

1-1-2014

Evaluation Of Nozzle Geometry On High Pressure Gasoline Direct Injection Spray Atomization

Mark Shost

Wayne State University,

Follow this and additional works at: http://digitalcommons.wayne.edu/oa_dissertations



Part of the [Mechanical Engineering Commons](#)

Recommended Citation

Shost, Mark, "Evaluation Of Nozzle Geometry On High Pressure Gasoline Direct Injection Spray Atomization" (2014). *Wayne State University Dissertations*. Paper 1102.

This Open Access Dissertation is brought to you for free and open access by DigitalCommons@WayneState. It has been accepted for inclusion in Wayne State University Dissertations by an authorized administrator of DigitalCommons@WayneState.

**EVALUATION OF NOZZLE GEOMETRY ON HIGH PRESSURE
GASOLINE DIRECT INJECTION SPRAY ATOMIZATION**

by

MARK ANTHONY SHOST

DISSERTATION

Submitted to the Graduate School

of Wayne State University,

Detroit, Michigan

in partial fulfillment of the requirements

for the degree of

DOCTOR OF PHILOSOPHY

2014

MAJOR: MECHANICAL ENGINEERING

Approved by:

Advisor

Date

© COPYRIGHT BY
MARK ANTHONY SHOST
2014
All Rights Reserved

DEDICATION

I dedicate my dissertation work to my family. First to my loving parents, John and Pauline Shost, who supported me in every pursuit in my youth, including disassembling, sandblasting, welding, and painting my first car in their garage, and who always promoted education as a worthy pursuit. To my sister Sharon and to my late brother John Shost Jr. who was my model for an engineer's inquisitive mind.

I also dedicate this work to my wife Denise, who has been my partner in this and every challenge of my life, always supportive and encouraging including encouraging finishing this dissertation a few times. To my daughter Jessica who shares my love of history and science and was born during my business school classes and twenty years later always knew a dad taking classes, and to my son Michael who shares my love of math and science. I hope to have passed to my children my parents' value of education and my love of learning and scientific research as part of a rewarding and happy life.

ACKNOWLEDGEMENTS

It was a tremendous experience to study under my thesis advisor, Professor Ming-Chia Lai at Wayne State University, over the past eight years, his support and encouragement and his recognized knowledge in the injector spray field was invaluable. I also recognize and appreciate the time and effort of my dissertation committee of Professor Singh and Professor Bryzik of the mechanical engineering department and especially recognize Associate Professor Lebieczik from the math department for joining my committee.

I want to express my gratitude to Delphi Powertrain management for their support, foremost Scott Bailey and Skip Wagner who sponsored my degree pursuit as well as engineering management Jim Zizelman and Walter Piock for supporting this work over the past four years and recognize injector team member Dan Varble for his efforts in coordinating hardware design and prototyping. I also recognize and thank Dr. Bizhan Befrui for his coordination of simulation & testing in Luxembourg. My discussions with Bizhan as the project and our learning progressed and his generous sharing of time and insights helped guide the overall success of the work.

TABLE OF CONTENTS

Dedication	ii
Acknowledgements	iii
List of Tables	vii
List of Figures	viii
Chapter 1 Background	1
1.1 Gasoline engine and fuel system evolution	1
1.2 Understanding of turbulence	8
1.3 Understanding of primary atomization.....	13
Chapter 2 Previously Related Researches.....	15
2.1 Blob or Stripping-Rate Model	15
2.2 Taylor Analogy Breakup (TAB) Model	18
2.3 Computational Fluid Dynamics (CFD) Models	21
2.3.1 Reynolds-Averaged Navier-Stokes Equations (RANS)	23
2.3.2 Large Eddy Simulation (LES)	33
2.3.3 Injector Nozzle Studies	39
Chapter 3 Objectives of the Study	42
Chapter 4 Outline of the Study Methodology	45
4.1 Defined Terms	45
4.2 Test Hardware	49
4.3 Test Equipment and Data Acquisition Systems	55

4.3.1 Shadowgraph Optical Imaging	55
4.3.2 High Speed Integral Mie Imaging.....	58
4.3.3 Laser Diffraction Technique	59
4.3.4 High Speed Near Nozzle Spray Imaging by Mie Scatter	62
4.3.5 Phase-contrast X-ray Imaging.....	63
4.4 Simulation and Modeling	65
4.4.1 Conservation Equations of Multi-Phase System.....	65
4.4.2 Large-Eddy-Simulation Method	66
4.4.3 VOF-Based Interface-Tracking Method	67
4.4.4 Vortex Identification Method	68
4.4.5 The Numerical Solution Method	69
4.4.6 Computational Domain and Mesh	70
4.4.7 Boundary Conditions	71
Chapter 5 Outline of the Results.....	73
5.1 Large Eddy Simulation of GDi Axis-symmetric single-hole Nozzles	73
5.1.1 Base Nozzle Geometry	74
5.1.2 Influence of Counterbore	81
5.1.3 Influence of Nozzle Taper	84
5.1.4 Influence of Nozzle l/d Ratio.....	87
5.1.5 Theoretical Jet Breakup Comparison.....	90

5.1.6 Summary/Conclusions	92
5.2 GDi Injector Spray Characterization	95
5.2.1 Prototype Injector Manufacture	95
5.2.2 Test Conditions	97
5.2.3 Injector Spray Characterization	98
5.2.4 Summary/Conclusion on Physical Test and Modified Project Scope Direction	111
5.3 GDi Skew-Angled Nozzle Flow and Near-Field Spray Analysis using Optical and X-ray Imaging and VOF-LES Computational Fluid Dynamics.....	113
5.3.1 Nozzle Geometry	113
5.3.2 Nozzle Geometry A, without Counterbore	114
5.3.3 Nozzle Geometry B, with Counterbore	120
5.3.4 Summary/Conclusions on Counterbore effect	132
5.4 GDi Nozzle Parameter Studies Using LES and Spray Imaging Methods.....	134
5.4.1 Nozzle Geometry A, $l/d = 1.1$	136
5.4.2 Nozzle Geometry C, $l/d = 0.55$	142
5.4.3 Summary/Conclusions on l/d and Pressure effects	148
Chapter 6 Summary	150
6.1 Summary of Conclusions	150
6.2 Recommendations for Future Work	153
Appendix A Prototype Injector Seat Drawing	154
Appendix B Injector Flow Rate	156

Appendix C Rochester Spray Lab Results.....	157
Appendix D Phase-contrast X-ray Images.....	178
Appendix E Shadowgraph Images.....	186
Appendix F Mie Scatter Images, Side View.....	219
Appendix G Mie Scatter Images, Bottom View	252
Appendix H Mie Scatter Images, Near-Field	262
Appendix I Phase-contrast X-ray Images	265
References	271
Abstract	279
Autobiographical Statement.....	280

LIST OF TABLES

Table 1 Overview of Primary Spray Characterization Variables	47
Table 2 Injector spray study prototype seat definition.....	52
Table 3 Injectors for Spray Characterization Luxembourg Spray Laboratory	54
Table 4 Turbulent Length Scales for 3-hole skew-angled nozzles	70
Table 5 CPU runtime for Flow Simulation of the 5M cell grid.....	71
Table 6 The base nozzle liquid jet non-dimensional parameters	90
Table 7 The base nozzle liquid jet atomization parameters, based on the jet linear stability / breakup theories	91
Table 8 Physical properties of the spray test liquids n-Heptane and Viscor-16B2	97
Table 9 Non-dimensional parameters for the spray shadow-imaging experiments.....	97
Table 10 Injector Spray Droplet size distribution measured at 50mm from nozzle tip.....	108
Table 11 Summary of key findings with index to VOF Figures and Spray Images Index.....	151

LIST OF FIGURES

Figure 1 Carburetor from 1 st generation of gasoline fuel systems.....	1
Figure 2 Multi-point Fuel Injector, MPFI, the 2 nd generation of gasoline fuel systems.....	3
Figure 3 Gasoline Direct Injection, GDi, the 3 rd generation of gasoline fuel systems	4
Figure 4 Gasoline Direct Injection System comprised of high-pressure pump, fuel rail, and side or center mount injector	5
Figure 5 Side-mount and Center-mount GDi systems.....	7
Figure 6 Studies of Water passing Obstacles and Falling, notes and drawings by Leonardo da Vinci (circa 1507)	8
Figure 7 Drawings from Reynolds' investigation of circumstances which determine whether the motion of water in parallel channels shall be direct or sinuous.....	10
Figure 8 Theory of Turbulent Cascades from Integral to Taylor to Kolmogorov scale	11
Figure 9 Droplet breakup regimes: Rayleigh, First wind-induced, Second wind-induced and Atomization	15
Figure 10 Reitz blob model showing Kelvin-Helmholtz instabilities on the liquid surface.....	15
Figure 11 O'Rourke's Taylor Analogy Breakup (TAB) model applies a spring-mass system to predict breakup.....	18
Figure 12 Combined model uses Blob method for primary atomization and TAB for secondary atomization	20
Figure 13 Graphic Representation of Solutions: DNS, LES, and RANS	23
Figure 14 Velocity decomposed into Average Velocity and Fluctuating Velocity	24
Figure 15 Field velocity profile for Laminar and Turbulent flows between plates	28
Figure 16 Turbulent energy across the length scale.....	30
Figure 17 Velocity decomposed into Large Scale and Small Scale components	33
Figure 18 Spectral Decomposition of Total Energy into Large Scale and Small Scale Components.....	34

Figure 19 Application of side-mount and central-mount GDi injectors	42
Figure 20 Visualization of spray plume targeting in side and central-mount GDi injectors	43
Figure 21 Definition of thru-hole, counterbore and skew angle geometry	44
Figure 22 Hexagonal Grid for Injector Pattern Determination	48
Figure 23 Determination of the SAE J2715 Spray Angle and Spray Bend Angle from a Digital Image of the Spray	48
Figure 24 Nomenclature for near-field Plume angle	48
Figure 25 Cross-section views of GDi injector and Seat Nozzle geometry	50
Figure 26 Definition of thru-hole, Counterbore and skew angle geometry	51
Figure 27 Tapered Nozzle definitions with common exit diameter	53
Figure 28 Test Configurations for Shadowgraph Optical Image Capture	56
Figure 29 Spray Image Capture definitions for Single Spray Plumes and Complete Sprays	57
Figure 30 Test Configurations for High Speed integral Mie Image Capture	58
Figure 32 Comparisons of Shadowgraph and High Speed Mie Imaging for Injector AK29-11-3-002	59
Figure 33 Particle Size Distribution determined using Laser Diffraction Technique	60
Figure 34 Test Configurations for Spray Particle Size Measurement	61
Figure 35 Test Configurations for High Speed Near Nozzle Spray Image Capture	62
Figure 36 Test Configurations for Phase-Contrast X-ray Image Capture	64
Figure 37 Computational domain, mesh, and boundaries	72
Figure 38 Case studies using axis-symmetric injector nozzles: Base Nozzle, Nozzle w/o Counterbore, Tapered Nozzle, and Long l/d Nozzle	73
Figure 39 Nozzle geometry and dimensional parameters	74
Figure 40 Iso-surface plots of VOF= 0.5, colored by instantaneous local velocity	75
Figure 41 VOF Contour plots on a cut-plane across the nozzle diameter	77

Figure 42 Stationary nozzle flow and liquid jet breakup structure (depicted by VOF =0.5 Iso- surface plots) at t=100,110,120 μ s after SOI.....	78
Figure 43 Stationary jet breakup structure (depicted by VOF iso-surface and contour plot) at t=110 μ s after SOI.....	78
Figure 44 Stationary jet breakup structure (depicted by VOF iso- surface and contour plots) at t=110 μ s after SOI.....	79
Figure 45 Stationary jet breakup structure (depicted by VOF =0.5 and Q =1.E+13 iso-surfaces) at t=110 μ s after SOI	80
Figure 46 Stationary jet breakup structure (depicted by VOF and Q iso-surfaces) at t=110 μ s after SOI.....	82
Figure 47 Comparison of jet breakup structure (depicted by VOF=0.5 and Q=1.E+13 iso- surfaces) for base nozzle with/without counterbore, at t=110 μ s after SOI.....	83
Figure 48 Stationary jet breakup structure for the tapered nozzle (depicted by the VOF=0.5 iso-surfaces and the VOF contour plot) at t=110 μ s after SOI	85
Figure 49 Comparison of jet breakup structures (depicted by the VOF =0.5 iso-surface, VOF contours, and the Q=1.E+13 iso- surface plots) for the base and tapered nozzles, at t=110 μ s after SOI.....	86
Figure 50 Stationary jet breakup structure for the large nozzle l/d (depicted by the VOF=0.5 iso-surfaces and the VOF contour plot) at t=110 μ s after SOI	88
Figure 51 Comparison of jet breakup structures (depicted by the VOF =0.5 iso-surface, VOF contours, and Q=1.E+13 iso- surface plot) for the base and large l/d nozzles, at t=110 μ s after SOI.....	89
Figure 52 Injector Seat Solid Model	95
Figure 53 Finished Prototype seat with grind	95
Figure 54 Silicone mold to reveal internal seat geometry	96
Figure 55 Prototype Cylindrical and Tapered thru-hole	97
Figure 56 Injector Test Request, for Hexcell Patternation, Backlight Imaging, and Laser drop size profile.....	99
Figure 57 Spray Plume Characterization using Hexcell Patternator, S/N AK29-07-001	100
Figure 58 Shadowgraph Image at 0° and 90° for 3-hole seat injector.....	101

Figure 59 Phase-Contrast X-ray images revealing turbulent structure	102
Figure 60 Spray Penetration after injection 0°, 90° at 10 and 20MPa calculated from Shadowgraph Images	104
Figure 61 Spray Penetration after injection 0°, 90° at 10 and 20MPa calculated from Mie Scatter Images	105
Figure 62 Spray Angle after injection 0°, 90° at 10 and 20MPa calculated from Shadowgraph Images	105
Figure 63 Spray Angle after injection 0°, 90° at 10 and 20MPa calculated from Mie Scatter Images	106
Figure 64 Spray Penetration after injection 0°, 90° at 10 and 20MPa calculated from Shadowgraph Images, 3-hole	106
Figure 65 Spray penetration after injection at 10 and 20MPa calculated from Mie Scatter Images, 3-hole	107
Figure 66 Spray angle after injection at 10 and 20MPa calculated from Shadowgraph Images, 3-hole	107
Figure 67 Spray angle after injection at 10 and 20MPa calculated from Mie Scatter Images, 3-hole	108
Figure 68 Spray Droplet size distributions for single and 3-hole injectors	109
Figure 69 Spray Droplet size distributions single nozzle, $d \approx .20$ & $d \approx .15$, at 10 and 20MPa, and 3-hole nozzle, $l/d=1.1$ & $l/d=3.96$, at 10 and 20MPa	109
Figure 70 Spray Droplet size effect of Counterbore	110
Figure 71 Spray Droplet size effect of Skew angle at 10, 20MPa	110
Figure 72 Shadowgraphic Spray Images for axis-symmetric, skewed angled and 3-hole seats.	111
Figure 73 Patternization tests for 10°, 20°, and 30° skew angle seats	112
Figure 74 Geometry of the GDi 3-hole seat and nozzles	113
Figure 75 Nozzle Geometry A and B with associated dimensional parameters	114
Figure 76 Shadowgraph imaging of the nozzle near-field spray plume (fuel pressure= 10MPa, t=time ASIE)	115

Figure 77 Nozzle near-field plume structure, primary breakup and atomization (fuel pressure=10MPa, t=470 μ s ASIE)	116
Figure 78 Spray plume shot-to-shot variation and statistical PDF (liquid-phase probability density function) (fuel pressure =10MPa, t =700 μ s ASIE)	117
Figure 79 Nozzle A X-ray phase-contrast imaging (fuel pressure=10MPa, t=time ASIE)	119
Figure 80 Shadowgraph imaging of the nozzle near-field spray plume (fuel pressure=10MPa, t=time ASIE)	120
Figure 81 Nozzle near-field plume structure, primary breakup, and atomization (fuel pressure=10MPa, t=470 μ s ASIE)	121
Figure 82 Spray plume shot-to-shot variation and statistical PDF (liquid –phase probability density function) fuel pressure=10MPa, t =700 μ s ASIE	122
Figure 83 Nozzle B X-ray imaging of the nozzle near-field spray plume (fuel pressure=10MPa, t=time ASIE)	123
Figure 84 Iso-surface plots of VOF= 0.5, colored by the instantaneous local velocity magnitude, at selected times ASOS	124
Figure 85 VOF Contour plots on the nozzle symmetry plane, at selected times ASOS.....	124
Figure 86 VOF Contour plots on planes normal to nozzle axis, in nozzle hole and at locations z=0 and 5*d (t = ASOS)	125
Figure 87 Flow stream-lines colored by local instantaneous velocity (t= 60 μ s ASOS).....	126
Figure 88 Iso-surface plots of Q=5E12, 1E13, and 5E13 (colored by the instantaneous local velocity magnitude) at t=60 μ s ASOS	127
Figure 89 Iso-surface plots of VOF= 0.5, colored by instantaneous local velocity, at selected times ASOS.....	128
Figure 90 VOF Contour plots on the nozzle symmetry plane, at selected times ASOS.....	128
Figure 91 VOF Contour plots on planes normal to nozzle axis, within the nozzle-hole, counterbore, and location z = 5*d downstream of injector (t=ASOS)	129
Figure 92 Iso-surface plots of Q=5E12, 1E13, and 5E13 (colored by the instantaneous local velocity magnitude) at t=60 μ s ASOS	129

Figure 93 Nozzle A - Comparison of the plume images (at $t=700\mu\text{s}$ ASIE) and VOF-LES simulations (at $t=60\mu\text{s}$ ASOS) of the instantaneous plume near-field breakup structure.....	130
Figure 94 Geometry of the GDi 3-hole seat and nozzle	134
Figure 95 Nozzle Geometry A and C with associated dimensional parameters.....	135
Figure 96 Spray velocity and VOF for Nozzle A at 10MPa at 10, 20, and $60\mu\text{s}$	136
Figure 97 Particle Streamlines for Nozzle A	137
Figure 98 Spray for Nozzle A at 5, 10, & 20MPa at 20, 60 at time = $140\mu\text{s}$, grid is 2 x 2mm..	138
Figure 99 Spray plume statistical PDF (liquid phase probability density function) based on 5 injections for Nozzle A, $l/d=1.1$, Fuel Pressure = 10MPa, time = $700\mu\text{s}$	139
Figure 100 Spray plume statistical PDF versus injection pressure for Nozzle A, $l/d=1.1$, time = $700\mu\text{s}$	140
Figure 101 Spray plume statistical PDF compared to LES modeled spray plume for Nozzle A, $l/d=1.1$, Fuel Pressure =10MPa, time = $700\mu\text{s}$ image, $60\mu\text{s}$ simulation..	140
Figure 102 Spray plume X-ray optical imaging for varying injection pressure Nozzle A, $l/d = 1.1$, time = $60\mu\text{s}$	141
Figure 103 Spray velocity and VOF for Nozzle C at 10MPa at 10, 20, and $60\mu\text{s}$	142
Figure 104 Particle Streamlines for Nozzle C	143
Figure 105 Spray Shadowgraph for Nozzle C at 5, 10, & 20MPa at 20, 60 & $140\mu\text{s}$	144
Figure 106 Spray plume statistical PDF compared to LES modeled spray plume for Nozzle C, $l/d=0.55$, Fuel Pressure =10MPa, time = $740\mu\text{s}$ image, $60\mu\text{s}$ simulation	145
Figure 107 Spray plume statistical PDF (liquid phase density function) compared to LES modeled spray plume for Nozzle C, $l/d=0.55$, Fuel Pressure=20MPa, time= $740\mu\text{s}$ image, $60\mu\text{s}$ simulation	146
Figure 108 Spray plume statistical PDF (liquid phase probability density function) versus injection pressure for Nozzle C, $l/d=0.55$, time = $740\mu\text{s}$	147
Figure 109 Spray plume X-ray optical imaging for varying injection pressure Nozzle A, $l/d = 0.55$, time = $70\mu\text{s}$	147

CHAPTER 1 BACKGROUND

1.1 Gasoline engine and fuel system evolution

The gasoline-fueled spark-ignited internal combustion engine has long dominated as the powertrain of choice for passenger car and light duty truck applications. Over history, fuel systems have gone through three major technological changes starting with mechanical carburetion transitioning to electronic port fuel injection and recently to today's high-pressure

Mechanical Carburetor

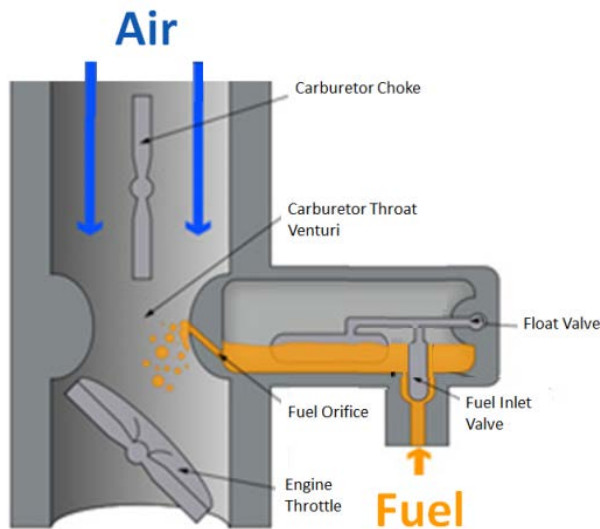


Figure 1 Carburetor from 1st generation of gasoline fuel systems

direct fuel injection. Early applications, dating back to Karl Benz, Gottlieb Daimler, and Henry Ford's model T, utilized carburetors, like shown in Figure 1, to meter fuel with intake air. Carburetors work on the Bernoulli principle by funneling air through a venturi whose restriction increases the air velocity while decreasing its static pressure. The resulting reduction in static pressure provides the opportunity to introduce gasoline at a low

pressure port. Fuel is then metered into the air stream as a function of vacuum, which itself is a function of mass airflow. This effect maintains a relatively constant air to fuel ratio across the varying mass airflows required for engine operation. To vary the airflow, a throttle valve is connected by linkage to the driver's pedal for engine load demand control, and the proper targeted fueling mix is controlled by the carburetor design. The desired air to fuel mixture varies slightly based on engine operating conditions, but is targeted around the stoichiometric air/fuel

ratio of 14.7/1 where the combustion reaction in the engine will fully consume the gasoline reagent with the air oxidizer. To provide the best vehicle drivability, carburetors evolved with additional mechanisms to vary the air/fuel ratio based on conditions. For example, when the driver wants more power to the wheels, he depresses the pedal or “tips-in” to the throttle. To adjust more quickly to the increased air-flow, accelerator pumps were added to the carburetor to add extra fuel for tip-in conditions so no lag would be experienced by the driver as the fuel would adjust to the increased air-flow condition. Likewise, to aid in start-up an additional function was added, called a “choke”, to limit airflow in the carburetor throat, thus providing a lower air to fuel ratio thereby operating more rich to aid in initial engine firing, especially at cold temperatures. In the 1970’s, internal combustion engines further developed to improve the exhaust emission characteristics. A phenomenon called “smog” was being experienced, especially prevalent in cities like Los Angeles where air inversion caused by mountains produced an unhealthy haze. Early research identified incomplete combustion of gasoline fuel, resulting in high levels of hydrocarbon and carbon monoxide, to be a main cause. Automakers solved this problem with the adoption of engine after-treatment devices called catalytic converters. In 1974, General Motors introduced oxidation catalysts, which promoted the complete oxidation of engine out hydrocarbons and the conversion of carbon monoxide to carbon dioxide. Within a few years, reduction catalysts were also added to the engine aftertreatment to reduce the oxides of nitrogen (NO_x), the ozone affecting gas. This culminated in the invention of the three-way catalyst, which provided both the oxidation function for hydrocarbons and the reduction of NO_x . The three-way catalyst was a major breakthrough in providing the clean emission operation of gasoline engines. The caveat to maintain optimum performance with the three-way catalysts is precise control of the air-fuel mixture around the stoichiometric point. To aid in this control, a

closed-loop feedback was added to the engine management system with the adoption of an exhaust oxygen sensor. Oxygen sensors located in the engine exhaust stream measure the partial pressure of oxygen in the exhaust gas. The presence of oxygen, or lean operation, indicates more fuel is necessary to reach stoichiometric operation. The absence of oxygen means the engine is operating at the stoichiometric point or in a rich regime with excess fuel. The engine management system adjusts the fueling command based on the output of the switching-style oxygen sensor around the switching voltage, which indicates the stoichiometric combustion desired for efficient catalytic converter operation. These demands for more precise fueling that could be dynamically adjusted led to “electronic” carburetors, but cost and complexity soon gave way to the next era in fuel control, the electronic fuel injector in the 1980s. Fuel injectors have the advantage of not relying on the air flow to set the fuel flow, instead using the engine control module to operate an electric solenoid to open a fuel flow orifice. With the adoption of fuel injection, engine management systems could now provide any fuel flow desired for engine operation based on vehicle

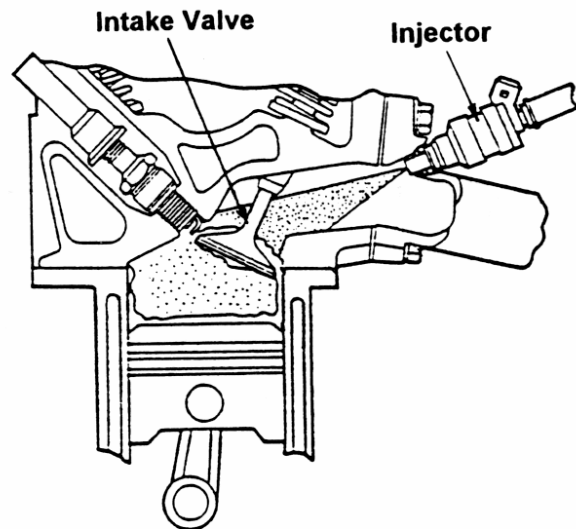


Figure 2 Multi-point Fuel Injector, MPFI, the 2nd generation of gasoline fuel systems

drivability, performance, or exhaust emission after-treat requirements. Early systems were either throttle body injection, which maintained a central injector for the entire engine, or multi-point injection where individual injectors are located closer to the intake port of each cylinder. This multi-point fuel injection (MPFI) scheme, as shown in Figure 2, became the norm in the 1990's. Since its introduction, MPFI development focused on improved atomization of the fuel to

promote air and fuel mixing for enhanced combustion and emission characteristics. Generally, the quest for smaller fuel droplet sizes drove the desire for higher fuel pressures or reduced fuel orifice diameters achieved by additional director plate holes for the given fuel flow rate. Injector targeting was also improved to avoid fuel impinging on surfaces, however, the fueling operated as closed-intake valve injection, and as such, still relied on the vacuum caused by the piston motion to pull the air and fuel mixture into the cylinder during the intake stroke for naturally aspirated engines. The pursuit of improved fuel economy driven by consumer's reaction to higher fuel prices, Corporate Average Fuel Economy, CAFE, regulations in the US, and CO₂

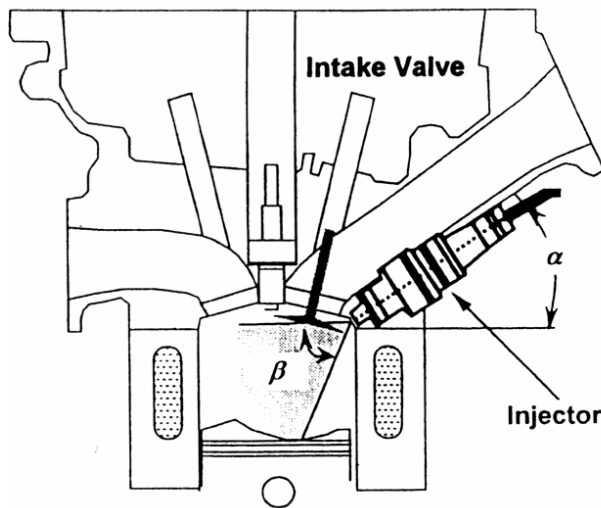


Figure 3 Gasoline Direct Injection, GDi, the 3rd generation of gasoline fuel systems

regulations in Europe drove automakers to search for alternatives to the naturally aspirated MPFI gasoline engine. The 1990s saw a large penetration of turbocharged direct-injected common rail diesel engines in Europe. The new common rail injection technology provided for split injection, which dramatically improved the Noise, Vibration, and Harshness (NVH) characteristics of the

diesel powertrain, and combined with turbocharging, provided the vehicle excellent drivability due to the high cylinder pressures achievable, hence high levels of engine torque. However, diesel engines still suffered somewhat compared to gasoline engines for noise, vibration, and harshness, and since diesel combustion has excess air, exhaust aftertreatment is more costly as

three way catalysts cannot be applied. An alternative technology, Gasoline Direct Injection (GDi), shown in Figure 3, was introduced by Mitsubishi in 1996 where the fuel injection point moved from the intake port to the combustion chamber. This direct means of injection improves volumetric efficiency since the intake port and gas exchange process only has to transfer air to the combustion chamber. Another benefit of direct injection into the chamber is the charge



Figure 4 Gasoline Direct Injection System comprised of high-pressure pump, fuel rail, and side or center mount injector

cooling effect due to fuel evaporation that acts to boost the effective engine knock tolerance. Lastly, direct injection decoupled the timing of the fuel injection from the intake valve timing. This permits techniques, like demonstrated in diesel engines, where multiple injections could be provided, even during the compression stroke when the intake valve is closed, to affect combustion. In order to achieve proper atomization of the fuel, direct injection requires that the injection pressures are raised to 100 bar, 1,450 PSI, and above. This represents a 30 fold increase over port fuel injectors, but still 1/10 of the pressures utilized by diesel injectors. To

produce and accommodate the higher pressures, a high pressure pump, typically cam lobe driven, and strengthened fuel lines and rails are adopted in GDi systems, as shown in Figure 4. GDi technology is also well suited for use in combination with turbocharging since cylinder

scavenging could be increased without a hydrocarbon issue and much higher levels of cylinder pressure achieved. This allows smaller engines to provide the maximum Brake Mean Effective Pressure, BMEP, or torque of larger engines when power is demanded, while maintaining the fuel saving characteristics of a smaller engine for lower demand driving. The charge cooling effect of direct injection also works well with turbocharging where engine knock limits spark advance for fuel efficiency or boost levels for power. Therefore, this technology employed with down-sizing of engine displacement, can realize fuel economy gains of 12% as demonstrated by Ford's roll-out of their "EcoBoost" Powertrain brand in a 3.5L V6 [1]. A trend starting in Europe currently is the development of 3-cylinder turbocharged GDi engines to replace the turbo-diesel powertrains, while offering similar low fuel consumption and good low-end torque characteristics, but without the need for costly exhaust after-treatment for NO_x and particulate matter. The new Turbocharged GDi engine technology using the down sized and down speeded concept is more costly than the MPFI technology it replaces due to the higher pressure fuel system and turbocharger additions, but is still significantly cheaper than the diesel alternative. The GDi engine has higher injection and cylinder pressures, and can provide additional vehicle packaging advantages since no complex diesel aftertreatment is required.

Vehicle segments with the most cost sensitivity, like compacts under 1,400 kilograms, are expected to adopt Turbocharged GDi Powertrains to meet the CO₂ challenge, while maintaining an attractive customer offering [2]. This



work will focus on the spray Figure 5 Side-mount and Center-mount GDi systems

characteristics of GDi injectors that are the foundation for achieving the combustion required to meet the demands on modern gasoline engines. GDi systems are configured either as side-mount, where the injector is located below the intake port, or as has been the industry trend, central-mount, where the injector is located in the center of the combustion chamber near the spark plug location, as shown on the right in Figure 5. The trend to center-mount is due to the fuel/air mixing advantages the location can provide, especially important for any lean operation where air/fuel mixture concentrations near the spark electrode are critical for reliable ignition and flame front propagation of the combustion system. Although the center-mount location requires a longer injector than side mount, as shown in Figure 4, the valve group's seat and nozzle geometry are similar, but require adjustments to spray plume targeting to match the application combustion chamber.

1.2 Understanding of turbulence

Given the dominant influence of fuel atomization and mixing on engine performance and emissions, it is expected that this physical mechanism has been well-studied. In fact, observations on fluid turbulence and flow of liquid jets date back more than 500 years to Leonardo da Vinci's studies of water and blood flow in an effort to determine the underlying physical laws, see Figure 6. Leonardo da Vinci in 1507 named the phenomenon he observed in swirling flow “la turbolenza” and described the following:

“Observe the motion of the surface of the water, which resembles that of hair, which has two motions, of which one is caused by the weight of the hair, the other by the direction of the curls; thus the water has eddying motions, one part of which is due to the principal current, the other to random and reverse motion.”

Formal definitions of turbulence are surprisingly difficult for a readily observable natural phenomenon, but da Vinci noted two key characteristics the curls or eddies form,

they have the velocity components of the main current and another component to a random motion. Although a concise definition is elusive, most researchers note the characteristics of



Figure 6 Studies of Water passing Obstacles and Falling, notes and drawings by Leonardo da Vinci (circa 1507)

turbulent flow, Bakker [3] does a comprehensive list as follows:

- One characteristic of turbulent flows is their irregularity or randomness. A full deterministic approach is very difficult. Turbulent flows are usually described statistically. Turbulent flows are always chaotic, but not all chaotic flows are turbulent.
- The diffusivity of turbulence causes rapid mixing and increased rates of momentum, heat, and mass transfer. A flow that looks random, but does not exhibit the spreading of velocity fluctuations through the surrounding fluid is not turbulent. If a flow is chaotic, but not diffusive, it is not turbulent. The trail left behind a jet plane that seems chaotic, but does not diffuse for miles is then not turbulent.
- Turbulent flows always occur at high Reynolds numbers. They are caused by the complex interaction between the viscous terms and the inertia terms in the momentum equations.
- Turbulent flows are rotational; that is, they have non-zero vorticity. Mechanisms such as the stretching of three-dimensional vortices play a key role in turbulence.
- Turbulent flows are dissipative. Kinetic energy gets converted into heat due to viscous shear stresses. Turbulent flows die out quickly when no energy is supplied. Random motions that have insignificant viscous losses, such as random sound waves, are not turbulent.
- Turbulence is a continuum phenomenon. Even the smallest eddies are significantly larger than the molecular scales. Turbulence is therefore governed by the equations of fluid mechanics.
- Turbulence is a feature of fluid flow, not of the fluid. When the Reynolds number is high enough, most of the dynamics of turbulence are the same whether the fluid is an actual fluid or a gas. Most of the dynamics are then independent of the properties of the fluid.

Osborne Reynolds (1883) was the first to systematically investigate the transition from laminar to turbulent flow in pipes by injecting a dye streak into flow through a pipe having smooth transparent walls [4]. His observations led to identification of a single dimensionless parameter representing the ratio of fluid inertial forces to viscous forces, now known as the Reynolds number.

$$Re = \frac{\rho UL}{\mu} \quad \text{where } \begin{array}{l} \rho = \text{density, } \mu = \text{kinematic viscosity} \\ U = \text{velocity, } L = \text{length scale} \end{array}$$

His experiments showed that the distinction between laminar and turbulent flow depended on a relationship between the dimensions of space and velocity, see Figure 7. Reynolds determined the transition to turbulent flow inside a pipe occurred when the Reynolds number exceeded a certain range ($2,000 \leq Re \leq 2,300$). Reynolds also noted that the transition from the streamline (laminar) flow to the sinuous (turbulent) flow was quite abrupt. Reynolds went on to decompose the velocities of turbulent flow in terms of

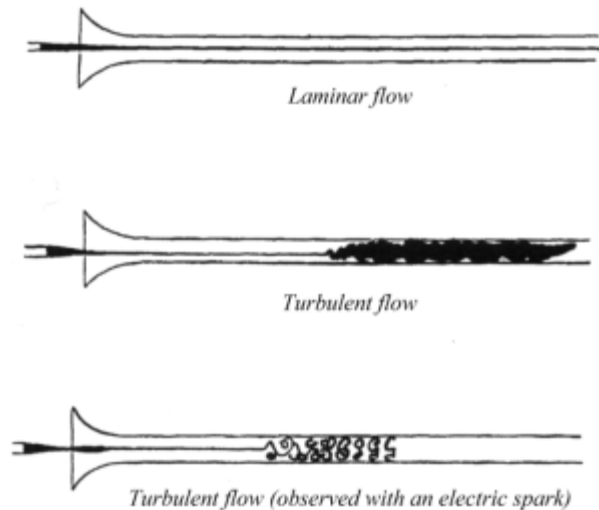


Figure 7 Drawings from Reynolds' investigation of circumstances which determine whether the motion of water in parallel channels shall be direct or sinuous

components representing its mean and eddying parts, a concept that will serve as the core for future fluid dynamic modeling.

The study of turbulence is of primary interest in several scientific fields, one of which is meteorology. In 1922 Lewis Richardson, an English mathematician, developed a novel method of weather forecasting by solution of differential equations [5]. Richardson laid out a method where discrete calculations would be performed in subsections based on local instantaneous data. Calculations of the subsections were used by surrounding subsections and all activity was coordinated by a supervisor to maintain the timing of all calculations. The described method, predating computing machines, represented well the method of turbulent flow modeling, using finite differences, which would be made practical with the advent of modern computers. Richardson is best remembered for his rhyme in this work to describe the turbulent cascade.

“When making a drawing of a rising cumulus from a fixed point; the details change before the sketch can be completed.’

We realize thus that:

Big whirls have little whirls
Which feed on their velocity;
And little whirls have lesser whirls,
And so on to viscosity
in the molecular sense.”

The concept of turbulent energy and its transition from large eddies to smaller eddies, the turbulent cascade, represent another key concept for representing turbulent flow in fluid models.

Russian mathematician Andrei Nikolaevich Kolmogorov in 1941 proposed a mathematical theory for Turbulent Cascades, see Figure 8, defining a mechanism to calculate turbulent scales for length, velocity, and time [6]. His theory is based on the premise that the unstable large eddies breakup and transfer energy to smaller eddies, which in turn breakup and transfer to even smaller eddies. This cascading of energy continues until a small enough scale is reached where the eddy motion is stable and viscous dissipation converts the kinetic

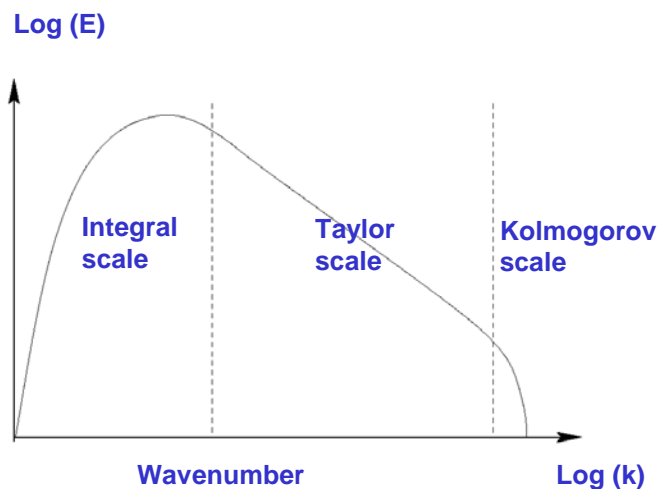


Figure 8 Theory of Turbulent Cascades from Integral to Taylor to Kolmogorov scale

energy into thermal energy. Turbulent Cascade theory requires the energy transfer is in only one direction from large eddies to smaller eddies. Although evidence exists to show smaller eddies

can interact to form larger eddies, a process known as backscatter, the forward progression from large to small energy cascade accounts for the vast majority of energy transfer. Kolmogorov noted that no closed mathematical solution would exist, but that a method involving random functions of several variables would be needed to match the irregularities seen in experimental data.

1.3 Understanding of primary atomization

Qualitative study of jets and their breakup dates back to Savart in 1833 noting that liquid atomization drops come from the rupture of objects having the form of threads or ligaments, where the liquid jet eventually ends in a train of droplets. In 1873, Plateau explained why the initial jet state is unstable, thus recognizing the crucial role of surface tension in the breakup phenomena. The liquid jet is unstable to any perturbation that reduces its surface area. This can be visualized as drops form from a slow flowing sink faucet stream. As the liquid column velocity is reduced, the liquid inertial and surface tension forces converge in magnitude. Drops are formed as the surface tension tries to minimize the surface area of the liquid mass, the liquid column narrows and subsequently “pinches-off” the spherical drop. Plateau showed the perturbations were unstable if their wavelength exceeded $\lambda_{\text{critical}} / \text{nozzle radius} = 2\pi \approx 6.28$. Lord Rayleigh (1879) applying acoustic excitation to the jet, found among all the unstable wavelengths the one with the fastest growth rate will dominate and determined:

$$\lambda_{\text{optimal}} = 9.01 * \text{nozzle radius}$$

Further, he described the theory of linear stability analysis of a liquid jet using these physical relationships. Wolfgang von Ohnesorge completed a PhD thesis “Application of a cinematographic high frequency apparatus with mechanical control of exposure for photographing the formation of drops and the breakup of liquid jets” in 1937. This work was instrumental in documenting the jet breakup phenomena with high temporal resolution. Ohnesorge varied the fluid properties experimentally using water, aniline, glycerin, and two hydrocarbon fuels in his study. From his work he noted four distinct breakup regimes:

- I. Slow dripping from the nozzle under gravity with no jet formation
- II. Breakup of a cylindrical jet by axisymmetric perturbations, according to Rayleigh

- III. Breakup by screw-like perturbations of the jet, according to Weber-Haenlein
- IV. Atomization of the jet

A review of dimensional analysis evaluating the relative contributions of fluid viscosity, inertia, surface tension, and nozzle diameter led to a new dimensionless parameter to clearly define the four breakup regimes now referred to as the Ohnesorge number:

$$Oh = \frac{\mu}{\sqrt{\rho\sigma d}} \text{ where } \begin{matrix} \mu=\text{viscosity}, & \rho=\text{density} \\ \sigma=\text{surface tension}, & d=\text{nozzle diameter} \end{matrix}$$

$$Oh = \frac{\sqrt{We}}{Re} \text{ where } \begin{matrix} We=\text{Weber number} \\ Re=\text{Reynolds number} \end{matrix}$$

CHAPTER 2 PREVIOUSLY RELATED RESEARCHES

2.1 Blob or Stripping-Rate Model

In many applications, such as ink jet printing, powder metallurgy, or fuel spray considered here, it is sometimes advantageous to hasten breakup, for fuel spray plumes to avoid liquid impingement on a surface like the cylinder wall or piston. While other times it is desirable to suppress the jet breakup mechanism, for instance, in fuel spray to target air/fuel mixture in a specific region of the combustion chamber. Therefore, a rigorous

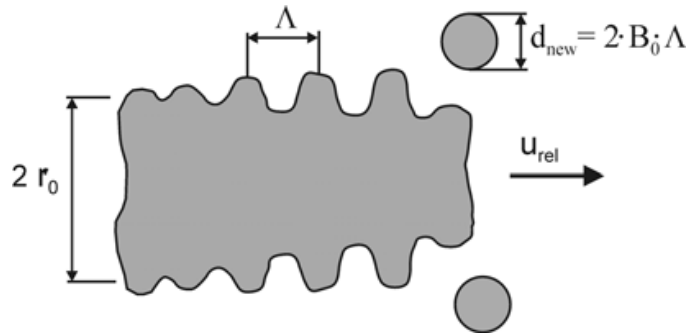


Figure 10 Reitz blob model showing Kelvin-Helmholtz instabilities on the liquid surface

understanding of the mechanism and the ability to model or predict atomization is desired. Since the combustion efficiency and exhaust particle emissions are dominated by the effectiveness of atomization, an understanding of the nozzle design parameters on the spray plume and the resulting particle size and distribution is desired. The classic Kelvin-Helmholtz instability model by Reitz, [7] [8] [9] still cited today, also known as the blob or stripping rate model, shown in

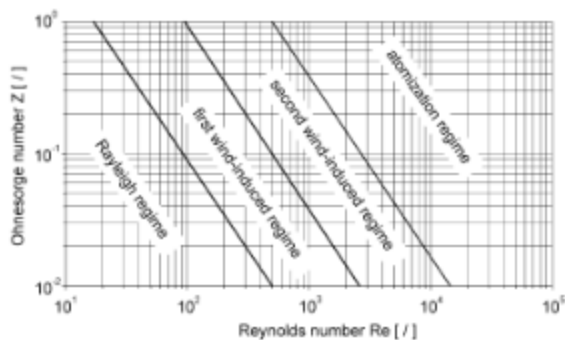


Figure 9 Droplet breakup regimes: Rayleigh, First wind-induced, Second wind-induced and Atomization

Figure 9, used viscosity, surface tension, and aerodynamic forces to predict the primary atomization. Reitz defined the jet breakup in four main regimes, as shown in Figure 10, and provided equations to predict the maximum growth wavelength and jet breakup length based on different

combinations of liquid inertia, surface tension, and aerodynamic forces acting on the jet. The Rayleigh breakup regime, dominated by growth of capillary waves along the jet surface, is characterized by drops larger than nozzle diameter initiating many nozzle diameters downstream. As velocity increases, interaction with aerodynamic forces yields the first wind-induced regime with drops on the order of the nozzle diameter with breakup occurring earlier, but still many nozzle diameters downstream. As velocity increases still further, the breakup shifts to the breakup characteristic of the second wind-induced regime with drops smaller than nozzle diameter, starting some nozzle diameters downstream. Finally, highest velocity jets operate in the Atomization Regime with droplets much smaller than nozzle diameter starting at the nozzle exit. Reitz also derived empirical relations for the jet-interface maximum growth-rate wave and its wave-length, based on the round-jet linear stability analysis:

$$\frac{\Lambda}{a} = 9.02 \frac{(1. + 0.45Z^{0.5})(1. + 0.4T^{0.7})}{(1. + 0.87We_{gas}^{1.67})^{0.6}}$$

$$\Omega \left[\frac{\rho_{liquid} a^3}{\sigma} \right]^{0.5} = \frac{(0.34 + 0.38We_{gas}^{1.5})}{(1. + Z)(1. + 1.4T^{0.6})}$$

With the dimensionless parameters defined as:

$$Z = \frac{\sqrt{We_{liquid}}}{Re_{liquid}}, \quad T = Z\sqrt{We_{air}}, \quad We_{air} = \frac{\rho_{air} a}{\sigma}, \quad Re_{liquid} = \frac{Ua}{\nu_{liquid}}$$

Where U is the liquid jet relative velocity and $a(= 0.5d)$ is the jet radius.

The relations the round jet breakup length (in a quiescent ambient) L/a are derived from the Taylor's analysis of high-speed liquid jet breakup, as:

$$\frac{L}{a} = \frac{B \sqrt{\frac{\rho_{liquid}}{\rho_{gas}}}}{f(T)}$$

With the parameter $B = 4.04$, recommended for typical diesel spray nozzles.

The Taylor's parameter T and $f(T)$ defined as:

$$T = \left(\frac{\rho_{liquid}}{\rho_{gas}} \right) \left(\frac{Re_{liquid}}{We_{liquid}} \right)^2$$

$$f(T) = \frac{\sqrt{3}}{6} [1 - e^{-10T}]$$

Reitz and other researchers showed these relationships correlated well to diesel sprays under study. It is not clear if they would expect to translate well to the GDi injector with a factor lower pressure, since there is no explicit account for internal jet turbulence, vortices, or cavitation, but rather semi-empirical coefficients. Investigation in this work will evaluate predicted breakup length and droplet size as well as calculate indicated coefficients based physical spray experimental results.

2.2 Taylor Analogy Breakup (TAB) Model

A second major development in jet modeling was the Taylor Analogy Breakup (TAB) model proposed by O'Rourke [10]. The analogy suggested originally by Taylor was between an oscillating and distorting droplet and a spring mass system where the restoring force is the surface tension force and the external force is the aerodynamic force, as depicted in Figure 11.

This method seems intuitively well suited to secondary breakup where larger droplets or ligaments are breaking to form smaller particles.

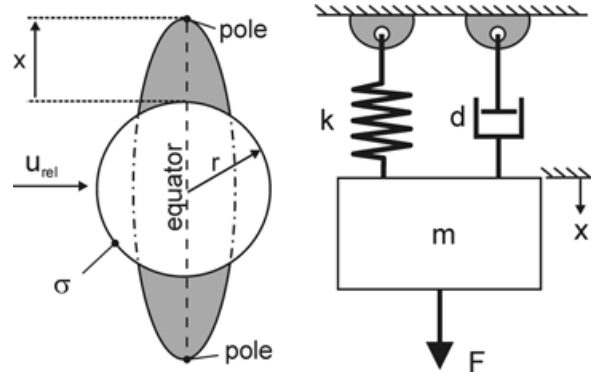


Figure 11 O'Rourke's Taylor Analogy Breakup (TAB) model applies a spring-mass system to predict breakup

This provides several advantages over Reitz's KH Instability model. First, there is not one unique critical Weber number for breakup, which is consistent with experimental evidence. Second, liquid viscosity effects are included, which can significantly affect the oscillations of small drops. Third, the model predicts the droplet state of oscillation and distortion, which can be used in calculation of exchange rates for mass, momentum, and energy between the droplet and the gas. Fourth, the model has shown better correlation with experimental data for drop size and spray angle. The model is based on the equation of a damped, forced harmonic oscillator:

$$m\ddot{x} = F - kx - d\dot{x} \quad \text{where} \quad \begin{array}{l} m = \text{drop mass, } F = \text{aerodynamic force} \\ kx = \text{restoring surface tension force, } d\dot{x} = \text{liquid viscous damping force} \end{array}$$

$$\frac{F}{m} = C_F \frac{\rho_g W^2}{\rho_l r_p}, \quad \frac{k}{m} = C_k \frac{\sigma}{\rho_l r_p^3}, \quad \frac{d}{m} = C_d \frac{\mu_l}{\rho_l r_p^2}$$

We assume the drop breakup only occurs if $x > C_b r$ and then nondimensionalize by setting $y = x/C_b r$ gives:

$$\ddot{y} = \frac{C_F}{C_b} \frac{\rho_g}{\rho_l} \frac{U^2}{r_p^2} - C_k \frac{\sigma}{\rho_l r_p^3} y - C_d \frac{\mu_l}{\rho_l r_p^2} \dot{y} \quad \text{This linear, nonhomogeneous, second-order}$$

differential equation has an exact solution

$$y(t) = \frac{C_F}{C_k C_b} We + e^{-t/t_d} \left[\left(y_0 - \frac{C_F}{C_k C_b} We \right) \cos \omega t + \frac{1}{\omega} \left(\dot{y}_0 + \frac{y_0 - \frac{C_F}{C_k C_b} We}{t_d} \right) \sin \omega t \right]$$

$$\text{Where } We = \frac{\rho_g U^2 r_p}{\sigma}, \quad \frac{1}{t_d} = \frac{C_d}{2} \frac{\mu_l}{\rho_l r_p^2}, \quad \omega^2 = C_k \frac{\sigma}{\rho_l r_p^3} - \frac{1}{t_d^2}, \quad y_0 = y(0), \quad \dot{y}_0 = \frac{dy}{dt}(0)$$

Experimental data suggests $C_F = \frac{1}{3}, C_b = \frac{1}{2}, C_k = 8, C_d = 5, t_d = \infty, y_0 = \dot{y}_0 = 0$

Substituting into $y(t)$ and solving for Weber Number critical for breakup $We_{crit} \approx 6$

The breakup time is defined when Weber Number is close to its critical value as:

$$t_{bu} = U \sqrt{\frac{\rho_l r^3}{8\sigma}} \quad \text{where } We \approx We_{crit} \quad \text{and Drop normal velocity } \dot{y} \approx \frac{C_F}{C_k C_b} We \omega^2 t_{bu}$$

Spray angle θ can be found as $\tan \frac{\theta}{2} = C_v \frac{\sqrt{3}}{3} \sqrt{\frac{\rho_g}{\rho_l}}$ the experimental result was found as

$$\tan \frac{\theta}{2} = \frac{\sqrt{3}}{3} \frac{2U}{3 + \frac{L/d}{3.6}} \sqrt{\frac{\rho_g}{\rho_l}} \quad \text{these agree when } C_v = 1, \text{ hole length to diameter } L/d = 11.8 \text{ to}$$

predict the drop size, the energy of the parent drop, the sum of its minimum surface energy, and the oscillation and distortion energy:

$$E_{surf} = (4\pi r^2 \sigma)$$

$$E_{osc} = K \frac{4\pi}{5} \rho_l r_p^3 (\dot{x} + \omega^2 x^2) = K \frac{\pi}{5} \rho_l r_p^5 (\dot{y}^2 + \omega^2 y^2)$$

$E_{parent} = E_{surf} + E_{osc} = (4\pi r^2 \sigma) + K \frac{\pi}{5} \rho_l r_p^5 (\dot{y}^2 + \omega^2 y^2)$ After breakup, assuming the product drops are not oscillating, the energy becomes the sum of the minimum surface energy and the kinetic energy of the product drops.

$E_{product} = 4\pi r^2 \sigma \frac{r}{r_{32}} + \frac{U}{6} r^5 \rho_l \dot{y}^2$ Where r_{32} is the Sauter-Mean Radius (SMR) after secondary atomization, equating energy of parent to energy of product and rearranging we get:

$$r_{32} = \frac{4\pi r^3 \sigma}{E_{parent} - \frac{\pi}{6} r^5 \rho_l \dot{y}^2}$$

Another approach is a combined model, as depicted in Figure 12, where near-field primary breakup is modeled using the Blob method and TAB is utilized for secondary atomization.

These works are still phenomenological based on certain relevant conditions and not broad general solutions to the fluid dynamics of interest. The difficulty in a robust solution to the primary jet atomization problem is the competition of forces acting on the jet surface between cohesive and disruptive forces. It is

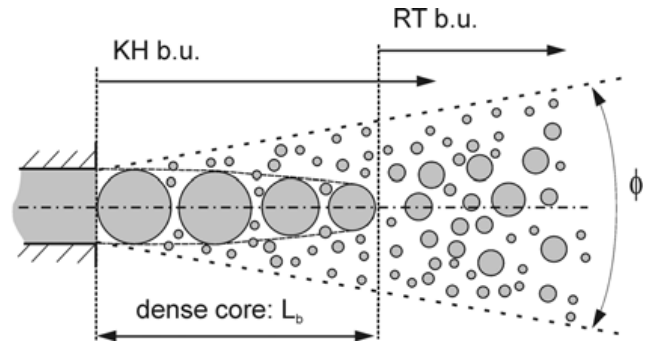


Figure 12 Combined model uses Blob method for primary atomization and TAB for secondary atomization

also heavily influenced by the jet's turbulence, which itself is a function of conditions upstream of the nozzle exit.

2.3 Computational Fluid Dynamics (CFD) Models

The last twenty years have seen new approaches to the Navier Stokes closure problem using computational fluid dynamic (CFD) methods. Given the increase in computing power and CFD methodologies, researchers aspired to solve the Navier-Stokes equations directly, a method referred to as direct numerical simulation (DNS), avoiding the need for any empirical coefficients. In order to accomplish a fully resolved solution, we apply the Navier Stokes equations, simplified in this example for incompressible flow.

In Cartesian coordinates (x, y, z) with the components of the velocity given by $\mathbf{u} = (u, v, w)$ the conservation of mass is defined as:

$$\nabla \mathbf{u} = 0 \quad \text{or} \quad \frac{\partial u}{\partial x} + \frac{\partial v}{\partial y} + \frac{\partial w}{\partial z} = 0$$

We can apply the same treatment to Navier Stokes or the x, y, and z momentum equations:

$$\frac{\partial \mathbf{u}}{\partial t} + \mathbf{u} \nabla \mathbf{u} = \frac{-1}{\rho} \nabla p + \nu \nabla^2 \mathbf{u}$$

$$\frac{\partial u}{\partial t} + u \frac{\partial}{\partial x} (u) + v \frac{\partial}{\partial y} (u) + w \frac{\partial}{\partial z} (u) = \frac{-1}{\rho} \frac{\partial p}{\partial x} + \nu \left(\frac{\partial^2 u}{\partial x^2} + \frac{\partial^2 u}{\partial y^2} + \frac{\partial^2 u}{\partial z^2} \right)$$

$$\frac{\partial v}{\partial t} + v \frac{\partial}{\partial x} (v) + u \frac{\partial}{\partial y} (v) + w \frac{\partial}{\partial z} (v) = \frac{-1}{\rho} \frac{\partial p}{\partial y} + \nu \left(\frac{\partial^2 v}{\partial x^2} + \frac{\partial^2 v}{\partial y^2} + \frac{\partial^2 v}{\partial z^2} \right)$$

$$\frac{\partial w}{\partial t} + u \frac{\partial}{\partial x} (w) + v \frac{\partial}{\partial y} (w) + w \frac{\partial}{\partial z} (w) = \frac{-1}{\rho} \frac{\partial p}{\partial z} + \nu \left(\frac{\partial^2 w}{\partial x^2} + \frac{\partial^2 w}{\partial y^2} + \frac{\partial^2 w}{\partial z^2} \right)$$

We can identify the characteristics of each term

$$\frac{\partial \mathbf{u}}{\partial t} + \mathbf{u} \nabla \mathbf{u} = -\frac{1}{\rho} \nabla p + \nu \nabla^2 \mathbf{u}$$

The terms are: unsteady acceleration, convective acceleration, pressure-gradient, and turbulent viscosity. Several observations can be made on the equations; first, the equations are expressed in velocity terms rather than position. The unsteady acceleration indicates the velocity is a function of time. The convective acceleration term is nonlinear, representing a change in velocity with position not just time, and the dependent variables appear in each equation yielding, at any given time, 4 coupled equations (continuity and x, y, and z momentum) with 4 unknowns (u, v, w, p) requiring an iterative solution for time step. The complication is that the model's grid size needs to account for the smallest eddies in the turbulent flow field, therefore reducing the uncertainty imposed by simplified models that estimate unresolved scales comes at the expense of extremely challenging computational requirements. The goal of resolving all the length and time scales is reasonably attainable when the flow is a single phase jet, but as the breakup process progresses, the smallest length scale approaches zero as the droplet is pinched-off the ligament to form an independent body. To deal with this limitation, modeling is introduced to facilitate a practical solution while still maintaining sufficient solution fidelity. The two dominate methods for turbulent modeling are Large-Eddy Simulation (LES) proposed by Smagorinsky [11] and Deardorff [12] and Reynolds-Averaged Navier-Stokes Equations (RANS) proposed by Deardorff [12] in the 1970's. A graphical representation of the solution techniques is provided in Figure 13, showing both the resolved and modeled portions of the DNS, LES, and RANS closures to Navier Stokes equations from Bakker [13].

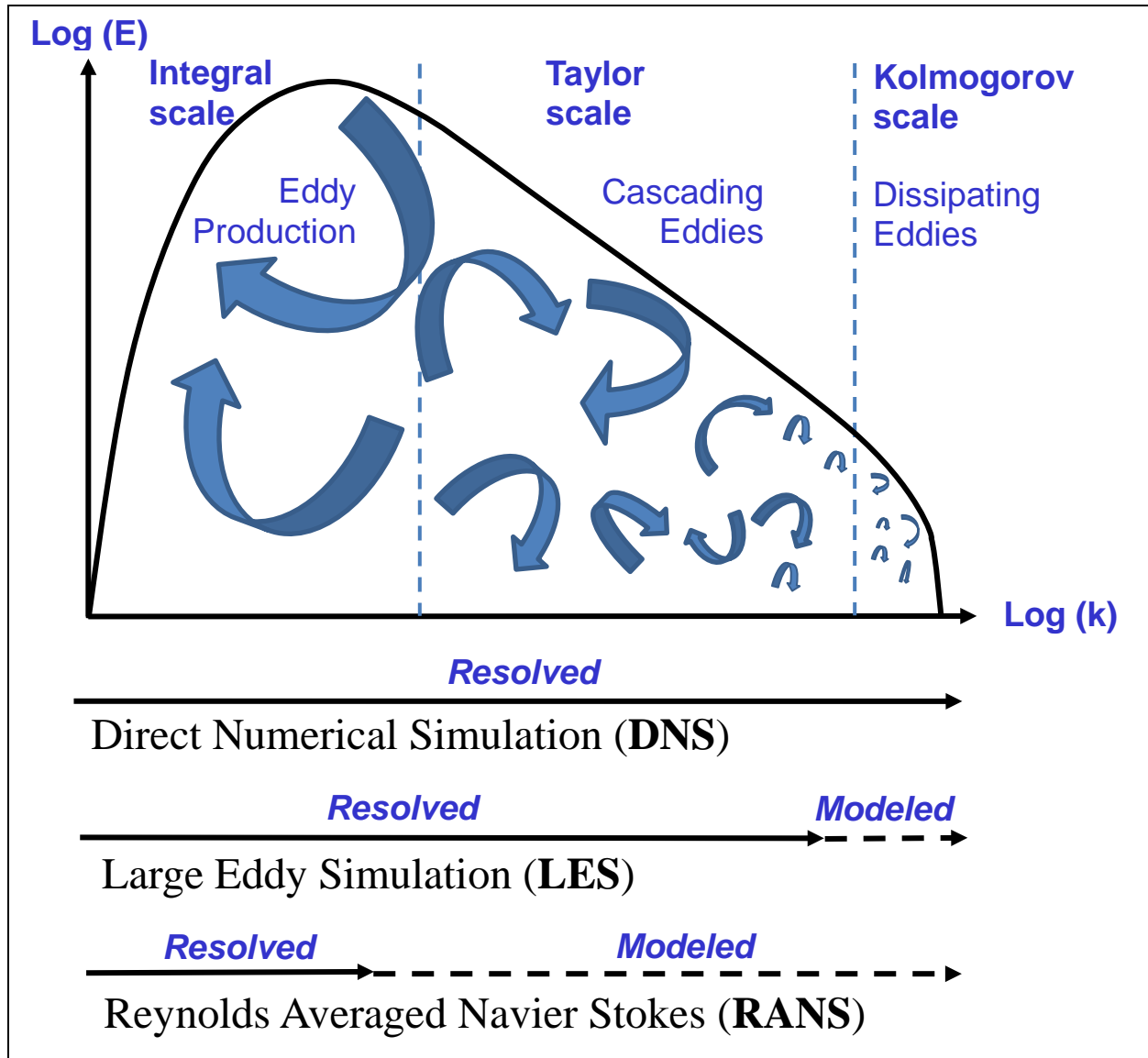


Figure 13 Graphic Representation of Solutions: DNS, LES, and RANS

2.3.1 Reynolds-Averaged Navier-Stokes Equations (RANS)

Modeling by use of Reynolds-Averaged Navier-Stokes Equations (RANS) is an attempt to close the Navier-Stokes equations by splitting them into averaged ($\bar{\mu}$) and varying (μ') parts. If we define a velocity $\mu(x)$ varying in time this can be viewed as:

$$\mu(x, t) = \bar{\mu}(x, t) + \mu'(x, t)$$

The splitting, or decomposition, concept is shown in Figure 14, where the variable Velocity is decomposed into an average and fluctuating signal. Likewise, this approach can be applied to pressure and other properties of the fluid field.

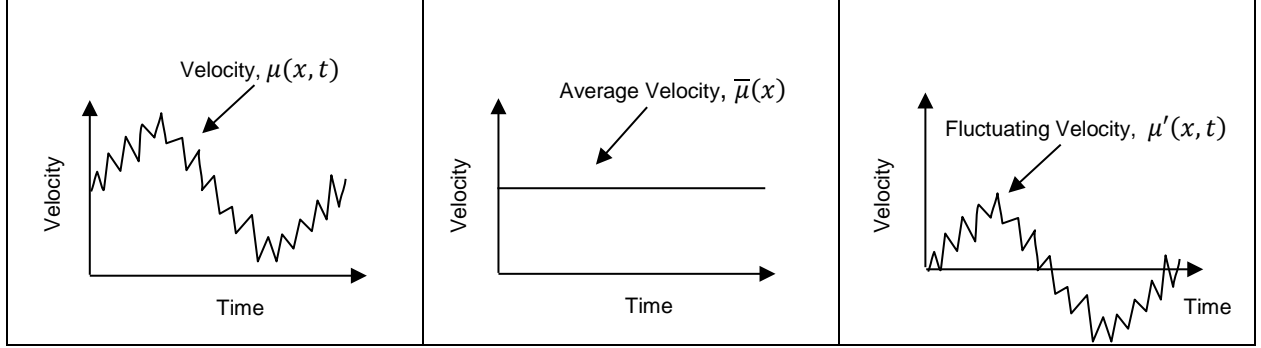


Figure 14 Velocity decomposed into Average Velocity and Fluctuating Velocity

The averaging operation is associated with time averaging:

$$\bar{\mu}(x, t) \approx \bar{\mu}(x) = \lim_{T \rightarrow \infty} \frac{1}{T} \int_0^T \mu(x, t) dt, \text{ and the decomposition is: } u = \bar{u} + u'$$

From this we see \bar{u} is constant over time and therefore $\overline{\bar{u}} = \bar{u}$ and by definition $\overline{u'} = 0$

If we apply the concept of average and fluctuating components to the continuity equation we get:

$$\frac{\partial u}{\partial x} + \frac{\partial v}{\partial y} + \frac{\partial w}{\partial z} = \frac{\partial (\bar{u} + u')}{\partial x} + \frac{\partial (\bar{v} + v')}{\partial y} + \frac{\partial (\bar{w} + w')}{\partial z} = 0$$

Distributing the partial differentiation:

$$\frac{\partial \bar{u}}{\partial x} + \frac{\partial u'}{\partial x} + \frac{\partial \bar{v}}{\partial y} + \frac{\partial v'}{\partial y} + \frac{\partial \bar{w}}{\partial z} + \frac{\partial w'}{\partial z} = 0$$

Now if we take the average of the equation we get:

$$\overline{\frac{\partial \bar{u}}{\partial x} + \frac{\partial u'}{\partial x} + \frac{\partial \bar{v}}{\partial y} + \frac{\partial v'}{\partial y} + \frac{\partial \bar{w}}{\partial z} + \frac{\partial w'}{\partial z}} = \bar{0}$$

And from our earlier identities we can substitute since the averages of the average part $\overline{\overline{u}} = \overline{u}$ and the average of the fluctuating part $\overline{u'} = 0$ resulting in **the averaged continuity equation:**

$$\boxed{\frac{\partial \overline{u}}{\partial x} + \frac{\partial \overline{v}}{\partial y} + \frac{\partial \overline{w}}{\partial z} = 0} \quad (1)$$

We can apply the same treatment to the x-momentum equation:

$$\frac{\partial u}{\partial t} + \frac{\partial}{\partial x} (u^2) + \frac{\partial}{\partial y} (uv) + \frac{\partial}{\partial z} (uw) = \frac{-1}{\rho} \frac{\partial p}{\partial x} + \nu \left(\frac{\partial^2 u}{\partial x^2} + \frac{\partial^2 u}{\partial y^2} + \frac{\partial^2 u}{\partial z^2} \right)$$

Again we take the average of both sides of the equation

$$\overline{\frac{\partial u}{\partial t} + \frac{\partial}{\partial x} (u^2) + \frac{\partial}{\partial y} (uv) + \frac{\partial}{\partial z} (uw)} = \overline{\frac{-1}{\rho} \frac{\partial p}{\partial x} + \nu \left(\frac{\partial^2 u}{\partial x^2} + \frac{\partial^2 u}{\partial y^2} + \frac{\partial^2 u}{\partial z^2} \right)}$$

Applying the properties of averaging to addition and multiplication we get:

$$\frac{\partial \overline{u}}{\partial t} + \frac{\partial}{\partial x} (\overline{u^2}) + \frac{\partial}{\partial y} (\overline{uv}) + \frac{\partial}{\partial z} (\overline{uw}) = \frac{-1}{\rho} \frac{\partial \overline{p}}{\partial x} + \nu \left(\frac{\partial^2 \overline{u}}{\partial x^2} + \frac{\partial^2 \overline{u}}{\partial y^2} + \frac{\partial^2 \overline{u}}{\partial z^2} \right)$$

Substituting the decomposition, $u = \overline{u} + u'$ we get:

$$\begin{aligned} \frac{\partial \overline{u}}{\partial t} + \frac{\partial}{\partial x} (\overline{u^2} + \overline{u'u'}) + \frac{\partial}{\partial y} (\overline{uv} + \overline{u'v'}) + \frac{\partial}{\partial z} (\overline{uw} + \overline{u'w'}) \\ = \frac{-1}{\rho} \frac{\partial \overline{p}}{\partial x} + \nu \left(\frac{\partial^2 \overline{u}}{\partial x^2} + \frac{\partial^2 \overline{u}}{\partial y^2} + \frac{\partial^2 \overline{u}}{\partial z^2} \right) \end{aligned}$$

Next we can rearrange the equation by moving the fluctuating part to the right hand side

generating **the averaged x-momentum equation:**

$$\begin{aligned} & \frac{\partial \bar{u}}{\partial t} + \frac{\partial}{\partial x} (\bar{u^2}) + \frac{\partial}{\partial y} (\bar{uv}) + \frac{\partial}{\partial z} (\bar{uw}) \\ = & \frac{-1}{\rho} \frac{\partial \bar{p}}{\partial x} + \nu \left(\frac{\partial^2 \bar{u}}{\partial x^2} + \frac{\partial^2 \bar{u}}{\partial y^2} + \frac{\partial^2 \bar{u}}{\partial z^2} \right) + \frac{\partial}{\partial x} (\bar{u'u'}) + \frac{\partial}{\partial y} (\bar{u'v'}) + \frac{\partial}{\partial z} (\bar{u'w'}) \end{aligned} \quad (2)$$

We can add **the averaged y-momentum equation:**

$$\begin{aligned} & \frac{\partial \bar{v}}{\partial t} + \frac{\partial}{\partial x} (\bar{uv}) + \frac{\partial}{\partial y} (\bar{v^2}) + \frac{\partial}{\partial z} (\bar{vw}) \\ = & \frac{-1}{\rho} \frac{\partial \bar{p}}{\partial y} + \nu \left(\frac{\partial^2 \bar{v}}{\partial x^2} + \frac{\partial^2 \bar{v}}{\partial y^2} + \frac{\partial^2 \bar{v}}{\partial z^2} \right) + \frac{\partial}{\partial x} (\bar{u'v'}) + \frac{\partial}{\partial y} (\bar{v'v'}) + \frac{\partial}{\partial z} (\bar{v'w'}) \end{aligned} \quad (3)$$

And **the averaged z-momentum equation:**

$$\begin{aligned} & \frac{\partial \bar{w}}{\partial t} + \frac{\partial}{\partial x} (\bar{uw}) + \frac{\partial}{\partial y} (\bar{vw}) + \frac{\partial}{\partial z} (\bar{w^2}) \\ = & \frac{-1}{\rho} \frac{\partial \bar{p}}{\partial z} + \nu \left(\frac{\partial^2 \bar{w}}{\partial x^2} + \frac{\partial^2 \bar{w}}{\partial y^2} + \frac{\partial^2 \bar{w}}{\partial z^2} \right) + \frac{\partial}{\partial x} (\bar{u'w'}) + \frac{\partial}{\partial y} (\bar{v'w'}) + \frac{\partial}{\partial z} (\bar{w'w'}) \end{aligned} \quad (4)$$

We now have derived the Reynolds-Averaged Navier-Stokes Equations (RANS). We started with 4 equations (continuity and x, y, z momentum) and 4 unknowns (u, v, w, p) after applying decomposition into average ($\bar{u}, \bar{v}, \bar{w}, \bar{p}$) and fluctuating parts (u', v', w', p') we have 10 unknowns ($\bar{u}, \bar{v}, \bar{w}, \bar{p}, \bar{u'u'}, \bar{u'v'}, \bar{u'w'}, \bar{v'v'}, \bar{v'w'}, \bar{w'w'}$) It should be noted that the fluctuating parts (u', v', w', p') do not appear directly, but as the averaged products of fluctuating parts ($\bar{u'u'}, \bar{u'v'}, \bar{u'w'}, \bar{v'v'}, \bar{v'w'}, \bar{w'w'}$).

So closure of the Navier-Stokes equations is not possible unless some simplification or substitution is provided to eliminate some of the 10 unknowns. The 6 fluctuating products could be of magnitudes that are positive, negative, or zero value. First, let us consider if any of the 6 fluctuating products could be ignored or considered as zero or of negligible value. By definition

of having turbulent flow, the turbulent flux terms $\left(\overline{u'u'}, \overline{v'v'}, \overline{w'w'}\right)$ are non-zero, since then the flow would be laminar not turbulent, nor are they negative, since the terms are squared. Experimentally, we find the magnitude of the turbulent term at times is similar to the averaged magnitude; therefore, the terms cannot be ignored as negligible. The Reynold stress cross product terms $\left(\overline{u'v'}, \overline{u'w'}, \overline{v'w'}\right)$ can be positive or negative, but cannot be assumed of zero magnitude. In 1877, French mathematician Joseph Valentin Boussinesq proposed the “Boussinesq Hypothesis” [13] defining a turbulent shear stress that is proportional to the mean flow strain rate, or “gradient transport”:

$$\overline{u'v'} \approx \frac{1}{2} \left(\frac{\partial \bar{u}}{\partial y} + \frac{\partial \bar{v}}{\partial x} \right) \quad \text{or} \quad -\overline{u'v'} \approx \vartheta_t \left(\frac{\partial \bar{u}}{\partial y} + \frac{\partial \bar{v}}{\partial x} \right), \quad \vartheta_t = \frac{-\overline{u'v'}}{\frac{1}{2} \left(\frac{\partial \bar{u}}{\partial y} + \frac{\partial \bar{v}}{\partial x} \right)}$$

The premise of the hypothesis is Newton’s law for laminar flow where viscosity is the proportional constant of shear stress to strain rate. The value of the hypothesis is clear since it allows for closure of the RANS equation by giving turbulent averaged substitutions for the turbulent fluctuating terms. Now the validity of the hypothesis is challenged on several fronts as well discussed in the literature [15]. Unlike viscosity, which is a function of the fluid, turbulent eddy viscosity, ϑ_t , like turbulence itself, is a function of the flow, and even with the hypothesis would be more properly defined as a vector rather than a scalar to match the local flow characteristics. Second, the hypothesis is based on a relation of small scale behavior, $\overline{u'}, \overline{v'}, \overline{w'}$, to large scale behavior, $\bar{u}, \bar{v}, \bar{w}$, contradicting our energy cascade framework for energy input, transfer, and dissipation. With serious reservations aside, the hypothesis does provide a pathway to closure if we have an estimate for turbulent viscosity, ϑ_t , which Boussinesq himself warned might be very difficult.

2.3.1.1 Zero dimensional model, mixing length model or algebraic model

The simplest solution is to define ϑ_t as a constant, meaning the turbulent contribution would vary in proportion to the mean flow velocity. We can construct this problem by evaluating our solution to flow between two parallel plates of infinite length as shown in

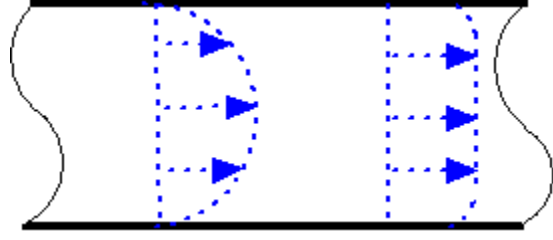


Figure 15 Field velocity profile for Laminar and Turbulent flows between plates

Figure 15.

The averaged continuity and momentum equations in 2-D are:

$$\frac{\partial \bar{u}}{\partial x} + \frac{\partial \bar{v}}{\partial y} = 0$$

$$0 = \frac{-1}{\rho} \frac{\partial \bar{p}}{\partial x} + \vartheta_t \left(\frac{\partial \bar{u}}{\partial y} + \frac{\partial \bar{v}}{\partial x} \right) - \frac{\partial \overline{u'^2}}{\partial x} - \frac{\partial \overline{u'v'}}{\partial y}$$

If $\overline{u'v'} = 0$ then the velocity profile would be identical to that of laminar flow, therefore ϑ_t must be some non-zero value as defined as:

$$-\overline{u'v'} = \vartheta_t \left(\frac{\partial \bar{u}}{\partial y} + \frac{\partial \bar{v}}{\partial x} \right)$$

$$0 = C + \frac{\partial}{\partial y} \left(\vartheta \frac{\partial \bar{u}}{\partial y} + \vartheta_T \frac{\partial \bar{u}}{\partial y} \right)$$

$$C = \frac{\partial}{\partial y} (\vartheta + \vartheta_T) \frac{\partial \bar{u}}{\partial y}$$

$$C = \frac{\partial}{\partial y} (\vartheta (1 + c_1)) \frac{\partial \bar{u}}{\partial y} \text{ where } \vartheta_T = c_1 \vartheta$$

$$\vartheta_T = C\vartheta \frac{\partial^2 \bar{u}}{\partial y^2}$$

If ϑ_T is related to ϑ by a constant, while the velocity itself may vary in magnitude, the shape of the velocity profile must remain consistent with laminar flow adjusted by a scalar multiple, which is not the case. In order to affect the velocity profile in our simple flow between infinite plates example, we see that ϑ_t must vary for the flow as a function of distance from the plate or $\vartheta_t = f(y)$. Starting with our continuity and x-momentum equation:

$$\frac{\partial \bar{u}}{\partial x} + \frac{\partial \bar{v}}{\partial y} = 0$$

$$\frac{\partial \bar{u}^2}{\partial x} + \frac{\partial \bar{u}\bar{v}}{\partial y} = \frac{-1}{\rho} \frac{\partial \bar{p}}{\partial x} + \vartheta \left(\frac{\partial \bar{u}}{\partial y} \right) - \frac{\partial \overline{u'^2}}{\partial x} - \frac{\partial \overline{u'v'}}{\partial y}$$

our y-momentum equation:

$$\frac{\partial \bar{u}\bar{v}}{\partial x} + \frac{\partial \bar{v}^2}{\partial y} = \frac{-1}{\rho} \frac{\partial \bar{p}}{\partial y} + \vartheta \left(\frac{\partial \bar{v}}{\partial x} \right) - \frac{\partial \overline{u'v'}}{\partial x} - \frac{\partial \overline{v'^2}}{\partial y}$$

Substitution yields:

$$\vartheta \left(\frac{\partial \bar{u}}{\partial y} \right) = \vartheta \left(\frac{\partial^2 \bar{u}}{\partial x^2} + \frac{\partial^2 \bar{u}}{\partial y^2} \right) = \frac{\partial}{\partial x} \left(\vartheta \frac{\partial \bar{u}}{\partial x} \right) + \frac{\partial}{\partial y} \left(\vartheta \frac{\partial \bar{u}}{\partial y} \right)$$

Applying the Boussinesq hypothesis:

$$-\overline{u'^2} = \vartheta_t \left(\frac{\partial \bar{u}}{\partial x} \right), \quad -\overline{u'v'} = \vartheta_t \left(\frac{\partial \bar{u}}{\partial y} \right), \quad -\overline{v'^2} = \vartheta_t \left(\frac{\partial \bar{v}}{\partial y} \right)$$

We can express the RANS equation as:

$$\frac{\partial \bar{u}^2}{\partial x} + \frac{\partial \bar{u}\bar{v}}{\partial y} = \frac{-1}{\rho} \frac{\partial \bar{p}}{\partial x} + \frac{\partial}{\partial x} \left((\vartheta + \vartheta_T) \frac{\partial \bar{u}}{\partial x} \right) + \frac{\partial}{\partial y} \left((\vartheta + \vartheta_T) \frac{\partial \bar{u}}{\partial y} \right)$$

In 1925, Prandtl [16] suggested considering the flow a collection of fluid particles where each fluid particle has influence on surrounding particles. This influence is important as by definition $\overline{u'v'} \neq 0$ since u' and v' are not independent. So visualizing an eddy of swirling motion, the effect of the mean flow velocity \bar{u}' has effect on the adjacent flow velocity \bar{v}' as eddy convection. High rates of convection yield increased rates of heat exchange and mixing of turbulent flow. These eddies vary in size across the broad range of length scales as illustrated in Figure 16 so mixing is well distributed. If we consider the full spectrum of kinetic turbulent energy, E , it is defined as:

$$E = \frac{1}{2} (\overline{u^2} + \overline{v^2} + \overline{w^2})$$

$$\vartheta_t = |\overline{u'v'}|, | \quad | + \text{coefficient}$$

$$|\overline{u'v'}| \approx \left| \left(l \frac{\partial \bar{u}}{\partial y} \right) \left(l \frac{\partial \bar{u}}{\partial y} \right) \right|$$

$$\approx l^2 \left| \frac{\partial \bar{u}}{\partial y} \right| \left| \frac{\partial \bar{u}}{\partial y} \right|$$

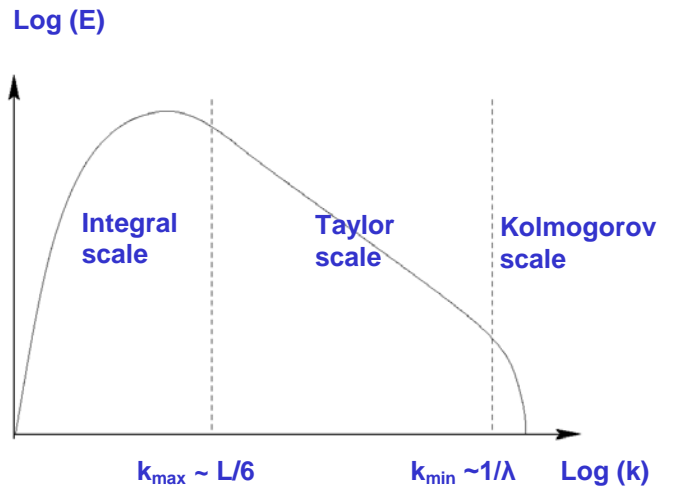


Figure 16 Turbulent energy across the length scale

Prandtl used experimental data to determine if a coefficient could be found such that mixing length l_{mix} could be simply determined.

$$l_{mix} = C\delta(x) \text{ where } \delta \text{ is the characteristic length, like jet diameter}$$

A range of cases have been explored in literature and the value of the constant varied from 0.08 for a round jet to 0.18 for a far wave [17]. The value for k_{max} is established by the geometry, the distance between the two plates in our example, and the ratio of $k_{max}/k_{min} \sim 10^3$ where k_{min} represents geometry-independent dissipating length scales in the Kolmogorov range. The mixing length model's main advantage is ease of application to represent wall effects for the turbulent flow, providing a proper velocity profile, but it lacks time history effects in fully local solutions for the modeled turbulence yielding poor results for complex flows.

2.3.1.2 One-Equation Model,

One-equation model family includes Spalart-Allmaras, Smagorinsky, Baldwin-Barth, and Prandtl. One-equation RANS models are mostly used in the aerospace industry where boundary effects are negligible. The Prandtl model defines the kinematic eddy viscosity as:

$$\nu_t = \frac{1}{k^2} l = C_D \frac{k^2}{\varepsilon} \text{ where } \varepsilon = C_D \frac{k^{\frac{2}{3}}}{l}$$

Where the coefficient $C_D=0.08$

The main advantage of the one-equation model is it adds history effects to the RANS solution.

2.3.1.3 Two-Equation Model, k - ε model

The two-equation model family attempts to better match the physical characteristics of turbulence with the addition of two additional transport equations (partial differential equations) representing the turbulent energy cascade with turbulent energy production, turbulent energy transfer, and turbulent energy dissipation. The most widely utilized model with excellent

solution convergence characteristics is the k - ε model where the term k represents the turbulent kinetic energy and ε represents the turbulent kinetic energy dissipation rate given by:

$$k = \frac{1}{2}(\overline{u'^2} + \overline{v'^2} + \overline{w'^2})$$

$$\varepsilon = 2\vartheta \overline{s'_{ij}s'_{ij}} \text{ where fluctuating strain rate tensor } s'_{ij} = \frac{1}{2}\left(\frac{\partial u'_i}{\partial x_j} + \frac{\partial u'_j}{\partial x_i}\right)$$

$$\frac{\partial (k)}{\partial t} + \frac{\partial (k\overline{u_j})}{\partial x_j} = \frac{\partial}{\partial x_j} \left(\frac{\vartheta_t}{\sigma_k} \frac{\partial k}{\partial x_j} \right) + 2\vartheta_t S_{ij}S_{ij} - \rho\varepsilon, \quad \text{where } \vartheta_t = C_\vartheta \frac{k^2}{\varepsilon}$$

$$\frac{\partial (\varepsilon)}{\partial t} + \frac{\partial (\varepsilon\overline{u_j})}{\partial x_j} = \frac{\partial}{\partial x_j} \left(\frac{\vartheta_t}{\sigma_\varepsilon} \frac{\partial \varepsilon}{\partial x_j} \right) + C_{1\varepsilon} \frac{\varepsilon}{k} 2\vartheta_t S_{ij}S_{ij} - 2C_{2\varepsilon} \frac{\varepsilon^2}{k}$$

with widely used constants: $C_\vartheta = 0.09, \sigma_k = 1.0, \sigma_\varepsilon = 1.3, C_{1\varepsilon} = 1.44, C_{2\varepsilon} = 1.92,$

With this closure, our RANS solution is expressed in 6 equations with 6 unknowns, $\overline{u}, \overline{v}, \overline{w}, \overline{p}, k, \varepsilon$ but with the addition of 5 constants, which must be determined empirically.

Industry experience has shown k - ε model to be the most popular as the finite element solution is stable, converges quickly, and results have shown a fair representation of experimental data.

There are several limits of the model as it does not accurately capture the effects of wall or boundary surfaces, so separate wall models are applied in practice. The k - ε model also does not perform well in swirling flows or flows with large separation, and in general the solutions are overly dissipative, thus eliminating turbulent effects more quickly than experimental data suggests appropriate.

2.3.2 Large Eddy Simulation (LES)

Modeling by use of Large Eddy Simulation (LES) is an attempt to close the Navier-Stokes equations by splitting, or decomposing, turbulent kinetic energy into large scale resolved portions and small scale modeled parts. If we define a velocity $\mu(x)$ varying in time, this can be decomposed into filtered Large Scale ($\tilde{\mu}$) and Small Scale (μ') parts through the application of a spatial filter. If we define a velocity $\mu(x, t)$ varying in time this can be viewed as:

$$\mu(x, t) = \tilde{\mu}(x, t) + \mu'(x, t)$$

The decomposition concept is illustrated in Figure 17 where the low-frequency

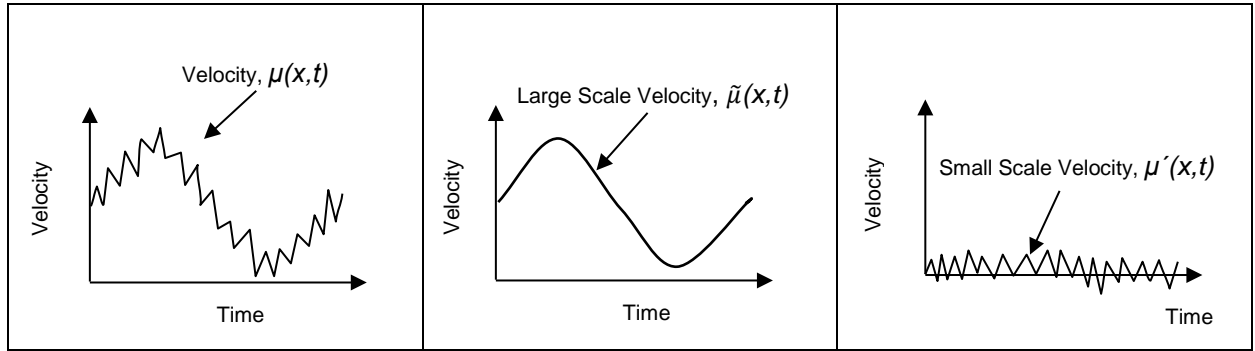


Figure 17 Velocity decomposed into Large Scale and Small Scale components

content of the Velocity signal is retained and directly resolved in the simulation, while the high frequency content, termed Sub-Grid-Stress (SGS), can be modeled. The filtering operation is associated with spatial averaging defined over domain Ω :

$$\tilde{\mu}(x, t) = \frac{1}{V_\Omega} \int_\Omega \mu(x, t) dx, \text{ where } V_\Omega \text{ represents Volume, and the decomposition is:}$$

$$u = \tilde{\mu} + u'$$

From Figure 17 we see that unlike RANS, time averaging \tilde{u} is not constant over time and therefore $\tilde{\tilde{u}} \neq \tilde{u}$ and $\tilde{u'} \neq 0$

As shown by Sagaut [18], we can also consider function $\mu(x, t)$ decomposition by defining the spatially-filtered function:

$$\tilde{\mu}(x, t) \equiv \frac{1}{V_\Omega} \int_{\Omega} G(x, x', |\Delta|) x' dx' \text{ where } G(x, x', |\Delta|) \text{ is the kernel of the filter}$$

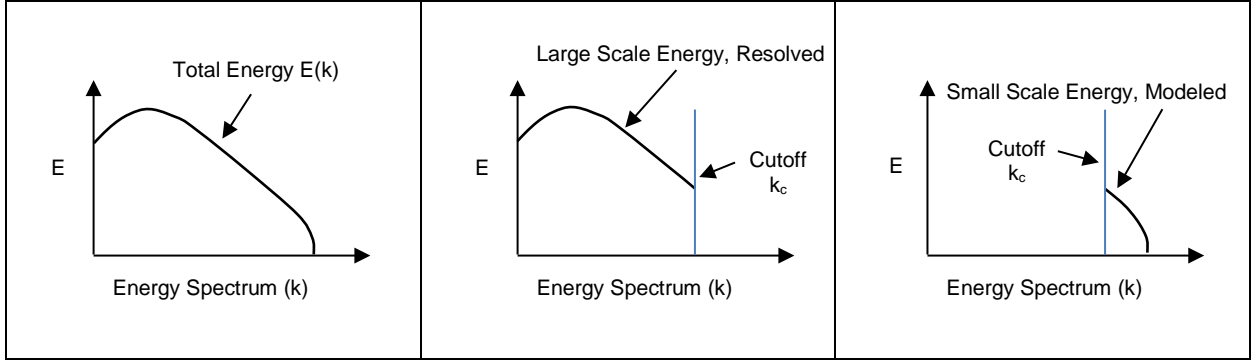


Figure 18 Spectral Decomposition of Total Energy into Large Scale and Small Scale components

Performing the decomposition, a low-pass filter provides the large-scale content to be resolved, and the high-pass filter portion yields the small-scale energy to be modeled, as illustrated in Figure 18. Various filter types: Gaussian, Box or Top-hat, or Sharp cutoff have been used and their specific filter characteristic impact the transformation.

The Gaussian filter is smooth where:

$$G(x, \Delta) = \sqrt{\frac{6}{\pi \Delta^2}} e^{\left(-\frac{6x^2}{\Delta^2}\right)}$$

The Box or Top-hat filter commonly applied to FE where the grid establishes Δ :

$$G(x, \Delta) = \begin{cases} \frac{1}{\Delta} & \text{where } (|x'| \leq \frac{\Delta}{2}) \\ 0 & \text{otherwise} \end{cases}$$

The Sharp cutoff filter can be thought of as a Fourier space transformation (FFT) removing wave numbers above a cutoff value, k_c , the sharp cutoff filter is the only true projection filter:

$$\dot{G}(k, \Delta) = \begin{cases} 1 & \text{where } (k \leq \frac{\pi}{\Delta}) \\ 0 & \text{otherwise} \end{cases}$$

The cutoff length, $\Delta(x)$, establishes the cutoff frequency k_c for the scale separation. Any cutoff length can be chosen, but a value smaller than the mesh size in the finite element model would be meaningless.

$$\Delta = \sqrt[3]{\Delta_x \Delta_y \Delta_z}$$

The filtered velocity is represented as:

$$\tilde{u}_i(x, t) \equiv \int G(x, x', \Delta) u_i(x', t) dx'$$

If we apply the concept to the conservation of mass we get **the filtered continuity equation:**

$$\boxed{\frac{\partial \tilde{u}}{\partial x} + \frac{\partial \tilde{v}}{\partial y} + \frac{\partial \tilde{w}}{\partial z} = 0} \quad (1)$$

We can apply the same filtered component to the x-momentum equation:

$$\frac{\partial \tilde{u}}{\partial t} + \frac{\partial (\tilde{u}\tilde{v})}{\partial y} = \frac{-1}{\rho} \frac{\partial \tilde{p}}{\partial x} + \vartheta \frac{\partial}{\partial y} \left(\frac{\partial \tilde{u}}{\partial y} + \frac{\partial \tilde{y}}{\partial x} \right) = \frac{-1}{\rho} \frac{\partial \tilde{p}}{\partial x} + 2\vartheta \frac{\partial}{\partial y} \tilde{S}_{xy}$$

$$\text{where fluctuating strain rate tensor } \tilde{S}_{xy} = \frac{1}{2} \left(\frac{\partial \tilde{u}}{\partial y} + \frac{\partial \tilde{y}}{\partial x} \right)$$

The non-linear term $\tilde{u}\tilde{v}$ must be expressed in terms of filtered variables for a solution.

2.3.2.1 Leonard's Decomposition for the non-linear term $\tilde{u}\tilde{v}$

An approach for decomposing the non-linear term $\tilde{u}\tilde{v}$ was proposed by Leonard [19] as:

$$\begin{aligned} \tilde{u}\tilde{v} &= (\tilde{u} + \widetilde{u'})(\tilde{v} + \widetilde{v'}) \\ &= \tilde{u}\tilde{v} + \tilde{u}\widetilde{v'} + \widetilde{u'}\tilde{v} + \widetilde{u'v'} \end{aligned}$$

Grouping the fluctuating terms per Germano [20] we can define a subgrid tensor τ_{ij} , as:

$$\tau_{xy} = \tilde{u}\widetilde{v'} + \widetilde{v'}\tilde{u} + \widetilde{u'v'} = \tilde{u}\tilde{v} - \widetilde{u'v'}$$

The $\widetilde{u'v'}$ term requires a second application of the filter. Leonard proposed to express it in components that could be grouped to provide context to the physics of turbulence starting with

the Leonard Tensor L_{ij} , which represents the interaction of the large scales:

$$\begin{aligned}\widetilde{\tilde{u}\tilde{v}} &= (\widetilde{\tilde{u}\tilde{v}} - \tilde{u}\tilde{v}) + \tilde{u}\tilde{v} \\ &= L_{ij} + \tilde{u}\tilde{v} \quad \text{or} \quad L_{xy} = \widetilde{\tilde{u}\tilde{v}} - \tilde{u}\tilde{v}\end{aligned}$$

The Cross term tensor C_{ij} represents the interactions between the large and small scales, and the Reynolds subgrid scale tensor R_{ij} represents the subgrid scale interactions.

$$C_{ij} = \widetilde{\tilde{u}v'} + \widetilde{\tilde{v}u'}$$

$$R_{ij} = \widetilde{u'v'}$$

The resulting subgrid tensor as defined is a function of the grid size, and as $\Delta \rightarrow 0$ the stress tensor $\tau \rightarrow 0$, therefore the LES model approaches the DNS solution. The Leonard tensor and Cross tensor are not Galilean invariant, although the entire SGS tensor τ is, leading to modeling of the entire SGS tensor as the preferred solution.

Now substituting $\widetilde{u\tilde{v}} = \tau_{xy} + \tilde{u}\tilde{v}$ we get **the filtered x-momentum equation:**

$$\begin{aligned}\frac{\partial \tilde{u}}{\partial t} + \frac{\partial (\widetilde{u\tilde{v}})}{\partial y} &= -\frac{1}{\rho} \frac{\partial \tilde{p}}{\partial x} + 2\vartheta \frac{\partial}{\partial y} \tilde{S}_{xy} \\ \frac{\partial \tilde{u}}{\partial t} + \frac{\partial (\tau_{xy} + \tilde{u}\tilde{v})}{\partial y} &= -\frac{1}{\rho} \frac{\partial \tilde{p}}{\partial x} + 2\vartheta \frac{\partial}{\partial y} \tilde{S}_{xy} \\ \frac{\partial \tilde{u}}{\partial t} + \frac{\partial (\tilde{u}\tilde{v})}{\partial y} &= -\frac{1}{\rho} \frac{\partial \tilde{p}}{\partial x} + 2\vartheta \frac{\partial}{\partial y} \tilde{S}_{xy} - \frac{\partial \tau_{xy}}{\partial y}\end{aligned}$$

$$\boxed{\frac{\partial \tilde{u}}{\partial t} + \frac{\partial (\tilde{u}\tilde{v})}{\partial y} = -\frac{1}{\rho} \frac{\partial \tilde{p}}{\partial x} + 2\vartheta \frac{\partial}{\partial y} \tilde{S}_{xy} - \frac{\partial \tau_{xy}}{\partial y}} \quad (2)$$

Similarly **the filtered y-momentum equation:**

$$\boxed{\frac{\partial \tilde{v}}{\partial t} + \frac{\partial (\tilde{v}\tilde{w})}{\partial z} = -\frac{1}{\rho} \frac{\partial \tilde{p}}{\partial y} + 2\vartheta \frac{\partial}{\partial z} \tilde{S}_{yz} - \frac{\partial \tau_{yz}}{\partial z}} \quad (3)$$

Similarly **the filtered z-momentum equation:**

$$\boxed{\frac{\partial \tilde{w}}{\partial t} + \frac{\partial (\tilde{w}\tilde{z})}{\partial x} = -\frac{1}{\rho} \frac{\partial \tilde{p}}{\partial z} + 2\vartheta \frac{\partial}{\partial x} \tilde{S}_{zx} - \frac{\partial \tau_{zx}}{\partial x}} \quad (4)$$

Therefore, we now have 4 filtered equations with 4 filtered unknowns ($\tilde{u}, \tilde{v}, \tilde{w}, \tilde{p}$) plus Subgrid

Stress Tensor terms ($\tau_{xy}, \tau_{yz}, \tau_{zx}$), which must be modeled.

2.3.2.2 Smagorinsky Model

The Smagorinsky Model [11] was first used by Deardorff [12] in his original work for closure of LES equations. This occurred in the same time period of RANS work, and not surprisingly, the Smagorinsky or Smagorinsky-Lilly [21] closure is based on the Boussinesq hypothesis used in RANS closure work of the same time period. It should be noted, however, one significant difference in LES solutions is that the SGS models represent a smaller portion of the turbulent solution than the RANS closure counterpart, resulting in a comparably smaller error being introduced. The essence of the Smagorinsky model is the assumption that the small scales are in equilibrium and thus entirely dissipate all the energy transferred from the resolved larger scales.

The SGS Tensor is defined as:

$$\tau_{SGSij} = -2\vartheta_{SGS}\tilde{S}_{ij}, \quad \text{and } \vartheta_{SGS} = (C_S\Delta)^2|\tilde{S}|$$

Experimental data supports a turbulent deceleration coefficient range where $0.18 \leq C_S \leq 0.23$, but empirical data also indicate the model is overly dissipative and in many situations near walls, which results in high shear rates, the constant must be decreased.

2.3.2.3 one-equation eddy viscosity SGS Model

Given the shortcomings of the algebraic model closure, alternative solutions add complexity to the simulation to better reflect the experimental data. As done earlier for the RANS closure, the first choice is a one-dimensional model like Spalart-Allmaras. A one-equation model was defined by Yoshizawa [22] defining a transport term where ε is the turbulent dissipation rate and Δ is the SGS length scale.

$$\frac{\partial K}{\partial t} + \nabla(K\tilde{u}) = \nabla[(\vartheta + \vartheta_{SGS})\nabla K] - \varepsilon - \tau\tilde{S} \quad \text{where } \vartheta_{SGS} = C_k K^{\frac{1}{2}}\Delta, \quad \varepsilon = \frac{C_\varepsilon K^{\frac{3}{2}}}{\Delta}$$

Empirical data suggests Model constants $C_k \approx 0.07$ and $C_\varepsilon \approx 1.05$

2.3.2.4 Scale Similarity SGS Model

Scale similarity models provide for additional interactions across turbulent scales by introducing a second level of filtering where:

$$\tau_{SGSij} = L_{ij} + C_{ij} + R_{ij}$$

$$\text{where } L_{ij} = \widetilde{\widetilde{u}}\widetilde{\widetilde{v}} - \widetilde{u}\widetilde{v}, C_{ij} = (\widetilde{u} - \widetilde{\widetilde{u}})\widetilde{\widetilde{v}} + (\widetilde{v} - \widetilde{\widetilde{v}})\widetilde{\widetilde{u}}, R_{ij} = (\widetilde{u} - \widetilde{\widetilde{u}})(\widetilde{v} - \widetilde{\widetilde{v}})$$

This simplifies to:

$$\tau_{SGSij} = \widetilde{\widetilde{u}}\widetilde{\widetilde{v}} - \widetilde{u}\widetilde{v} \text{ Allowing for direct approximation based on filtered properties}$$

2.3.2.5 SGS Model study

A study of the SGS closure methods: Smagorinski, one-equation eddy viscosity, and scale similarity was conducted by Weller [23] using a C++ based open source finite element code named FOAM (field operation and manipulation). The study case involved bluff bodies where the comparison was to a RANS $k-\varepsilon$ model, RANS Launder-Gibson Reynolds stress model and RNG model. The results showed the RANS $k-\varepsilon$ model performed poorly and the RANS Launder-Gibson Reynolds as well as the LES one-equation eddy viscosity models predicted flow near the obstacle well. Based on this conclusion, Delphi CFD analysis using open FOAM formulation is based on LES one-equation eddy viscosity model for closure according to Yoshizawa [22]

$$\frac{\partial K}{\partial t} + \nabla(K\tilde{u}) = \nabla[(\vartheta + \vartheta_{SGS})\nabla K] - \varepsilon - \tau\tilde{S} \quad (7)$$

$$\text{where } \vartheta_{SGS} = C_k K^{\frac{1}{2}} \Delta, \varepsilon = \frac{C_\varepsilon K^{\frac{3}{2}}}{\Delta}$$

Where ε is the SGS turbulence dissipation rate, ν_{SGS} the SGS turbulent viscosity, and Δ is the SGS length scale (equivalent to the local computational cell size). The turbulence model constants have the values $C_K = 0.07$ and $C_\varepsilon = 1.05$, in accordance with Yoshizawa.

2.3.3 Injector Nozzle Studies

Over the recent two decades, there has been significant recognition of the influence of the injector valve group design on the flow structure within the injector nozzle and the subsequent liquid jet primary breakup and atomization characteristics of the spray. The nozzles representative of the diesel fuel injectors have received extensive R&D attention, leading to identification of multiple fluid dynamic phenomena as influential factors that affect the spray primary breakup, including the cavitation [24] [25] [26] [27], turbulence [7] [28] [9], and vortices [29] [30] [31] that form after nozzle exit, upstream of the breakup, or within the valve group with subsequent breakup immediately at nozzle exit. It is notable that often these phenomena are concurrent and coupled; for instance, cavitation or separation can markedly influence the nozzle jet velocity distribution as well as impact jet turbulence levels.

The GDi multi-hole injector valve-group and spray atomization is receiving more attention [32] [33] [34] in line with the broad adoption of direct injection for gasoline engines as well as advances of the GDi combustion system, including the application of center-mount injectors for well-mixed homogenous charge combustion systems, and the more stringent requirements on fuel economy and emissions, especially the particulate number emission targets implemented in Europe. The experimental data indicates dependence of the spray plume structure and atomization on the GDi nozzle geometry, in addition to expected influence of the pintle-sac volume, due to its influence on the flow velocity field and formation of turbulent eddies. In this respect, despite the conceptual similarity with the diesel injectors, it is expected

that the differences in the GDI nozzle geometry, in particular the nozzle thru-hole, length-to-diameter ratio, and injection pressure modify the profile of the velocity field, rate of acceleration, and nozzle-exit liquid jet velocity, are significant to render the key nozzle fluid dynamic and breakup features different than diesel injector nozzles. For example, it is expected that the short nozzle l/d renders the jet breakup characteristics more sensitive to the nozzle thru-hole entrance conditions and provides the potential occurrence of the hydraulic flip phenomenon [25]. The implication is that an accurate computational analysis of the flow within the injector valve group is an integral component of the analysis of the spray near-field breakup and atomization characteristics.

The VOF-LES method for analysis of the jet breakup process has been under development and verification over the past decade. The capability of the method has been broadly demonstrated [35] [36] [37] [38], although in all cases, the injector internal flow domain was excluded and the liquid jet VOF-LES simulations were performed with assumed nozzle-exit flow conditions or with imposed disturbances to represent turbulent fluctuations. The importance of the nozzle-exit flow condition on the jet breakup was investigated in the DNS “numerical experiments” of Sander and Weigand [38] [39] that demonstrated significant influence of the issuing jet velocity profile and turbulence disturbances on the jet primary breakup. The recent combined VOF-LES and spray imaging studies of the GDI conical [40] and planar-sheet [41] liquid jet atomization incorporated the injector valve group into the computational domain in order to couple the injector internal flow with the jet primary breakup process and to alleviate uncertainty or complexity associated with prescribing the nozzle-exit spatial and temporal initial conditions. These simulations provided good quantitative predictions of the jet breakup process, including the prediction of the Kelvin-Helmholtz instability wave length, and demonstrated both

the strong dependence of the spray geometry and atomization characteristics on the details of the nozzle geometry, as well as the capability of the VOF-LES method to capture the effect of nozzle design on the jet primary breakup structure. Therefore, the VOF-LES of the injector valve-group internal flow and near-field primary breakup offers a useful tool for the investigation of the GDI multi-hole specific nozzle design geometry and the associated effect on the liquid plume structure and its primary breakup to be analyzed in this work.

CHAPTER 3 OBJECTIVES OF THE STUDY

The optimization of the multi-hole GDI injector spray characteristics: atomization, spray plume angle, spray plume penetration, and spray targeting within the constraints imposed by engine geometry, to avoid spray impingement on all solid surfaces, is a crucial component of the combustion system optimization to meet the fuel consumption and emission objectives.

The GDI multi-hole injector must fulfill several requirements:

- 1) Precise fuel metering with a uniform or defined hole-to-hole flow rate distribution to promote proper charge mixing for combustion
- 2) Precise spray plume targeting geometry and defined plume penetration to avoid impingement on surfaces
- 3) Required atomization characteristics of plume angle and spray droplet-size distribution to promote evaporation and clean combustion

The simultaneous fulfillment of these requirements renders design optimization of the GDI injector valve group for specific combustion chamber geometry a non-trivial, and often iterative, process. This complexity owes to the inherent coupling of the injector fuel metering, spray targeting, and atomization characteristics as a result of the influence of the nozzle geometry on

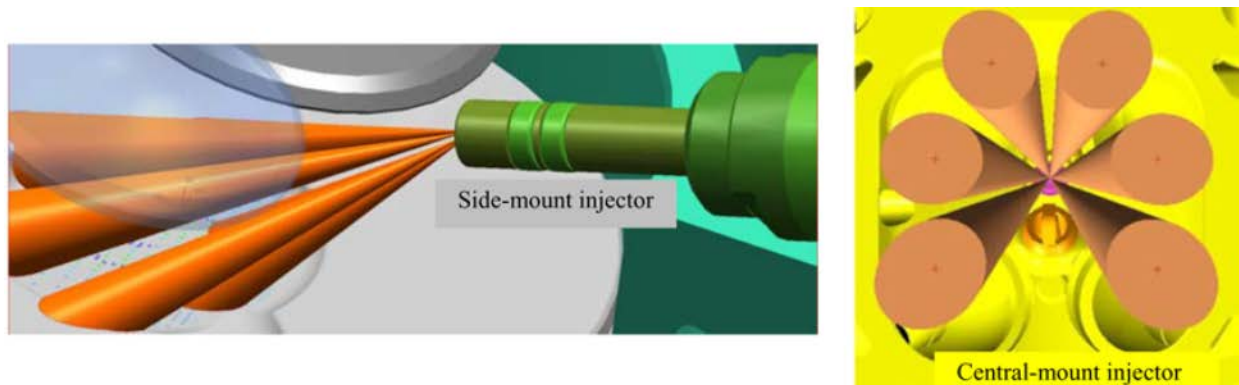


Figure 19 Application of side-mount and central-mount GDI injectors

all features of the spray. Although the physical packaging of the injector may vary for side or central-mount applications, the targeting goal of the spray plumes is consistent: targeting specific locations to avoid impingement on the valves, piston, and cylinder bore wall while providing excellent mixture distribution, especially near the spark plug electrode for proper emissions, as shown on Figure 19. These plume targets are typically defined relative to a downstream target, see Figure 20, and confirmed in a spray lab with a patternator (described in 4.3 Test Equipment), which calculates the mass centroid of each spray plume.

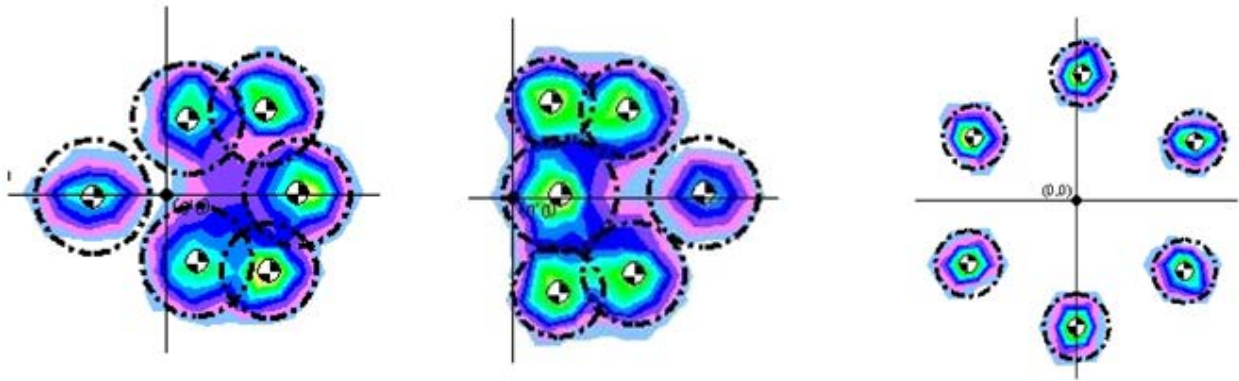


Figure 20 Visualization of spray plume targeting in side and central-mount GDI injectors

Currently, the GDI injector seat and nozzle design draws on significant empirical knowledge, developed through experimental valve-group hardware design and test programs. The major drawback of this method, apart from the cost and time requirement, is the difficulty to investigate one aspect of the spray characteristics in isolation (without affecting other spray features) in order to establish a direct and conclusive correlation of nozzle geometry to spray characteristics. One approach to address this complexity and establish a fundamental understanding of the relationship between the seat nozzle geometry and the spray characteristics is through application of advanced computational fluid dynamic (CFD) methods. In order to establish model verification, physical hardware and appropriate test methodology will be applied.

The fundamental geometry of interest for the nozzle, as defined in Figure 21 is:

- 1) Thru-hole length to diameter ratio (l/d)
- 2) Counterbore interaction with spray (D/d), $(l+L)/d$
- 3) Spray plume skew angle for targeting (β)

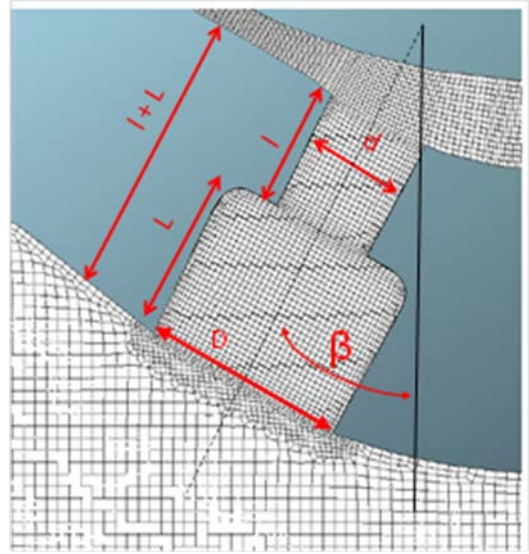


Figure 21 Definition of thru-hole, counterbore and skew angle geometry

CHAPTER 4 OUTLINE OF THE STUDY METHODOLOGY

4.1 Defined Terms

ASIE - after the start of injector energizing

ASOS - after the start of simulation

SOF - start of fuel, visual jet exiting the nozzle

d – nozzle thru-hole diameter

l – nozzle thru-hole length of diameter d

(l/d) – thru-hole length to diameter ratio

D – nozzle counterbore diameter

L – nozzle counterbore length of counterbore diameter D

(D/d) – ratio of counterbore diameter to thru-hole diameter

$(l+L)/d$ – ratio of thru-hole length plus counterbore length to thru-hole diameter

β - spray plume skew angle for targeting

D_{V90} – The drop diameter value that is a statistical indicator of the largest drops in the spray.

90% of the spray liquid volume and mass is contained within drops that have a diameter less than or equal to D_{V90}

D_{V50} – The drop diameter value that is a statistical indicator of the median drop size. Half the spray volume and mass is contained in smaller, while half in larger drops. D_{V50} is also sometimes referred to as the Mass Median Diameter (MMD) or Volume Mean Diameter (VMD)

Sauter Mean Diameter (SMD) – The drop diameter, which has the same ratio of the volume to surface area as that of the entire spray. This diameter is particularly useful for spray combustion modeling, can also be expressed at D_{V32}

u, U - fluid velocity field

(u, v, w) the (x, y, z) components of the fluid velocity u

\bar{u} - averaged fluid velocity, where $u = \bar{u} + u'$ applies to pressure and other averaged variables

u' - fluctuating fluid velocity

$(\bar{u}, \bar{v}, \bar{w})$ - the averaged (x, y, z) components of the fluid velocity averaged fluid velocity \bar{u}

\tilde{u} - filtered fluid velocity, where $u = \tilde{u} + u'$ applies to pressure and other filtered variables

$(\tilde{u}, \tilde{v}, \tilde{w})$ - the filtered (x, y, z) components of the fluid velocity filtered fluid velocity \tilde{u}

ϑ – kinematic viscosity

ϑ_t - turbulent kinematic viscosity

Re - Reynolds number, $= \rho_{\text{liquid}} U L_s / \mu$

We – Weber number, $= \rho_{\text{liquid}} U^2 L_s / \sigma$

Oh – Ohnesorge number, $= \mu / \sqrt{(\rho \sigma L_s)}$

Ma – Mach number, $= U / \text{speed sound}$

ρ - density

μ – viscosity

L_s – Length scale

σ – surface tension

τ - stress tensor

LES - Large Eddy Simulation

RANS - Reynolds Averaged Navier Stokes

DNS - Direct Numerical Simulation

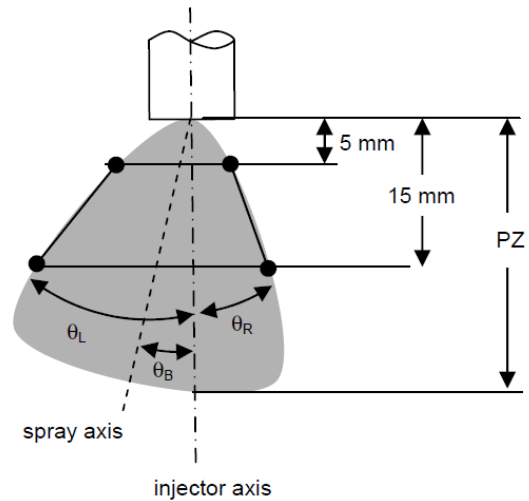
This work will follow the SAE standard J2715 for spray nomenclature and measurement specification [42] terminology. Since fuel spray measurement and characterization is critical to

the automotive industry, a comprehensive industry-wide set of measurement and reporting procedures and nomenclature was established to correct a situation where many spray parameters and test procedures had been created and utilized within individual automotive manufacturers, tier-one fuel system manufacturers, and third-party testing laboratories and universities. The SAE standard provides very detailed procedures and test specifications for all of the spray parameters, and establishes a neutral, unbiased test for each defined spray parameter. The adoption of a standard permits researchers to compare results from various published works with expectation of consistent definition and measure.

Table 1 Overview of Primary Spray Characterization Variables

SPRAY CHARACTERIZATION PARAMETER (SAE Primary Set)	TYPE OF TEST PROCEDURE IN SAE J2715			
	Spray Imaging	High-Res Patternation	Phase-Doppler Interferometry	Laser Diffraction
Spray Angle	✓ (G-DI)	×	×	×
Main Spray Tip Penetration	✓ (G-DI)	×	×	×
Sac Spray Tip Penetration	✓ (G-DI)	×	×	×
Cone Angle	×	✓ (PFI)	×	×
Separation Angle (Dual Spray Injector)	×	✓ (PFI)	×	×
Cone Bend Angle (Bent Spray Injector)	×	✓ (PFI)	×	×
Centroid Angle	×	✓ (PFI)	×	×
Sauter Mean Diameter	×	×	✓ (PFI & G-DI)	✓ (PFI & G-DI)
Dv90	×	×	✓ (PFI & G-DI)	✓ (PFI & G-DI)
Dv50	×	×	×	✓ (PFI & G-DI)

PZ = penetration
 θ_L = left spray half-angle
 θ_R = right spray half-angle
 θ_S = spray angle = $\theta_L + \theta_R$
 θ_B = spray bend angle = $|\theta_L - \theta_R|/2$



PZ = penetration
 θ_S = spray angle = $|\theta_L - \theta_R|$
 θ_B = spray bend angle = $\theta_R + |\theta_L - \theta_R|/2$

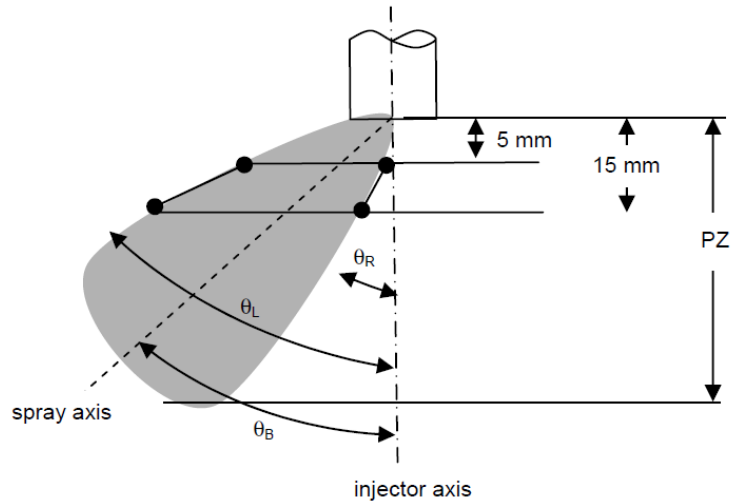


Figure 23 Determination of the SAE J2715 Spray Angle and Spray Bend Angle from a Digital Image of the Spray

The spray angle is a measure of the angular extent of a GDI fuel spray, and is determined by backlit imaging. It is defined as the angle between the spray edges at 5mm and 15mm axially downstream from the injector tip at 1.5ms after the start of fuel (SOF). This angle is denoted as θ_s , and is illustrated schematically in Figure 23. The details

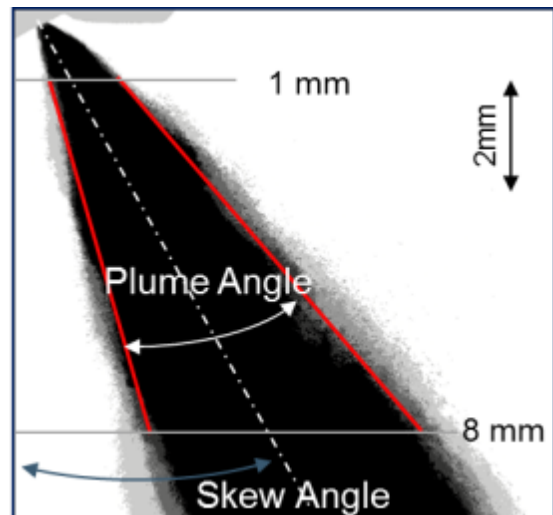


Figure 24 Nomenclature for near-field Plume angle

of how the test for spray angle is to be conducted and reported are provided in Section 6.1 of the SAE standard. For the purpose of this paper, some measures of individual plumes in the near-field are desired. The nomenclature used will be plume angle, as shown in Figure 24. It is important to note that the spray angle, represented and described for GDi injectors, differs conceptually from the cone angle of a PFI spray, which is not calculated by imaging, but by a patternation test. Some literature still refers to cone angle when discussing GDi sprays; however, since the spray angle for GDi is determined by optical spray imaging, it will provide only a measure of the angular extent between spray edges, not the mass distribution between them. Hence, the distinctly different and non-interchangeable names, spray angle (GDi) and cone angle (PFI), describing two different metrics should *not* be interchanged.

4.2 Test Hardware

GDi injector and special seats for study are based on production applications of the side-mount and center-mount type shown in Figure 4. The design of the product was developed using a Design for Six Sigma innovation methodology [43]. Several unique features resulted from the methodology including a decoupled armature, providing for low bounce thus minimizing audible noise and after-closing injections, a valve group optimized for fast response and low shot-to-shot flow variation, and a valve group designed for accurate spray targeting. A cross-section of the injector showing the actuator coil and armature details and valve seat group is presented in Figure 25.

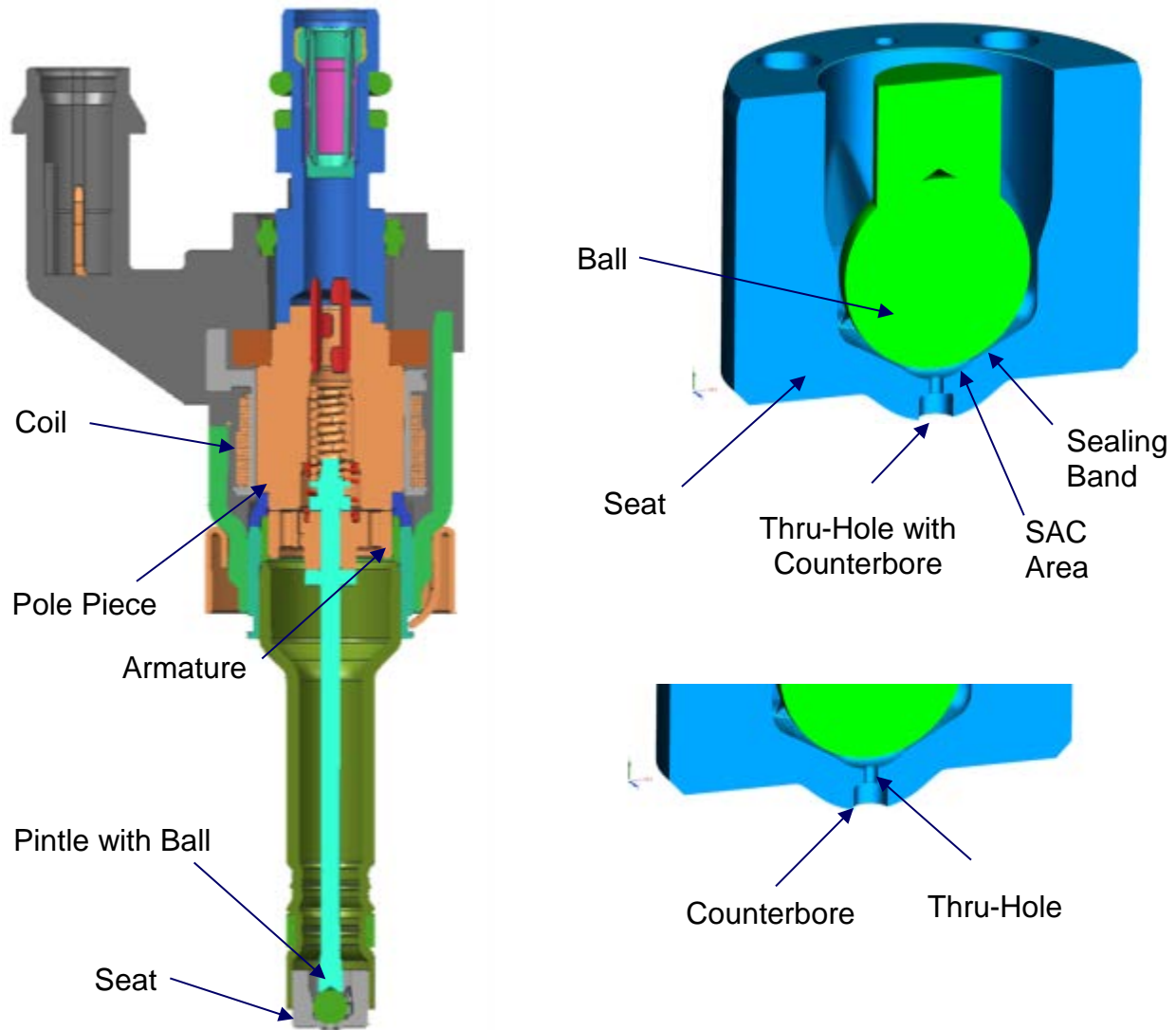


Figure 25 Cross-section views of GDI injector and Seat Nozzle geometry

To facilitate the study of nozzle parameter design on spray characteristics, a series of special seats were designed incorporating the desired geometry per the definition provided in Figure 26, as shown in Table 2, Injector spray study prototype seat definition. The initial study focused on axis-symmetric single-hole nozzles, seats 1-6, and 10-12. This direction followed previous work on diesel nozzles with the desired benefit of a clearer view of the spray morphology by focusing on a single spray plume downstream unaffected by other plumes. A typical GDI injector application has 5 to 6 spray plumes and a temporal spray study would be

difficult due to the high liquid density, especially at the higher 20MPa injection pressure test conditions. The baseline nozzle is typical of production GDi injectors with a $\approx 0.20\text{mm}$ diameter thru-hole of $\approx 0.22\text{mm}$ length exiting in a $\approx 0.50\text{mm}$ diameter counterbore of $\approx 0.37\text{mm}$ length. More specific values are not included at the request of Delphi to maintain proprietary information; however, all listed approximations are scaled to the $\approx 0.20\text{mm}$ reference, and therefore the calculations for ratios that are key to

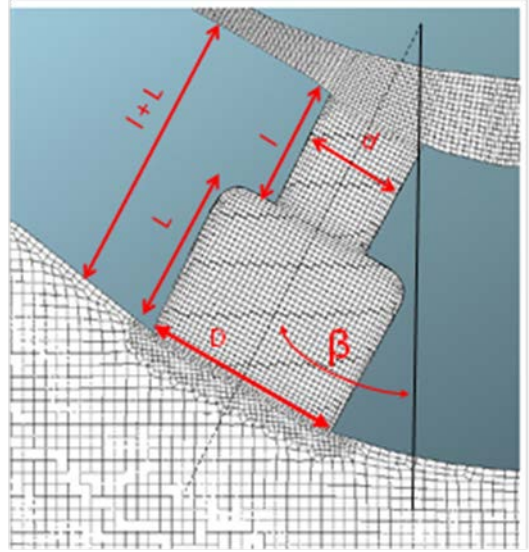


Figure 26 Definition of thru-hole, Counterbore and skew angle geometry







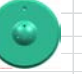






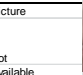







this work, are accurately represented. The counterbore serves several functions; first it allows the thru-hole l/d to be in a practical range for manufacture while maintaining the overall seat thickness of $l+L$ to maintain structural integrity for the high pressure. The counterbore also provides a buffer for the thru-hole exit from the high temperatures of the combustion chamber. One critical design requirement is robustness to buildup of deposits at the nozzle exit since they directly impact spray morphology and hence combustion performance. The defined baseline geometry for seat 1 is then defined as:


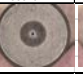
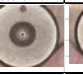



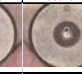


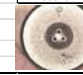



$$\frac{l}{d} = \frac{\approx 0.2}{\approx 0.22} = 1.10 \qquad \frac{(l+L)}{d} = \frac{(\approx 0.22 + \approx 0.37)}{\approx 0.22} = 2.95 \qquad \frac{D}{d} = \frac{\approx 0.5}{\approx 0.2} = 2.50$$

Seat 2 targeting a long l/d is produced by elimination of the majority of the counterbore increasing l to $\approx 0.60\text{mm}$. Seat 3 was defined as the baseline with the counterbore ground off generating the same l/d to isolate the effect of the counterbore. Seats 4-6 repeated the sequence, but with a different thru-hole diameter also indicative of production GDi injectors, to isolate the effect of d independently of ratio l/d . Seats 10-12 duplicated the geometry, but with a skew

angle of 30°, typical of application where each spray plume is defined to target areas in the combustion chamber for optimized atomization and mixing, while avoiding impingement on surfaces of the valves, piston, or cylinder wall. Seats 7-9, derived from the baseline geometry, also included a skew angle, and as well added additional thru-holes to understand the effects that multi-hole fluid motion has on spray morphology.

Table 2 Injector spray study prototype seat definition

AK29	01	02	03	04	05	06	07	08	09	10	11	12
test nozzles	SHN(baseline)	SHN2(Long)	SHN3(short)	SHN4(small)	SHN5(s-L)	SHN6(s-s)	3HN(baseline)	3HN2(long)	3HN3(short)	SHN4(small)	SHN5(s-L)	SHN6(s-s)
d(mm)	≈0.20	≈0.20	≈0.20	≈0.15	≈0.15	≈0.15	≈0.20	≈0.20	≈0.20	≈0.15	≈0.15	≈0.15
l (mm)	≈0.22	≈0.60	≈0.22	≈0.16	≈0.60	≈0.16	≈0.22	≈0.60	≈0.22	≈0.16	≈0.60	≈0.16
D(mm)	≈0.50	≈0.22	ground	≈0.37	≈0.15	ground	≈0.55	≈0.22	ground	≈0.37	≈0.15	ground
L (mm)	≈0.37	na	na	≈0.43	na	na	≈0.407	na	na	≈0.43	na	na
β	0°	0°	0°	0°	0°	0°	~30°	~30°	~30°	~30°	~30°	~30°
l+L (mm)	≈0.60	≈0.60	≈0.22	≈0.60	≈0.60	≈0.16	≈0.60	≈0.60	≈0.22	≈0.60	≈0.60	≈0.16
l/d	1.10	2.95	1.10	1.10	3.96	1.10	1.10	2.95	1.10	1.10	3.96	1.10
(l+L)/d	2.95	na	na	3.96	na	na	2.95	na	1.10	3.96	na	na
D/d	2.50	na	na	2.50	na	na	2.50	na	na	2.50	na	na
Effects of # of Holes	1	1	c-bore	1	1	1	multi-hole	l/d	c-bore	1	1	1
			This is the same as #2, but grind flat on tip just to the bottom of the CB			This is the same as #5, but grind flat on tip just to the bottom of the CB			This is the same as #7, but grind flat on tip just to the bottom of the CB			This is the same as #11, but grind flat on tip to the bottom of the CB
Qty of Seats	5	5	5	5	5	5	5	5	5	5	5	5
Seat P/N	28331614A	28331614B	28331614C	28331614D	28331614E	28331614F	28331614G	28331614H	28331614I	28331614J	28331614K	28331614L
Solid Model												
Seat Prototype												

EWO	Proposed 2012 round of seats										Added to order 11JUL12		
AK29	13	14	15	16	17	18	19	20	21	22	23	24	07
	SHN(baseline)	l/d short	l/d mid	mid c/b	m c/b w/ 30 angle	narrow c/b	n c/b w/ 30 angle	B w/ 10 angle	B w/ 20 angle	B w/ 30 angle	B w/ 10 angle	B w/ 20 angle	3HN(baseline)
d(mm)	≈0.20	≈0.20	≈0.20	≈0.20	≈0.20	≈0.20	≈0.20	≈0.20	≈0.20	≈0.20	≈0.20	≈0.20	≈0.20
l (mm)	≈0.22	≈0.11	≈0.33	≈0.22	≈0.22	≈0.22	≈0.22	≈0.22	≈0.22	≈0.22	≈0.22	≈0.22	≈0.22
D(mm)	≈0.50	≈0.50	≈0.50	≈0.40	≈0.40	≈0.30	≈0.30	≈0.50	≈0.50	≈0.50	≈0.50	≈0.50	≈0.50
L (mm)	≈0.37	≈0.48	≈0.28	≈0.37	≈0.37	≈0.37	≈0.37	≈0.37	≈0.37	≈0.37	≈0.37	≈0.37	≈0.37
β	0°	0°	0°	0°	30°	0°	30°	10°	20°	30°	10°	20°	~30°
l+L (mm)	≈0.60	≈0.60	≈0.60	≈0.60	≈0.60	≈0.60	≈0.60	≈0.60	≈0.60	≈0.60	≈0.60	≈0.60	≈0.60
l/d	1.10	0.55	1.65	1.10	1.10	1.10	1.10	1.10	1.10	1.10	1.10	1.10	1.10
(l+L)/d	2.95	2.95	2.95	2.95	2.95	2.95	2.95	2.95	2.95	2.95	2.95	2.95	2.95
D/d	2.50	2.50	2.50	2.00	2.00	1.50	1.50	2.50	2.50	2.50	2.50	2.50	2.50
Effects of		l/d	l/d	D/d	D/d & β	D/d	D/d & β	β	β	β	β	β	multi-hole
# of Holes	1	1	1	1	1	1	1	1	1	1	3	3	3
Qty of Seats	5	5	5	5	5	5	5	5	5	5	5	5	5
seat P/N	28331614M	28331614N	28331614O	28331614P	28331614Q	28331614R	28331614S	28331614T	28331614U	28331614V	28331614T	28331614U	28331614G
Seat Prototype													

An additional seat added to the study was a tapered nozzle similar to those used in diesel injectors. The geometry was defined to have an identical exit diameter as the comparable cylindrical seat and an 8° taper to the thru-hole inlet at the injector sac, as shown in Figure 27.

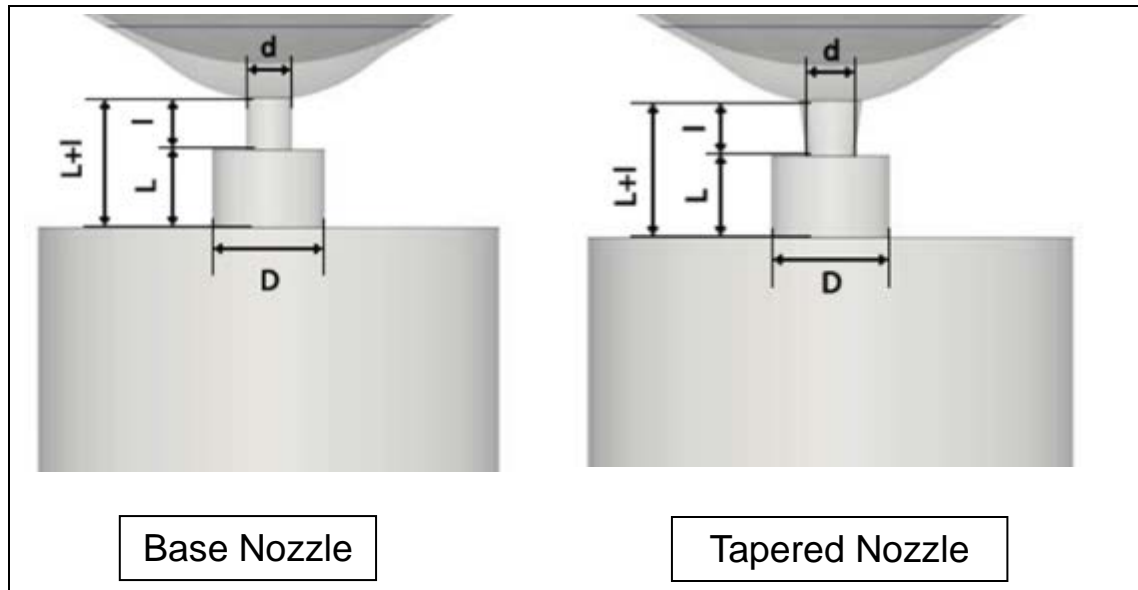


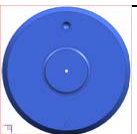








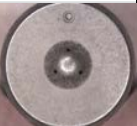


Figure 27 Tapered Nozzle definitions with common exit diameter

Following the first year of study, an adjusted prototype seat matrix was selected based on initial spray analysis at Technical Center Rochester for evaluation in the Spray Lab at Customer Technical Centre Luxembourg, these seats are listed in Table 3.

Table 3 Injectors for Spray Characterization Luxembourg Spray Laboratory

EWO	AK29-3	AK29-3	AK29-6	AK29-9			AK29-10	AK29-11
suffix	-001	-002	-002	-001			-3-003	-2-002
Feature	Single hole	Single hole	Single hole	hole 1	hole2	hole 3	3-hole	3-hole
d(mm)	≈0.20	≈0.20	≈0.15	≈0.20	≈0.20	≈0.20	≈0.15	≈0.15
l (mm)	≈0.22	≈0.22	≈0.16	≈0.22	≈0.22	≈0.22	≈0.16	≈0.60
D(mm)	ground	ground	ground	ground	≈0.55	≈0.55	≈0.37	na
L (mm)	na	na	na	na	≈0.407	≈0.407	≈0.43	na
β	0°	0°	0°	~30°	~30°	~30°	~30°	~30°
l+L (mm)	na	na	na	na	≈0.60	≈0.60	≈0.60	na
l/d	1.10	1.10	1.10	1.10	1.10	1.10	1.10	3.96
(l+L)/d	1.10	1.10	1.10	na	2.95	2.95	3.96	na
D/d	na	na	na	na	2.50	2.50	2.50	na
Effects of	Baseline	Baseline	small d	CB	CB	CB	small d, CB	Long l/d
# of Holes	1	1	1	3	3	3	3	3
g/s @ 10MPa	3.34	3.14	1.86	7.69	7.69	7.69	5.29	5.46
g/s @ 10MPa	3.34	3.14	1.86	2.56	2.56	2.56	1.76	1.82
			identical l/d with smaller d	Seat with 1 hole ground to eliminate CB			identical l/d with smaller d	Long l/d no CB
Seat S/N	28331614	28331614	28331614	28331614	28331614	28331614	28331614	28331614
Injector S/n	1304	1304	1306	1308	1308	1308	1313	1315
Solid Model								
Seat Prototype								

4.3 Test Equipment and Data Acquisition Systems

4.3.1 Shadowgraph Optical Imaging

The experimental spray bench at Delphi Customer Technical Centre Luxembourg comprises of the fuel supply, test injector fixture, illumination source, camera mounting, and additional spray measurement equipment. It incorporates a multi-functional capability that enables complementary laser diagnostic techniques. The spray imaging investigations utilize a shadowgraph imaging technique for visualization of the spray development, which with the aid of data analysis software, enables automatic extraction of the relevant spray spatial-temporal development data. In the optical investigations, the spray “side” imaging arrangements is used to capture the spray breakup structure, trajectory (especially deviation from the nozzle skew angle), and plume angle. The imaging utilizes laser illumination and a macroscopic zoom lens in order to capture the structure of the high-speed spray in close proximity of the nozzle exit. The Shadowgraph Optical Imaging experimental setup, shown in Figure 28, employs a laser light source, fluorescence screen dye diffuser plate, target injector for spray with pressurized fuel supply, and CCD camera. Synchronization of the camera, light source, and injector actuation is realized by the imaging system.

Analysis of the image is performed by an automated image capture program using parameters defined per SAE [42], as shown in Figure 29. It should be noted that Spray angle, as defined by SAE, envelopes all spray plumes in each view. In this work, we will focus only on single plume structures, and when evaluating near field spray, alternative measurement lengths of 1mm and 8mm downstream from the nozzle tip will be utilized, as documented in 4.1 Defined Terms.

Shadowgraph Optical Image acquisition instrumentation & set-up:

CCD-Camera: LaVision Flow Master
 Camera lens: Nikon 50mm, f#1.8 (retro mounting)
 Camera lens aperture: 4
 Back light: ND-YAG Laser combined with Dye Diffuser Plate
 Fluorescence screen: LaVision Dye Diffuser Plate
 [Light output pulse duration (@ 5 ns input): 20 ns, 580nm]

ND YAG Laser: Quantel Big Sky Laser Twins Ultra (25mJ per cavity)
 Image size: 9 x 8mm (width x height)
 Camera Orientation: 0° & 120° to Injector
 Image acquisition: shot imaging (one spray image per injection)

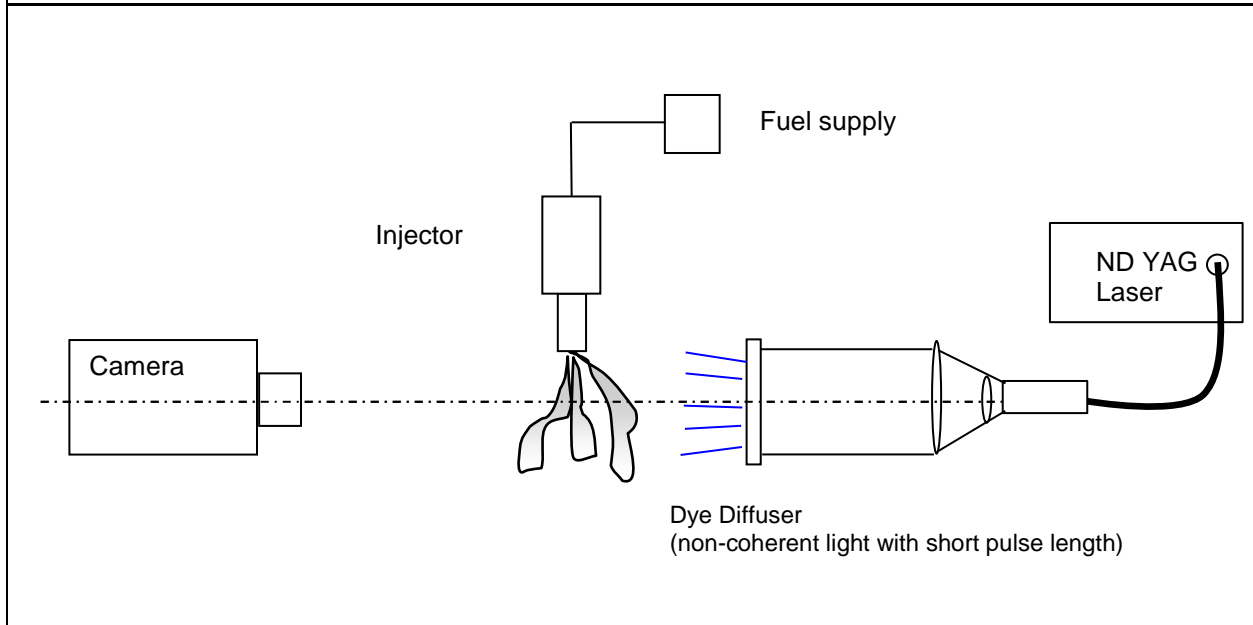


Figure 28 Test Configurations for Shadowgraph Optical Image Capture

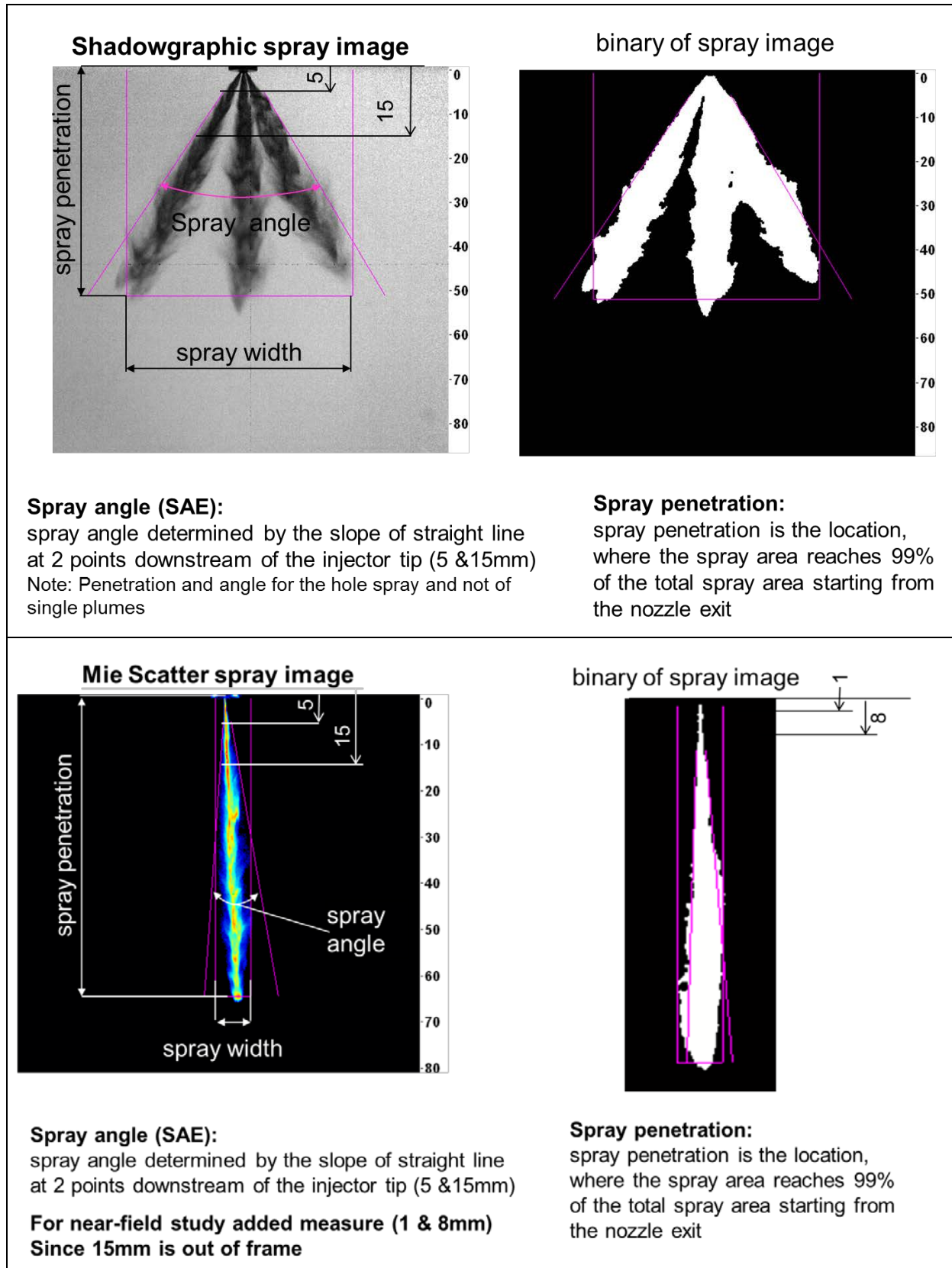


Figure 29 Spray Image Capture definitions for Single Spray Plumes and Complete Sprays

4.3.2 High Speed Integral Mie Imaging

An alternative to shadowgraph imaging is high speed integral Mie imaging to capture spray morphology. LED flash panels provide the light source and a special CCD camera captures the image. The bench setup for front and side views is shown in Figure 30, the configuration can also rotate to capture spray progression from below the injector. Similar to shadowgraph imaging, analysis of the image is performed by an automated image capture program using parameters defined per SAE [42], as shown in Figure 29. A comparison of sprays for injector AK29-11-3-002 captured in both techniques is shown in Figure 31. It can be seen there were plume issues for this injector and both imaging techniques capture the phenomena.

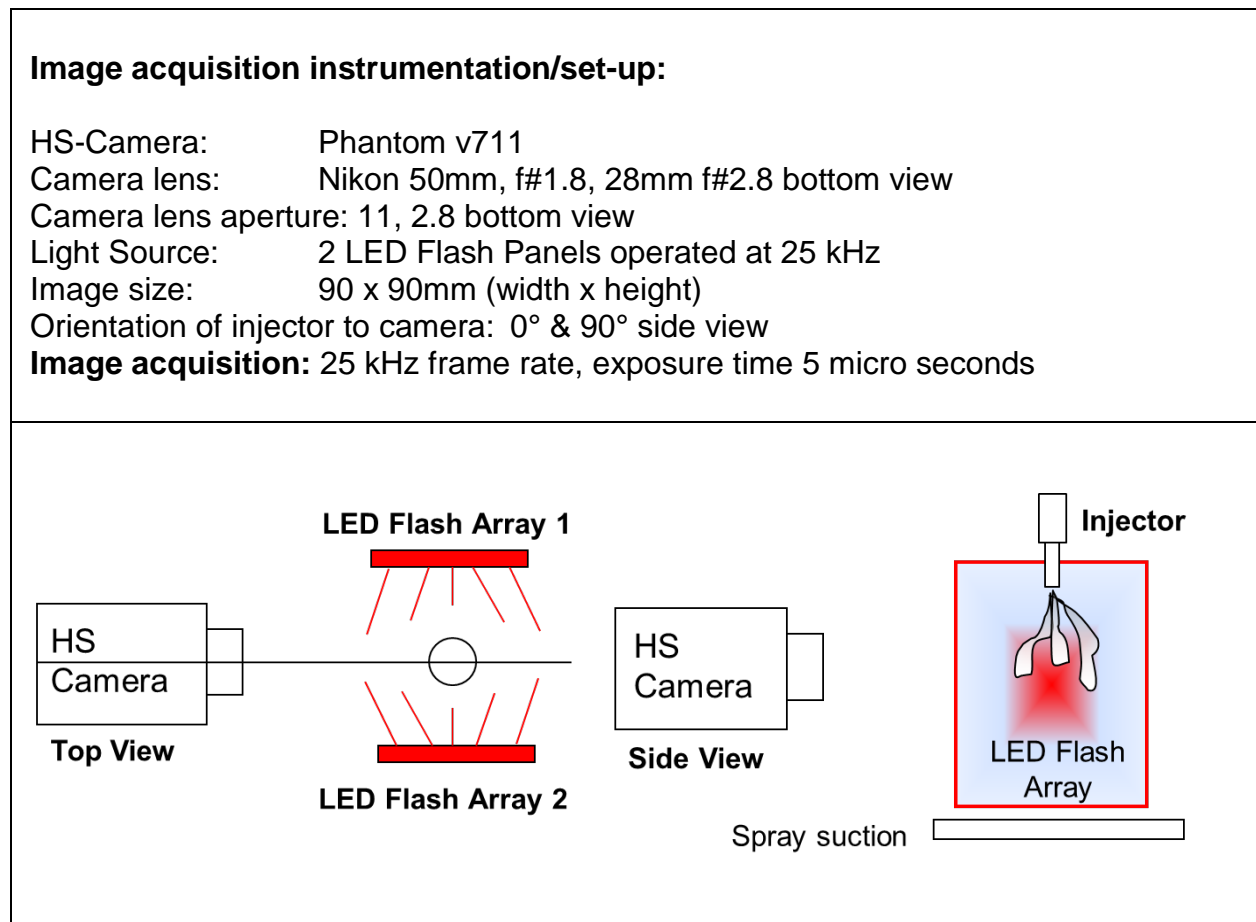


Figure 30 Test Configurations for High Speed integral Mie Image Capture

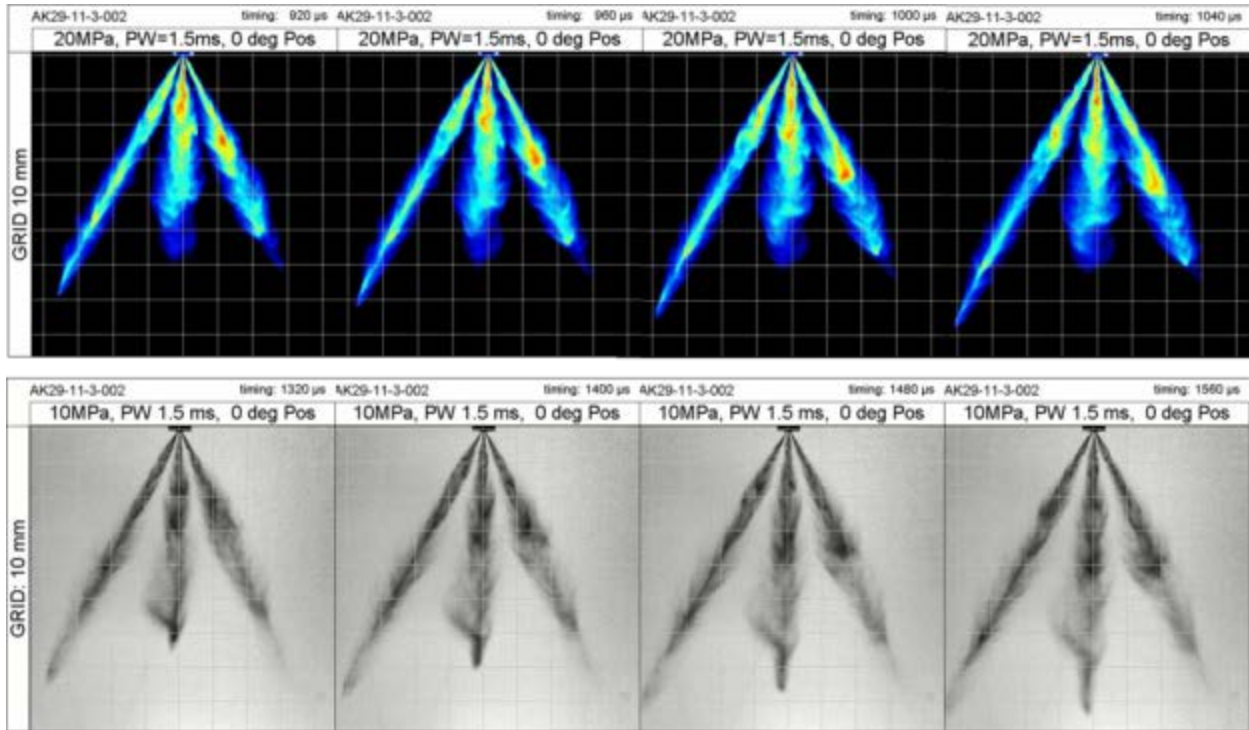


Figure 31 Comparisons of Shadowgraph and High Speed Mie Imaging for Injector AK29-11-3-002

4.3.3 Laser Diffraction Technique

A key characteristic of injector spray is spray particle, or droplet size, determination. The Delphi spray lab test bench, shown in Figure 32, uses a commercially available Laser Diffraction product, the Malvern Spraytec 2000 [44], which measures droplet size distributions using the technique of laser diffraction. The technique is Fraunhofer diffraction where the scattering of light around particles produces varying intensities of wavelengths proportional to the particle size. Malvern can also use Mie theory diffraction, which provides for better small particle resolution when reference data for the fluid is available. Diffraction requires the angular intensity of light scattered from a spray to be measured as it passes through a laser beam. The recorded scattering pattern is then analyzed using a proprietary multiple scattering algorithm to yield a size distribution. The angular range where scattering measurements are made has been optimized to ensure diverse size distributions are fully resolved. This ensures accurate particle size distributions can be measured at up to 98% obscuration. The test setup shows the laser

passes through the spray at 50mm distance per the SAE standard, as shown in Figure 33. For this work, the 3-hole injectors were rotated so direct comparisons to the single-hole injectors could be made.

Malvern Spraytec 2000

- Method: Fraunhofer diffraction of parallel monochromatic light
diffraction angle $\sim 1/d_{\text{particle}}$
- Line of sight measurement
limited by dense sprays: extinction of beam $< 8\%$
- Sampling frequency: 20 kHz
Scan interval: 30 μ s at 20 kHz

Focal length 200mm
Laser beam diameter 15mm
Injection Frequency 10Hz
No. of repetitions 20
Integration time: 0-7 ms after ASOI

- Size range (focal length lense)

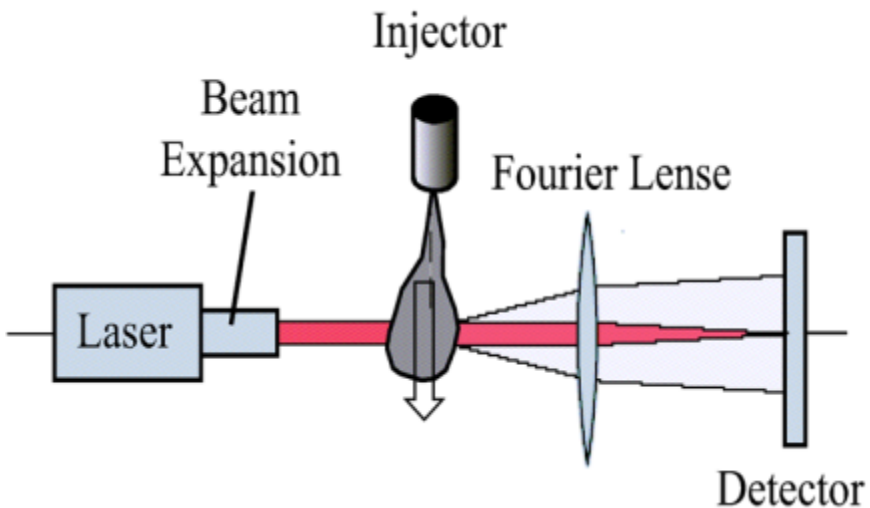
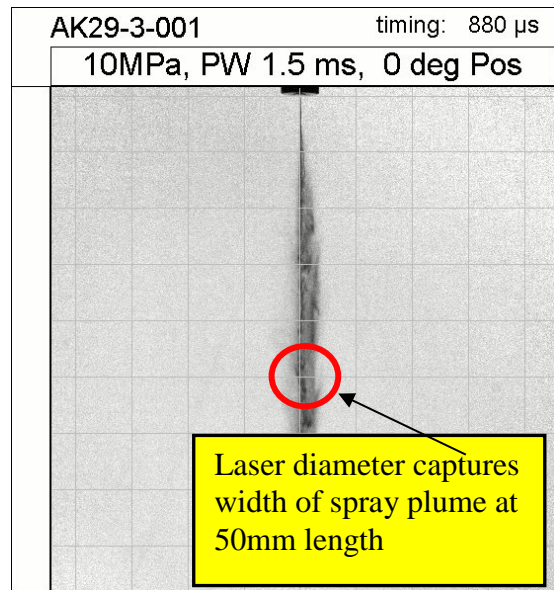
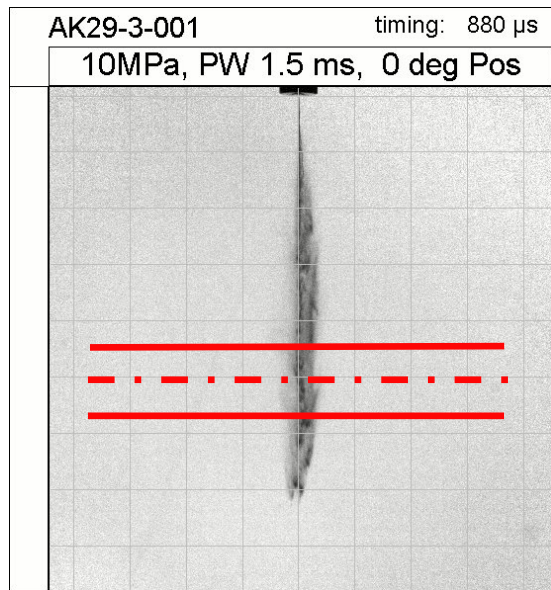
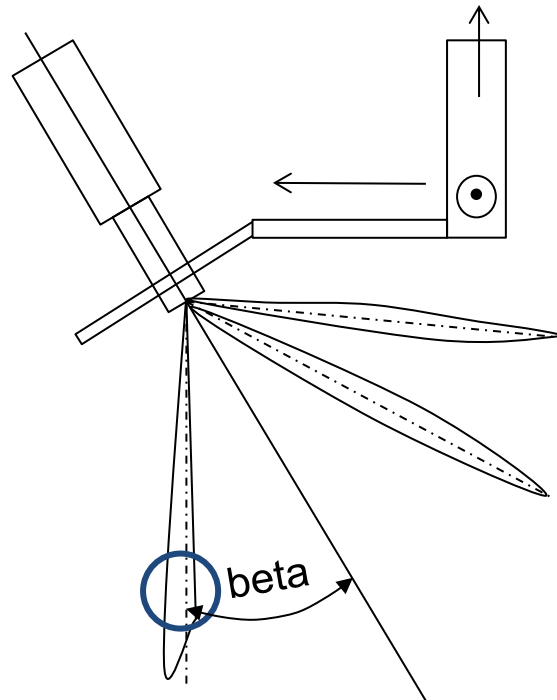


Figure 32 Particle Size Distribution determined using Laser Diffraction Technique

For the 3-hole injectors the spray plume has been oriented, so that the spray is vertical, similar to the single-hole injectors



The laser beam center line is located at 50mm vertical distance from the tip
The laser beam (diameter 15mm) is perpendicular to the spray axis, therefore almost of the spray is captured by the measurement system

Figure 33 Test Configurations for Spray Particle Size Measurement

4.3.4 High Speed Near Nozzle Spray Imaging by Mie Scatter

For the purpose of this study, the ability to capture near field spray development in the immediate vicinity of the nozzle exit was desired. A technique similar to the high speed Mie shadowgraph technique is high speed near-nozzle imaging, applied with changes to the CCD camera and the replacement of the LED flash banks with a continuous monochromatic white light source. Videos are captured at 300 frames per second, providing analysis of the near field spray development. The test setup is shown in Figure 34.

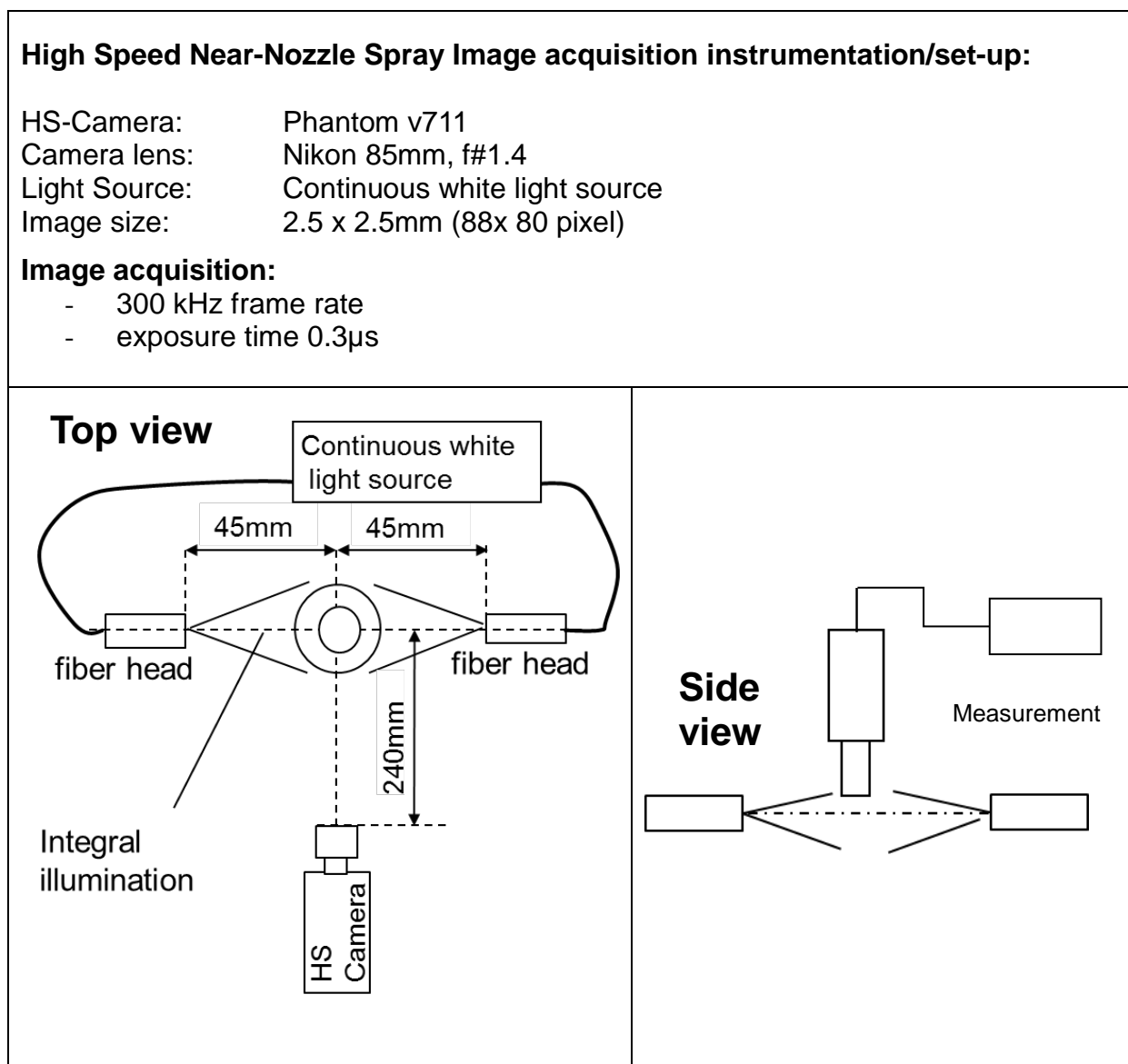


Figure 34 Test Configurations for High Speed Near-Nozzle Spray Image Capture

4.3.5 Phase-contrast X-ray Imaging

The Advanced Photon Source (APS) at the Argonne National Lab experimental bench, shown in Figure 35, utilizes slow and fast shutters, an injector fixture with variable pressure fuel supply, scintillator crystal to convert signal to visible light, and a 45° mirror to direct light to a CCD camera. The X-ray beam is generated from an insertion device (undulator) in the APS electron storage ring. The special beam pattern (hybrid singlet mode), shown in Figure 35, was used in this experiment. This pattern contains a single electron bunch (150ps duration and carrying 16 mA current) isolated from the remaining electron train bunch (472 ns long, 96 mA) by symmetrical 1.594 μ s gaps. To reduce the heat power, the X-ray beam is gated by two mechanical shutters: the slow shutter operating at 1Hz frequency with 10ms opening duration and the fast shutter operating at 2kHz frequency with 9 μ s opening duration. Synchronized operation of these two shutters cuts-off more than 99% of the beam heat power. After being transmitted through the spray, the X-ray beam generates the phase-contrasted image on the scintillator crystal (LYSO:Ce), which converts the transmitted X-ray beam into the visible light spectrum (432nm). This image is reflected by a 45° mirror and then captured by a charge coupled device (CCD) camera (Sensicam, 1376x1040 pixels, from Cooke). The camera was gated at the timing when only the singlet electron bunch passed through the shutters. The remaining electron bunches were cut-off by closing the camera gate at 1.5 μ s after the gate opening (yielding exposure time of 1.5 μ s). The field of view of the camera was 1.75mm x 1.32mm when a 10x objective lens (NA=0.14) was used. The fuel was injected into a spray chamber using a high pressure rail GDi injection system composed of fuel tank, motor, high-pressure pump, pressure control valve, and high-pressure rail. The pressure inside the rail was controlled via feedback control of measured pressure inside the rail and bleeding fuel flow rate

of the pressure valve. The spray chamber has two Kapton windows, which allow the X-ray beam to pass through this without loss of intensity. Synchronization of the camera, the shutters, and the injector actuation is realized by the imaging system.

Phase-Contrast X-ray Image acquisition instrumentation & set-up:

CCD-Camera: Cooke Sensicam, 1376×1040 pixels,
Scintillator crystal: (LYSO:Ce), converts X-ray beam into visible light (432 nm).

Synchrotron X-ray: 150 ps duration from a single 16mA electron bunch
Image size: 1.74×1.32mm
Camera Orientation: 0° to injector (normal to spray)
Image acquisition: 1.26μm/pixel with 5x objective lens

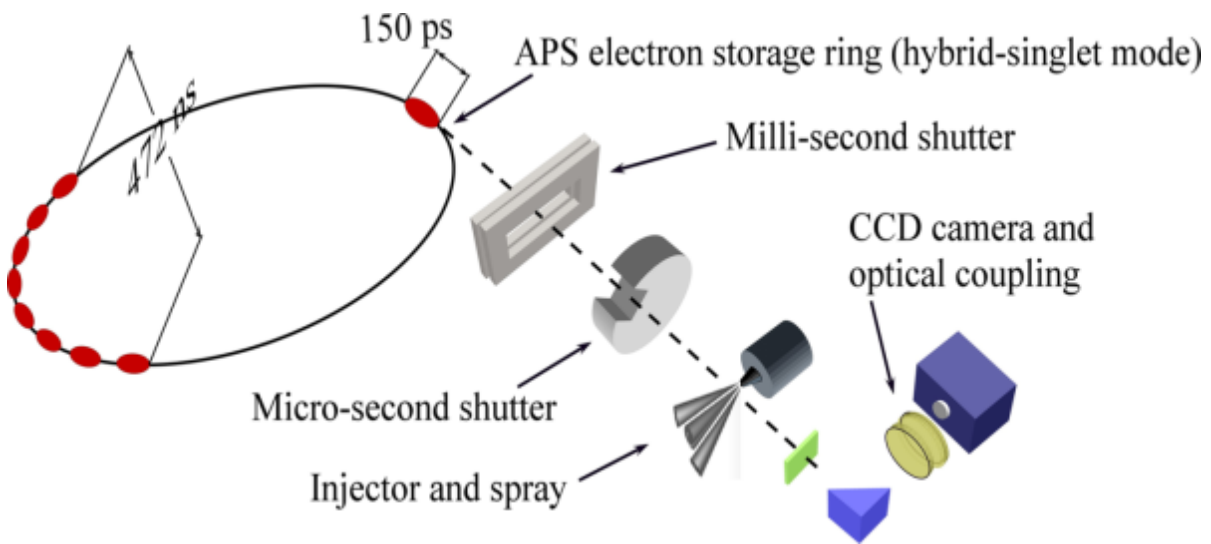


Figure 35 Test Configurations for Phase-Contrast X-ray Image Capture

4.4 Simulation and Modeling

4.4.1 Conservation Equations of Multi-Phase System

The mathematical modeling practice is similar to de Villiers [44] [45], based on the transport equations for the conservation of mass and momentum of a two-phase flow system, comprised of two immiscible, incompressible Newtonian fluids, including the surface tension.

The single set of conservation equations that describe the flow of a two-phase mixture are:

$$\frac{\partial \rho}{\partial t} + \nabla \cdot (\rho U) = 0 \quad (1)$$

$$\frac{\partial \rho U}{\partial t} + \nabla \cdot (\rho U \otimes U) = -\nabla P + \nabla \cdot \tau + \int_{S(t)} \sigma \kappa' n' \delta(x - x') ds \quad (2)$$

Where, U is the velocity, ρ is the density, σ is the surface tension coefficient, τ is the stress tensor, κ is the curvature of the liquid surface, n represents a unit vector normal to the liquid surface, and $\nabla ()$ and $\nabla \cdot ()$ denote the gradient and the divergence operations, respectively.

The integral term in equation (2) represents the momentum source due to surface tension: it is effective at the interface of the liquid surface $S(t)$ over the entire liquid volume. This is an important source term in the numerical simulation of the liquid jet breakup process. The evaluation of this term is achieved through the Continuum Surface Force (CSF) model of Brackbill [46] as:

$$\int_{S(t)} \sigma \kappa' n' \delta(x - x') ds \approx \sigma \kappa \nabla \alpha \quad (3)$$

Where α is the “volume-of-liquid” phase-fraction, which is obtained from solution of a transport equation, and κ is the “curvature of the interface”, estimated from the solution of the phase-

fraction α as:

$$\kappa = \nabla \cdot \left(\frac{\nabla \alpha}{|\nabla \alpha|} \right) \quad (4)$$

Equation (4) is valid for cases with constant surface tension, as in the case of the present study.

In case of variable surface tension, e.g. in case of spatially non-uniform composition or temperature distribution, surface tension gradients are encountered that generate additional shear stress at the interface that must be taken into account.

4.4.2 Large-Eddy-Simulation Method

The VOF-LES equations are derived from equations (1) to (3), through a process of local volume averaging of the phase-weighted hydrodynamic variables. This entails decomposition of the dependent variables into resolvable and computational sub-grid scales of turbulent fluctuations, and application of a filter that removes the sub-grid scale fluctuations from the direct numerical simulation. The filtering process, in conjunction with the non-linear term in equation (2), produces additional terms, involving correlations of the hydrodynamic variable fluctuations at sub-grid scales that require closure with the aid of mathematical models. The most notable of these terms is the Sub-Grid-Scale (SGS) stress tensor that represents the effect of unresolved scales of turbulence on the momentum transport process and its viscous dissipation.

The Sub-Grid-Scale (SGS) stress is defined as:

$$\tau_{sgs} = (\widetilde{U\tilde{U}}) - \tilde{U}\tilde{U} \quad (5)$$

Where \tilde{U} is the filtered instantaneous velocity field. The closure of the SGS stress is provided through a sub-grid-scale “eddy-viscosity” model as:

$$\tau_{sgs} = \frac{2}{3} \kappa \mathbf{I} - \frac{\mu_{sgs}}{\rho} (\nabla \tilde{U} + \nabla \tilde{U}^T) \quad (6)$$

Where K is the SGS turbulence kinetic energy and μ_{sgs} is the SGS turbulent viscosity. These SGS turbulence parameters are obtained through solution of a transport equation for the SGS turbulence kinetic energy, according to Yoshizawa [21].

$$\frac{\partial K}{\partial t} + \nabla \cdot (K \tilde{U}) = -\nabla \cdot \left[(\nu + \nu_{sgs}) \nabla K + \tau_{sgs} \cdot \tilde{U} \right] - \frac{1}{2} \tau_{sgs} : (\nabla \tilde{U} + \nabla \tilde{U}^T) - \varepsilon \quad (7)$$

Where $\varepsilon = C_\varepsilon K^{3/2} / \Delta$ is the SGS turbulence dissipation rate, $\nu_{sgs} = C_K K^{1/2} \Delta$, and Δ is the SGS length scale (equivalent to the local computational cell size). The turbulence model constants have the values $C_K = 0.07$ and $C_\varepsilon = 1.05$, in accordance with Yoshizawa [22].

The additional SGS terms associated with the transport equations involve correlations of the sub-grid fluctuations of the phase-fraction, density, surface tension, etc., that are neglected in the absence of mathematical closure models, following the work of de Villiers et al [45].

4.4.3 VOF-Based Interface-Tracking Method

The principle of the “Volume of Fluid” (VOF) approach is that a two- (or indeed multi-) phase system can be represented as a mixture of phases where the phase-fraction distribution includes sharp, yet resolvable, transitions between the phases. Accordingly, the interface in a two-phase flow system is computed with the aid of the transport equation for the liquid volume fraction as the indicator function to locate the interface. The transport equation for the phase fraction α , for two incompressible fluids, is:

$$\frac{\partial \rho \alpha}{\partial t} + \nabla \cdot (\rho U \alpha) = 0 \quad (8)$$

According to the definition of α , the mixture thermo-physical properties are calculated as:

$$\rho = \alpha \rho_f + (1 - \alpha) \rho_g \quad (9)$$

$$\mu = \alpha \mu_f + (1 - \alpha) \mu_g \quad (10)$$

The VOF interface capture and tracking method is a simple and flexible approach for simulation of multi-phase systems with free surfaces, especially for circumstances where the surface tension effects are not dominant. The main challenge of the VOF methodology relates to the accuracy of the numerical scheme, in order to assure that it simultaneously provides the boundedness and conservation of the flow variables, and that the interface remains sharp, yet is not affected by numerical dispersion and mesh alignment bias [48]. In the present simulations, an advanced method formulated by Open-FOAM Ltd. [49] that adopts a two-fluid formulation of the conventional volume-of-fluid concept, within the frame-work of the finite-volume method, is used. The method employs a formulation of the phase transport equation that includes a “compression velocity” term [50], which acts to “compress” the VOF interface and maintain a sharp interface resolution. Appropriate numerical schemes are employed to ensure the bounded temporal and spatial discretization with minimum mesh biasing of the compression term and convection of the phase fraction transport equation, but without numerical diffusion or dispersion of the liquid-gas interface.

A comparison of the VOF interface capturing, and tracking, and the numerical solution method in the Open-FOAM code with the alternative “Interface Reconstruction” scheme [51] for prediction of a Rayleigh jet breakup, provides closely similar predictions of the jet structure, breakup length, and droplet size between the two computational methods, in close agreement with the measurements and theoretical analysis [51].

4.4.4 Vortex Identification Method

Identification of vortical coherent structure is an important component of LES allowing for flow visualization or rotating velocity fields. In this work, the term Q will be used for

quantified rotation energy of vortex cores following the most cited convention in the literature [52] [53]. The quantity Q is defined as:

$$Q = \frac{1}{2} (\|W\|^2 - \|S\|^2)$$

Where W is defined as the anti-symmetric part of the velocity gradient tensor:

$$\|W\| = (W:W)^{\frac{1}{2}}$$

$$W = \frac{1}{2} (\nabla \tilde{U} - (\nabla \tilde{U})^T)$$

Where S is the local rate of strain tensor

$$\|S\| = \frac{1}{2} (S:S)^{\frac{1}{2}}$$

$$S = \frac{1}{2} (\nabla \tilde{U} + (\nabla \tilde{U})^T)$$

A large value for Q represents a flow region where the rate of strain is dominated by the rate of rotation.

4.4.5 The Numerical Solution Method

The simulations are performed using Open-FOAM, an open-source finite-volume CFD tool-box [54]. The solution method for the VOF-LES conservation equations in Open-FOAM incorporates a “compressive” formulation of the phase-fraction transport equation, employs special NVD/TVD and a blend of central/upwind schemes for spatial discretization of the transport terms, and a combination of the Crank-Nicholson and Euler-implicit integration schemes for the phase-fraction and the governing conservation equations. The numerical method is intended to afford second-order spatial and temporal discretization maintaining integration accuracy and to assure that the schemes are bounded and preserve the proper physical limits of the fluid dynamic variables.

The “pressure implicit with splitting of operators” (PISO) [55] algorithm, specifically suited to transient flows, is employed for coupled solution of the mass and momentum conservation equations through coupling of the velocity and the pressure fields. The method starts with an initial estimate for the pressure field based on the last time step result. The momentum equation is then used to yield the approximate matching velocity field. The pressure Poisson equation is applied with the divergence of the partial velocity flux as a source term to estimate the pressure field. The corrected pressure field is then used to correct the velocity field. These steps are repeated until convergence criteria are met. In the calculations, the numerical integration time-step is dynamically adjusted according to various stability criteria, and is of the order 1 E-10 to 1 E-9 second.

4.4.6 Computational Domain and Mesh

Figure 36 presents the three-dimensional computational domain that comprises the injector valve-group flow domain and its immediate near-field ambient. The computational mesh is of the order 5 M cells (1 M cells within the injector domain and 4 M cells within the ambient) and affords a spatial resolution in the range 2-5 μm (within the injector seat-nozzle) to 10 μm (within the ambient domain). The effective filter is 2 times the grid size, therefore, 4-10 E-6 m suggests resolved scales will include the Integral scale eddy production range and cascading eddies into the Taylor microscale range and smaller than 4-10 E-6 m will be modeled as Kolmogorov dissipating eddies in the Sub-Grid-Scale (SGS) term.

Table 4 Turbulent Length Scales for 3-hole skew-angled nozzle

<i>Turbulent Reynolds number $Re_L = k^2/\epsilon v$</i>	<i>Integral Scale Eddy production $l_0 = \eta Re_L^{3/4}$</i>	<i>Taylor microscale Cascading eddy $\lambda = (15vu^2/\epsilon)^{1/2}$</i>	<i>Kolmogorov scale Dissipating eddy $\eta = (v^3/\epsilon)^{1/4}$</i>
1.5 E3	3.3 E-5 m	4 E-6 m	2 E-7 m

The simulation run time for this model of 5M cells, covering into the Taylor microscale range, running on a HP Z800 workstation with 2 CPUs each CPU with 6 cores operating at clock speed of 2.4GHz, is listed in Table 5 for 3-hole injector geometry. The CPU execution time depends on the conditions as the simulation time step adjusts dynamically to meet the convergence criteria, generally, 1 μ s of flow simulation required between 2.8 to 3.9 hours of CPU run time.

Table 5 CPU runtime for Flow Simulation of the 5M cell grid

<i>Flow Simulation</i>	<i>CPU time</i>	<i>CPU time</i>
1 μ s	14,000 sec	10,000 sec
	3.9 hours	2.8 hours
100 μ s	389 hours	278 hours
	16.2 days	11.6 days
120 μ s	467 hours	333 hours
	19.5 days	13.9 days

Skew-angled 3-hole nozzles converged with average simulation time step $\sim 1.e-9s - 4.e-9s$ of simulation, and required 100 μ s to reach steady state conditions. Axis-symmetric hole were more time consuming due to the long physical-time to evacuate the air in the sac volume, the calculations required a time step of order $1e-10s$, and at least 120 μ s to reach steady state, or more than one month of execution runtime.

The pintle motion is not included in the simulation due to severe requirements of the VOF-LES method for mesh geometric quality (e.g. orthogonal arrangement, aspect ratio, etc.) that would not permit the extensive mesh deformation required to accommodate the pintle displacement of approximately 45 μ m. Hence, the transient simulation of the seat-nozzle flow development is performed on a fixed geometry mesh with the pintle at the nominal open stroke position. The initial condition fills the nozzle from the inlet to the pintle sealing band with liquid at rest, while the remainder of the computational domain, downstream of the sealing band, is

filled with stagnant air at ambient conditions of the near field. At the start of the calculation, the liquid phase at the inlet boundary is instantaneously accelerated to its nominal velocity corresponding to the static flow for the fuel injection pressure being evaluated.

4.4.7 Boundary Conditions

In the present calculations, the liquid is n-Heptane at $T=293^{\circ}\text{K}$ temperature. The following boundary conditions are employed:

- Inlet: Uniform inlet velocity, corresponding to the nozzle static flow for injection fuel pressure, without imposition of any artificial velocity disturbances
- Outlets : Non-reflective, uniform static ambient pressure
- Walls: zero-slip velocity condition, with law-of-the-wall treatment of the wall shear stress

The outlet boundaries are at sufficient distance from the nozzle to ensure minimum reflection of pressure disturbances that may influence the jet breakup process.

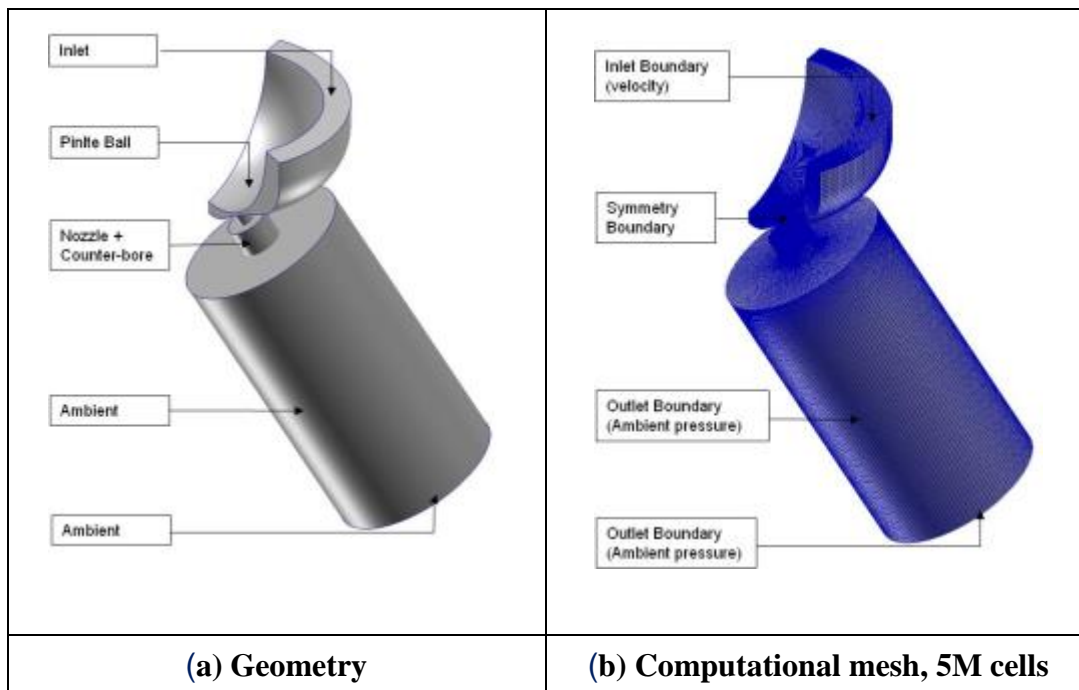


Figure 36 Computational domain, mesh, and boundaries

CHAPTER 5 OUTLINE OF THE RESULTS

5.1 Large Eddy Simulation of GDI Axis-symmetric single-hole Nozzles

The results of this section were published [56] and presented at the SAE World Congress in Detroit in April of 2012. This section summarizes a Large Eddy Simulation of 4 case studies using single-hole axis-symmetric nozzles, as shown in Figure 37. The contrast between the baseline nozzle and nozzle without counterbore should help to understand the effect of the counterbore on spray. Likewise, comparison of the nozzle without counterbore and the long l/d nozzle should show influence of l/d. Lastly, a tapered nozzle similar to those used in diesel applications is introduced to understand its impact on spray.

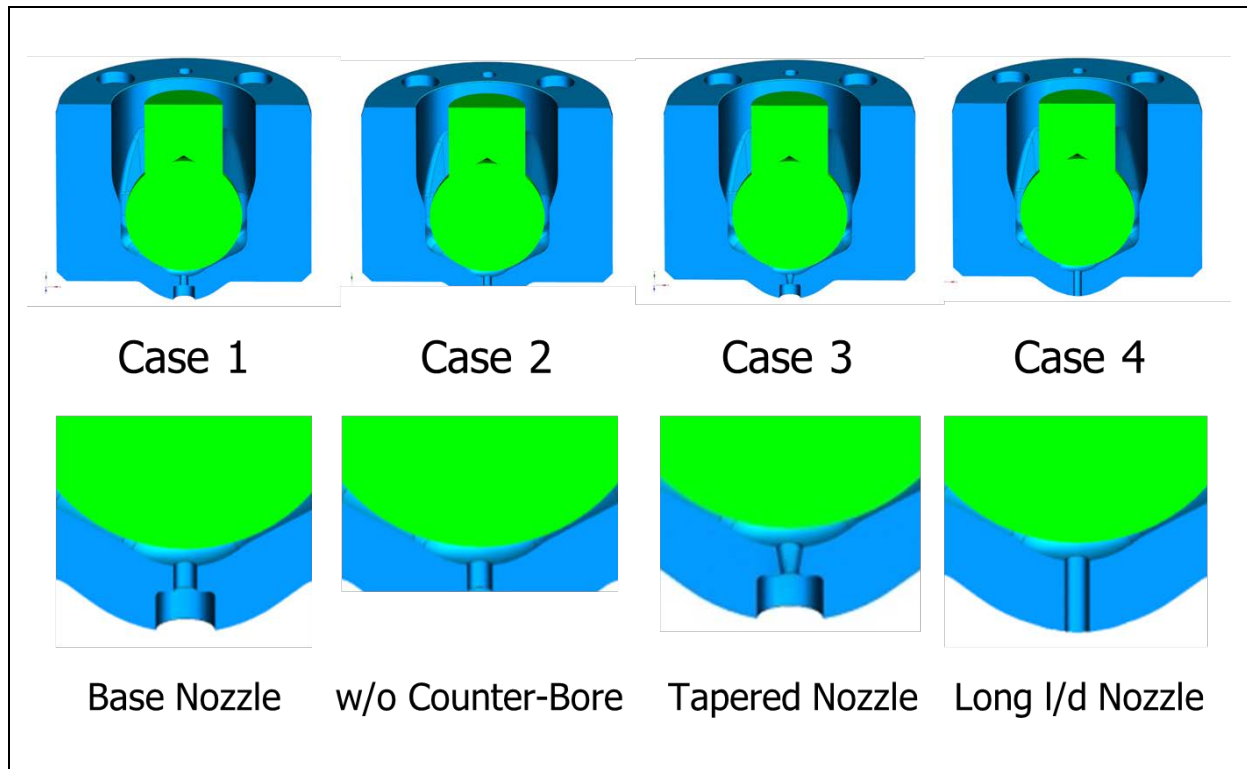


Figure 37 Case studies using axis-symmetric injector nozzles: Base Nozzle, Nozzle w/o Counterbore, Tapered Nozzle, and Long l/d Nozzle

THE SIMULATION RESULTS

5.1.1 Base Nozzle Geometry

The geometry and nozzle dimensions of the Base GDi nozzle are presented in Figure 38. The nozzle diameter, d , is of order 0.2mm. This geometry is representative of the design features of the current production GDi nozzles that incorporate a counterbore to achieve a small nozzle l/d ratio, irrespective of the seat thickness imposed by the structural integrity considerations.

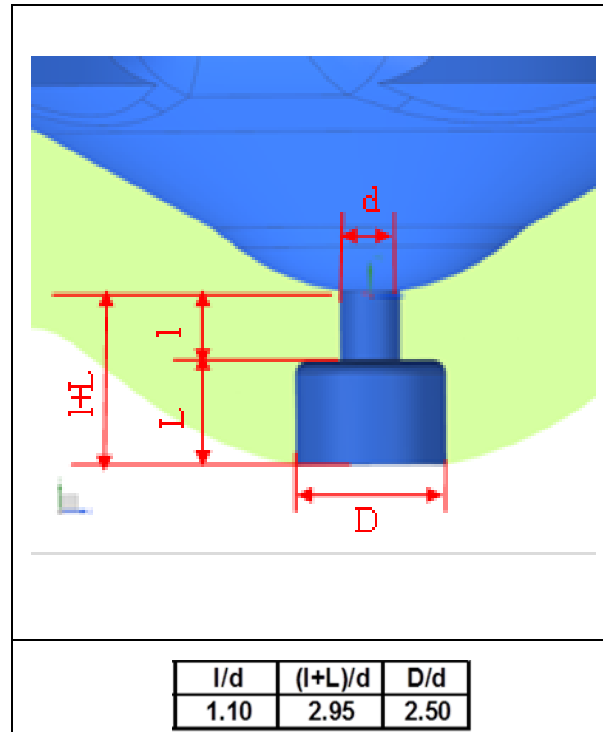


Figure 38 Nozzle geometry and dimensional parameters

The transient development of the flow within the injector seat and nozzle is illustrated by the evolution of the iso-surface plots of $VOF=0.5$, colored by the instantaneous velocity at selected times after the start of simulation, as shown in Figure 39. Figure 40 presents the corresponding VOF contour plots on a symmetry cut-plane through the geometry.

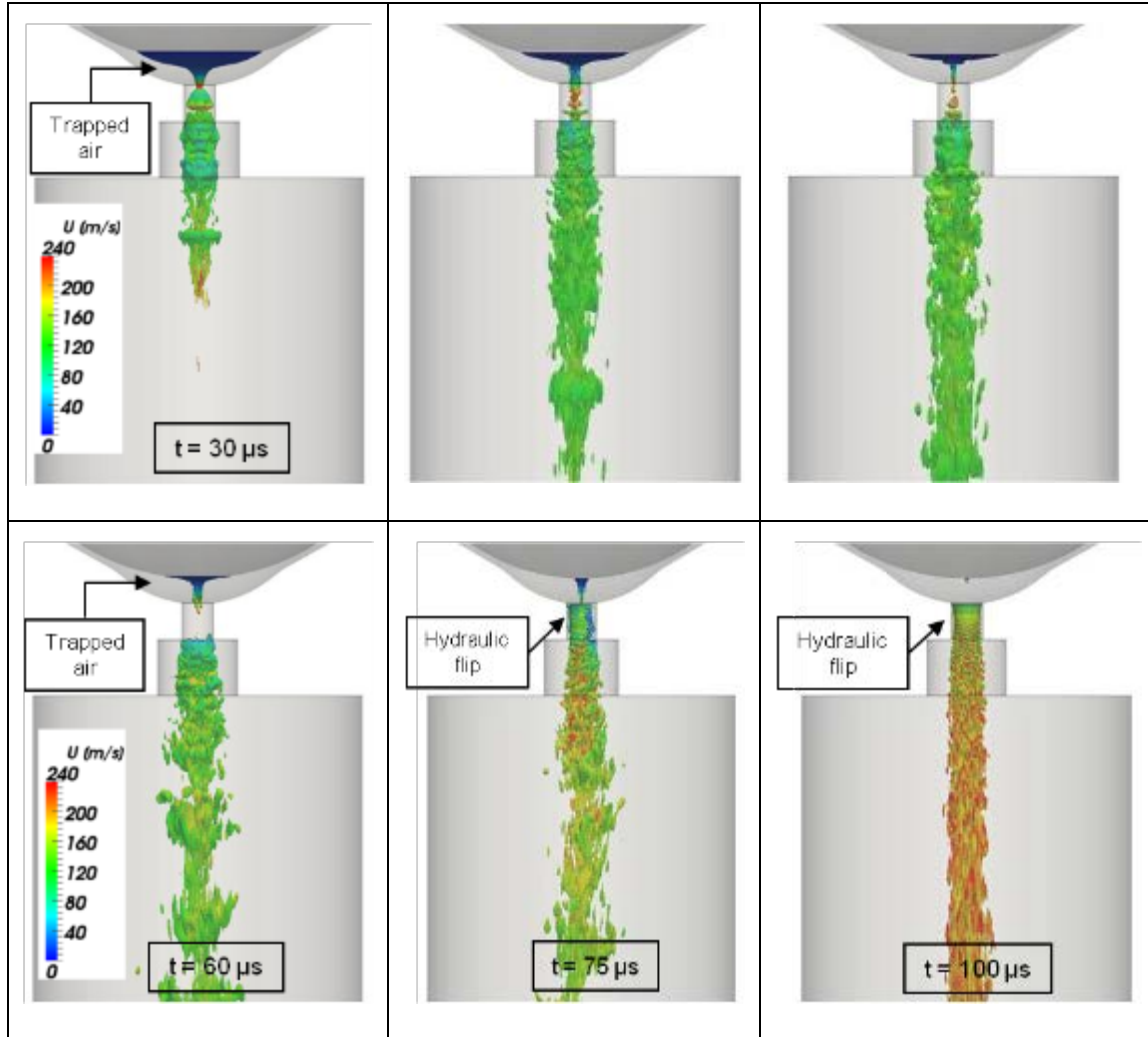


Figure 39 Iso-surface plots of VOF= 0.5, colored by instantaneous local velocity

The transient nozzle flow is markedly affected by the entrapped air in the sac volume, beneath the pintle. The initial liquid jet is fully attached at the nozzle entrance. The entrapment and discharge of the trapped air by the liquid causes formation of an attached liquid jet with an unsteady air core, as illustrated by the VOF iso-surface contour plots for $t = 30\mu\text{s}$, $40\mu\text{s}$, and $50\mu\text{s}$. Also notable is the perfect axisymmetric structure of the flow within the nozzle, which is indicative of the high level of resolution and numerical accuracy of the solution. The VOF plots at $40\mu\text{s}$ already show the development of the liquid jet irregular instabilities within the immediate downstream of the nozzle exit.

With diminishing of the sac volume entrapped air and reduction of the jet core air volume flow rate, the liquid jet separates at the nozzle entrance edge and, owing to the short nozzle l/d , the separation extends through the nozzle exit. This causes ingestion of the ambient air into the nozzle, thus forming an air annulus that separates the liquid jet from the nozzle wall. The phenomenon is known as “hydraulic flip” and its occurrence is indicated in Figure 39 by the VOF plot at $t = 75\mu s$. The full establishment of the hydraulic flip takes between $75\mu s$ and $100\mu s$; thereafter, the liquid jet is fully detached at the nozzle entrance and the ingested air penetrates the full nozzle length, thus completing the hydraulic flip. This is the structure of the steady-state stationary turbulent jet that prevails for $t > 100\mu s$. This structure is very stable, without temporal or cyclic variation of the jet separation, yielding consistent jet velocity profile, and downstream Kelvin-Helmholtz interface waves.

It must be underlined that the present simulation method excludes a cavitation model; hence, the hydraulic flip is engendered solely due to liquid flow separation at the nozzle entrance. It is expected that inclusion of cavitation, causing formation of a cavitation ring at the nozzle entrance, would promote separation and the hydraulic flip process, as well as augmentation of the jet inertial instabilities and impact on the breakup process.

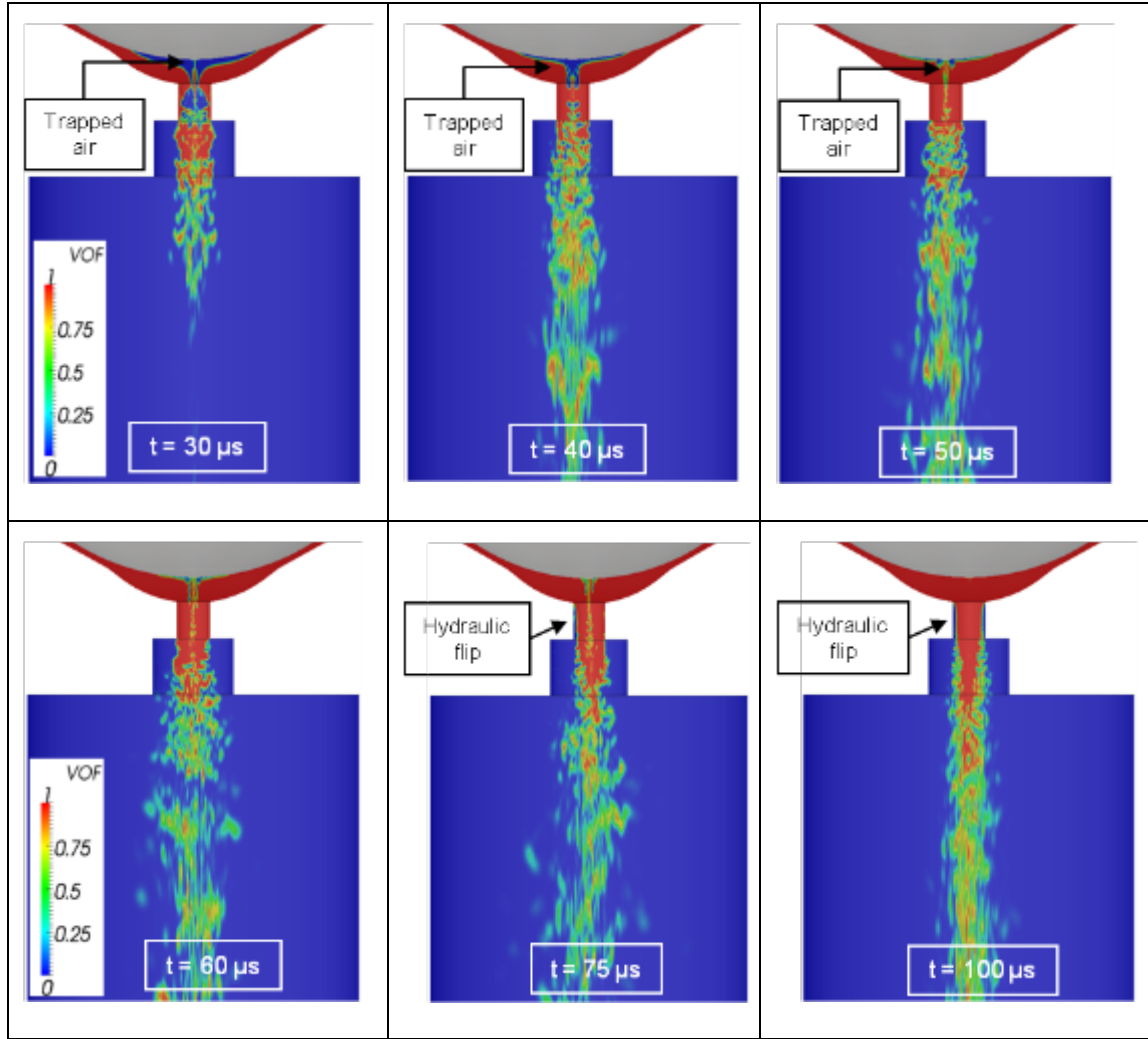


Figure 40 VOF Contour plots on a cut-plane across the nozzle diameter

Stationary Liquid Jet Breakup Structure

The structure of the stationary liquid jet, including the Kelvin-Helmholtz interface waves, is remarkably stable, as shown by the $VOF = 0.5$ iso-surface plots of the nozzle flow with separated liquid jet at $t = 100\mu s$, $110\mu s$, and $120\mu s$ in Figure 41. It is worth mention that presence of a disturbance at the nozzle entrance, due to velocity perturbation or edge irregularity, is expected to engender an asymmetric and instationary Kelvin-Helmholtz wave development, although jet breakup ‘mean’ features, trajectory, spray plume angle, etc., remain stationary.

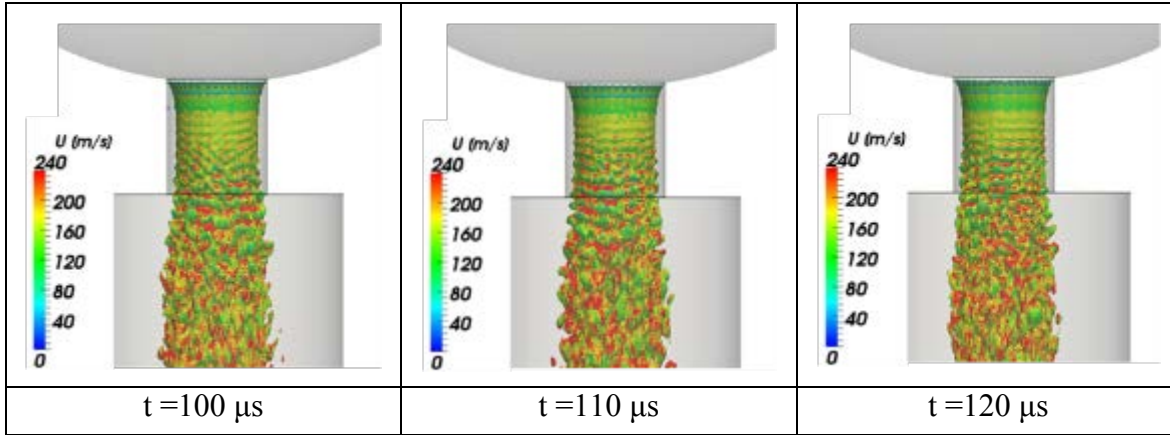


Figure 41 Stationary nozzle flow and liquid jet breakup structure (depicted by VOF =0.5 iso-surface plots) at $t=100, 110, 120 \mu s$ after SOI

As further illustrated in Figure 42, the nozzle flow is characterized by the full circumferential flow separation at the nozzle entry and formation of a liquid jet accompanied by the full hydraulic flip and resulting detachment of the liquid jet from the nozzle wall, shielded by the air

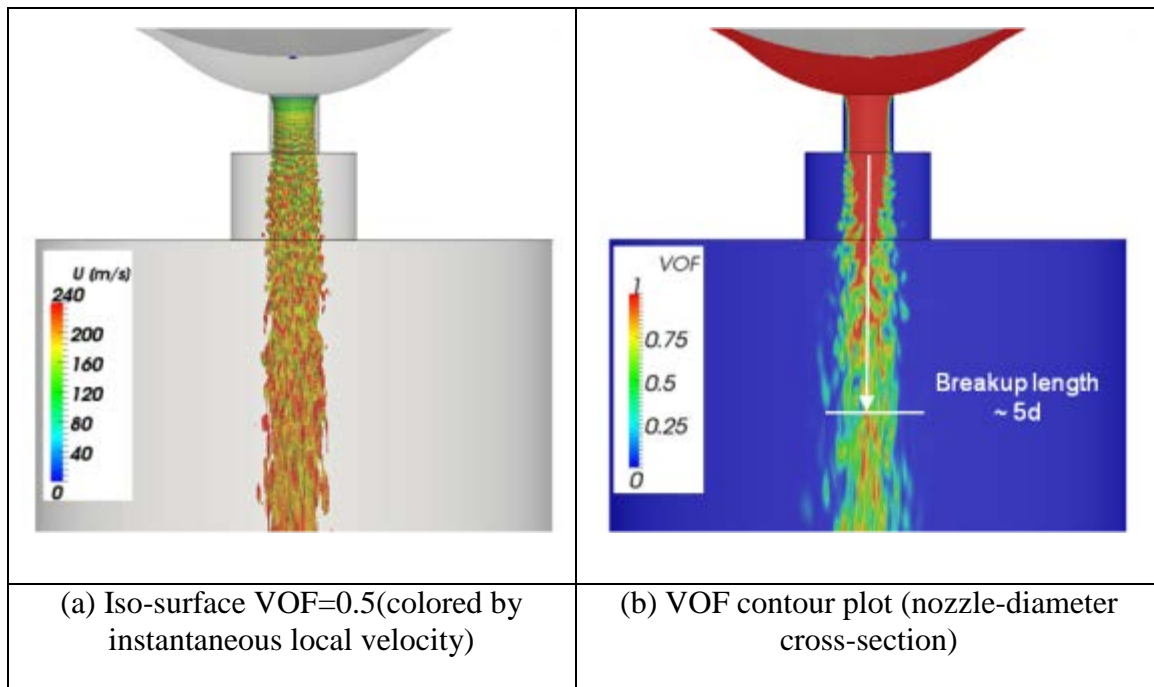


Figure 42 Stationary jet breakup structure (depicted by VOF iso-surface and contour plot) at $t=110 \mu s$ after SOI

ingested from the spray ambient. The VOF contour plots show initiation and growth of the Kelvin-Helmholtz jet interface instabilities within the nozzle hole. The amplification and transformation of the ring-vortex Kelvin-Helmholtz structures, also shown in the plot of Q in

Figure 42, in the counterbore space and turbulence leads to liquid jet primary breakup at a distance of $\sim 5d$ downstream of the nozzle hole exit plane. Figure 43 displays the VOF=0.5 iso-surface and the VOF contour plots at four cut-planes at locations $z = l/2$, $z = l$, $z = l+L/2$, and $z = l+L$. The results show the uniform circumferential separation of the liquid jet at the nozzle-hole entrance. The separated liquid jet within the nozzle-hole exhibits a remarkable circumferential

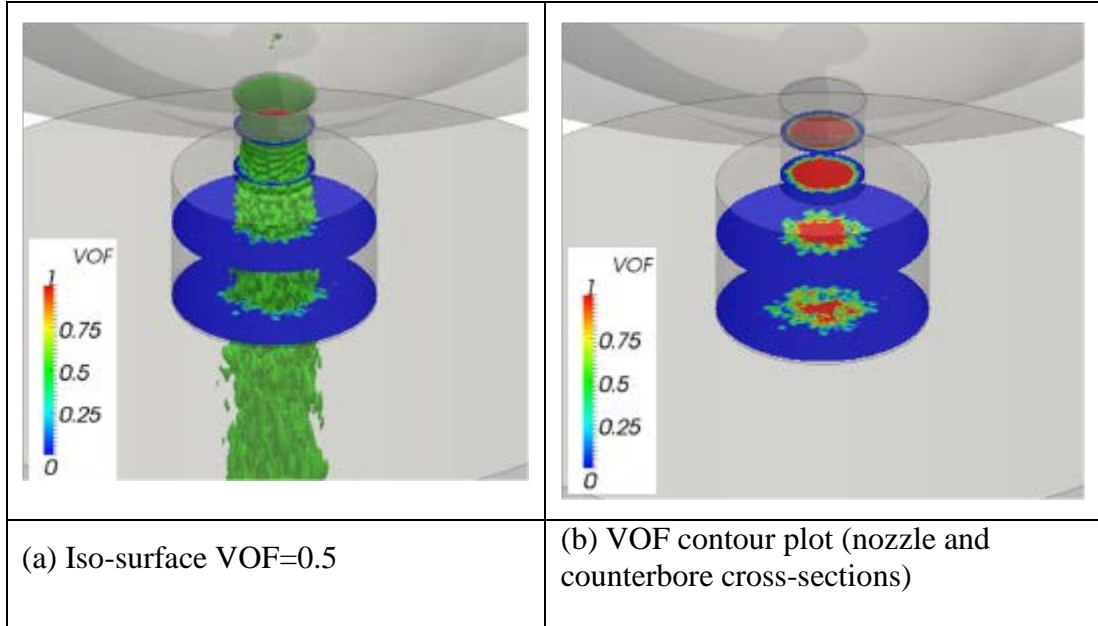


Figure 43 Stationary jet breakup structure (depicted by VOF iso- surface and contour plots) at $t=110 \mu s$ after SOI

symmetry and temporal consistency, with the evidence of perturbation of its interface by the Kelvin-Helmholtz waves. The progression of the Kelvin-Helmholtz circumferentially-symmetric ring-vortex instabilities into three-dimensional instabilities within the counterbore space engenders the irregular primary breakup of the liquid jet, as clearly shown by the VOF contour plots (at $z = l+L/2$ and $z = l+L$). This phenomenon is similar to that observed in the VOF-LES simulations of the primary breakup of the accelerated planar-sheet liquid jets [41].

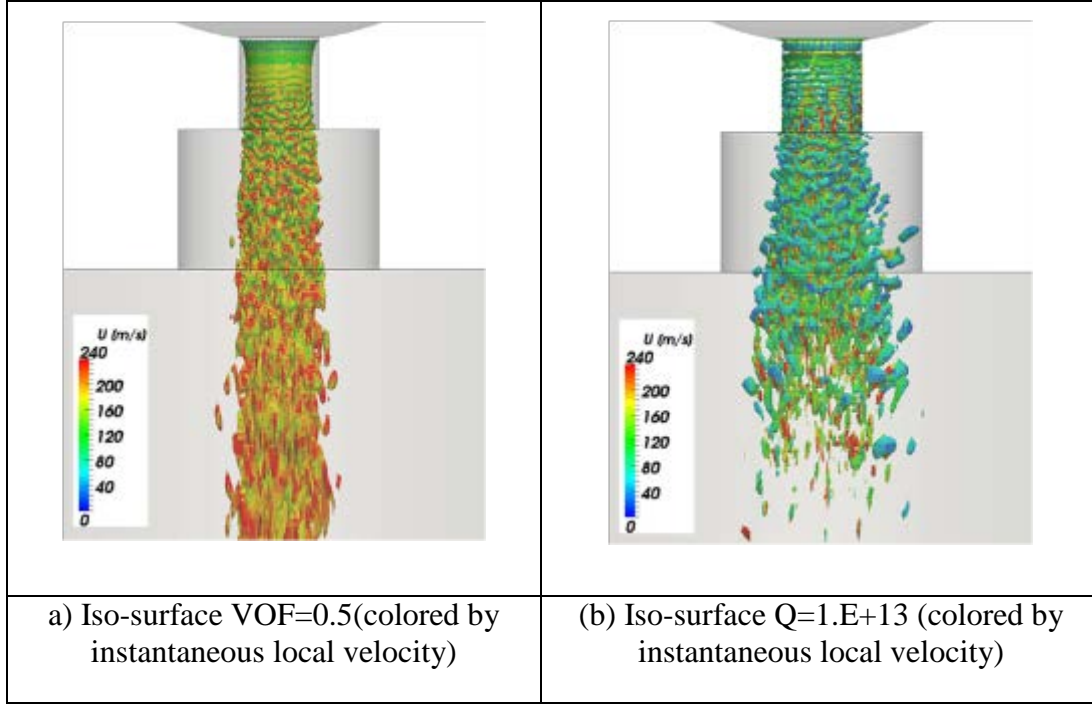


Figure 44 Stationary jet breakup structure (depicted by VOF =0.5 and $Q=1.E+13$ iso- surfaces) at $t=110\mu s$ after SOI

Figure 44 displays the structure of the liquid jet-air interface instabilities with the aid of the VOF = 0.5 and the $Q = 1.E+13$ iso-surfaces. The Q plot in Figure 44 shows imparting of high levels of vorticity onto the liquid jet at the nozzle entrance and formation of vortex-ring structures along the nozzle length at the liquid jet to air interface extending to the nozzle wall, that corresponds to the Kelvin-Helmholtz interface waves. The Q vortex-ring structures extend to the nozzle wall and indicate merging of the vorticity at the liquid jet to air interface with that of the surrounding air boundary layer, although the structure underlines the prominence of the jet interface instability in vorticity formation.

The deformation and breakup of the regular ring-vortex structures, concurrent with similar circumferential deformation of KH interface waves, along the nozzle hole is evident. In the immediate vicinity downstream of the nozzle hole, Q is enhanced by the amplification of the three-dimensional KH interface instabilities that diffuse vorticity into the surrounding air. The

level of Q rapidly diminishes with the jet primary breakup as the linear motion of the stretched liquid ligaments forms droplets.

5.1.2 Influence of Counterbore

The influence of counterbore on the liquid jet atomization is of special interest, as it provides a practical means to affect the atomization features; plume angle, droplet-size distribution, penetration, etc., of the individual spray plumes of the GDI multi-hole injector without resorting to complex and restrictive nozzle-hole geometry modifications, which simultaneously affect other features of the spray plume, such as the flow rate or targeting. The effect of counterbore geometry on the spray plume features is investigated through hardware experiments conducted on varying designs that have provided indication of its influence on the plume angle and penetration. Therefore, it is of particular interest to investigate the mechanism of this influence with the aid of VOF-LES.

Figure 45 presents the stationary nozzle flow and the liquid jet primary breakup structure for the base nozzle geometry without the counterbore. The transient nozzle flow development is identical to that of base geometry since it is dependent on features of the seat-nozzle geometry that determine the flow upstream of the nozzle hole, and is not presented. The VOF plots in Figure 45 depict a fully detached liquid jet within the nozzle with a jet surface corrugated by growth of the KH interface instability waves within the nozzle, and a jet breakup length of $\sim 5.5d$, almost identical to $\sim 5d$ of the base geometry.

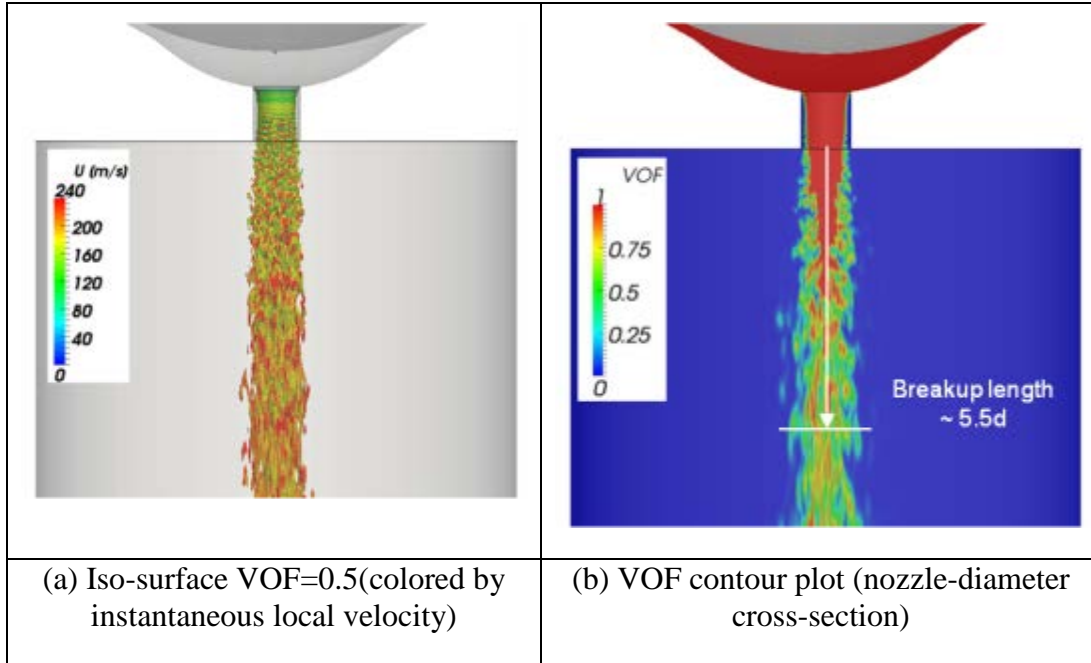


Figure 45 Stationary jet breakup structure (depicted by VOF and Q iso-surfaces) at $t=110 \mu\text{s}$ after SOI

Figure 46 displays a direct comparison of the liquid jet interface structure and Q levels for the base geometry and without the counterbore. The structure of the liquid jet within and downstream of the nozzle, including the features of the development of the KH interface instabilities, are practically identical for the two cases, which is remarkable considering that they display instantaneous and not statistically averaged field values. Also, as illustrated by the super-positioned lines that mark the spray interface for Case 1, there is no discernible difference between the spray plume angles for Case 1 and Case 2. However, there is noticeable difference in the Q iso-surface plots between the two cases, as seen in Figure 46 (a.2) vs. (b.2), with Case 1 showing a noticeable spread of vorticity from the jet into the surrounding air within and downstream of the counterbore, which is absent in Case 2. The explanation is that the combination of jet-induced air motion and pressure disturbances, engendered by the Kelvin-Helmholtz instabilities, excites the air within the counterbore with the effect of generating

energetic vortex structures within the surrounding air. However, as shown by the plots of VOF and Q , especially the location of decay of Q , the phenomenon does not have a marked influence

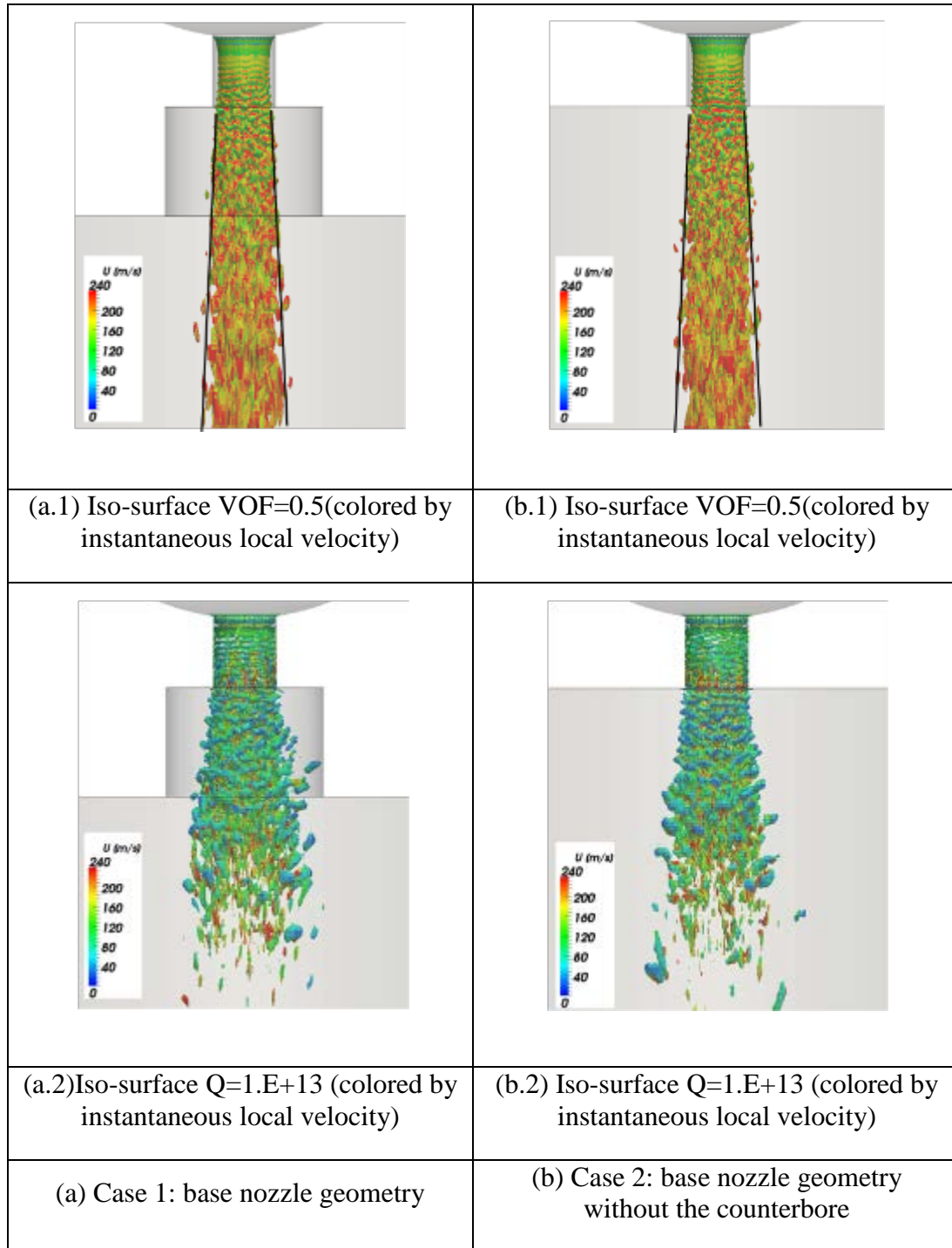


Figure 46 Comparison of jet breakup structure (depicted by $VOF=0.5$ and $Q=1.E+13$ iso- surfaces) for base nozzle with/without counterbore, at $t=110\mu s$ after SOI

on the liquid jet breakup process. The possible explanations are 1) the jet breakup is an inertial process that is predominantly controlled by the instabilities of the liquid jet and the air disturbances do not play a major role due to the large density ratio, or 2) the counterbore dimensions are outside the range that could influence the jet breakup. Further investigation is required to understand the underlying mechanism.

5.1.3 Influence of Nozzle Taper

One practical method to influence the flow structure within the nozzle hole is through tapered nozzle geometry. The ‘positive tapered’, or convergent nozzle, is considered to be advantageous as it enables reduction of the nozzle entrance losses, thus increasing nozzle C_d in addition to a reduction of the flow cavitation potential. However, it has a disadvantage that the flow acceleration tends to suppress turbulence within the nozzle and consequently adversely impacts the initiation and growth-rate of the KH instabilities. This subject has been the focus of attention in the field of diesel injector nozzle development [26] [57] [58] [59], and received significant consideration for the GDi multi-hole injectors. Therefore, it is of special interest to investigate the potential benefits of the GDi multi-hole tapered nozzle geometry with respect to the spray atomization characteristics. Figure 47 present the stationary nozzle flow and spray near-field breakup structure for a tapered nozzle with same flow-metering nozzle exit diameter as the base nozzle geometry. The most notable feature of the simulation results are:

- Fully attached flow in the nozzle hole,
- Initiation and growth of the KH interface waves downstream of the nozzle exit, with the consequent significant increase of the jet breakup length.
- Significant increase of the nozzle discharge coefficient ($C_d \sim 0.9$) for the tapered versus that of the cylindrical nozzle hole ($C_d \sim 0.6$).

- Significant increase in jet breakup length and deterioration of the jet breakup process.

Therefore, the pressure loss characteristic of a nozzle is not necessarily a negative feature of its design, as it contributes the energy for the atomization process. An energy budget of the nozzle flow losses from pressure fluctuations, Reynolds stresses, etc., is necessary to establish the linkage between the nozzle entrance losses and the jet breakup enhancement.

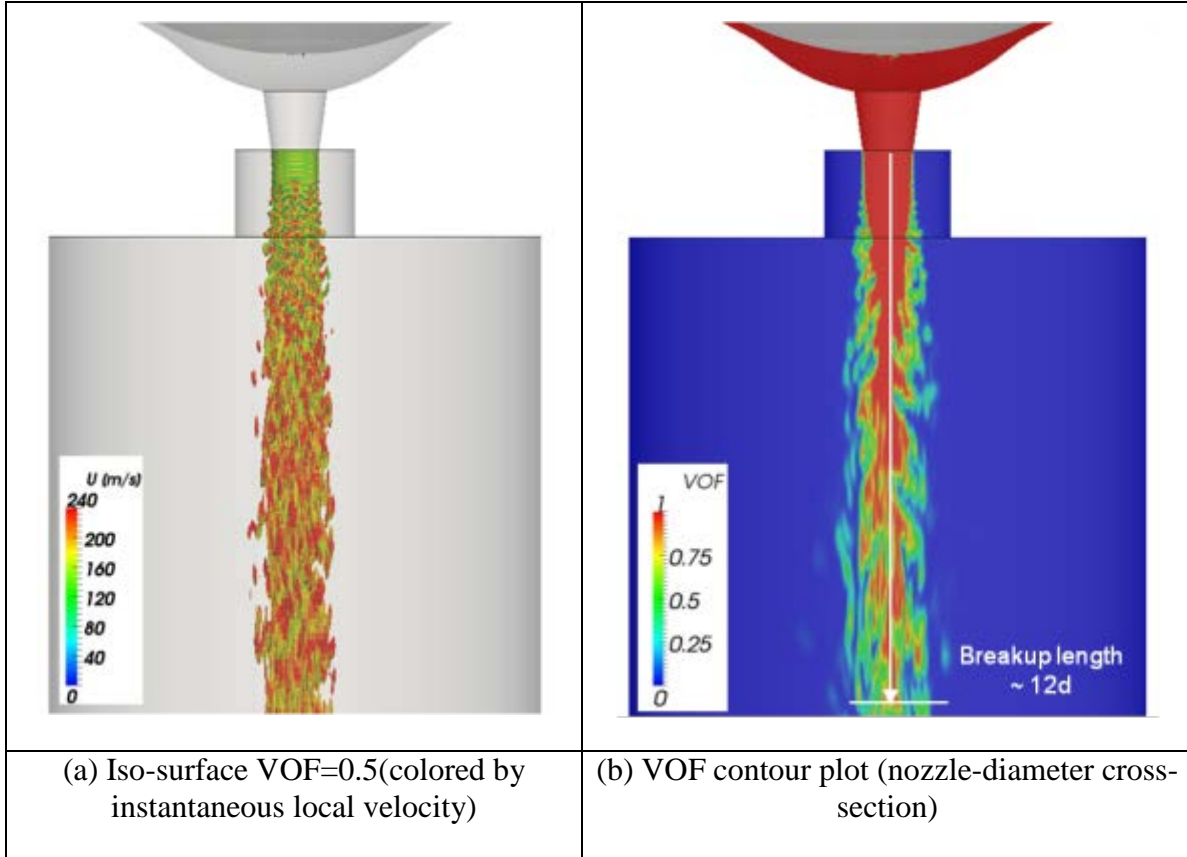


Figure 47 Stationary jet breakup structure for the tapered nozzle (depicted by the VOF=0.5 iso-surfaces and the VOF contour plot) at $t=110 \mu\text{s}$ after SOI

Figure 48 provides a direct comparison of the nozzle flow, liquid jet instability, and breakup for the cylindrical and the tapered nozzles with the aid of the VOF iso-surface contour-plots at several locations downstream of the nozzle and the iso-surface plots of the quantity Q , representative of the magnitude of the jet interface vortical structures.

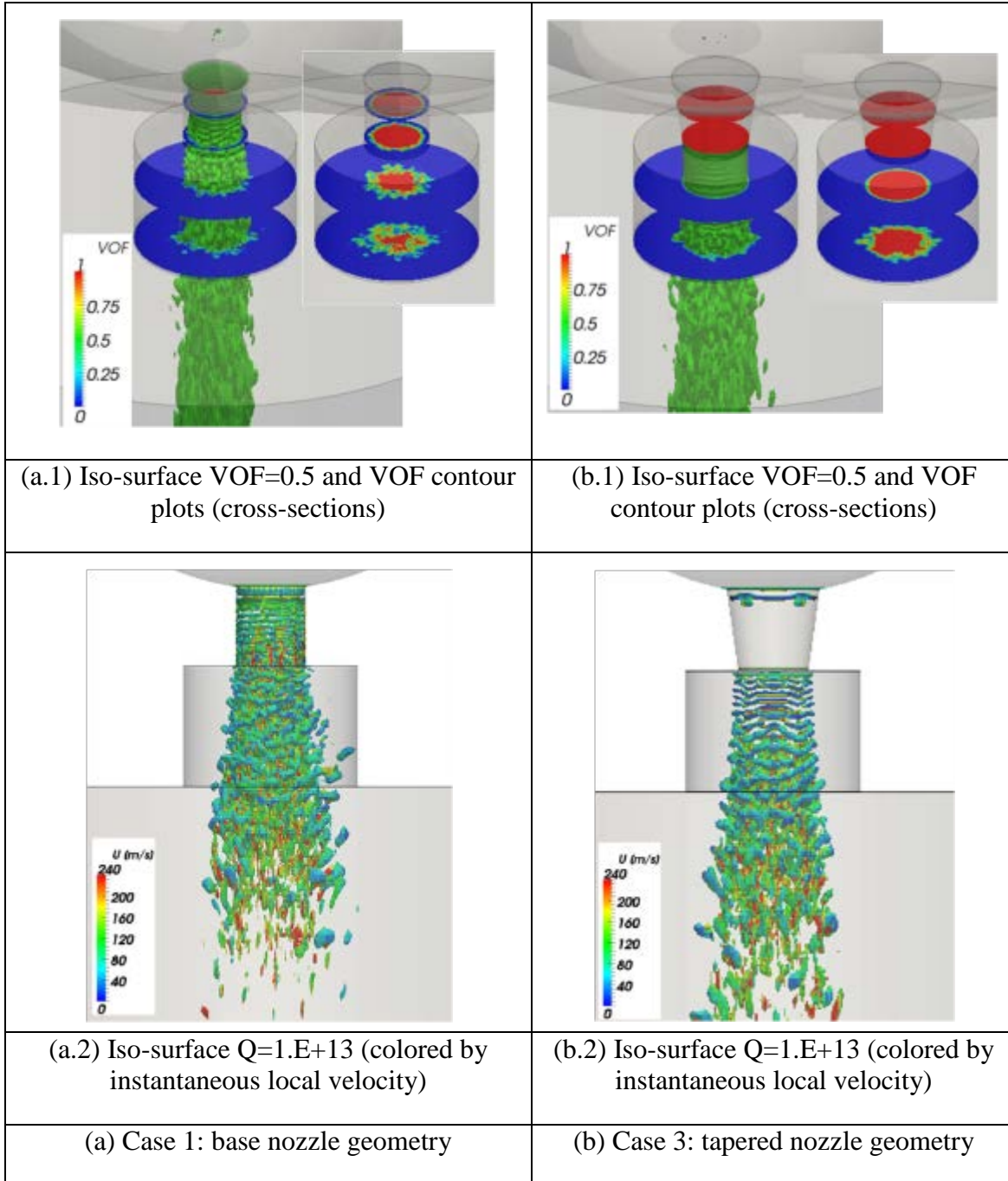


Figure 48 Comparison of jet breakup structures (depicted by the VOF =0.5 iso-surface, VOF contours, and the $Q=1.E+13$ iso- surface plots) for the base and tapered nozzles, at $t=110 \mu s$ after SOI

The VOF contour plots in Figure 48 illustrate the attached flow within the tapered nozzle and the consequent effect on the temporal and spatial development of the KH jet interface instabilities and the jet breakup. The Q iso-surface plots show the retarded formation of the jet-air interface

vorticity, in spatial correspondence with the development of the KH waves, downstream of the nozzle. Notably, the Q iso-plot indicates formation of vorticity at the nozzle entrance edge, but this is not amplified by the nozzle wall boundary layer likely due to the suppression effect of acceleration on turbulence.

5.1.4 Influence of Nozzle l/d Ratio

The GDi multi-hole nozzle has a short l/d ratio, of the order 0.8-1.5, compared with the diesel nozzles. It is of interest to investigate the flow and spray structure from a GDi multi-hole seat without a counterbore. Figure 49 presents the stationary spray near-field breakup structure for the long nozzle, with $l/d \sim 3$, and illustrates the effect of large nozzle l/d on the nozzle flow and the spray breakup process. The most notable features of the simulation results are:

- Absence of flow separation at nozzle entrance and the associated hydraulic flip
- Initiation and growth of the KH interface waves downstream of the nozzle exit, with the consequent significant increase of the jet breakup length.
- Significant increase of the nozzle discharge coefficient ($C_d \sim 0.8$) for the large l/d (~ 3) nozzle versus that of the small l/d (~ 1.1) nozzle hole ($C_d \sim 0.6$). Similar to the simulations for the tapered-hole geometry, the gain in the discharge coefficient is at the expense of deterioration of the jet breakup process.

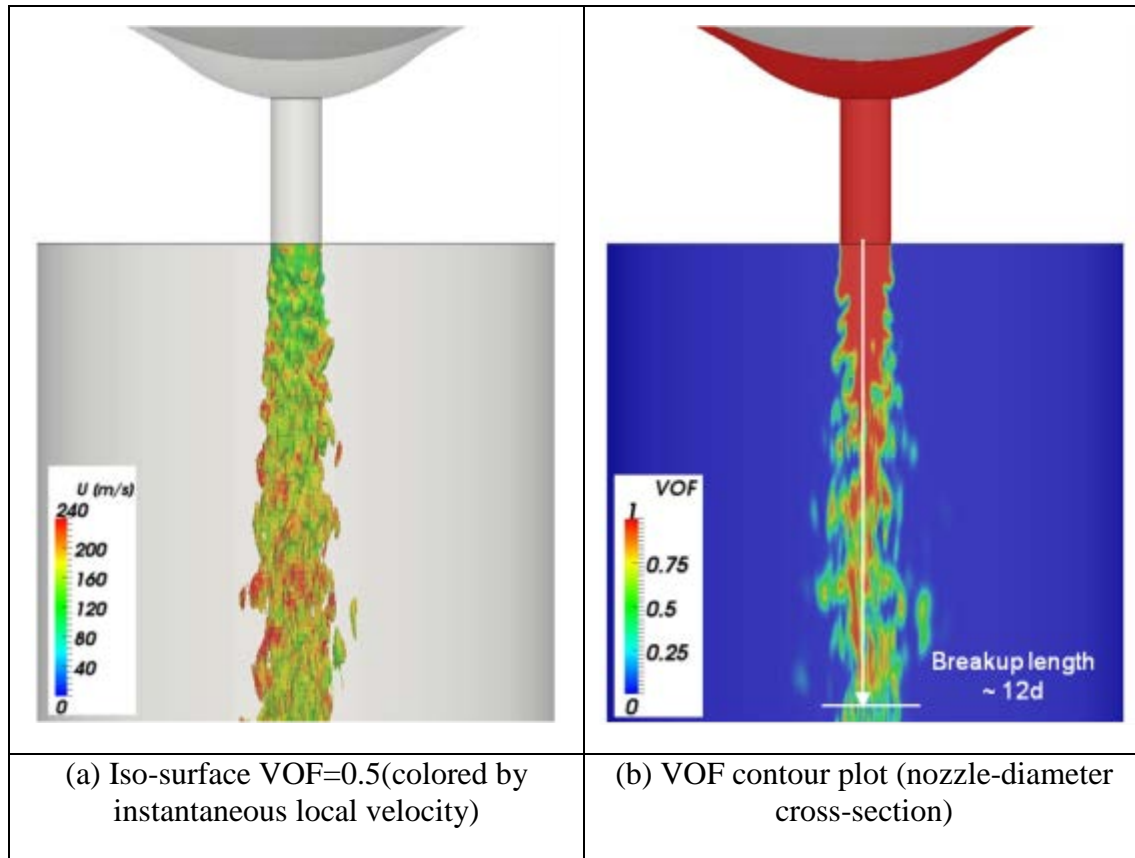


Figure 49 Stationary jet breakup structure for the large nozzle l/d (depicted by the VOF=0.5 iso-surfaces and the VOF contour plot) at $t=110 \mu s$ after SOI

Figure 50 provides a direct comparison of the nozzle flow and the liquid jet breakup structure for the long and short l/d nozzles with the aid of the VOF iso-surface contour-plots at several locations downstream of the nozzle entrance and iso-surface plots of the quantity Q , representative of the magnitude of the jet interface vorticity.

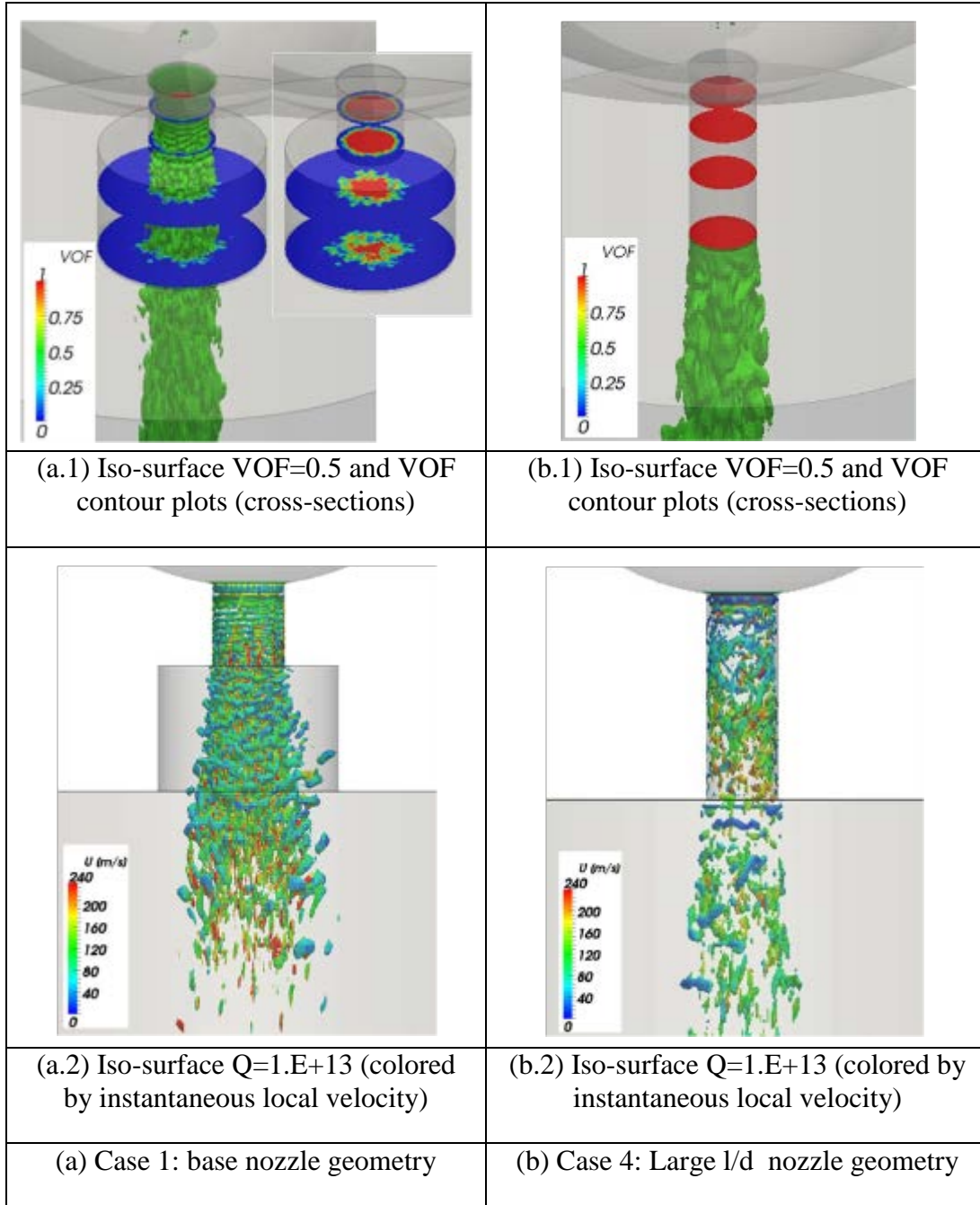


Figure 50 Comparison of jet breakup structures (depicted by the VOF =0.5 iso-surface, VOF contours, and $Q=1.E+13$ iso- surface plot) for the base and large l/d nozzles, at $t=110 \mu s$ after SOI

The VOF contour plots in Figure 50 illustrate the attached flow within the long nozzle, and the consequent effect on the downstream development of the KH jet interface instabilities and the jet breakup. It is noteworthy that the jet momentum is significantly larger for the long nozzle, which is due to its superior flow discharge coefficient. Most notably, the Q iso-plot for the large

l/d nozzle shows formation of vorticity at the nozzle entrance edge and its amplification within the nozzle due to turbulent flow development. The Q iso-surface highlights the distinct difference in the mechanisms of vorticity production between the short and the long nozzle, and that the vorticity production by KH interface instability of short nozzle is markedly more effective.

It must be underscored that the present VOF-LES method does not include a cavitation modeling capability. In the case of the long nozzle, the cavitation inception at the nozzle entrance is expected to play a significant influence on the flow field and turbulence within the nozzle and the subsequent jet breakup process. The present simulations primarily serve to highlight the significant difference between the nozzle flow and atomization features of typical GDi multi-hole and diesel injector nozzles.

5.1.5 Theoretical Jet Breakup Comparison

The VOF-LES simulations provide evidence of Kelvin-Helmholtz instability as the primary jet breakup mechanism for the GDi representative nozzle geometry and fuel pressure, as well as notable influence of nozzle-hole geometry on the jet primary breakup process. A comparison of the VOF-LES predictions with the jet breakup relations derived from the linear stability theory and semi-empirical analysis of the round-jet atomization [7] [9] [55] is of interest, especially since these relations take no account of the nozzle geometry and the nozzle internal flow. The important jet hydrodynamic parameters for the base nozzle geometry are presented in Table 6.

Table 6 The base nozzle liquid jet non-dimensional parameters

$Re_L = \rho_{liquid} Ua / \mu$	$We_L = \rho_{liquid} U^2 a / \sigma$	$We_G = \rho_{gas} U^2 a / \sigma$	$Oh = \mu / \sqrt{(\rho \sigma a)}$
2.70E+04	8.10E+04	1.40E+02	1.00E-02

Where U is the nozzle-exit jet superficial velocity, a ($=0.5d$) is the nozzle radius, and the liquid properties pertain to n-Heptane. It must be noted that Re_L , We_L , and We_G are larger for the tapered and long nozzles, due to their superior discharge coefficients. The We_G value is significantly larger than 40.3, the upper limit for the second wind-induced breakup regime [9], and so the atomization regime prevails, whereby the primary atomization mechanism is the Kelvin-Helmholtz liquid to air interface instability, and the start of atomization is expected at the nozzle exit [9]. The VOF-LES simulations reveal that, for all the nozzle geometries, Kelvin-Helmholtz waves are seen immediately at the nozzle exit consistent with primary jet breakup mechanism due to KH instability, but they indicate a much shorter jet breakup length range of $L/a \sim 10-24$ (note $l/d = 5-12$) than predicted. Some of this apparent discrepancy can be attributed to the jet divergent plume angle obscuring the visual criterion used for determining the jet atomization regime that is caused by the Kelvin-Helmholtz wave deformation of the jet surface in the immediate vicinity of the nozzle, as evident in Figure 45 and Figure 49, in spite of the presence of a core liquid jet. The corresponding jet atomization parameters, calculated from the relations shown in section 2.1 Blob or Stripping-Rate Model, are presented in Table 7.

Table 7 The base nozzle liquid jet atomization parameters, based on the jet linear stability / breakup theories

Λ / a	Ω [1/s]	T (Taylor's Parameter)	f (T)	$L_{breakup} / a$
8.00E-02	2.00E+08	6.30E+01	2.90E-01	3.40E+02

The jet breakup characteristics are defined by the frequency, Ω , and the associated wave-length Λ of the maximum growth-rate wave, produced by an infinitesimal axisymmetric disturbance on the liquid jet interface at the nozzle exit. The VOF-LES simulations indicate the KH wave-length values in the range $\Lambda/a \sim 0.2$ (base nozzle) – 1. ($l/d \sim 3$ nozzle), which are notably larger than the value predicted by the linear stability theory. Conversely, VOF-LES simulations of the

jet breakup length are in the range $L/a \sim 10$ (base nozzle) - 24 ($l/d \sim 3$ nozzle), which are significantly smaller than provided by linear stability theory. In this regard, it is likely that the value of parameter $B = 4.04$, pertinent to the sprays from diesel nozzles, is inappropriate for the GDi nozzle's small l/d nozzle geometry. The VOF-LES simulations indicate a suitable value for the GDi nozzles is in the range $B \sim 0.1 - 0.3$.

It should be noted that the present VOF-LES simulations exclude in-flow disturbances and nozzle geometry imperfections, like those at the nozzle inlet edge. These are expected to be present and influential in the jet breakup experiments, and hence assimilated into the semi-empirical atomization models. With regards to the influential computational factors, the computational mesh resolution of the current VOF-LES simulations has been shown to be sufficient for quantitatively reliable simulation of the jet breakup from GDi-representative nozzle geometries [40] [41]. Nevertheless, the predicted results require confirmation through comparison with experimental data.

5.1.6 Summary/Conclusions

The VOF-LES simulations provide insight into the salient nozzle flow and jet-breakup features of the current GDi nozzle design and the important influences of the nozzle geometry.

The simulations highlight for the axis-symmetric single-hole nozzles:

- The full flow detachment, caused by flow separation at the nozzle entrance, accompanied by hydraulic flip, is a major feature of the GDi nozzle geometry ($l/d \sim 0.8-1.5$).
- Initiation and growth of the Kelvin-Helmholtz instabilities within the nozzle, engendered by the flow separation at nozzle entrance, with jet primary breakup within a short nozzle downstream distance ($\sim 5 \times$ nozzle diameter).

- Formation of unsteady vortical flow within the counterbore volume, induced by the Kelvin-Helmholtz instabilities. However, these do not augment the jet breakup process. The likely explanation is that the liquid jet breakup is controlled by the jet inertial instabilities and the kinetic energy of the surrounding air disturbances is insufficient to influence the process.

In the case of a tapered nozzle, the attached nozzle flow yields a significant increase of the nozzle discharge coefficient ($C_d \sim 0.9$ vs ~ 0.6 for the detached cylindrical nozzle). However, vorticity is reduced, and therefore the initiation and growth of KH interface instabilities are arrested, thus resulting in a marked increase of the jet primary breakup length.

The LES predictions of the KH wave-length and the jet breakup length are not in quantitative conformity with the values obtained from the jet stability and breakup theories [9] [55]. The empirical parameters in the jet breakup relations may require modification for spray predictions with GDi multi-hole injector nozzle geometry.

Simulation results for the large l/d (~ 3) nozzle highlight the marked influence of the flow separation at the nozzle entrance on the mechanism for production of vorticity and the jet breakup process. This is, in conjunction with the nozzle-entrance cavitation, a distinction between the GDi multi-hole and the diesel injector nozzle flow and breakup processes.

The stationary nozzle flow structure and the liquid jet breakup process are remarkably stable: there is no transient instability of the nozzle flow detachment, the liquid jet trajectory, or the development of the Kelvin-Helmholtz instabilities (including transition to irregular waves) in the jet breakup structure.

Overall, the VOF-LES results reveal that the nozzle flow characteristics of GDi nozzle holes are markedly different from the diesel nozzles, owing to the relatively short nozzle l/d (of order 1,

vs. 6 - 7 for the diesel nozzles). This renders the hydraulic flip an important feature of the nozzle flow and the jet primary breakup process.

It is worth mentioning that the higher nozzle discharge coefficients of the tapered and large l/d nozzles enable smaller nozzle sizes for the same static flow as the base GDi nozzle geometry.

This study highlights the potential capability of the VOF-LES method for analysis of the liquid to air interface dynamics of the jet breakup and influence of the GDi multi-hole injector valve-group specific design features. Experimental studies are required to quantitatively verify the VOF-LES simulations. Also, more realistic GDi multi-hole nozzle geometries, taking into account the nozzle hole skew angle, are subjects of investigation.

5.2 GDi Injector Spray Characterization

5.2.1 Prototype Injector Manufacture

Based on the test hardware defined in section 4.2 Test Hardware, injector seat drawings were generated to provide the l/d, counterbore, and skew angle geometry desired, the drawings are provided in Appendix A, and the solid model is shown in Figure 51. GDi Production seat blanks used in this study are manufactured by powder metal forming process and production blanks were sent to a supplier, Leer, with Electric Discharge Machining (EDM) equipment, to generate the nozzle thru-hole

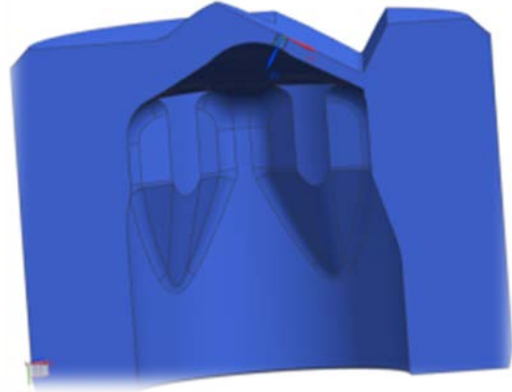


Figure 51 Injector Seat Solid Model

geometry and subsequently to a second supplier, Arnprior, to machine the counterbores. A grinding process was then used to create the short l/d and non-counterbored seats by removing material through surface grinding to achieve the desired geometry on the finished seat, as shown in Figure 52. This was viewed as the best method to achieve representative geometry, but the material removal does result in thinner seat material cross-section raising concerns for structural strength, however, assuring representative prototype injector nozzle thru-hole features. As can be partially seen



Figure 52 Finished Prototype seat with grind

in the interior of the seat has 5 internal ribs and thru-hole geometry was established to provide flow streamlines representative of production 5 and 6 hole injectors. It should be noted that if

the number of holes $\neq 5$ some asymmetry is introduced affecting flow between ribs and thru-hole entrance.

Completed injector seats were inspected to assure resulting geometry was achieved. Due to the critical nature of the thru-hole inlet edge condition, a positive silicone mold was produced, shown in Figure 53, to analyze the transition from the seat sac volume to thru-hole inlet. The mold confirmed the thru-hole inlet transition to be a

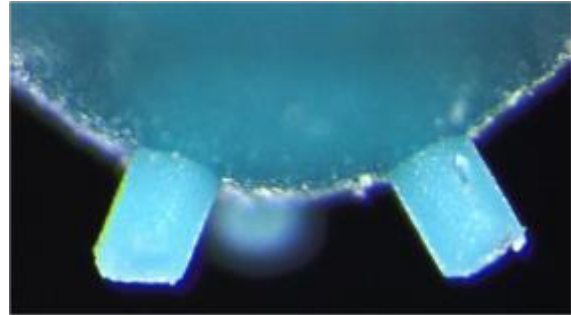


Figure 53 Silicone mold to reveal internal seat geometry

sharp corner, less than .002mm radius, desired for production of fluid turbulence. A study of the effects using LES was conducted and determined a rounded inlet radius had significant effect on the discharge coefficient for the nozzle confirming the importance the thru-hole inlet edge plays in engendering turbulent structures that aid atomization.

A list of initial prototype seats and their respective geometry is provided in Table 2. The matrix provided the range of l/d, counterbore, and skew angles outlined in Chapter 3 . Additionally, a tapered seat geometry, shown in Figure 54, was added to further the understanding of inlet geometry implications on spray formation as discussed in section 5.1.3 Influence of Nozzle Taper.

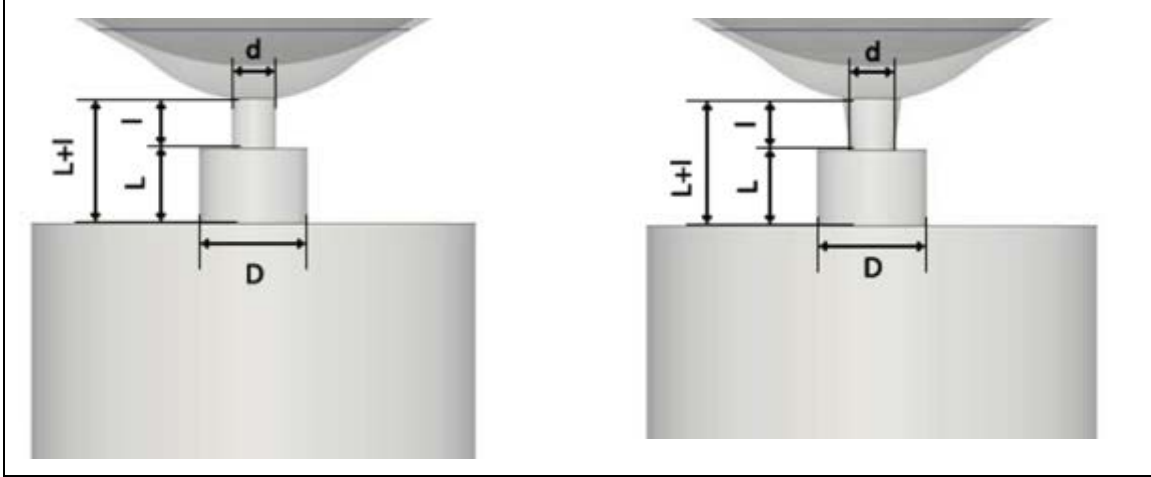


Figure 54 Prototype Cylindrical and Tapered thru-hole

5.2.2 Test Conditions

The spray imaging was performed using n-Heptane fuel, with system fuel pressure of 10MPa, and injection into the atmospheric ambient. In the case of the phase-contrast X-ray imaging, the Viscor calibration fluid 16B substitute was used [34]. Table 8 provides the relevant physical properties of the working liquids at 23°C for 10MPa injection pressure.

Table 8 Physical properties of the spray test liquids n-Heptane and Viscor-16B2

<i>Fluid</i>	ρ [kg/m ³]	μ [cP]	σ [N/m]	<i>P</i> vapor [Pa]
n-Heptane	684	0.41	0.02	5.3E+3
Viscor 16B2	778	0.9	0.024	- (low)

The relevant spray plume non-dimensional parameters based on LES nozzle exit velocities and n-Heptane material properties are provided in Table 9.

Table 9 Non-dimensional parameters for the spray shadow-imaging experiments

$Re = \rho_{liquid}UL / \mu$	$We = \rho_{liquid}U^2L/\sigma$	$Oh = \mu / \sqrt{(\rho\sigma L)}$	$Ma = U / a$
38,000	80,000	0.007	0.33

5.2.3 Injector Spray Characterization

Injector Spray Characterization was conducted per test request # 6500035516 listed in plume angle. The X-ray image does reveal extensive turbulent structures immediately at nozzle exit. The structures are also similar across injection pressures of 25, 50, and 75MPa. Following an initial evaluation discussed in section 5.2.4 Summary/Conclusion on Physical Test and Modified Project Scope Direction the injector series listed in Table 3 was selected and evaluated at the Delphi Luxembourg Spray laboratory Figure 55 according to the SAE standard J2715 for spray nomenclature and measurement specification [42]. To verify seat geometry, Hexcell Patternization was utilized to record plume centroid location and mass distribution for comparison to the target geometry and plume angle, as shown in Figure 56. For initial inspection of spray plume formation and penetration, backlight images were captured at 0° and 90° view angles as illustrated in Figure 57. The Hexcell Patternization and spray imaging conducted in the Rochester Spray lab for the complete seat matrix is provided in Appendix C. It should be noted in the table the seat # with red indicates that this portion of the label was omitted in the marked injector. Tests were also conducted at Argonne National Lab using the Advanced Photon Source (APS) to characterize the near-field spray turbulence. Testing conducted at Argonne National Lab (APS) focused on the single-hole injectors representing l/d of 2.95 and 3.96, and the series of image captures is presented in Appendix D. A typical time sequence is shown in Figure 58, and similar to the shadowgraph images for axis-symmetric single-hole nozzles, we see long penetration and spray plumes that contract as the penetration increases in contrast to the 30° skew angle nozzles typical of GDi injectors in application.

REQUEST FOR TEST ENGINEERING			
¹ TEST REQUEST # <u>PU927-AQ18</u>		REQUESTER <u>Varble/Mergler</u>	
SUBJECT <u>Spray Request for AK29 Injectors - Mark Shost</u> <u>Project</u>		SUPERVISOR <u>Dom Dalo</u>	
SAP IO #(s) <u>650035516</u>		DATE <u>12-Jan-2012</u>	
TDP/ADP/PDP Status _____		DEPT. <u>15640</u> PHONE <u>x6795</u>	
<input type="radio"/> TDP <input type="radio"/> ADP <input type="radio"/> Analytical Design Confirmation <input type="radio"/> Design Confirmation		<input checked="" type="radio"/> Development Model Shop	
<input type="radio"/> Design Validation <input type="radio"/> Product Validation <input type="radio"/> MCIP <input checked="" type="radio"/> Other <u>Spray angle</u>		<input type="radio"/> Production Intent Model Shop	
TEST CLOSURE METHOD: _____		<input type="radio"/> Production Equipment	
<input type="radio"/> REPORT/SUMMARY <input checked="" type="radio"/> DATA ONLY		<input type="radio"/> MQ1 <input type="radio"/> MQ2	
² DATE SAMPLES AVAILABLE <u>12-Jan-2012</u>		DATE RESULTS REQUIRED <u>18-Jan-2012</u>	
SAMPLE DISPOSITION		<input type="radio"/> RETAIN PER PROC 1001 <input checked="" type="radio"/> RETURN TO <u>Dan Varble</u>	
³ DESCRIPTION OF WHAT IS TO BE TESTED:		PART NAME: <u>Beta Spray Mule</u>	
PART NO. <u>AK29 Spray Mule</u>		MODEL YEAR <u>N/A</u>	
REV. _____		QTY. <u>3 ea of 12 TC's</u>	
SERIAL NO. <u>AK29-01, AK29-02....to AK29-12 plus 3 hole versions of AK10-3, AK11-3 & AK12-3</u>		SUPPLIER <u>Leer/Armprior</u>	
⁴ PPAP DATE _____		SOP DATE _____	
BEN # _____		BEN TEST COMPLETION DATE _____	
BACKGROUND INFORMATION & SPECIAL FEATURES			
Seat Part No.: NA Fuel Pressure: 10 Mpa Static Flow Rate: 1 to 3 g/sec @ 10Mpa Stoddard (65 um stroke) Other Information (e.g. GDi injector driver, GDi spray orientation, special fixturing, etc.): Please use HMC nominal pressure waveform, "HMC_IDM3Lv19_Nom30FFT_10-9-10"			
TEST OBJECTIVE			
Background: (3) injectors of (12) different seat configurations for a total of (36) injectors. These seats were EDM'ed at Leer and spray mules built at Armprior. (9) single hole seats and (3) three hole seats. Flow rates are very low on the order of 1-3 g/sec! For flow: Please calibrate in Stoddard to 10% of SF using "SW9_Std65V_Nom_Beta_SprayMule.s28" drive waveform. Please record SF (in Stoddard) and stroke in spray mule file. Flow work was requested under AJ84. Note first injectors (2&5) arrived 6/24, and were previously shipped, so not available for spray testing. Have Extra 3 hole Versions of 10,11&12. for testing. Spray: Use N-Heptane. HexCell / Patternation: all spray mules Imaging / Penetration: all spray mules LD / drop size all spray mules			
SUGGESTED PROCEDURE #: _____			
PASS/FAIL CRITERIA			
N/A			
⁵ TEST COMPLETED WITH DATA ONLY - NO REPORT REQUIRED			
RESULTS _____ (Quantity)		<input type="checkbox"/> Pages <input type="checkbox"/> Files FORWARDED TO _____ METHOD _____ <input type="checkbox"/> Disks	
FORWARDED BY _____		TEST SUPERVISOR APPROVAL _____	
<input type="checkbox"/> Hard Copy		<input type="checkbox"/> E-Mail	
<input type="checkbox"/> CD/Disks		<input type="checkbox"/> Network Drive	
ON _____ (Date)		Attachments? <input checked="" type="radio"/> Yes <input type="radio"/> No	

Figure 55 Injector Test Request, for Hexcell Patternation, Backlight Imaging, and Laser drop size profile

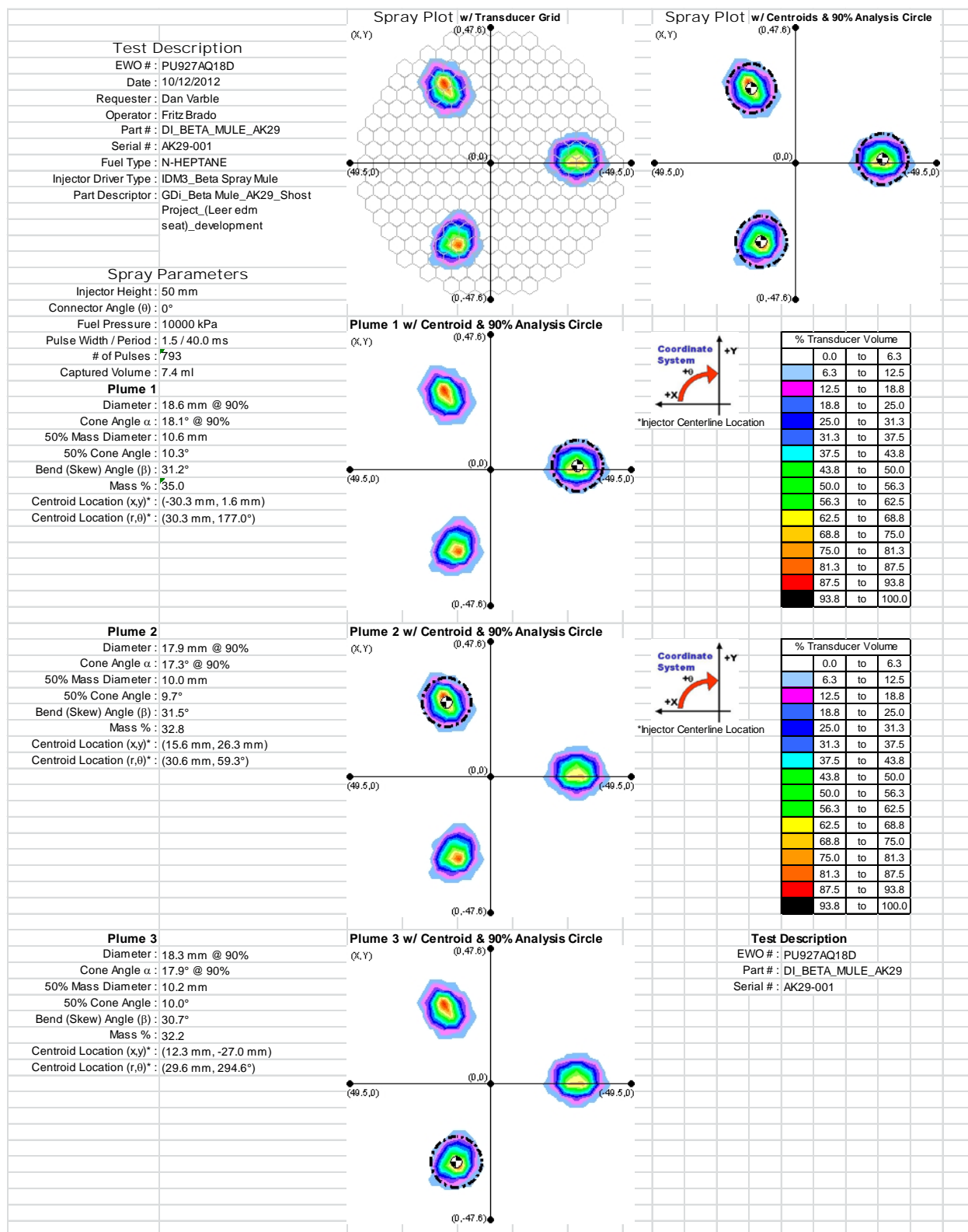


Figure 56 Spray Plume Characterization using Hexcell Patternator, S/N AK29-07-001

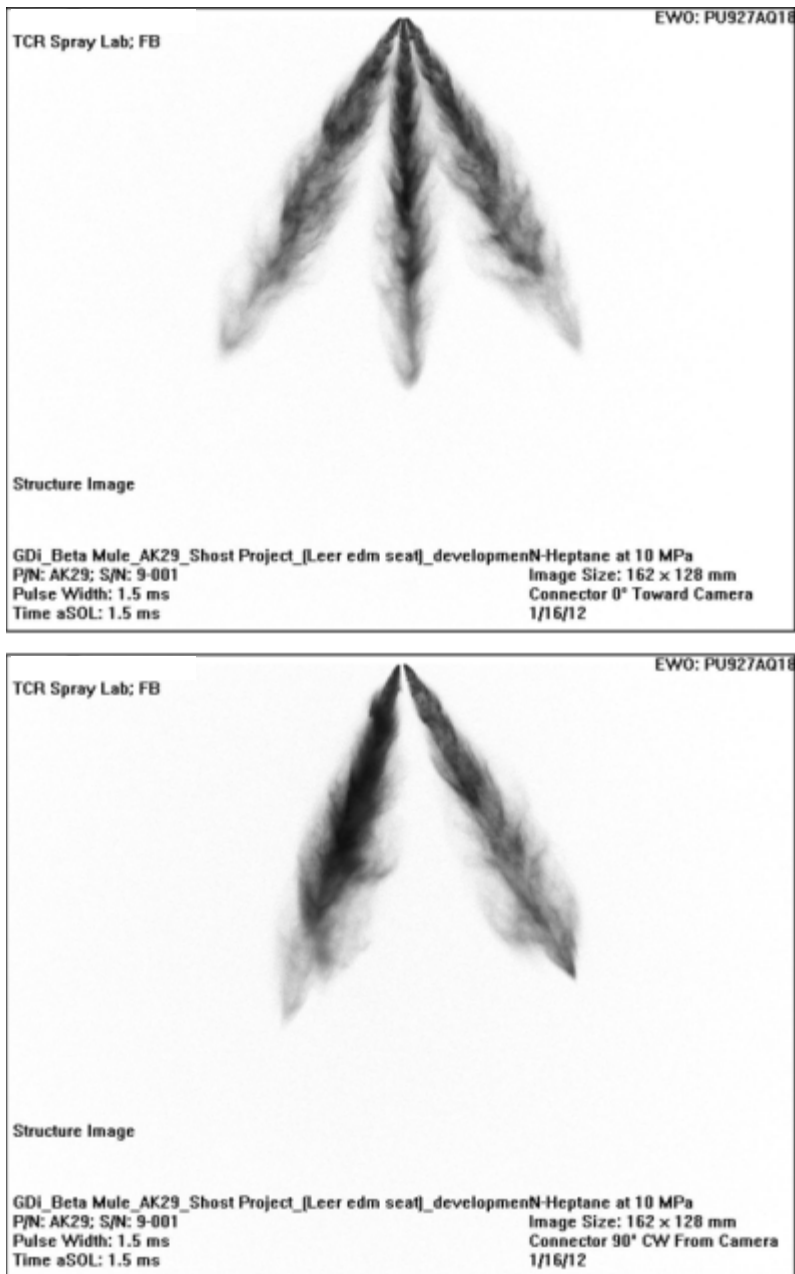


Figure 57 Shadowgraph Image at 0° and 90° for 3-hole seat injector

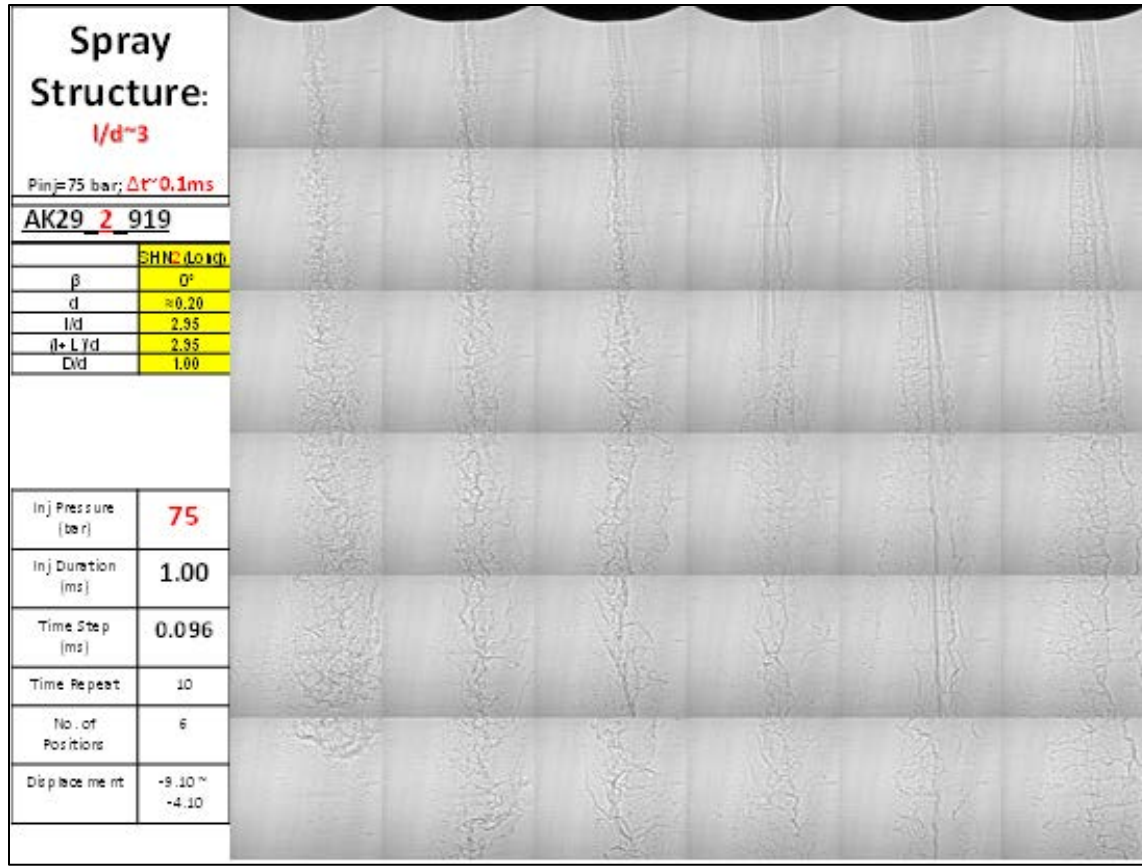


Figure 58 Phase-Contrast X-ray images revealing turbulent structure

Testing in the Delphi Luxembourg spray lab was conducted per the SAE standard documented in 4.1 Defined Terms. To understand the differences of methodology, calculations for plume angle and penetration were conducted using both Shadowgraph and Mie Images.

The following summarize the presented data:

- High speed shadowgraph images from the side view are presented in Appendix E
- High speed integral Mie Images from the side view are presented in Appendix F
- Bottom-view high speed integral Mie Images are presented in Appendix G
- Mie Scatter Images of near-field Spray are presented in Appendix H

Calculated spray penetration length for the axis-symmetric single-hole nozzles from the Shadowgraph images at 0° and 90° orientations, and 10 and 20MPa injection pressures, is shown

in Figure 59 and indicates a consistent penetration $\approx 88\text{mm}$ across the range of pressure. While seat AK29-3 and AK29-6 both had an $l/d = 1.1$, the thru-hole diameters varied with AK29-3 $\approx .20\text{mm}$ and diameter of AK29-6 $\approx .15\text{mm}$. A similar penetration calculation using the Mie Imaging data is presented in Figure 60. The data documents a slightly shorter penetration $\approx 86\text{mm}$, again unaffected by injection pressure. Calculated spray angle for the axis-symmetric single-hole nozzles from the Shadowgraph images at 0° and 90° orientations, and 10 and 20MPa injection pressures, shown in Figure 61, reveals variation in the plume angle over time from 4 - 14° with a mean value ≈ 6 - 8° , while Figure 62 with Mie Scatter images indicate similar variability with a mean ≈ 8 - 10° . Analysis was also conducted on the 3-hole seats AK29-9, AK29-10, and AK29-11 with results presented on Figure 63 for the Shadowgraph images at 0° and 90° orientations, and 10 and 20MPa injection pressures. Similar results were found using Mie Scatter images, as shown in Figure 64. There is a noticeable anomaly for seat AK29-10 at the 90° orientation exhibiting a markedly lower penetration on the shadowgraph images. The lower penetration is also seen in the Mie Scatter image calculations, but to a somewhat reduced amount. Additionally seat AK29-11 shows some larger penetration rates at around $1000\mu\text{s}$ ASIE, this can be seen clearly in the Mie scatter image, presented in Appendix F, with one nozzle plume exhibiting far greater penetration and narrower plume angle. Spray angle is presented for the 3-hole seats in Figure 65 for the Shadowgraph images at 0° and 90° orientations with 10 and 20MPa injection pressures. The results are more consistent than the single-hole nozzles with variation between 60 - 80° . In this case, the results are very similar for the Mie Scatter images provided in Figure 66. Spray droplet measurements were conducted using the Malvern Spraytec 2000, as defined in 4.3.3 Laser Diffraction Technique, at 10 and 20MPa with calculated key spray statistics for Dv_{10} - Dv_{90} , Dv_{32} , and Sauter Mean Diameter

(SMD), listed in Table 10. The results indicate similar droplet distribution for all nozzles with the tendency for smaller droplets at 20MPa injection pressure. This would indicate the deeper penetrating axis-symmetric single-hole nozzles showed no degradation in particle size as measured at 50mm from injector tip. Distributions of the droplet size for the single-hole and 3-hole injectors at 10 and 20MPa are presented in Figure 67 and Figure 68, showing a tendency of a larger quantity of smaller droplets for 3-hole injectors, but with a similar mean characteristic. Figure 69 compares similar nozzles constructed with and without counterbores and the graph of nearly identical droplet size distributions indicates no discernable influence of the counterbore. The last comparison was for skew angle, as presented on Figure 70, where AK29-3, skew angle = 0° , showed a greater propensity of small droplets compared to AK29-3 with skew angle = 30° .

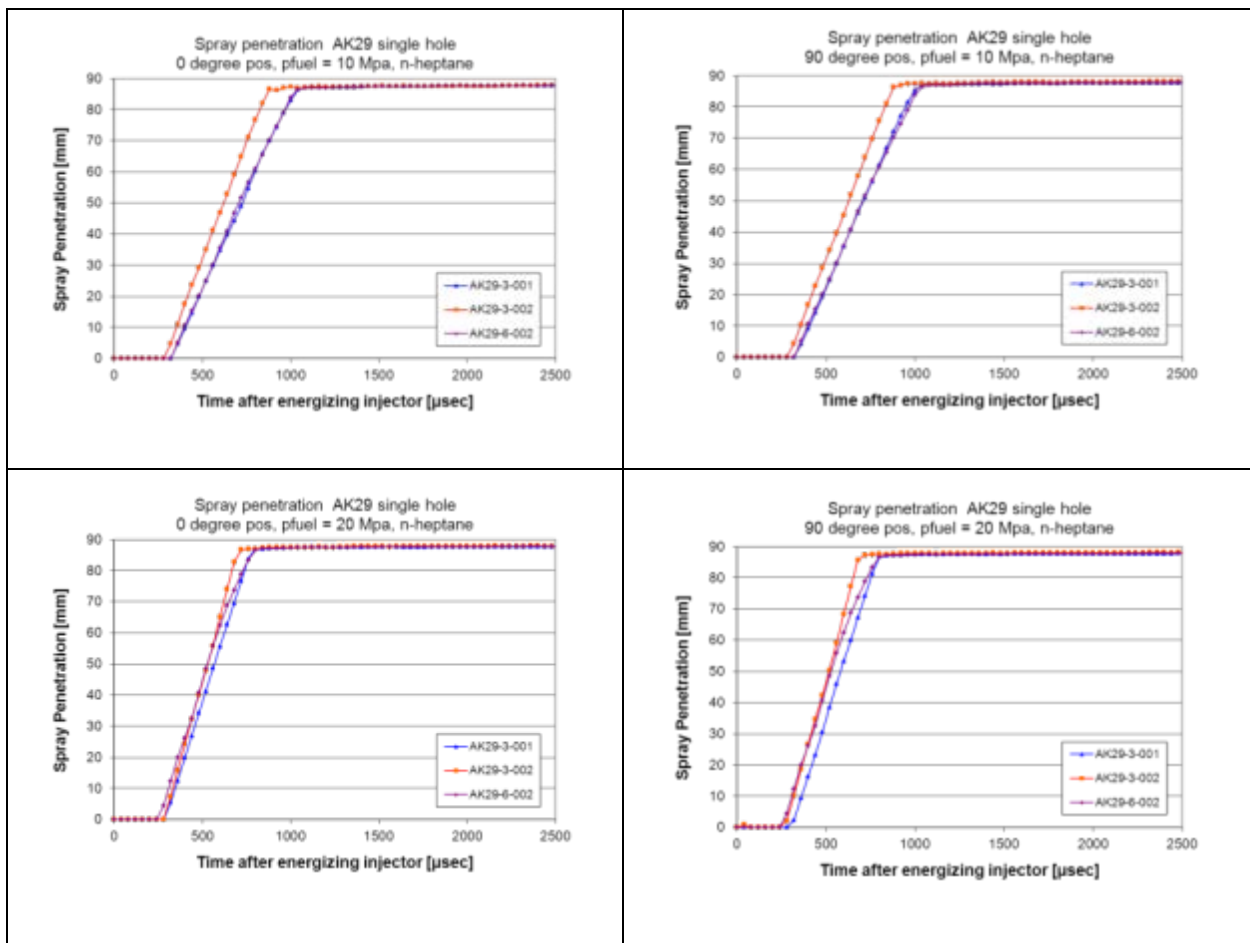


Figure 59 Spray Penetration after injection 0° , 90° at 10 and 20MPa calculated from Shadowgraph Images

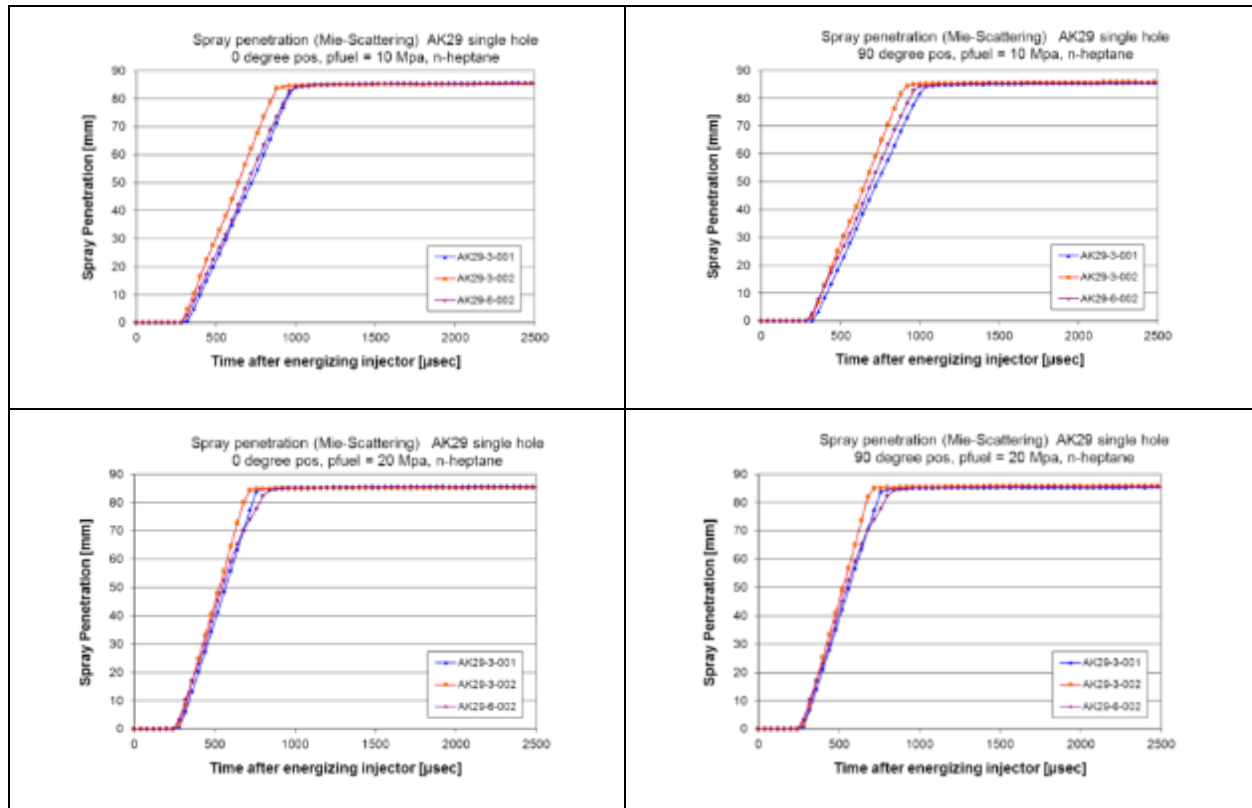


Figure 60 Spray Penetration after injection 0°, 90° at 10 and 20MPa calculated from Mie Scatter Images

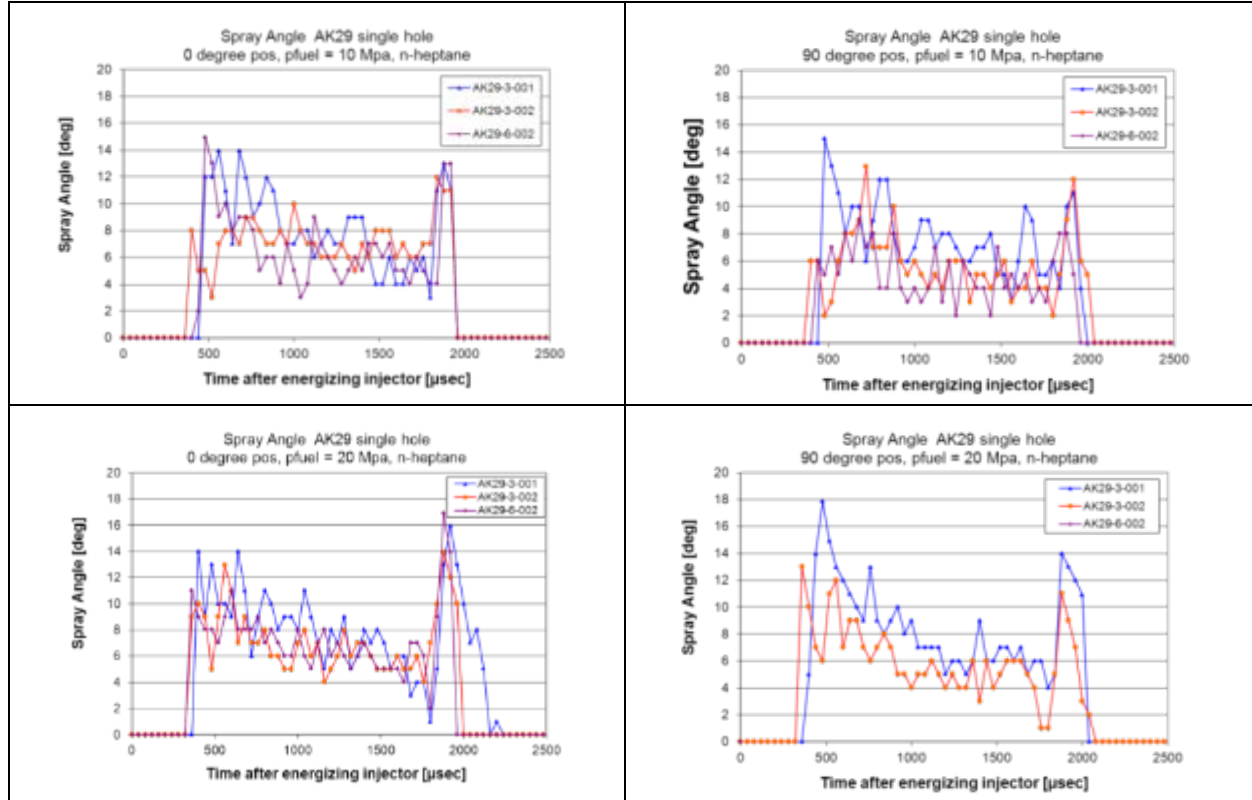


Figure 61 Spray Angle after injection 0°, 90° at 10 and 20MPa calculated from Shadowgraph Images

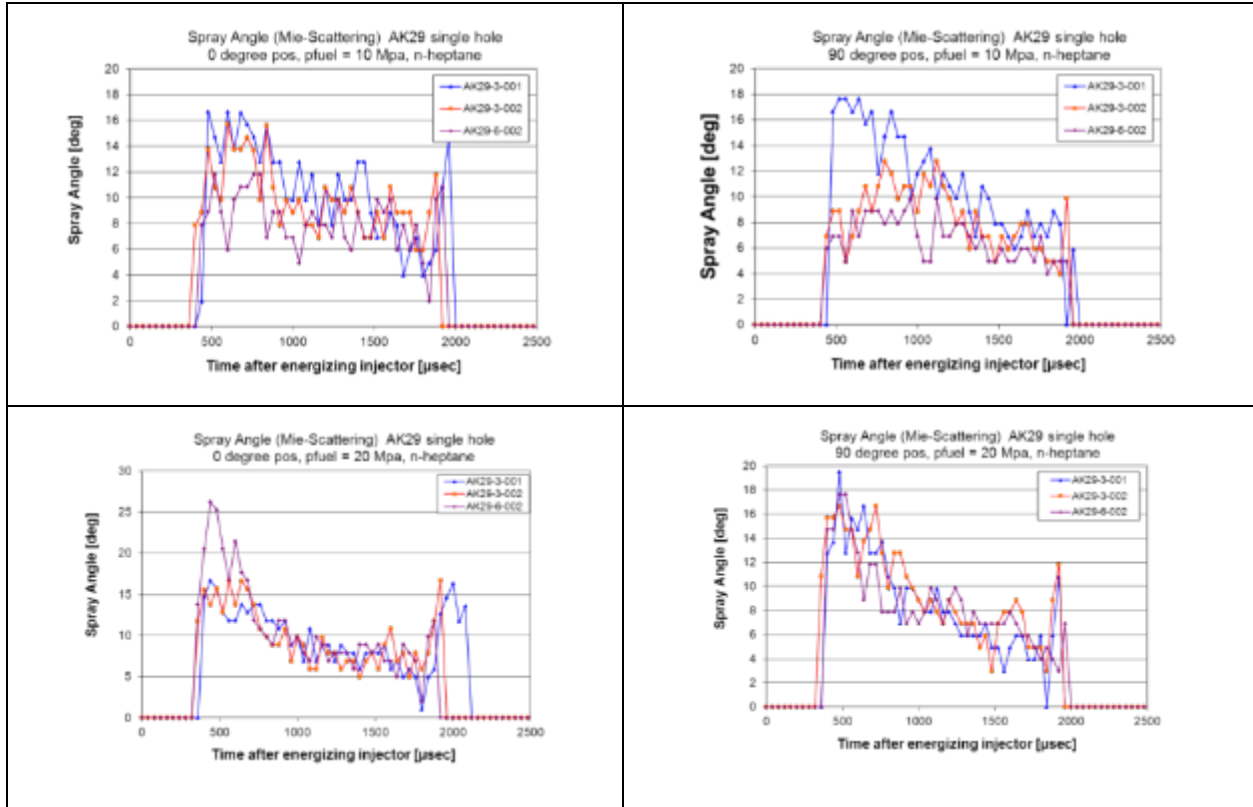


Figure 62 Spray Angle after injection 0°, 90° at 10 and 20MPa calculated from Mie Scatter Images

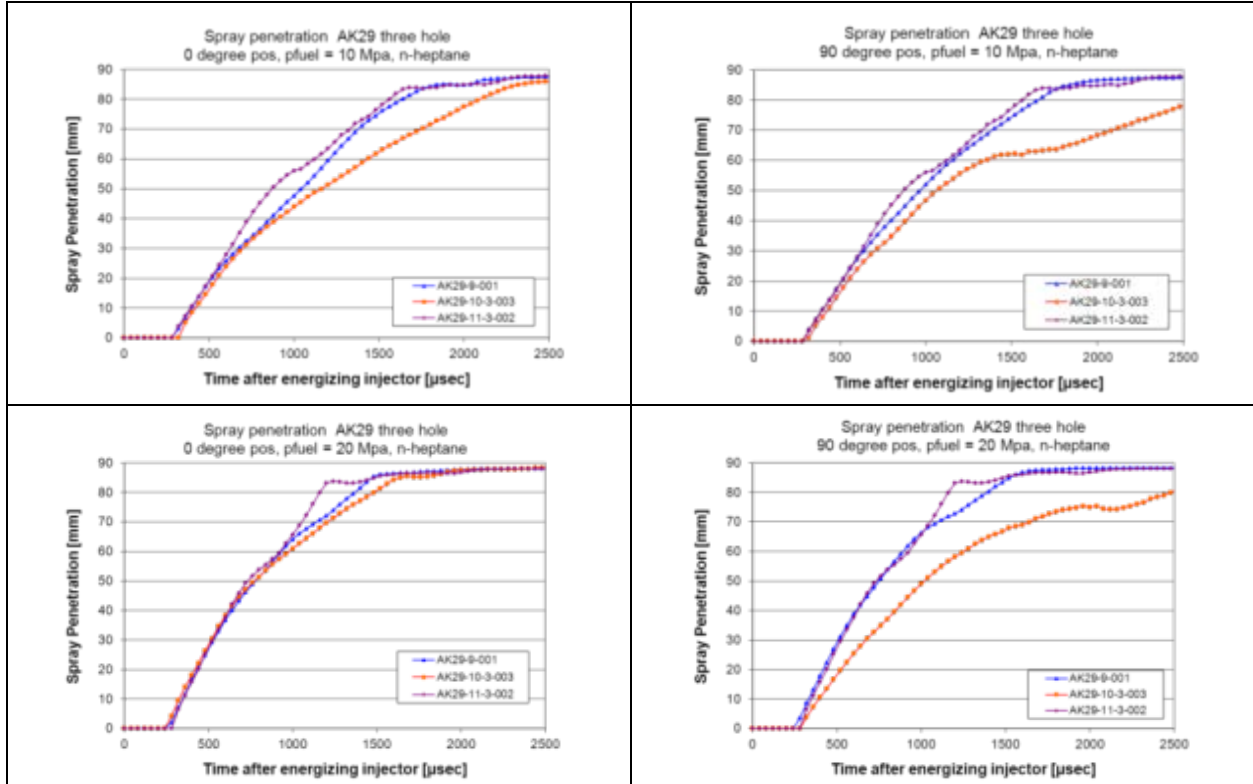


Figure 63 Spray Penetration after injection 0°, 90° at 10 and 20MPa calculated from Shadowgraph Images, 3-hole

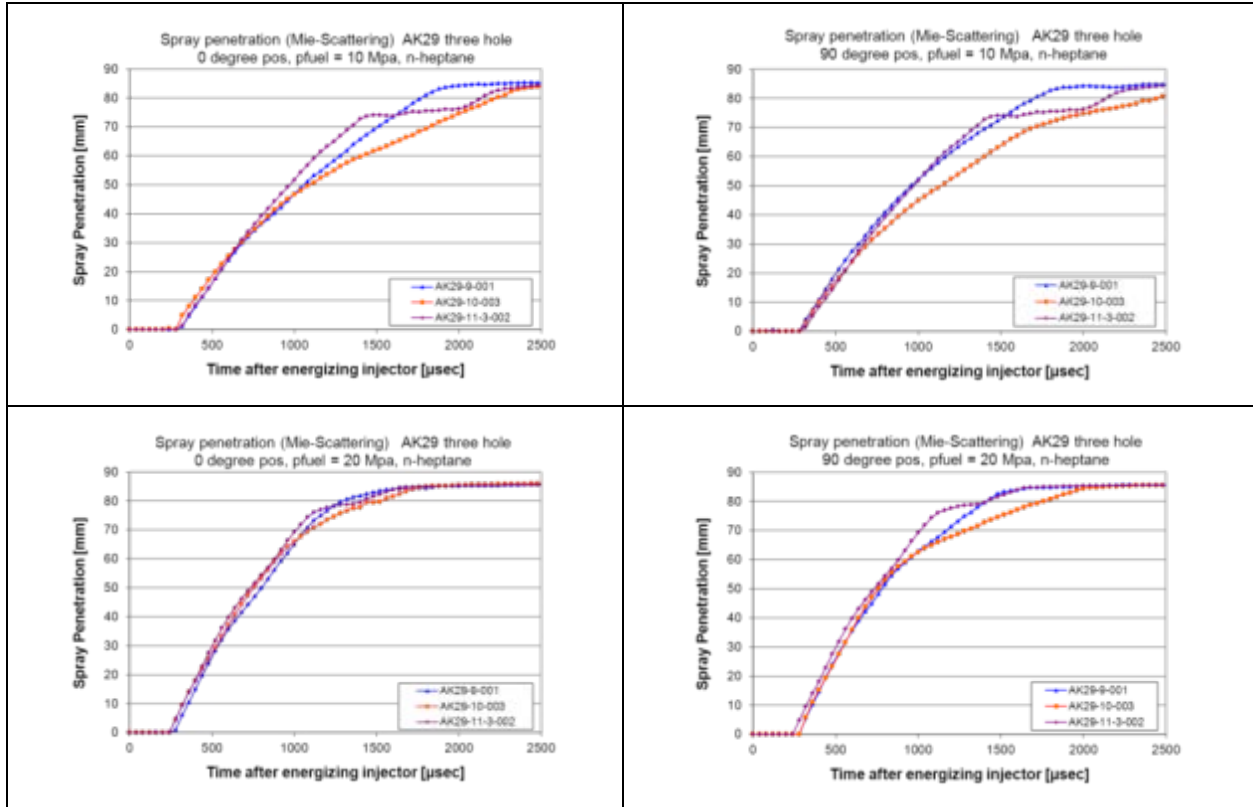


Figure 64 Spray penetration after injection at 10 and 20MPa calculated from Mie Scatter Images, 3-hole

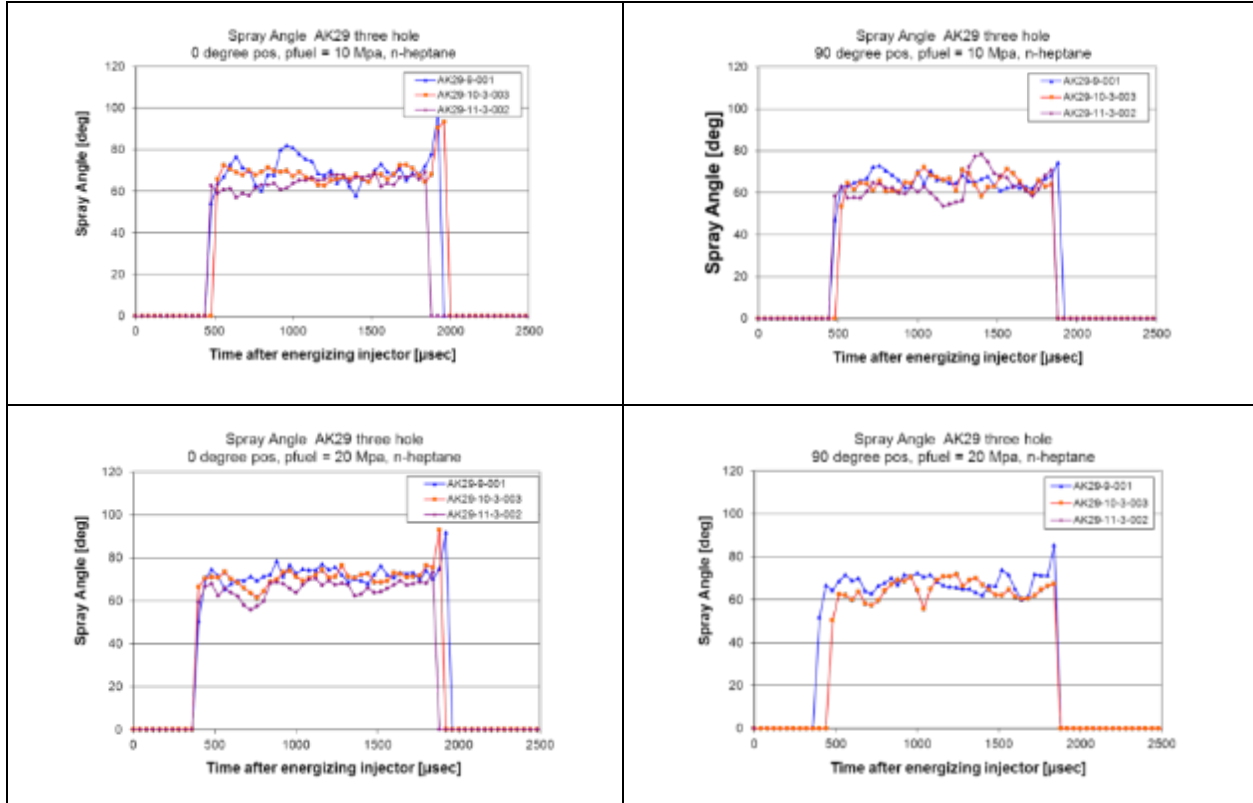


Figure 65 Spray angle after injection at 10 and 20MPa calculated from Shadowgraph Images, 3-hole injectors

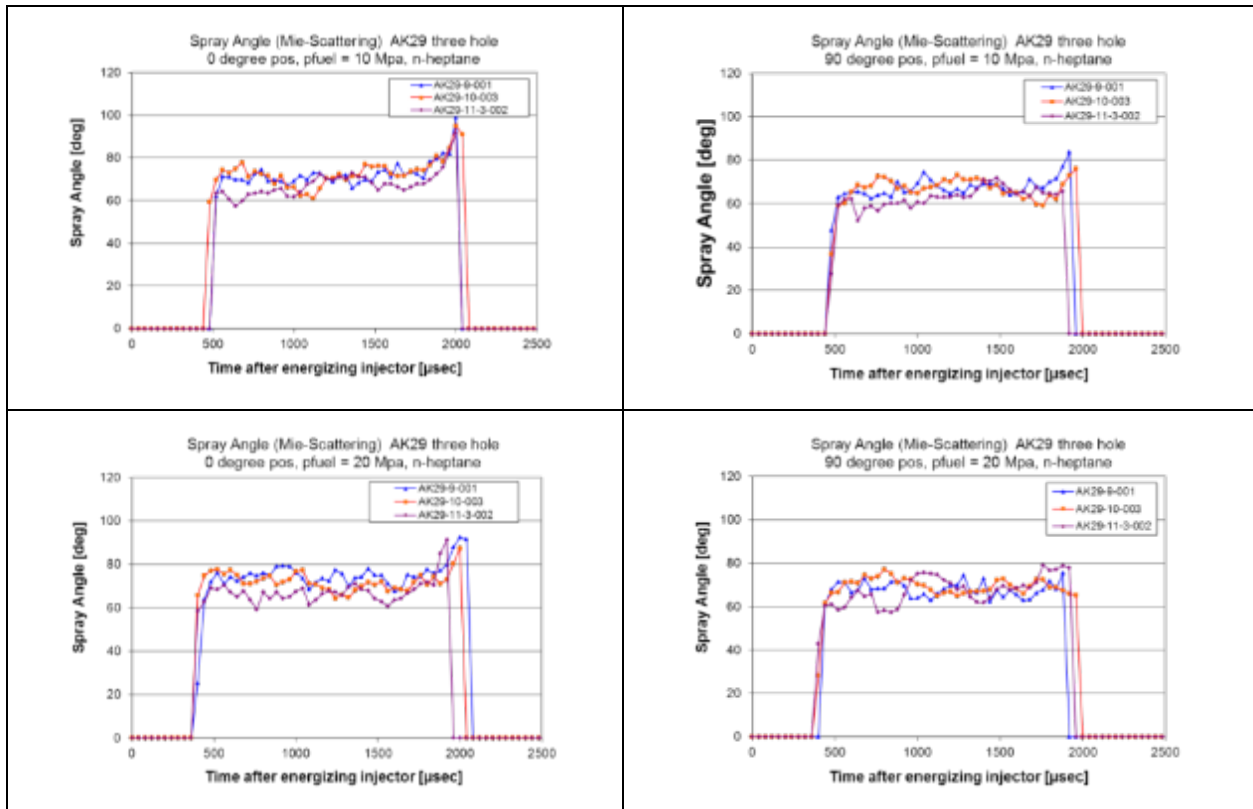


Figure 66 Spray angle after injection at 10 and 20MPa calculated from Mie Scatter Images, 3-hole injectors

Table 10 Injector Spray Droplet size distribution measured at 50mm from nozzle tip

Injector	Nozzle holes	Nozzle Key Feature	Fuel pressure [Mpa]	Sauter mean Dv32 [μm]	Dv43 [μm]	Dv10 [μm]	Dv50 [μm]	Dv90 [μm]
AK29-3-001	1	$d \approx .20$, $l/d=1.1$	10	7.3	15.6	3.5	11.9	30.5
AK29-3-002	1	$d \approx .20$, $l/d=1.1$	10	6.4	13.2	3.1	10.3	26.3
AK29-6-002	1	$d \approx .15$, $l/d=1.1$	10	6.6	14.8	3.1	10.9	29.6
AK29-9-001	3	$d \approx .20$, $l/d=1.1$	10	8.6	15.6	4.8	12.9	27.9
AK29-10-3-003	3	$d \approx .15$, $l/d=1.1$	10	8.3	16.3	4.3	13.1	30.6
AK29-11-3-002	3	$d \approx .15$, $l/d=3.96$	10	8.8	16.9	4.7	13.6	31.2
Injector	Nozzle holes	Nozzle Key Feature	Fuel pressure [Mpa]	Dv32 [μm]	Dv43 [μm]	Dv10 [μm]	Dv50 [μm]	Dv90 [μm]
AK29-3-001	1	$d \approx .20$, $l/d=1.1$	20	4.4	8.9	2.0	6.9	17.7
AK29-3-002	1	$d \approx .20$, $l/d=1.1$	20	4.4	8.6	2.0	6.8	17.1
AK29-6-002	1	$d \approx .15$, $l/d=1.1$	20	3.8	8.0	1.6	5.8	16.5
AK29-9-001	3	$d \approx .20$, $l/d=1.1$	20	5.6	10.2	2.8	8.5	18.8
AK29-10-3-003	3	$d \approx .15$, $l/d=1.1$	20	5.2	10.1	2.5	8.1	19.1
AK29-11-3-002	3	$d \approx .15$, $l/d=3.96$	20	5.6	10.6	2.7	8.7	19.6

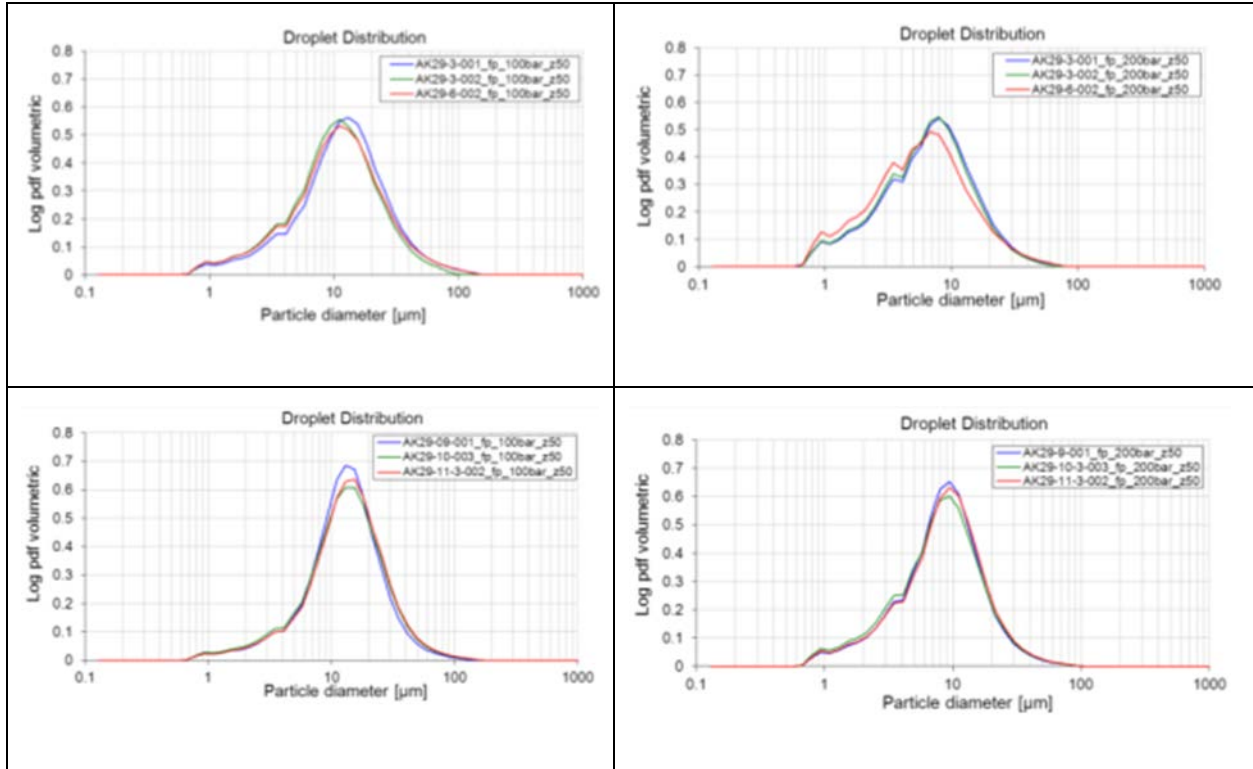


Figure 67 Spray Droplet size distributions for single and 3-hole injectors

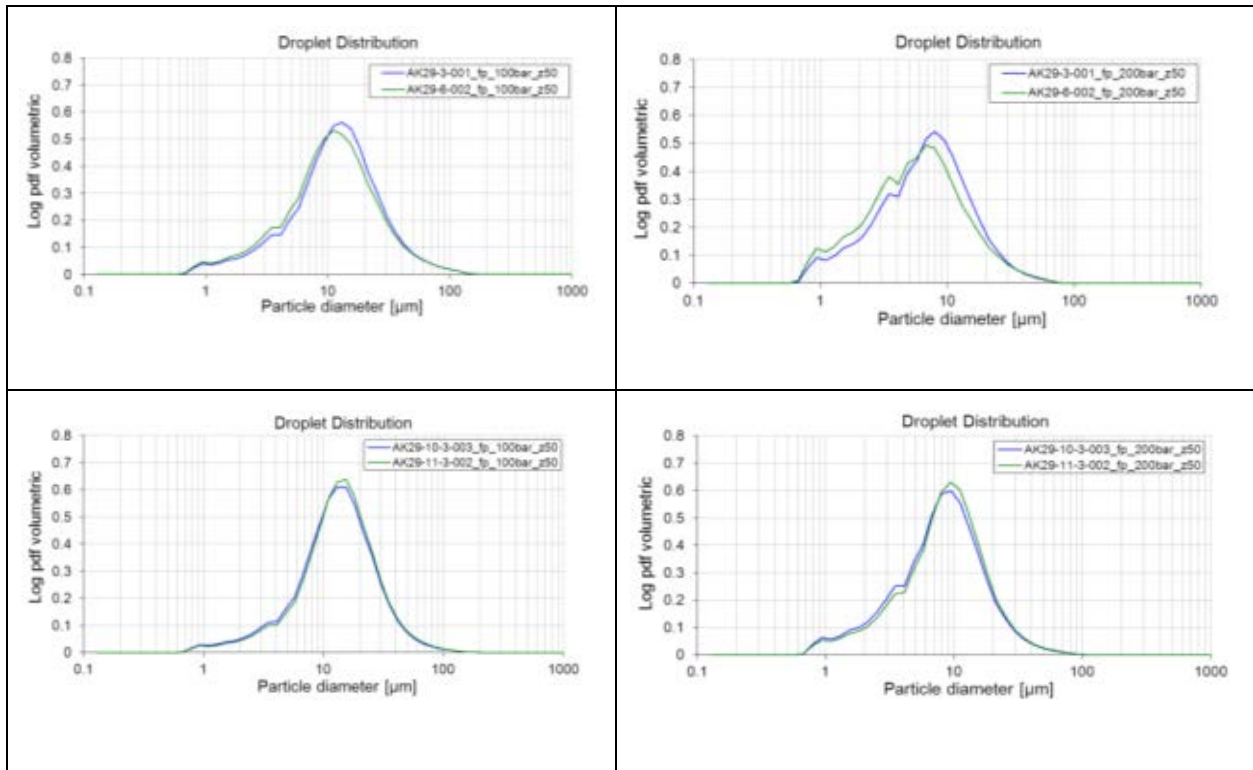


Figure 68 Spray Droplet size distributions single nozzle, $d \approx 20$ & $d \approx 15$, at 10 and 20 MPa, and 3-hole nozzle, $l/d=1.1$ & $l/d=3.96$, at 10 and 20 MPa

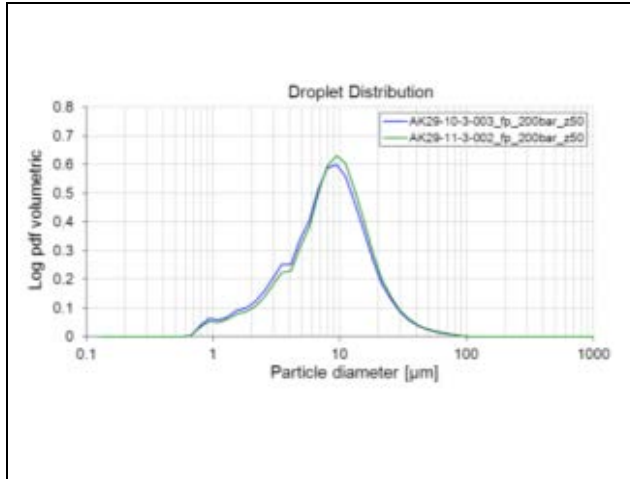


Figure 69 Spray Droplet size effect of Counterbore

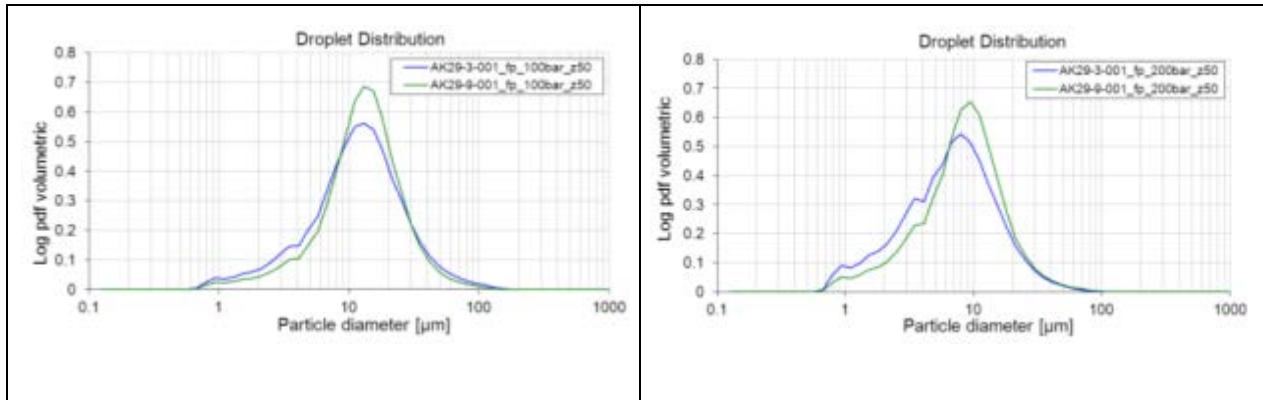


Figure 70 Spray Droplet size effect of Skew angle at 10, 20MPa

5.2.4 Summary/Conclusion on Physical Test and Modified Project Scope Direction

Review of the spray imaging revealed that axis-symmetric single-hole seats produced spray plumes with a slightly narrower plume angle and a much longer penetration than single-hole nozzles with a 30° skew angle or the 3-hole seats as shown in Figure 71. The spray morphology of seats with approximately a 30° skew angle more resemble production 5 or 6 hole injectors. Testing of 3-hole seats with 30°, 20°, and 10° skew angles, shown on Figure 72, revealed the same tendency. The 20° geometric skew angle injectors demonstrated a spray plume skew angle of approximately 17° and the 10° geometric skew angle nozzles collapsed into a single spray plume. Based on these findings, the prototype seats underway for calendar year 2012 testing were adjusted to add more focus on 3-hole seat configurations with 30° skew angles, which are expected to provide representative and thus more meaningful results for future GDi injector nozzle design. The injector test plan, injector solid models with FEA meshes, and LES simulations were

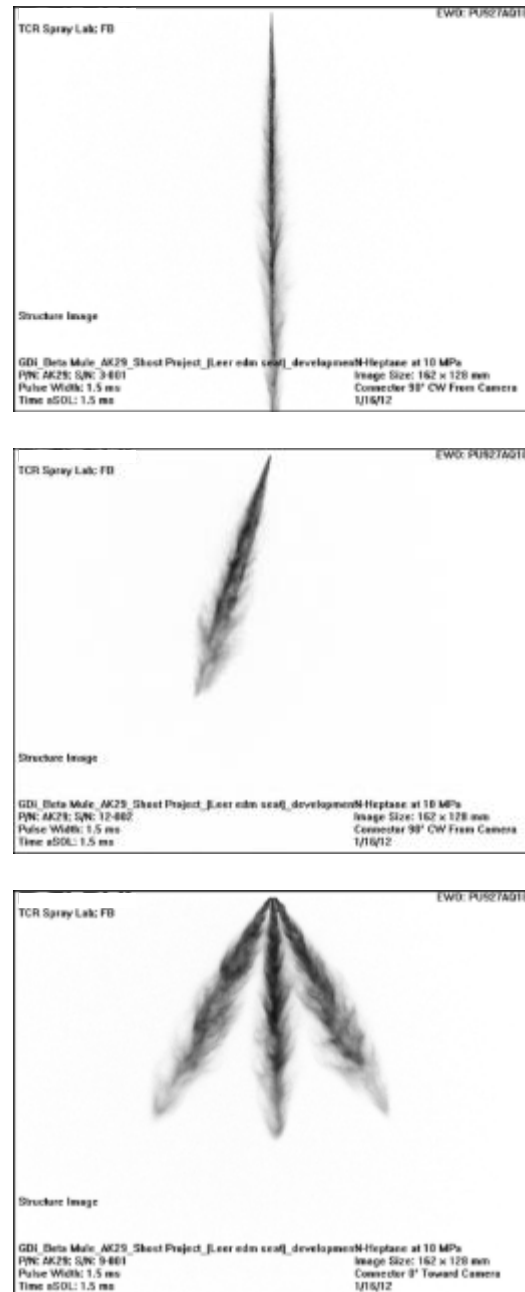


Figure 71 Shadowgraphic Spray Images for axis-symmetric, skewed angled and 3-hole seats

re-focused accordingly. The impact of this change would add approximately 1 year to the study, as previous modeling and testing would be redone. The intended second SAE paper expected to conclude this work, which was to focused on axis-symmetric single-hole nozzle test results, would be replaced by two future SAE papers each including LES simulation and experimental results focused on the injector design parameters established in Chapter 4 .

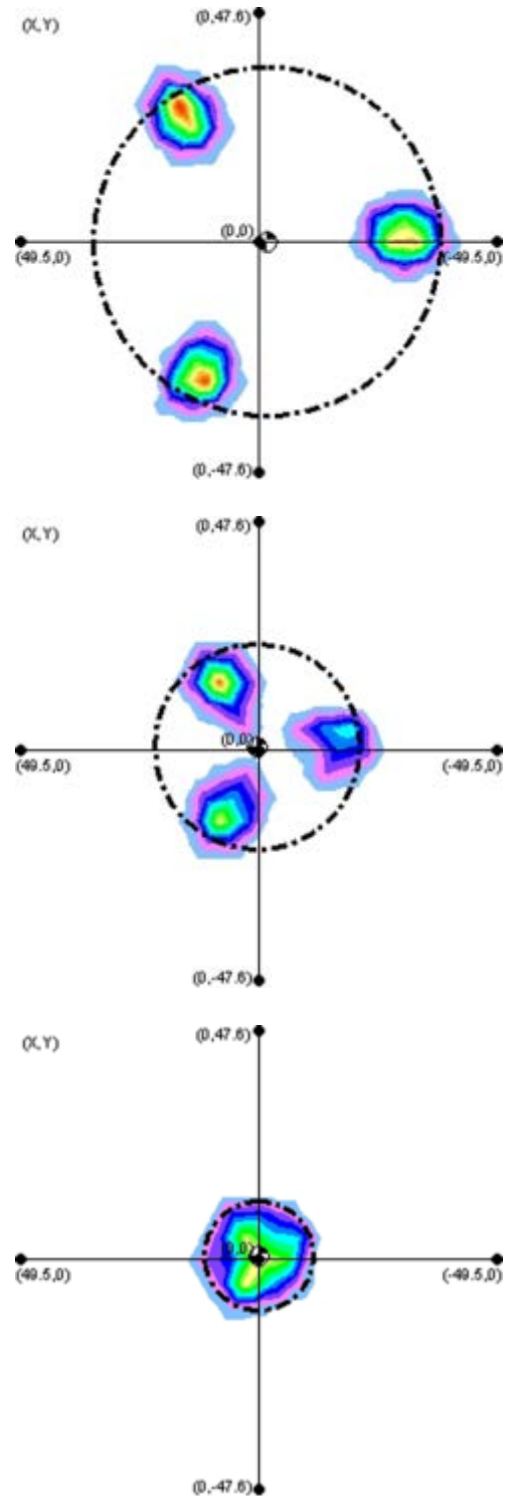


Figure 72 Patternization tests for 10°, 20°, and 30° sk

5.3 GDi Skew-Angled Nozzle Flow and Near-Field Spray Analysis using Optical and X-ray Imaging and VOF-LES Computational Fluid Dynamics

The results of this section were published [60] and presented at the SAE World Congress held in Detroit in April of 2013. The objective of this study is optical imaging investigation of the nozzle near-field jet breakup structure and the influence of nozzle geometry on the spray primary atomization. Of specific interest, especially for comparison with the VOF-LES model, is the nozzle near-field spray primary breakup structure and relevant geometric parameters. The data is obtained with the aid of conventional shadowgraph optical imaging techniques at the Delphi Technology Centre Luxembourg and phase-contrast X-ray imaging using high-intensity and high-brilliance X-ray beams available at the Advanced Photon Source (APS) at Argonne National Lab.

5.3.1 Nozzle Geometry

Figure 73 presents views of the purpose-built 3-hole GDi seat geometry. For this investigation, the same injector seat contained nozzle A and B geometry. This was accomplished by using a purpose-built seat containing 3

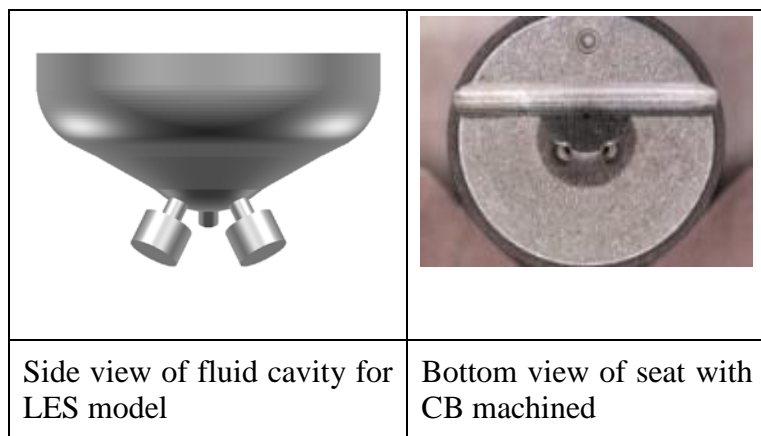


Figure 73 Geometry of the GDi 3-hole seat and nozzles

holes having identical thru-hole and counterbore dimensions arranged at 120° circumferential spacing. A secondary process was used on the seat of nozzle B geometry to precisely grind the seat of one hole to remove seat material to the depth of the counterbore, thus producing nozzle geometry as shown in the 4.2 Test Hardware. Figure 74 provides a view of the nozzle-hole

geometry for nozzle A and B and their associated dimensional parameters. The thru-hole diameter (d) is of the order 0.2mm, and the skew-angle from the injector axis (β), thru-hole length (l), counterbore diameter (D), and counterbore length (L) is representative of modern multi-hole GDi seats. The skew-angle $\beta=30^\circ$ was particularly selected to precipitate nozzle flow separation and, thereby, enable predictive accuracy of the VOF-LES method for prediction of the deviation between the plume trajectory and the nozzle axis direction for typical production GDi nozzles.

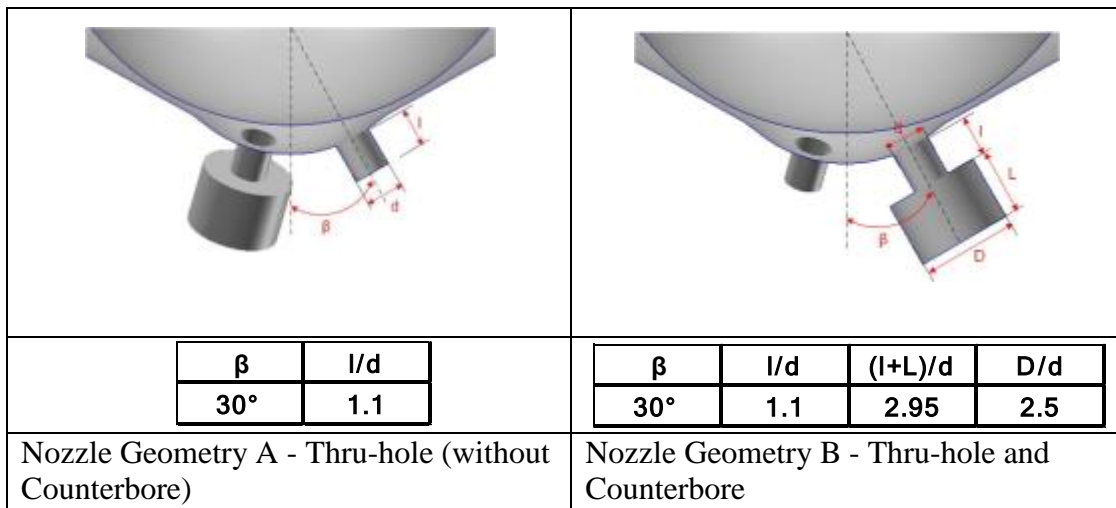


Figure 74 Nozzle Geometry A and B with associated dimensional parameters

5.3.2 Nozzle Geometry A, without Counterbore

Figure 75 presents the temporal development of the spray plume near-field with snapshot images at selected instances after the start of injector energizing (ASIE) for the fuel system pressure of 10MPa. The images provide evidence of an “atomization regime” turbulent jet breakup. The jet primary breakup happens within close vicinity of the nozzle, almost immediately after the injector opening and plume emergence. Remarkably, the development of the jet Kelvin-Helmholtz interface instabilities and primary breakup is detectable within 2mm vicinity of the nozzle exit. The most notable feature of the spray plume morphology is the

intermittent jet breakup structure, which is evident in the wave pattern of spatial liquid mass distribution longitudinal with the plume propagation.

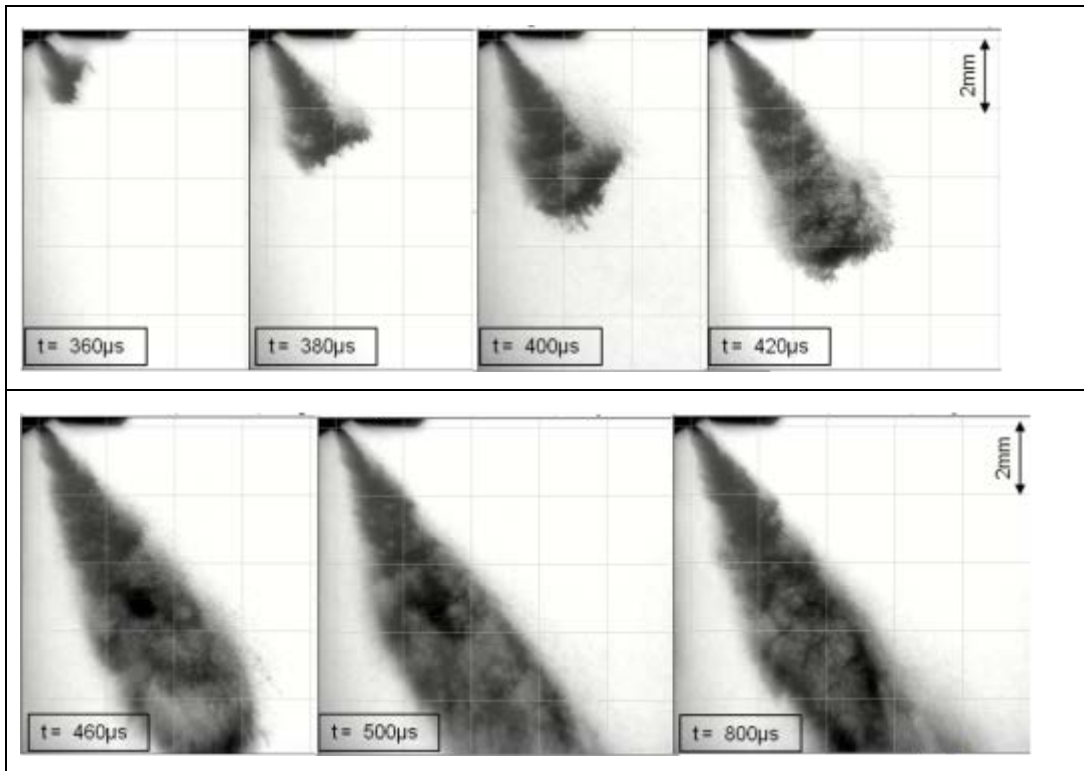


Figure 75 Shadowgraph imaging of the nozzle near-field spray plume (fuel pressure=10MPa, t=time ASIE)

The plume intermittent morphology is clearly discernible in Figure 76. This shows the concurrent development of the interface instabilities close to the nozzle exit, intermittent spatial mass distribution and associated wave-like jet breakup into concentrated ligament structures that subsequently atomize through interaction with the air. This plume morphology is caused by the injection rate pulsations that are induced by the high-frequency hydraulic pressure oscillations in the injector valve group. This structure is also attributed to unsteady vortex shedding and cavitation in the GDI multi-hole nozzles, although it shows correlation with the nozzle pressure

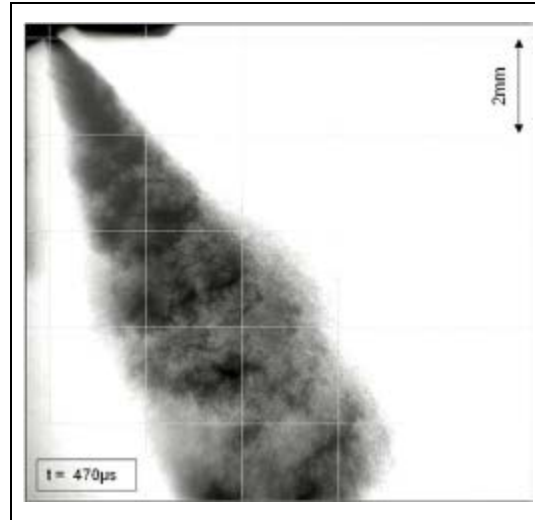


Figure 76 Nozzle near-field plume structure, primary breakup and atomization (fuel pressure=10MPa, $t=470\mu\text{s}$ ASIE)

and the injection rate oscillations [61]. It is also detectable in the measurements of diesel sprays [62]. This morphology is notable, since it highlights the coupling of the injector design hydraulic features with the spray breakup structure and atomization. The concurrent plume breakup and the atomization of ligaments are through interactions with the ambient air accompanied by the spray lateral dispersion. It is expected that the plume intermittent structure influences all aspects the spray-air interactions, such as air entrainment rate, penetration, etc., that affect its mixture preparation characteristic.

Figure 77 provides an indication of the spray plume shot-to-shot variation, for five repetitions at $t=700\mu\text{s}$ ASIE, and the associated statistical average (normalized liquid-phase probability density function) for the plume geometry. Since the SAE standard method for quantifying the plume geometry [42] is not applicable to the nozzle near-field, the plume angle is characterized per section 4.1 Defined Terms based on the plume width between 1mm and 8mm downstream of the nozzle along the injector axis. Figure 77 (a) shows that the intermittent formation and atomization of the massive ligaments, due to interactions with the ambient air,

cause stochastic variations of the plume spatial structure, lateral dispersion, and trajectory. Figure 77 (b) shows the alignment of jet center-line with the nozzle axis and statistical variation of the plume angle in the range $\phi = 19^\circ - 26^\circ$ due to shot-to-shot plume breakup variability.

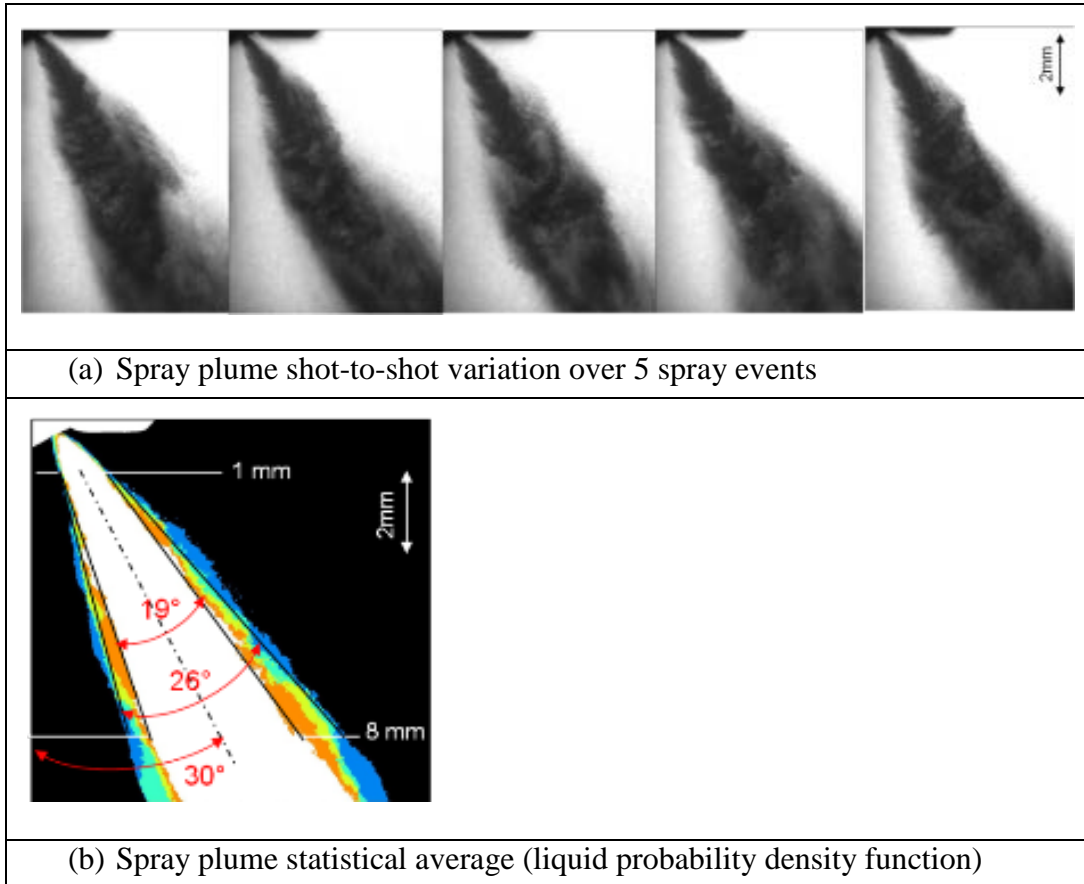


Figure 77 Spray plume shot-to-shot variation and statistical PDF (liquid-phase probability density function) (fuel pressure =10MPa, $t=700\mu\text{s}$ ASIE)

The optical image shadowgraph provides good insight into the spray plume structure. However, the use of conventional optical techniques to provide information about the internal structure of high-speed jets in immediate vicinity of the nozzle exit has proven problematic due to the multiple scattering by droplets and interfaces, and the high density of the near-field jet. This problem becomes exacerbated as fuel pressures rise, as noted in the optical images at 20MPa, and spray masses yield a larger level of spatial liquid concentration and higher jet velocity, therefore the jet breakup structure is not as sharp and discernible. For this reason,

researchers have often concentrated more on the leading edges of the spray field. In previous research, in order to provide more insight into the near field structures, ultrafast synchrotron X-ray full-field phase-contrast imaging has been used [63]. This technique reveals instantaneous velocity and internal structure of optically dense sprays with a combined spatial and time resolution. It is employed in this work to gain insight to the turbulent jet characteristics at the near-field of nozzle exit. The test fluid used in the X-ray visualization is Viscor-16B2, whose physical properties compared with n-heptane used in the shadowgraph tests are listed in Table 6. The spray field is captured in a series of 1.32mm tall by 1.74mm wide image blocks. In order to provide a view of the spray plume formation a series of five optical image panels, taken at the same time ASIE, are used to form a mosaic covering the spatial range of interest, as shown in Figure 78. In prior work done by the author for diesel sprays with injection pressures of 30-100MPa [63], good spatial coherence of the composite images resulted from excellent shot-to-shot repeatability of the structures. However, when this technique was extended to GDi multi-hole injectors operated at 5-10MPa, the spray was found to be highly temporally and spatially stochastic [34]. In order to construct a view of the developing spray, multiple pictures were taken for each panel, and then a collection of panels was selected to form the best spatially coherent composite picture, or mosaic, representative of a typical temporal event.

Figure 78 presents the phase-contrast X-ray imaging for nozzle geometry A at 10MPa. As shown in the figure, spray has enveloped the 4mm visual field by 430 μ s ASIE. Inspection of the image at 430 μ s reveals a stochastic pattern of waves that is consistent from nozzle exit through the spatial field, 0-4mm distance. The plume structure suggests breakup at the nozzle exit with established disturbances that originated inside the nozzle and turbulent dispersion perpendicular to the spray axis. The chaotic jet breakup structure and shot-to-shot variation of

the plume angle is visible. There is substantial difference between the GDi plume morphology, shown in Figure 78, and the X-ray phase-contrast images of the diesel nozzle near-field plume breakup structure [64] [65]. The data signify the influence of the seat-nozzle geometry on the plume breakup mechanism and spray morphology.

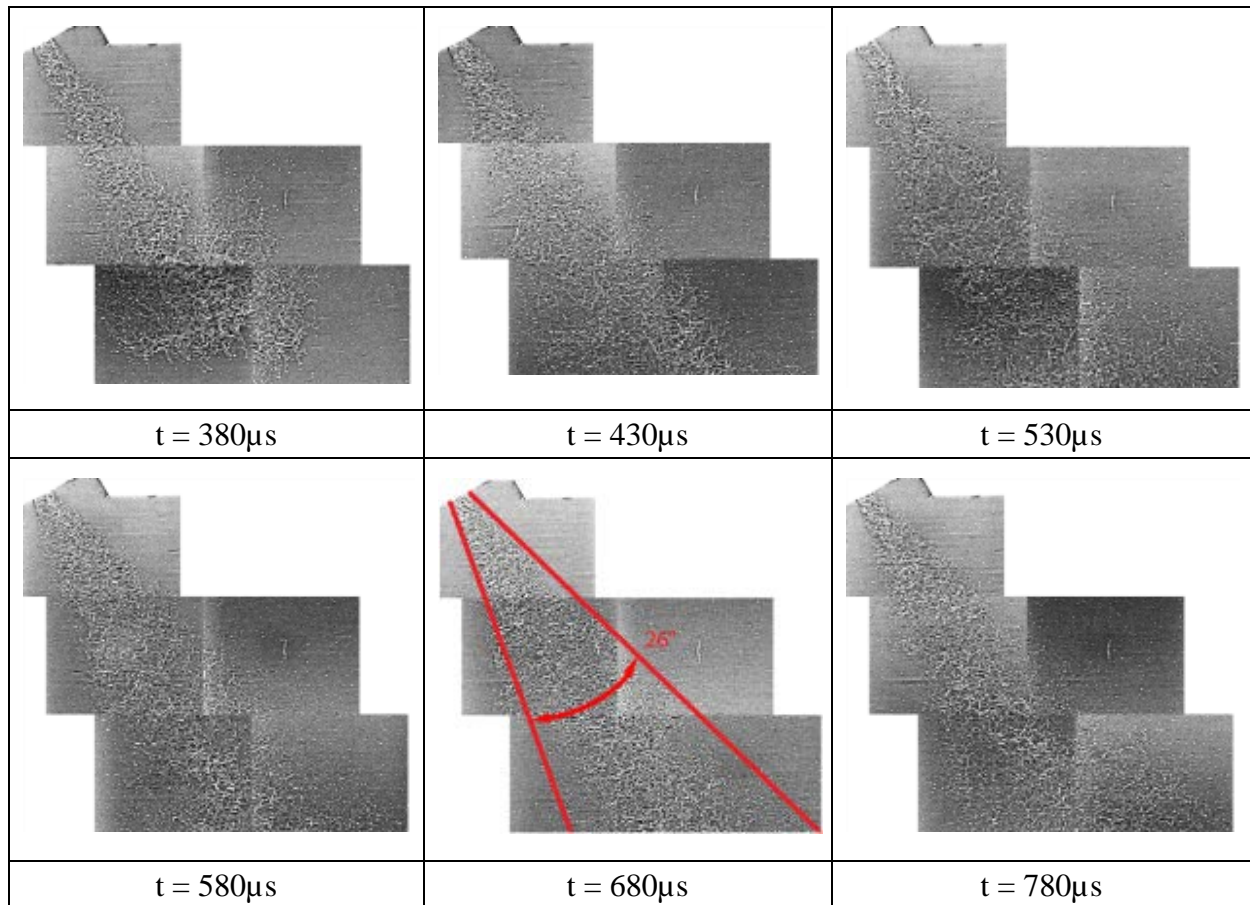


Figure 78 Nozzle A X-ray phase-contrast imaging (fuel pressure=10MPa, t=time ASIE)

A notable feature of the spray plume imaging data, in Figure 75 to Figure 78, is the alignment of the plume trajectory with the geometric nozzle axis direction. This differs from previous studies of the GDi nozzle internal flow and spray for different seat-nozzle geometry [33] that highlighted the liquid-phase flow separation in a skew-angle nozzle as a primary cause of the commonly observed deviation of the plume trajectory from the nozzle axis direction. The alignment in the present study suggests absence of a major liquid-phase flow separation within

the nozzle, as indicated by the VOF-LES simulation. This dissimilarity is attributable to the differences in the seat-nozzle geometries of the two studies; notably the hole-to-hole circumferential separation, 120° in present study vs. 60° in Ref. [33], and the nozzle skew angle, $\beta=30^\circ$ simple vs. compound angle in Ref [33]. The geometric differences alter the nozzle-entrance velocity condition, which alters the structure of the nozzle flow and the jet velocity distribution and turbulence condition.

5.3.3 Nozzle Geometry B, with Counterbore

The imaging data for the nozzle geometry B provides a comparison of the influence of counterbore on the spray breakup structure. Figure 79 presents the temporal development of the

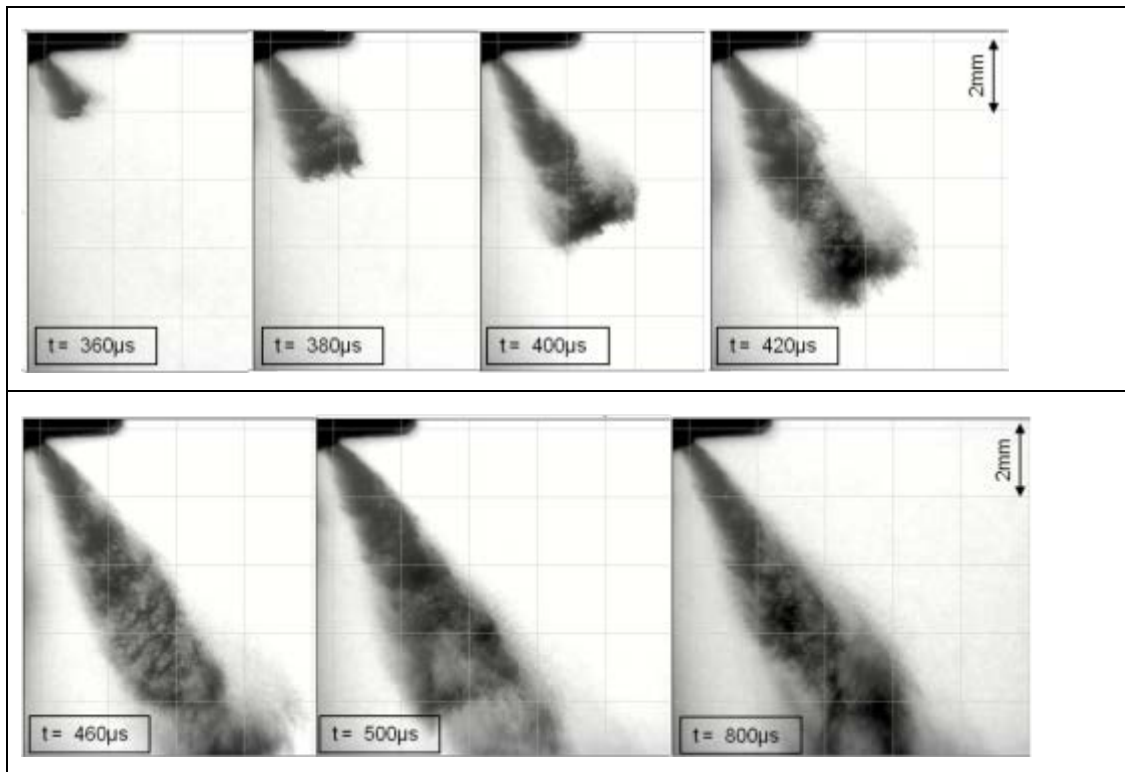


Figure 79 Shadowgraph imaging of the nozzle near-field spray plume (fuel pressure=10MPa, t=time ASIE)

spray plume near-field for the fuel system pressure of 10MPa. The images show evidence of the spray plume breakup and atomization, taking place immediately after the jet emergence, within close vicinity of the nozzle. As in the case of Nozzle A, the most notable feature of the temporal-

spatial plume development is the intermittent jet breakup morphology induced by the hydraulic pressure oscillations in the injector valve group.

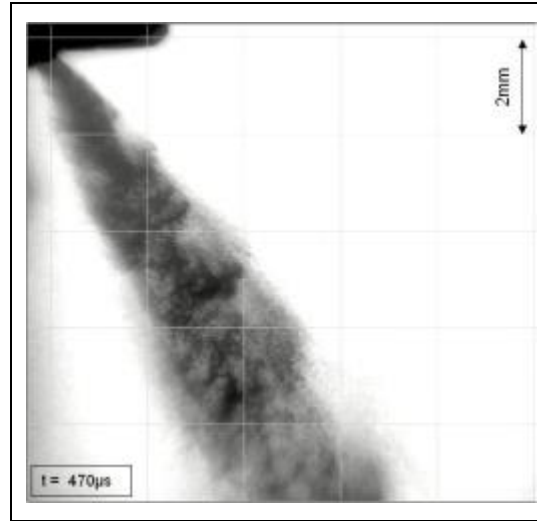


Figure 80 Nozzle near-field plume structure, primary breakup, and atomization (fuel pressure=10MPa, $t=470\mu\text{s}$ ASIE)

Figure 80 displays the nozzle-near-field plume primary breakup and atomization structure. The jet morphology appears similar to that of nozzle A, shown in Figure 75, which illustrates the development of interface instabilities, intermittent liquid jet breakup, formation of large ligaments, which deform and spread the plume in the lateral direction and atomize through interaction with the ambient air.

Figure 81 provides an illustration of the extent of spray plume shot-to-shot variation. It presents five repetitions of the plume image at $t = 700\mu\text{s}$ ASIE and the associated statistical average (liquid-phase probability density function) for the fuel pressure of 10MPa. The plume trajectory is aligned with the nozzle axis, but there is notable reduction in plume angle compared to nozzle A. One likely explanation, provided by the VOF-LES simulation, is the physical plume interaction with the counterbore wall, which imposes restriction on the plume angle. This explanation is supported by the plume images in Figure 79 to Figure 82 that show spray plume at

the nozzle exit emerges with the width of the counterbore, although this does not prove a preceding physical interaction.

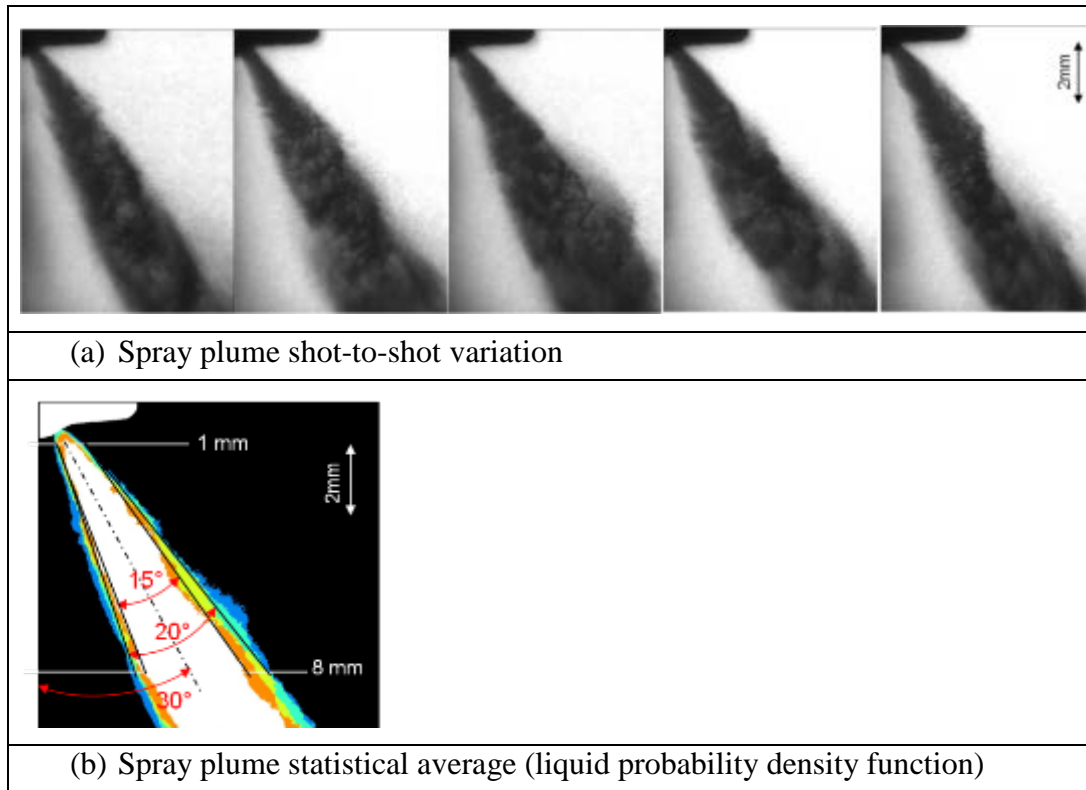


Figure 81 Spray plume shot-to-shot variation and statistical PDF (liquid –phase probability density function) fuel pressure=10MPa, $t = 700\mu\text{s}$ ASIE

Figure 82 presents the phase-contrast X-ray imaging for nozzle geometry B at 10MPa. Similar jet breakup morphology to that of nozzle A is evident throughout the temporal progression to $780\mu\text{s}$ ASIE. The notable characteristics are the jet breakup in the immediate vicinity of the nozzle with a stochastic pattern indicating transverse structures normal to the plume axis. Some discrete particles appear surrounding the structures in all of the time exposures. It is unclear whether these droplets result from breakup due to interaction of near-field spray ligaments and surrounding ambient air, or result from spray plume interaction with the counterbore wall. The quantity of droplets does appear qualitatively greater than evidenced in nozzle A.

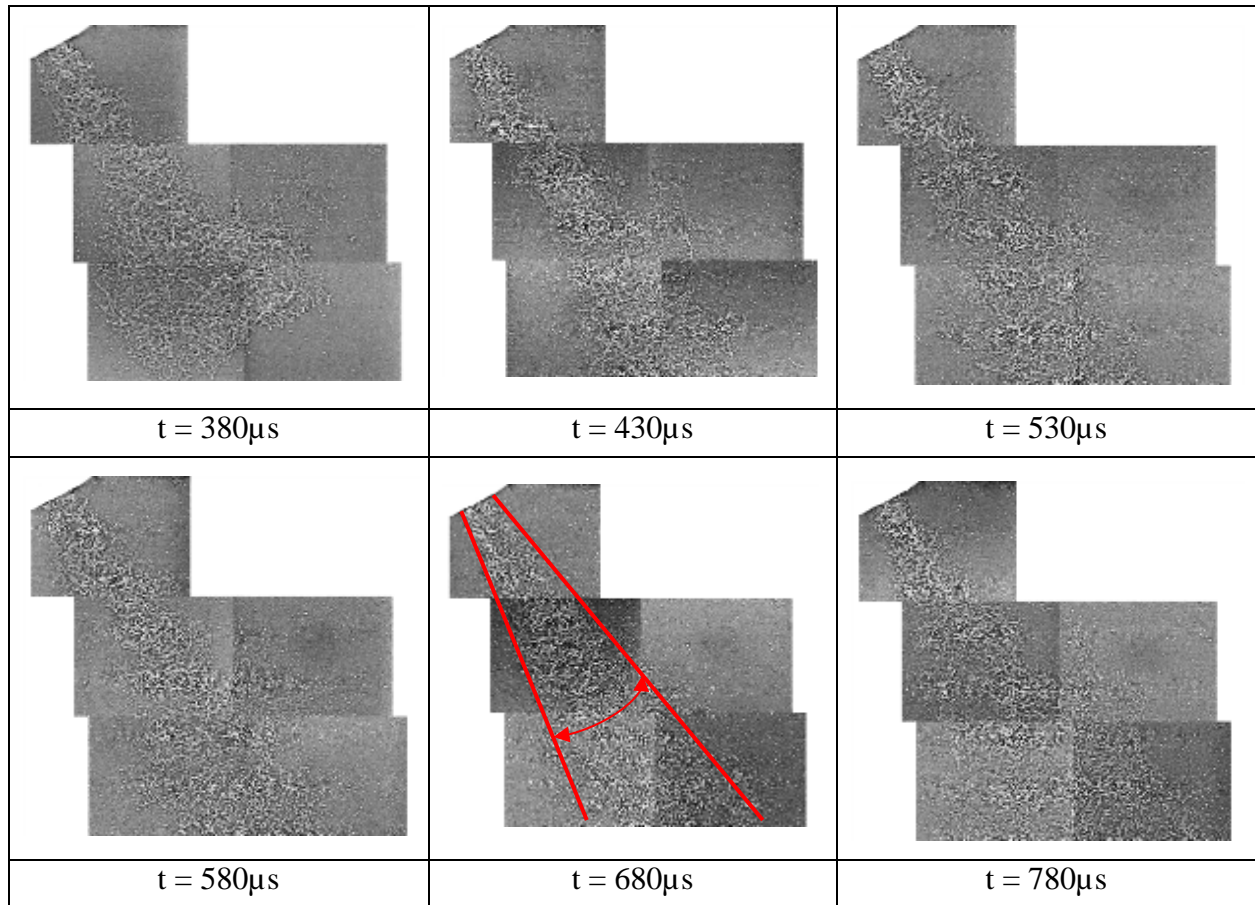


Figure 82 Nozzle B X-ray imaging of the nozzle near-field spray plume (fuel pressure=10MPa, t=time ASIE)

Nozzle geometry A – w/o Counterbore

The transient development of the flow within the injector seat and the nozzle near-field jet primary breakup structure is illustrated by the plots of evolution of the VOF=0.5 iso-surface, colored by the instantaneous velocity, at selected times after the start of simulation (ASOS), in Figure 83. The VOF=0.5 iso-surface is commonly used as the median value (Air = $0 \leq \text{VOF} \leq 1$ = Liquid) to present the liquid-air interface geometry. Figure 84 presents the corresponding VOF contour plots on the nozzle symmetry plane, and aids to elucidate the jet primary atomization structure.

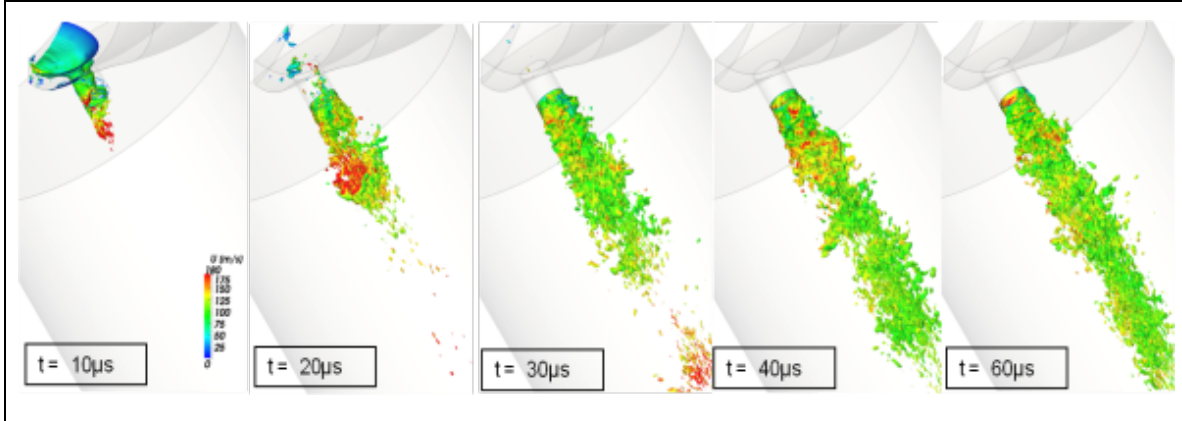


Figure 83 Iso-surface plots of VOF= 0.5, colored by the instantaneous local velocity magnitude, at selected times ASOS

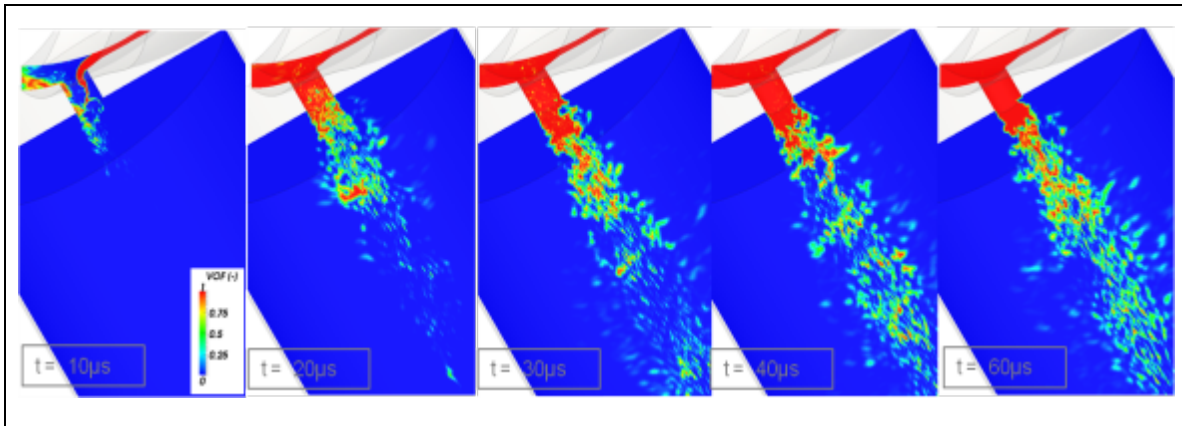


Figure 84 VOF Contour plots on the nozzle symmetry plane, at selected times ASOS

The initial stage of the transient nozzle flow is affected by the scavenging of the entrapped air within in the sac volume. This phase is characterized by transition of a separated liquid jet within the nozzle, concurrent with a ‘slug’ type two-phase flow, to a fully attached nozzle flow that produces a full-cone liquid jet. This is accompanied by the transient expelling of the air entrapped in the sac volume in the form of transition of the nozzle flow from the initial slug type two-phase flow to a dispersed bubble type flow. After complete discharge of the sac air, the nozzle flow and the liquid jet attain a stationary structure at $t=40\mu s$. Nevertheless, Figure 83 and Figure 84 illustrate the unsteady character of the jet primary breakup, caused by the

nozzle turbulent velocity disturbances in addition to the boundary pressure oscillations induced by the imposed acceleration of the inlet velocity boundary condition.

The unsteady character of the jet primary breakup is further illustrated in Figure 85 by the VOF contour plots on the planes normal to the jet axis, within the nozzle, and at locations $z = 0$ (corresponding to the counterbore exit plane in Nozzle B), and $z = 5 \cdot d$ downstream of the injector.

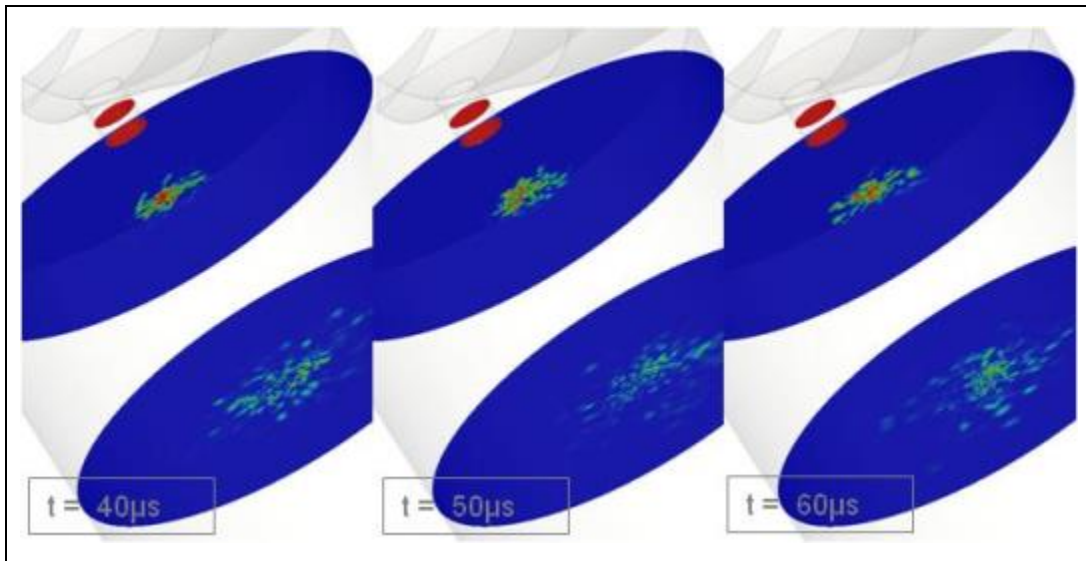


Figure 85 VOF Contour plots on planes normal to nozzle axis, in nozzle hole and at locations $z = 0$ and $5 \cdot d$ ($t = ASOS$)

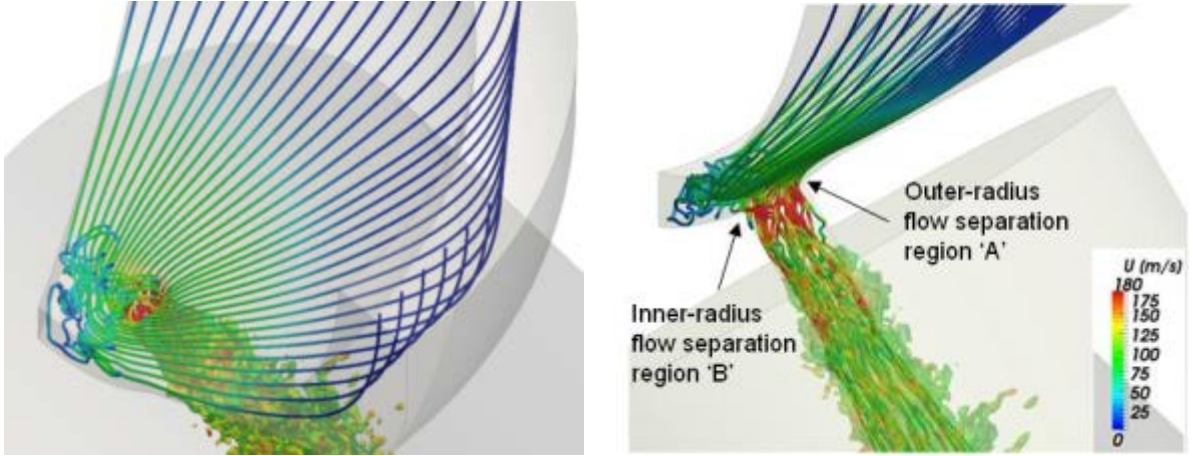


Figure 86 Flow stream-lines colored by local instantaneous velocity ($t = 60 \mu\text{s}$ ASOS)

A notable feature of the VOF-LES predictions is the absence of flow separation at the nozzle entrance. Flow separation at nozzle entrance was predicted in a previous VOF-LES analysis of the GDi multi-hole skew-angled nozzle geometry [33] and identified as a cause of deviation of the liquid jet trajectory from the nozzle-hole axis. As noted earlier, the primary difference between the present VOF-LES analysis and that of reference [33] is associated with the seat-nozzle topology. Figure 86 presents flow stream-line plots that illustrate the effect of the three-hole 120° segment seat geometry on the circumferential distribution of the nozzle entrance flow, which inhibits flow separation at the outer and inner radius locations of the nozzle entrance.

The quantity Q is the 2^{nd} invariant of the velocity gradient tensor, commonly adopted for vortex visualization in DNS and LES studies of wall-bounded flows [52]. Figure 87 presents the iso-surface plots of $Q = 5.E12$, $1.E13$, and $5.E13$ colored with the magnitude of the instantaneous local velocity. It shows the cascade structure and intensity of the vortical flows within the nozzle, the near-field liquid jet, and the surrounding ambient air. The highest level of vorticity is found in vortex cores with dimension of the order $0.1 \cdot d$ (i.e. the order of length-scale of the

energy-containing turbulent eddies). These high intensity vortical eddies induce a cascade of vortical flow structures, which extend upstream of the nozzle into the seat volume to cause formation of the ‘string cavitation’ [66] [67] and propagate downstream to engender the jet breakup through combined internal shear and temporal/spatial inertial and pressure perturbations.

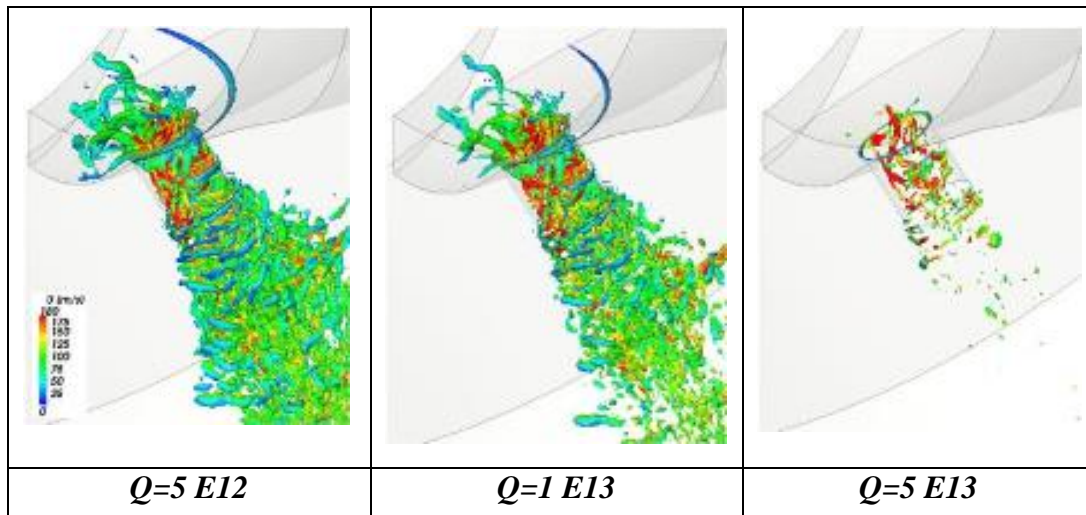


Figure 87 Iso-surface plots of $Q=5E12$, $1E13$, and $5E13$ (colored by the instantaneous local velocity magnitude) at $t=60\mu s$ ASOS

Nozzle geometry B – w/ Counterbore

Figure 88 and Figure 89 illustrate the transient development of the flow within the injector seat, nozzle, and the near-field jet primary breakup structure, with the aid of plots of evolution of the $VOF=0.5$ iso-surface, colored by the instantaneous velocity, and corresponding VOF contour plots displayed on the nozzle symmetry plane at selected times after the start of simulation.

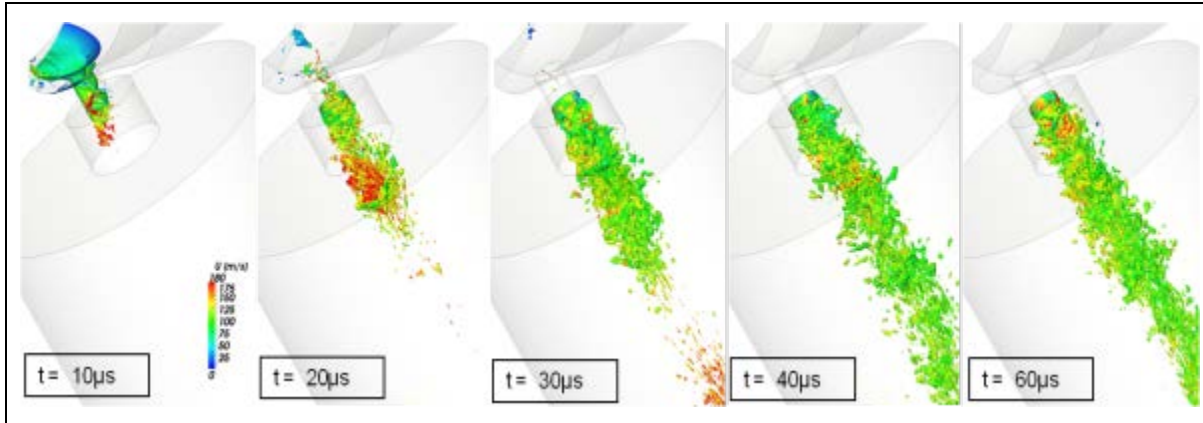


Figure 88 Iso-surface plots of VOF= 0.5, colored by instantaneous local velocity, at selected times ASOS

The transient development of seat-nozzle flow and morphology of the jet primary breakup is identical to the case of nozzle A. The exceptional feature of nozzle B plume is the indication of physical interaction of the jet primary breakup process with the counterbore wall which constrains the plume lateral dispersion as well as causing liquid splash from the surface.

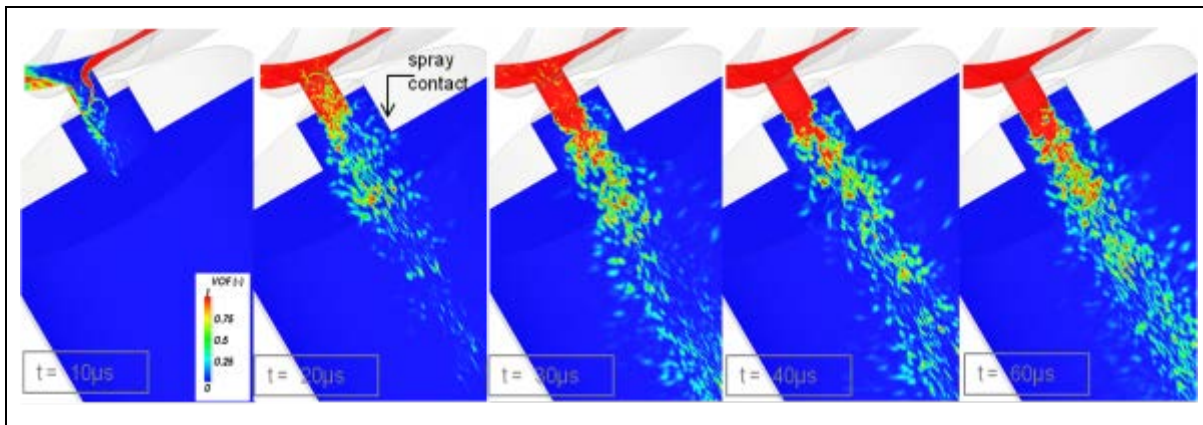


Figure 89 VOF Contour plots on the nozzle symmetry plane, at selected times ASOS

Figure 90 illustrates the unsteady character of the jet primary breakup and the spray contact with the counterbore wall with the aid of VOF contour plots on multiple display planes, normal to the jet axis, within the nozzle, the counterbore, and the location $z=5*d$ downstream of the injector ($z = 0$ corresponds to the counterbore exit plane).

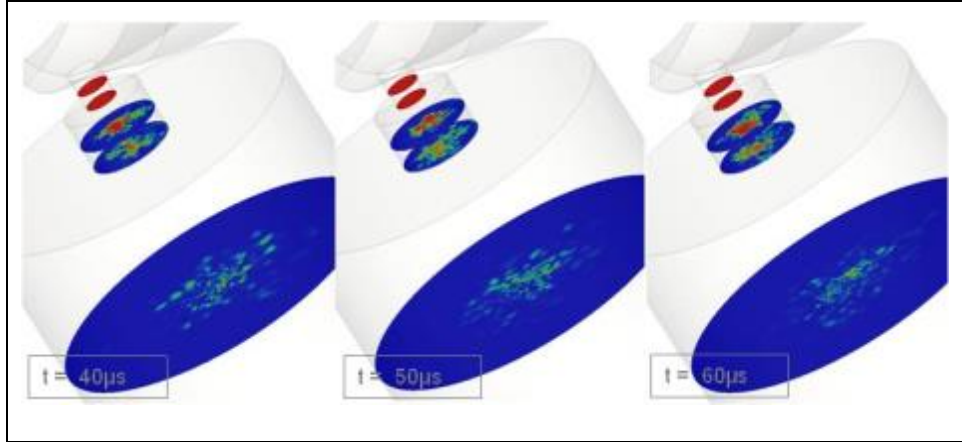


Figure 90 VOF Contour plots on planes normal to nozzle axis, within the nozzle-hole, counterbore, and location $z = 5*d$ downstream of injector ($t=ASOS$)

Figure 91 presents the contour plots of $Q=5.E12$, $1.E13$, and $5.E12$ in order to illustrate the structure and intensity of vortical flows within the nozzle and the nozzle near-field liquid jet. The most notable aspect of the results is the evident suppression of the diffusion of vorticity into the surrounding air within the counterbore space compared with the nozzle A. This is in contrast

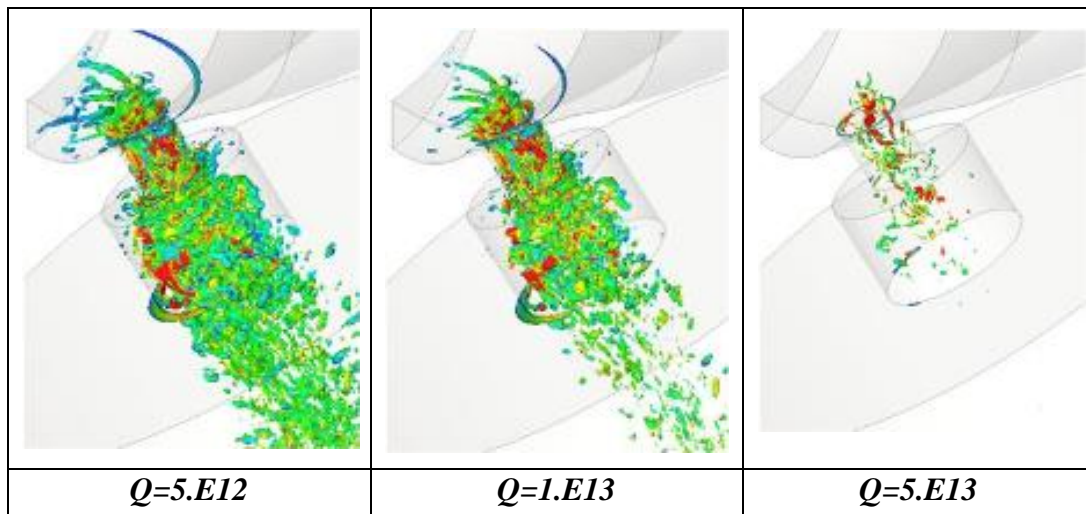


Figure 91 Iso-surface plots of $Q=5E12$, $1E13$, and $5E13$ (colored by the instantaneous local velocity magnitude) at $t=60\mu s$ ASOS

with the enhancement of vorticity of the air in the counterbore observed in the VOF-LES simulations of the GDi axisymmetric nozzles [56], and underscores the significance of the nozzle geometric parameters on the hydrodynamic and aerodynamic of the jet primary atomization.

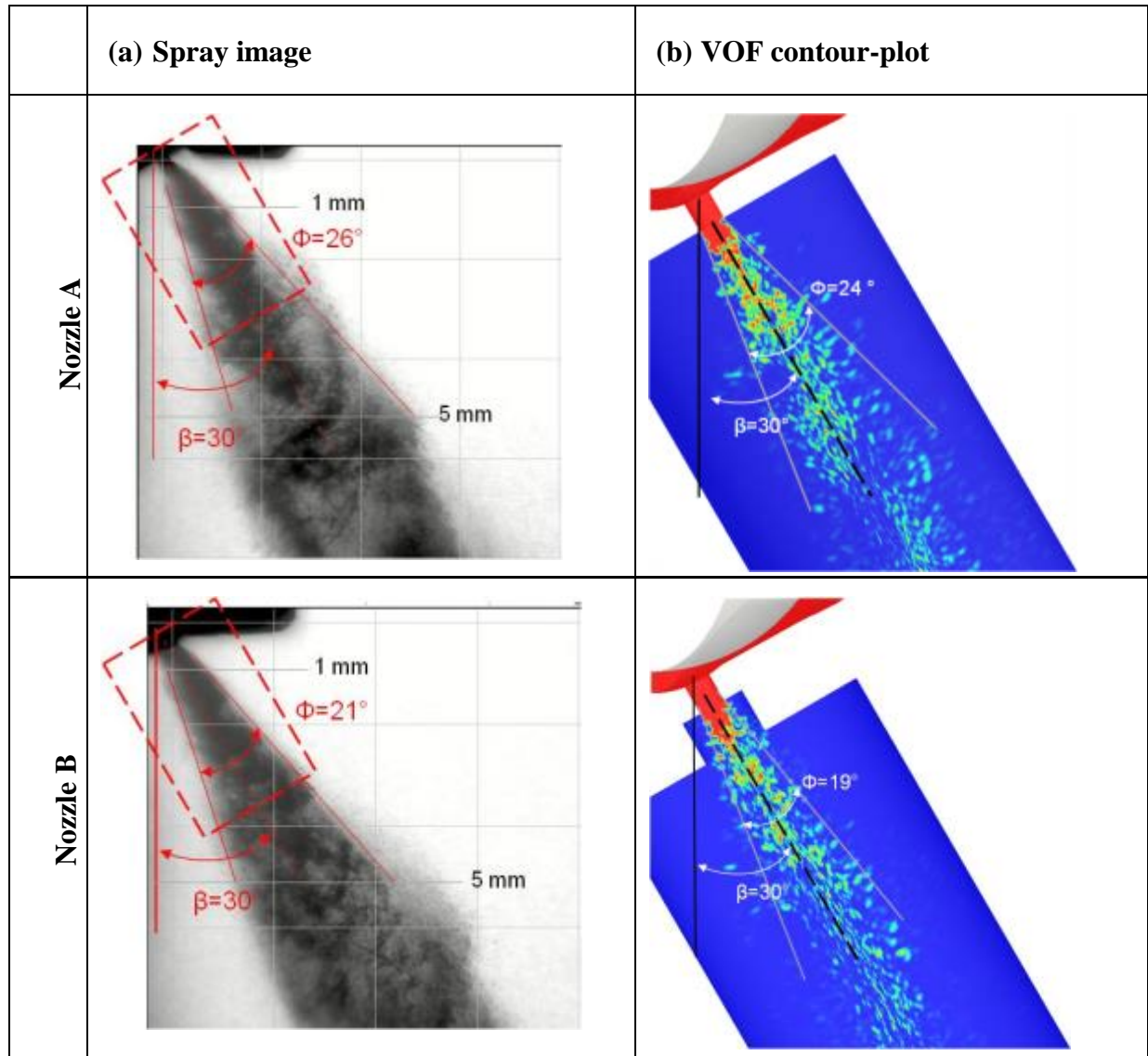


Figure 92 Nozzle A - Comparison of the plume images (at $t=700\mu\text{s}$ ASIE) and VOF-LES simulations (at $t=60\mu\text{s}$ ASOS) of the instantaneous plume near-field breakup structure

Comparison with Imaging Data

The comparison of the instantaneous VOF-LES simulation of the stationary jet primary breakup structure, at $t=60\mu\text{s}$ ASOS, for the nozzles A and B with the respective single-shot

images of the plume near-field, at $t=700\mu\text{s}$ ASIE, is presented in Figure 92. The computational domain for the VOF-LES simulation is indicated by the dashed-line rectangles in Figure 92(a).

Figure 92 provides a side by side view of the effect of counterbore on the plume structure as quantified by the plume angle and quantitative comparison with the VOF-LES simulations. There is evidence of the good predictive accuracy of the VOF-LES method with respect to (a) the initiation of the jet primary breakup in the immediate vicinity of the nozzle exit, (b) the plume trajectory angle ($\beta=30^\circ$), aligned with the nozzle axis, and (c) the near-field plume angle. The imaging data exhibits excellent correspondence of the single-shot plume macro scale geometry, center-line axis, and plume angle with that of the statistical plume analysis in Figure 77 and Figure 81. The agreement between the plume imaging data and the VOF-LES prediction of the plume angle is good (Nozzle A: experimental $\phi=26^\circ$ vs. VOF-LES prediction of $\phi=24^\circ$. Nozzle B: experimental $\phi=21^\circ$ vs. VOF-LES prediction of $\phi=19^\circ$). It can be concluded that the predictive accuracy of the VOF-LES method is satisfactorily validated for analysis of the influence of nozzle design on the plume geometric features.

It is worth noting that the present VOF-LES method does not provide a cavitation simulation capability. Therefore, cavitation is excluded in the simulations. The good predictive accuracy of the VOF-LES jet primary breakup structure and plume macro scale parameters does not warrant concluding absence of flow cavitation in the nozzle flow experiments.

5.3.4 Summary/Conclusions on Counterbore effect

The conclusions of this experimental and computational study of the GDi multi-hole nozzle geometry can be summarized as:

- The near-field plume imaging provides evidence of the jet primary breakup in the immediate vicinity of the nozzle exit, almost immediately after start of injection. The GDi plume breakup morphology is indicative of the “atomization” regime.
- There is evidence of the influence of intermittent injector valve-group hydraulic pressure oscillations on the jet breakup structure. This is expected to influence the air entrainment, and associated combustion-relevant characteristics of the spray plume.
- There is evidence of the physical interaction and influence of counterbore on the jet primary breakup process, with consequent effects on the plume trajectory, plume angle, and atomization.
- The VOF-LES simulations of the plume near-field breakup structure are in good agreement with the imaging data. Specifically, the important plume near-field macro scale characteristics: plume trajectory, plume angle, and the trend of influence of nozzle geometry on the plume breakup structure are in satisfactory agreement with data.
- The VOF-LES simulations indicate the atomization effectiveness of the GDi nozzle is associated with the vorticity and turbulence imparted on the flow at nozzle entrance.

The VOF-LES results and corresponding plume imaging data, in conjunction with previous GDi multi-hole seat-nozzle flow and spray investigations, underscore the major

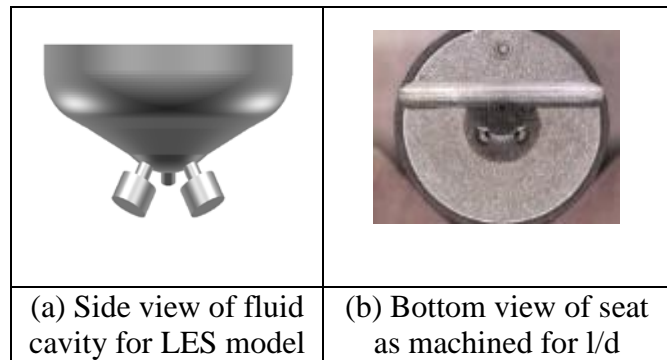
importance of the seat-nozzle topology and geometry on the hydrodynamics of the nozzle flow and structure of the plume primary atomization. Further investigations of the GDi multi-hole nozzle design influence on the plume primary breakup structure and evaluation of the predictive accuracy of the VOF-LES method are in progress. The objective is to establish a key knowledge of the prominent features of the relationship of GDi nozzle design and the spray near-field and far-field characteristics.

5.4 GDi Nozzle Parameter Studies Using LES and Spray Imaging Methods

The results of this section were published [68] and presented at the SAE World Congress held in Detroit in April of 2014. This study provides analyses of GDi skew-angled nozzles with $\beta=30^\circ$ skew (bend) angle and varying nozzle geometries. This work is an extension of previous work [56] [60] where the effect of counterbore geometry on spray was analyzed. In this current study, the effect of nozzle thru-hole length over diameter ratio ($l/d = .55$ and 1.10) and fuel pressure (5, 10, and 20MPa) on spray skew angle, spray plume angle, and primary breakup length is studied. The work is a combination of Large Eddy Simulation (LES) providing insight into physical mechanisms behind underlying spray results, validated by spray imaging testing using optical shadowgraph to evaluate spray plume geometry and phase-contrast X-ray imaging to focus on near-field structures within the dense spray plumes. Overall, the LES and spray imaging results are in qualitative and quantitative agreement and the model is successfully validated.

Nozzle Geometries

Figure 93 presents the solid model and experimental hardware views of the purpose-built 3-hole GDi seat used in this study. Specific geometry was accomplished



by using a purpose built seat containing 3

Figure 93 Geometry of the GDi 3-hole seat and nozzle

holes arranged at 120° circumferential spacing having identical thru-hole diameters. A secondary process was used on the seat to precisely grind the face of one hole, normal to the thru-hole, to remove seat material and vary the length of the thru-hole producing nozzle A and C geometry with varying length to diameter ratio

(l/d), as shown in the Figure 93(b). Figure 94 provides a view of the nozzle-hole geometry for nozzle A and C, and their associated dimensional parameters. The thru-hole diameter (d) is of the order 0.2mm, and the skew-angle (β) is 30° from the injector axis.

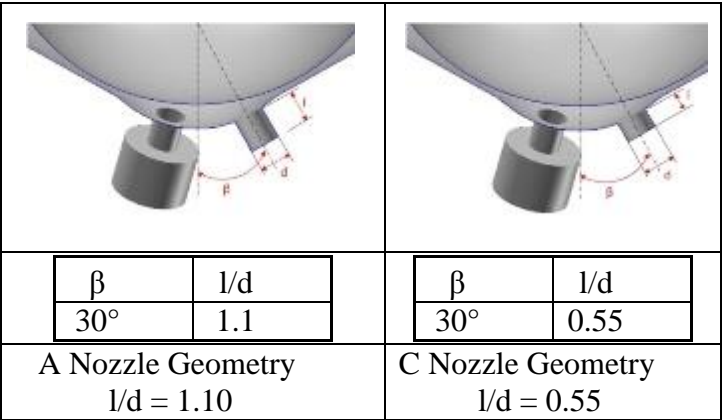


Figure 94 Nozzle Geometry A and C with associated dimensional parameters

A skew angle and varying l/d ratios representative of production injectors were selected to understand nozzle flow separation, and, thereby, enable evaluation of the accuracy of the VOF-LES method for prediction of the deviation between the plume trajectory and the nozzle thru-hole geometric axis direction.

5.4.1 Nozzle Geometry A, $l/d = 1.1$

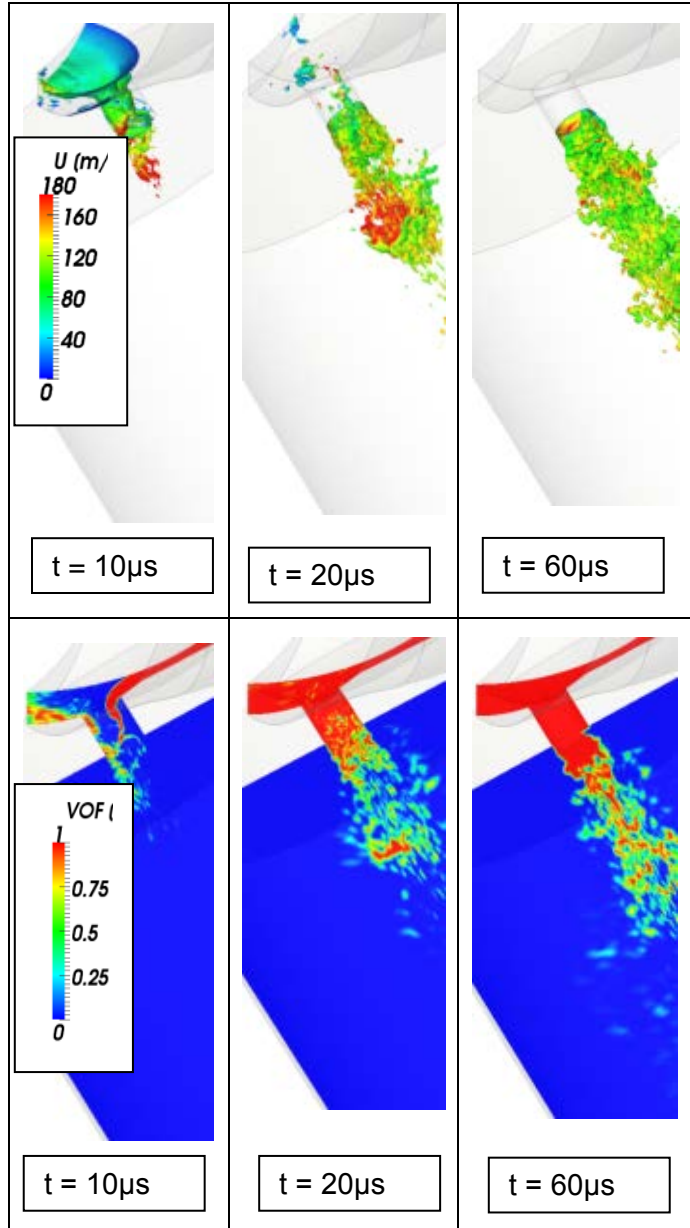


Figure 95 Spray velocity and VOF for Nozzle A at 10MPa at 10, 20, and 60 μ s

5.4.1.1 Simulation Results

Figure 95 shows the simulation results for Nozzle A, $l/d = 1.1$, as flow progresses after start of injector energizing. As can be seen in the VOF plot, the injector sac volume is initially filled with air and the liquid starts to enter the thru-hole at 10 μ s. Liquid completely fills the sac volume by 20 μ s, and fills the thru-hole by 60 μ s. It can be noted that there is no separation at the thru-hole entrance, and the spray plume jet follows the thru-hole geometry on exit. The velocity plot for VOF=.5 shows breakup of particles immediately at the nozzle exit and particle velocities in the range of 120m/s.

Fluid particle motion was tracked to provide a visualization of the flow path,

specifically at the thru-hole inlet, and is presented in Figure 96. As can be seen in the plot, the flow lines start with well-defined axial travel at a velocity of 20m/s. The side view shows that the streamlines undulate at the thru-hole entrance and particles accelerate as they enter the thru-

hole. Particle velocity reaches its maximum of approximately 180m/s in the thru-hole. The figure reveals that particle flow generally moves on axis of the thru-hole as expected, however, at some points, the figure reveals some streamlines move normal to the hole axis, which suggests turbulent vortices develop in the transition from the nozzle sac to the thru-hole inlet and are present in the thru-hole prior to the exit. The plot indicates attached flow in the thru-hole and at the nozzle exit and the particle streams exit the thru-hole following the nozzle seat thru-hole geometry. The particle stream decelerates upon exiting the injector traveling at approximately 120m/s.

5.3.1.2 Shadowgraph Optical Imaging Results

Shadowgraph optical imaging spray plume progression from start of injector energizing is presented in Figure 97. The reference grid is 2 x 2mm at time snap shots taken for 20, 60, and 140 μ s. The test was performed at 5, 10, and 20MPa fuel pressures. As shown in the captured

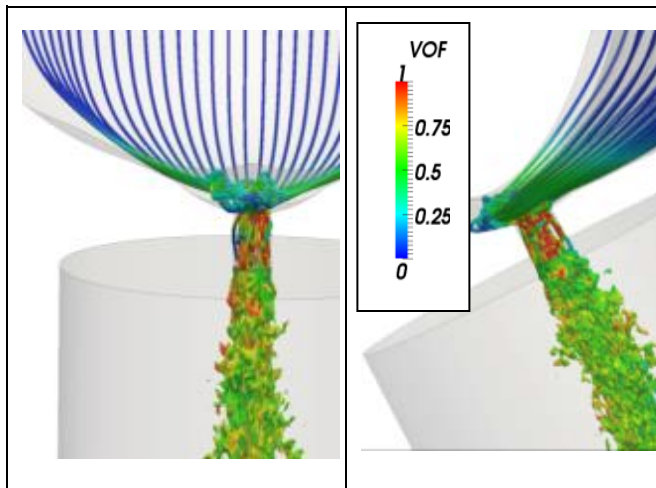


Figure 96 Particle Streamlines for Nozzle A

images, the spray plume penetration is 1-2mm at 20 μ s, and spray breakup is evident immediately at the exit of the nozzle at all fuel pressures. Spray penetration increases to between 4-6mm at 60 μ s, and evidence of a consistent spray plume angle of approximately 26° can be observed. The

spray progression at 60 μ s also reveals

optically more dense waves of droplets progressing at a regular spatial interval, at approximately 1.7mm spacing, across the plume penetration length, which indicates a dynamic disturbance in the nozzle or valve group at a given frequency is the likely cause. At 140 μ s the penetration the

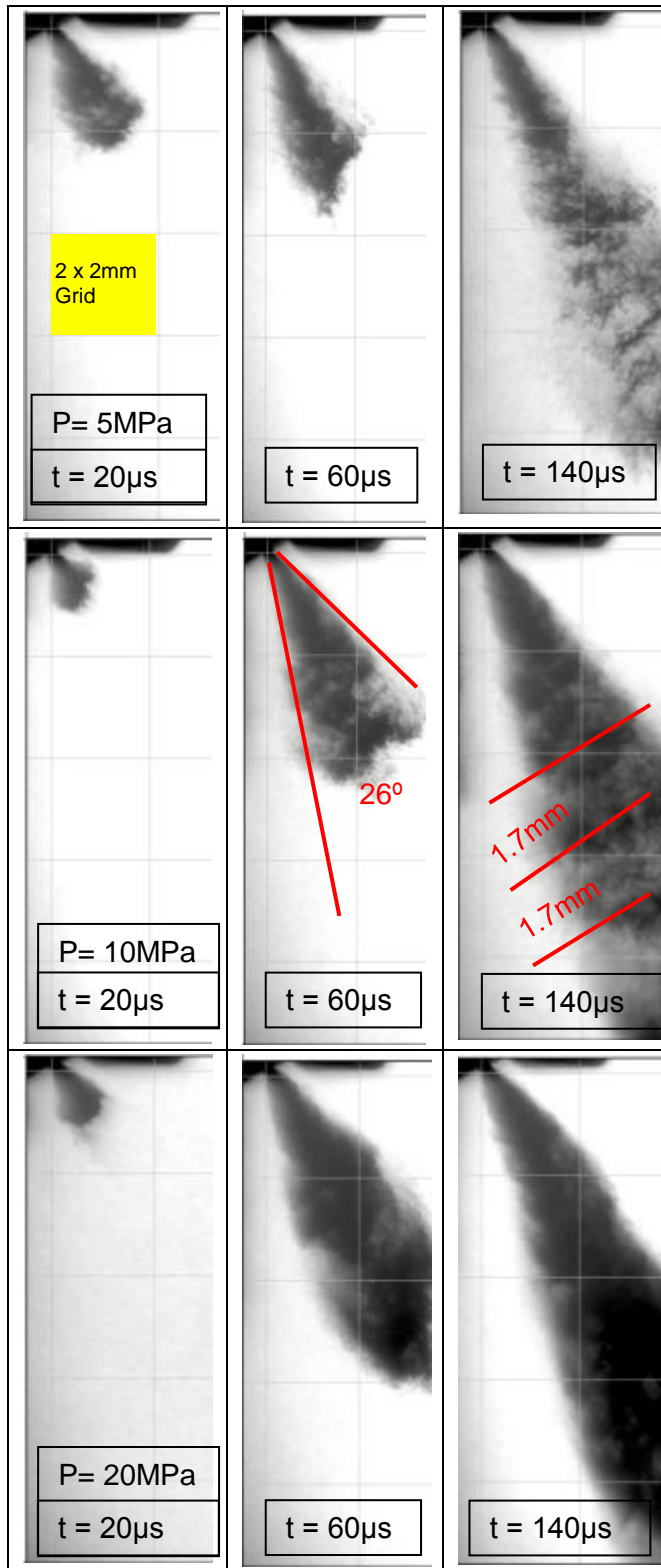


Figure 97 Spray for Nozzle A at 5, 10, & 20MPa at 20, 60 at time = 140 μ s, grid is 2 x 2mm

Spray plumes have exceeded 8mm of penetration and maintain characteristics of consistent spray plume angle and waves of heavier droplet density along the penetration length. The spray plumes also increase optical density with increasing injection pressures and at the highest pressure of 20MPa distinguishing droplets and waves is more difficult due to the high optical density. To better assess the spray plume geometry, a statistical PDF (liquid phase probability density function) is calculated for the 10MPa fuel pressure test point at 700 μ s, where the spray is fully developed, based on 5 spray plumes to account for any shot to shot variation. The results in Figure 98 indicate 100% liquid phase is captured at a spray plume angle of 19° and the majority of liquid is captured within a 26° plume angle. The spray plume skew axis is 30° matching the thru-hole geometry.

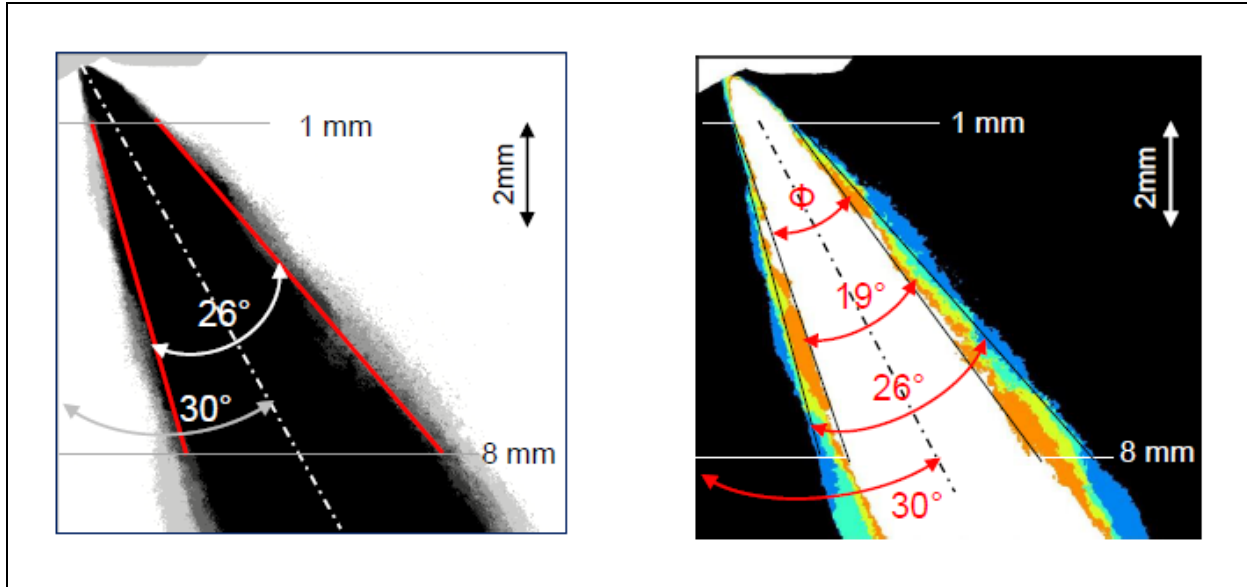


Figure 98 Spray plume statistical PDF (liquid phase probability density function) based on 5 injections for Nozzle A, $l/d=1.1$, Fuel Pressure = 10MPa, time = 700 μ s

The statistical PDF can also evaluate the plume geometry at 5, 10, and 20MPa fuel pressures tested to understand the effect of pressure on the geometry. As seen in Figure 99, fuel pressure did not show a significant effect over the range of 5-20MPa when tested, with the PDF indicating a plume angle between 19°-26° well captures the liquid phase spray. The statistical PDF can also be compared to the LES simulation as shown in Figure 100 where the spray is fully developed for 10MPa fuel pressure at 700 μ s.

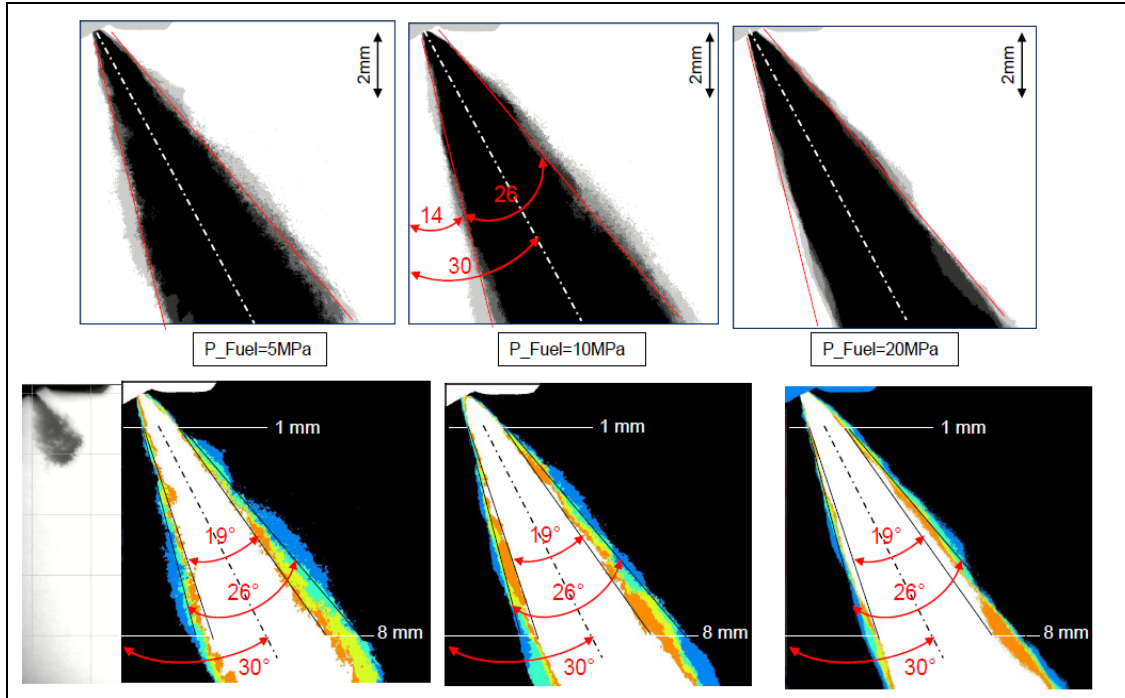


Figure 99 Spray plume statistical PDF versus injection pressure for Nozzle A, $l/d=1.1$, time = 700 μ s

As shown in the figure, the LES confirms well the spray plume skew angle of 30°. The LES would indicate a spray plume angle of approximately 24°, well within the 19°-26° range indicated by the PDF. Overall, the LES and optical spray imaging are in excellent quantitative agreement for injector spray plume angle, spray plume skew angle, and particle breakup length. Previous work of the authors [69] showed the LES model predicted spray plume and skew angles were unaffected by injection pressure. The LES particle tracking streamlines also provide good

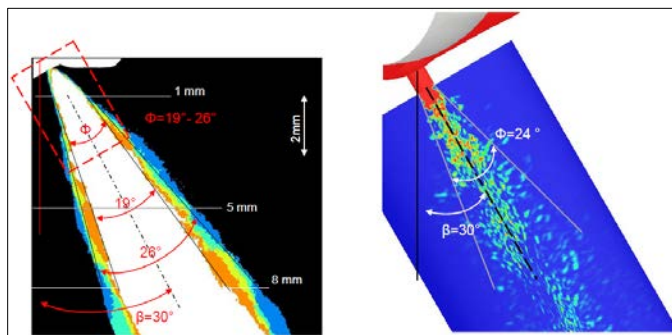
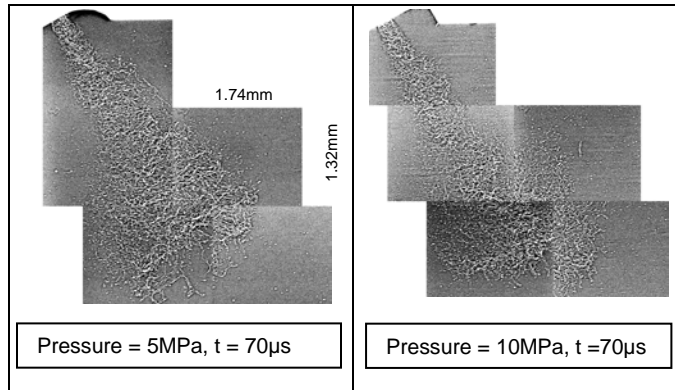


Figure 100 Spray plume statistical PDF compared to LES modeled spray plume for Nozzle A, $l/d=1.1$, Fuel Pressure = 10MPa, time = 700 μ s image, 60 μ s simulation

insight into the role of the thru-hole inlet in developing turbulent eddies in the accelerating fluid flow in the thru-hole.

5.3.1.3 Phase contrast X-ray Optical imaging

As was evidenced in Figure 97, it is difficult to discern spray morphology near the nozzle exit due to the optical density of the GDi spray using a shadowgraph method. This condition is only exacerbated with increasing fuel pressures,



as seen in the 20MPa optical image. It is important to understand this structure to

Figure 101 Spray plume X-ray optical imaging for varying injection pressure Nozzle A, $l/d = 1.1$, time = $60\mu s$

help confirm whether the primary driver of spray breakup occurs in the nozzle or in friction interactions with the air through Kelvin-Helmholtz mechanism. X-ray optical images for nozzle A are presented in Figure 101 at varying injection pressure. At $70\mu s$ the spray plume has penetrated approximately 5mm into the chamber. The X-ray passes through the dense spray and reveals a stochastic pattern of waves that is consistent from nozzle exit through the spatial field. The plume structure breakup at the nozzle exit suggests disturbances originated inside the nozzle, and turbulent dispersion perpendicular to the spray axis can be seen similar to that predicted within the thru-hole by the particle streamlines. The chaotic jet breakup structures appear similar for 5 and 10MPa operating pressures with turbulence evident immediately at nozzle exit prior to any interaction with ambient air in the chamber.

5.4.2 Nozzle Geometry C, $l/d = 0.55$

5.4.2.1 Simulation Results

Figure 102 shows the simulation results for Nozzle C, $l/d = 0.55$, as flow progresses after start of injector energizing. As can be seen in the VOF plot the injector sac volume is initially filled with air and the liquid starts to enter the thru-hole at approximately $10\mu\text{s}$. Liquid completely fills the sac volume by $20\mu\text{s}$ and the thru-hole by $60\mu\text{s}$. However, in contrast to nozzle A there is evidence of unsteady flow separation at the thru-hole outboard edge. The separation starts at the thru-hole inlet, and the distance of separation increases as the flow in the thru-hole progress, thus causing a deviation of the spray plume jet from the thru-hole geometry on exit. The implication of flow separation is that the observed spray plume skew (bend) will be

narrower than the geometric angle. The velocity plot for $\text{VOF}=0.5$ shows the fluid starts at approximately 20m/s and accelerates to 40m/s in the sac volume and to $120\text{--}160\text{m/s}$ in the thru-

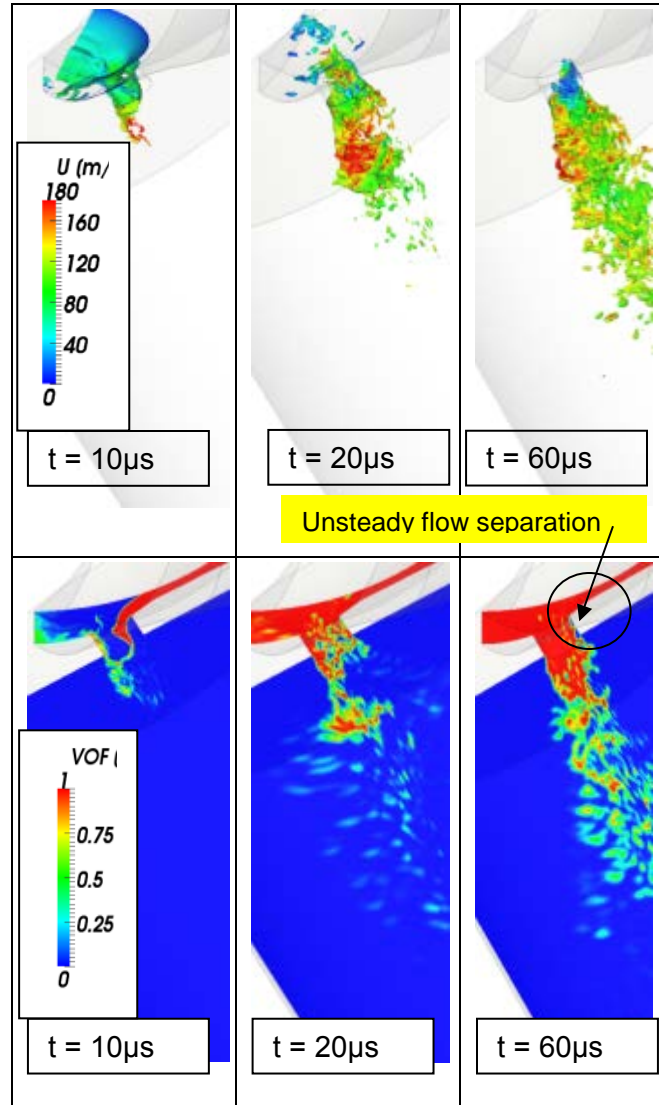


Figure 102 Spray velocity and VOF for Nozzle C at 10MPa at 10, 20, and $60\mu\text{s}$

hole with breakup to particles immediately at the nozzle exit and particle velocities in the range of 120m/s.

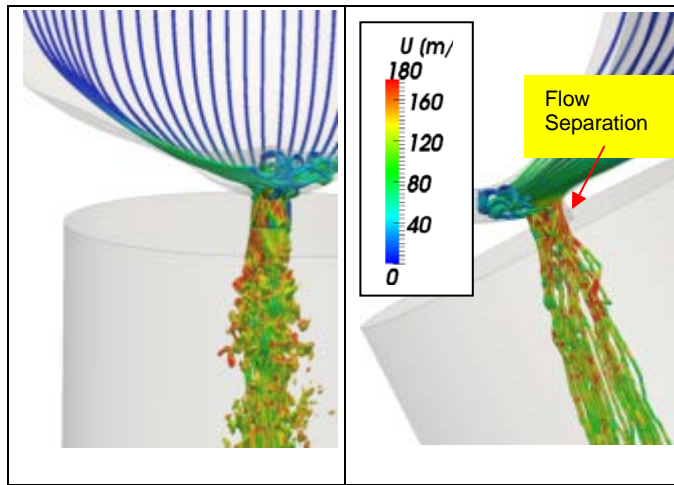


Figure 103 Particle Streamlines for Nozzle C

Fluid particle motion tracking is presented in Figure 103. As can be seen in the plot, the flow lines start with well-defined axial travel at a velocity of 20m/s. As the side view shows, the flow lines undulate as they wrap around the far edge of the thru-hole, but enter the near edge with minimum deviation. Thereby,

maintaining the streamline momentum passing through the nozzle and exiting at an angle narrower than the geometric skew angle. The particles accelerate with velocity reaching its maximum in the thru-hole moving up to 180m/s. Particle flow is bi-modal with near edge streamlines leaving the nozzle at a narrower than geometric skew angle, while far edge streamlines show evidence of turbulent vortices deviating the path of travel and impacting the relative near edge streamlines. The plot indicates unsteady flow separation starting at the near edge inlet to the thru-hole and separation distance from the wall growing as the streamline progresses due to the deviation of streamline angle to the geometric angle.

5.4.2.2 Shadowgraph Optical

Imaging Results

Shadowgraph optical imaging of spray plume progression from the start of injector energizing is presented in Figure 104. The reference grid is 1 x 1mm (note smaller grid than Nozzle A imaging) at time snap shots taken for 20, 60, and 140 μ s. The test was performed at 5, 10, and 20MPa fuel pressures. As shown in the captured images, the spray plume penetration is 1-2mm at 20 μ s, and spray breakup is evident immediately at the exit of the nozzle at all fuel pressures. Spray penetration increases to between 4-6mm at 60 μ s and evidence of a consistent spray plume angle of approximately 33° can be observed. Again, similar to Nozzle A, the spray progression at 60 μ s also reveals optically more dense waves of droplets progressing at a regular spatial interval, approximately 1.7mm in length, across the plume penetration length, likely indicating

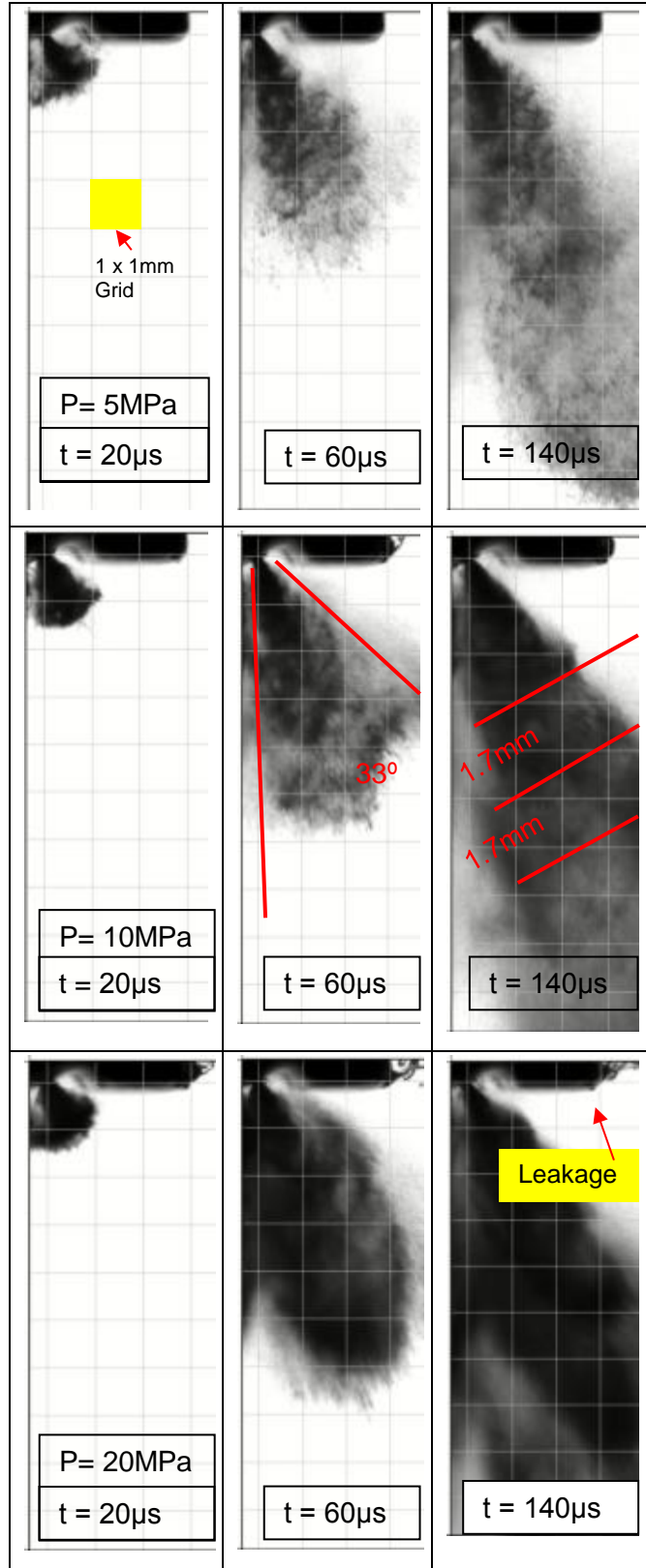


Figure 104 Spray Shadowgraph for Nozzle C at 5, 10, & 20MPa at 20, 60 & 140 μ s

a dynamic disturbance in the nozzle or valve group at a given frequency. At $140\mu\text{s}$, the spray plumes have exceeded 8mm of penetration and maintain characteristics of consistent spray plume angle and waves of heavier droplet density along the penetration length. The spray plumes also increase optical density with increasing injection pressures, and at the highest pressure of 20MPa distinguishing droplets and waves is more difficult due to the high optical density. Significant seat leakage is also visible at 20MPa, forming a film on the seat surface and large droplets shedding from the seat edge.

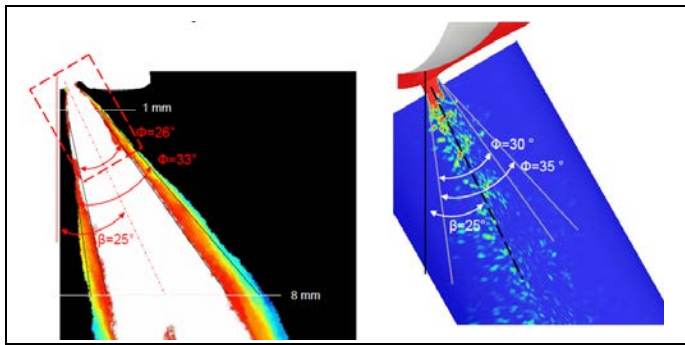


Figure 105 Spray plume statistical PDF compared to LES modeled spray plume for Nozzle C, $l/d=0.55$, Fuel Pressure =10MPa, time = $740\mu\text{s}$ image, $60\mu\text{s}$ simulation

To better assess the spray plume geometry, a statistical PDF (liquid phase probability density function) is calculated for the 10MPa fuel pressure test point at $700\mu\text{s}$, where the spray is fully developed, based on 5 spray plumes to account for any shot to shot variation.

The results, shown in Figure 105, indicate 100% liquid phase is captured at a spray plume angle of 26° , and the majority of liquid is captured within a 33° plume angle. The plume skew axis is 25° , narrower than the thru-hole geometry.

Similar to Nozzle A, the statistical PDF can also be compared to the LES simulation. This comparison at 10MPa fuel pressure test point and $700\mu\text{s}$, where the spray is fully developed, is provided in Figure 105. As shown in the figure, the LES confirms well the narrowed spray plume skew angle of 25° . The LES would indicate a spray plume angle of approximately 30° - 35° , slightly greater than the 26° - 33° range indicated by the PDF. Overall, the LES and optical spray imaging are in excellent quantitative agreement for injector spray plume

angle, spray plume skew angle, and particle breakup length. The LES particle tracking streamlines in the case of Nozzle C illustrated the mechanism of how near edge streamlines separated, starting at the thru-hole inlet edge and followed a trajectory exiting the nozzle resulting in a reduction of the skew angle. Like Nozzle A, the entrance of the fluid into the thru-hole created turbulent eddies.

The statistical PDF comparing optical imaging to the LES simulation is provided in Figure 106 at $700\mu\text{s}$ where the spray is fully developed for 20MPa fuel pressure. The LES would indicate a spray plume angle of approximately 30° - 35° , slightly greater than the 21° - 29° range indicated by the PDF. In case of $l/d = 0.55$, simulation and imaging data indicates there is no effect of fuel pressure on the plume skew angle trajectory. As in the case of $l/d = 1.1$,

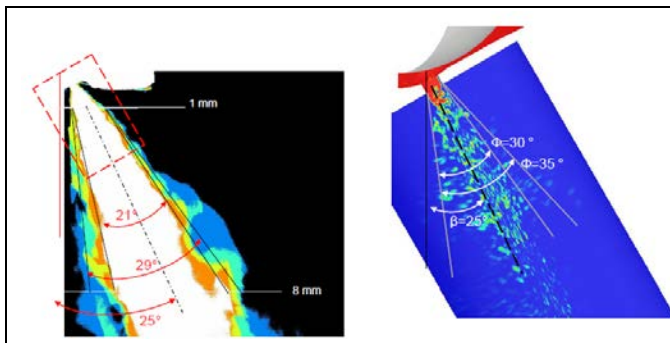


Figure 106 Spray plume statistical PDF (liquid phase density function) compared to LES modeled spray plume for Nozzle C, $l/d=0.55$, Fuel Pressure =20MPa, time = $740\mu\text{s}$ image, $60\mu\text{s}$ simulation

simulations predict no effect of pressure on spray plume angle, however, the imaging data suggest the effect is notable and complex. Figure 106 shows a significant increase of plume spray angle as pressure increases from 5MPa (24° - 28°) to 10MPa (28° - 33°), followed by a

reduction of the plume spray angle, concurrent with marked increase of shot-to-shot variations, as pressure is further increased from 10MPa (28° - 33°) to 20MPa (21° - 29°). The author's hypothesis is that the observed effect of fuel pressure increase was associated with deformation of the cracked seat, a result of machining, which caused a disproportionate increase of fuel leakage with increased pressure that substantially interacted with and influenced the spray development.

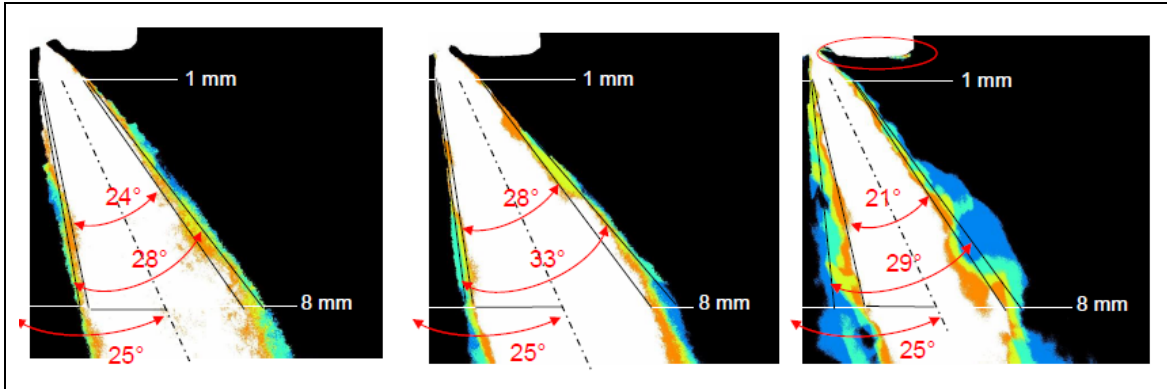


Figure 107 Spray plume statistical PDF (liquid phase probability density function) versus injection pressure for Nozzle C, $l/d=0.55$, time = $740\mu s$

5.3.2.3 Phase contrast X-ray Optical imaging

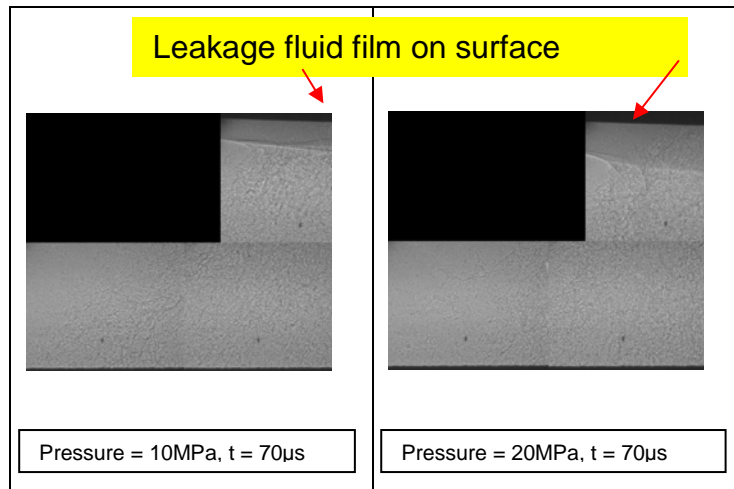


Figure 108 Spray plume X-ray optical imaging for varying injection pressure Nozzle A, $l/d = 0.55$, time = $70\mu s$

X-ray images for nozzle C are presented in Figure 108 at varying injection pressure. At $70\mu s$, the spray plume has penetrated approximately 5mm into the chamber. The X-ray passes through the dense spray and reveals a stochastic pattern of waves that is

consistent from nozzle exit through the spatial field. The X-ray also shows the injector leakage leaves a deposit of fluid on the seat surface that the spray plume penetrates (limited contrast of particles in image). It can also be seen that the film thickness increased with increasing pressure. The plume structure breakup at the nozzle exit suggests disturbances originated inside the nozzle, and turbulent dispersion perpendicular to the spray axis can be seen similar to that predicted within the thru-hole by the particle streamlines. The chaotic jet breakup structures appear similar

for 10 and 20MPa operating pressures with turbulence evident in both immediately at nozzle exit prior to any interaction with ambient air in the chamber.

5.4.3 Summary/Conclusions on l/d and Pressure effects

Overall, the GDi nozzle parameter studies using LES and spray imaging methods were very successful. LES and optical spray imaging are in agreement for injector spray plume angle, spray plume skew angle, and jet breakup length. There exists some imprecision in the assessments as plume angle and breakup length are visually based on the droplet distribution in the instantaneous VOF field and the VOF field, like the experimental images, have temporal variations. The LES particle tracking streamlines also provide good insight into the role of the thru-hole inlet in developing turbulent eddies with the accelerating fluid flow in the thru-hole as well as the mechanism of flow separation and resulting narrower skew angle for shorter l/d nozzles. The X-ray imaging revealed a stochastic pattern of waves that is consistent from nozzle exit through the spatial field and turbulent dispersion perpendicular to the spray axis similar to that predicted within the thru-hole by the particle streamlines. The complementary analysis of CFD methods and empirical data supported definitive conclusions on parameter effects as well as provided an understanding of the underlying physical mechanism involved. The conclusions of the LES and experimental spray imaging study of GDi nozzle parameters can be summarized as:

Spray Breakup Structure:

Simulation, shadowgraph imaging, and X-ray imaging all reveal jet primary atomization in close vicinity of the nozzle exit, evidenced immediately after start of fueling at all fuel pressures evaluated, even in the 5MPa case. The simulation and optical imaging data suggests that nozzle

induced vorticity/turbulence is the primary cause of jet breakup. X-ray imaging confirms the turbulence is present at nozzle exit prior to any interaction with ambient air.

The effect nozzle l/d reduction:

Simulation and optical imaging showed spray plume angle increased approximately 7° as nozzle thru-hole l/d was reduced:

l/d = 1.1 spray plume angle = 19° - 26°

l/d = 0.55 spray plume angle = 26° - 33°

The plume skew angle deviated approximately 5° from thru-hole nozzle geometric axis for the shorter l/d due to separation at the nozzle inlet as follows:

l/d = 1.1 skew angle = 30° , deviation angle = 0°

l/d = 0.55 skew angle = 25° , deviation angle = -5°

Effect of Fuel pressure:

In the case of l/d=1.1, simulation and imaging data show the absence of a significant, and consistent, effect of fuel pressure on the near-field plume breakup, spray plume angle, and plume skew angle.

In the case of l/d=0.55, simulation and imaging data indicates there is no effect of fuel pressure on the plume skew angle trajectory. As in the case of l/d = 1.1, simulations predict no effect of pressure on spray plume angle; however, the imaging data suggested a notable and complex effect. The hypothesis is that the observed effect of fuel pressure increase was associated with deformation of the cracked seat, a result of machining, which caused a disproportionate increase of fuel leakage with increased pressure that substantially interacted with and influenced the spray development.

CHAPTER 6 SUMMARY

6.1 Summary of Conclusions

Overall, the GDI nozzle parameter studies using LES and spray imaging methods were very successful. LES was validated by optical spray imaging for injector spray plume angle, spray plume skew angle, and jet breakup length. There exists some imprecision in the assessments as spray angle and breakup length are visually based on the droplet distribution in the instantaneous VOF field and, like the experimental images, the VOF field have temporal variations. The success of the VOF-LES model is noteworthy given the varying flow conditions accurately predicted: separation with full hydraulic flip without influence of counterbore for axis symmetric nozzles, fully attached flow following geometric skew angle with spray plume angle counterbore influence for skew angled nozzles of $l/d \sim 1$, and detached flow with separation on the leading edge with effect on spray skew angle and spray plume angle for small $l/d \sim .6$ skew angled nozzles. All of these effects were predicted without model coefficients or other adjustment parameters but solely on the nozzle geometry and imposed initial velocity of the flow field without any disturbances. The LES particle tracking streamlines also provided good insight into the role of the thru-hole entrance in development of turbulent eddies within the accelerating fluid flow in the thru-hole as well as the mechanism of flow separation and resulting narrower skew angle for shorter l/d nozzles. The X-ray imaging revealed a stochastic pattern of turbulent waves that is consistent from the immediate nozzle exit through the spatial field, as well as turbulent dispersion perpendicular to the spray axis similar to that predicted within the thru-hole by the particle streamlines. The complementary analysis of CFD methods and empirical data supported definitive conclusions on parameter effects as well as provided an understanding of the underlying physical mechanism involved. Several findings changed the “understanding of

spray formation” that existed at the start of this work. Overall, the study reveals that the nozzle flow characteristics of GDi nozzle holes are markedly different from the diesel nozzles, owing to the relatively short nozzle $l/d \sim 1$ versus $l/d \sim 6-7$ for the diesel nozzles. The VOF-LES simulations of the plume near-field breakup structure are in good agreement with the shadowgraph, Mie scatter, and X-ray imaging data. Specifically, the important plume near-field macro-scale characteristics of plume trajectory, plume spray angle, plume penetration, and the trend of influence of nozzle geometry on the plume breakup structure are in satisfactory agreement with data to validate the model. The summary of key findings with an index to relevant VOF-LES Figures and Test Images are presented in Table 11.

Table 11 Summary of key findings with index to VOF Figures and Spray Images Index

Evaluation	VOF-LES Figures	Test Images	Spray Morphology Conclusion
axis-symmetric single-hole nozzles	39-44	Appendix C 157,158 Appendix E 187-193 Appendix F 120-131	Separation at inlet full hydraulic flip Narrowed spray plume at exit No counterbore contact Extremely long penetration
Skew-angled Nozzle with and without counterbore	83-92	Appendix E 199-205 Appendix F 232-238	Spray contact with counterbore narrows spray plume $\approx 5^\circ$
Injection pressures 5, 10 and 20Mpa	95	Figure 97, 99 Appendix E 205-211 Appendix F 238-244	No change in plume angle No change in skew angle
Nozzle l/d reduced from 1.1 to 0.55	95, 102, 103	Figure 97, 104	Separation at top-of inlet edge Spray plume angle increases $\approx 7^\circ$ Spray skew angle deviates $\approx 5^\circ$ from geometric

In summary, the supported conclusions are:

GDi plume breakup morphology is indicative of the “Atomization” regime

The near-field plume imaging provides evidence of the jet primary breakup in the immediate vicinity of the nozzle exit, almost immediately after start of injection.

There is evidence of the influence of injector valve-group hydraulic pressure oscillations on the near-field jet breakup structure, revealed in regular waves of optically dense spray.

Evidence of Kelvin-Helmholtz interface instability waves was shown in both VOF-LES modeling and spray imaging; however, the ligament formation stemming from vorticity internal to the jet dominated as the breakup mechanism occurring immediately at nozzle exit.

The VOF-LES simulations indicate the atomization effectiveness of the GDi nozzle is associated with the vorticity and turbulence imparted on the flow at nozzle thru-hole entrance.

- **Effect of Nozzle Counterbore:**

There is evidence of the physical interaction and influence of counterbore on the jet primary breakup process with consequent effects on the plume trajectory, plume angle, and atomization. This counterbore interaction yields smaller spray plume angles for nozzle geometry typical for GDi production. It should be noted, as the geometric skew angle approaches 0° , the effect of the counterbore will diminish as was demonstrated with axis-symmetric nozzles.

- **Effect of Nozzle l/d:**

Simulation and optical imaging showed spray plume angle increased approximately 7° as nozzle thru-hole l/d was reduced:

- l/d = 1.1 spray plume angle = 19° - 26°
- l/d = 0.55 spray plume angle = 26° - 33°

The observed plume skew angle deviated approximately 5° from thru-hole nozzle geometric axis for the shorter l/d due to separation at the nozzle inlet as follows:

- l/d = 1.1 skew angle = 30° , deviation angle = 0°
- l/d = 0.55 skew angle = 25° , deviation angle = -5°

- **Effect of Nozzle d:**

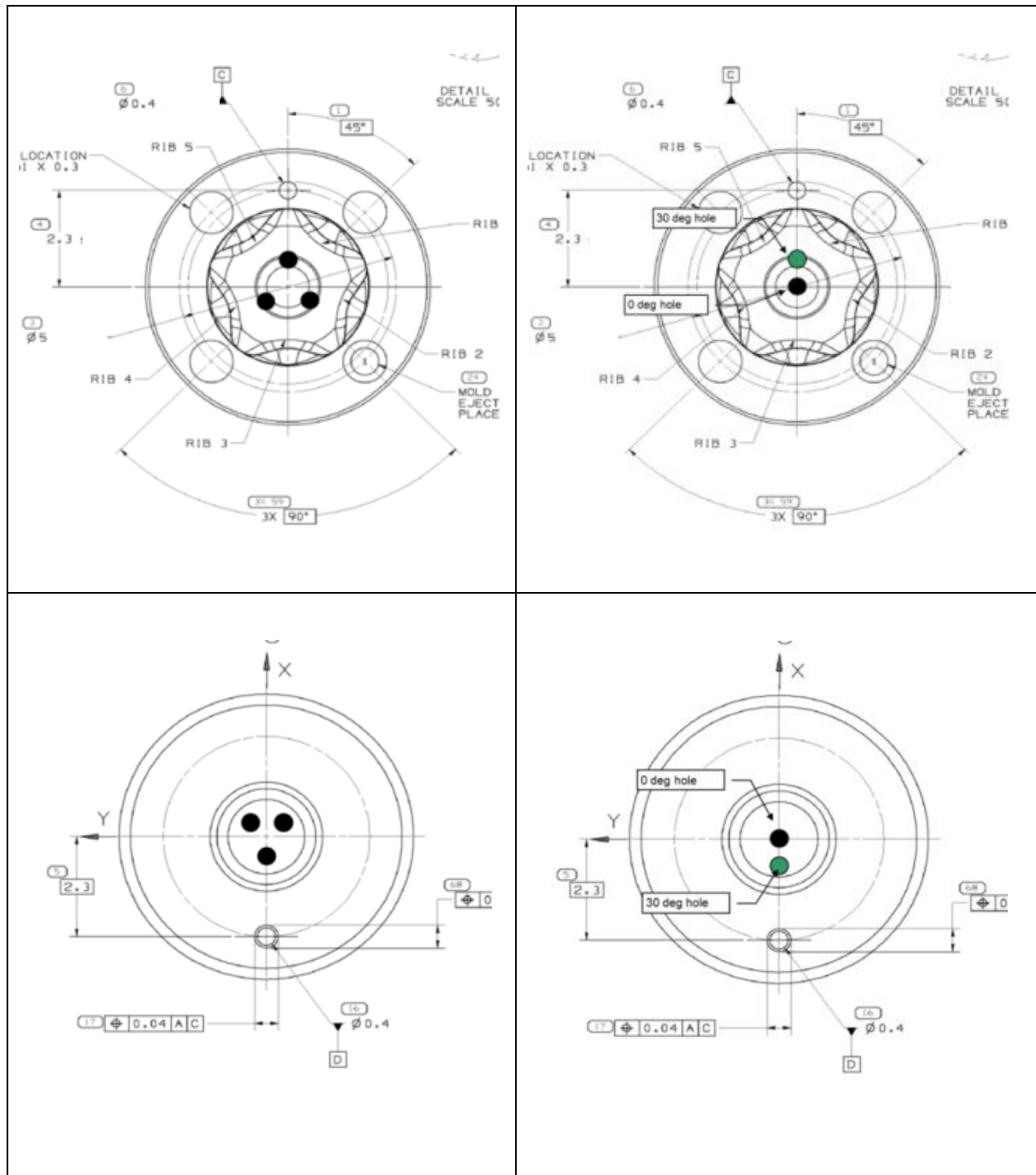
The plume angle was shown to be a function of l/d and nozzles of $d \approx 20\text{mm}$ and $d \approx 15\text{mm}$ demonstrated similar plume angle.

- **Effect of Fuel Pressure:**

In the case of $l/d=1.1$, typical of production GDi injectors, simulation and imaging data show the absence of a significant, and consistent, effect of fuel pressure on the near-field plume breakup, spray plume angle, and plume skew angle.

6.2 Recommendations for Future Work

While this work provided new insights into the turbulent dynamics of GDi nozzle flow and validated a methodology for use in GDi nozzle design, it also opens several areas of research focus for future work. The first of these is already being pursued, the extension of the VOF-LES modeling of internal injector flow and near-field jet breakup analysis to spray droplet formation [70] and predicted droplet distribution developed in the far field. It will be interesting to understand the nozzle design variable influences since the laser diffraction measurement of this work indicated droplet distribution was fairly independent of nozzle l/d or counterbore presence. Another area of interest that was observed in the experimental images of this work was the clear and consistent pulsed frequency of optically dense spray plume waves, future work incorporating pintle movement in the simulation is recommended to confirm the interaction of the injector valve group dynamics, non-ideal asymmetries as exist with internal seat features and nozzle hole placements, and seat sac volume on spray plume morphology. Likewise, as this work excluded cavitation which is known to significantly contribute to turbulent structure as l/d increases, future work to develop stable CFD solutions that permit inclusion of cavitation in the analysis is desired. Finally, a study of element mesh size impact on the simulation result to understand the effect of LES resolved versus modeled scales as the solution ranges from near Reynolds Averaged Navier Stokes solution to Direct Numerical Simulation for the GDi nozzle could establish guidelines for predictive accuracy and computational expense so that future work may target an appropriate compromise required for injector development.



HOLE POSITIONS ON BOLT CIRCLE (x,y)-COORDINATE SYSTEM

Comments

input in green cells

number of holes **3**
 position of Hole #1 **180** deg (Typically 180 deg or less)
 Posalux EDM Hole position Offset **180** deg (Typically 180 deg for the posalux)
 Equally distributed spacing calc **120.00** deg between holes

		Hole Location			
		Bolt Circle [mm]			0.75
		Z Coordinate [mm]			-0.16
	Print Bolt Circle Angular Hole	Coordinates [mm]			
		Z			
Hole #	Position	X	Y	Z	EDM Hole Pos. sizes for bubble plot
1	180.0	-0.375	0.000	-0.180	0.0 1.01
2	60.0	0.188	0.325	-0.180	120.0 1.02
3	-60.0	0.188	-0.325	-0.180	240.0 1.03
4	-180.0	10.000	0.000	-0.180	360.0 1.04
5	-300.0	10.000	0.325	-0.180	480.0 1.05
6	-420.0	10.000	-0.325	-0.180	600.0 1.06
7	-540.0	10.000	0.000	-0.180	720.0 1.07
8	-660.0	10.000	0.325	-0.180	840.0 1.08

For Reference	bolt circle	Z-coord
BRAVO	0.65	-0.13
BETA3.175	0.75	-0.185
BETA 3.0	0.75	-0.16

Hole Numbering System

Hole # 1 on X-axis closest to seat dot

View from Inside Seat

Hole's ordered CCW – starting at seat dot or CCW from seat dot

View from Outside Seat

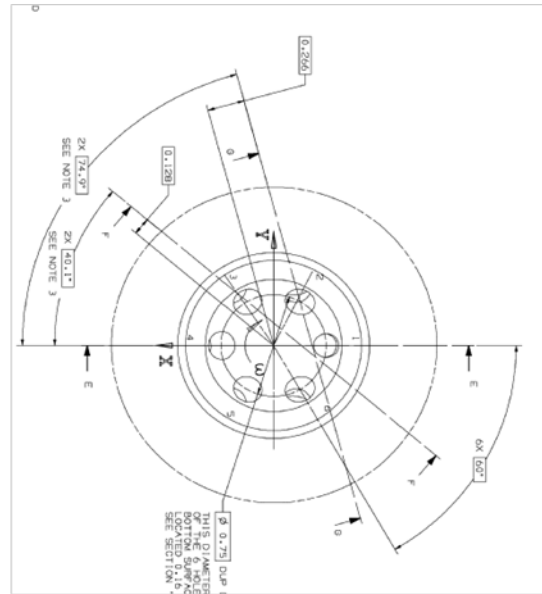
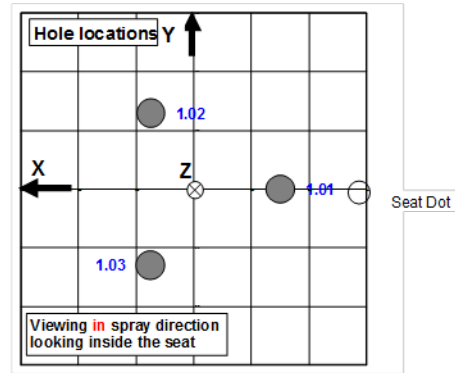
Hole's ordered CW – starting seat dot or CW from seat dot

Reference coordinate system

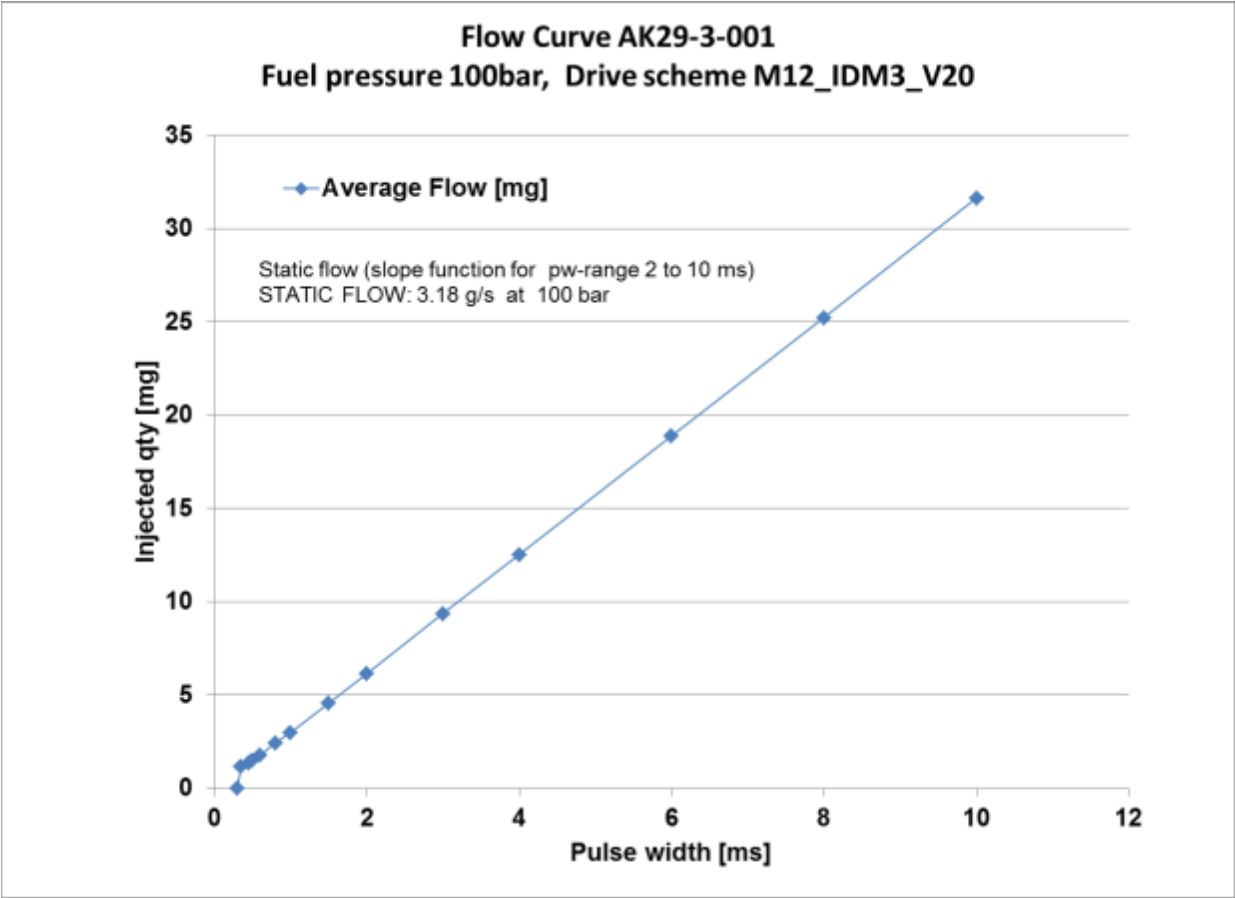
X axis identified by Seat Dot - on negative X

Y axis 90 degrees to X axis

Z axis in direction of spray



APPENDIX B INJECTOR FLOW RATE

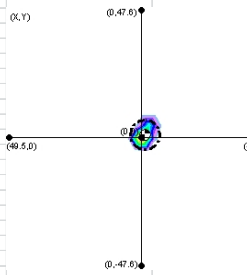
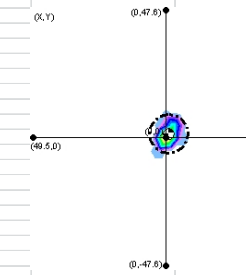
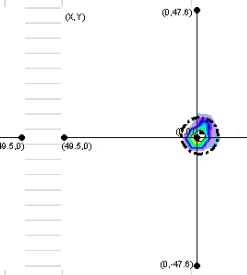
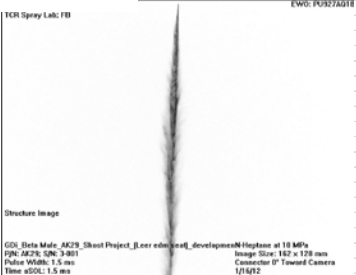
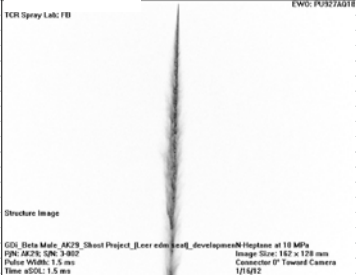
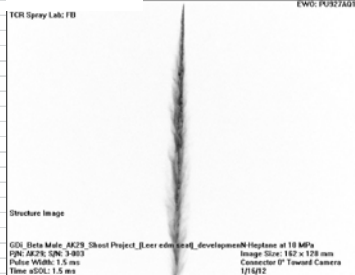
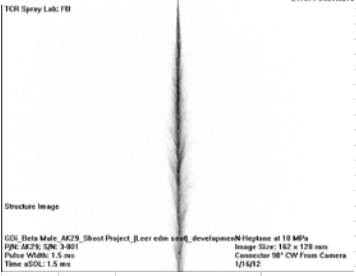

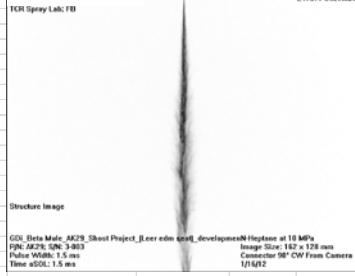


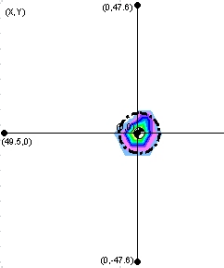
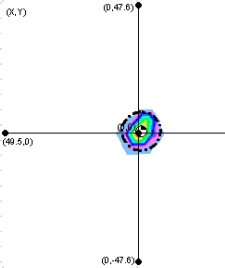
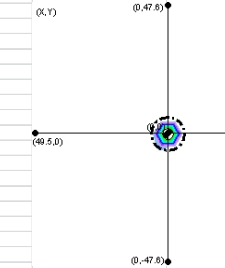
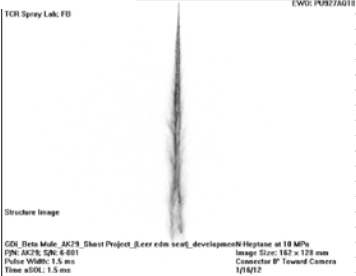
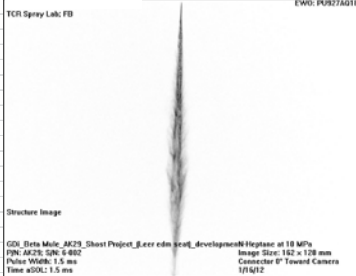
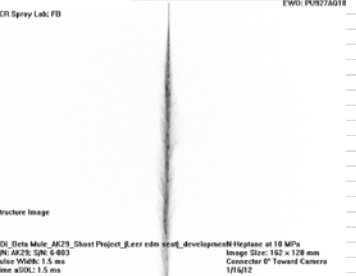
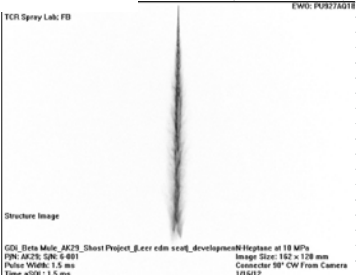
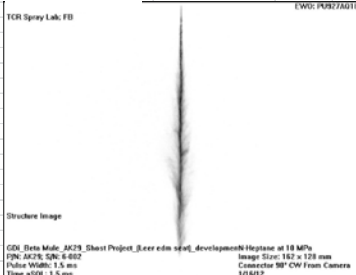
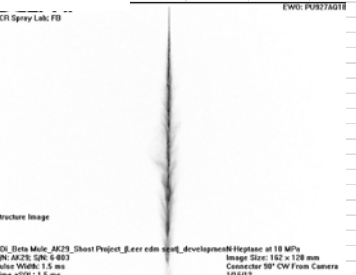
Injector	AK29-3-001		
Drive Scheme	M12_IDM3_V20		
Fuel pressure [bar]			
Test Number	29475		
Pulse width [ms]	Average Flow [mg]	Pulse width [ms]	Average Flow [mg]
0.30	0.00	8.00	25.22
0.35	1.17	10.00	31.64
0.45	1.37		
0.50	1.50	Slope	3.18 g/s
0.60	1.79	Intercept	-0.21
0.80	2.42		
1.00	2.99		
1.50	4.57		
2.00	6.15		

APPENDIX C ROCHESTER SPRAY LAB RESULTS

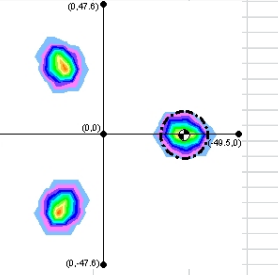


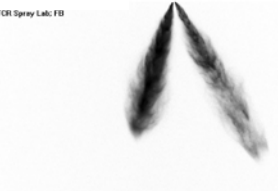
Injector Patternization for targeting centroid, plume angle and shadowgraphic image from Rochester spray lab, seat # **xx**- indicates number omitted in s/n label

Sheet #	Seat #	# holes	d (mm)	β	l/d	(l+L) /d	D/d	Inj. Pres.	Plume Angle	View Angle
1	AK29-03-001	1	≈ 20	0°	1.1	na	na	10MPa	13.5°	0°, 90°
1	AK29-03-002	1	≈ 20	0°	1.1	na	na	10MPa	17.1°	0°, 90°
1	AK29-03-003	1	≈ 20	0°	1.1	na	na	10MPa	16.1°	0°, 90°
2	AK29-06-001	1	≈ 15	0°	1.1	na	na	10MPa	17.6°	0°, 90°
2	AK29-06-002	1	≈ 15	0°	1.1	na	na	10MPa	17.4°	0°, 90°
2	AK29-06-003	1	≈ 15	0°	1.1	na	na	10MPa	14.9°	0°, 90°
3	AK29-09-001	3	≈ 20	30°	1.1	na	na	10MPa	16.6°	0°, 90°
3	AK29-09-002	3	≈ 20	30°	1.1	na	na	10MPa	16.2°	0°, 90°
3	AK29-09-003	3	≈ 20	30°	1.1	na	na	10MPa	17.5°	0°, 90°
4	AK29-10-3-001	3	≈ 15	30°	3.96	na	na	10MPa	16.0°	0°, 90°
4	AK29-10-3-002	3	≈ 15	30°	3.96	na	na	10MPa	17.2°	0°, 90°
4	AK29-10-3-003	3	≈ 15	30°	3.96	na	na	10MPa	16.2°	0°, 90°
5	AK29-11-3-001	3	≈ 15	30°	1.1	na	na	10MPa	13.4°	0°, 90°
5	AK29-11-3-002	3	≈ 15	30°	1.1	na	na	10MPa	14.2°	0°, 90°
5	AK29-11-3-003	3	≈ 15	30°	1.1	na	na	10MPa	15.5°	0°, 90°
6	AK29-12-3-002	3	≈ 15	30°	1.1	na	na	10MPa	13.2°	0°, 90°
6	AK29-12-3-003	3	≈ 15	30°	1.1	na	na	10MPa	15.1°	0°, 90°
6	AK29-12-3-004	3	≈ 15	30°	1.1	na	na	10MPa	13.0°	0°, 90°
7	AK29-12-001	1	≈ 15	30°	1.1	na	na	10MPa	13.7°	0°, 90°
7	AK29-12-002	1	≈ 15	30°	1.1	na	na	10MPa	15.8°	0°, 90°
7	AK29-12-003	1	≈ 15	30°	1.1	na	na	10MPa	13.5°	0°, 90°
8	AK29-13-003	1	≈ 20	0°	1.1	2.95	2.5	10MPa	18.5°	
8	AK29-13-004	1	≈ 20	0°	1.1	2.95	2.5	10MPa	21.7°	
9	AK29-14-005	1	≈ 20	0°	.55	2.95	2.5	10MPa	18.3°	
9	AK29-14-006	1	≈ 20	0°	.55	2.95	2.5	10MPa	18.1°	
10	AK29-15-007	1	≈ 20	0°	1.65	2.95	2.5	10MPa	17.9°	
10	AK29-15-008	1	≈ 20	0°	1.65	2.95	2.5	10MPa	18.3°	
11	AK29-16-009	1	≈ 20	0°	1.1	2.95	2.0	10MPa	21.5°	
11	AK29-16-010	1	≈ 20	0°	1.1	2.95	2.0	10MPa	18.1°	
12	AK29-17-011	1	≈ 20	30°	1.1	2.95	2.0	10MPa	17.6°	
12	AK29-17-012	1	≈ 20	30°	1.1	2.95	2.0	10MPa	18.9°	
13	AK29-18-013	1	≈ 20	0°	1.1	2.95	1.5	10MPa	18.1°	
13	AK29-18-014	1	≈ 20	0°	1.1	2.95	1.5	10MPa	18.0°	
14	AK29-19-015	1	≈ 20	30°	1.1	2.95	1.5	10MPa	14.7°	
14	AK29-19-016	1	≈ 20	30°	1.1	2.95	1.5	10MPa	14.4°	
15	AK29-20-017	1	≈ 20	10°	1.1	2.95	2.5	10MPa	23.3°	
15	AK29-20-018	1	≈ 20	10°	1.1	2.95	2.5	10MPa	21.9°	
16	AK29-21-019	1	≈ 20	20°	1.1	2.95	2.5	10MPa	17.6°	
16	AK29-21-020	1	≈ 20	20°	1.1	2.95	2.5	10MPa	18.1°	
17	AK29-22-021	1	≈ 20	30°	1.1	2.95	2.5	10MPa	19.5°	
17	AK29-22-022	1	≈ 20	30°	1.1	2.95	2.5	10MPa	20.1°	
18	AK29-23-023	3	≈ 20	10°	1.1	2.95	2.5	10MPa	26.0°	
19	AK29-24-024	3	≈ 20	20°	1.1	2.95	2.5	10MPa	20.9°	
19	AK29-24-025	3	≈ 20	20°	1.1	2.95	2.5	10MPa	21.5°	
20	AK29-07-001	3	≈ 20	30°	1.1	2.95	2.5	10MPa	18.1°	
20	AK29-07-002	3	≈ 20	30°	1.1	2.95	2.5	10MPa	18.7°	

AK29-03-001		AK29-03-002		AK29-03-003		Average St. Dev.							
Spray Parameters		Spray Parameters		Spray Parameters									
Injector Height : 50 mm		Injector Height : 50 mm		Injector Height : 50 mm									
Connector Angle (θ) : 0°		Connector Angle (θ) : 0°		Connector Angle (θ) : 0°									
Fuel Pressure : 10000 kPa		Fuel Pressure : 10000 kPa		Fuel Pressure : 10000 kPa									
Pulse Width / Period : 1.5 / 40.0 ms		Pulse Width / Period : 1.5 / 40.0 ms		Pulse Width / Period : 1.5 / 40.0 ms									
# of Pulses : 183		# of Pulses : 193		# of Pulses : 218		198		18.03		183		11.9	
Captured Volume : 1.0 ml		Captured Volume : 1.3 ml		Captured Volume : 1.3 ml						193		15.1	
Plume 1		Plume 1		Plume 1						218		14.2	
Diameter : 11.9 mm @ 90°		Diameter : 15.1 mm @ 90°		Diameter : 14.2 mm @ 90°		13.73		1.85		198		13.73333	
Cone Angle α : 13.5° @ 90°		Cone Angle α : 17.1° @ 90°		Cone Angle α : 16.1° @ 90°		15.57		1.86		18.02776		1.650253	
50% Mass Diameter : 6.8 mm		50% Mass Diameter : 7.8 mm		50% Mass Diameter : 7.3 mm									
50% Cone Angle : 8.9°		50% Cone Angle : 8.9°		50% Cone Angle : 8.4°									
Bend (Skew) Angle (β) : 2.0°		Bend (Skew) Angle (β) : 2.2°		Bend (Skew) Angle (β) : 1.7°									
Mass % : 100.0		Mass % : 100.0		Mass % : 100.0									
Centroid Location (x,y)* : (-1.1 mm, 1.4 mm)		Centroid Location (x,y)* : (-0.9 mm, 1.7 mm)		Centroid Location (x,y)* : (-0.9 mm, 1.2 mm)									
Centroid Location (r,θ)* : (1.8 mm, 130.4°)		Centroid Location (r,θ)* : (1.9 mm, 117.4°)		Centroid Location (r,θ)* : (1.5 mm, 128.6°)									
Static Flow [g/s] per hole @ 10 Mpa		Static Flow [g/s] per hole @ 10 Mpa		Static Flow [g/s] per hole @ 10 Mpa		3.14		3.34		3.25			
Plume 1 w/ Centroid & 90° Analysis Circle		Plume 1 w/ Centroid & 90° Analysis Circle		Plume 1 w/ Centroid & 90° Analysis Circle									
													
TCR Spray Lab: FB		TCR Spray Lab: FB		TCR Spray Lab: FB									
													
Structure Image		Structure Image		Structure Image									
GDI_Beta Male_AK29_Shoot Project_B_err edn test_developmenN Hoptone at 10 MPa F/N: AK29; S/N: 3-801 Pulse Width: 1.5 ms Time aSOL: 1.5 ms		GDI_Beta Male_AK29_Shoot Project_B_err edn test_developmenN Hoptone at 10 MPa F/N: AK29; S/N: 3-802 Pulse Width: 1.5 ms Time aSOL: 1.5 ms		GDI_Beta Male_AK29_Shoot Project_B_err edn test_developmenN Hoptone at 10 MPa F/N: AK29; S/N: 3-803 Pulse Width: 1.5 ms Time aSOL: 1.5 ms									
TCR Spray Lab: FB		TCR Spray Lab: FB		TCR Spray Lab: FB									
													
Structure Image		Structure Image		Structure Image									
GDI_Beta Male_AK29_Shoot Project_B_err edn test_developmenN Hoptone at 10 MPa F/N: AK29; S/N: 3-801 Pulse Width: 1.5 ms Time aSOL: 1.5 ms		GDI_Beta Male_AK29_Shoot Project_B_err edn test_developmenN Hoptone at 10 MPa F/N: AK29; S/N: 3-802 Pulse Width: 1.5 ms Time aSOL: 1.5 ms		GDI_Beta Male_AK29_Shoot Project_B_err edn test_developmenN Hoptone at 10 MPa F/N: AK29; S/N: 3-803 Pulse Width: 1.5 ms Time aSOL: 1.5 ms									

AK29-06-001		AK29-06-002		AK29-06-003		Average St. Dev.					
Spray Parameters		Spray Parameters		Spray Parameters							
Injector Height : 50 mm		Injector Height : 50 mm		Injector Height : 50 mm							
Connector Angle (θ) : 0°		Connector Angle (θ) : 0°		Connector Angle (θ) : 0°							
Fuel Pressure : 10000 kPa		Fuel Pressure : 10000 kPa		Fuel Pressure : 10000 kPa							
Pulse Width / Period : 1.5 / 40.0 ms		Pulse Width / Period : 1.5 / 40.0 ms		Pulse Width / Period : 1.5 / 40.0 ms							
# of Pulses : 335		# of Pulses : 398		# of Pulses : 288		340.33		55.19		335	
Captured Volume : 1.5 ml		Captured Volume : 1.7 ml		Captured Volume : 0.9 ml						15.5	
Plume 1		Plume 1		Plume 1						17.4	
Diameter : 15.5 mm @ 90°		Diameter : 15.3 mm @ 90°		Diameter : 13.1 mm @ 90°		14.63		1.33		398	
Cone Angle α : 17.6° @ 90°		Cone Angle α : 17.4° @ 90°		Cone Angle α : 14.9° @ 90°		16.63		1.50		288	
50% Mass Diameter : 8.3 mm		50% Mass Diameter : 8.4 mm		50% Mass Diameter : 6.1 mm						13.1	
50% Cone Angle : 9.5°		50% Cone Angle : 9.6°		50% Cone Angle : 6.9°						14.9	
Bend (Skew) Angle (β) : 0.7°		Bend (Skew) Angle (β) : 1.5°		Bend (Skew) Angle (β) : 0.2°						16.63333	
Mass % : 100.0		Mass % : 100.0		Mass % : 100.0						1.504438	
Centroid Location (x,y)* : (-0.5 mm, 0.2 mm)		Centroid Location (x,y)* : (-1.0 mm, 0.9 mm)		Centroid Location (x,y)* : (0.2 mm, 0.0 mm)							
Centroid Location (r,θ)* : (0.6 mm, 160.9°)		Centroid Location (r,θ)* : (1.3 mm, 135.4°)		Centroid Location (r,θ)* : (0.2 mm, 346.0°)							
Static Flow [g/s] per hole @ 10 Mpa		Static Flow [g/s] per hole @ 10 Mpa		Static Flow [g/s] per hole @ 10 Mpa		1.89					
1.87		1.86									
Plume 1 w/ Centroid & 90° Analysis Circle		Plume 1 w/ Centroid & 90° Analysis Circle		Plume 1 w/ Centroid & 90° Analysis Circle							
											
											
Structure Image GDI, Beta Mule, AK29, Shoot Project, Error edm src'd_developmentN Height at 10 MPa PIN: AK29; SN: 6-001 Pulse Width: 1.5 ms Time aSOL: 1.5 ms Image Size: 162 x 128 mm Connector 8" Toward Camera 1/16/12		Structure Image GDI, Beta Mule, AK29, Shoot Project, Error edm src'd_developmentN Height at 10 MPa PIN: AK29; SN: 6-002 Pulse Width: 1.5 ms Time aSOL: 1.5 ms Image Size: 162 x 128 mm Connector 8" Toward Camera 1/16/12		Structure Image GDI, Beta Mule, AK29, Shoot Project, Error edm src'd_developmentN Height at 10 MPa PIN: AK29; SN: 6-003 Pulse Width: 1.5 ms Time aSOL: 1.5 ms Image Size: 162 x 128 mm Connector 8" Toward Camera 1/16/12							
											
Structure Image GDI, Beta Mule, AK29, Shoot Project, Error edm src'd_developmentN Height at 10 MPa PIN: AK29; SN: 6-001 Pulse Width: 1.5 ms Time aSOL: 1.5 ms Image Size: 162 x 128 mm Connector 8" Toward Camera 1/16/12		Structure Image GDI, Beta Mule, AK29, Shoot Project, Error edm src'd_developmentN Height at 10 MPa PIN: AK29; SN: 6-002 Pulse Width: 1.5 ms Time aSOL: 1.5 ms Image Size: 162 x 128 mm Connector 8" Toward Camera 1/16/12		Structure Image GDI, Beta Mule, AK29, Shoot Project, Error edm src'd_developmentN Height at 10 MPa PIN: AK29; SN: 6-003 Pulse Width: 1.5 ms Time aSOL: 1.5 ms Image Size: 162 x 128 mm Connector 8" Toward Camera 1/16/12							

Note no relation SF vs. cone angle

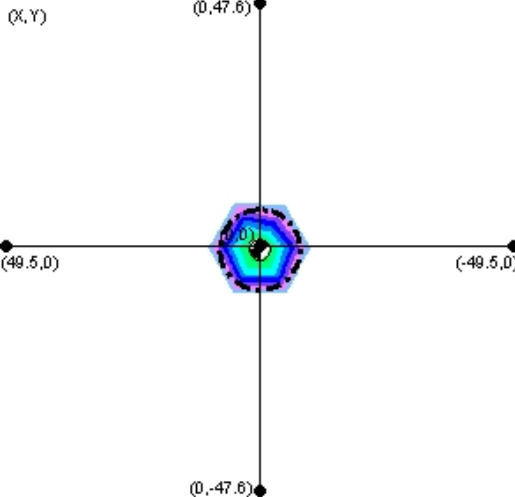
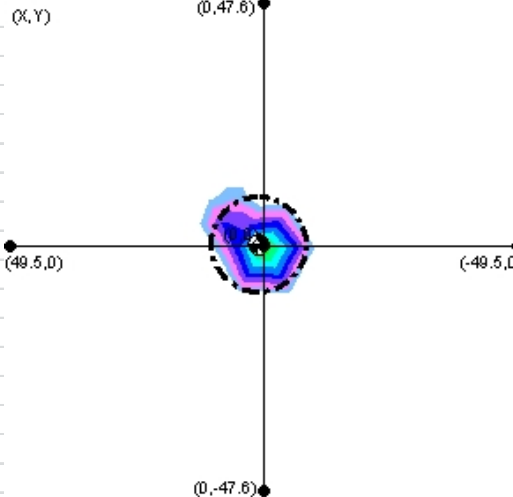
AK29-09-001		AK29-09-002		AK29-09-003		Average		St. Dev.			
Spray Parameters		Spray Parameters		Spray Parameters							
Injector Height : 50 mm		Injector Height : 50 mm		Injector Height : 50 mm							
Connector Angle (θ) : 0°		Connector Angle (θ) : 0°		Connector Angle (θ) : 0°							
Fuel Pressure : 10000 kPa		Fuel Pressure : 10000 kPa		Fuel Pressure : 10000 kPa							
Pulse Width / Period : 1.5 / 40.0 ms		Pulse Width / Period : 1.5 / 40.0 ms		Pulse Width / Period : 1.5 / 40.0 ms							
# of Pulses : 523		# of Pulses : 468		# of Pulses : 560		517.00		46.29		523	
Captured Volume : 6.1 ml		Captured Volume : 5.4 ml		Captured Volume : 6.7 ml						17	
Plume 1		Plume 1		Plume 1						16.2	
Diameter : 17.0 mm @ 90°		Diameter : 17.0 mm @ 90°		Diameter : 17.9 mm @ 90°		17.30		0.52		560	
Cone Angle α : 16.6° @ 90°		Cone Angle α : 16.2° @ 90°		Cone Angle α : 17.5° @ 90°		16.77		0.67		517	
50% Mass Diameter : 9.5 mm		50% Mass Diameter : 9.6 mm		50% Mass Diameter : 10.3 mm						16.76667	
50% Cone Angle : 9.2°		50% Cone Angle : 9.2°		50% Cone Angle : 10.1°							
Bend (Skew) Angle (β) : 33.8°		Bend (Skew) Angle (β) : 33.0°		Bend (Skew) Angle (β) : 30.5°							
Mass % : 35.3		Mass % : 35.2		Mass % : 33.8							
Centroid Location (x,y)* : (-29.8 mm, 0.8 mm)		Centroid Location (x,y)* : (-32.5 mm, 0.8 mm)		Centroid Location (x,y)* : (-29.4 mm, 0.1 mm)							
Centroid Location (r,θ)* : (29.8 mm, 178.5°)		Centroid Location (r,θ)* : (32.5 mm, 178.6°)		Centroid Location (r,θ)* : (29.4 mm, 179.8°)							
Static Flow [g/s] per hole @ 10 Mpa		Static Flow [g/s] per hole @ 10 Mpa		Static Flow [g/s] per hole @ 10 Mpa		2.55					
Plume 1 w/ Centroid & 90% Analysis Circle		Plume 1 w/ Centroid & 90% Analysis Circle		Plume 1 w/ Centroid & 90% Analysis Circle							
											
											
Structure Image		Structure Image		Structure Image							
GDI, Delta Male, AK29, Shost Project, Inner edn scall, development, Heptane at 18 MPa P/N: AK29, S/N: 9-001 Pulse Width: 1.5 ms Time at SOL: 1.5 ms		GDI, Delta Male, AK29, Shost Project, Inner edn scall, development, Heptane at 18 MPa P/N: AK29, S/N: 9-002 Pulse Width: 1.5 ms Time at SOL: 1.5 ms		GDI, Delta Male, AK29, Shost Project, Inner edn scall, development, Heptane at 18 MPa P/N: AK29, S/N: 9-003 Pulse Width: 1.5 ms Time at SOL: 1.5 ms							
											
Structure Image		Structure Image		Structure Image							
GDI, Delta Male, AK29, Shost Project, Inner edn scall, development, Heptane at 18 MPa P/N: AK29, S/N: 9-001 Pulse Width: 1.5 ms Time at SOL: 1.5 ms		GDI, Delta Male, AK29, Shost Project, Inner edn scall, development, Heptane at 18 MPa P/N: AK29, S/N: 9-002 Pulse Width: 1.5 ms Time at SOL: 1.5 ms		GDI, Delta Male, AK29, Shost Project, Inner edn scall, development, Heptane at 18 MPa P/N: AK29, S/N: 9-003 Pulse Width: 1.5 ms Time at SOL: 1.5 ms							

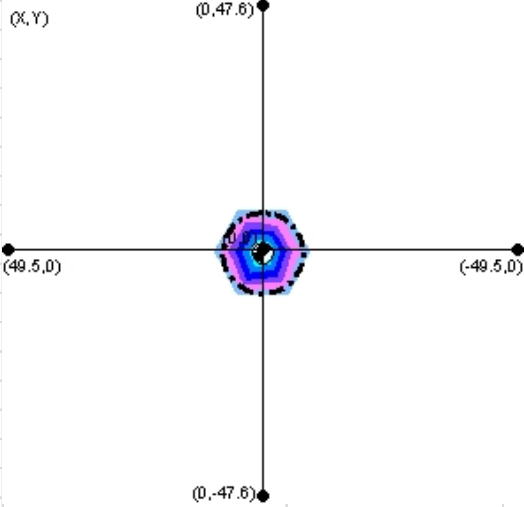
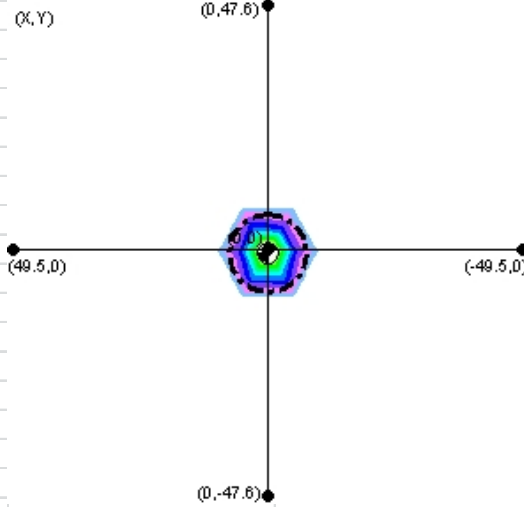
AK29-10-3-001		AK29-10-3-002		AK29-10-3-003		Average		St. Dev.					
Spray Parameters		Spray Parameters		Spray Parameters									
Injector Height : 50 mm		Injector Height : 50 mm		Injector Height : 50 mm									
Connector Angle (θ) : 0°		Connector Angle (θ) : 0°		Connector Angle (θ) : 0°									
Fuel Pressure : 10000 kPa		Fuel Pressure : 10000 kPa		Fuel Pressure : 10000 kPa									
Pulse Width / Period : 1.5 / 40.0 ms		Pulse Width / Period : 1.5 / 40.0 ms		Pulse Width / Period : 1.5 / 40.0 ms									
# of Pulses : 613		# of Pulses : 923		# of Pulses : 720		818.67		101.62		813		16.4	
Captured Volume : 6.6 ml		Captured Volume : 6.7 ml		Captured Volume : 5.9 ml						923		17.7	
Plume 1 Diameter : 16.4 mm @ 90°		Plume 1 Diameter : 17.7 mm @ 90°		Plume 1 Diameter : 16.6 mm @ 90°		16.90		0.70		720		16.6	
Cone Angle α : 16.0° @ 90°		Cone Angle α : 17.2° @ 90°		Cone Angle α : 16.2° @ 90°		16.47		0.64		101.6186		0.7	
50% Mass Diameter : 9.3 mm		50% Mass Diameter : 9.9 mm		50% Mass Diameter : 9.4 mm									
50% Cone Angle : 9.1°		50% Cone Angle : 9.7°		50% Cone Angle : 9.2°									
Bend (Skew) Angle (β) : 30.9°		Bend (Skew) Angle (β) : 31.2°		Bend (Skew) Angle (β) : 30.8°									
Mass % : 34.6		Mass % : 36.3		Mass % : 37.0									
Centroid Location (x,y)* : (-29.9 mm, 0.9 mm)		Centroid Location (x,y)* : (-30.3 mm, 0.0 mm)		Centroid Location (x,y)* : (-29.7 mm, 1.1 mm)									
Centroid Location (r,θ)* : (29.9 mm, 178.3°)		Centroid Location (r,θ)* : (30.3 mm, 179.9°)		Centroid Location (r,θ)* : (29.8 mm, 177.9°)									
Static Flow [g/s] per hole @ 10 Mpa		Static Flow [g/s] per hole @ 10 Mpa		Static Flow [g/s] per hole @ 10 Mpa									
1.69		1.76		1.76									
Plume 1 w/ Centroid & 90° Analysis Circle		Plume 1 w/ Centroid & 90° Analysis Circle		Plume 1 w/ Centroid & 90° Analysis Circle									
Structure Image		Structure Image		Structure Image									
GDI Beta Mule AK29_Short Project_Emer edn swaf_developmenHogplate at 10 MPa FPM AK29: SN: 19-3-001 Image Size: 162 x 128 mm Pulse Width: 1.5 ms Connector 8" Toward Camera Time ASD: 1.5 ms		GDI Beta Mule AK29_Short Project_Emer edn swaf_developmenHogplate at 10 MPa FPM AK29: SN: 19-3-002 Image Size: 162 x 128 mm Pulse Width: 1.5 ms Connector 8" Toward Camera Time ASD: 1.5 ms		GDI Beta Mule AK29_Short Project_Emer edn swaf_developmenHogplate at 10 MPa FPM AK29: SN: 19-3-003 Image Size: 162 x 128 mm Pulse Width: 1.5 ms Connector 8" Toward Camera Time ASD: 1.5 ms									
Structure Image		Structure Image		Structure Image									
GDI Beta Mule AK29_Short Project_Emer edn swaf_developmenHogplate at 10 MPa FPM AK29: SN: 19-3-001 Image Size: 162 x 128 mm Pulse Width: 1.5 ms Connector 8" Toward Camera Time ASD: 1.5 ms		GDI Beta Mule AK29_Short Project_Emer edn swaf_developmenHogplate at 10 MPa FPM AK29: SN: 19-3-002 Image Size: 162 x 128 mm Pulse Width: 1.5 ms Connector 8" Toward Camera Time ASD: 1.5 ms		GDI Beta Mule AK29_Short Project_Emer edn swaf_developmenHogplate at 10 MPa FPM AK29: SN: 19-3-003 Image Size: 162 x 128 mm Pulse Width: 1.5 ms Connector 8" Toward Camera Time ASD: 1.5 ms									

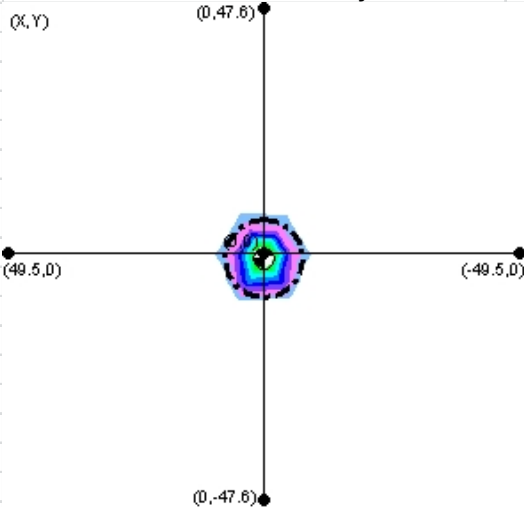
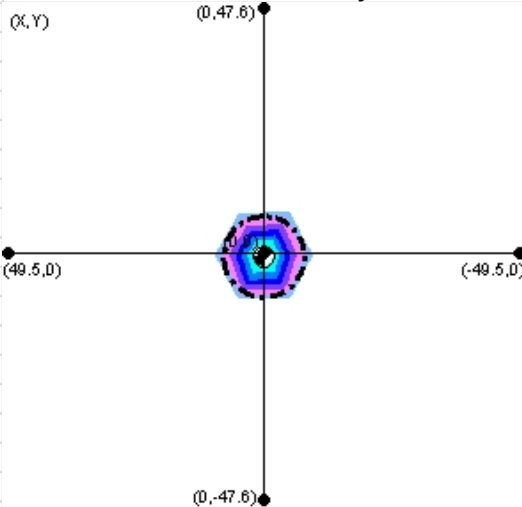
AK29-11-3-001		AK29-11-3-002		AK29-11-3-003		Average		St. Dev.					
Spray Parameters		Spray Parameters		Spray Parameters									
Injector Height : 50 mm		Injector Height : 50 mm		Injector Height : 50 mm									
Connector Angle (θ) : 0°		Connector Angle (θ) : 0°		Connector Angle (θ) : 0°									
Fuel Pressure : 10000 kPa		Fuel Pressure : 10000 kPa		Fuel Pressure : 10000 kPa									
Pulse Width / Period : 1.5 / 40.0 ms		Pulse Width / Period : 1.5 / 40.0 ms		Pulse Width / Period : 1.5 / 40.0 ms									
# of Pulses : 440		# of Pulses : 478		# of Pulses : 638		518.67		105.08		440		13.9	
Captured Volume : 4.1 ml		Captured Volume : 4.7 ml		Captured Volume : 5.5 ml						478		14.6	
Plume 1		Plume 1		Plume 1						638		15.7	
Diameter : 13.9 mm @ 90°		Diameter : 14.6 mm @ 90°		Diameter : 15.7 mm @ 90°		14.73		0.91		518.6667		14.73333	
Cone Angle α : 13.4° @ 90°		Cone Angle α : 14.2° @ 90°		Cone Angle α : 15.5° @ 90°		14.37		1.06		105.0777		0.907377	
50% Mass Diameter : 7.9 mm		50% Mass Diameter : 8.6 mm		50% Mass Diameter : 9.1 mm									
50% Cone Angle : 7.7°		50% Cone Angle : 8.4°		50% Cone Angle : 9.0°									
Bend (Skew) Angle (β) : 31.9°		Bend (Skew) Angle (β) : 31.1°		Bend (Skew) Angle (β) : 29.8°									
Mass % : 32.4		Mass % : 32.7		Mass % : 35.8									
Centroid Location (x,y)* : (-31.1 mm, 0.8 mm)		Centroid Location (x,y)* : (-30.2 mm, 1.1 mm)		Centroid Location (x,y)* : (-28.6 mm, -0.2 mm)									
Centroid Location (r,θ)* : (31.1 mm, 178.5°)		Centroid Location (r,θ)* : (30.2 mm, 177.9°)		Centroid Location (r,θ)* : (28.6 mm, 180.5°)									
Static Flow [g/s] per hole @ 10 Mpa	1.76	Static Flow [g/s] per hole @ 10 Mpa	1.82	Static Flow [g/s] per hole @ 10 Mpa	1.68								
Plume 1 w/ Centroid & 90% Analysis Circle		Plume 1 w/ Centroid & 90% Analysis Circle		Plume 1 w/ Centroid & 90% Analysis Circle									
													
													
<p>Structure Image</p> <p>GD: Beta Male AK29_Sheet Project_E Aer edn sea4_development\Hoptane at 10 MPa P/N: AK29: S/N: 11-3-001 Image Size: 162 x 128 mm Pulse Width: 1.5 ms Connector 9° Toward Camera 1/16112 Time at SOL: 1.5 ms</p>		<p>Structure Image</p> <p>GD: Beta Male AK29_Sheet Project_E Aer edn sea4_development\Hoptane at 10 MPa P/N: AK29: S/N: 11-3-002 Image Size: 162 x 128 mm Pulse Width: 1.5 ms Connector 9° Toward Camera 1/16112 Time at SOL: 1.5 ms</p>		<p>Structure Image</p> <p>GD: Beta Male AK29_Sheet Project_E Aer edn sea4_development\Hoptane at 10 MPa P/N: AK29: S/N: 11-3-003 Image Size: 162 x 128 mm Pulse Width: 1.5 ms Connector 9° Toward Camera 1/16112 Time at SOL: 1.5 ms</p>									
													
<p>Structure Image</p> <p>GD: Beta Male AK29_Sheet Project_E Aer edn sea4_development\Hoptane at 10 MPa P/N: AK29: S/N: 11-3-001 Image Size: 162 x 128 mm Pulse Width: 1.5 ms Connector 90° CW From Camera 1/16112 Time at SOL: 1.5 ms</p>		<p>Structure Image</p> <p>GD: Beta Male AK29_Sheet Project_E Aer edn sea4_development\Hoptane at 10 MPa P/N: AK29: S/N: 11-3-002 Image Size: 162 x 128 mm Pulse Width: 1.5 ms Connector 90° CW From Camera 1/16112 Time at SOL: 1.5 ms</p>		<p>Structure Image</p> <p>GD: Beta Male AK29_Sheet Project_E Aer edn sea4_development\Hoptane at 10 MPa P/N: AK29: S/N: 11-3-003 Image Size: 162 x 128 mm Pulse Width: 1.5 ms Connector 90° CW From Camera 1/16112 Time at SOL: 1.5 ms</p>									

	AK29-12-3-002	AK29-12-3-003	AK29-12-3-004	AverageSt. Dev.					
	Spray Parameters								
	Injector Height : 50 mm	Injector Height : 50 mm	Injector Height : 50 mm						
	Connector Angle (θ) : 0°	Connector Angle (θ) : 0°	Connector Angle (θ) : 0°						
	Fuel Pressure : 10000 kPa	Fuel Pressure : 10000 kPa	Fuel Pressure : 10000 kPa						
	Pulse Width / Period : 1.5 / 40.0 ms	Pulse Width / Period : 1.5 / 40.0 ms	Pulse Width / Period : 1.5 / 40.0 ms						
	# of Pulses : 570	# of Pulses : 765	# of Pulses : 388						
	Captured Volume : 4.4 ml	Captured Volume : 5.1 ml	Captured Volume : 3.5 ml						
	Plume 1	Plume 1	Plume 1						
	Diameter : 13.6 mm @ 90°	Diameter : 15.4 mm @ 90°	Diameter : 13.3 mm @ 90°						
	Cone Angle α : 13.2° @ 90°	Cone Angle α : 15.1° @ 90°	Cone Angle α : 13.0° @ 90°						
	50% Mass Diameter : 8.1 mm	50% Mass Diameter : 8.9 mm	50% Mass Diameter : 8.0 mm						
	50% Cone Angle : 7.8°	50% Cone Angle : 8.7°	50% Cone Angle : 7.8°						
	Bend (Skew) Angle (β) : 31.8°	Bend (Skew) Angle (β) : 31.0°	Bend (Skew) Angle (β) : 31.2°						
	Mass % : 35.9	Mass % : 35.4	Mass % : 37.3						
	Centroid Location (x,y)* : (-30.9 mm, 1.9 mm)	Centroid Location (x,y)* : (-30.0 mm, 1.3 mm)	Centroid Location (x,y)* : (-30.2 mm, 1.3 mm)						
	Centroid Location (r,θ)* : (30.9 mm, 176.6°)	Centroid Location (r,θ)* : (30.1 mm, 177.4°)	Centroid Location (r,θ)* : (30.3 mm, 177.5°)						
	Plume 1 w/ Centroid & 90% Analysis Circle	Plume 1 w/ Centroid & 90% Analysis Circle	Plume 1 w/ Centroid & 90% Analysis Circle						
									
g model									
model									
TCR Spray Lab: FB									
Structure Image									
GD: Beta Male_AK29_Short Project_1_err edn scatt_developmentH Height at 10 MPa	Image Size: 162 x 128 mm	GD: Beta Male_AK29_Short Project_1_err edn scatt_developmentH Height at 10 MPa	GD: Beta Male_AK29_Short Project_1_err edn scatt_developmentH Height at 10 MPa						
FW: AK29: SW: 12-3-882	Connector 0° Toward Camera	FW: AK29: SW: 12-3-883	FW: AK29: SW: 12-3-884						
Pulse Width: 1.5 ms	Time at SOL: 1.5 ms	Pulse Width: 1.5 ms	Pulse Width: 1.5 ms						
Time at SOL: 1.5 ms	Time at SOL: 1.5 ms	Time at SOL: 1.5 ms	Time at SOL: 1.5 ms						
TCR Spray Lab: FB									
Structure Image									
GD: Beta Male_AK29_Short Project_1_err edn scatt_developmentH Height at 10 MPa	Image Size: 162 x 128 mm	GD: Beta Male_AK29_Short Project_1_err edn scatt_developmentH Height at 10 MPa	GD: Beta Male_AK29_Short Project_1_err edn scatt_developmentH Height at 10 MPa						
FW: AK29: SW: 12-3-882	Connector 90° CW From Camera	FW: AK29: SW: 12-3-883	FW: AK29: SW: 12-3-884						
Pulse Width: 1.5 ms	Time at SOL: 1.5 ms	Pulse Width: 1.5 ms	Pulse Width: 1.5 ms						
Time at SOL: 1.5 ms	Time at SOL: 1.5 ms	Time at SOL: 1.5 ms	Time at SOL: 1.5 ms						

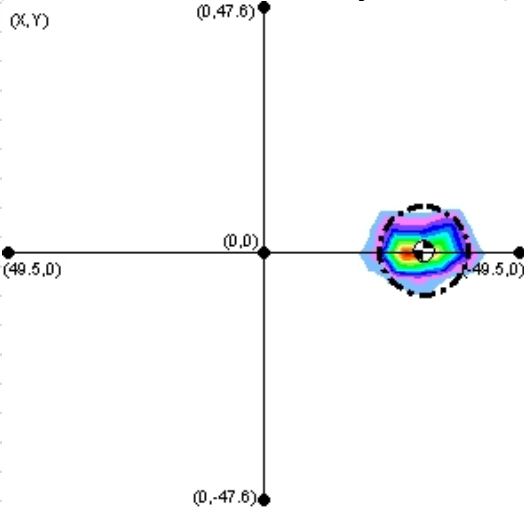
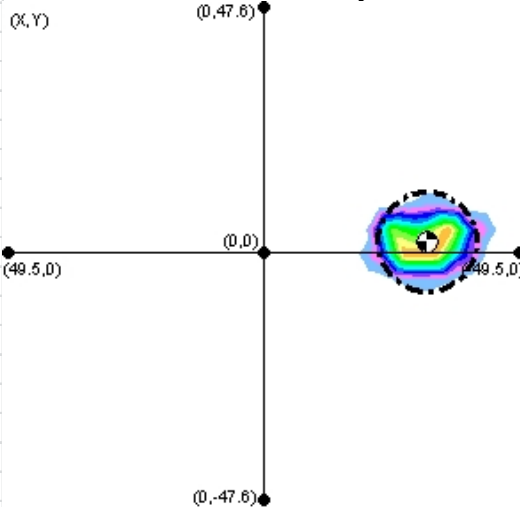
AK29-12-001		AK29-12-002		AK29-12-003		Average St. Dev.					
Spray Parameters		Spray Parameters		Spray Parameters							
Injector Height : 50 mm		Injector Height : 50 mm		Injector Height : 50 mm							
Connector Angle (θ) : 0°		Connector Angle (θ) : 0°		Connector Angle (θ) : 0°							
Fuel Pressure : 10000 kPa		Fuel Pressure : 10000 kPa		Fuel Pressure : 10000 kPa							
Pulse Width / Period : 1.5 / 40.0 ms		Pulse Width / Period : 1.5 / 40.0 ms		Pulse Width / Period : 1.5 / 40.0 ms							
# of Pulses : 510		# of Pulses : 575		# of Pulses : 480		521.67		48.56		510	
Captured Volume : 1.6 ml		Captured Volume : 2.1 ml		Captured Volume : 1.5 ml						575	
Plume 1		Plume 1		Plume 1						480	
Diameter : 13.9 mm @ 90°		Diameter : 16.0 mm @ 90°		Diameter : 13.8 mm @ 90°		14.57		1.24		510	
Cone Angle α : 13.7° @ 90°		Cone Angle α : 15.8° @ 90°		Cone Angle α : 13.5° @ 90°		14.33		1.27		575	
50% Mass Diameter : 8.3 mm		50% Mass Diameter : 9.5 mm		50% Mass Diameter : 7.9 mm						13.9	
50% Cone Angle : 8.2°		50% Cone Angle : 9.4°		50% Cone Angle : 7.8°						16	
Bend (Skew) Angle (β) : 30.3°		Bend (Skew) Angle (β) : 29.6°		Bend (Skew) Angle (β) : 30.8°						13.8	
Mass % : 100.0		Mass % : 100.0		Mass % : 100.0						14.33333	
Centroid Location (x,y)* : (13.3 mm, -26.0 mm)		Centroid Location (x,y)* : (13.3 mm, -25.0 mm)		Centroid Location (x,y)* : (14.9 mm, -25.8 mm)							
Centroid Location (r,θ)* : (29.2 mm, 297.1°)		Centroid Location (r,θ)* : (28.4 mm, 298.0°)		Centroid Location (r,θ)* : (29.8 mm, 300.1°)							
Plume 1 w/ Centroid & 90° Analysis Circle		Plume 1 w/ Centroid & 90° Analysis Circle		Plume 1 w/ Centroid & 90° Analysis Circle							
Structure Image		Structure Image		Structure Image							
GDI Beta Mole AK29_Short Project_Baser odm scat_developme@Higphase at 10 MPa PIN AK29: SN: 12 001 Pulse Width: 1.5 ms Time at SOL: 1.5 ms		GDI Beta Mole AK29_Short Project_Baser odm scat_developme@Higphase at 10 MPa PIN AK29: SN: 12 002 Pulse Width: 1.5 ms Time at SOL: 1.5 ms		GDI Beta Mole AK29_Short Project_Baser odm scat_developme@Higphase at 10 MPa PIN AK29: SN: 12 003 Pulse Width: 1.5 ms Time at SOL: 1.5 ms							
Image Size: 162 x 128 mm Connector 90° Toward Camera 1/16/12		Image Size: 162 x 128 mm Connector 90° Toward Camera 1/16/12		Image Size: 162 x 128 mm Connector 90° Toward Camera 1/16/12							
Structure Image		Structure Image		Structure Image							
GDI Beta Mole AK29_Short Project_Baser odm scat_developme@Higphase at 10 MPa PIN AK29: SN: 12 001 Pulse Width: 1.5 ms Time at SOL: 1.5 ms		GDI Beta Mole AK29_Short Project_Baser odm scat_developme@Higphase at 10 MPa PIN AK29: SN: 12 002 Pulse Width: 1.5 ms Time at SOL: 1.5 ms		GDI Beta Mole AK29_Short Project_Baser odm scat_developme@Higphase at 10 MPa PIN AK29: SN: 12 003 Pulse Width: 1.5 ms Time at SOL: 1.5 ms							
Image Size: 162 x 128 mm Connector 90° Toward Camera 1/16/12		Image Size: 162 x 128 mm Connector 90° Toward Camera 1/16/12		Image Size: 162 x 128 mm Connector 90° Toward Camera 1/16/12							

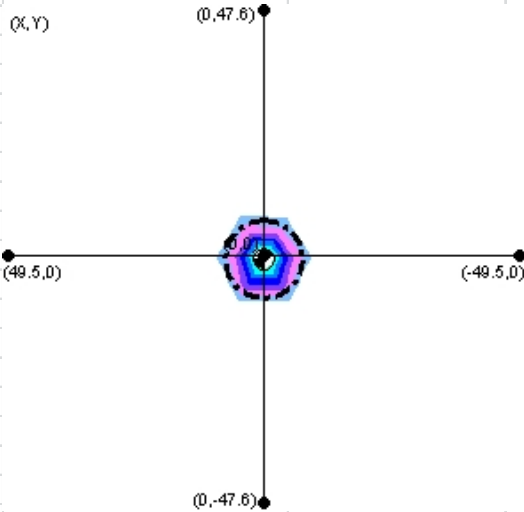
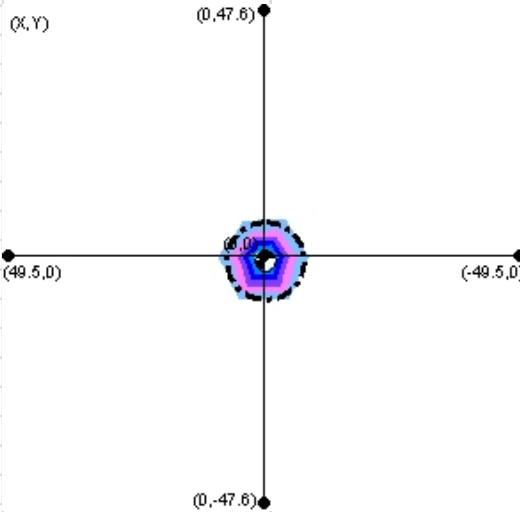
AK29-003		AK29-004	
Spray Parameters		Spray Parameters	
Injector Height : 50 mm		Injector Height : 50 mm	
Connector Angle (θ) : 0°		Connector Angle (θ) : 0°	
Fuel Pressure : 10000 kPa		Fuel Pressure : 10000 kPa	
Pulse Width / Period : 1.5 / 40.0 ms		Pulse Width / Period : 1.5 / 40.0 ms	
# of Pulses : 600		# of Pulses : 495	
Captured Volume : 2.0 ml		Captured Volume : 2.0 ml	
Plume 1		Plume 1	
Diameter : 16.3 mm @ 90%		Diameter : 19.2 mm @ 90%	
Cone Angle α : 18.5° @ 90%		Cone Angle α : 21.7° @ 90%	
50% Mass Diameter : 10.2 mm		50% Mass Diameter : 11.6 mm	
50% Cone Angle : 11.7°		50% Cone Angle : 13.2°	
Bend (Skew) Angle (β) : 0.4°		Bend (Skew) Angle (β) : 1.5°	
Centroid Location (x,y)* : (0.2 mm, -0.3 mm)		Centroid Location (x,y)* : (1.0 mm, 0.8 mm)	
Centroid Location (r, θ)* : (0.4 mm, 297.0°)		Centroid Location (r, θ)* : (1.3 mm, 37.3°)	
Plume 1 w/ Centroid & 90° Analysis Circle		Plume 1 w/ Centroid & 90° Analysis Circle	
			

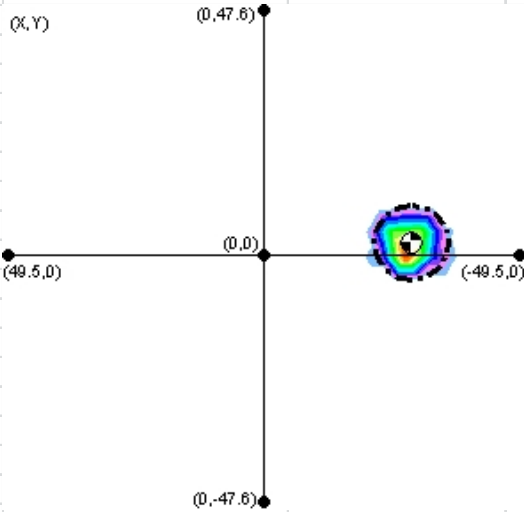
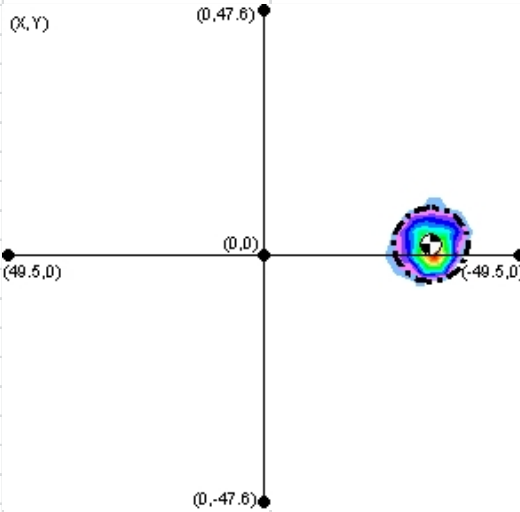
AK29-005		AK29-006	
Spray Parameters		Spray Parameters	
Injector Height : 50 mm		Injector Height : 50 mm	
Connector Angle (θ) : 0°		Connector Angle (θ) : 0°	
Fuel Pressure : 10000 kPa		Fuel Pressure : 10000 kPa	
Pulse Width / Period : 1.5 / 40.0 ms		Pulse Width / Period : 1.5 / 40.0 ms	
# of Pulses : 358		# of Pulses : 555	
Captured Volume : 1.4 ml		Captured Volume : 1.9 ml	
Plume 1		Plume 1	
Diameter : 16.1 mm @ 90%		Diameter : 15.9 mm @ 90%	
Cone Angle α : 18.3° @ 90%		Cone Angle α : 18.1° @ 90%	
50% Mass Diameter : 9.9 mm		50% Mass Diameter : 9.5 mm	
50% Cone Angle : 11.3°		50% Cone Angle : 10.8°	
Bend (Skew) Angle (β) : 0.4°		Bend (Skew) Angle (β) : 0.3°	
Centroid Location (x,y) [*] : (0.2 mm, -0.3 mm)		Centroid Location (x,y) [*] : (0.1 mm, -0.3 mm)	
Centroid Location (r,θ) [*] : (0.4 mm, 309.3°)		Centroid Location (r,θ) [*] : (0.3 mm, 283.4°)	
Plume 1 w/ Centroid & 90% Analysis Circle		Plume 1 w/ Centroid & 90% Analysis Circle	
			

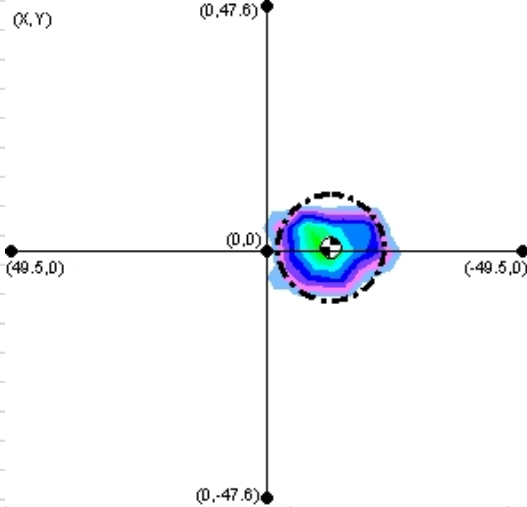
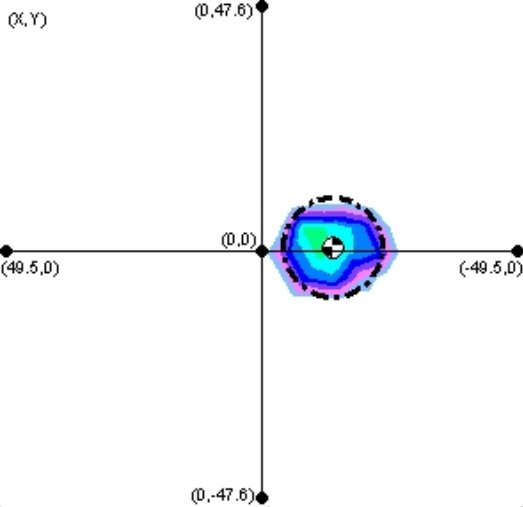
AK29-007		AK29-008	
Spray Parameters		Spray Parameters	
Injector Height : 50 mm		Injector Height : 50 mm	
Connector Angle (θ) : 0°		Connector Angle (θ) : 0°	
Fuel Pressure : 10000 kPa		Fuel Pressure : 10000 kPa	
Pulse Width / Period : 1.5 / 40.0 ms		Pulse Width / Period : 1.5 / 40.0 ms	
# of Pulses : 538		# of Pulses : 455	
Captured Volume : 1.5 ml		Captured Volume : 1.5 ml	
Plume 1		Plume 1	
Diameter : 15.7 mm @ 90%		Diameter : 16.1 mm @ 90%	
Cone Angle α : 17.9° @ 90%		Cone Angle α : 18.3° @ 90%	
50% Mass Diameter : 9.0 mm		50% Mass Diameter : 9.9 mm	
50% Cone Angle : 10.3°		50% Cone Angle : 11.3°	
Bend (Skew) Angle (β) : 0.9°		Bend (Skew) Angle (β) : 0.3°	
Centroid Location (x,y)* : (0.1 mm, -0.7 mm)		Centroid Location (x,y)* : (0.0 mm, -0.3 mm)	
Centroid Location (r, θ)* : (0.7 mm, 281.4°)		Centroid Location (r, θ)* : (0.3 mm, 279.2°)	
Plume 1 w/ Centroid & 90% Analysis Circle		Plume 1 w/ Centroid & 90% Analysis Circle	
			

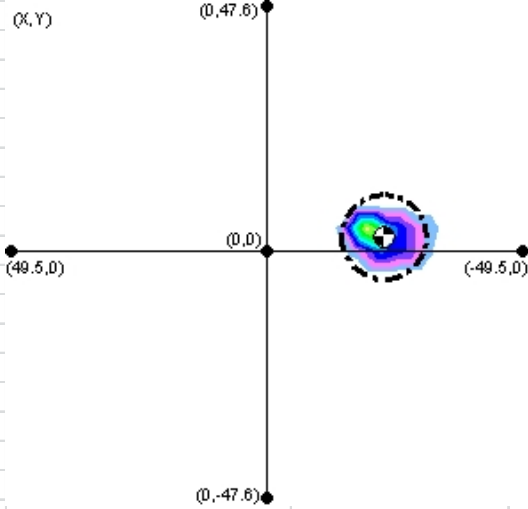
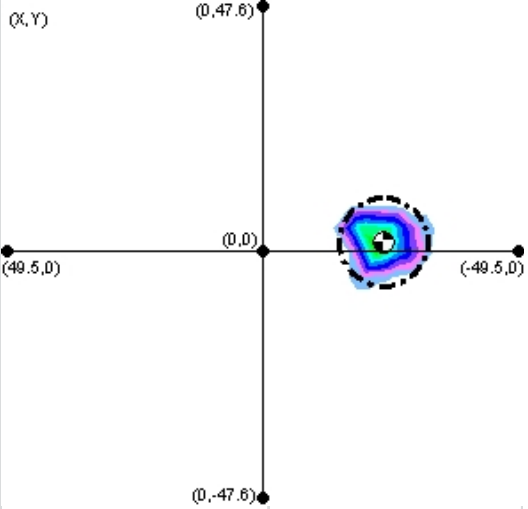
AK29-009		AK29-010	
Spray Parameters		Spray Parameters	
Injector Height : 50 mm		Injector Height : 50 mm	
Connector Angle (θ) : 0°		Connector Angle (θ) : 0°	
Fuel Pressure : 10000 kPa		Fuel Pressure : 10000 kPa	
Pulse Width / Period : 1.5 / 40.0 ms		Pulse Width / Period : 1.5 / 40.0 ms	
# of Pulses : 458		# of Pulses : 305	
Captured Volume : 1.7 ml		Captured Volume : 1.2 ml	
Plume 1		Plume 1	
Diameter : 19.0 mm @ 90%		Diameter : 15.9 mm @ 90%	
Cone Angle α : 21.5° @ 90%		Cone Angle α : 18.1° @ 90%	
50% Mass Diameter : 11.1 mm		50% Mass Diameter : 9.4 mm	
50% Cone Angle : 12.7°		50% Cone Angle : 10.8°	
Bend (Skew) Angle (β) : 1.1°		Bend (Skew) Angle (β) : 0.4°	
Centroid Location (x,y)* : (0.4 mm, 0.9 mm)		Centroid Location (x,y)* : (0.0 mm, -0.3 mm)	
Centroid Location (r, θ)* : (1.0 mm, 65.7°)		Centroid Location (r, θ)* : (0.3 mm, 261.7°)	
Plume 1 w/ Centroid & 90% Analysis Circle		Plume 1 w/ Centroid & 90% Analysis Circle	

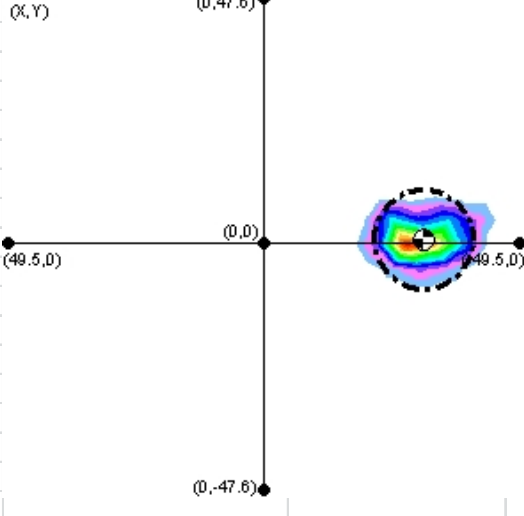
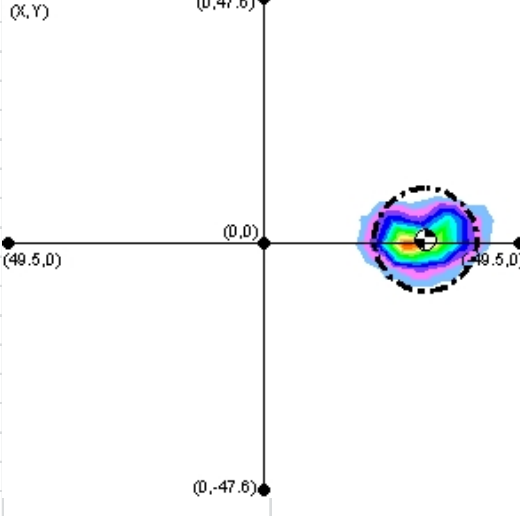
AK29-011		AK29-012	
Spray Parameters		Spray Parameters	
Injector Height : 50 mm		Injector Height : 50 mm	
Connector Angle (θ) : 0°		Connector Angle (θ) : 0°	
Fuel Pressure : 10000 kPa		Fuel Pressure : 10000 kPa	
Pulse Width / Period : 1.5 / 40.0 ms		Pulse Width / Period : 1.5 / 40.0 ms	
# of Pulses : 588		# of Pulses : 770	
Captured Volume : 2.3 ml		Captured Volume : 3.2 ml	
Plume 1		Plume 1	
Diameter : 18.1 mm @ 90%		Diameter : 19.6 mm @ 90%	
Cone Angle α : 17.6° @ 90%		Cone Angle α : 18.9° @ 90%	
50% Mass Diameter : 10.1 mm		50% Mass Diameter : 11.4 mm	
50% Cone Angle : 9.9°		50% Cone Angle : 11.1°	
Bend (Skew) Angle (β) : 31.4°		Bend (Skew) Angle (β) : 32.1°	
Centroid Location (x,y)* : (-30.5 mm, 0.8 mm)		Centroid Location (x,y)* : (-31.3 mm, 2.3 mm)	
Centroid Location (r, θ)* : (30.5 mm, 178.4°)		Centroid Location (r, θ)* : (31.4 mm, 175.7°)	
Plume 1 w/ Centroid & 90% Analysis Circle		Plume 1 w/ Centroid & 90% Analysis Circle	
			

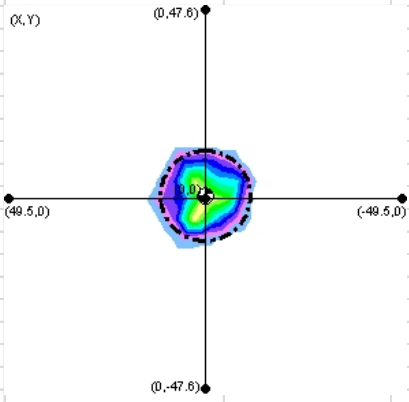
AK29-013		AK29-014	
Spray Parameters		Spray Parameters	
Injector Height : 50 mm		Injector Height : 50 mm	
Connector Angle (θ) : 0°		Connector Angle (θ) : 0°	
Fuel Pressure : 10000 kPa		Fuel Pressure : 10000 kPa	
Pulse Width / Period : 1.5 / 40.0 ms		Pulse Width / Period : 1.5 / 40.0 ms	
# of Pulses : 375		# of Pulses : 275	
Captured Volume : 1.3 ml		Captured Volume : 1.1 ml	
Plume 1		Plume 1	
Diameter : 15.9 mm @ 90%		Diameter : 15.8 mm @ 90%	
Cone Angle α : 18.1° @ 90%		Cone Angle α : 18.0° @ 90%	
50% Mass Diameter : 9.4 mm		50% Mass Diameter : 9.2 mm	
50% Cone Angle : 10.7°		50% Cone Angle : 10.5°	
Bend (Skew) Angle (β) : 0.6°		Bend (Skew) Angle (β) : 0.6°	
Centroid Location (x,y)* : (0.0 mm, -0.5 mm)		Centroid Location (x,y)* : (0.0 mm, -0.6 mm)	
Centroid Location (r, θ)* : (0.5 mm, 270.4°)		Centroid Location (r, θ)* : (0.6 mm, 269.6°)	
Plume 1 w/ Centroid & 90% Analysis Circle		Plume 1 w/ Centroid & 90% Analysis Circle	
			

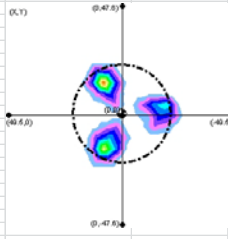
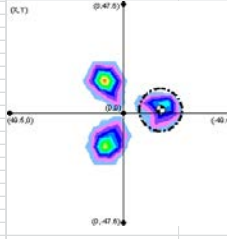
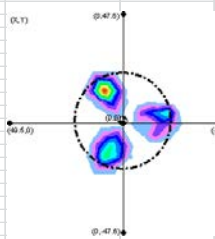
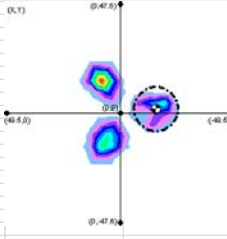
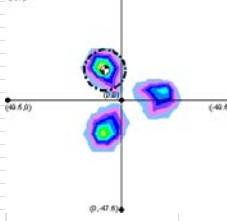
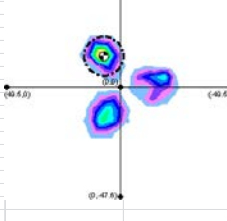
AK29-15		AK29-16	
Spray Parameters		Spray Parameters	
Injector Height : 50 mm		Injector Height : 50 mm	
Connector Angle (θ) : 0°		Connector Angle (θ) : 0°	
Fuel Pressure : 10000 kPa		Fuel Pressure : 10000 kPa	
Pulse Width / Period : 1.5 / 40.0 ms		Pulse Width / Period : 1.5 / 40.0 ms	
# of Pulses : 413		# of Pulses : 375	
Captured Volume : 1.9 ml		Captured Volume : 1.7 ml	
Plume 1		Plume 1	
Diameter : 14.8 mm @ 90%		Diameter : 15.1 mm @ 90%	
Cone Angle α : 14.7° @ 90%		Cone Angle α : 14.4° @ 90%	
50% Mass Diameter : 8.6 mm		50% Mass Diameter : 8.5 mm	
50% Cone Angle : 8.6°		50% Cone Angle : 8.2°	
Bend (Skew) Angle (β) : 29.6°		Bend (Skew) Angle (β) : 32.8°	
Centroid Location (x,y)* : (-28.2 mm, 2.6 mm)		Centroid Location (x,y)* : (-32.1 mm, 2.2 mm)	
Centroid Location (r, θ)* : (28.4 mm, 174.6°)		Centroid Location (r, θ)* : (32.2 mm, 176.0°)	
Plume 1 w/ Centroid & 90% Analysis Circle		Plume 1 w/ Centroid & 90% Analysis Circle	
 <p>Diagram showing the spray plume for AK29-15. The plume is centered at (0,0) and extends horizontally to (-49.5,0) and (49.5,0). The vertical axis is labeled (0,Y) at the top and (0,-47.6) at the bottom. A 90% analysis circle is shown around the centroid location (-28.2 mm, 2.6 mm). The plume is labeled (0,47.6) at the top and (0,-47.6) at the bottom.</p>		 <p>Diagram showing the spray plume for AK29-16. The plume is centered at (0,0) and extends horizontally to (-49.5,0) and (49.5,0). The vertical axis is labeled (0,Y) at the top and (0,-47.6) at the bottom. A 90% analysis circle is shown around the centroid location (-32.1 mm, 2.2 mm). The plume is labeled (0,47.6) at the top and (0,-47.6) at the bottom.</p>	

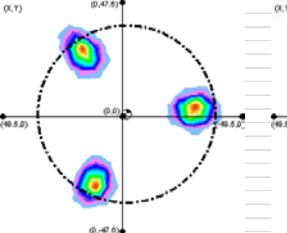
AK29-17		AK29-18	
Spray Parameters		Spray Parameters	
Injector Height : 50 mm		Injector Height : 50 mm	
Connector Angle (θ) : 0°		Connector Angle (θ) : 0°	
Fuel Pressure : 10000 kPa		Fuel Pressure : 10000 kPa	
Pulse Width / Period : 1.5 / 40.0 ms		Pulse Width / Period : 1.5 / 40.0 ms	
# of Pulses : 938		# of Pulses : 848	
Captured Volume : 2.7 ml		Captured Volume : 2.6 ml	
Plume 1		Plume 1	
Diameter : 21.2 mm @ 90%		Diameter : 20.0 mm @ 90%	
Cone Angle α : 23.3° @ 90%		Cone Angle α : 21.9° @ 90%	
50% Mass Diameter : 12.6 mm		50% Mass Diameter : 12.6 mm	
50% Cone Angle : 13.9°		50% Cone Angle : 13.9°	
Bend (Skew) Angle (β) : 13.6°		Bend (Skew) Angle (β) : 15.2°	
Centroid Location (x,y)* : (-12.0 mm, 0.9 mm)		Centroid Location (x,y)* : (-13.5 mm, 0.9 mm)	
Centroid Location (r, θ)* : (12.1 mm, 175.5°)		Centroid Location (r, θ)* : (13.6 mm, 176.1°)	
Plume 1 w/ Centroid & 90% Analysis Circle		Plume 1 w/ Centroid & 90% Analysis Circle	
			

AK29-19		AK29-20	
Spray Parameters		Spray Parameters	
Injector Height : 50 mm		Injector Height : 50 mm	
Connector Angle (θ) : 0°		Connector Angle (θ) : 0°	
Fuel Pressure : 10000 kPa		Fuel Pressure : 10000 kPa	
Pulse Width / Period : 1.5 / 40.0 ms		Pulse Width / Period : 1.5 / 40.0 ms	
# of Pulses : 315		# of Pulses : 435	
Captured Volume : 1.3 ml		Captured Volume : 1.6 ml	
Plume 1		Plume 1	
Diameter : 17.0 mm @ 90%		Diameter : 17.6 mm @ 90%	
Cone Angle α : 17.6° @ 90%		Cone Angle α : 18.1° @ 90%	
50% Mass Diameter : 9.5 mm		50% Mass Diameter : 9.8 mm	
50% Cone Angle : 9.8°		50% Cone Angle : 10.2°	
Bend (Skew) Angle (β) : 24.4°		Bend (Skew) Angle (β) : 24.8°	
Centroid Location (x,y)* : (-22.5 mm, 3.1 mm)		Centroid Location (x,y)* : (-23.0 mm, 2.1 mm)	
Centroid Location (r, θ)* : (22.7 mm, 172.3°)		Centroid Location (r, θ)* : (23.1 mm, 174.8°)	
Plume 1 w/ Centroid & 90% Analysis Circle		Plume 1 w/ Centroid & 90% Analysis Circle	
 <p>Diagram showing the spray plume for AK29-19. The plume is centered at (0,0) and is bounded by a 90% analysis circle. The centroid location is marked at (-22.5 mm, 3.1 mm). The diagram includes a coordinate system with points (0,47.6), (0,-47.6), (49.5,0), and (-49.5,0) marked.</p>		 <p>Diagram showing the spray plume for AK29-20. The plume is centered at (0,0) and is bounded by a 90% analysis circle. The centroid location is marked at (-23.0 mm, 2.1 mm). The diagram includes a coordinate system with points (0,47.6), (0,-47.6), (49.5,0), and (-49.5,0) marked.</p>	

AK29-21		AK29-22	
Spray Parameters		Spray Parameters	
Injector Height : 50 mm		Injector Height : 50 mm	
Connector Angle (θ) : 0°		Connector Angle (θ) : 0°	
Fuel Pressure : 10000 kPa		Fuel Pressure : 10000 kPa	
Pulse Width / Period : 1.5 / 40.0 ms		Pulse Width / Period : 1.5 / 40.0 ms	
# of Pulses : 688		# of Pulses : 650	
Captured Volume : 2.9 ml		Captured Volume : 2.7 ml	
Plume 1		Plume 1	
Diameter : 20.2 mm @ 90%		Diameter : 20.9 mm @ 90%	
Cone Angle α : 19.5° @ 90%		Cone Angle α : 20.1° @ 90%	
50% Mass Diameter : 11.5 mm		50% Mass Diameter : 11.7 mm	
50% Cone Angle : 11.2°		50% Cone Angle : 11.4°	
Bend (Skew) Angle (β) : 31.6°		Bend (Skew) Angle (β) : 31.7°	
Centroid Location (x,y)* : (-30.8 mm, 1.2 mm)		Centroid Location (x,y)* : (-30.9 mm, 1.1 mm)	
Centroid Location (r, θ)* : (30.8 mm, 177.8°)		Centroid Location (r, θ)* : (30.9 mm, 178.0°)	
Plume 1 w/ Centroid & 90% Analysis Circle		Plume 1 w/ Centroid & 90% Analysis Circle	
			

AK29-23				
Spray Parameters				
Injector Height : 50 mm				
Connector Angle (θ) : 0°		Likely the 3 plumes have coalesced into 1.		
Fuel Pressure : 10000 kPa				
Pulse Width / Period : 1.5 / 40.0 ms				
# of Pulses : 383				
Captured Volume : 4.3 ml				
Plume 1				
Diameter : 23.1 mm @ 90%				
Cone Angle α : 26.0° @ 90%				
50% Mass Diameter : 14.1 mm				
50% Cone Angle : 16.0°				
Bend (Skew) Angle (β) : 1.2°				
Centroid Location (x,y)* : (0.2 mm, 1.0 mm)				
Centroid Location (r, θ)* : (1.0 mm, 78.3°)				
Plume 1 w/ Centroid & 90% Analysis Circle				
				

AK29-24 Spray Parameters Injector Height : 50 mm Connector Angle (θ) : 0° Fuel Pressure : 10000 kPa Pulse Width / Period : 1.5 / 40.0 ms # of Pulses : 543 Captured Volume : 5.4 ml Spray Diameter : 43.3 mm @ 90° Cone Angle α : 46.8° @ 90° 50% Mass Diameter : 31.7 mm 50% Cone Angle : 35.2° Bend (Skew) Angle (β) : 1.2° Centroid Location (x,y) : (0.4 mm, 1.0 mm) Centroid Location (r,θ) : (1.1 mm, 66.9°)	AK29-24 Spray Parameters Injector Height : 50 mm Connector Angle (θ) : 0° Fuel Pressure : 10000 kPa Pulse Width / Period : 1.5 / 40.0 ms # of Pulses : 543 Captured Volume : 5.4 ml Plume 1 Diameter : 19.4 mm @ 90° Cone Angle α : 20.9° @ 90° 50% Mass Diameter : 11.4 mm 50% Cone Angle : 12.4° Bend (Skew) Angle (β) : 17.8° Mass % : 28.7 Centroid Location (x,y) : (-15.9 mm, 1.9 mm) Centroid Location (r,θ) : (16.1 mm, 173.3°)	AK29-25 Spray Parameters Injector Height : 50 mm Connector Angle (θ) : 0° Fuel Pressure : 10000 kPa Pulse Width / Period : 1.5 / 40.0 ms # of Pulses : 613 Captured Volume : 5.5 ml Spray Diameter : 42.7 mm @ 90° Cone Angle α : 46.2° @ 90° 50% Mass Diameter : 30.7 mm 50% Cone Angle : 34.1° Bend (Skew) Angle (β) : 1.7° Centroid Location (x,y) : (0.6 mm, 1.3 mm) Centroid Location (r,θ) : (1.5 mm, 65.2°)	AK29-25 Spray Parameters Injector Height : 50 mm Connector Angle (θ) : 0° Fuel Pressure : 10000 kPa Pulse Width / Period : 1.5 / 40.0 ms # of Pulses : 613 Captured Volume : 5.5 ml Plume 1 Diameter : 19.9 mm @ 90° Cone Angle α : 21.5° @ 90° 50% Mass Diameter : 12.3 mm 50% Cone Angle : 13.4° Bend (Skew) Angle (β) : 17.0° Mass % : 27.6 Centroid Location (x,y) : (-15.2 mm, 1.9 mm) Centroid Location (r,θ) : (15.3 mm, 172.8°)
Plume 1 w/ Centroid & 90% Analysis Circle 	Plume 1 w/ Centroid & 90% Analysis Circle 	Plume 1 w/ Centroid & 90% Analysis Circle 	Plume 1 w/ Centroid & 90% Analysis Circle 
	Spray Parameters Plume 2 Diameter : 18.3 mm @ 90° Cone Angle α : 19.8° @ 90° 50% Mass Diameter : 10.2 mm 50% Cone Angle : 11.1° Bend (Skew) Angle (β) : 17.1° Mass % : 35.8 Centroid Location (x,y) : (7.4 mm, 13.5 mm) Centroid Location (r,θ) : (15.4 mm, 61.0°)		Plume 2 Diameter : 18.0 mm @ 90° Cone Angle α : 19.5° @ 90° 50% Mass Diameter : 9.9 mm 50% Cone Angle : 10.9° Bend (Skew) Angle (β) : 17.3° Mass % : 36.5 Centroid Location (x,y) : (7.4 mm, 13.7 mm) Centroid Location (r,θ) : (15.5 mm, 61.6°)
	Plume 2 w/ Centroid & 90% Analysis Circle 		Plume 2 w/ Centroid & 90% Analysis Circle 

AK29-001	AK29-001	AK29-002	AK29-002
Spray Parameters Injector Height : 50 mm Connector Angle (θ) : 0° Fuel Pressure : 10000 kPa Pulse Width / Period : 1.5 / 40.0 ms # of Pulses : 793 Captured Volume : 7.4 ml	Spray Parameters Injector Height : 50 mm Connector Angle (θ) : 0° Fuel Pressure : 10000 kPa Pulse Width / Period : 1.5 / 40.0 ms # of Pulses : 793 Captured Volume : 7.4 ml	Spray Parameters Injector Height : 50 mm Connector Angle (θ) : 0° Fuel Pressure : 10000 kPa Pulse Width / Period : 1.5 / 40.0 ms # of Pulses : 898 Captured Volume : 7.8 ml	Spray Parameters Injector Height : 50 mm Connector Angle (θ) : 0° Fuel Pressure : 10000 kPa Pulse Width / Period : 1.5 / 40.0 ms # of Pulses : 898 Captured Volume : 7.8 ml
Spray Diameter : 72.9 mm @ 90° Cone Angle α : 72.1° @ 90° 50% Mass Diameter : 61.0 mm 50% Cone Angle : 62.8° Bend (Skew) Angle (β) : 1.8° Centroid Location (x,y)* : (-1.5 mm, 0.5 mm) Centroid Location (r,θ)* : (1.6 mm, 161.9°)	Plume 1 Diameter : 18.6 mm @ 90° Cone Angle α : 18.1° @ 90° 50% Mass Diameter : 10.6 mm 50% Cone Angle : 10.3° Bend (Skew) Angle (β) : 31.2° Mass % : 35.0 Centroid Location (x,y)* : (-30.3 mm, 1.6 mm) Centroid Location (r,θ)* : (30.3 mm, 177.0°)	Spray Diameter : 74.2 mm @ 90° Cone Angle α : 73.1° @ 90° 50% Mass Diameter : 61.1 mm 50% Cone Angle : 62.8° Bend (Skew) Angle (β) : 2.4° Centroid Location (x,y)* : (-1.7 mm, 1.3 mm) Centroid Location (r,θ)* : (2.1 mm, 141.9°)	Plume 1 Diameter : 19.2 mm @ 90° Cone Angle α : 18.7° @ 90° 50% Mass Diameter : 10.7 mm 50% Cone Angle : 10.5° Bend (Skew) Angle (β) : 31.0° Mass % : 35.7 Centroid Location (x,y)* : (-29.9 mm, 3.0 mm) Centroid Location (r,θ)* : (30.0 mm, 174.2°)
Plume 1 w/ Centroid & 90° Analysis Circle 	Plume 1 w/ Centroid & 90° Analysis Circle 	Plume 1 w/ Centroid & 90° Analysis Circle 	Plume 1 w/ Centroid & 90° Analysis Circle 
	Spray Parameters Plume 2 Diameter : 17.9 mm @ 90° Cone Angle α : 17.3° @ 90° 50% Mass Diameter : 10.0 mm 50% Cone Angle : 9.7° Bend (Skew) Angle (β) : 31.5° Mass % : 32.8 Centroid Location (x,y)* : (15.6 mm, 26.3 mm) Centroid Location (r,θ)* : (30.6 mm, 59.3°)		Spray Parameters Plume 2 Diameter : 19.6 mm @ 90° Cone Angle α : 18.8° @ 90° 50% Mass Diameter : 10.7 mm 50% Cone Angle : 10.4° Bend (Skew) Angle (β) : 32.2° Mass % : 32.6 Centroid Location (x,y)* : (16.2 mm, 27.0 mm) Centroid Location (r,θ)* : (31.5 mm, 59.0°)
	Plume 2 w/ Centroid & 90° Analysis Circle 		Plume 2 w/ Centroid & 90° Analysis Circle 

APPENDIX D PHASE-CONTRAST X-RAY IMAGES

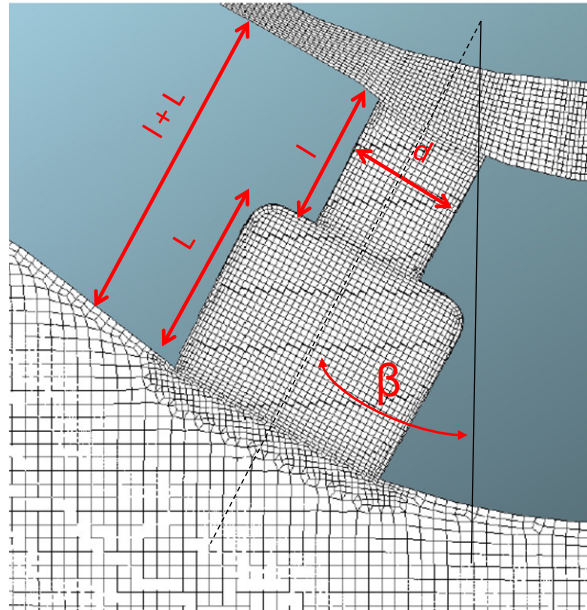
Phase Contrast X-ray images from Argonne testing for single-hole injectors

Image #	Sequence #	d (mm)	β	l/d	(l+L)/d	D/d	Injection Pressure (Bar)
1	AK29-2-919	$\approx .20$	0°	2.95	na	na	75
2	AK29-2-920	$\approx .20$	0°	2.95	na	na	75
3	AK29-2-921	$\approx .20$	0°	2.95	na	na	75
4	AK29-2-922	$\approx .15$	0°	3.96	na	na	75
5	AK29-2-923	$\approx .15$	0°	3.96	na	na	75
6	AK29-2-924	$\approx .15$	0°	3.96	na	na	75
7	Start & end of Injection						75
8	Varying Inj Pressure					Varying View angles	25,50,75
9	Needle motion						25,50,75

Current Geometry Matrix (7'11):

Single-Hole Injectors : only two types, three each, no counter-bore (L=0).

	SHN2(Long)	SHN5(s-L)
d(mm)	≈0.20	≈0.15
β	0°	0°
l/d	2.95	3.96
(l+L)/d	2.95	3.96
D/d	1.00	1.00
Effects of	l/d	l/d
# of Holes	1	1



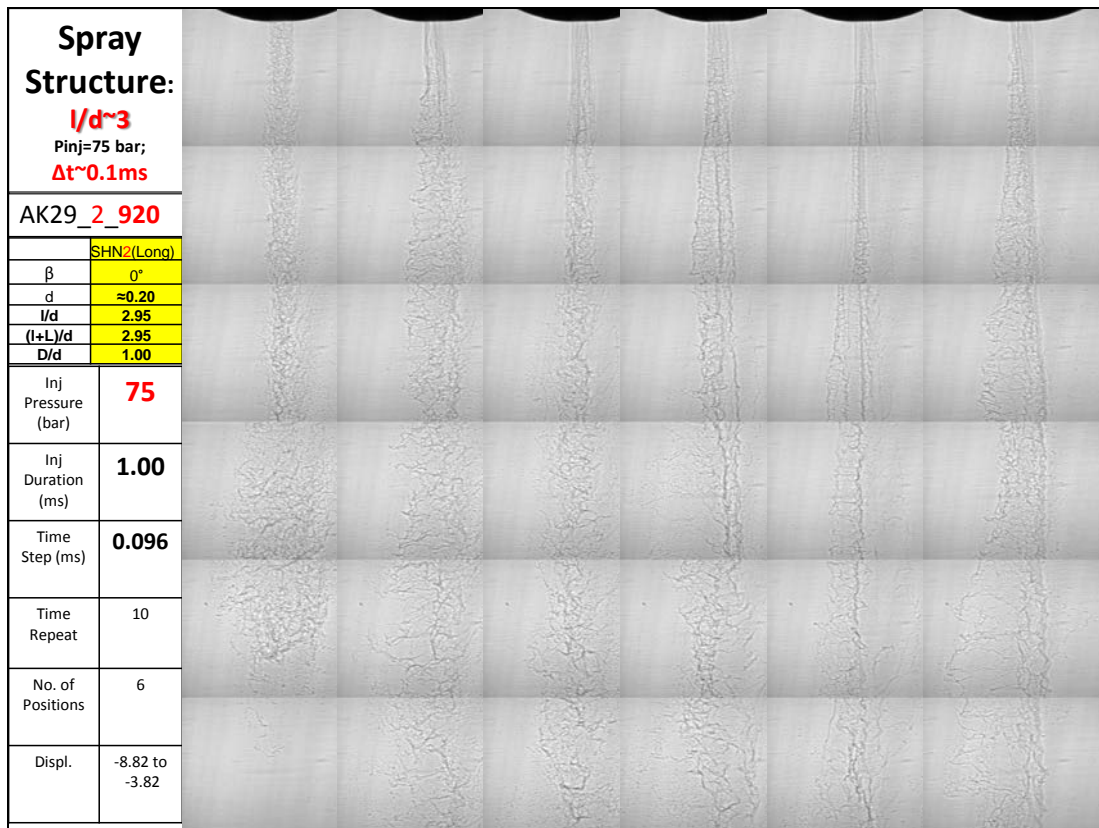
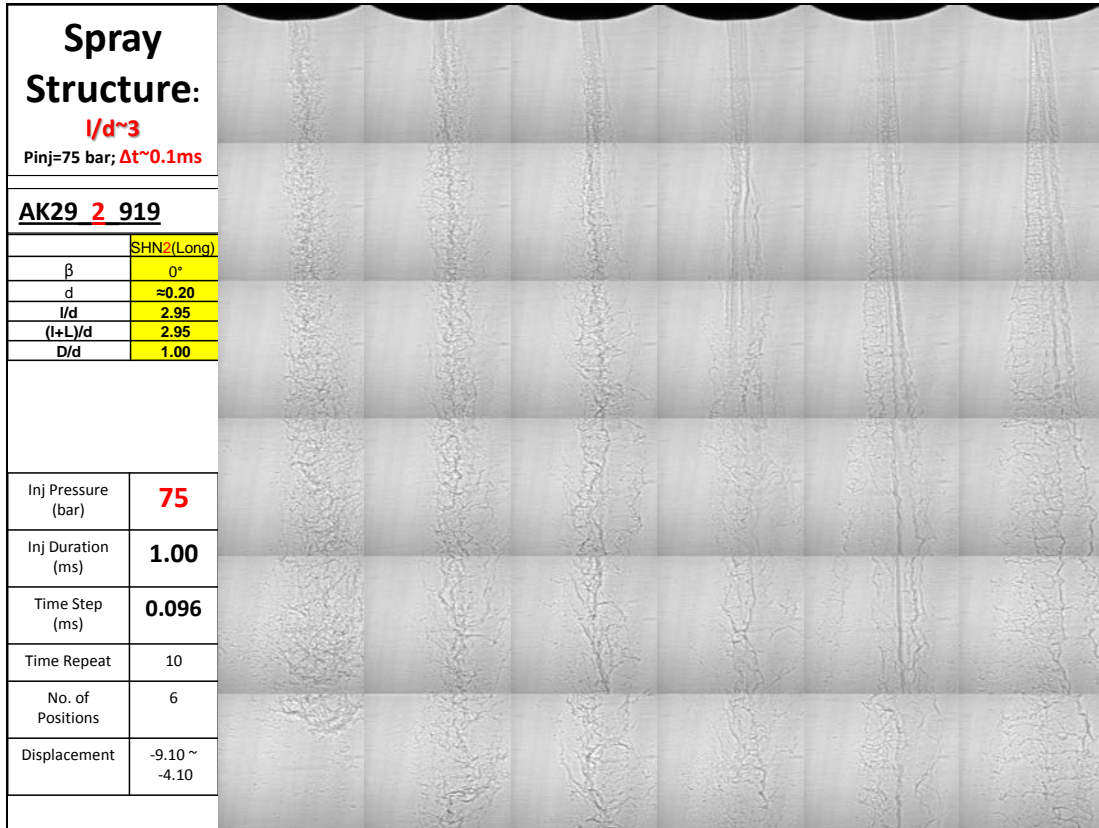
Current Nozzle Matrix (7'11):

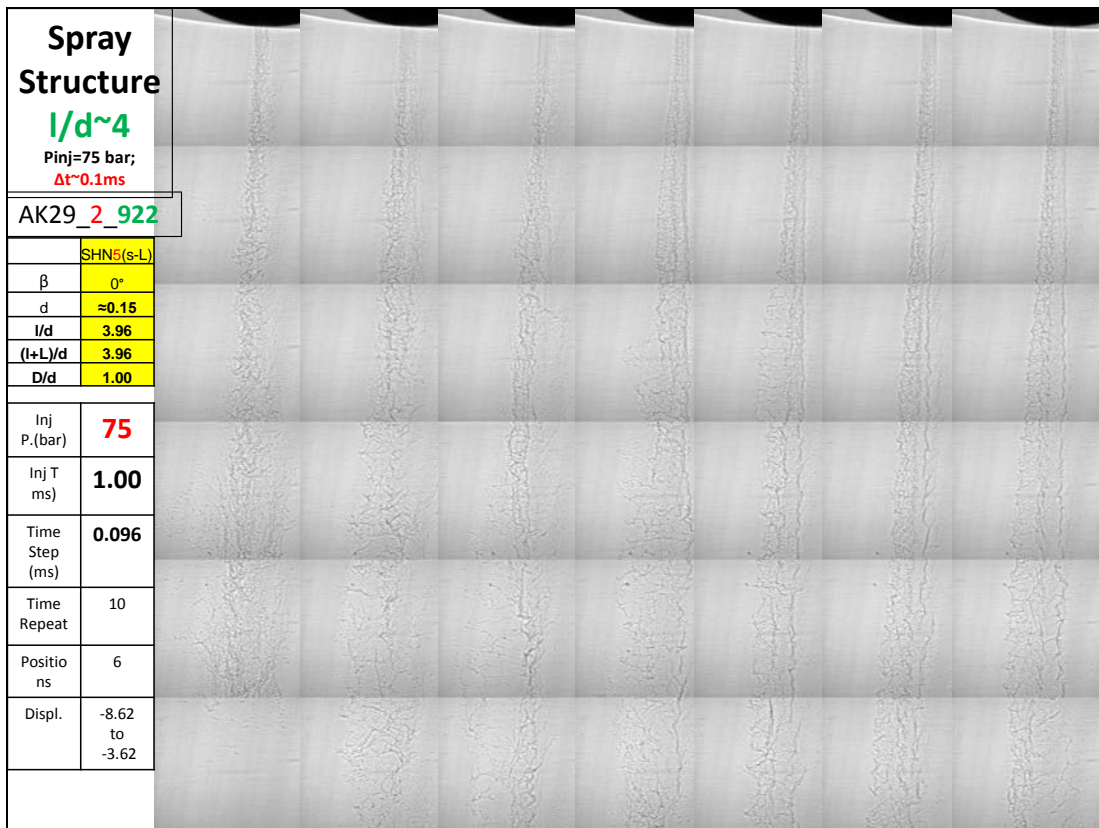
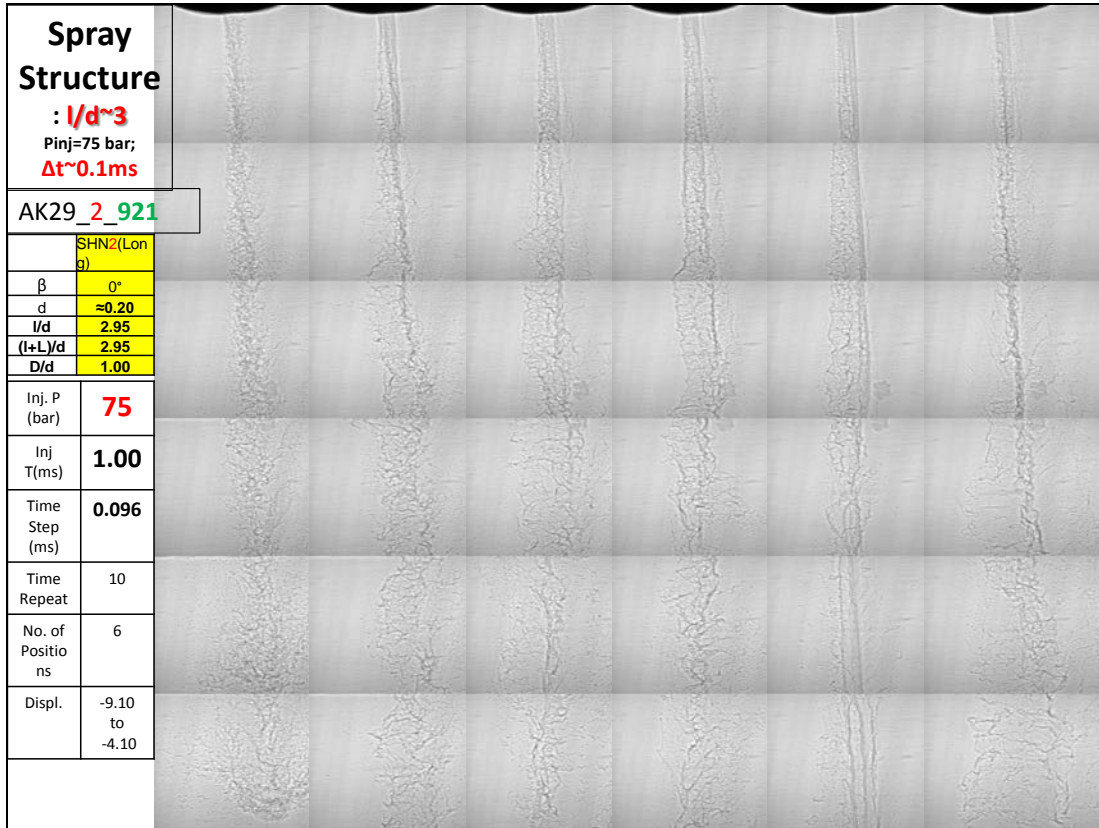
2 types of Single-Hole Injectors : d and l/d, three each, no counter-bore.

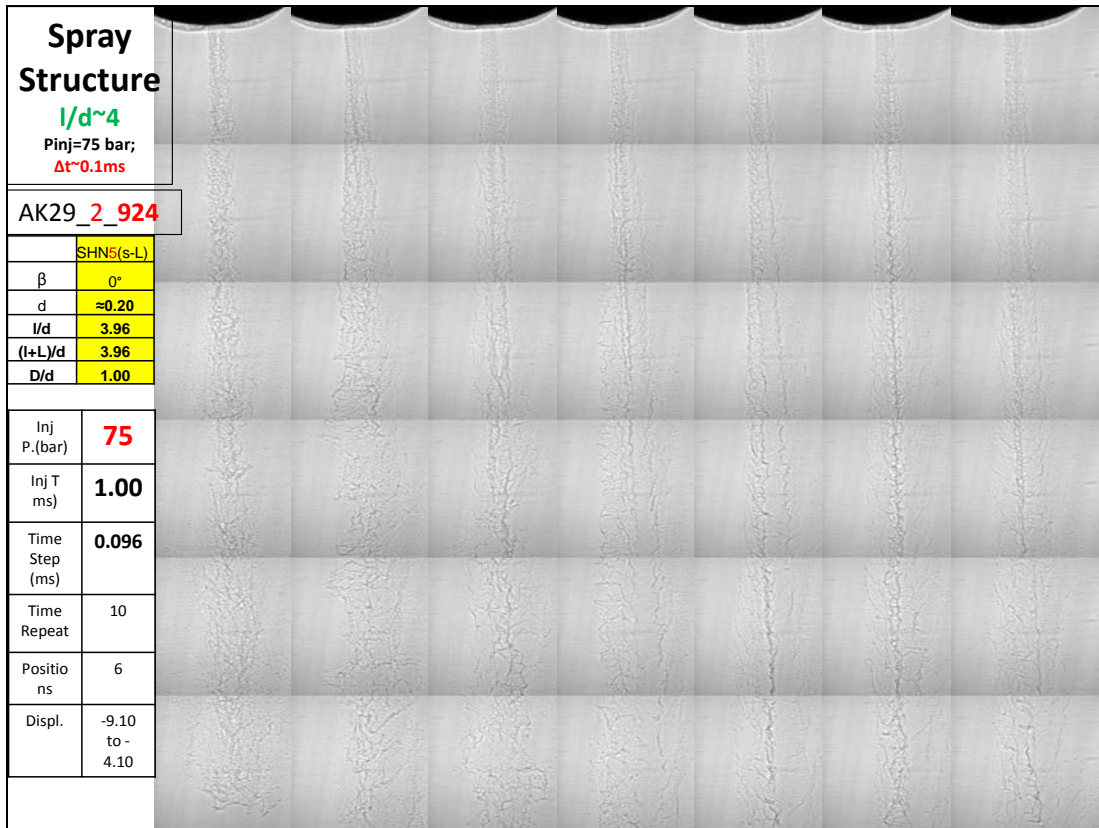
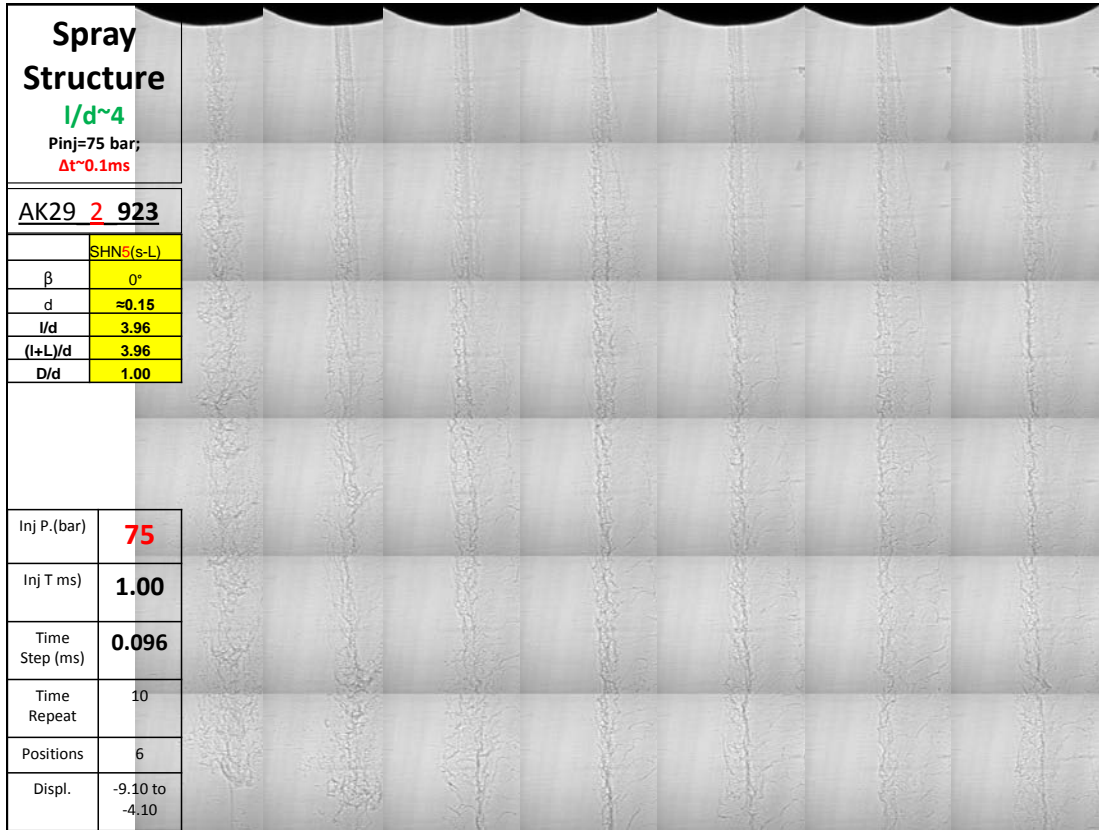
l/d			
	AK29_2_919	AK29_2_920	AK29_2_921
2.95	SF: 3.121 SP: 0.321	SF: 3.26 SP: 0.329	SF: 3.072 SP: 0.332
3.96	AK29_5_922 SF: 1.871 SP: 0.248 (15%)	AK29_5_923 SF: 1.873 SP: 0.208 (15%)	AK29_5_924 SF: 1.92 SP: 0.199

NOTES:

- SF** is the Static flow of the injector is 3.121 grams/sec, at calibration point (10 Mpa, with stoddard solvent).
- SP** is the dynamic flow (at calibration point) is 0.321 grams/sec of fuel with 1.0 msec pulse-width.

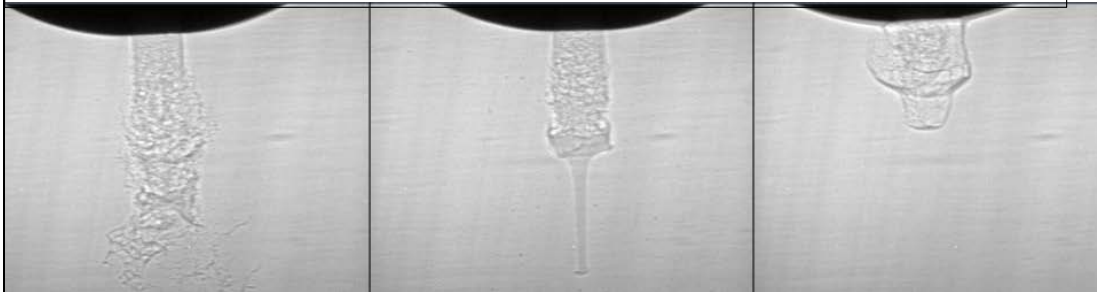




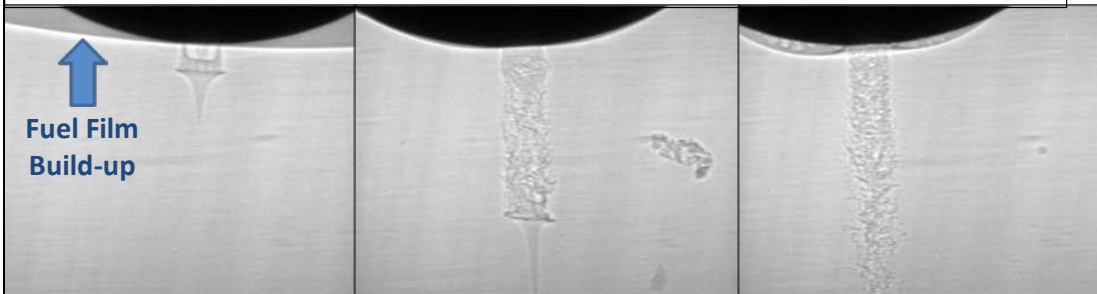


Start of Injection: Effect of L/D & nozzle variability; $P_{inj}=75\text{Bar}$

$l/d \sim 3$: AK29_2_919 AK29_2_920 AK29_2_921



$l/d \sim 4$: AK29_5_922 AK29_5_923 AK29_5_924

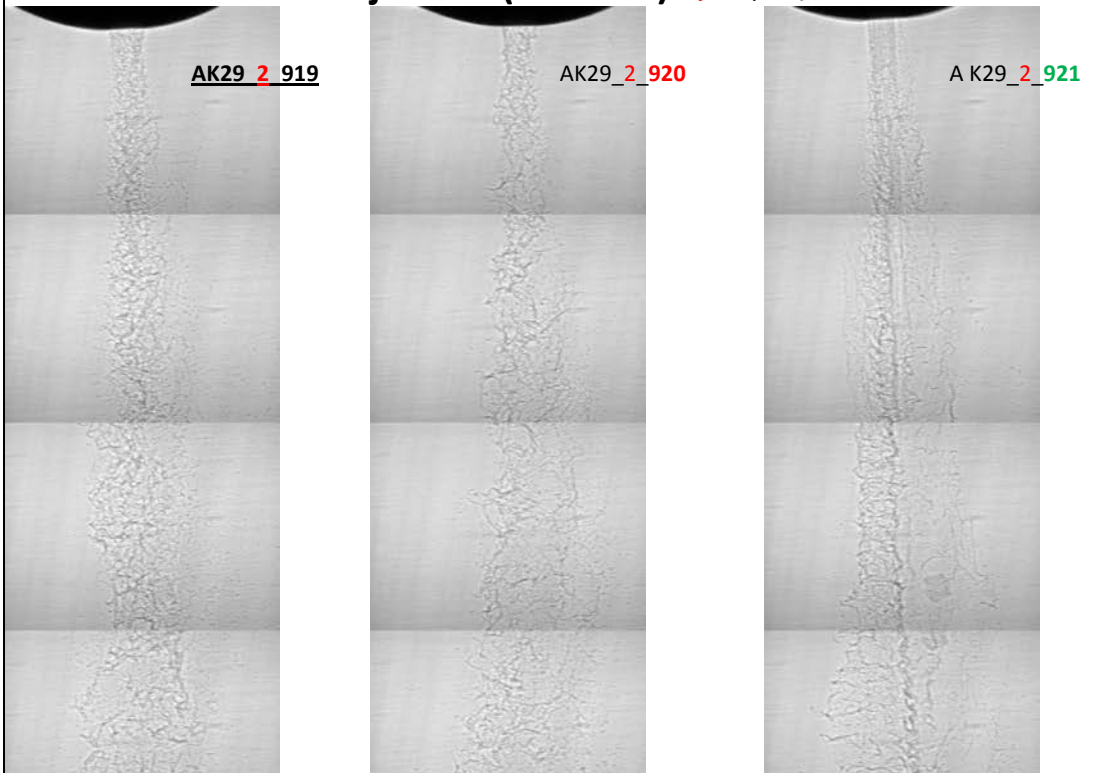


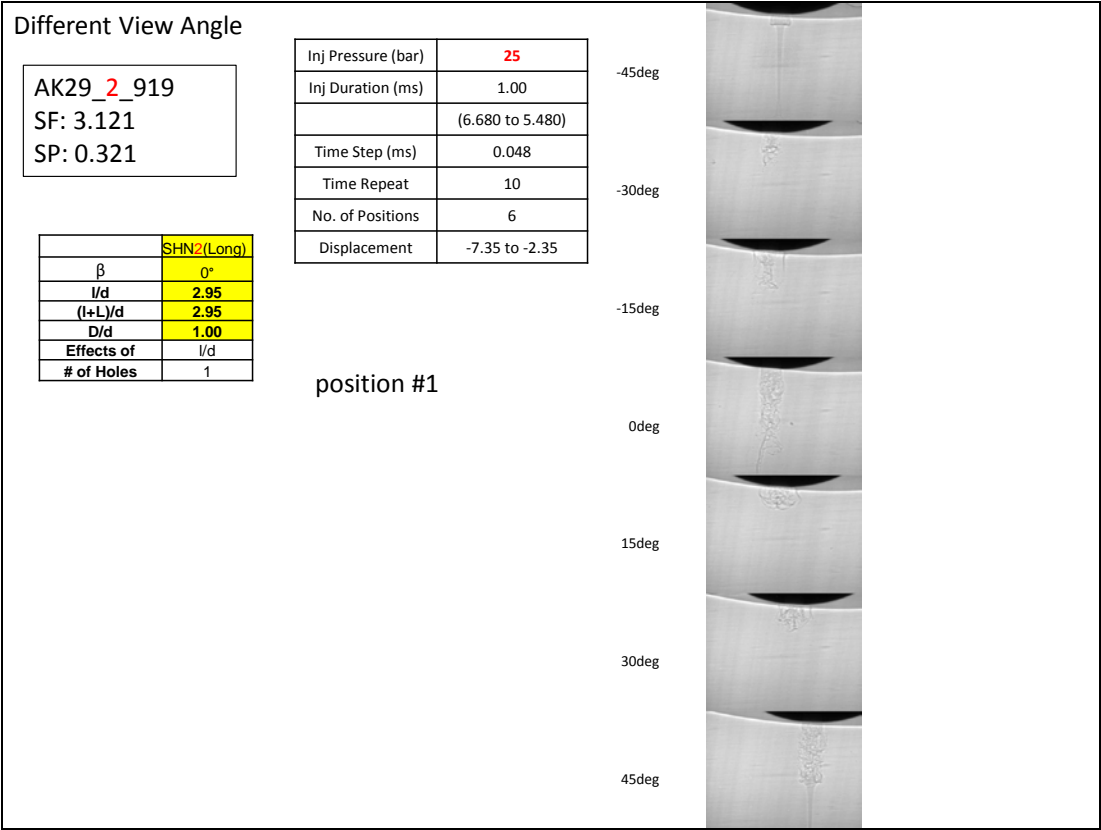
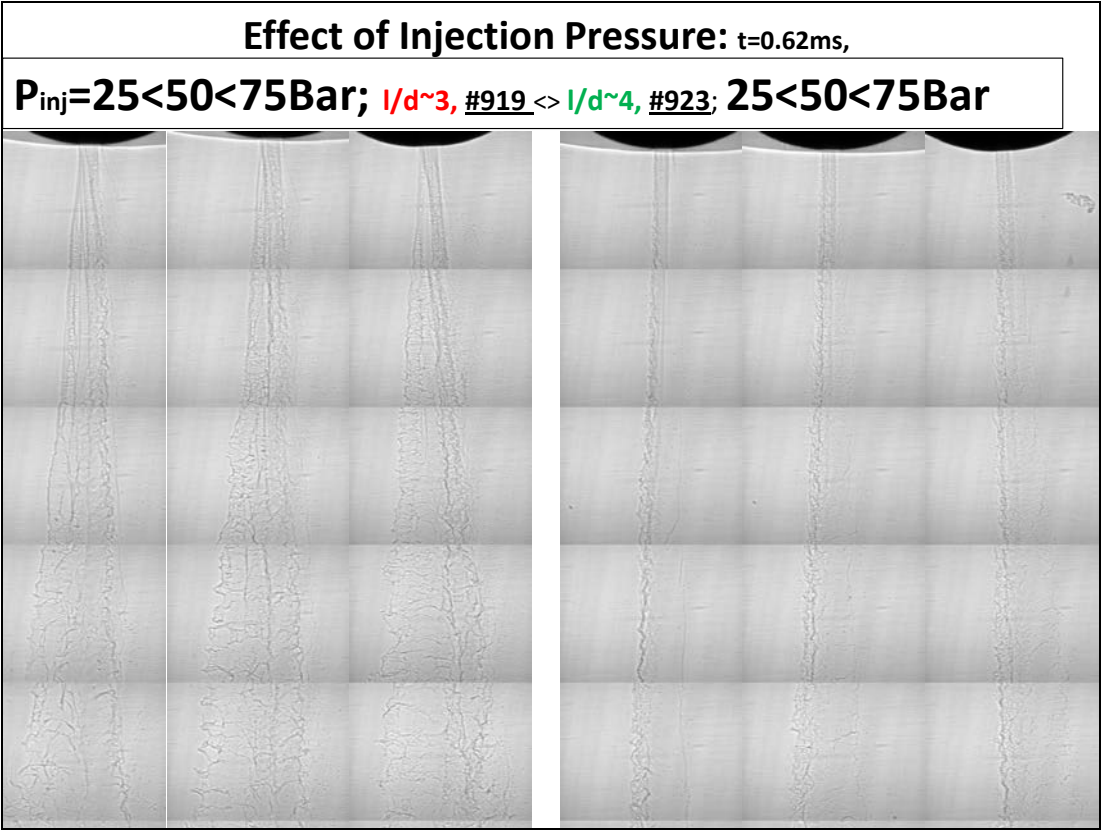
End of Injection ($t=1.1\text{ms}$): $l/d \sim 3$; $P_{inj}=75\text{Bar}$

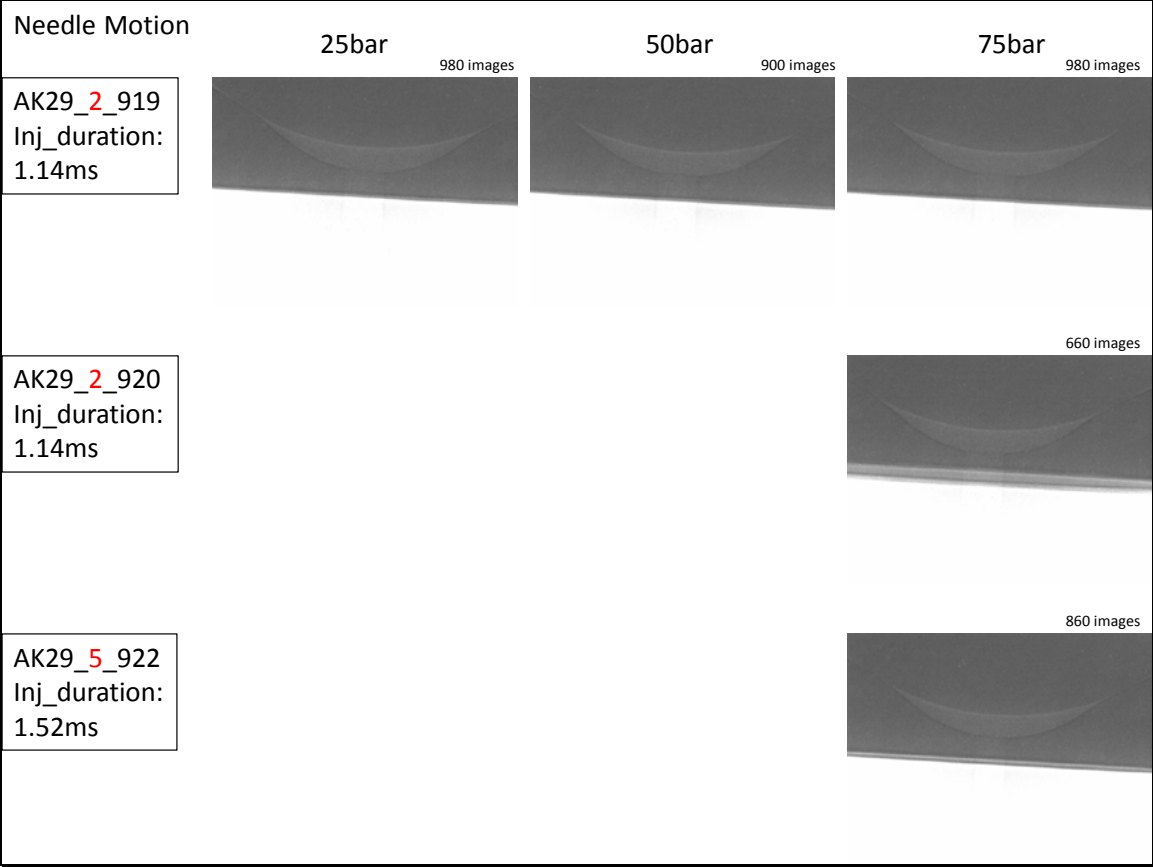
AK29_2_919

AK29_2_920

A K29_2_921





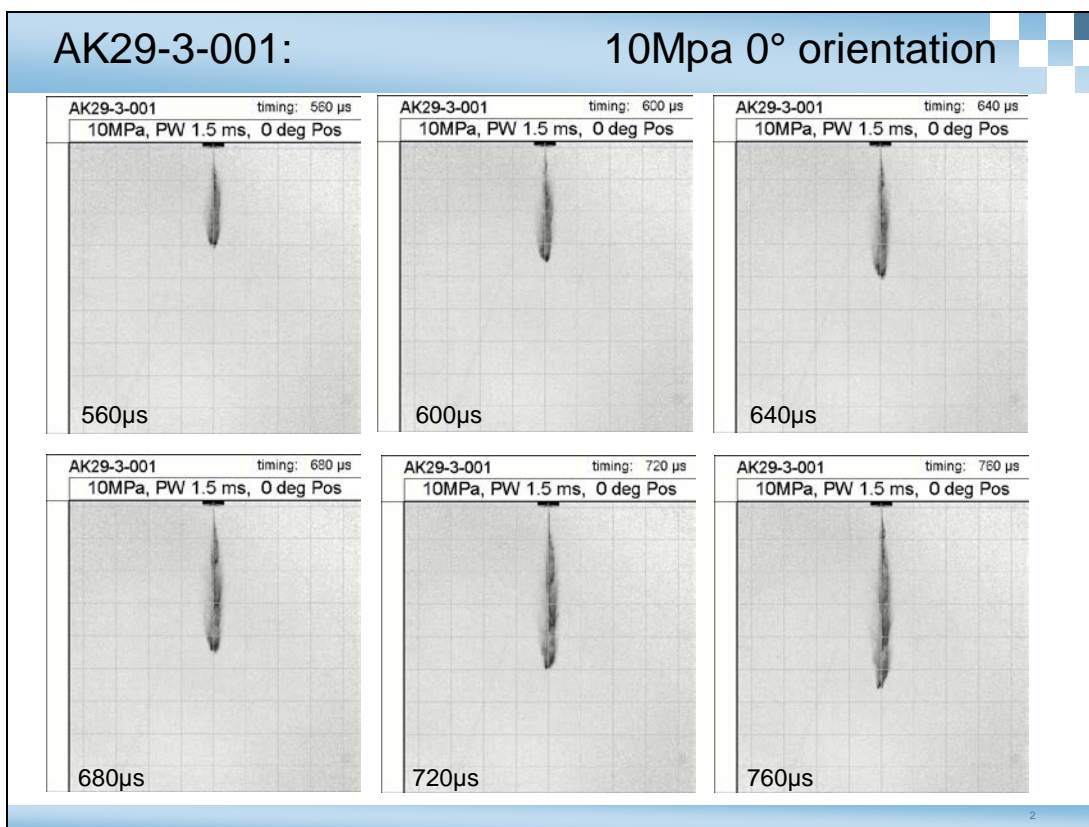
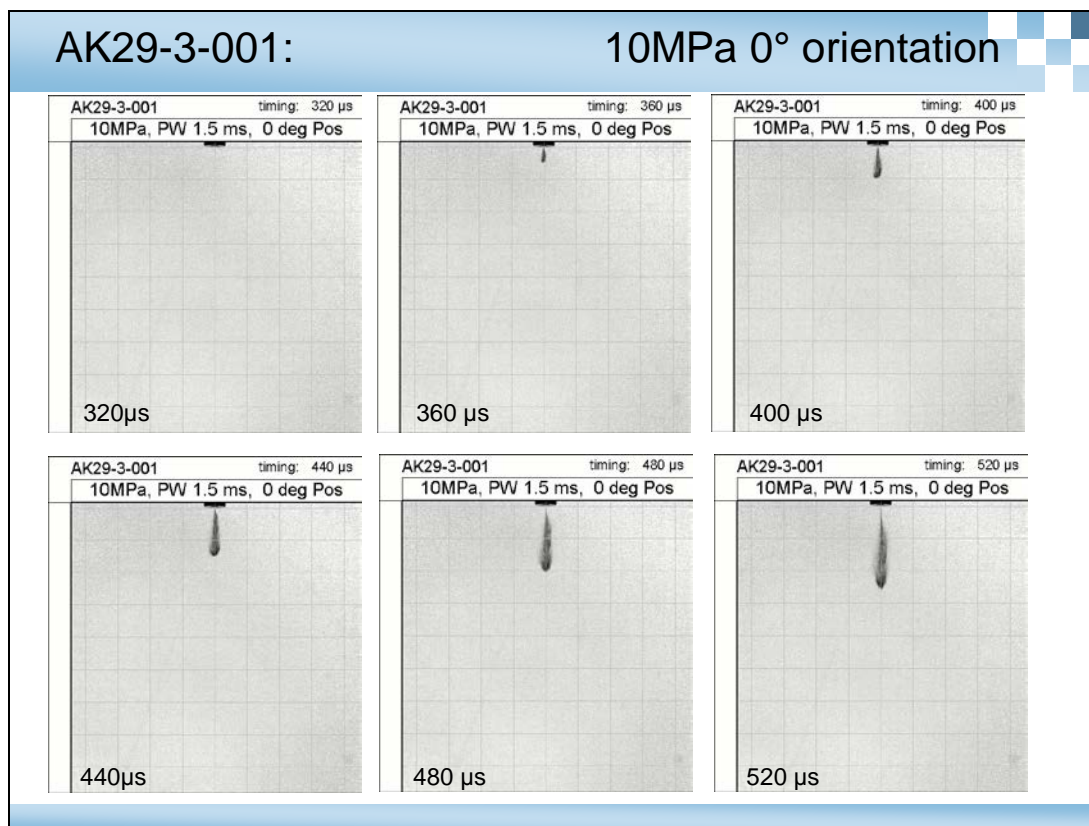


APPENDIX E SHADOWGRAPH IMAGES

High speed Shadowgraph Images (432 images) of Spray plumes from side view, Luxembourg Spray lab

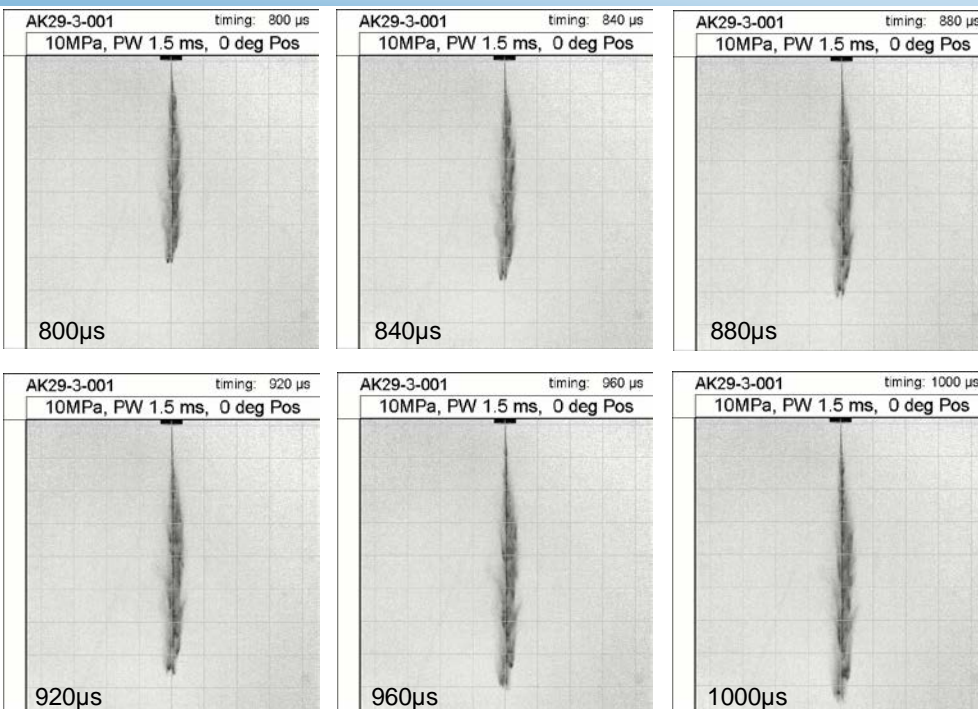
Image #	Seat #	d (mm)	β	l/d	(l+L)/d	D/d	Inj. Pres.	View Angle	Shadowgraph Time Images (μ s)
1-6	AK29-3-001	≈ 20	0°	1.1	na	na	10MPa	0°	320,360,400,440,470,520
7-12	AK29-3-001	≈ 20	0°	1.1	na	na	10MPa	0°	560,600,640,680,720,760
13-18	AK29-3-001	≈ 20	0°	1.1	na	na	10MPa	0°	800,840,880,920,960,1000
19-24	AK29-3-001	≈ 20	0°	1.1	na	na	10MPa	0°	1040,1080,1120,1160,1200,1240
1-6	AK29-3-001	≈ 20	0°	1.1	na	na	20MPa	0°	280,320,360,400,440,480
7-12	AK29-3-001	≈ 20	0°	1.1	na	na	20MPa	0°	520,560,600,640,680,720
13-18	AK29-3-001	≈ 20	0°	1.1	na	na	20MPa	0°	760,800,840,880,920,960
19-24	AK29-3-001	≈ 20	0°	1.1	na	na	20MPa	0°	1000,1040,1080,1120,1160,1200
1-6	AK29-3-002	≈ 20	0°	1.1	na	na	10MPa	0°	280,320,360,400,440,480
7-12	AK29-3-002	≈ 20	0°	1.1	na	na	10MPa	0°	520,560,600,640,680,720
13-18	AK29-3-002	≈ 20	0°	1.1	na	na	10MPa	0°	760,800,840,880,920,960
19-24	AK29-3-002	≈ 20	0°	1.1	na	na	10MPa	0°	1000,1040,1080,1120,1160,1200
1-6	AK29-3-002	≈ 20	0°	1.1	na	na	20MPa	0°	280,320,360,400,440,480
7-12	AK29-3-002	≈ 20	0°	1.1	na	na	20MPa	0°	520,560,600,640,680,720
13-18	AK29-3-002	≈ 20	0°	1.1	na	na	20MPa	0°	760,800,840,880,920,960
19-24	AK29-3-002	≈ 20	0°	1.1	na	na	20MPa	0°	1000,1040,1080,1120,1160,1200
1-6	AK29-6-002	≈ 15	0°	1.1	na	na	10MPa	0°	320,360,400,440,470,520
7-12	AK29-6-002	≈ 15	0°	1.1	na	na	10MPa	0°	560,600,640,680,720,760
13-18	AK29-6-002	≈ 15	0°	1.1	na	na	10MPa	0°	800,840,880,920,960,1000
19-24	AK29-6-002	≈ 15	0°	1.1	na	na	10MPa	0°	1040,1080,1120,1160,1200,1240
1-6	AK29-6-002	≈ 15	0°	1.1	na	na	20MPa	0°	240,280,320,360,400,440
7-12	AK29-6-002	≈ 15	0°	1.1	na	na	20MPa	0°	480,520,560,600,640,680
13-18	AK29-6-002	≈ 15	0°	1.1	na	na	20MPa	0°	760,800,840,880,920,960
19-24	AK29-6-002	≈ 15	0°	1.1	na	na	20MPa	0°	1000,1040,1080,1120,1160,1200
1-8	AK29-9-001	≈ 20	30°	1.1	na	na	10MPa	0°	280,320,360,400,440,480,520,560
9-16	AK29-9-001	≈ 20	30°	1.1	na	na	10MPa	0°	600,640,680,720,760,800,840,880
17-24	AK29-9-001	≈ 20	30°	1.1	na	na	10MPa	0°	920,1000,1080,1160,1240,1320,1400,1480
1-8	AK29-9-001	≈ 20	30°	1.1	na	na	10MPa	90°	280,320,360,400,440,480,520,560
9-16	AK29-9-001	≈ 20	30°	1.1	na	na	10MPa	90°	600,640,680,720,760,800,840,880
17-24	AK29-9-001	≈ 20	30°	1.1	na	na	10MPa	90°	920,1000,1080,1160,1240,1320,1400,1480
1-8	AK29-9-001	≈ 20	30°	1.1	na	na	20MPa	0°	280,320,360,400,440,480,520,560
9-16	AK29-9-001	≈ 20	30°	1.1	na	na	20MPa	0°	600,640,680,720,760,800,840,880
17-24	AK29-9-001	≈ 20	30°	1.1	na	na	20MPa	0°	920,1000,1080,1160,1240,1320,1400,1480
1-8	AK29-9-001	≈ 20	30°	1.1	na	na	20MPa	90°	280,320,360,400,440,480,520,560
9-16	AK29-9-001	≈ 20	30°	1.1	na	na	20MPa	90°	600,640,680,720,760,800,840,880
17-24	AK29-9-001	≈ 20	30°	1.1	na	na	20MPa	90°	920,1000,1080,1160,1240,1320,1400,1480

1-8	AK29-10-3-003	≈.15	30°	1.1	3.96	2.5	10MPa	0°	320,340,400,440,480,520,560,600
9-16	AK29-10-3-003	≈.15	30°	1.1	3.96	2.5	10MPa	0°	640,680,720,760,800,840,880,920
17-24	AK29-10-3-003	≈.15	30°	1.1	3.96	2.5	10MPa	0°	1000,1080,1160,1240,1320,1400,1480,1560
1-8	AK29-10-3-003	≈.15	30°	1.1	3.96	2.5	10MPa	90°	320,340,400,440,480,520,560,600
9-16	AK29-10-3-003	≈.15	30°	1.1	3.96	2.5	10MPa	90°	640,680,720,760,800,840,880,920
17-24	AK29-10-3-003	≈.15	30°	1.1	3.96	2.5	10MPa	90°	1000,1080,1160,1240,1320,1400,1480,1560
1-8	AK29-10-3-003	≈.15	30°	1.1	3.96	2.5	20MPa	0°	280,320,360,400,440,480,520,560
9-16	AK29-10-3-003	≈.15	30°	1.1	3.96	2.5	20MPa	0°	600,640,680,720,760,800,840,880
17-24	AK29-10-3-003	≈.15	30°	1.1	3.96	2.5	20MPa	0°	920,1000,1080,1160,1240,1320,1400,1480
1-8	AK29-10-3-003	≈.15	30°	1.1	3.96	2.5	20MPa	90°	280,320,360,400,440,480,520,560
9-16	AK29-10-3-003	≈.15	30°	1.1	3.96	2.5	20MPa	90°	600,640,680,720,760,800,840,880
17-24	AK29-10-3-003	≈.15	30°	1.1	3.96	2.5	20MPa	90°	920,1000,1080,1160,1240,1320,1400,1480
1-8	AK29-11-3-002	≈.15	30°	3.96	na	na	10MPa	0°	320,340,400,440,480,520,560,600
9-16	AK29-11-3-002	≈.15	30°	3.96	na	na	10MPa	0°	640,680,720,760,800,840,880,920
17-24	AK29-11-3-002	≈.15	30°	3.96	na	na	10MPa	0°	1000,1080,1160,1240,1320,1400,1480,1560
1-8	AK29-11-3-002	≈.15	30°	3.96	na	na	10MPa	90°	320,340,400,440,480,520,560,600
9-16	AK29-11-3-002	≈.15	30°	3.96	na	na	10MPa	90°	640,680,720,760,800,840,880,920
17-24	AK29-11-3-002	≈.15	30°	3.96	na	na	10MPa	90°	1000,1080,1160,1240,1320,1400,1480,1560
1-8	AK29-11-3-002	≈.15	30°	3.96	na	na	20MPa	0°	280,320,360,400,440,480,520,560
9-16	AK29-11-3-002	≈.15	30°	3.96	na	na	20MPa	0°	600,640,680,720,760,800,840,880
17-24	AK29-11-3-002	≈.15	30°	3.96	na	na	20MPa	0°	920,1000,1080,1160,1240,1320,1400,1480
1-8	AK29-11-3-002	≈.15	30°	3.96	na	na	20MPa	90°	280,320,360,400,440,480,520,560
9-16	AK29-11-3-002	≈.15	30°	3.96	na	na	20MPa	90°	600,640,680,720,760,800,840,880
17-24	AK29-11-3-002	≈.15	30°	3.96	na	na	20MPa	90°	920,1000,1080,1160,1240,1320,1400,1480



AK29-3-001:

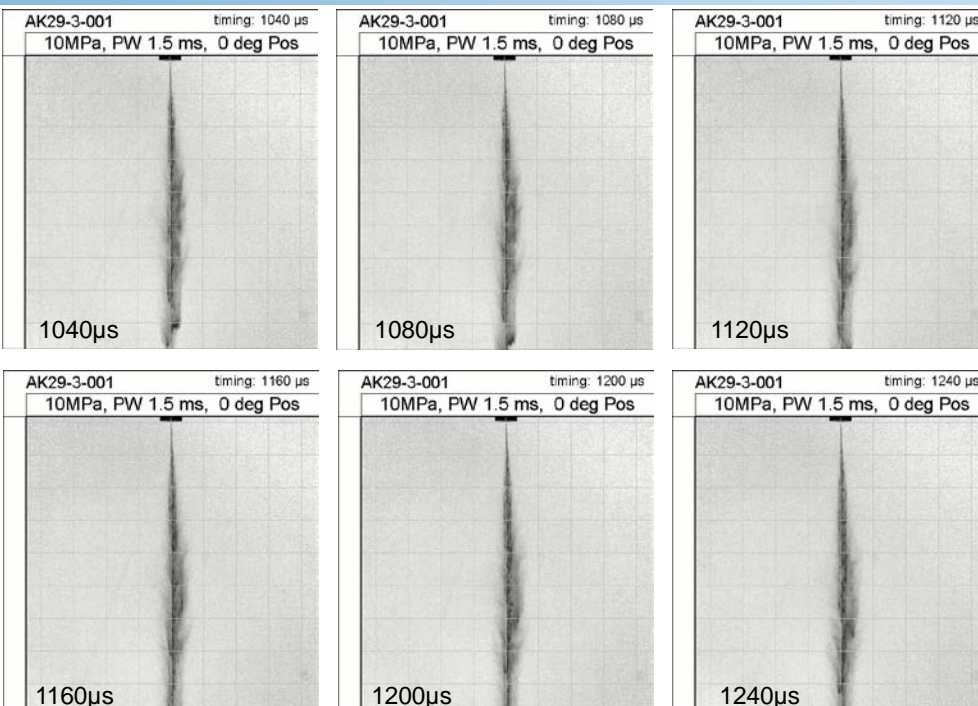
10MPa 0° orientation



3

AK29-3-001:

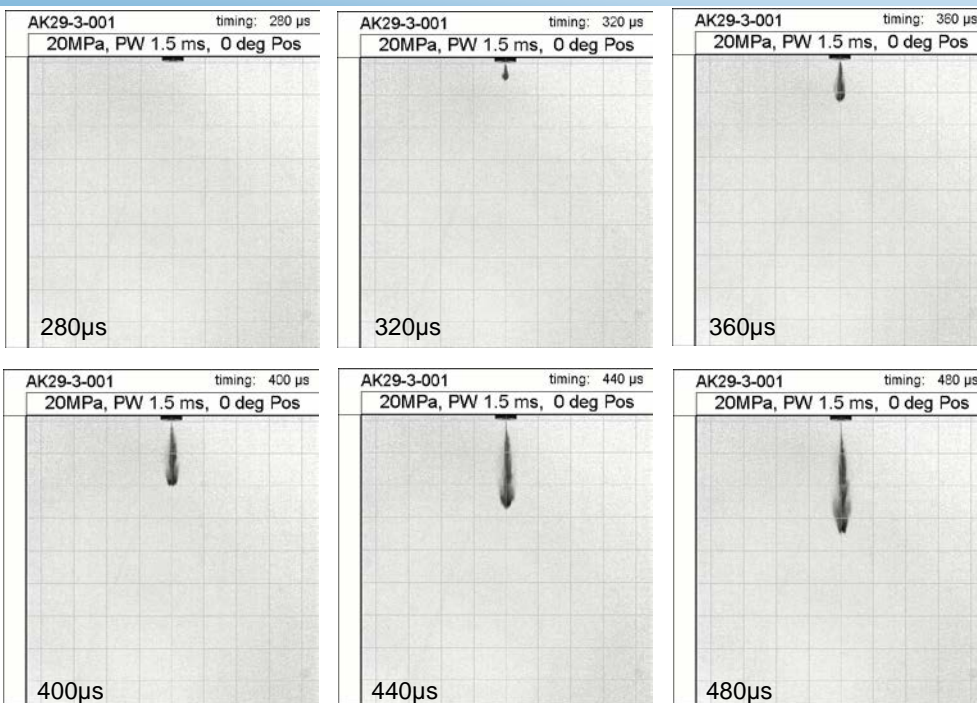
10MPa 0° orientation



4

AK29-3-001:

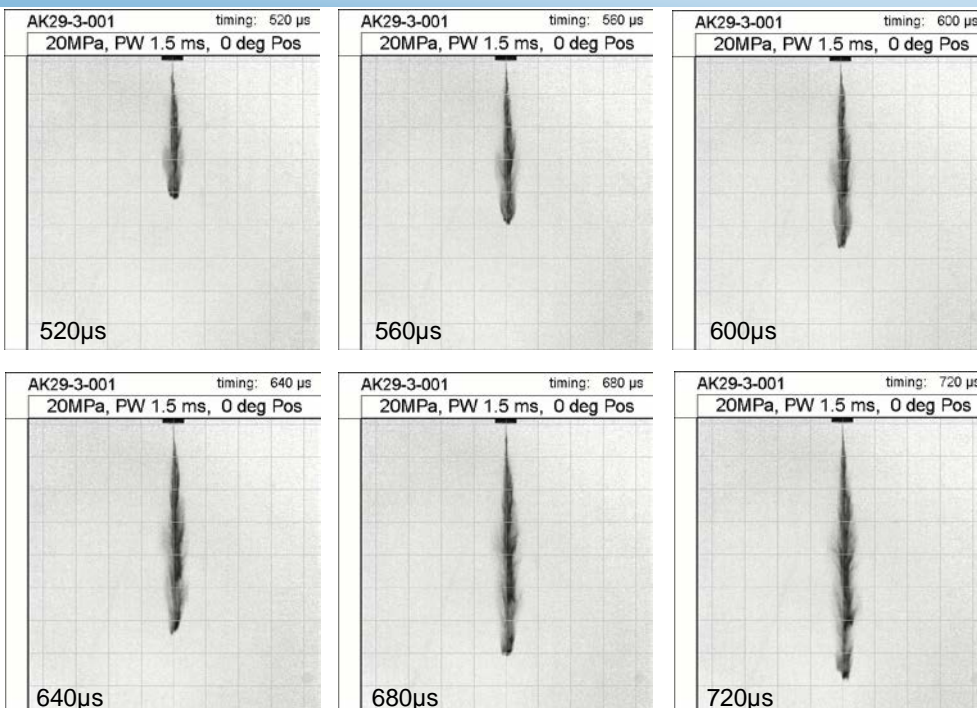
20MPa 0° orientation



5

AK29-3-001:

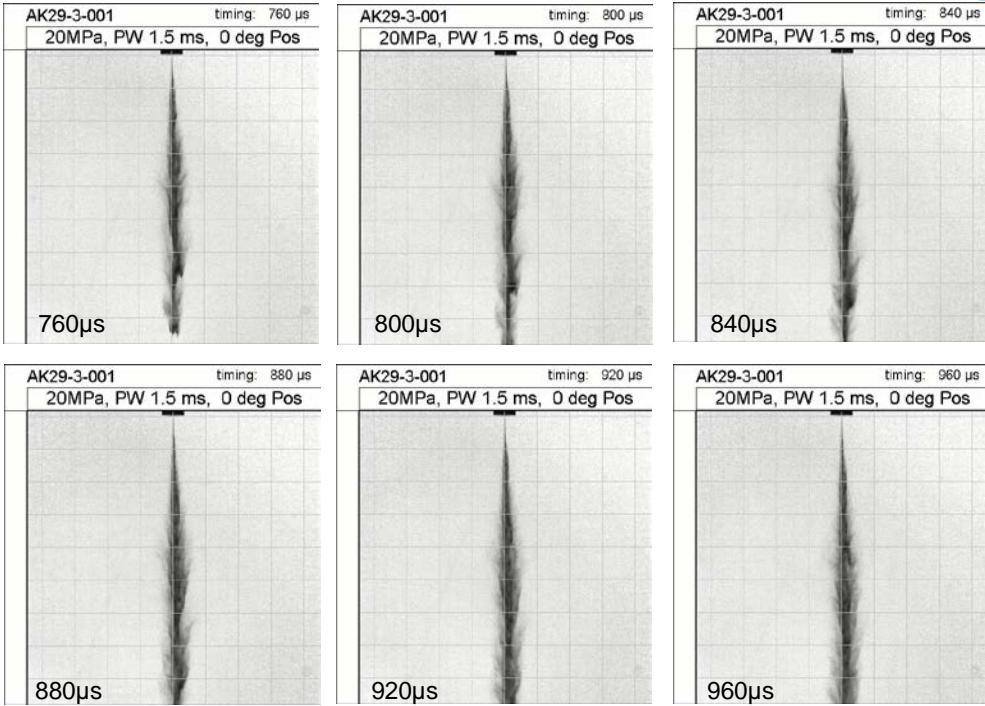
20MPa 0° orientation



6

AK29-3-001:

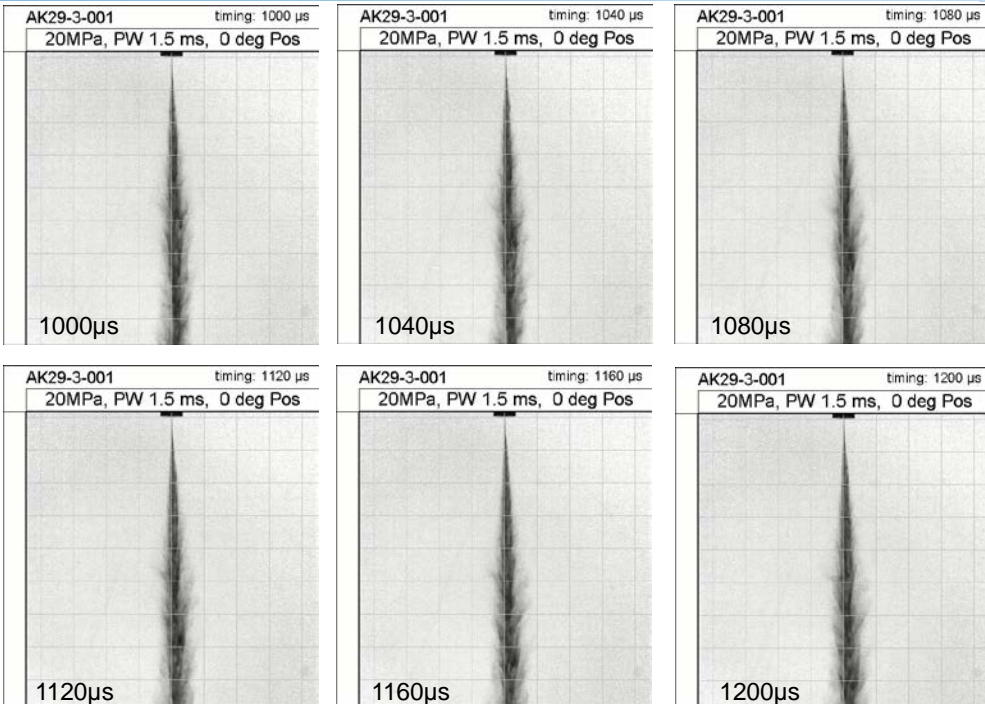
20MPa 0° orientation



7

AK29-3-001:

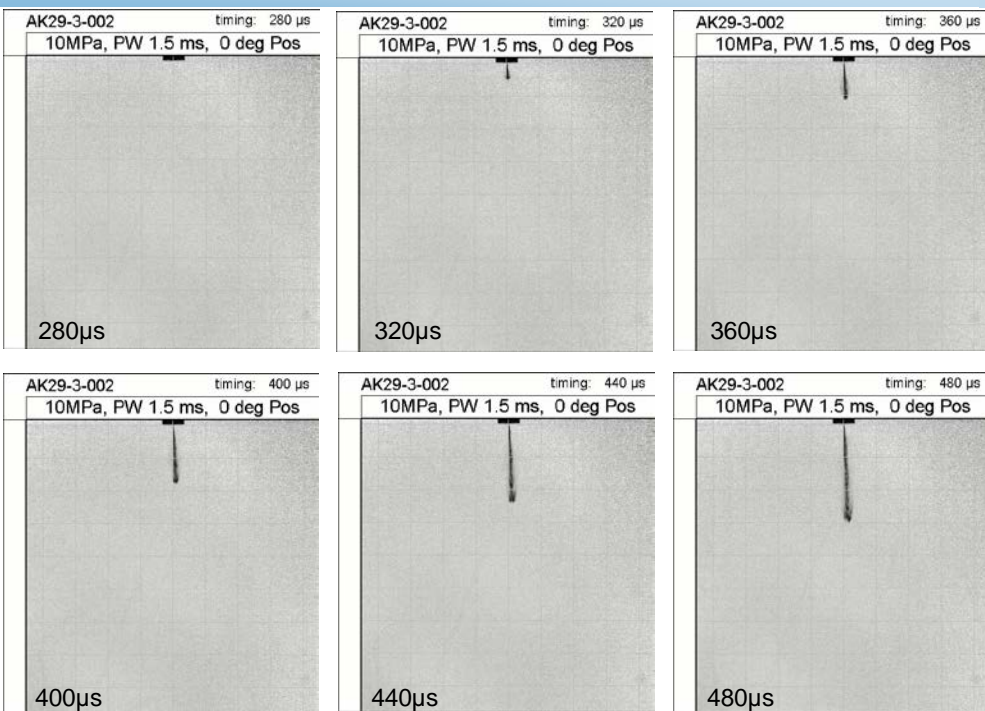
20MPa 0° orientation



8

AK29-3-002:

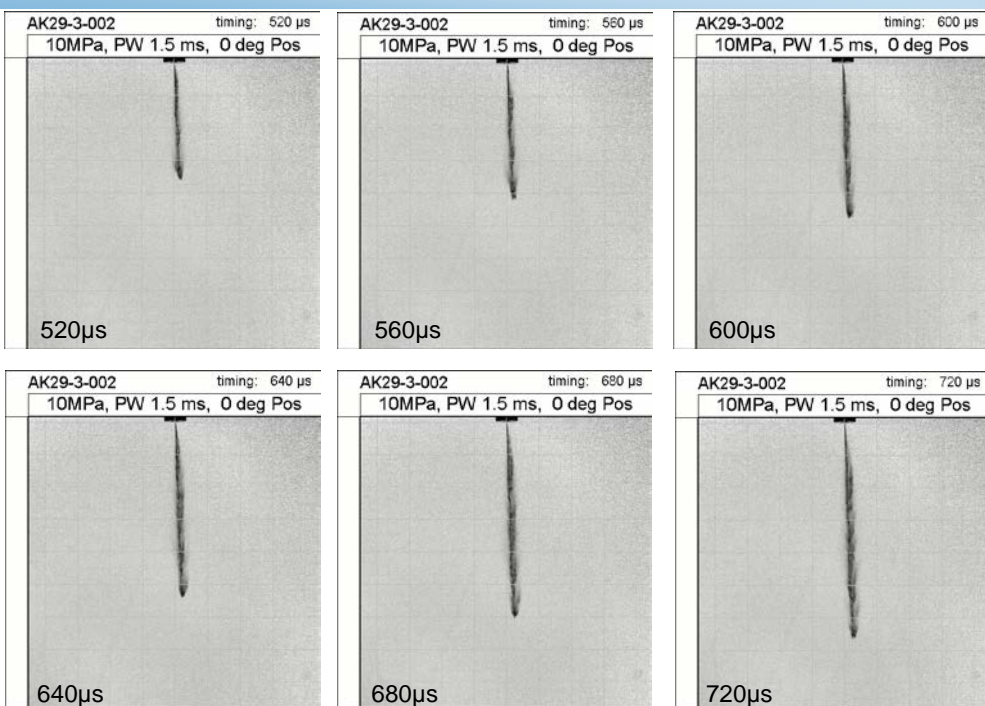
10MPa 0° orientation



9

AK29-3-002:

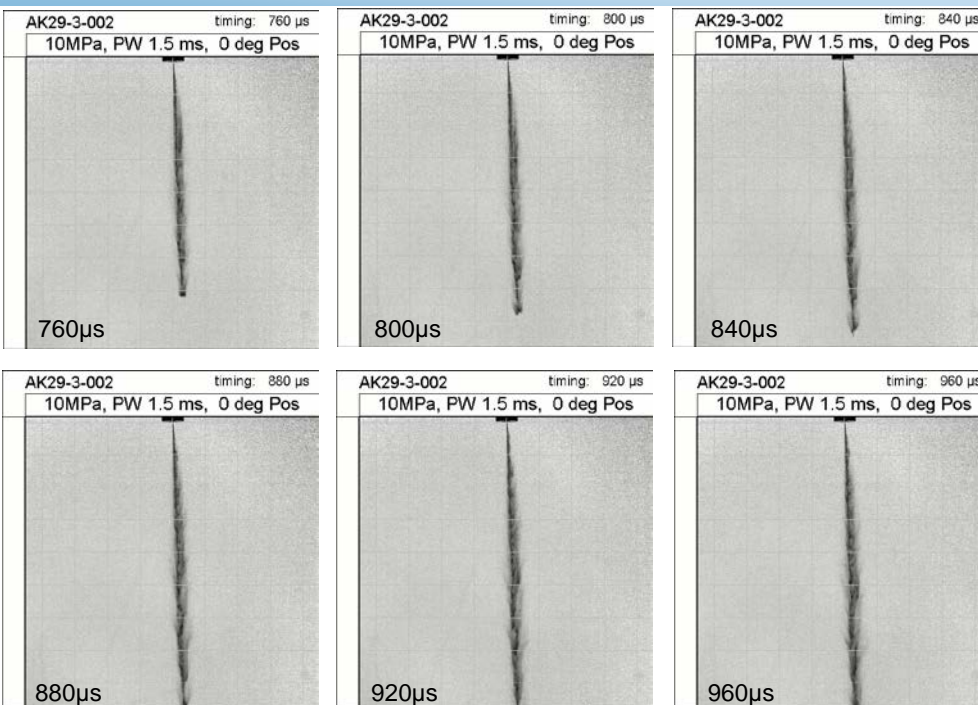
10MPa 0° orientation



10

AK29-3-002:

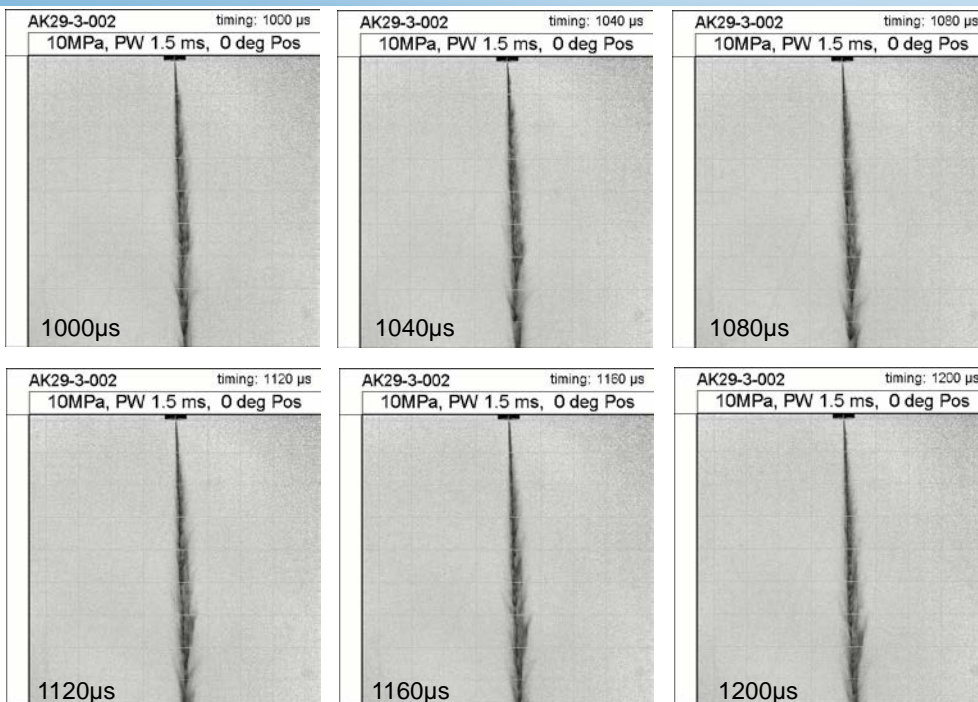
10MPa 0° orientation



11

AK29-3-002:

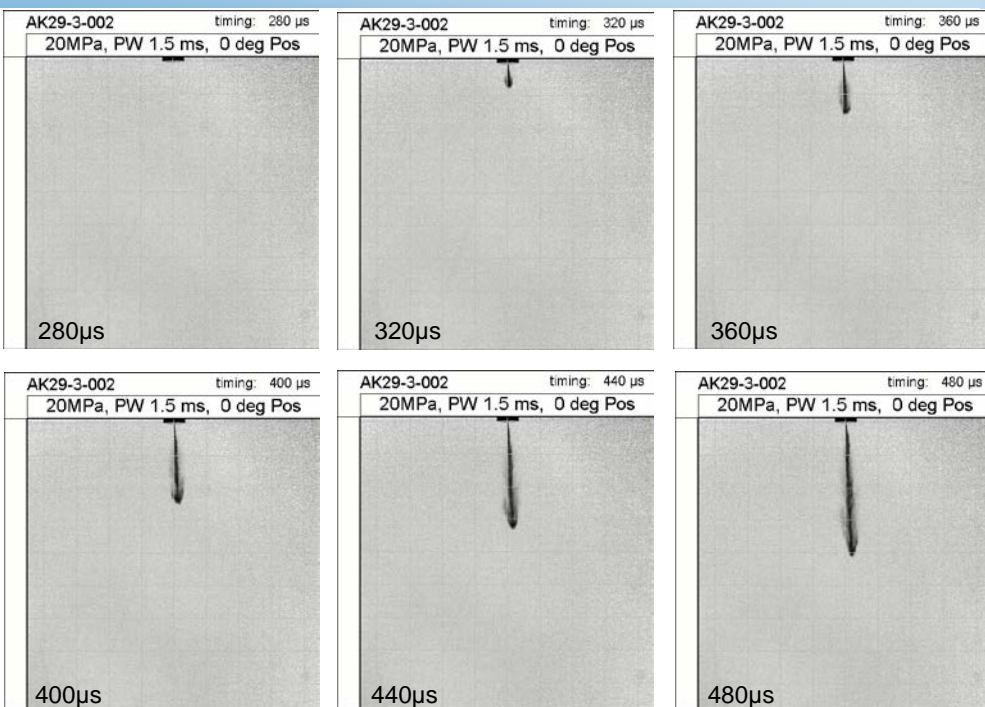
10MPa 0° orientation



12

AK29-3-002:

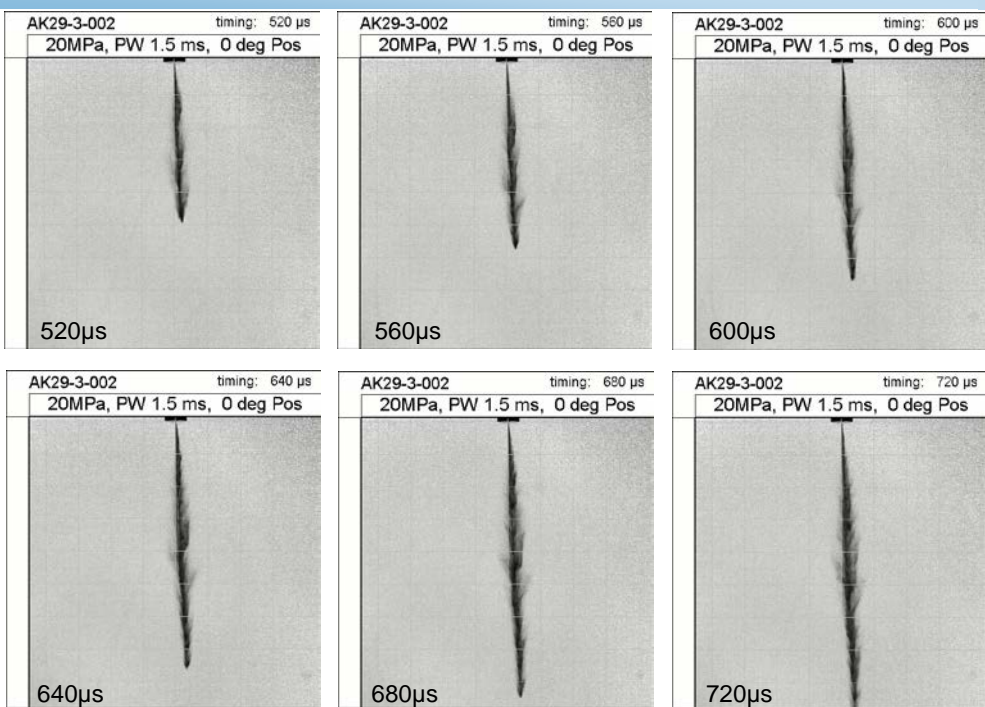
20MPa 0° orientation



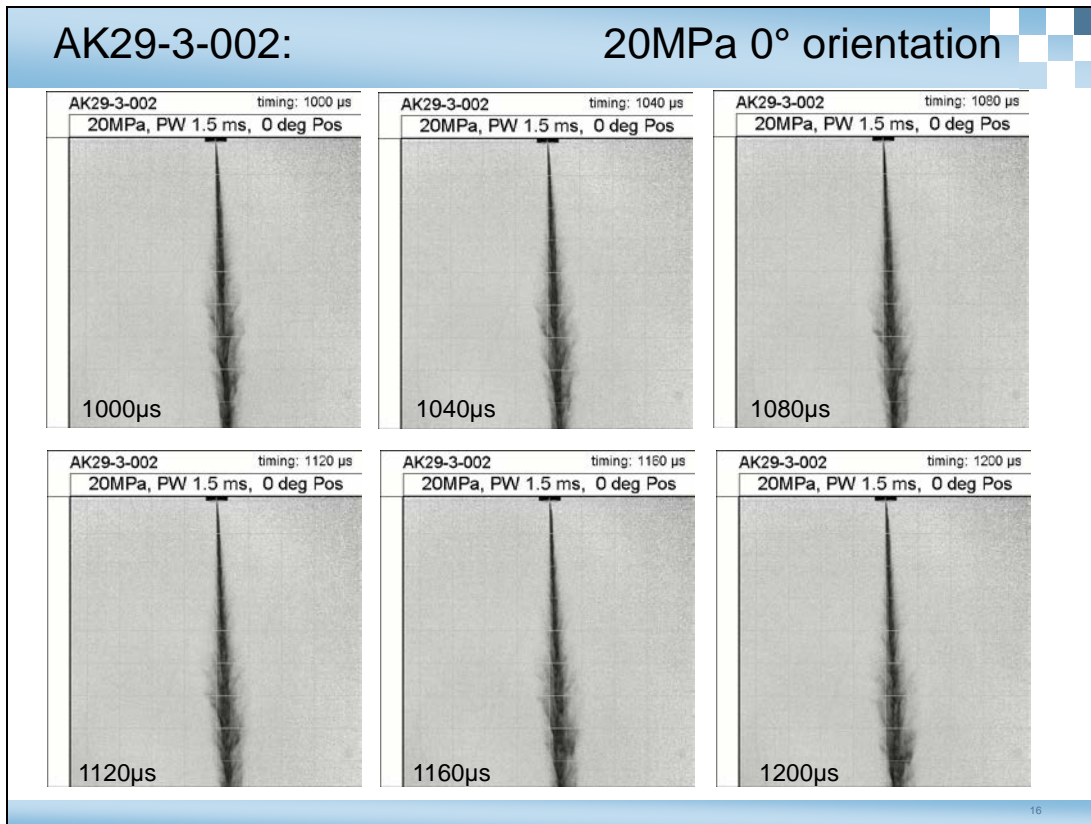
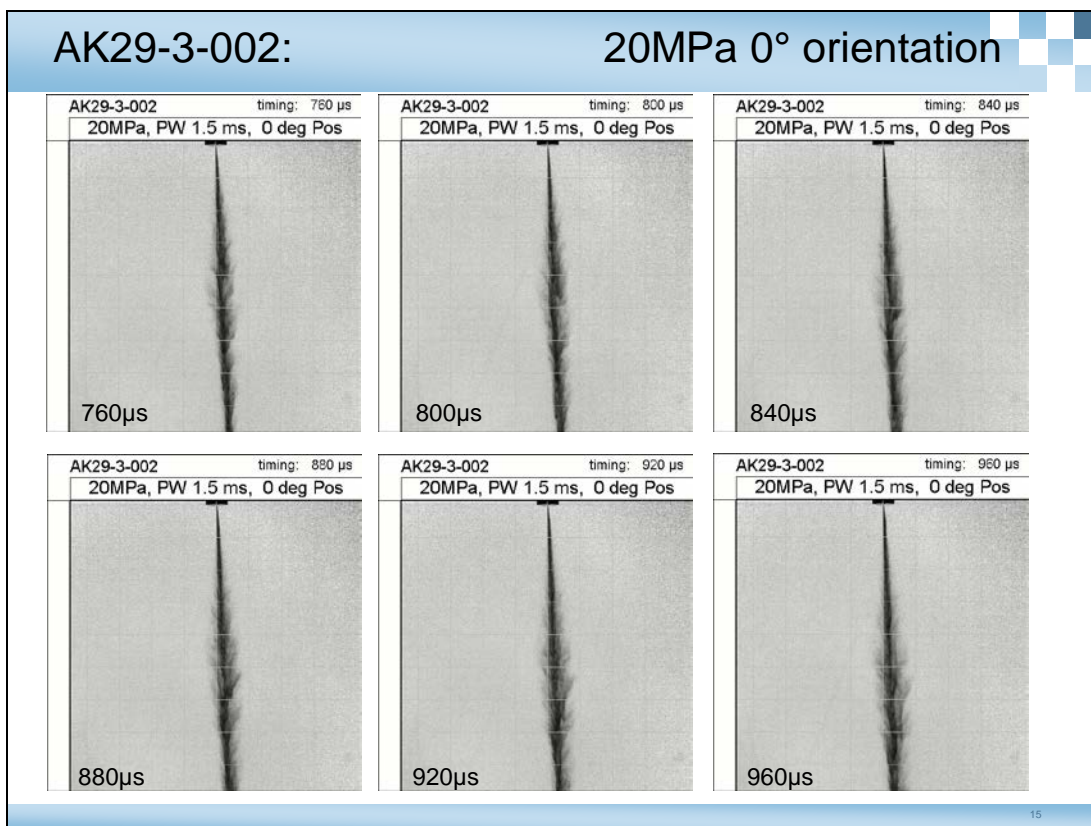
13

AK29-3-002:

20MPa 0° orientation

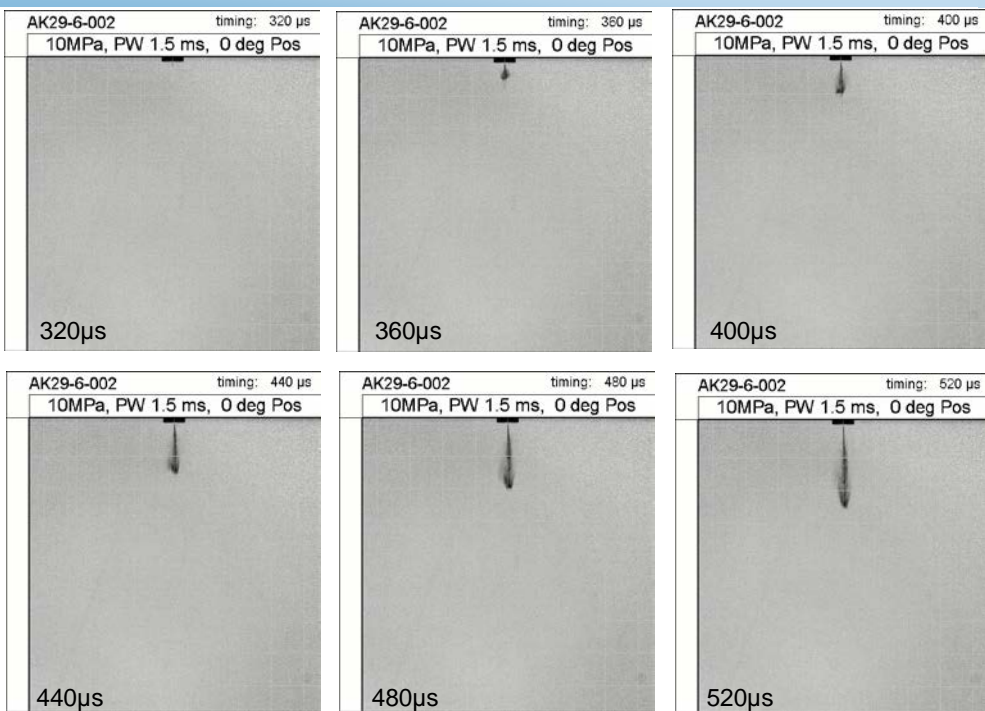


14



AK29-6-002:

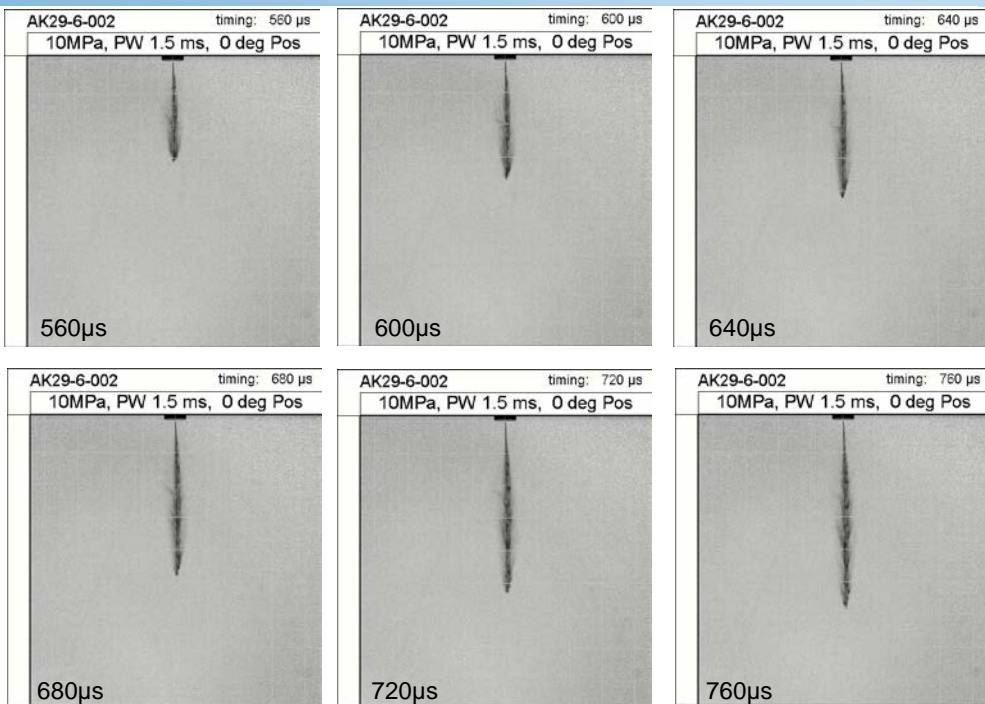
10MPa 0° orientation



17

AK29-6-002:

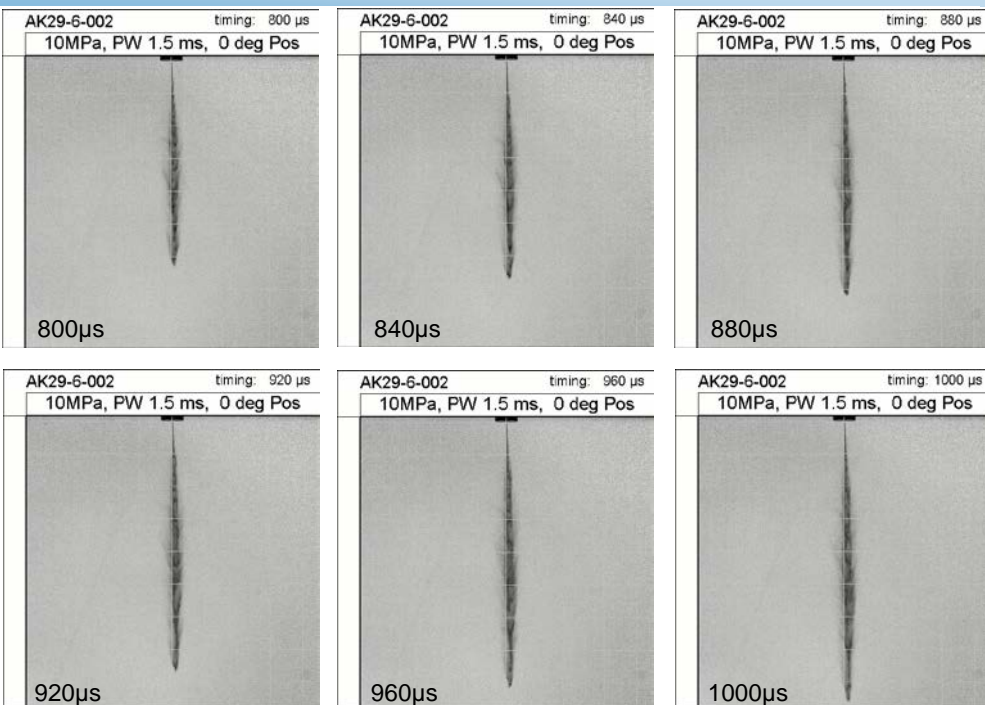
10MPa 0° orientation



18

AK29-6-002:

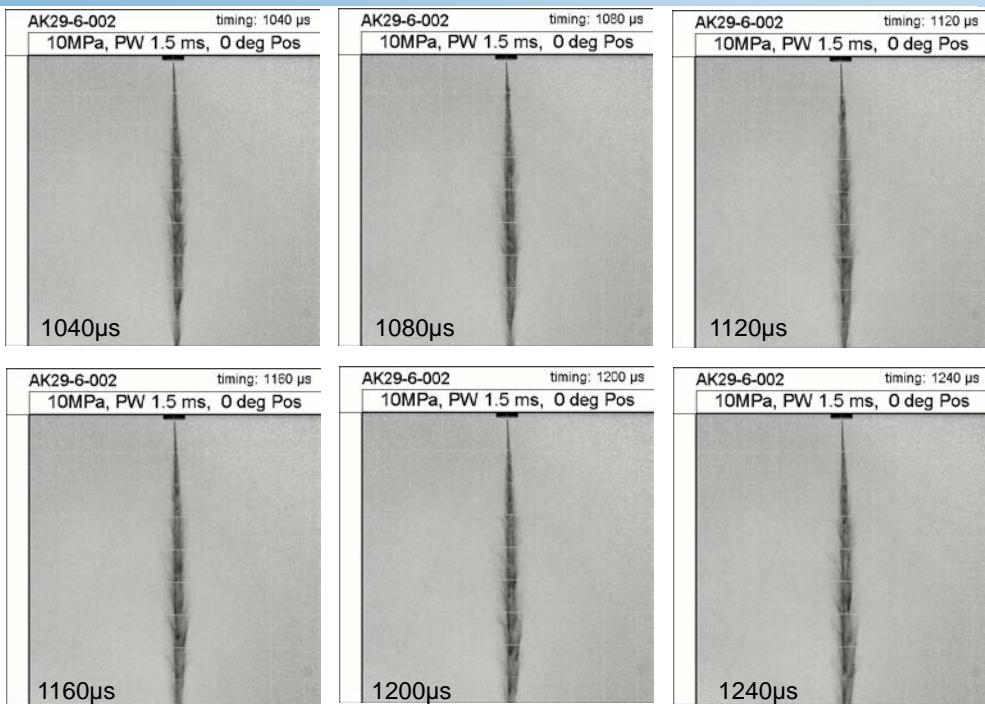
10MPa 0° orientation



19

AK29-6-002:

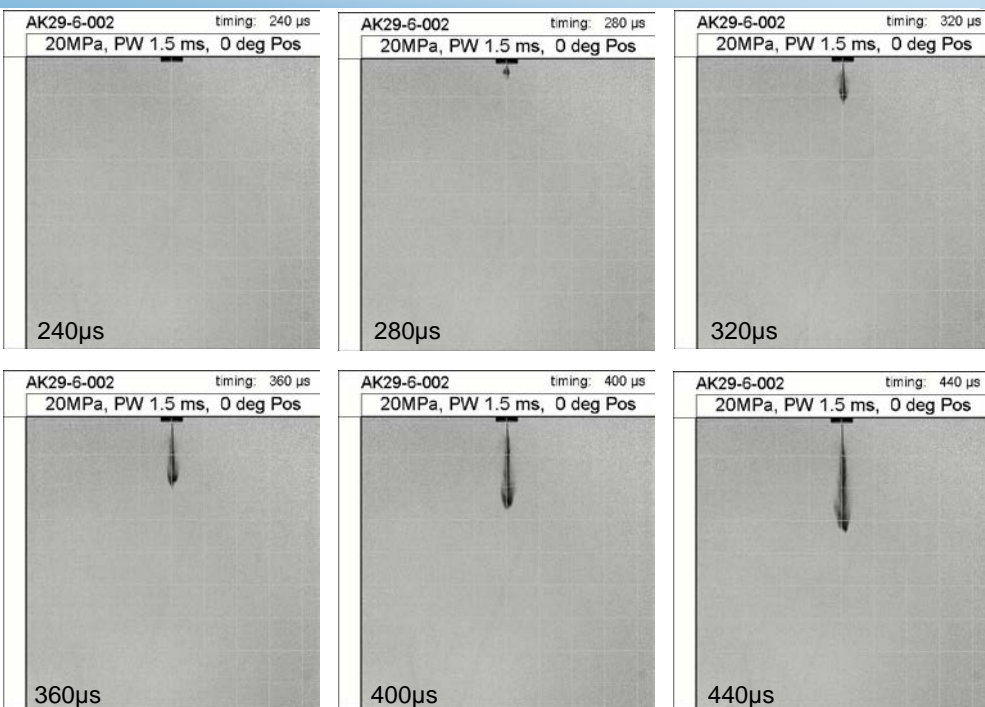
10MPa 0° orientation



20

AK29-6-002:

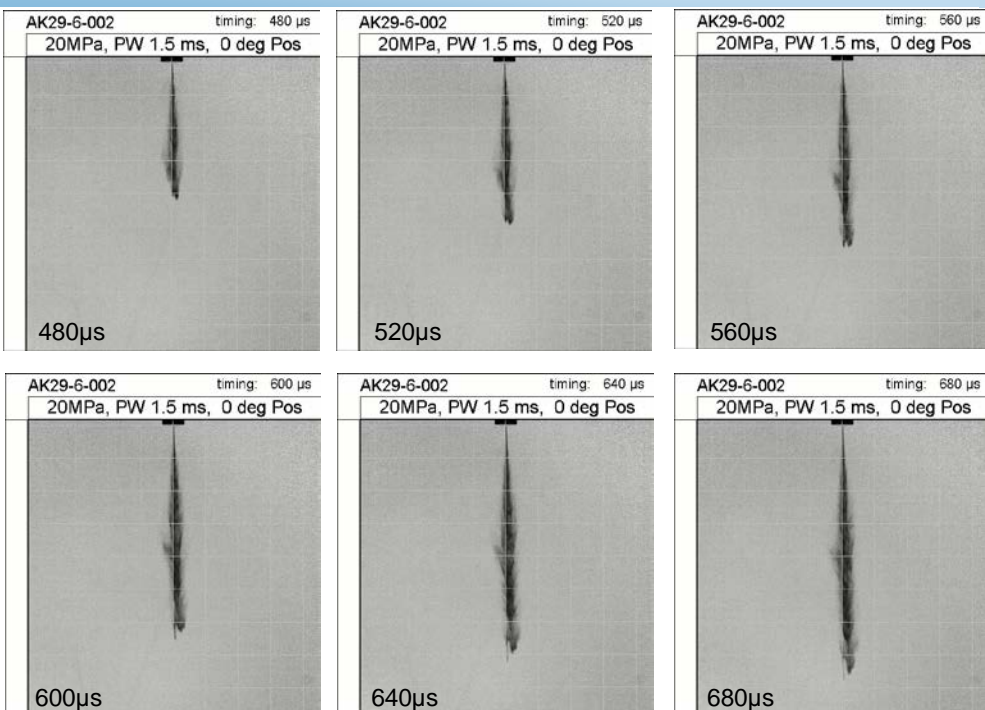
20MPa 0° orientation



21

AK29-6-002:

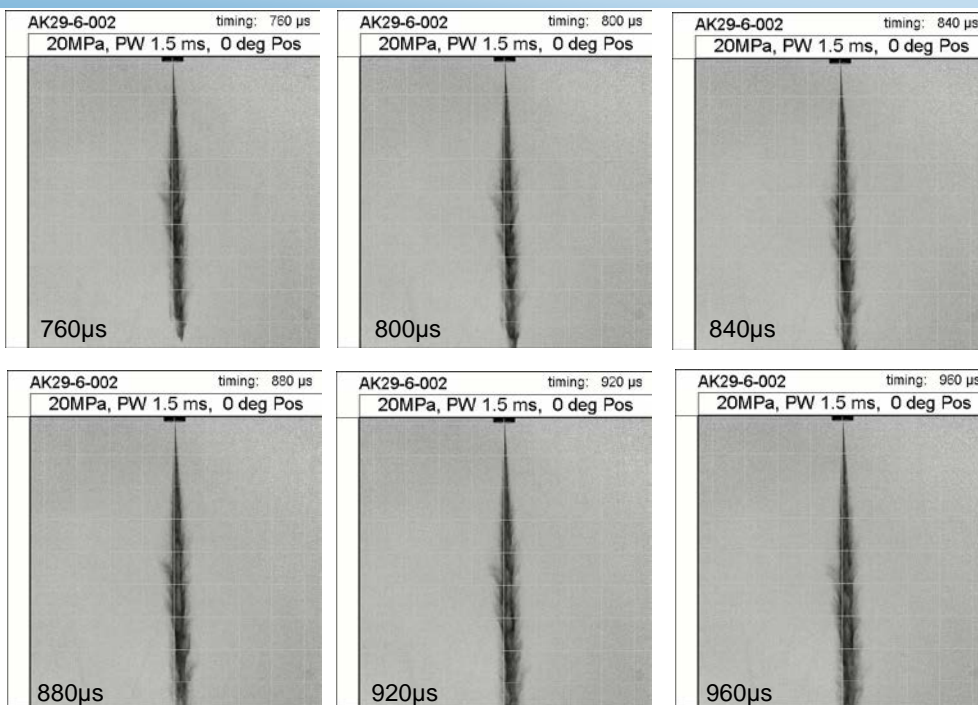
20MPa 0° orientation



22

AK29-6-002:

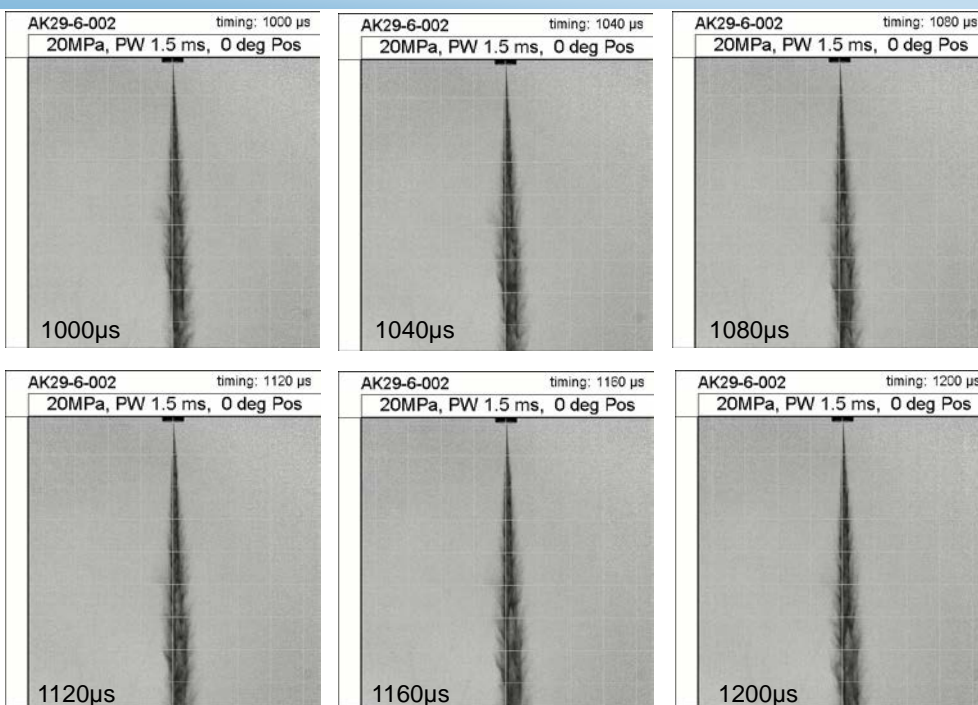
20MPa 0° orientation



23

AK29-6-002:

20MPa 0° orientation



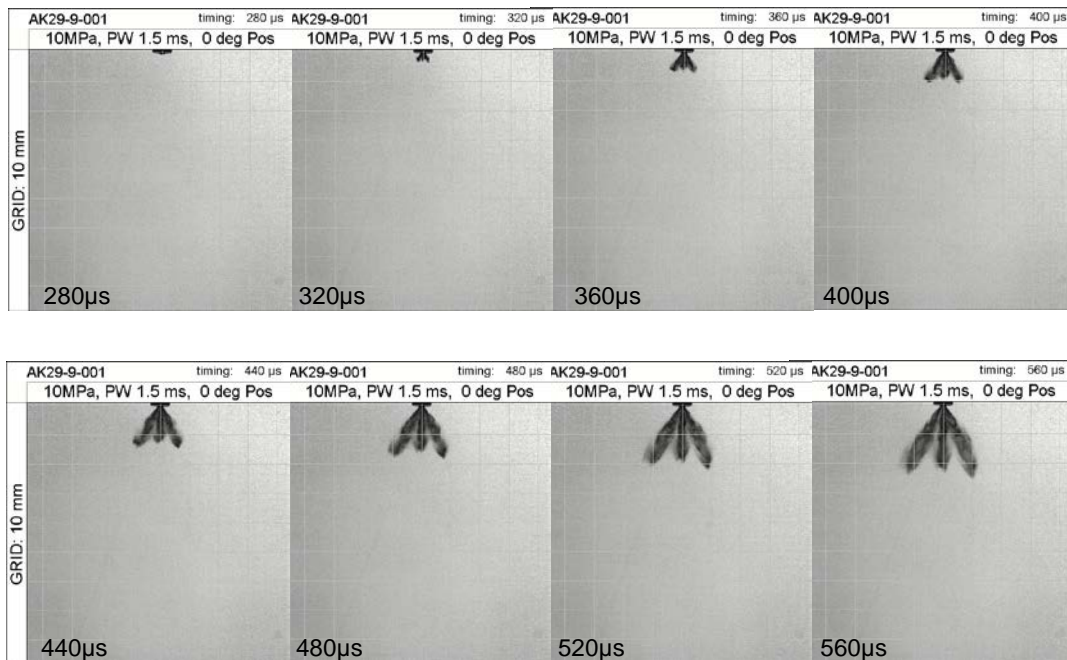
24

Shadow spray image

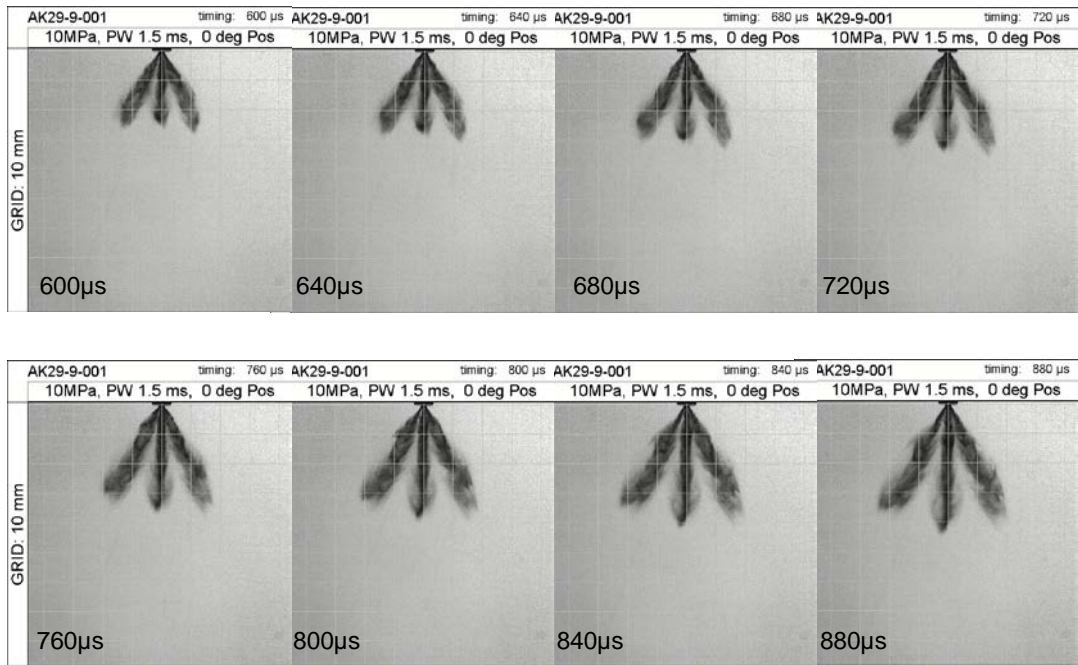
90° orientation

Shadow spray images for 90 degree orientation show similar behavior, so not shown.

AK29-9-001: 10MPa 0° orientation

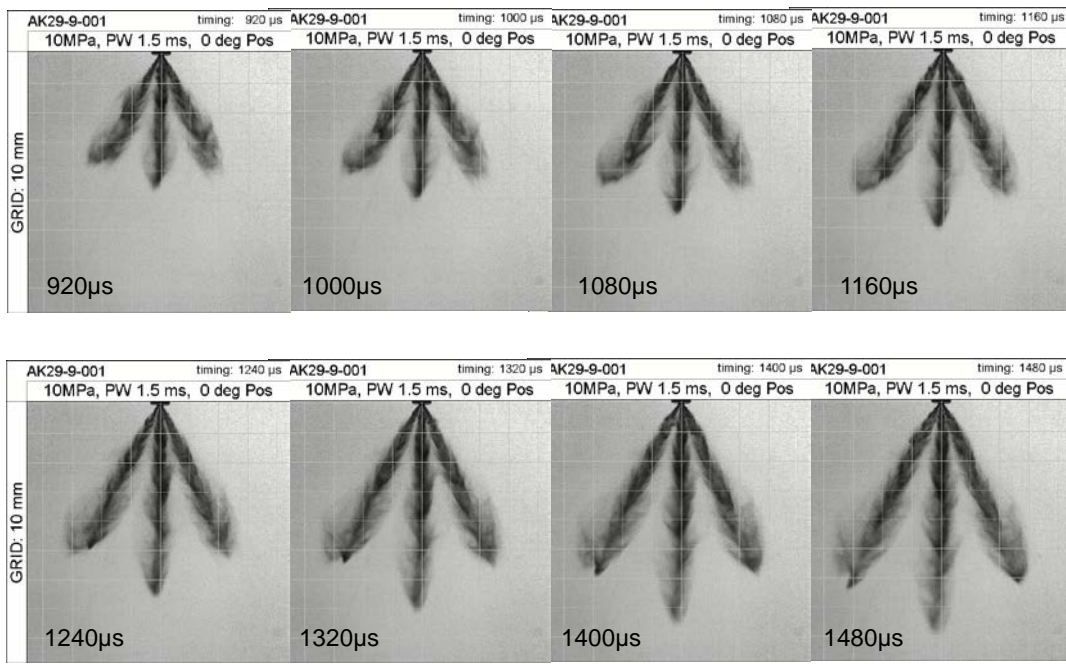


AK29-9-001: 10MPa 0° orientation



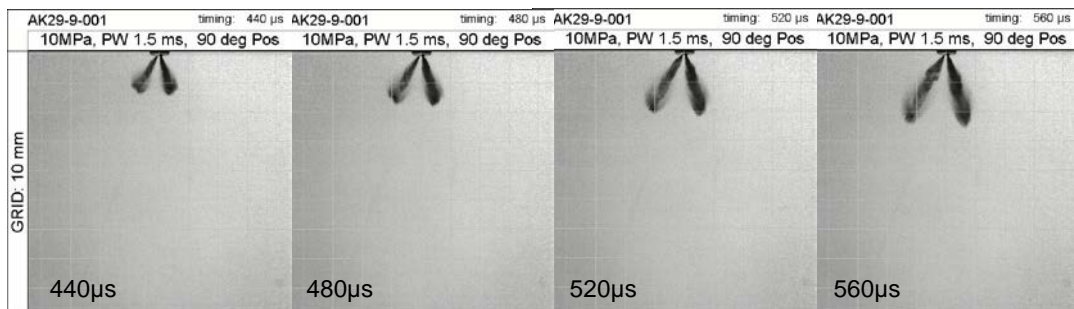
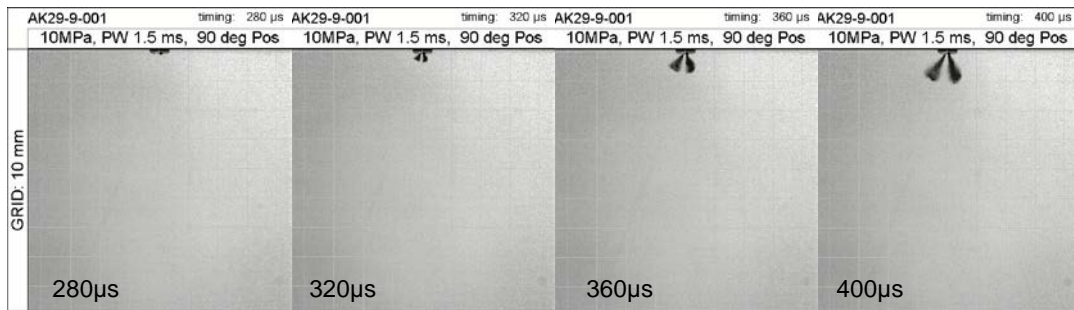
27

AK29-9-001: 10MPa 0° orientation



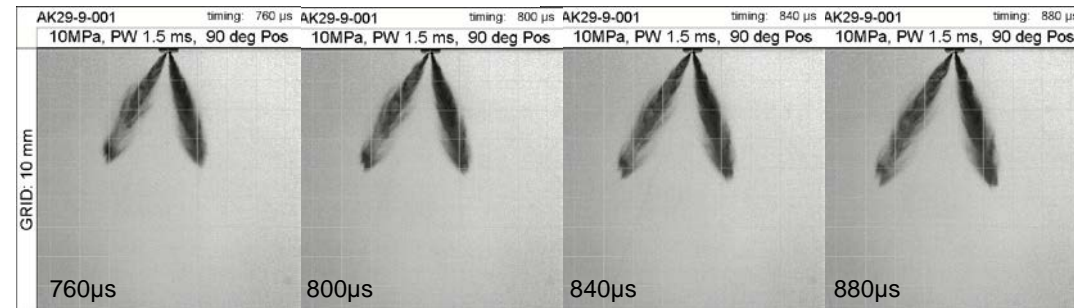
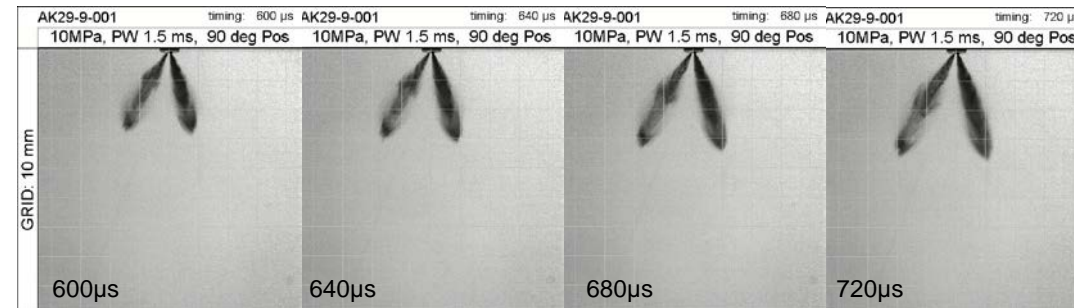
28

AK29-9-001: 10MPa, 90° orientation



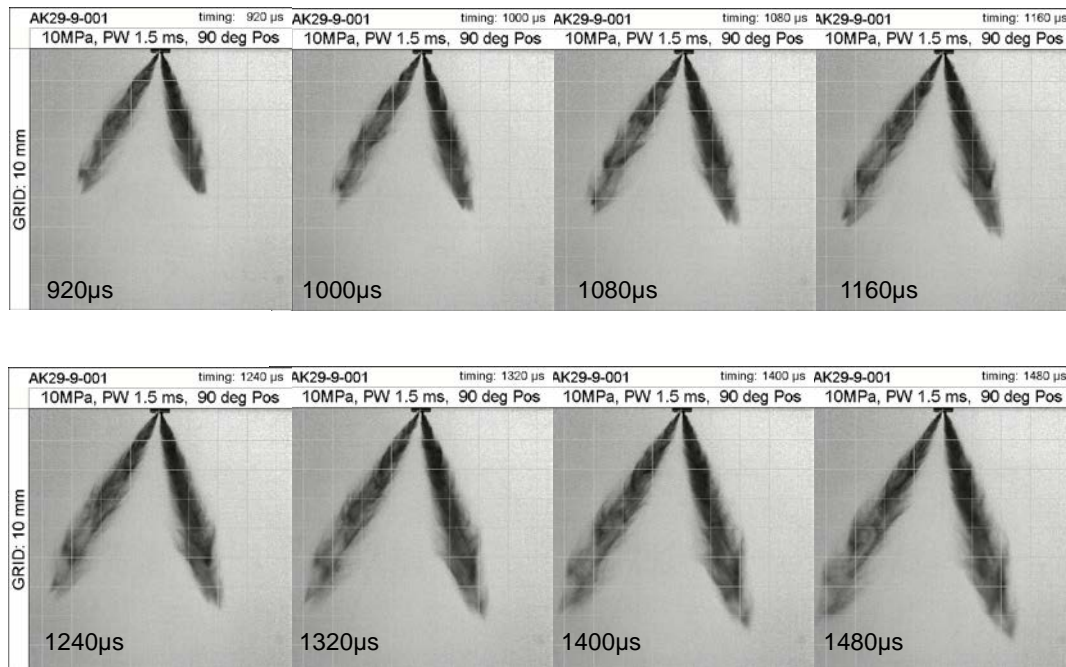
29

AK29-9-001: 10MPa, 90° orientation



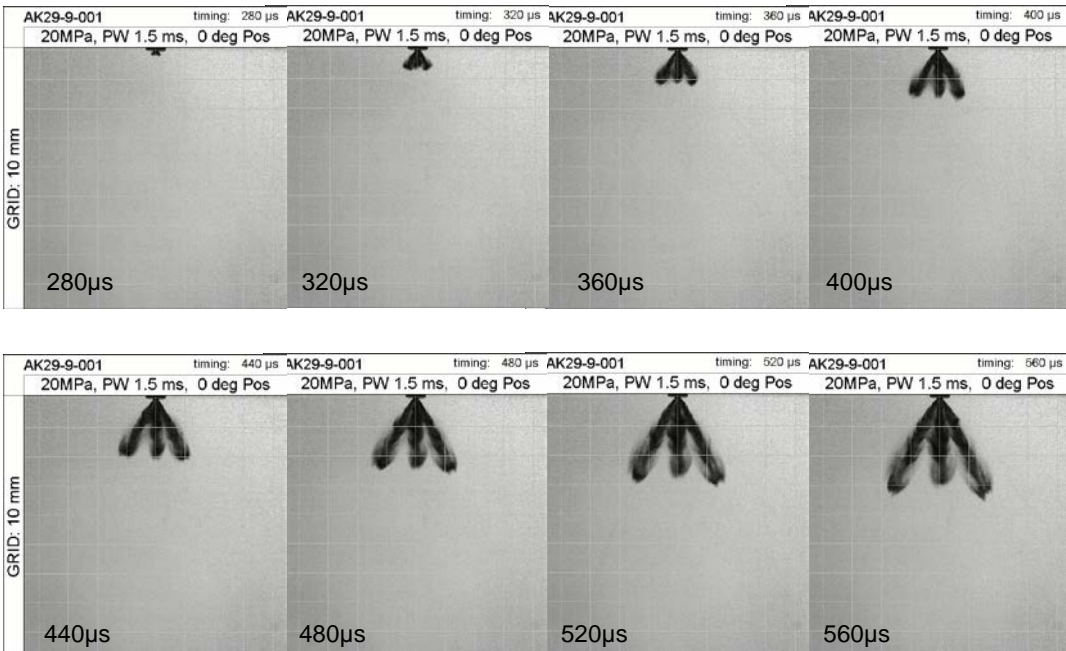
30

AK29-3-001: 10MPa, 90° orientation



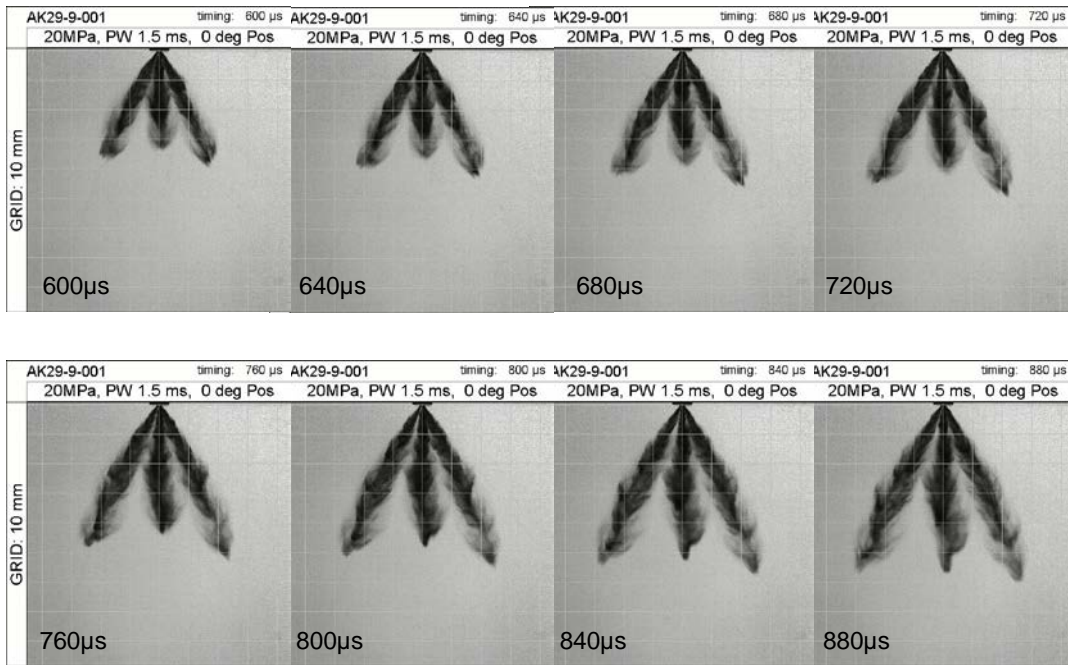
31

AK29-9-001: 20MPa 0° orientation



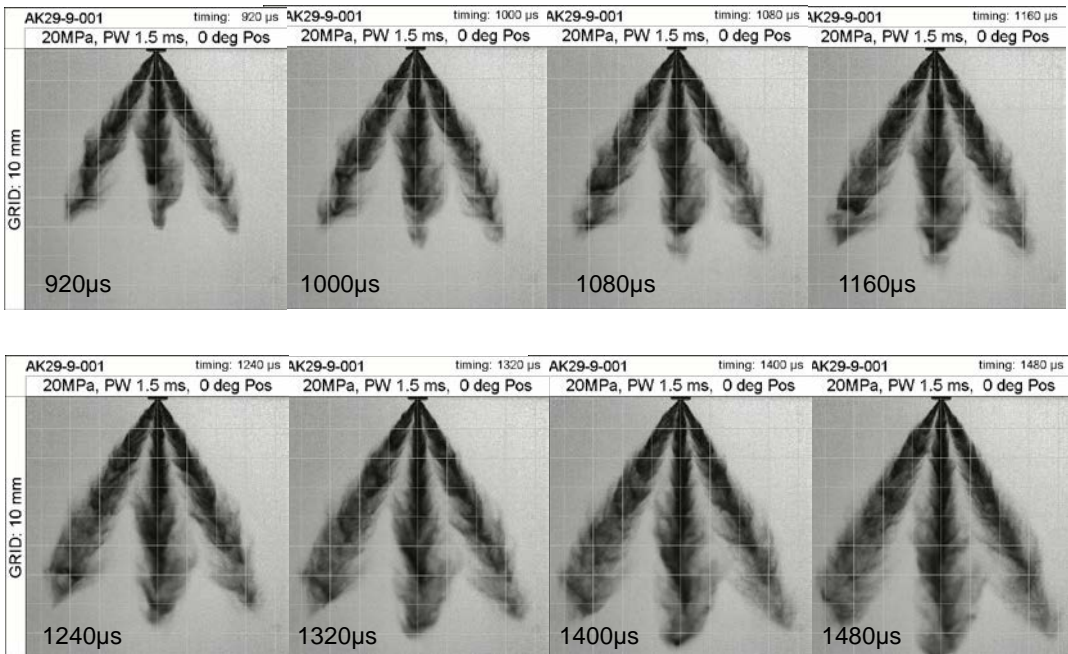
32

AK29-9-001: 20MPa 0° orientation



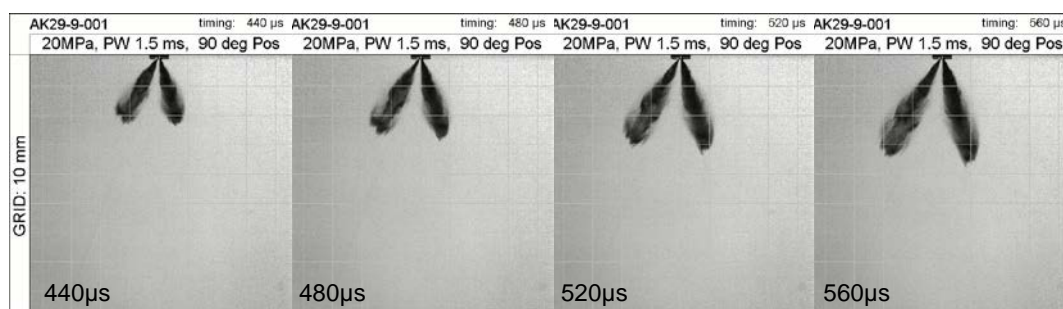
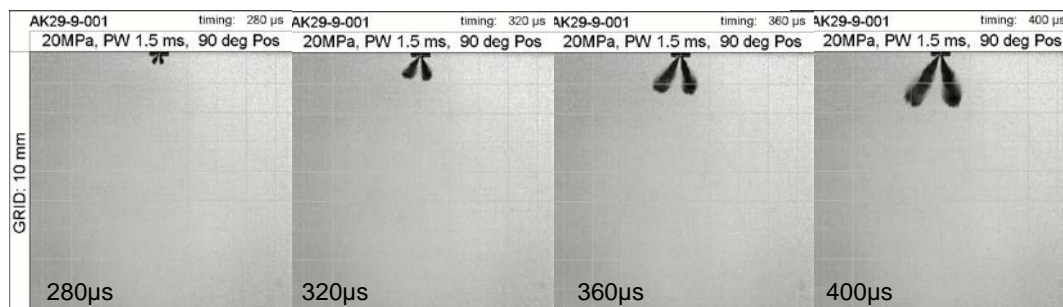
33

AK29-9-001: 20MPa 0° orientation



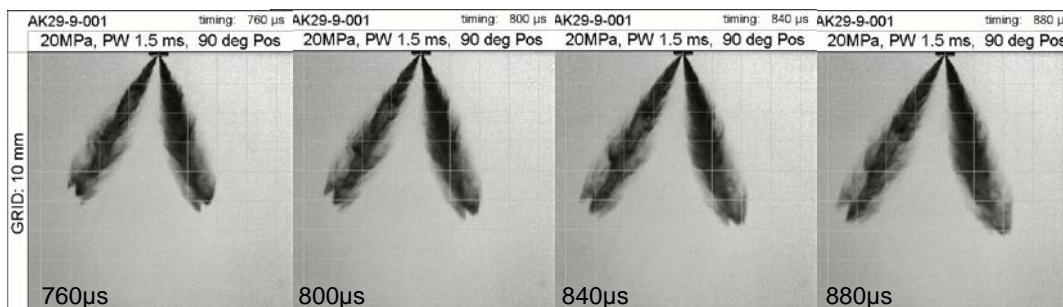
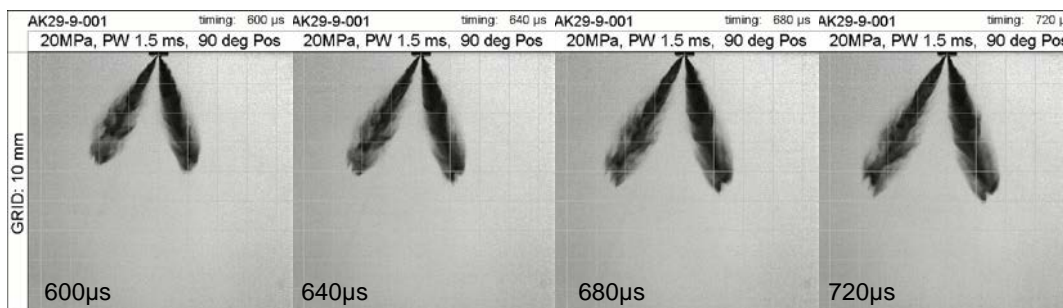
34

AK29-9-001: 20MPa, 90° orientation



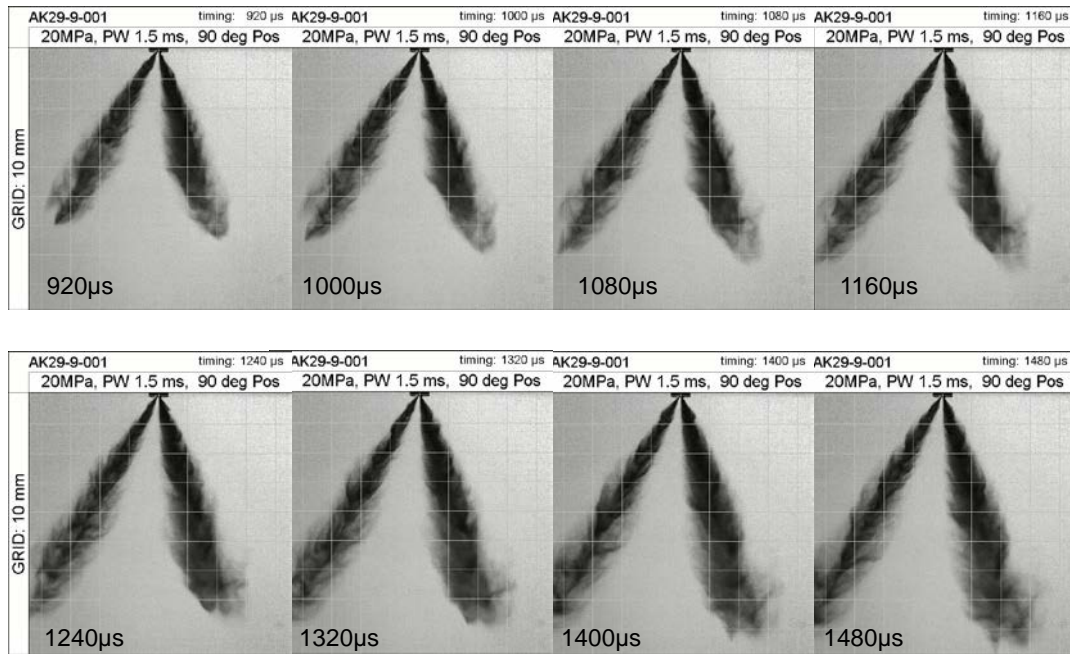
35

AK29-9-001: 20MPa, 90° orientation



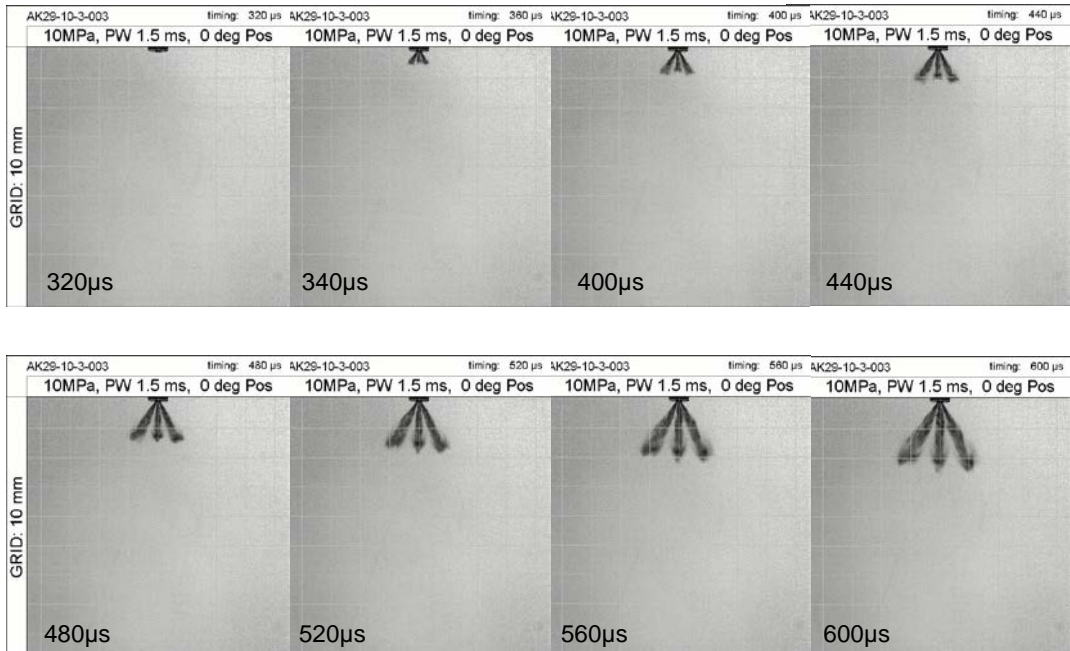
36

AK29-9-001: 20MPa, 90° orientation



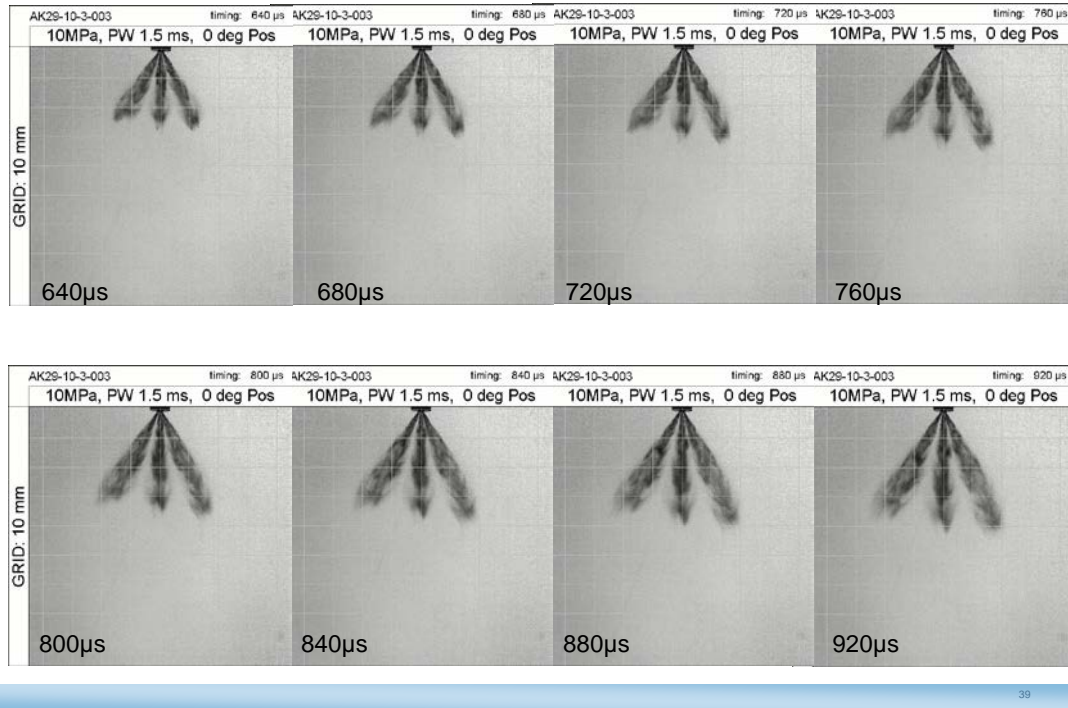
37

AK29-10-3-003: 10MPa 0° orientation

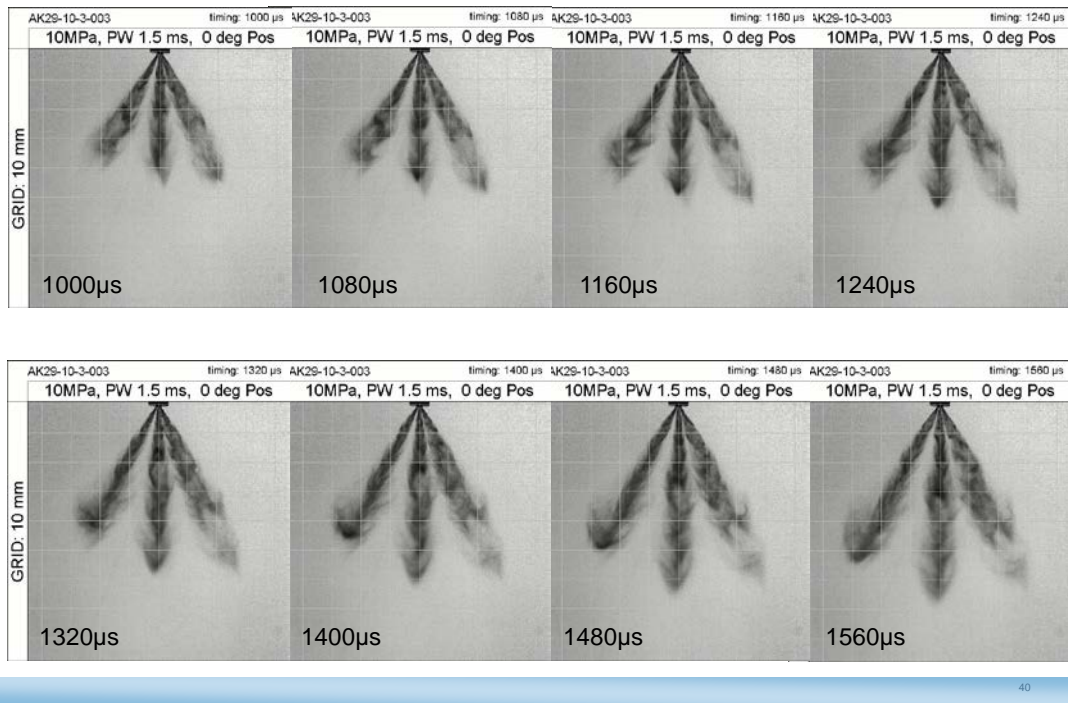


38

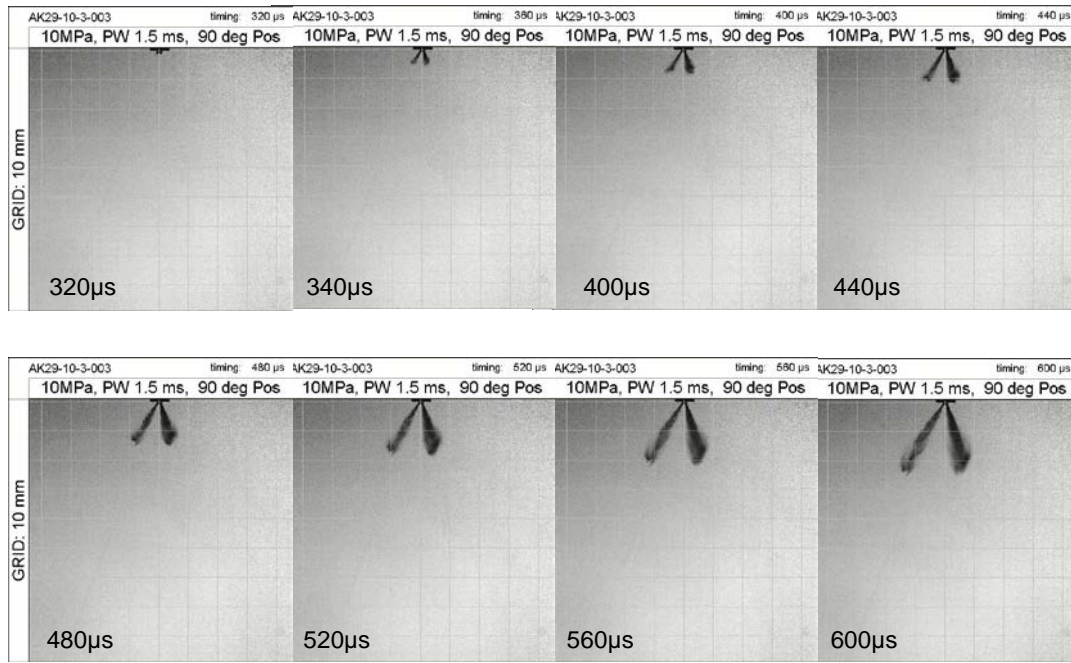
AK29-10-3-003: 10MPa 0° orientation



AK29-10-3-003: 10MPa 0° orientation

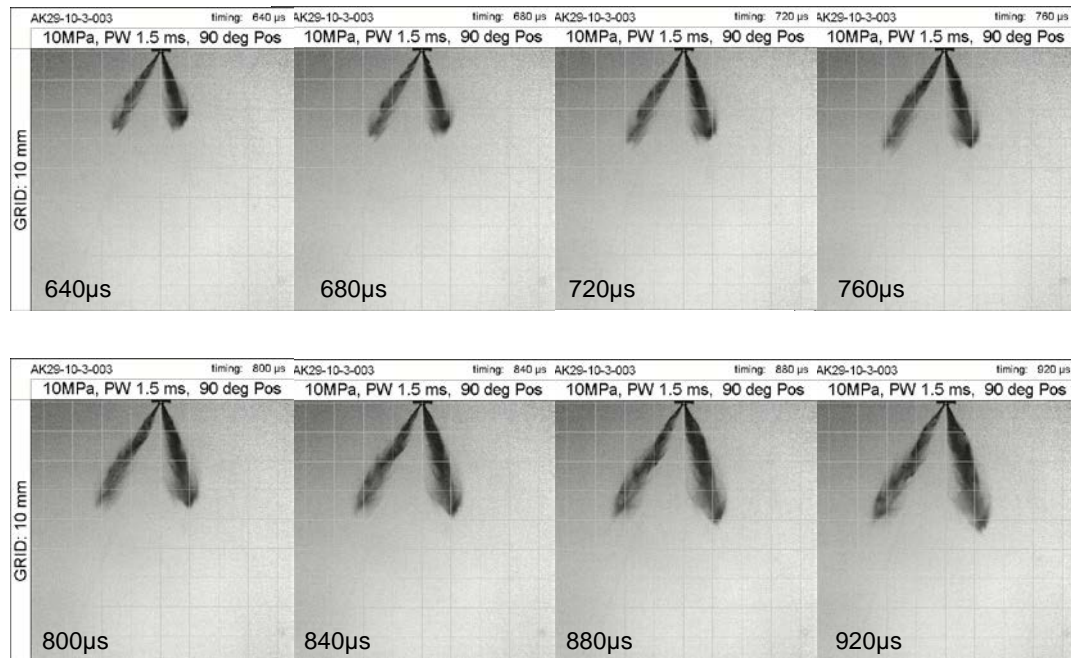


AK29-10-3-003: 10MPa, 90° orientation



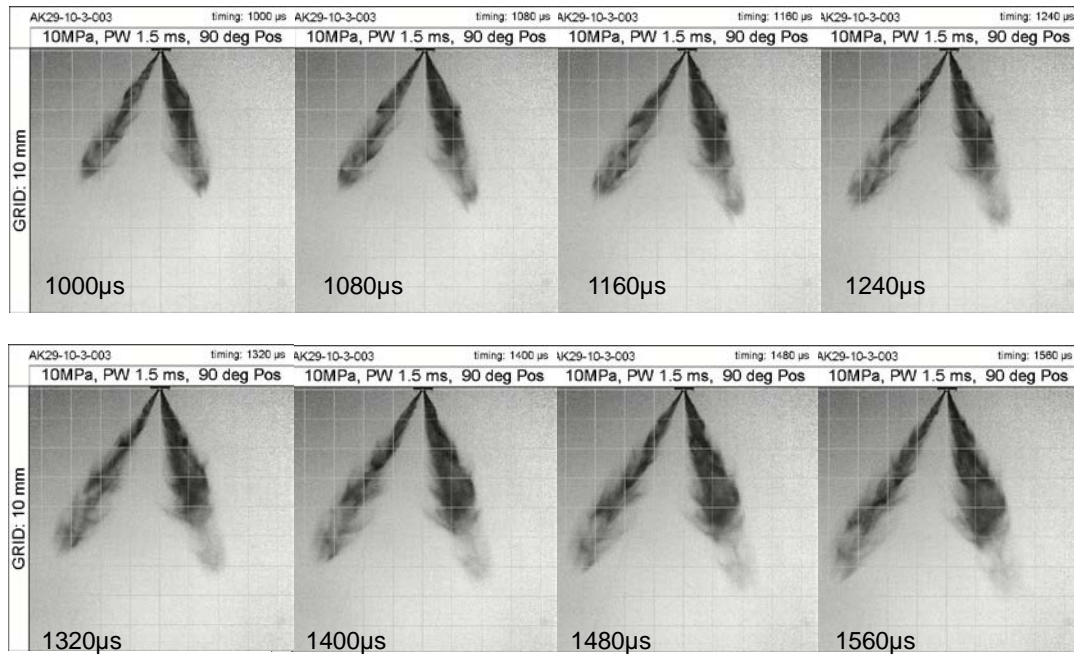
41

AK29-10-3-003: 10MPa, 90° orientation



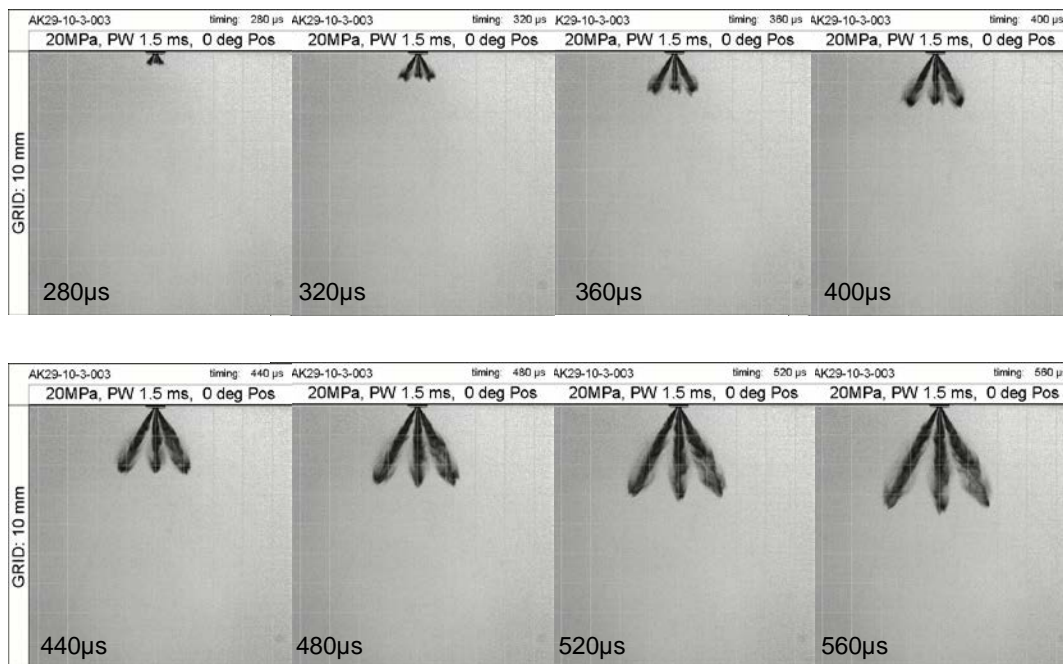
42

AK29-10-3-003: 10MPa, 90° orientation



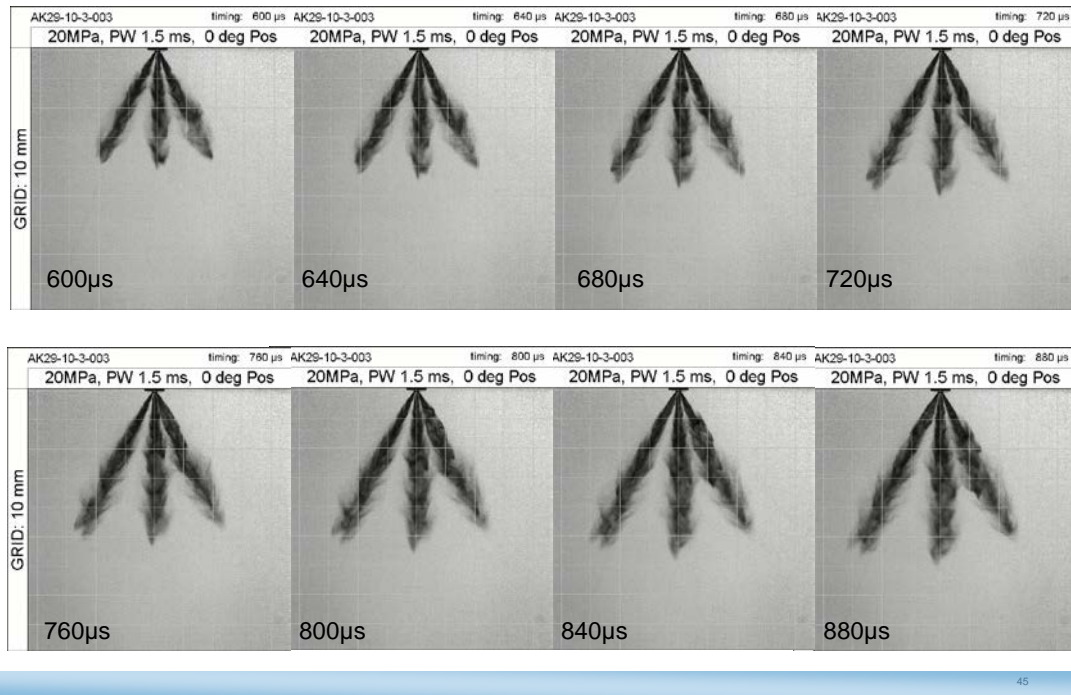
43

AK29-10-3-003 : 20MPa, 0° orientation

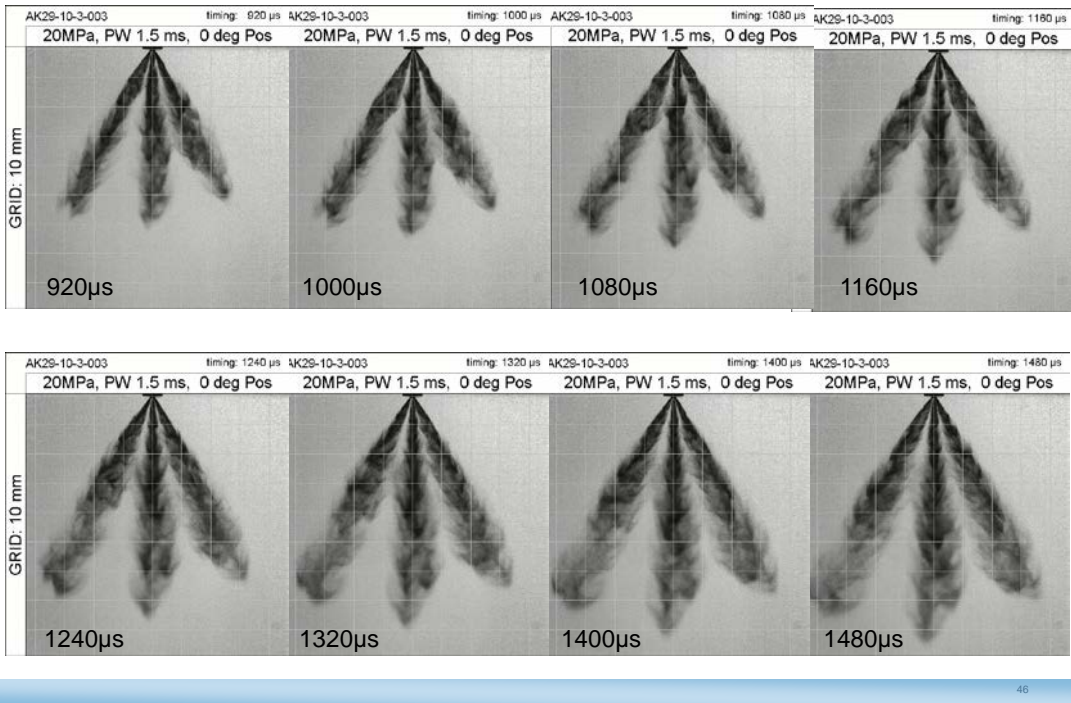


44

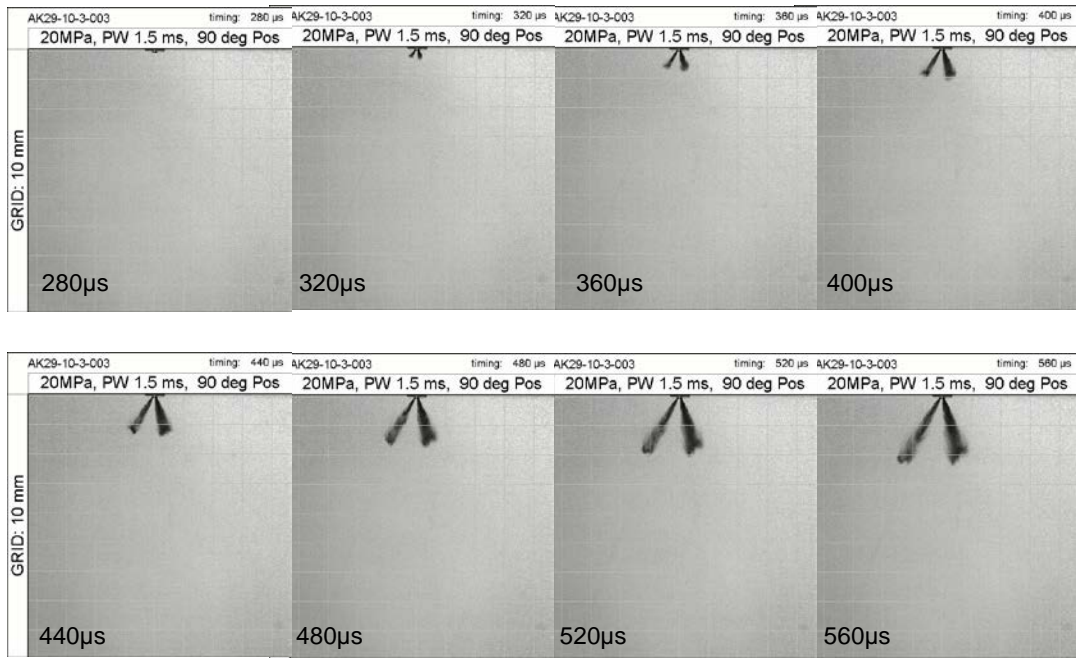
AK29-10-3-003 : 20MPa, 0° orientation



AK29-10-3-003: 20MPa, 0° orientation

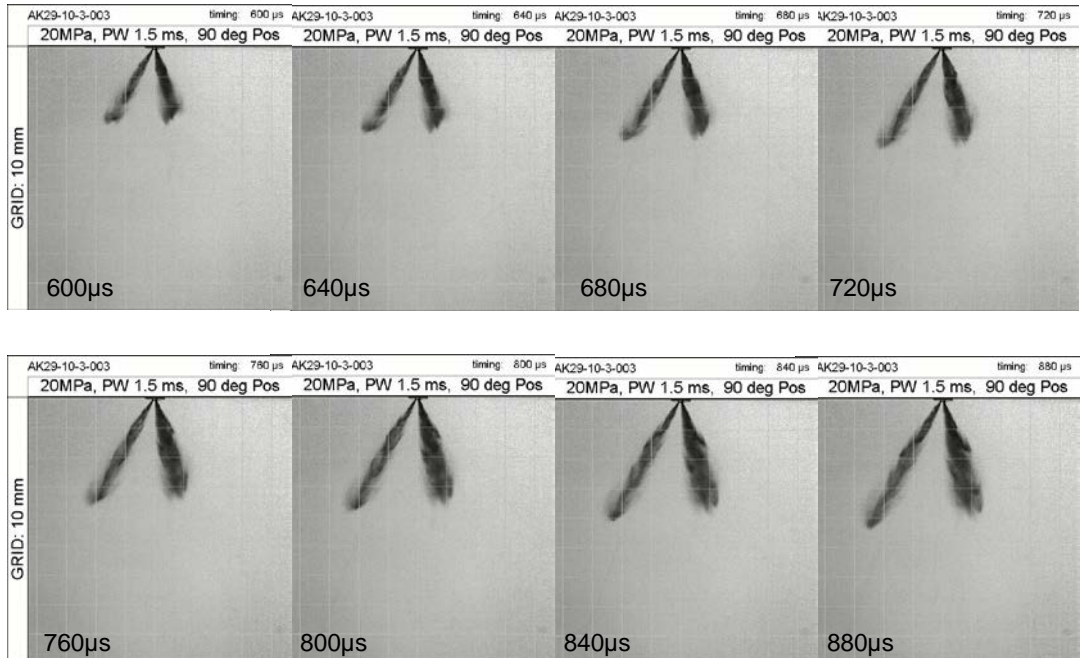


AK29-10-3-003 : 20MPa, 90° orientation



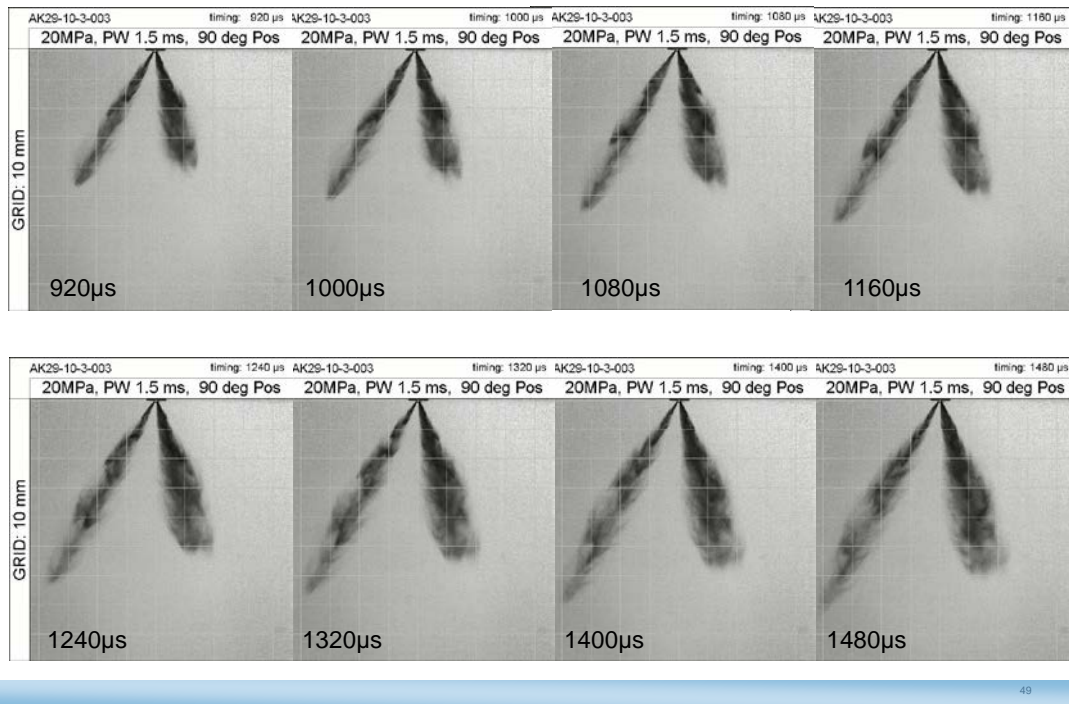
47

AK29-10-3-003 : 20MPa, 90° orientation

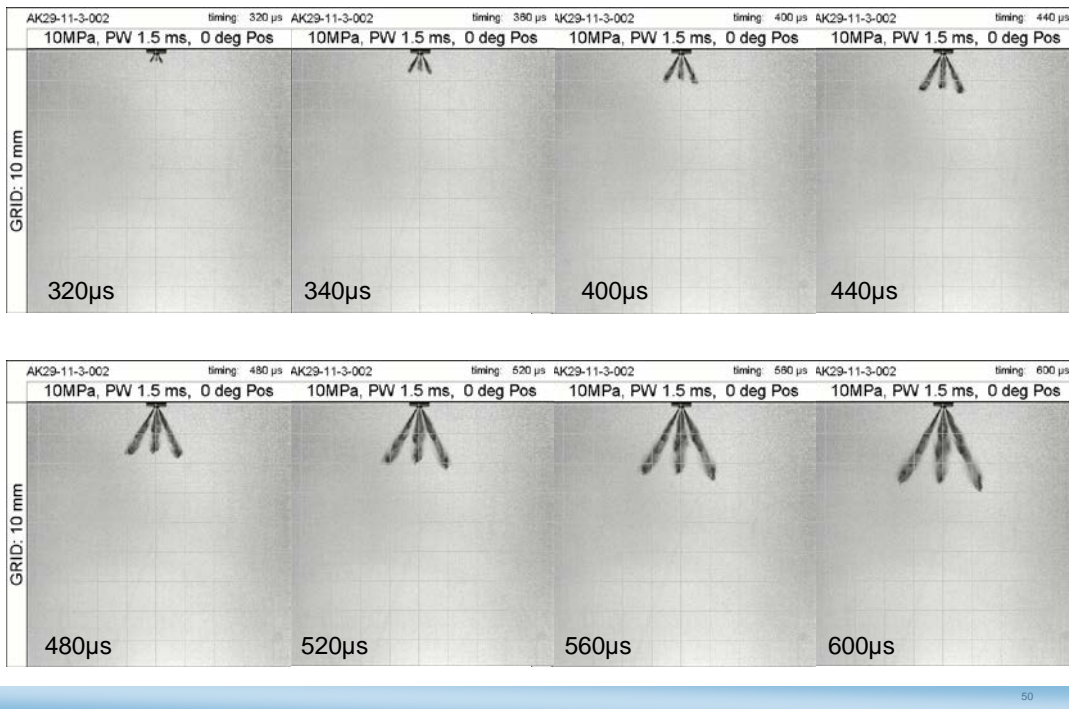


48

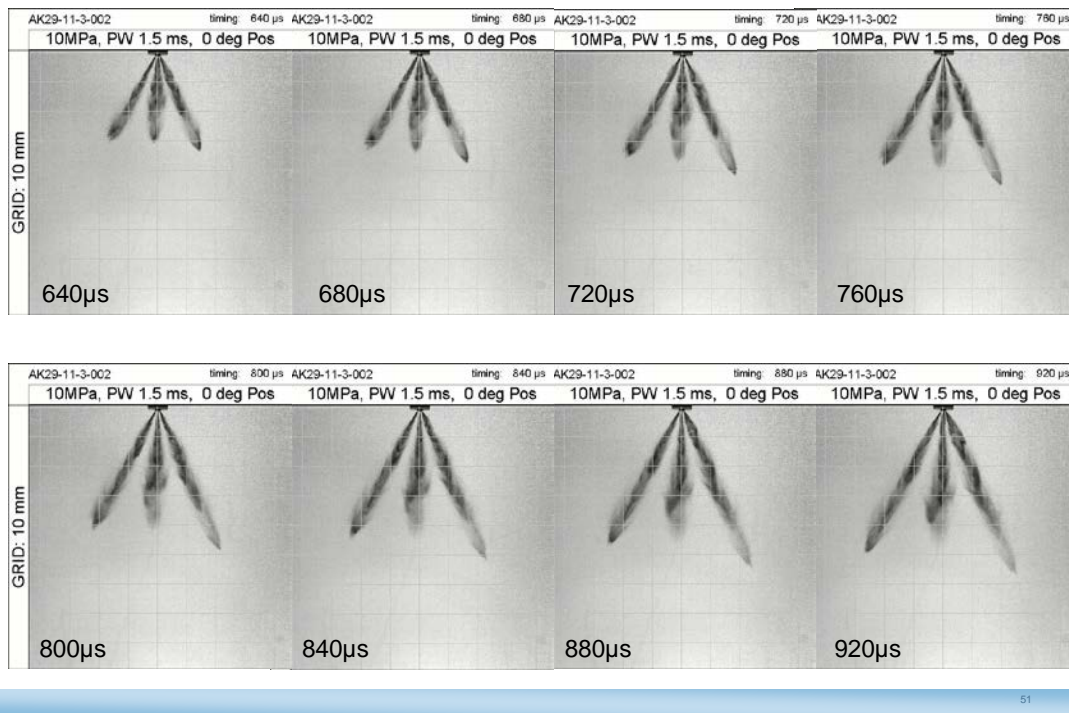
AK29-10-3-003: 20MPa, 90° orientation



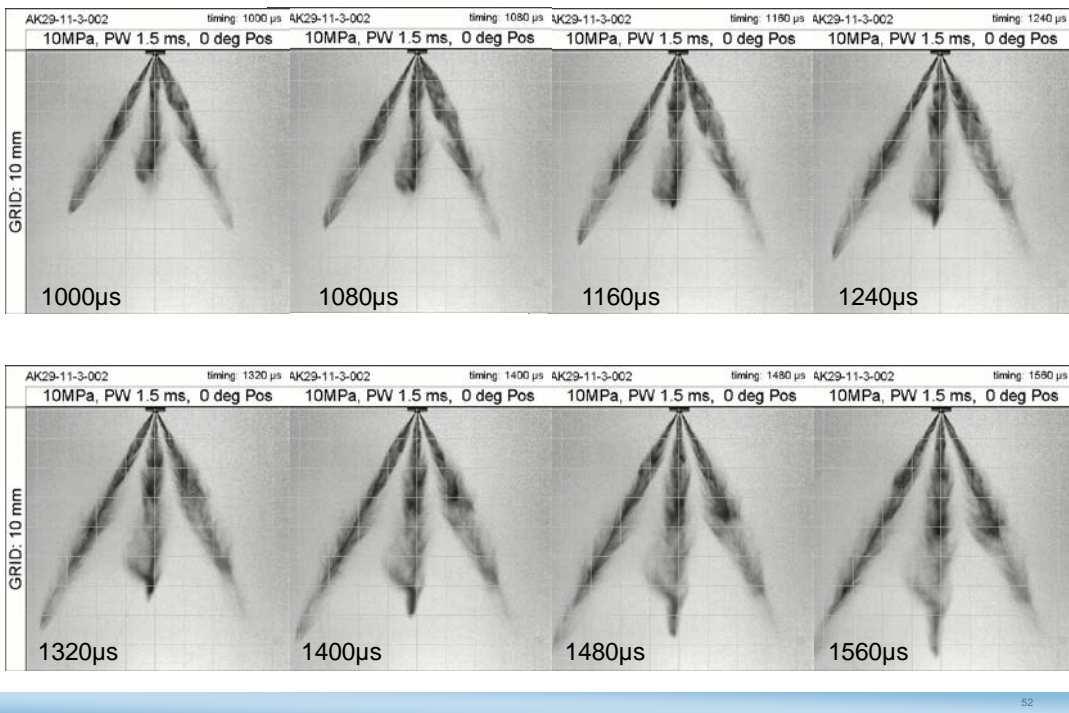
AK29-11-3-002: 10MPa 0° orientation



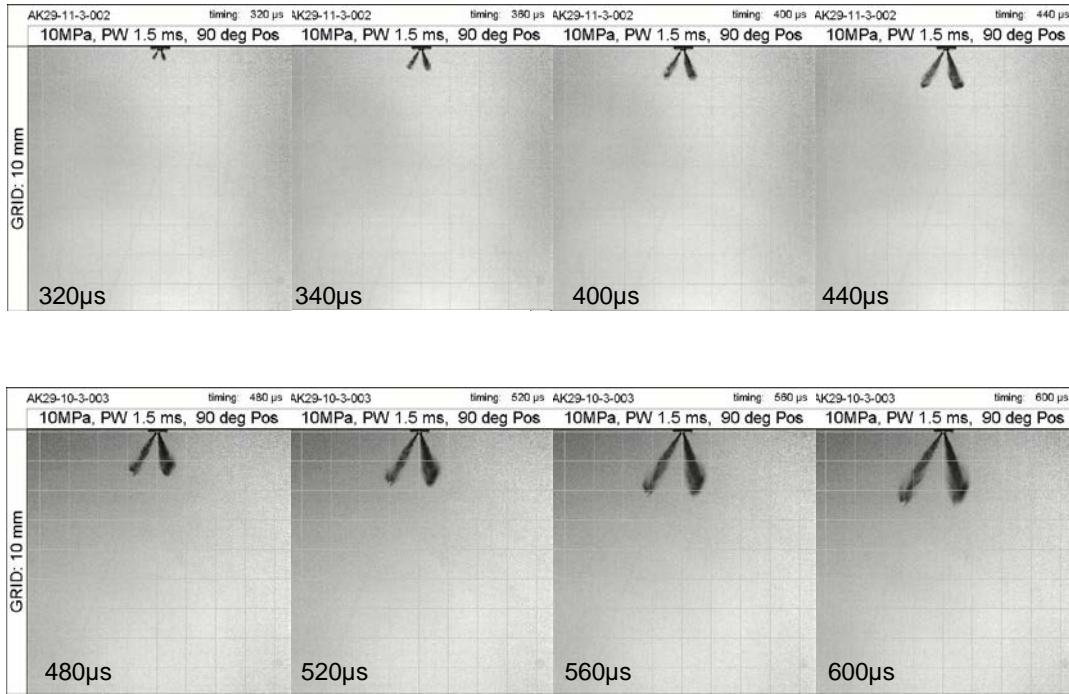
AK29-11-3-002: 10MPa 0° orientation



AK29-11-3-002: 10MPa 0° orientation

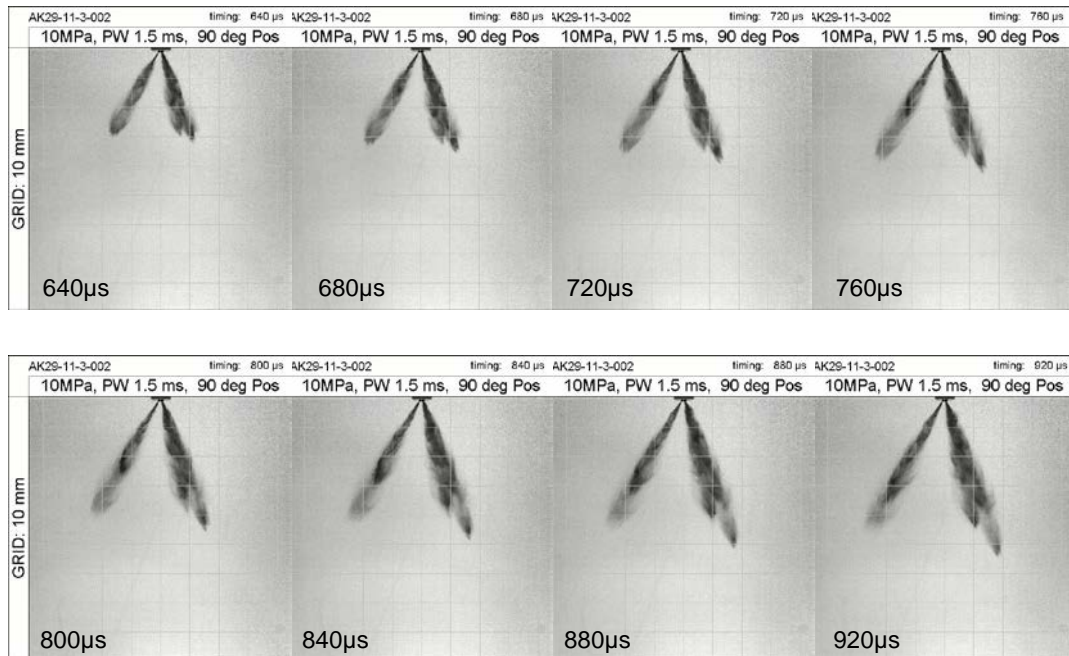


AK29-11-3-002: 10MPa, 90° orientation



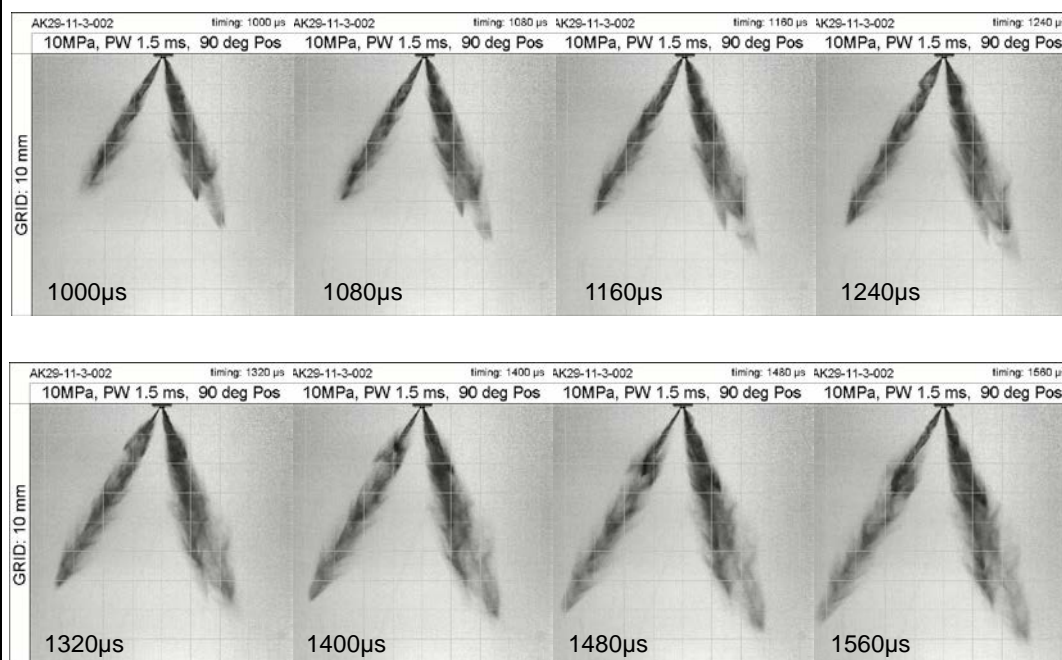
53

AK29-11-3-002: 10MPa, 90° orientation



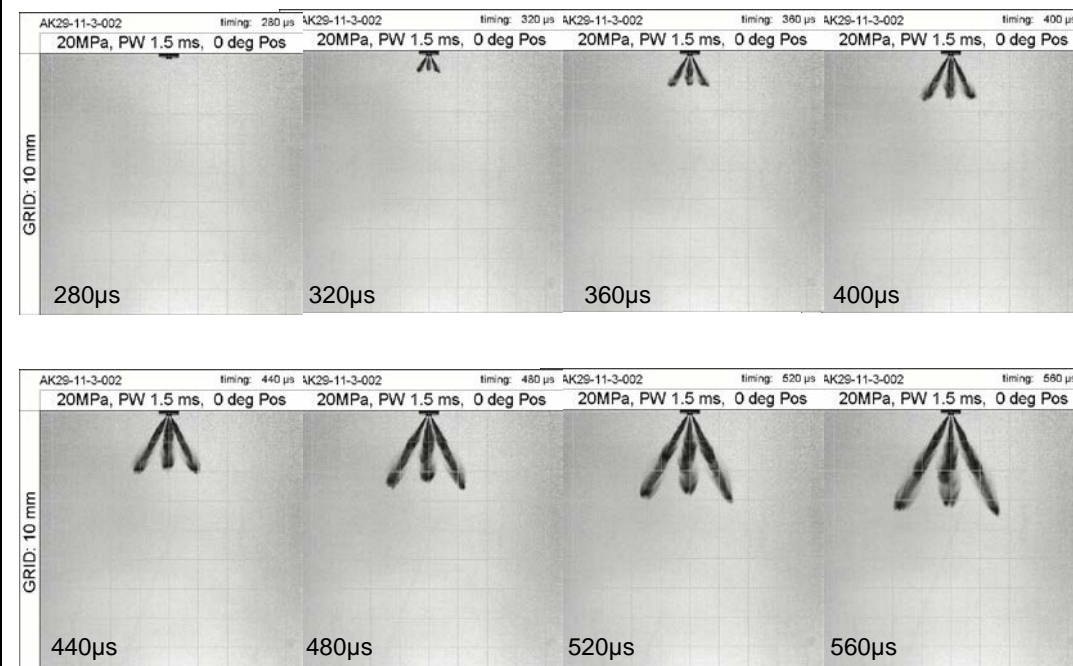
54

AK29-11-3-002: 10MPa, 90° orientation



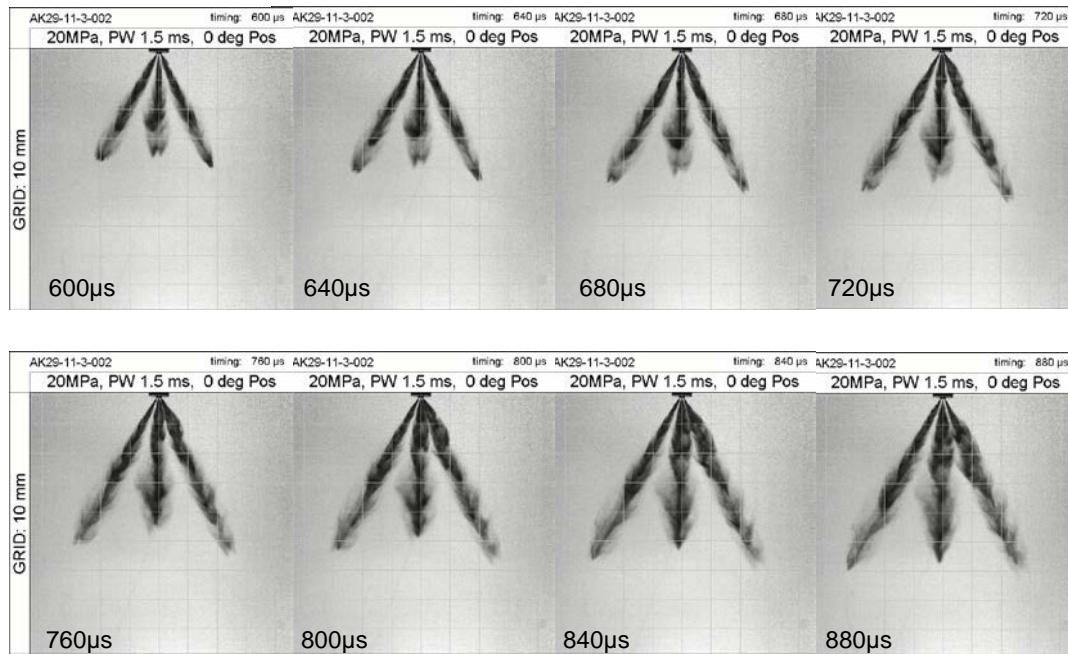
55

AK29-11-3-002: 20MPa, 0° orientation



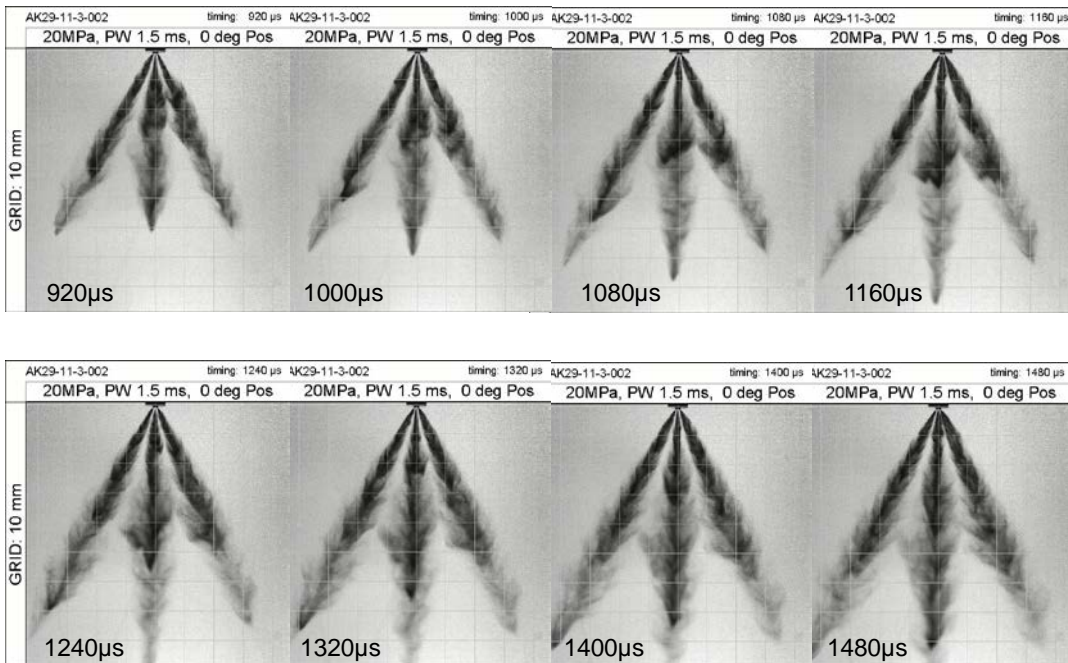
56

AK29-11-3-002: 20MPa, 0° orientation



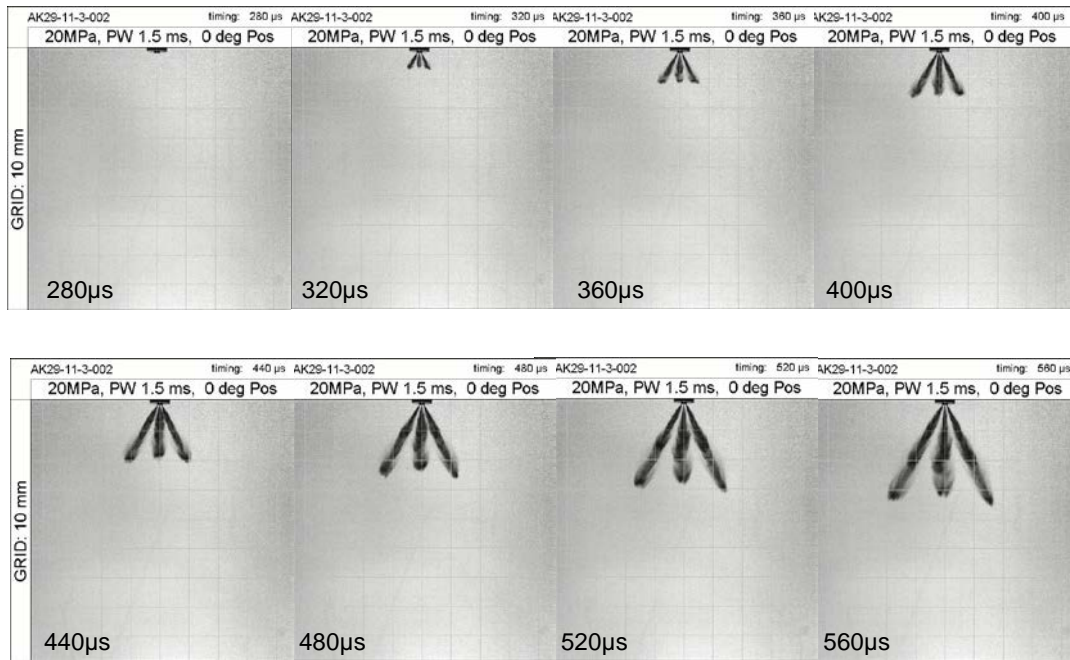
57

AK29-11-3-002: 20MPa, 0° orientation



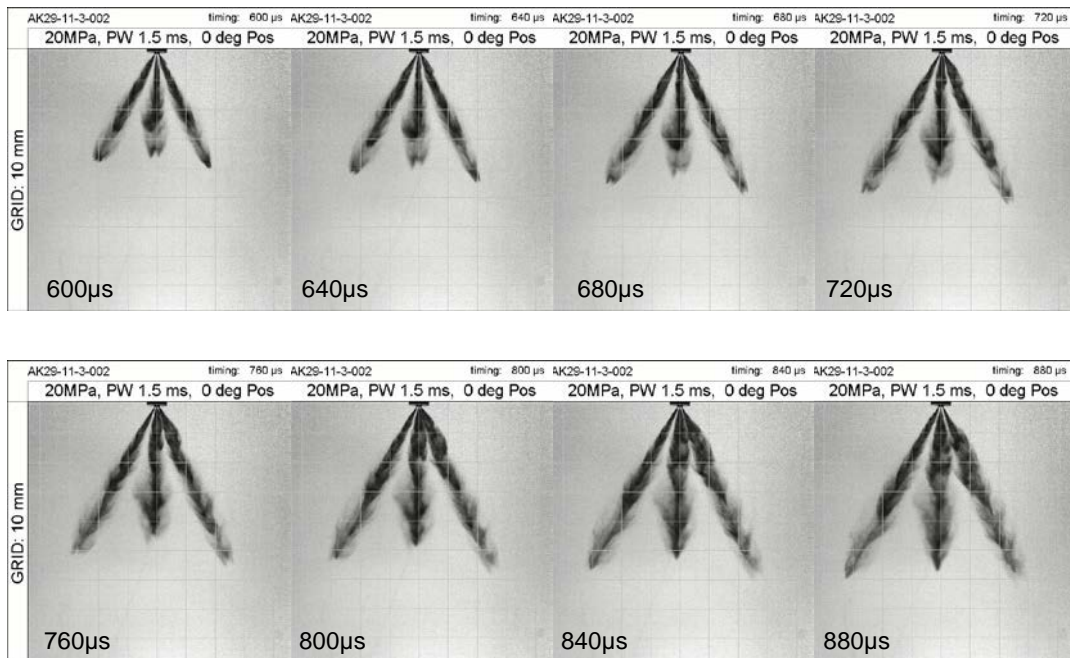
58

AK29-11-3-002: 20MPa, 90° orientation



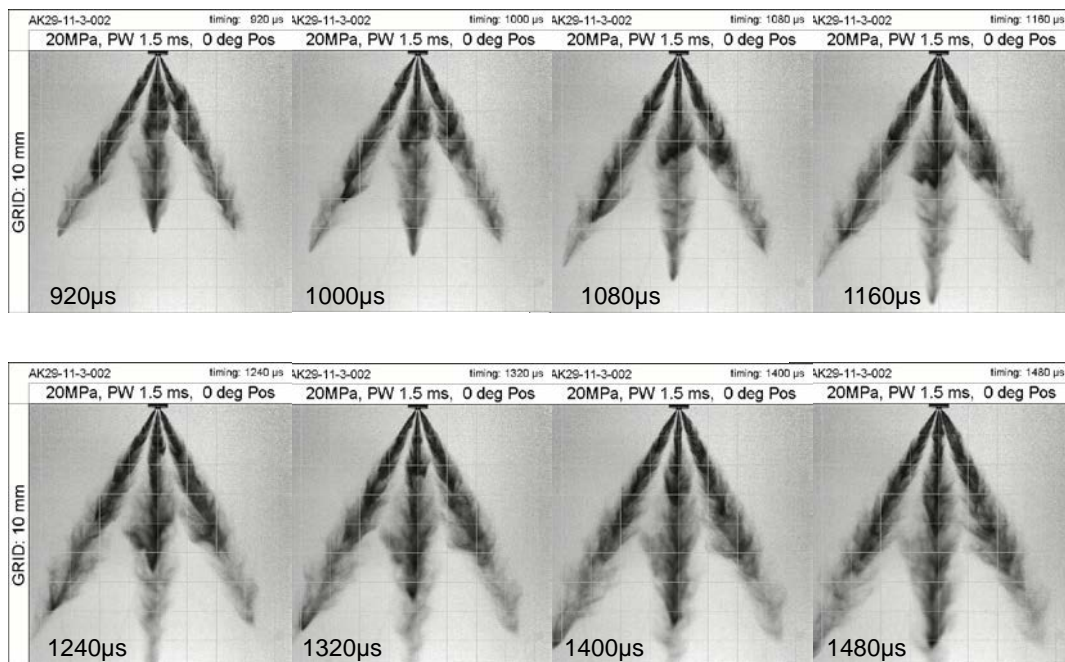
59

AK29-11-3-002: 20MPa, 90° orientation



60

AK29-11-3-002: 20MPa, 90° orientation



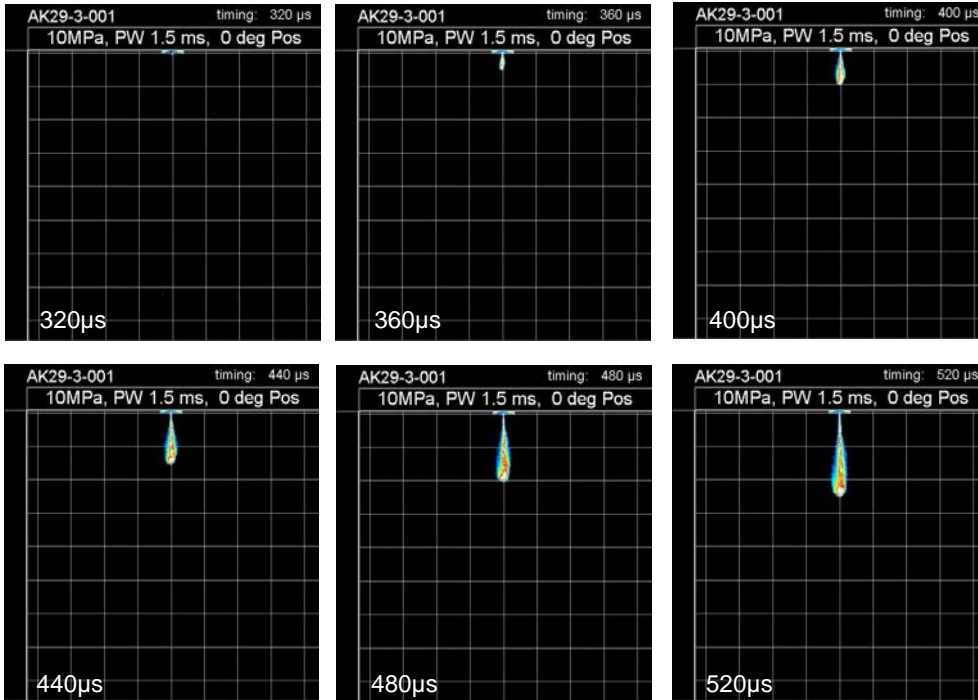
APPENDIX F MIE SCATTER IMAGES, SIDE VIEW

High speed Mie Imaging (408 images) of Spray plumes from side view, Luxembourg Spray lab

Image #	Seat #	d (mm)	β	l/d	(l+L)/d	D/d	Inj. Pres.	View Angle	Mie Scatter Time Images (μ s)
1-6	AK29-3-001	≈ 20	0°	1.1	na	na	10MPa	0°	320,360,400,440,470,520
7-12	AK29-3-001	≈ 20	0°	1.1	na	na	10MPa	0°	560,600,640,680,720,760
13-18	AK29-3-001	≈ 20	0°	1.1	na	na	10MPa	0°	800,840,880,920,960,1000
19-24	AK29-3-001	≈ 20	0°	1.1	na	na	10MPa	0°	1040,1080,1120,1160,1200,1240
1-6	AK29-3-001	≈ 20	0°	1.1	na	na	20MPa	0°	280,320,360,400,440,480
7-12	AK29-3-001	≈ 20	0°	1.1	na	na	20MPa	0°	520,560,600,640,680,720
13-18	AK29-3-001	≈ 20	0°	1.1	na	na	20MPa	0°	760,800,840,880,920,960
19-24	AK29-3-001	≈ 20	0°	1.1	na	na	20MPa	0°	1000,1040,1080,1120,1160,1200
1-6	AK29-3-002	≈ 20	0°	1.1	na	na	10MPa	0°	320,360,400,440,470,520
7-12	AK29-3-002	≈ 20	0°	1.1	na	na	10MPa	0°	560,600,640,680,720,760
13-18	AK29-3-002	≈ 20	0°	1.1	na	na	10MPa	0°	800,840,880,920,960,1000
19-24	AK29-3-002	≈ 20	0°	1.1	na	na	10MPa	0°	1040,1080,1120,1160,1200,1240
1-6	AK29-3-002	≈ 20	0°	1.1	na	na	20MPa	0°	280,320,360,400,440,480
7-12	AK29-3-002	≈ 20	0°	1.1	na	na	20MPa	0°	520,560,600,640,680,720
13-18	AK29-3-002	≈ 20	0°	1.1	na	na	20MPa	0°	760,800,840,880,920,960
19-24	AK29-3-002	≈ 20	0°	1.1	na	na	20MPa	0°	1000,1040,1080,1120,1160,1200
1-6	AK29-6-002	≈ 15	0°	1.1	na	na	10MPa	0°	320,360,400,440,470,520
7-12	AK29-6-002	≈ 15	0°	1.1	na	na	10MPa	0°	560,600,640,680,720,760
13-18	AK29-6-002	≈ 15	0°	1.1	na	na	10MPa	0°	800,840,880,920,960,1000
19-24	AK29-6-002	≈ 15	0°	1.1	na	na	10MPa	0°	1040,1080,1120,1160,1200,1240
1-6	AK29-6-002	≈ 15	0°	1.1	na	na	20MPa	0°	240,280,320,360,400,440
7-12	AK29-6-002	≈ 15	0°	1.1	na	na	20MPa	0°	480,520,560,600,640,680
13-18	AK29-6-002	≈ 15	0°	1.1	na	na	20MPa	0°	720,760,800,840,880,920
19-24	AK29-6-002	≈ 15	0°	1.1	na	na	20MPa	0°	960,1000,1040,1080,1120,1160
1-8	AK29-9-001	≈ 20	30°	1.1	na	na	10MPa	0°	320,360,400,440,470,520,560,600
9-16	AK29-9-001	≈ 20	30°	1.1	na	na	10MPa	0°	640,680,720,760,800,840,880,920
17-24	AK29-9-001	≈ 20	30°	1.1	na	na	10MPa	0°	1000,1080,1160,1240,1320,1400,1480,1560
1-8	AK29-9-001	≈ 20	30°	1.1	na	na	10MPa	90°	320,360,400,440,470,520,560,600
9-16	AK29-9-001	≈ 20	30°	1.1	na	na	10MPa	90°	640,680,720,760,800,840,880,920
17-24	AK29-9-001	≈ 20	30°	1.1	na	na	10MPa	90°	1000,1080,1160,1240,1320,1400,1480,1560
1-8	AK29-9-001	≈ 20	30°	1.1	na	na	20MPa	0°	280,320,360,400,440,480,520,560
9-16	AK29-9-001	≈ 20	30°	1.1	na	na	20MPa	0°	600,640,680,720,760,800,840,880
17-24	AK29-9-001	≈ 20	30°	1.1	na	na	20MPa	0°	920,1000,1080,1160,1240,1320,1400,1480
1-8	AK29-9-001	≈ 20	30°	1.1	na	na	20MPa	90°	280,320,360,400,440,480,520,560
9-16	AK29-9-001	≈ 20	30°	1.1	na	na	20MPa	90°	600,640,680,720,760,800,840,880
17-24	AK29-9-001	≈ 20	30°	1.1	na	na	20MPa	90°	920,1000,1080,1160,1240,1320,1400,1480
1-8	AK29-10-3-003	≈ 15	30°	1.1	3.96	2.5	10MPa	0°	320,340,400,440,480,520,560,600

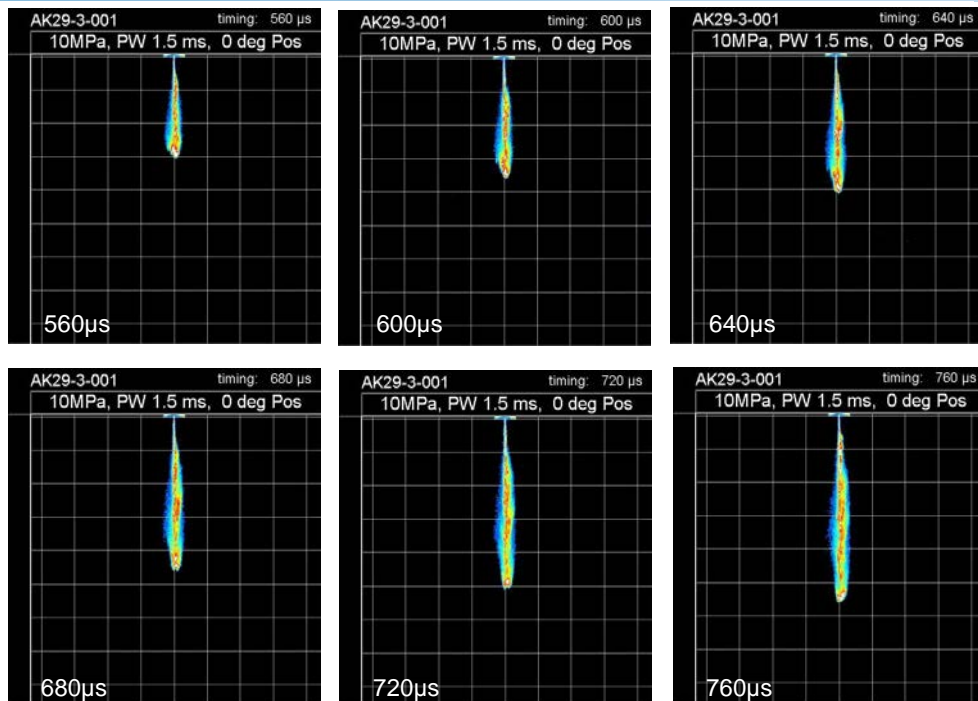
9-16	AK29-10-3-003	≈.15	30°	1.1	3.96	2.5	10MPa	0°	640,680,720,760,800,840,880,920
17-24	AK29-10-3-003	≈.15	30°	1.1	3.96	2.5	10MPa	0°	1000,1080,1160,1240,1320,1400,1480,1560
1-8	AK29-10-3-003	≈.15	30°	1.1	3.96	2.5	10MPa	90°	320,340,400,440,480,520,560,600
9-16	AK29-10-3-003	≈.15	30°	1.1	3.96	2.5	10MPa	90°	640,680,720,760,800,840,880,920
17-24	AK29-10-3-003	≈.15	30°	1.1	3.96	2.5	10MPa	90°	1000,1080,1160,1240,1320,1400,1480,1560
1-8	AK29-10-3-003	≈.15	30°	1.1	3.96	2.5	20MPa	0°	280,320,360,400,440,480,520,560
9-16	AK29-10-3-003	≈.15	30°	1.1	3.96	2.5	20MPa	0°	600,640,680,720,760,800,840,880
17-24	AK29-10-3-003	≈.15	30°	1.1	3.96	2.5	20MPa	0°	920,1000,1080,1160,1240,1320,1400,1480
1-8	AK29-10-3-003	≈.15	30°	1.1	3.96	2.5	20MPa	90°	280,320,360,400,440,480,520,560
9-16	AK29-10-3-003	≈.15	30°	1.1	3.96	2.5	20MPa	90°	600,640,680,720,760,800,840,880
17-24	AK29-10-3-003	≈.15	30°	1.1	3.96	2.5	20MPa	90°	920,1000,1080,1160,1240,1320,1400,1480
1-8	AK29-11-3-002	≈.15	30°	3.96	na	na	10MPa	0°	320,340,400,440,480,520,560,600
9-16	AK29-11-3-002	≈.15	30°	3.96	na	na	10MPa	0°	640,680,720,760,800,840,880,920
17-24	AK29-11-3-002	≈.15	30°	3.96	na	na	10MPa	0°	1000,1080,1160,1240,1320,1400,1480,1560
1-8	AK29-11-3-002	≈.15	30°	3.96	na	na	10MPa	90°	320,340,400,440,480,520,560,600
9-16	AK29-11-3-002	≈.15	30°	3.96	na	na	10MPa	90°	640,680,720,760,800,840,880,920
17-24	AK29-11-3-002	≈.15	30°	3.96	na	na	10MPa	90°	1000,1080,1160,1240,1320,1400,1480,1560
1-8	AK29-11-3-002	≈.15	30°	3.96	na	na	20MPa	0°	280,320,360,400,440,480,520,560
9-16	AK29-11-3-002	≈.15	30°	3.96	na	na	20MPa	0°	600,640,680,720,760,800,840,880
17-24	AK29-11-3-002	≈.15	30°	3.96	na	na	20MPa	0°	920,1000,1080,1160,1240,1320,1400,1480
1-8	AK29-11-3-002	≈.15	30°	3.96	na	na	20MPa	90°	280,320,360,400,440,480,520,560
9-16	AK29-11-3-002	≈.15	30°	3.96	na	na	20MPa	90°	600,640,680,720,760,800,840,880
17-24	AK29-11-3-002	≈.15	30°	3.96	na	na	20MPa	90°	920,1000,1080,1160,1240,1320,1400,1480

AK29-3-001 (Mie-Scatter): 10MPa 0° orientation



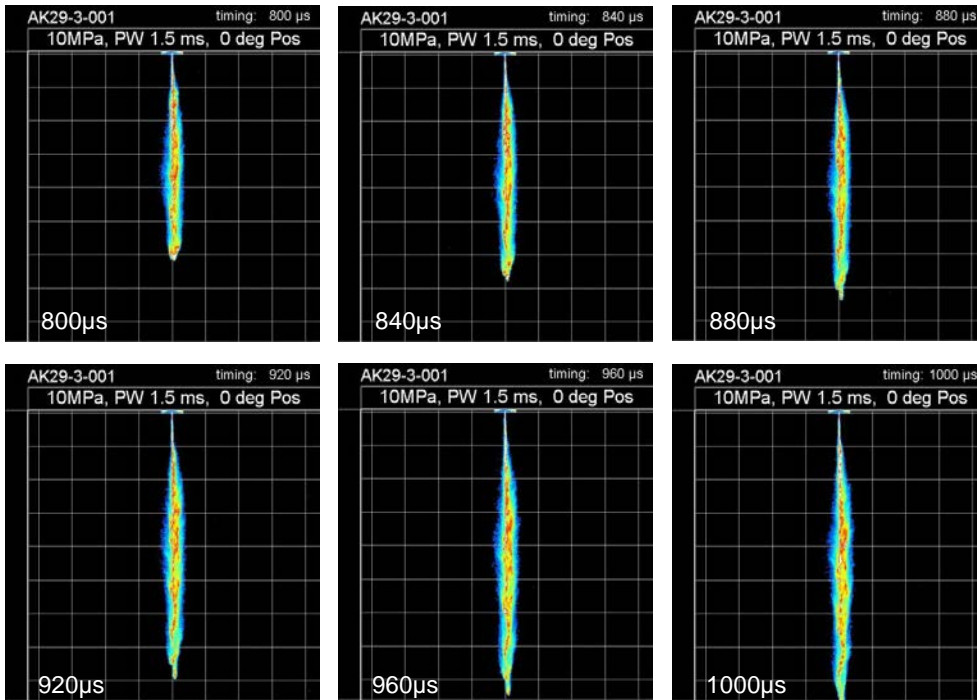
2

AK29-3-001 (Mie-Scatter): 10MPa 0° orientation



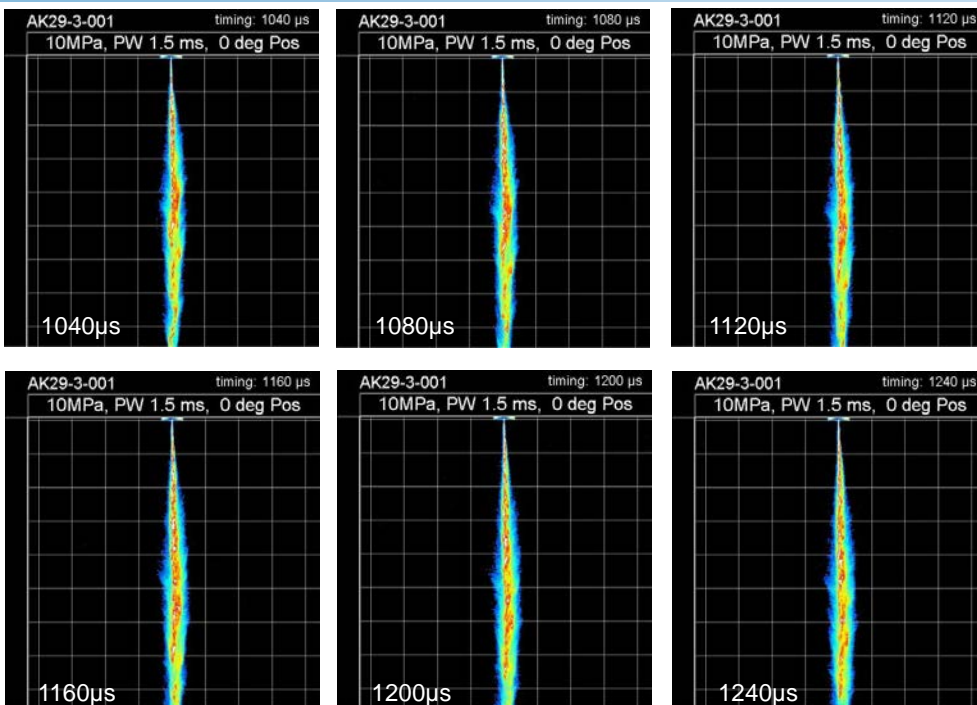
3

AK29-3-001 (Mie-Scatter): 10MPa 0° orientation



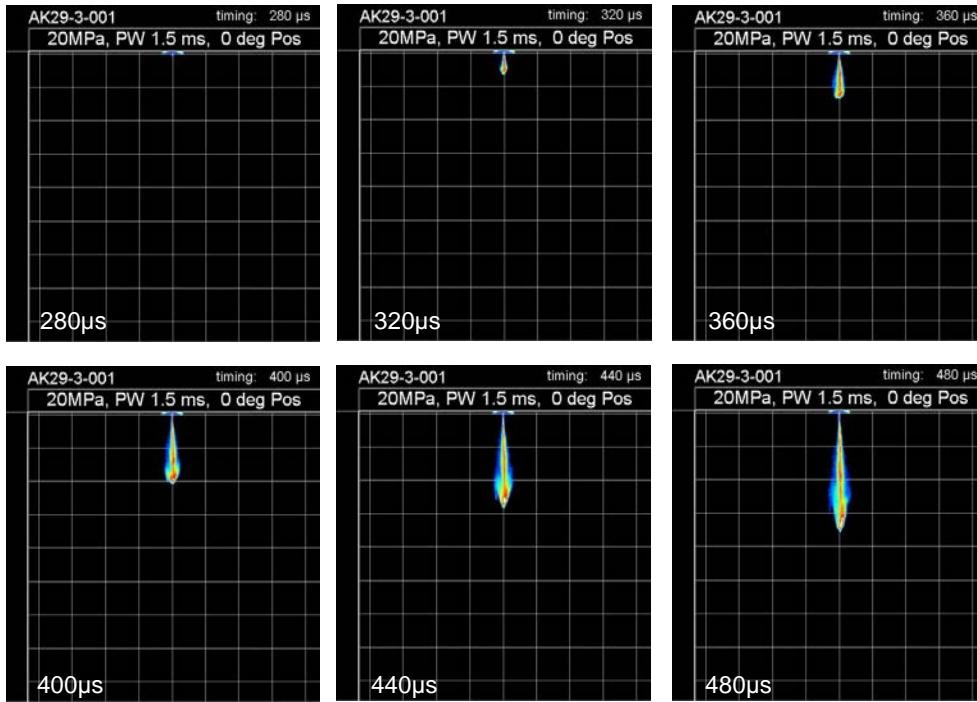
4

AK29-3-001 (Mie-Scatter): 10MPa 0° orientation



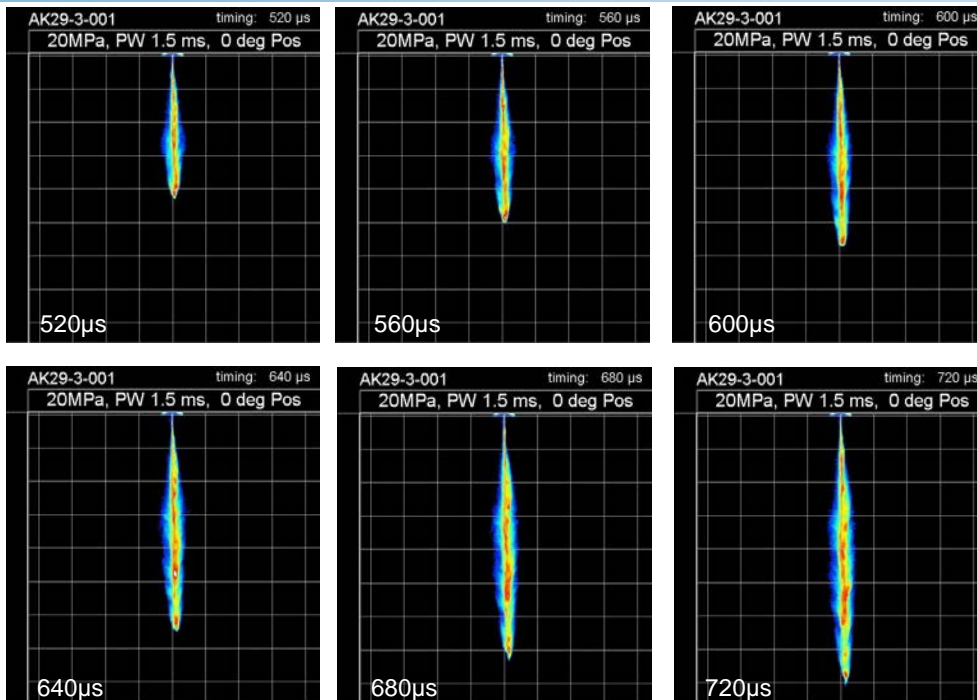
5

AK29-3-001 (Mie-Scatter): 20MPa 0° orientation



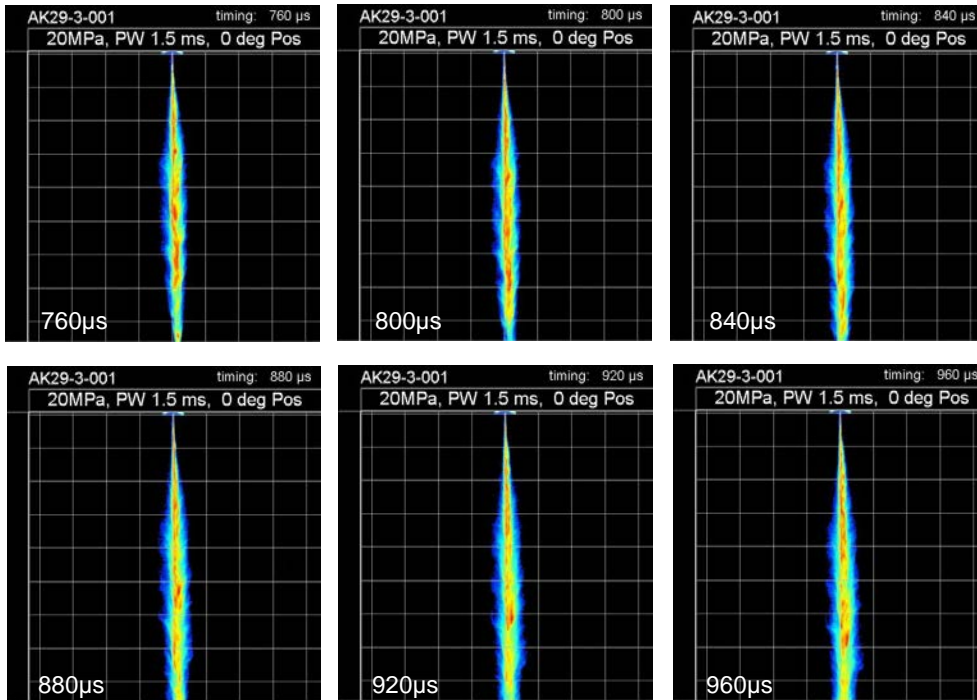
6

AK29-3-001 (Mie-Scatter): 20MPa 0° orientation



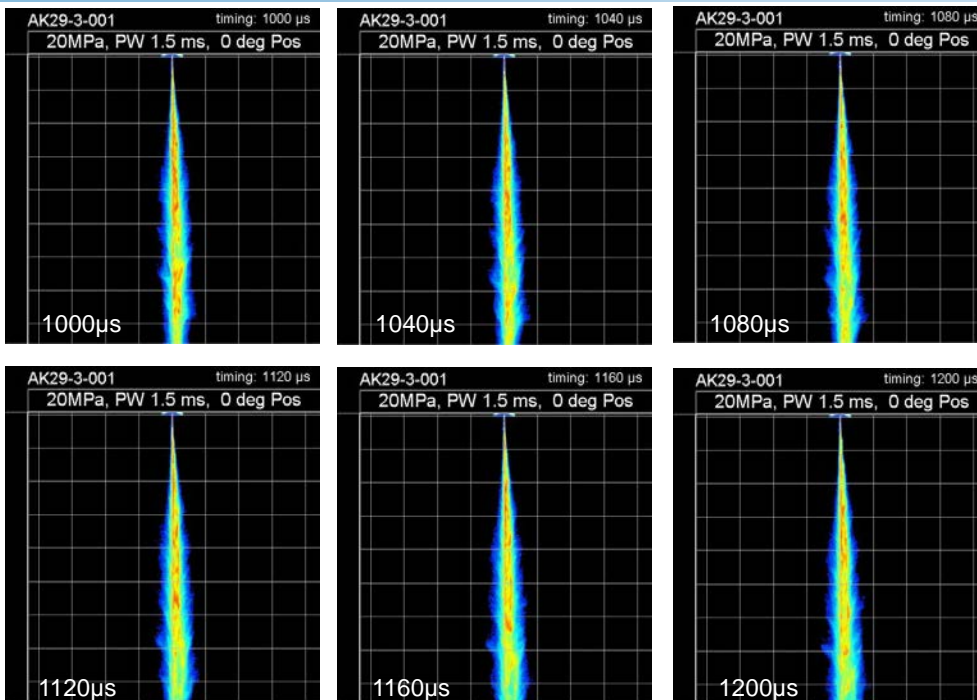
7

AK29-3-001 (Mie-Scatter): 20MPa 0° orientation



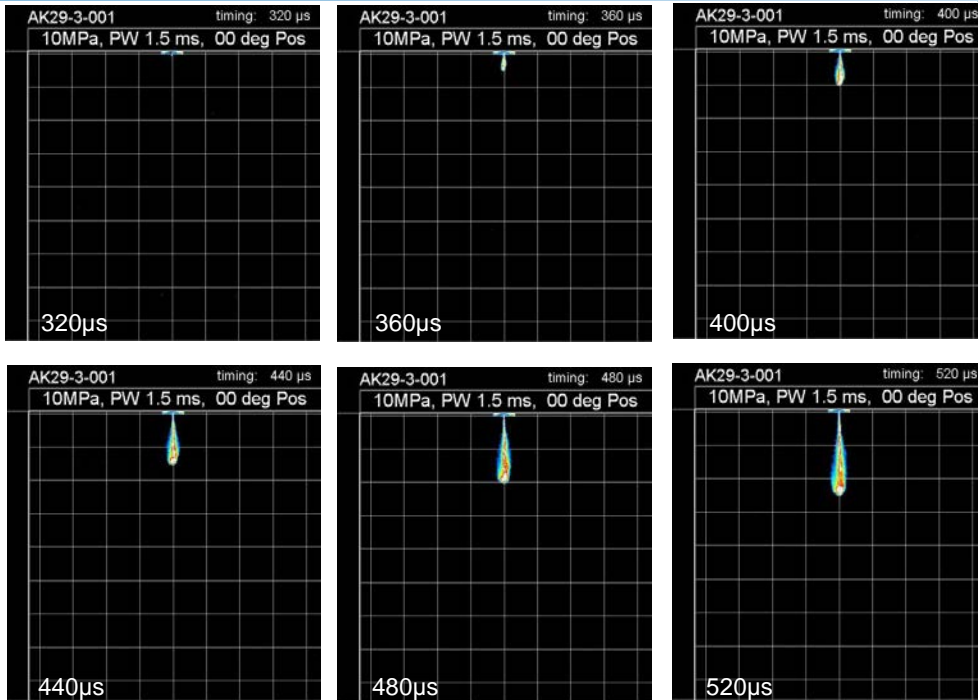
8

AK29-3-001 (Mie-Scatter): 20MPa 0° orientation



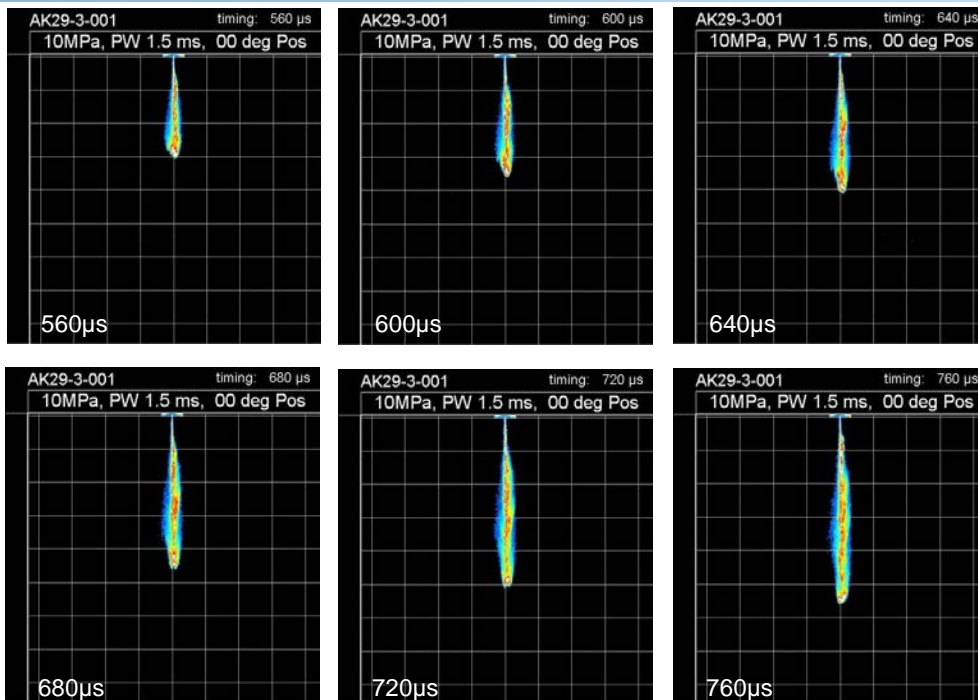
9

AK29-3-002 (Mie-Scatter): 10MPa 0° orientation



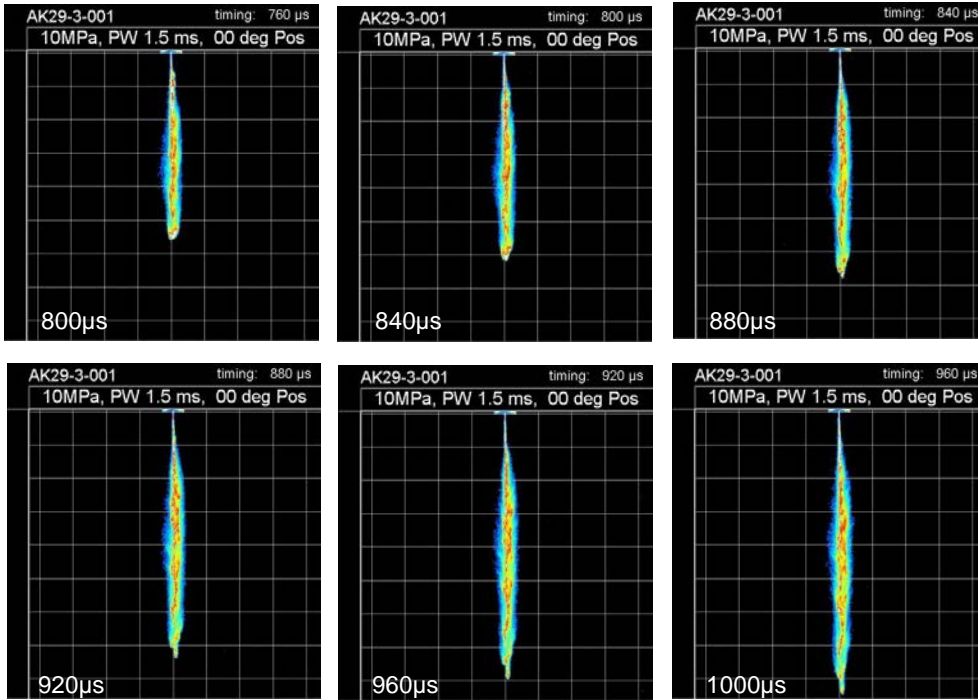
10

AK29-3-002 (Mie-Scatter): 10MPa 0° orientation



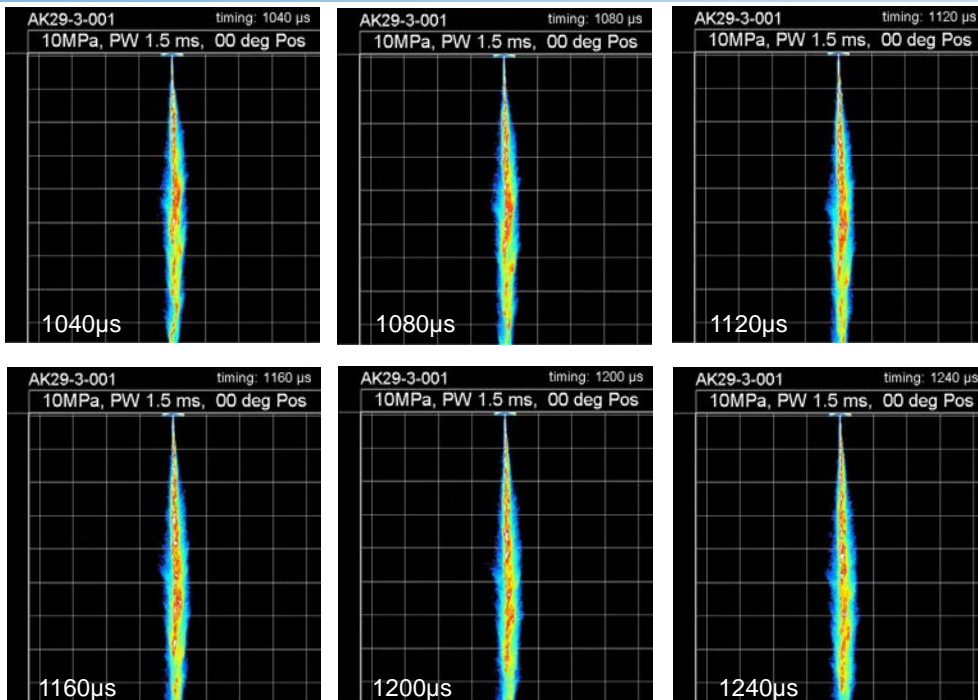
11

AK29-3-001 (Mie-Scatter): 10MPa 0° orientation



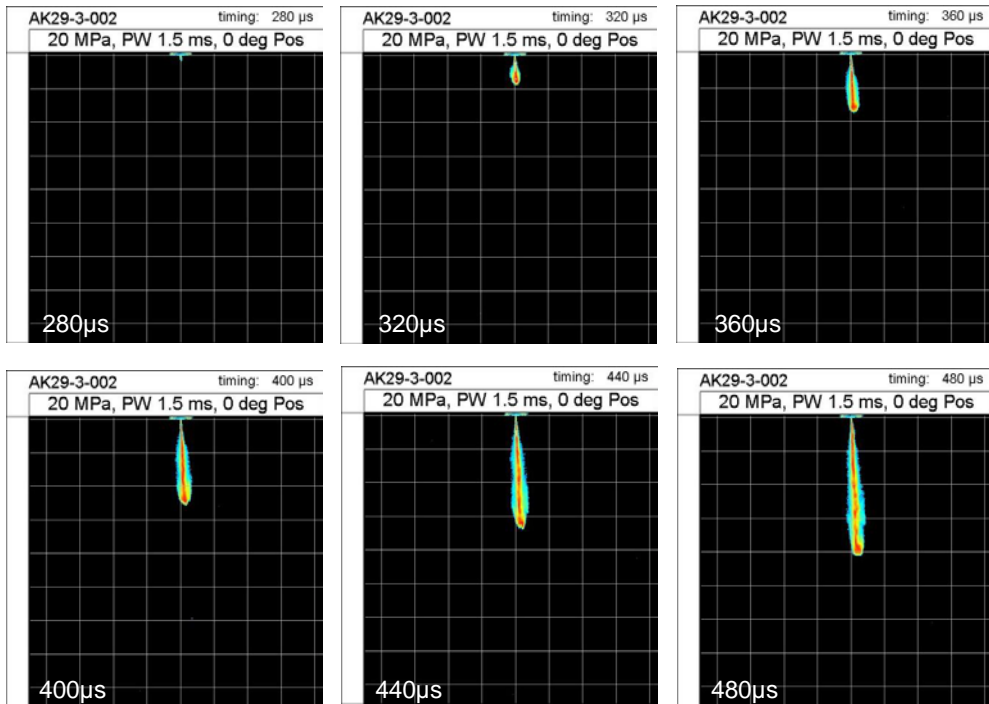
12

AK29-3-002 (Mie-Scatter): 10MPa 0° orientation



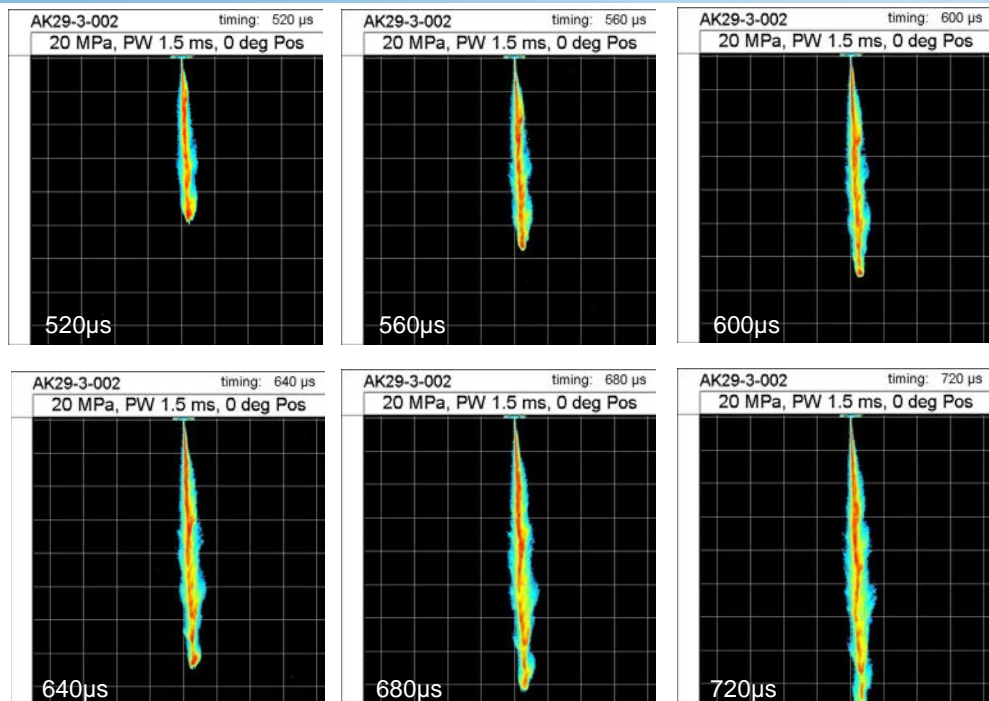
13

AK29-3-002 (Mie-Scatter): 20MPa 0° orientation



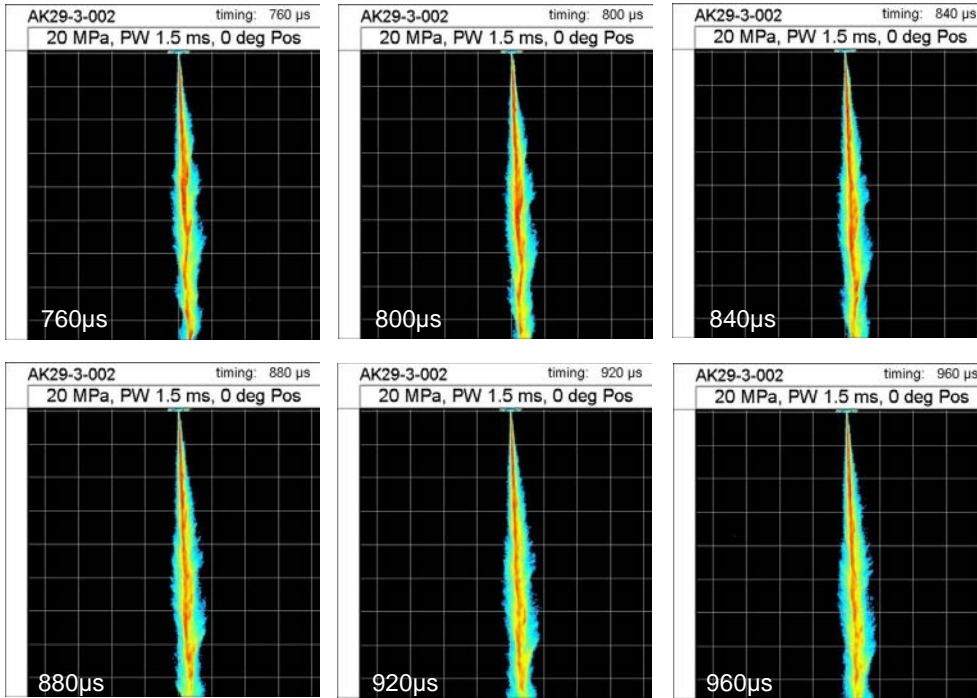
14

AK29-3-002 (Mie-Scatter): 20MPa 0° orientation



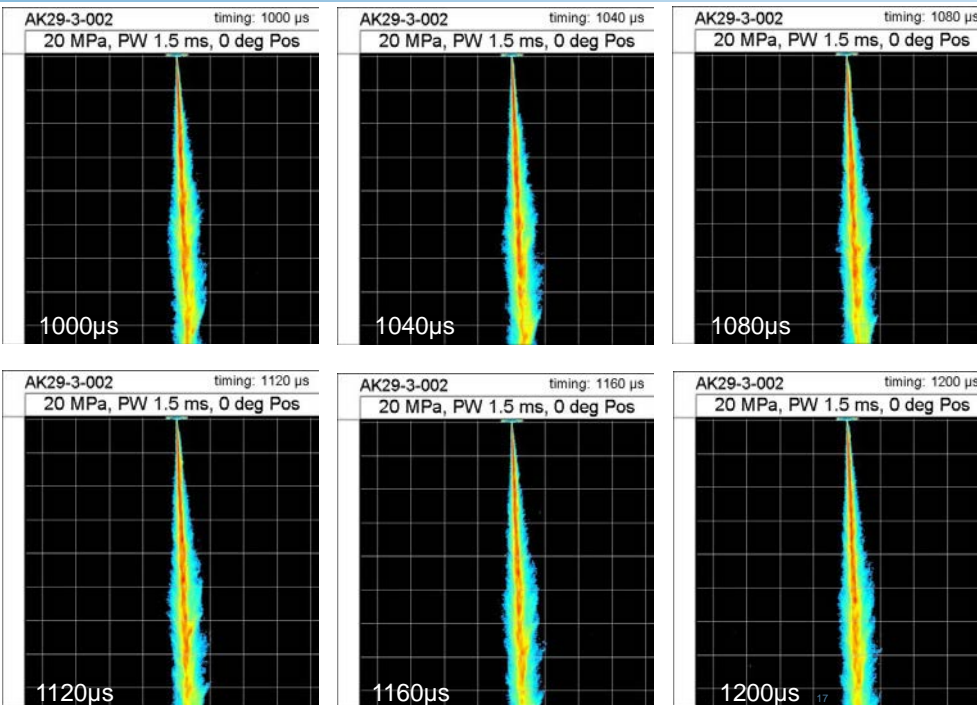
15

AK29-3-002 (Mie-Scatter): 20MPa 0° orientation



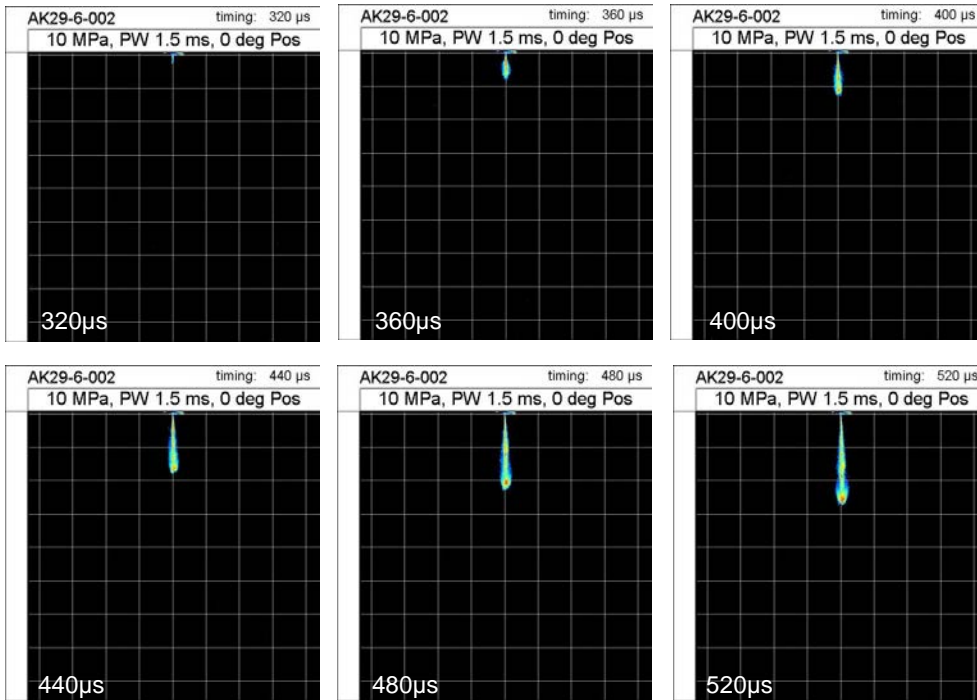
16

AK29-3-002 (Mie-Scatter): 20MPa 0° orientation



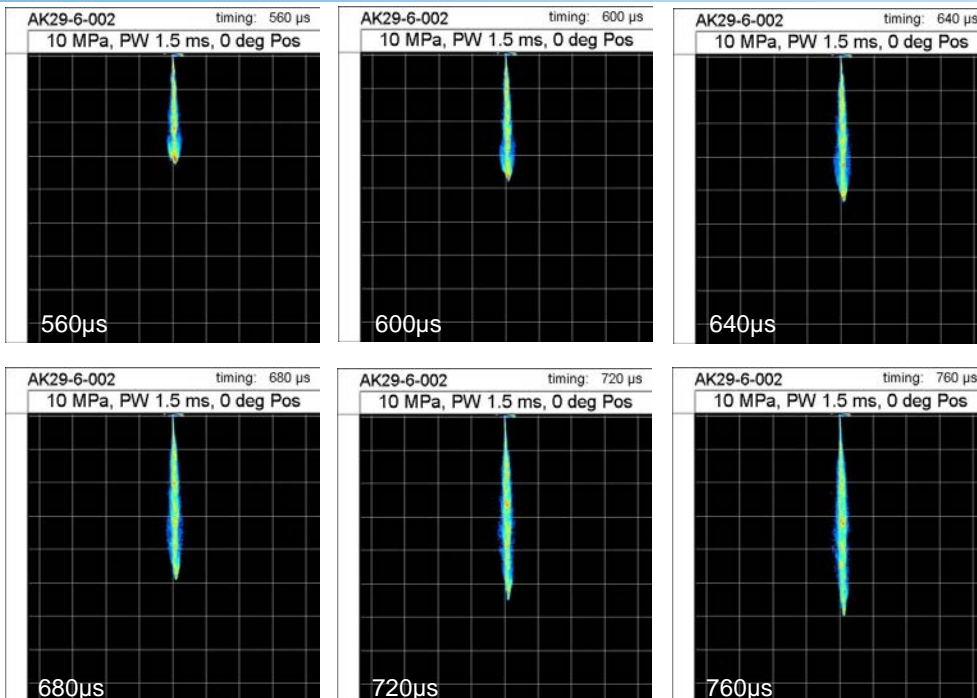
17

AK29-6-002 (Mie-Scatter): 10MPa 0° orientation



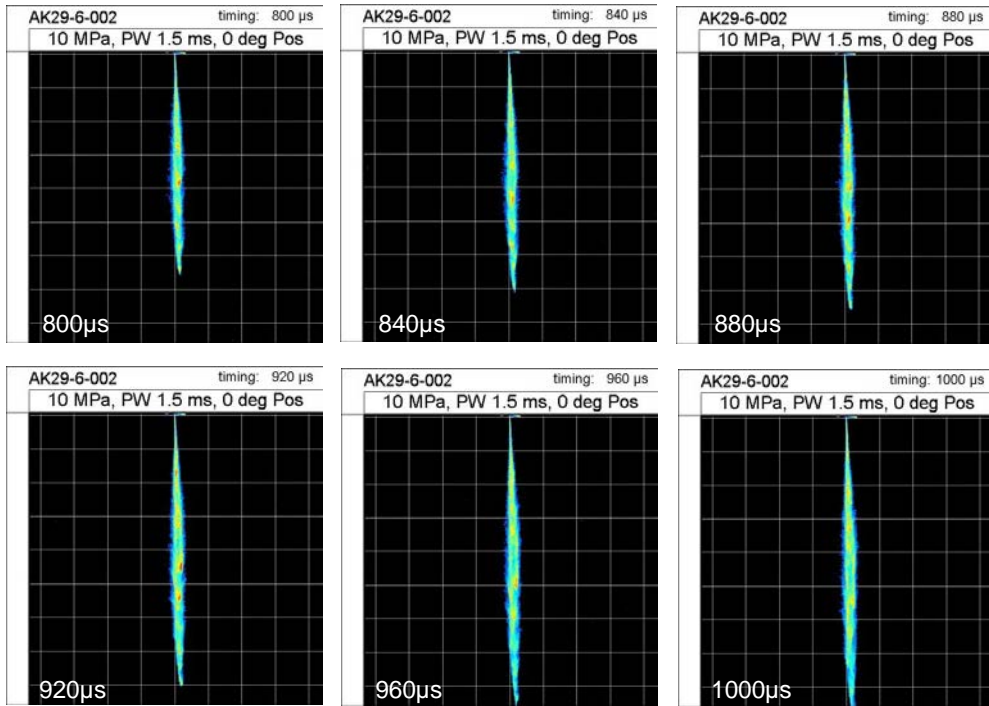
18

AK29-6-002 (Mie-Scatter): 10MPa 0° orientation



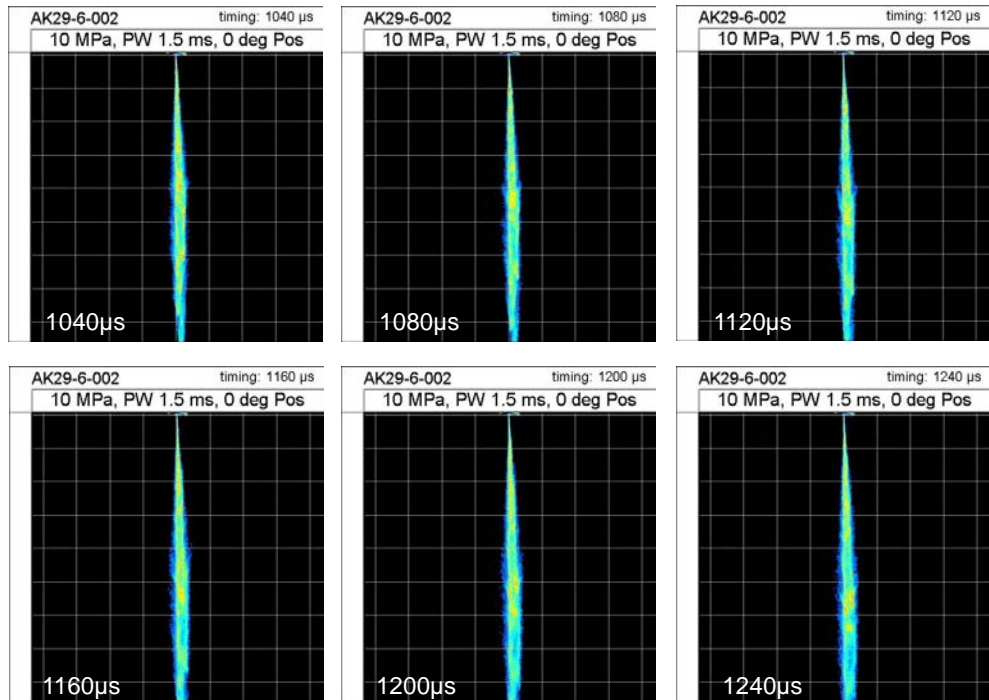
19

AK29-6-002 (Mie-Scatter): 10MPa 0° orientation



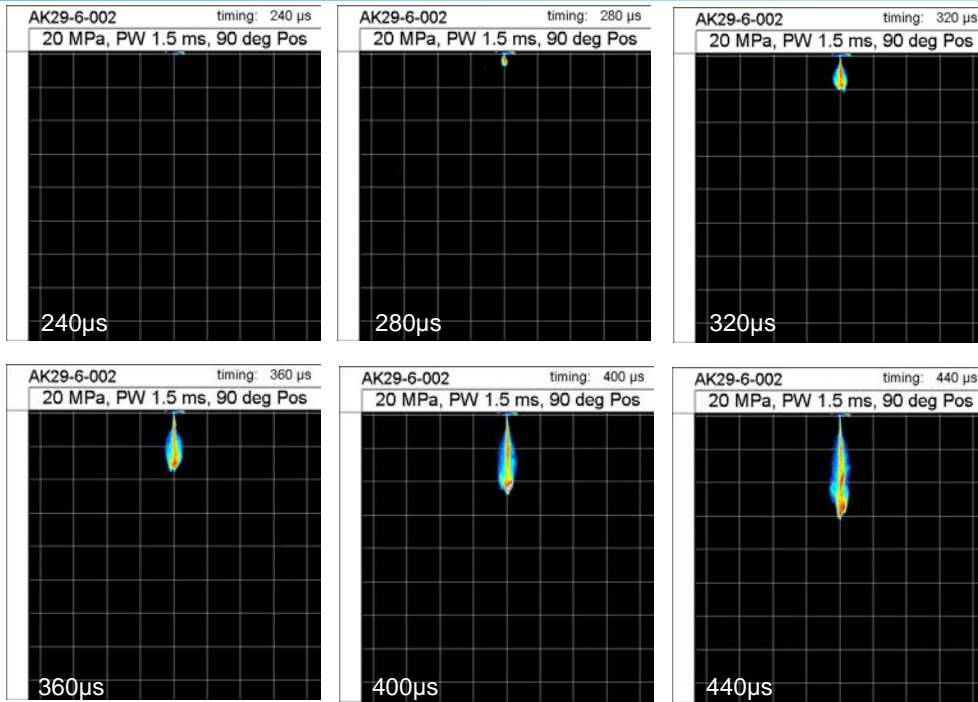
20

AK29-6-002 (Mie-Scatter): 10MPa 0° orientation



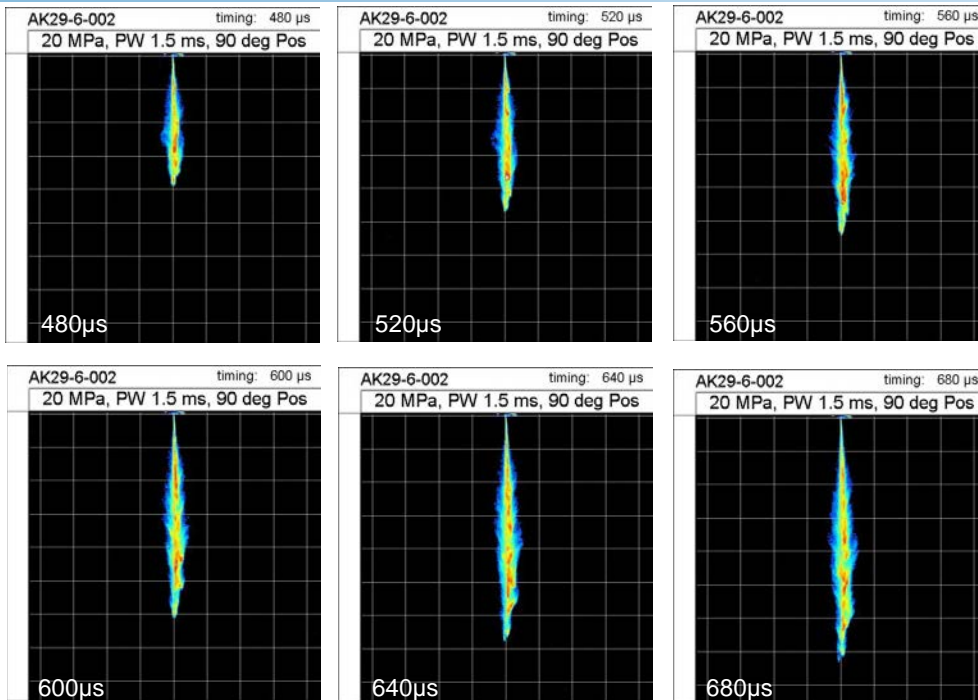
21

AK29-6-002 (Mie-Scatter): 20MPa 0° orientation



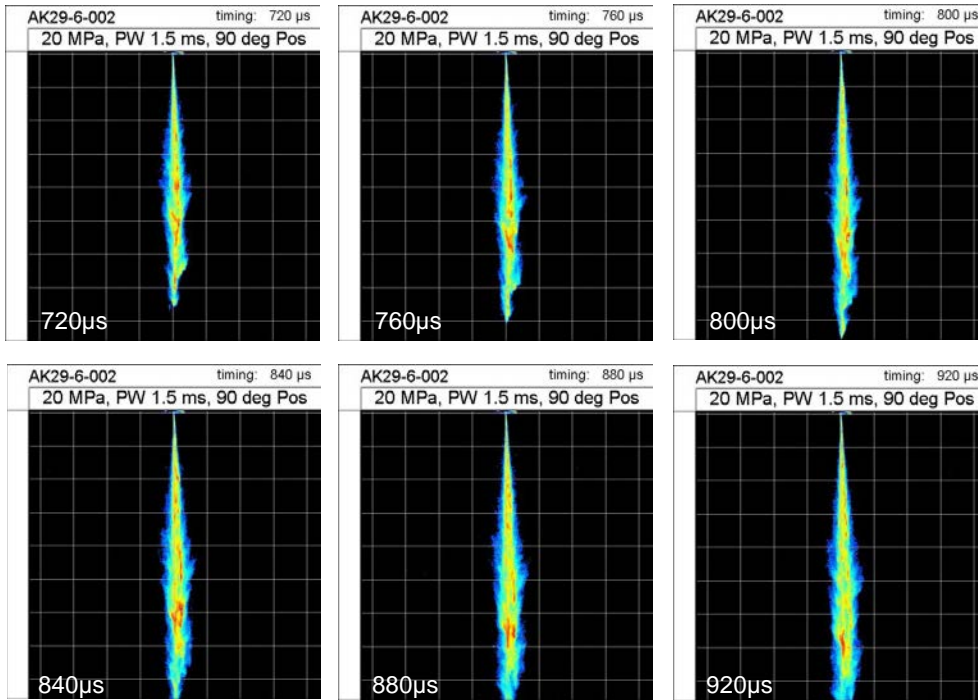
22

AK29-6-002 (Mie-Scatter): 20MPa 0° orientation



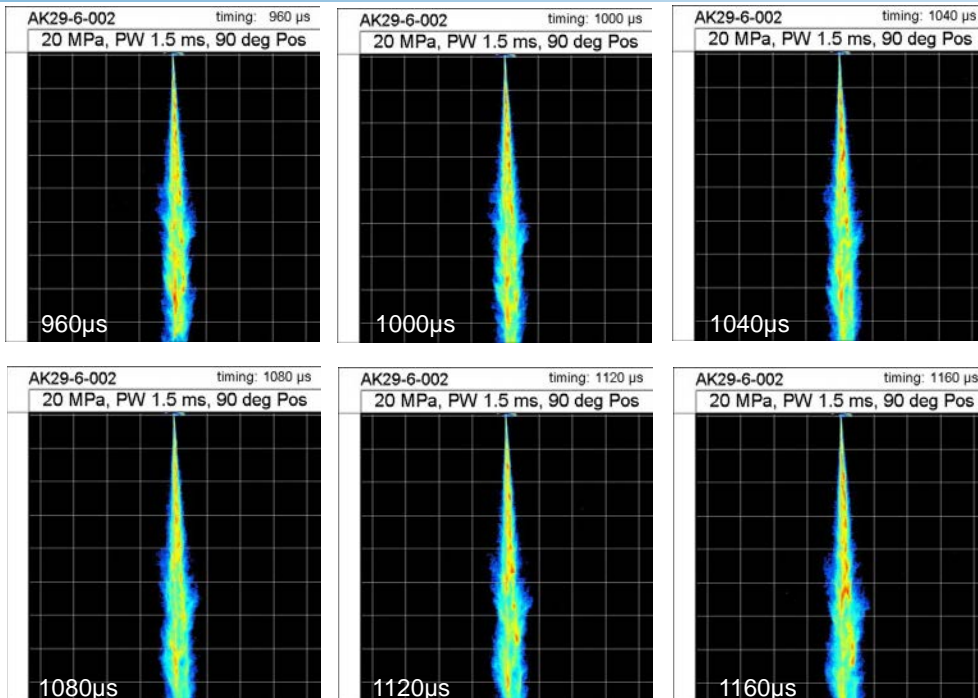
23

AK29-6-002 (Mie-Scatter): 20MPa 0° orientation



24

AK29-6-002 (Mie-Scatter): 20MPa 0° orientation



25

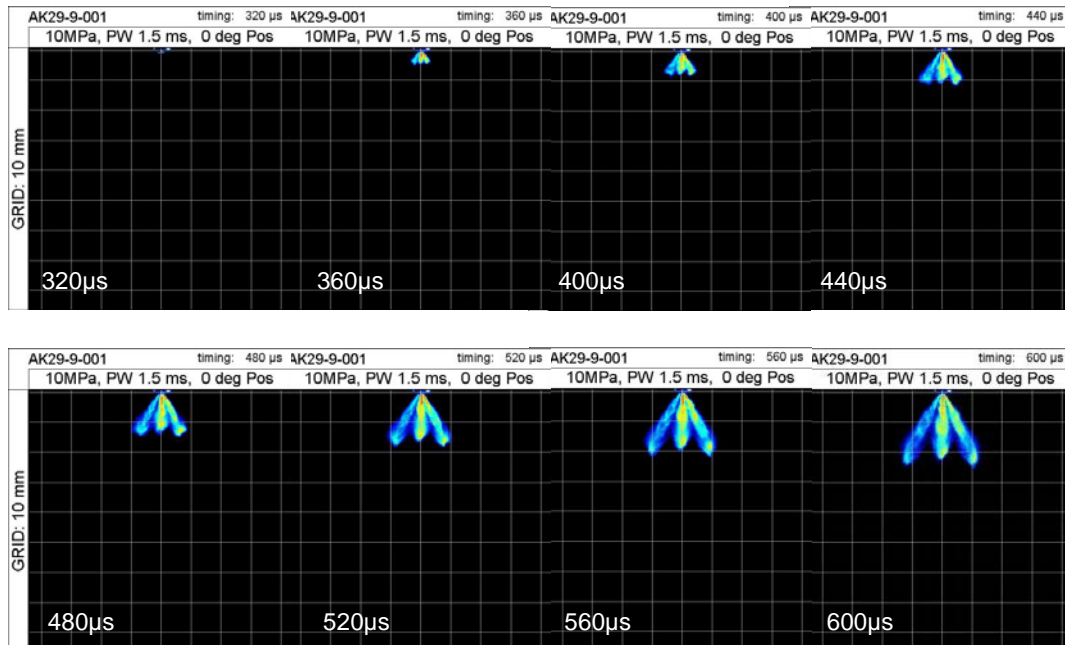
Mie spray images

90° orientation

Mie Scatter spray images for 90 degree orientation show similar behavior, therefore not shown here.

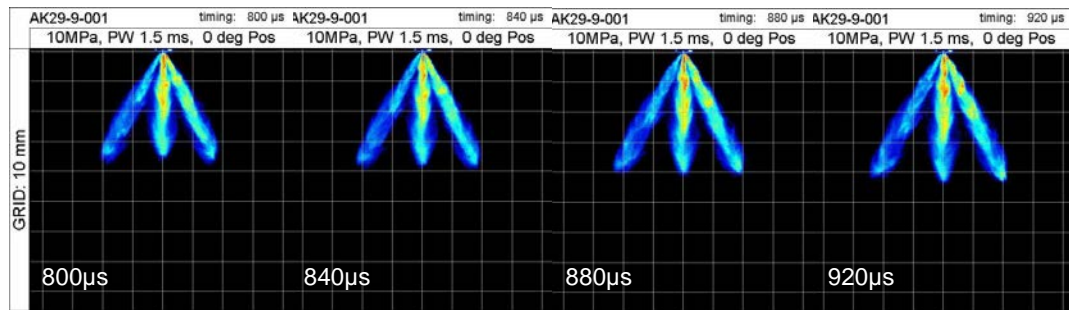
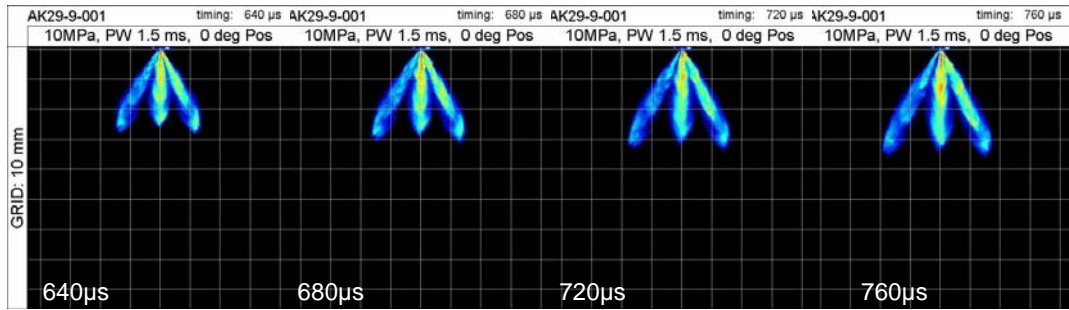
26

AK29-9-001 (Mie-Scatter): 10MPa, 0° orientation



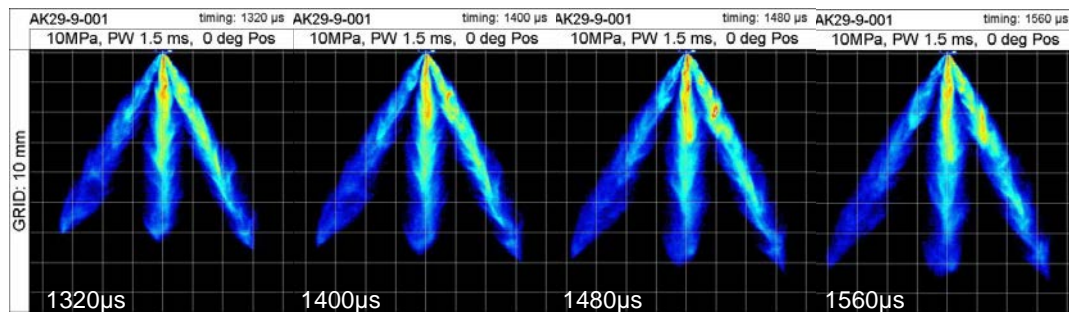
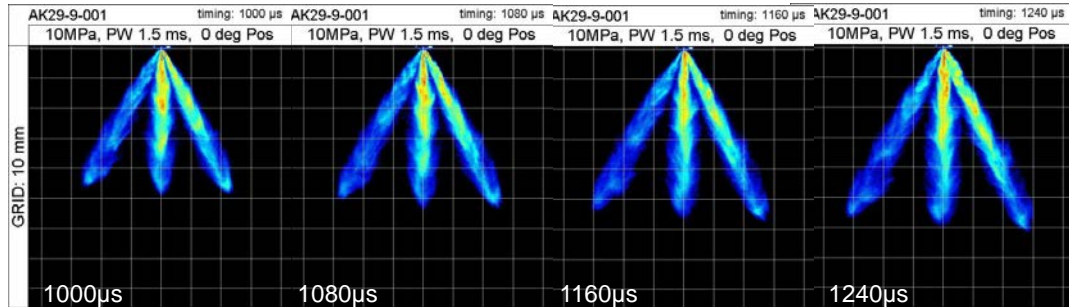
27

AK29-9-001 (Mie-Scatter): 10MPa, 0° orientation



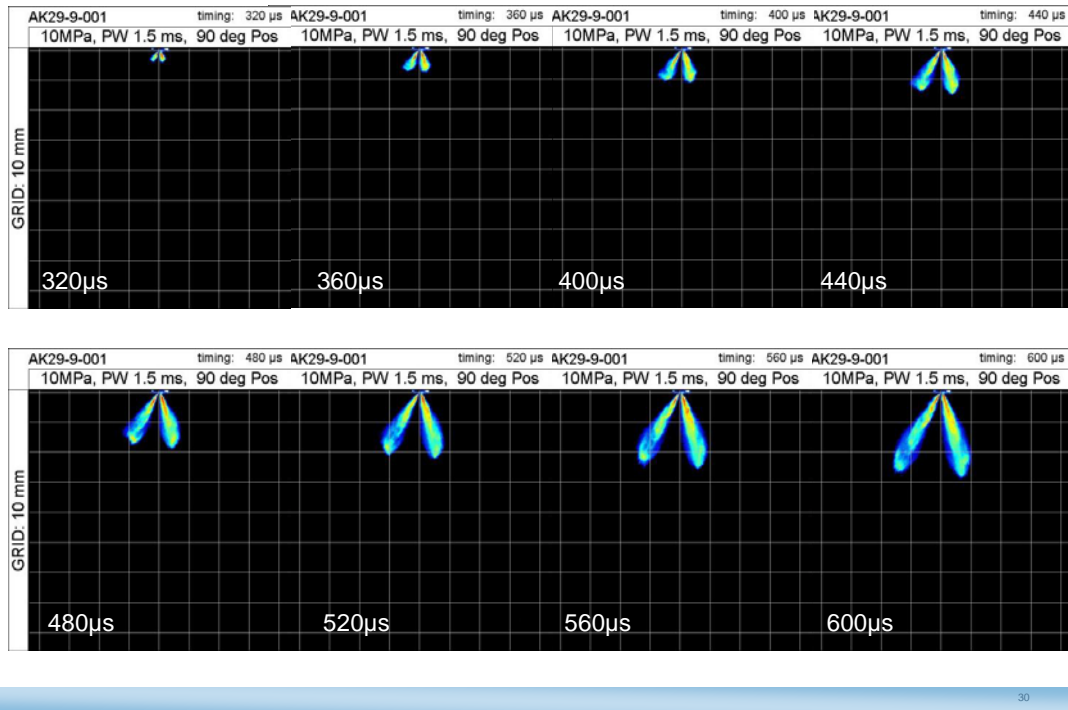
28

AK29-9-001 (Mie-Scatter): 10MPa, 0° orientation

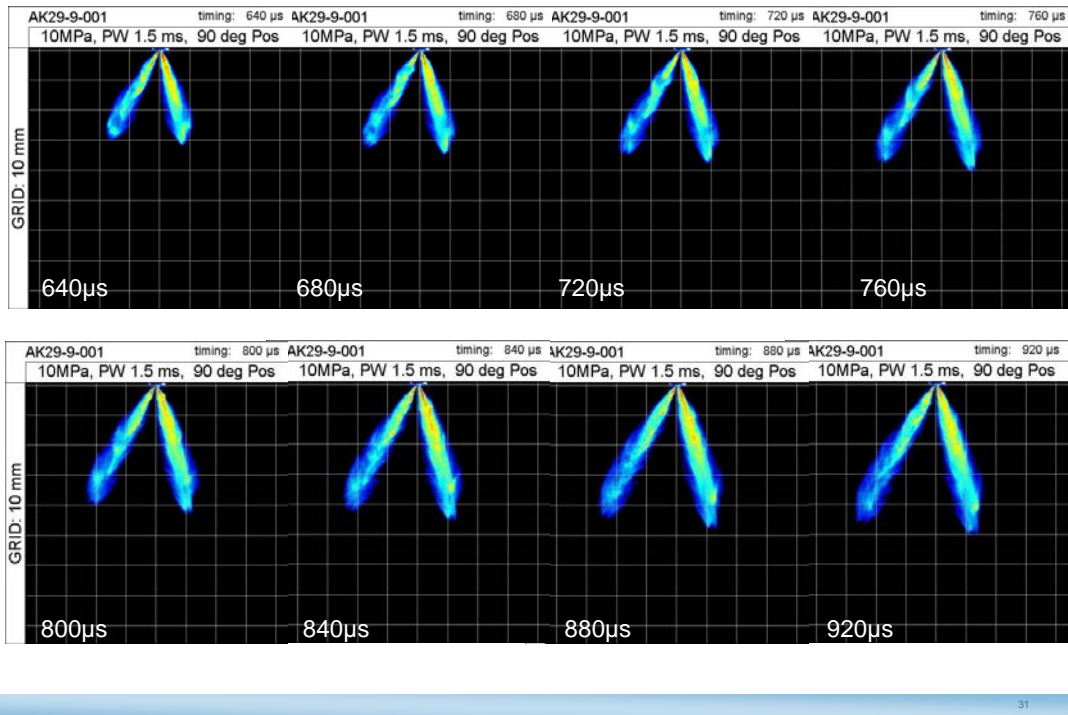


29

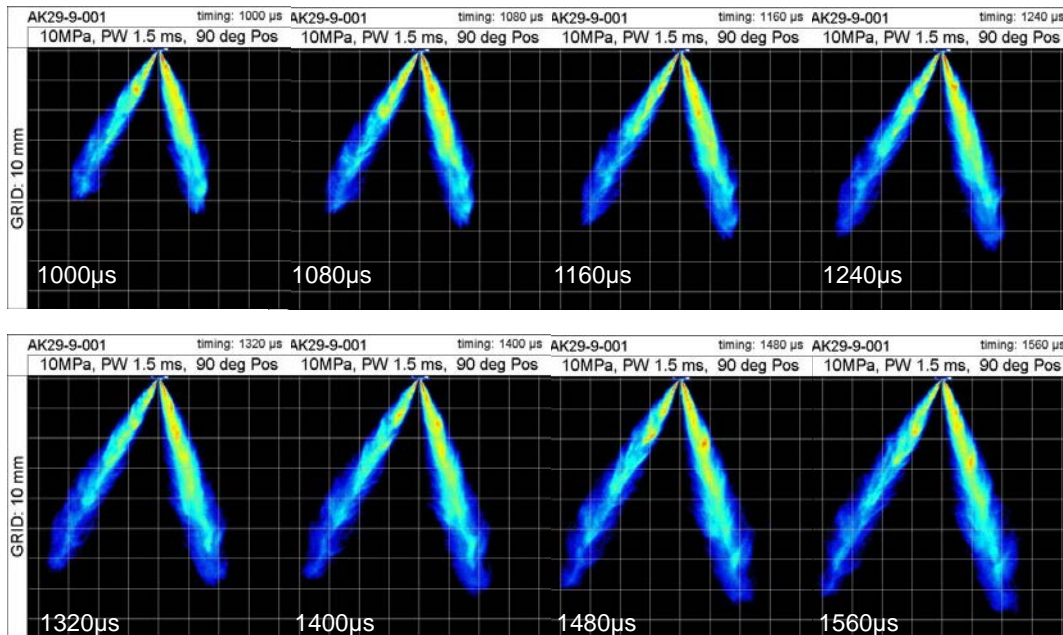
AK29-9-001 (Mie-Scatter): 10MPa, 90° orientation



AK29-9-001 (Mie-Scatter): 10MPa, 90° orientation

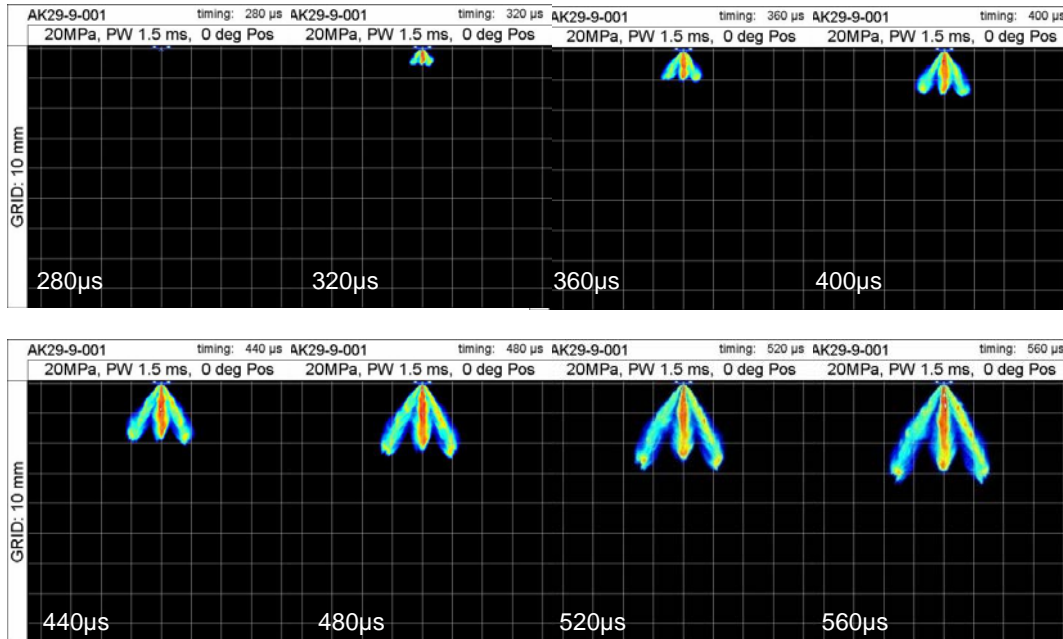


AK29-9-001 (Mie-Scatter): 10MPa, 90° orientation



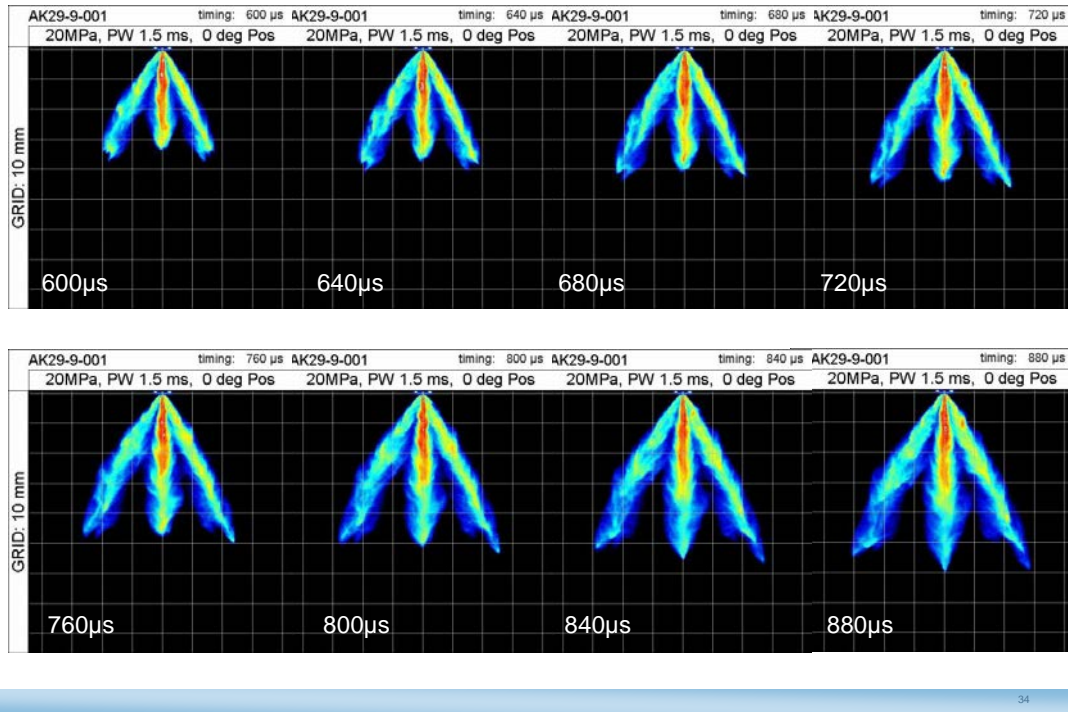
32

AK29-9-001 (Mie-Scatter): 20MPa, 0° orientation

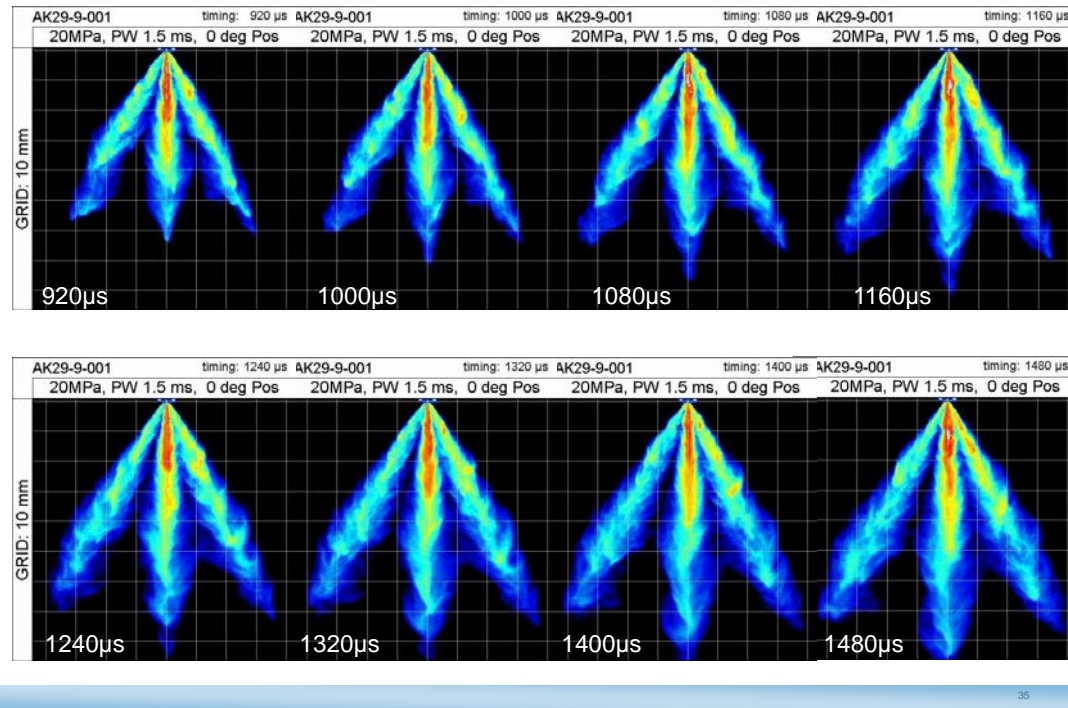


33

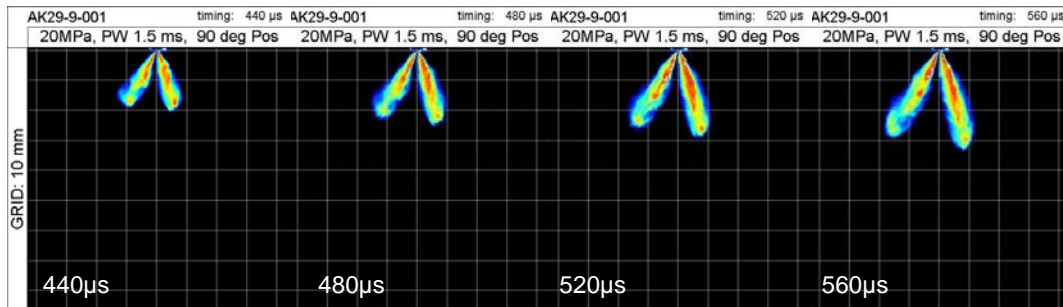
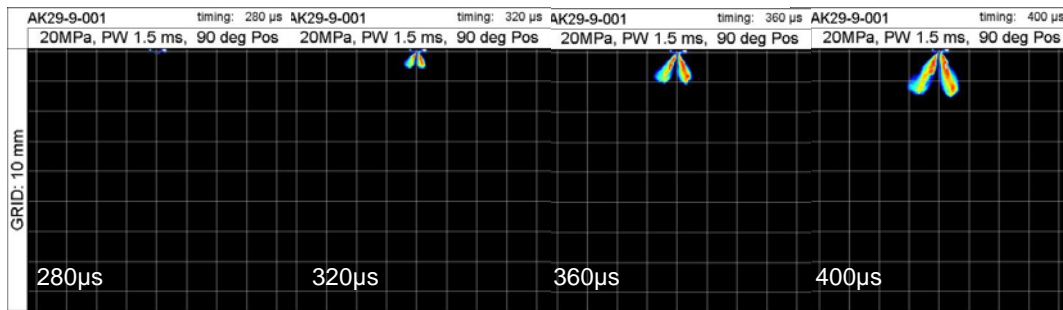
AK29-9-001 (Mie-Scatter): 20MPa, 0° orientation



AK29-9-001 (Mie-Scatter): 20MPa, 0° orientation

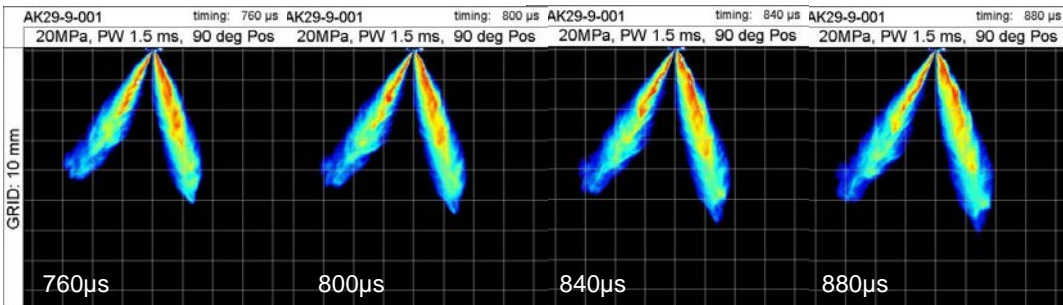
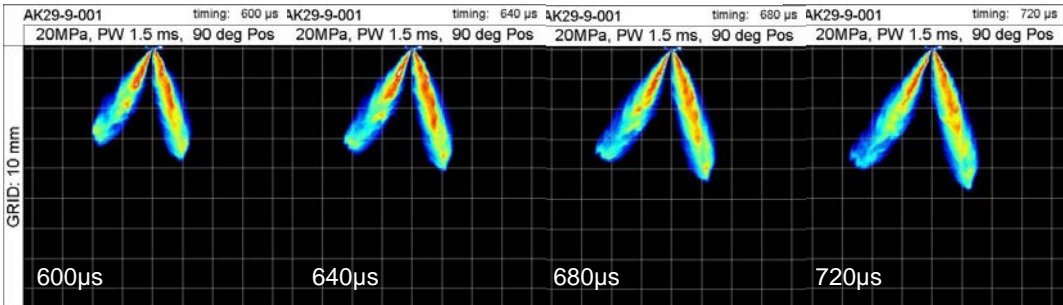


AK29-9-001 (Mie-Scatter): 20MPa, 90° orientation



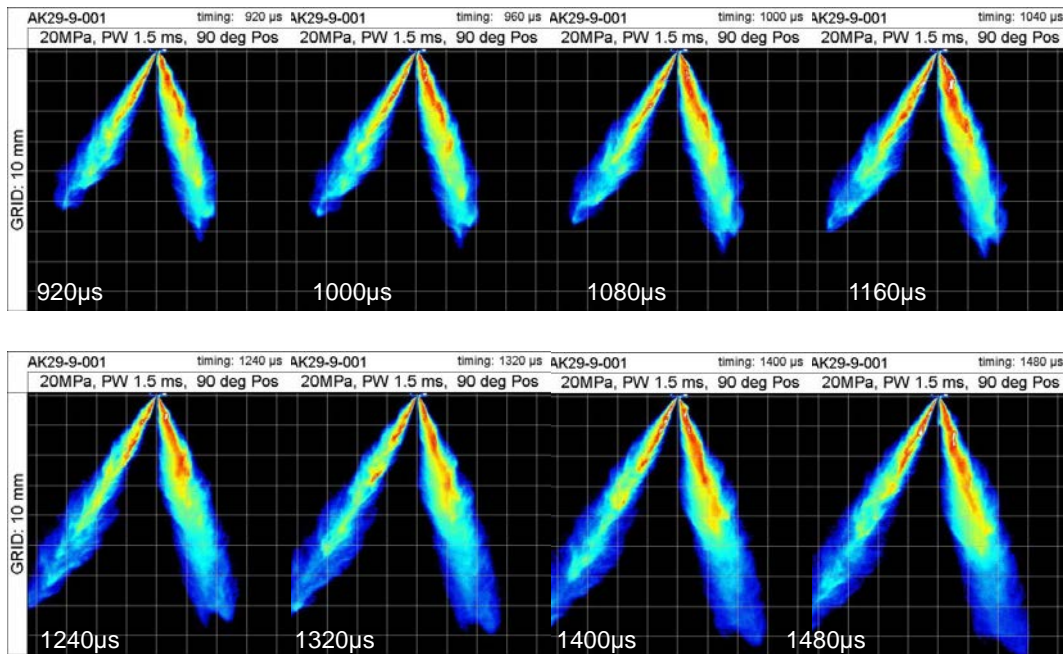
36

AK29-9-001 (Mie-Scatter): 20MPa, 90° orientation



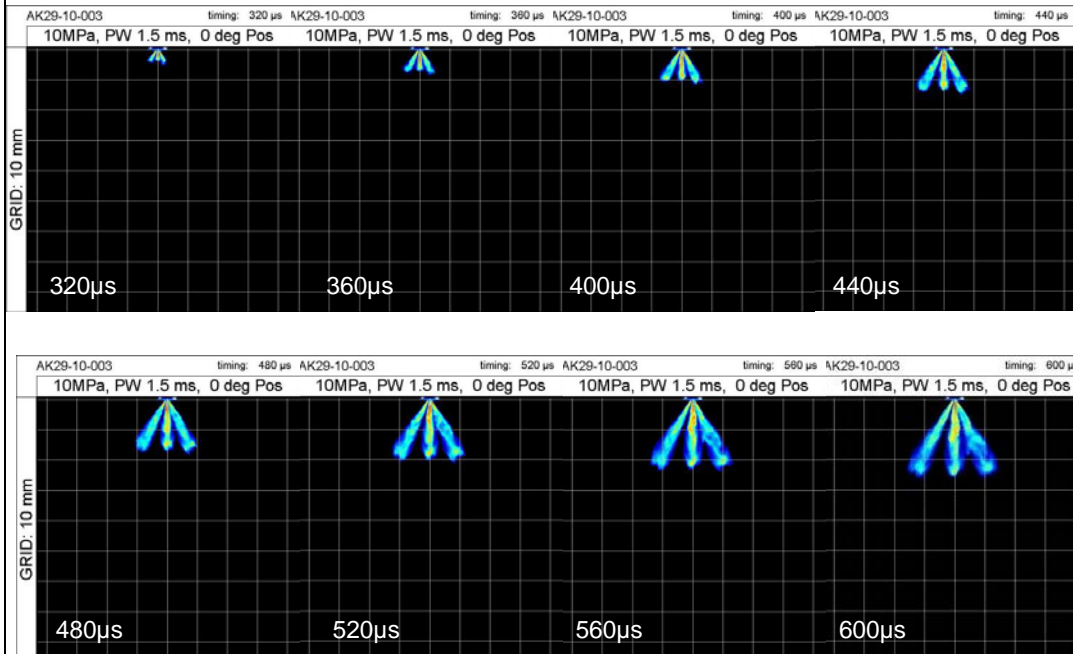
37

AK29-9-001 (Mie-Scatter): 20MPa, 90° orientation



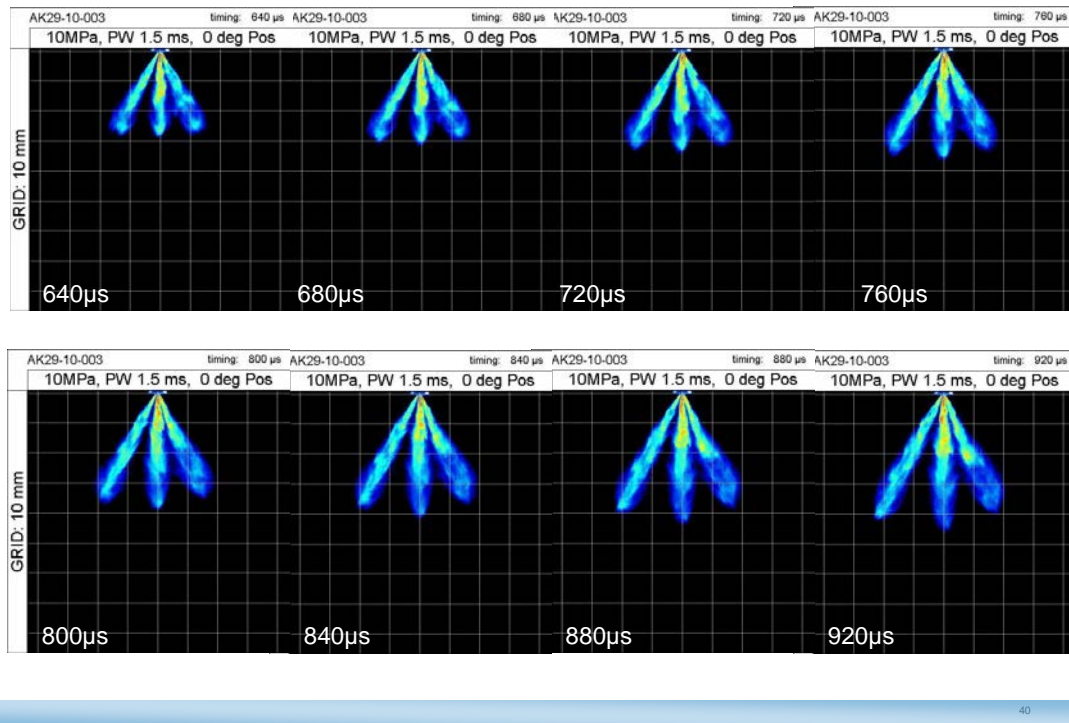
38

AK29-10-003 (Mie-Scatter): 10MPa 0° orientation

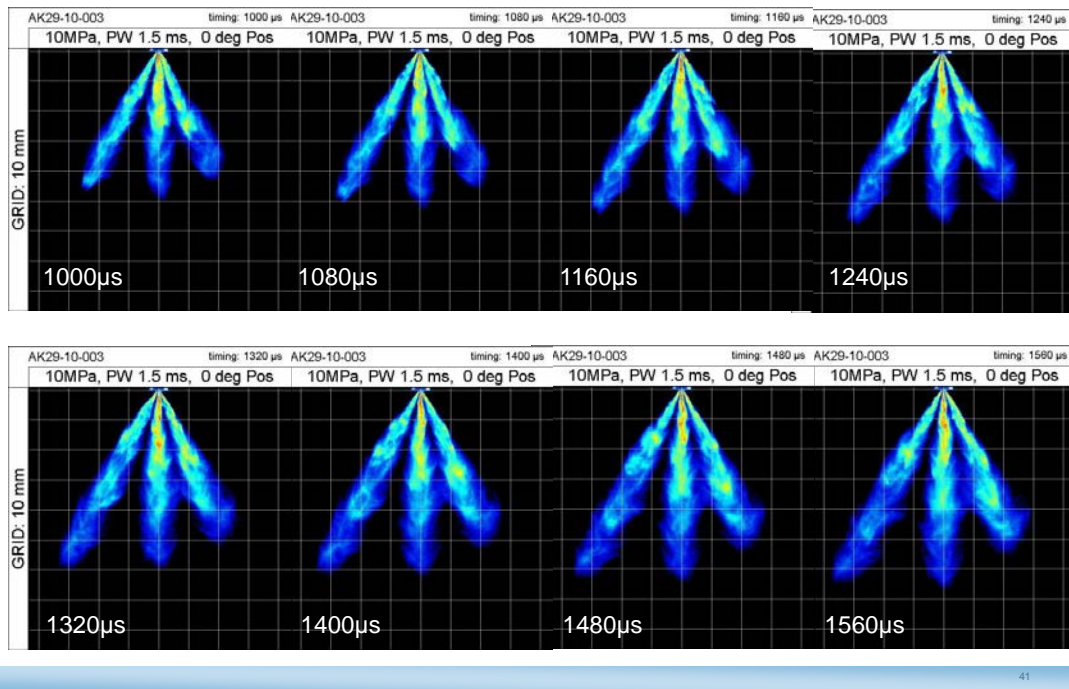


39

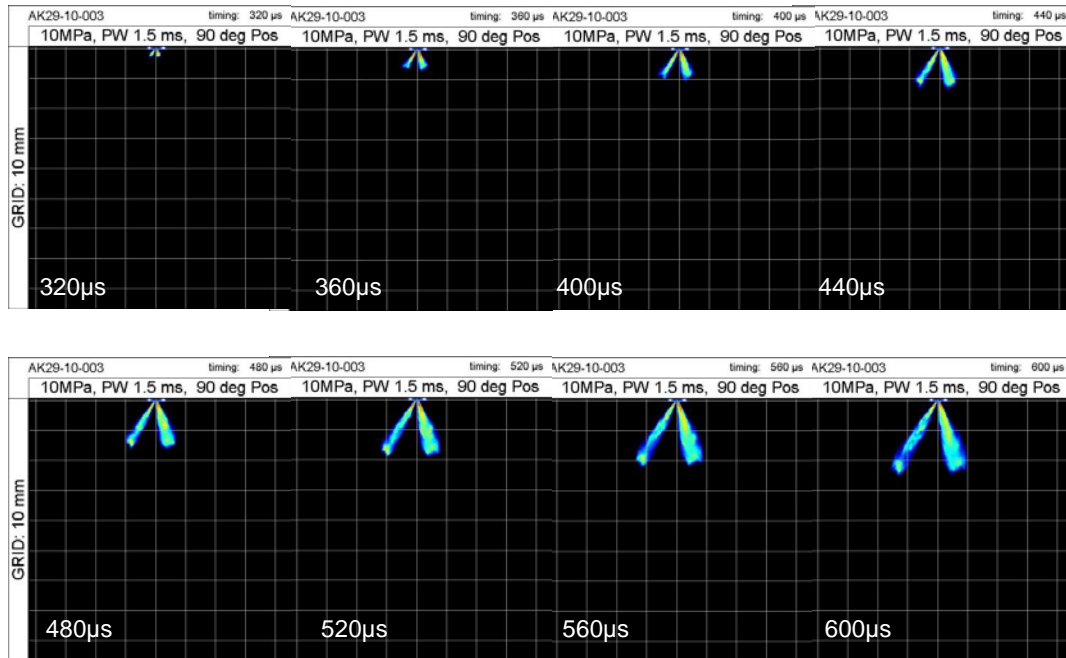
AK29-10-003 (Mie-Scatter): 10MPa 0° orientation



AK29-10-003 (Mie-Scatter): 10MPa 0° orientation

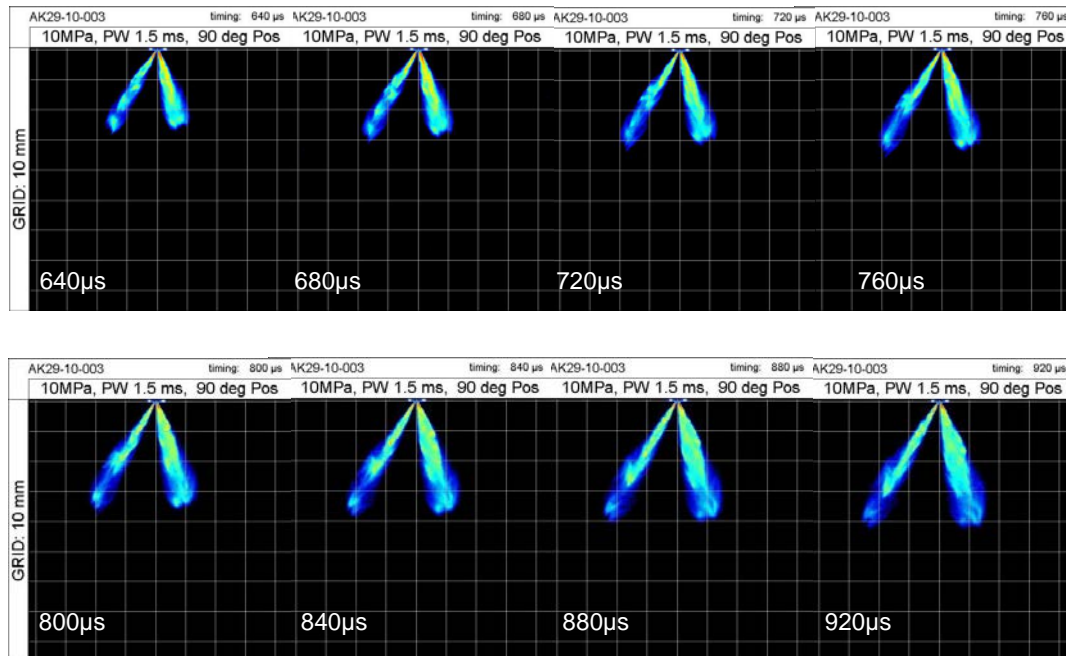


AK29-10-003 (Mie-Scatter): 10MPa 90° orientation



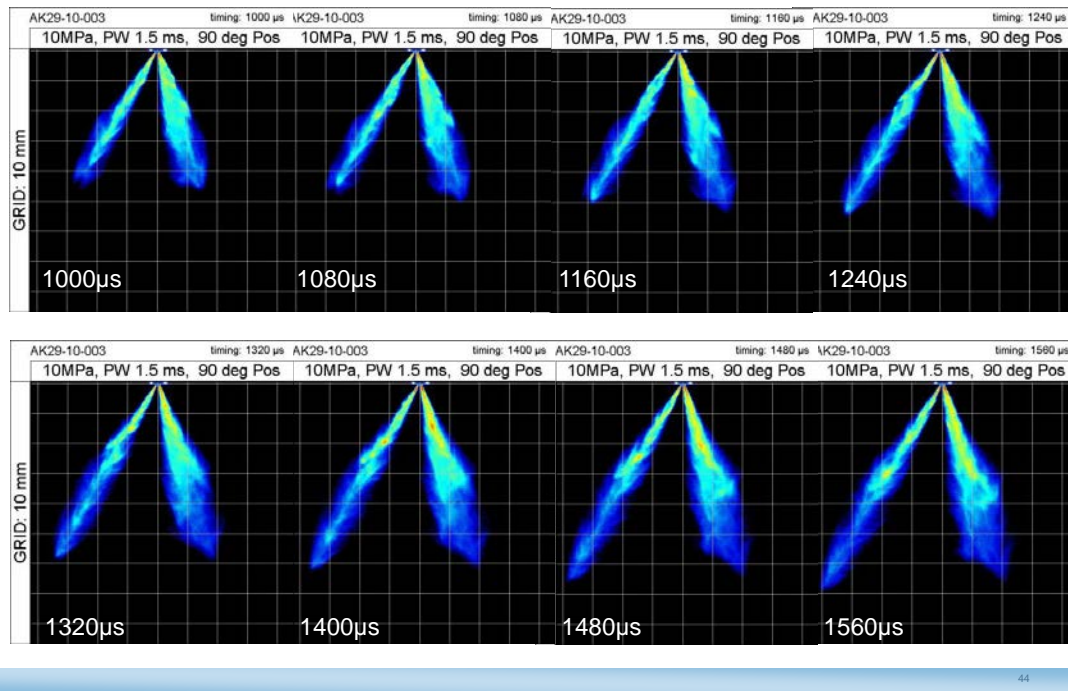
42

AK29-10-003 (Mie-Scatter): 10MPa 90° orientation

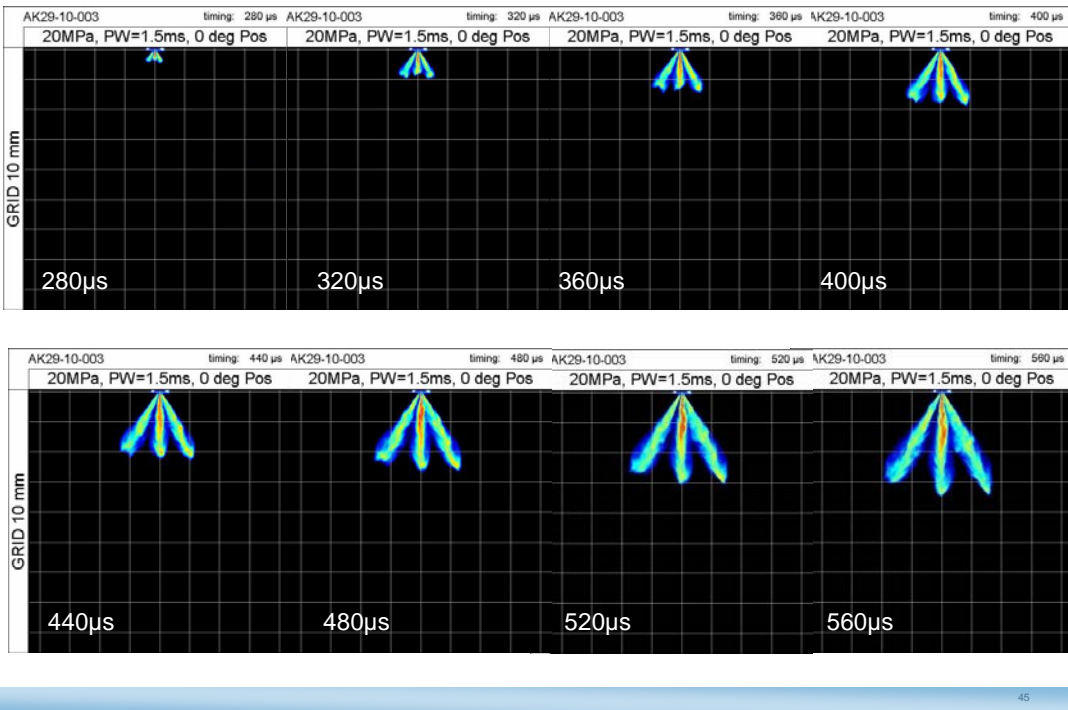


43

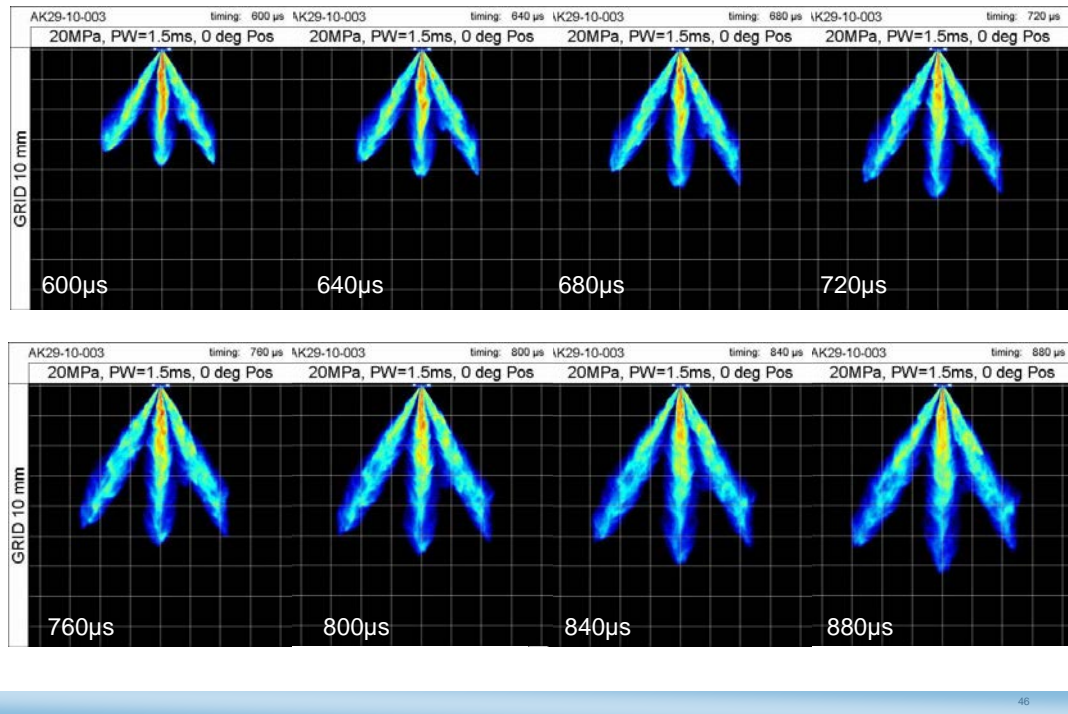
AK29-10-003 (Mie-Scatter): 10MPa 90° orientation



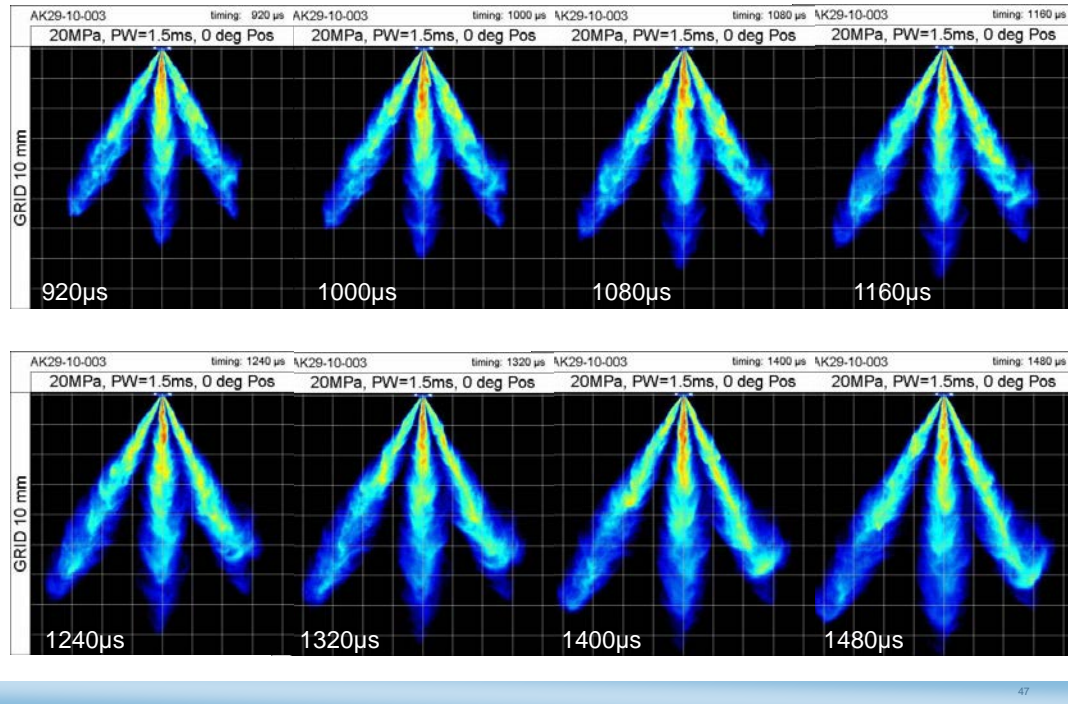
AK29-10-003 (Mie-Scatter): 20MPa 0° orientation



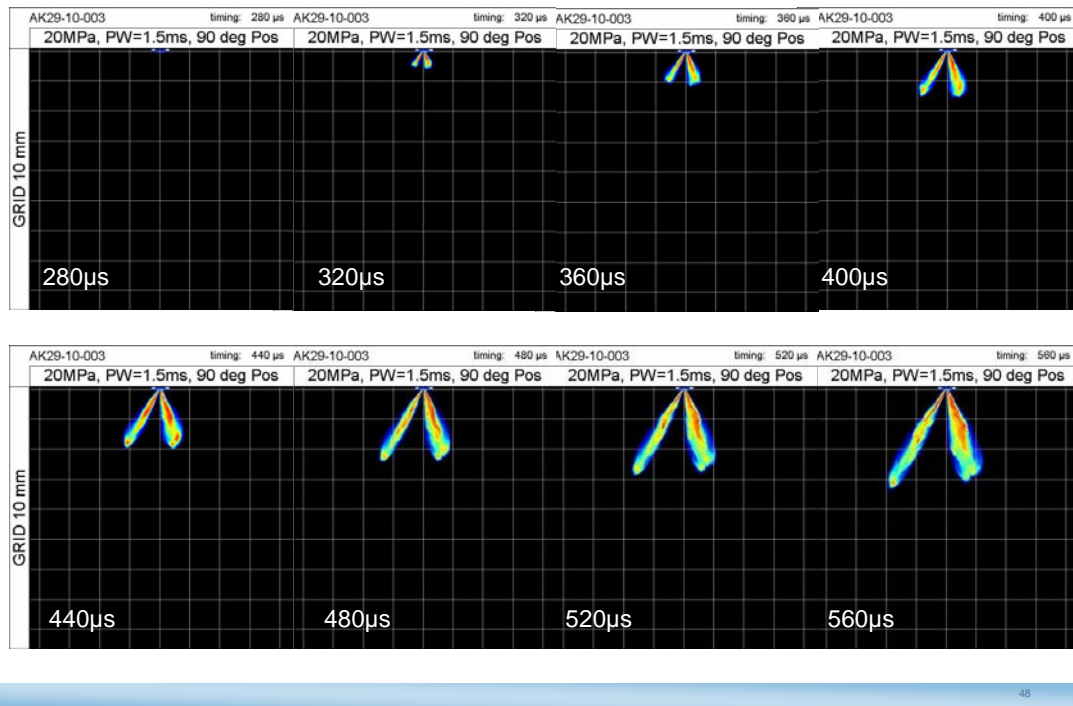
AK29-10-003 (Mie-Scatter): 20MPa 0° orientation



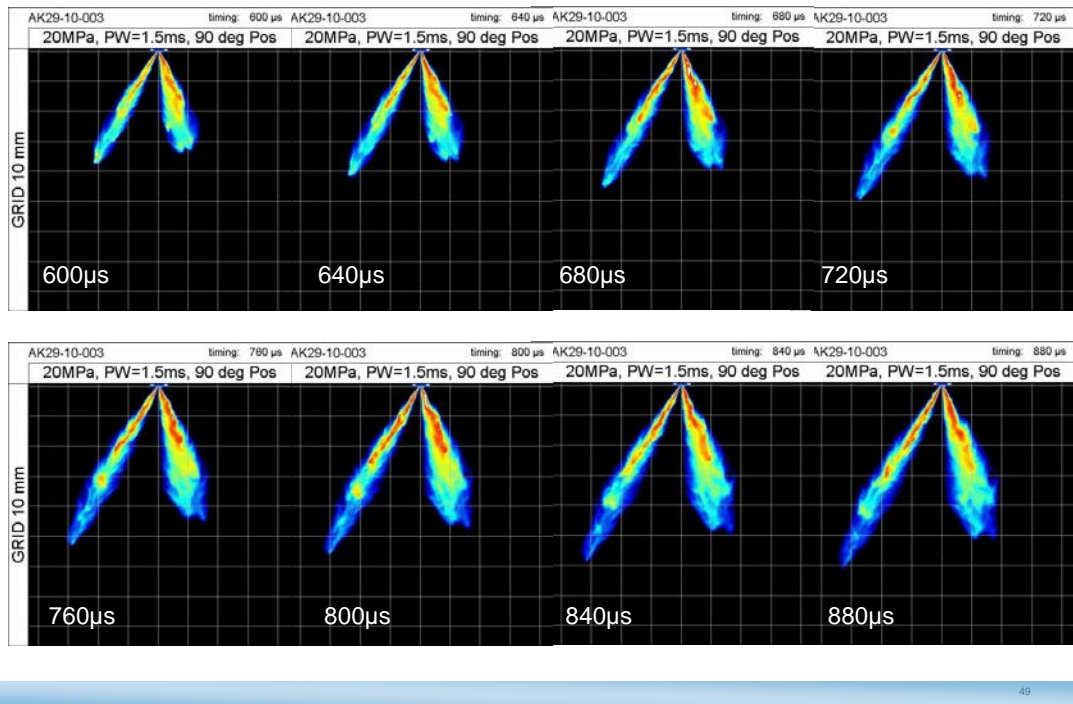
AK29-10-003 (Mie-Scatter): 20MPa 0° orientation



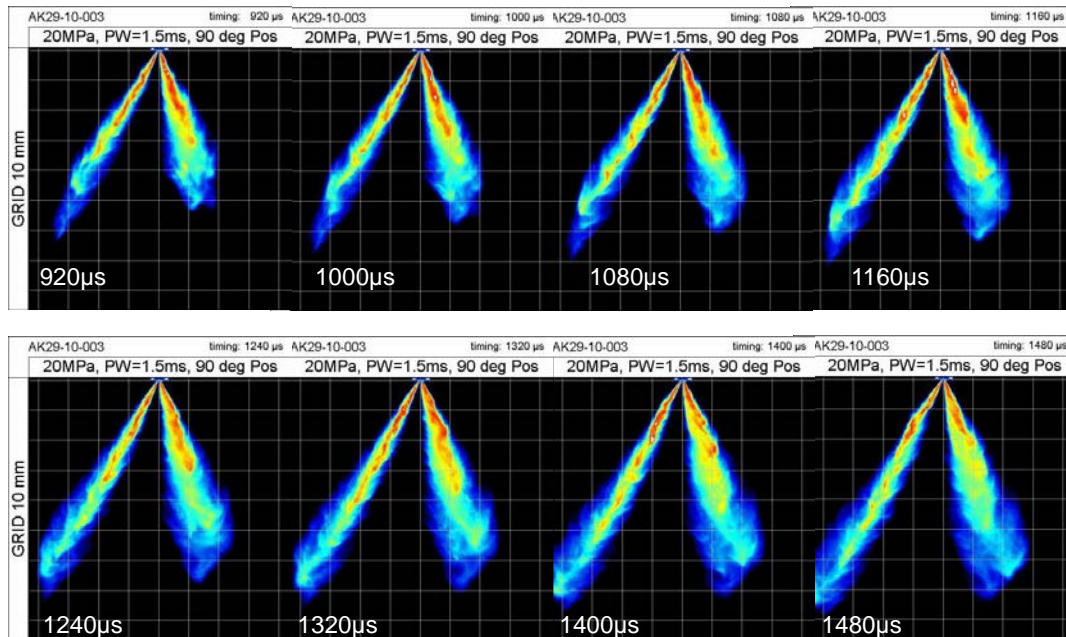
AK29-10-003 (Mie-Scatter): 20MPa 90° orientation



AK29-10-003 (Mie-Scatter): 20MPa 90° orientation

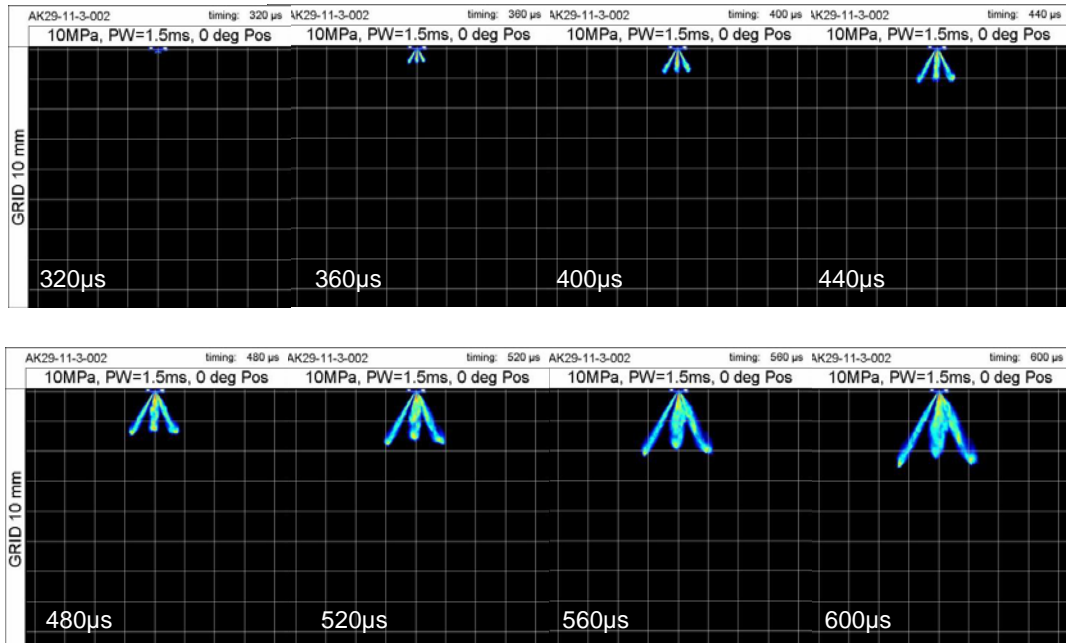


AK29-10-003 (Mie-Scatter): 20MPa 90° orientation



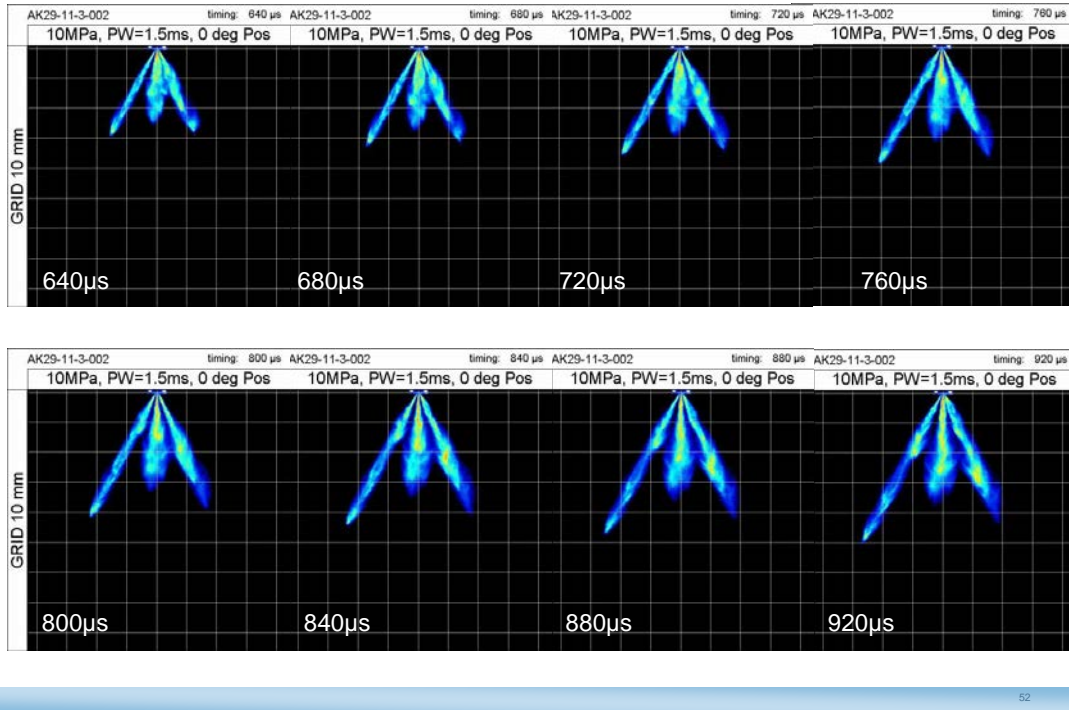
50

AK29-11-3-002 (Mie-Scatter): 10MPa, 0°orientation

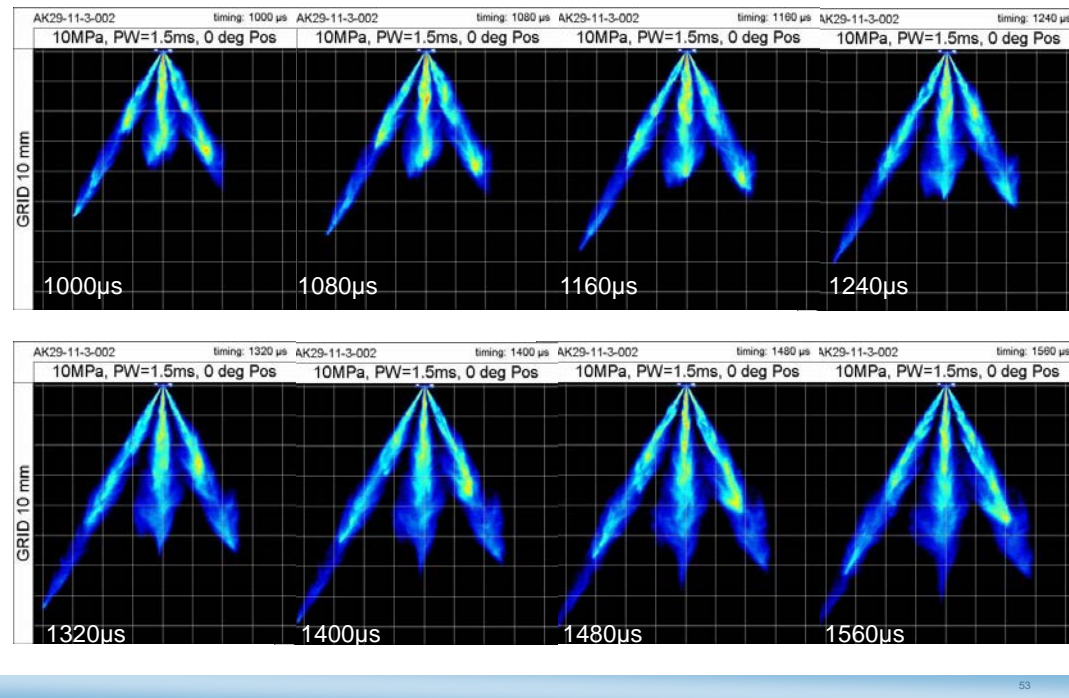


51

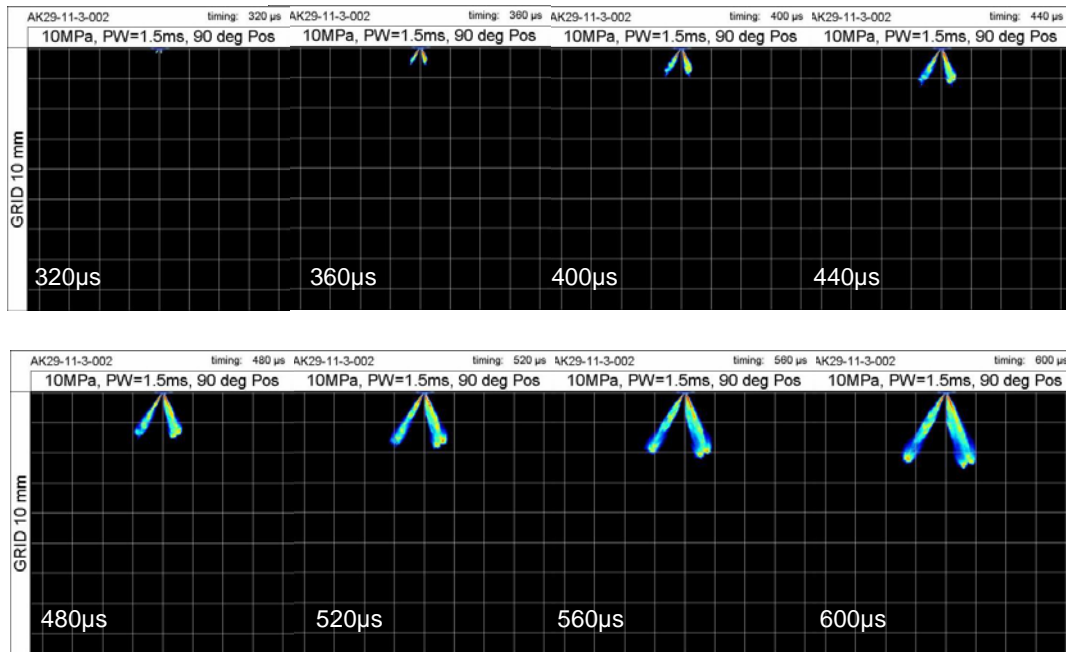
AK29-11-3-002 (Mie-Scatter): 10MPa, 0° orientation



AK29-11-3-002 (Mie-Scatter): 10MPa, 0°orientation

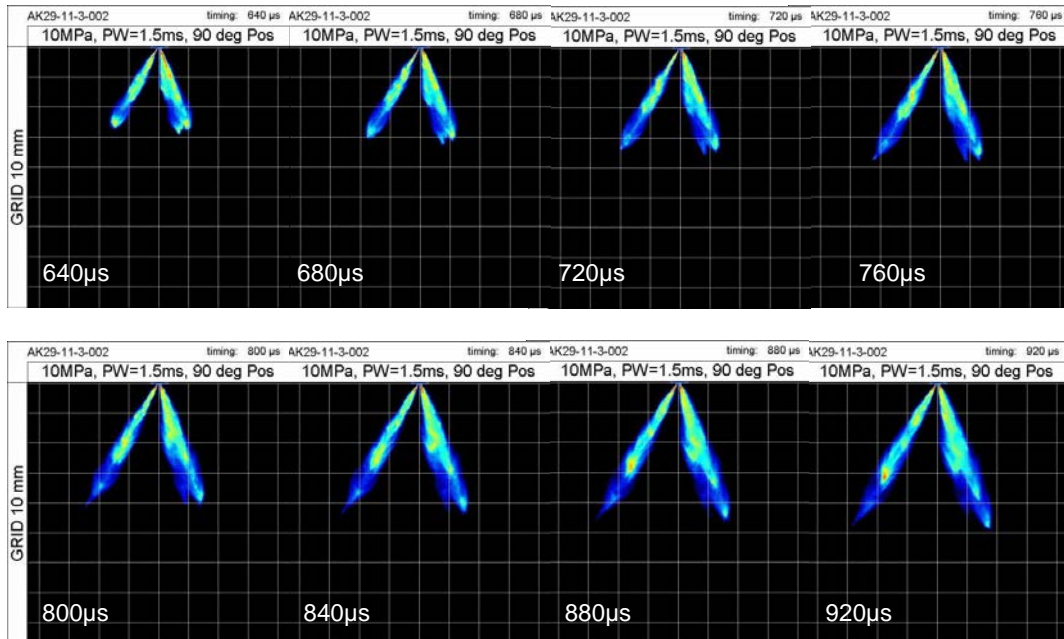


AK29-11-3-002 (Mie-Scatter): 10MPa, 90°orientation



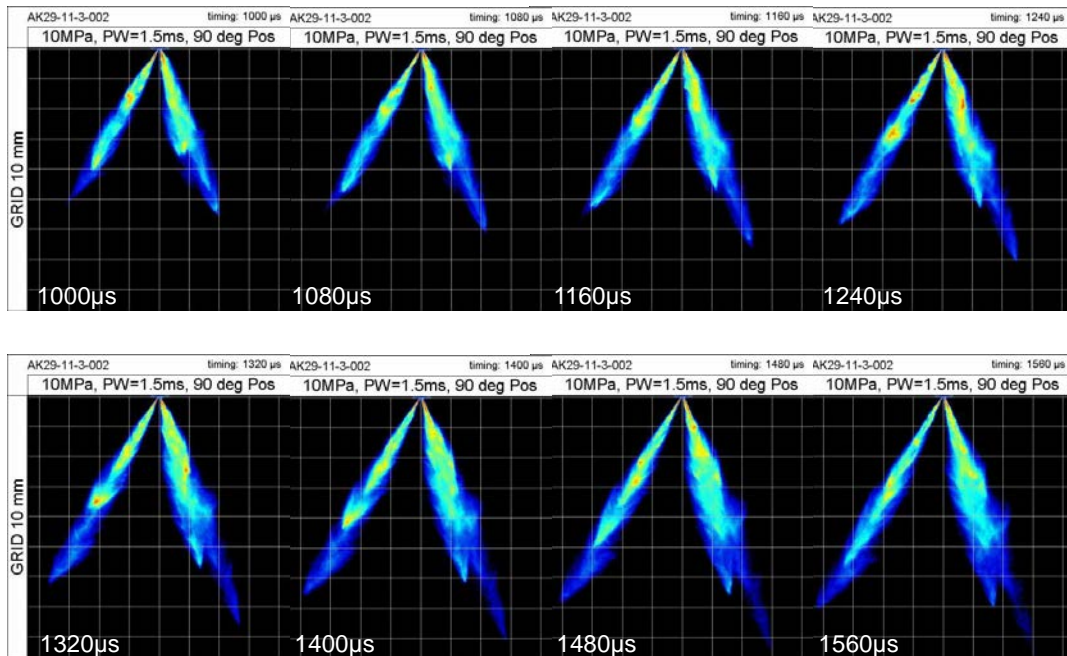
54

AK29-11-3-002 (Mie-Scatter): 10MPa, 90°orientation



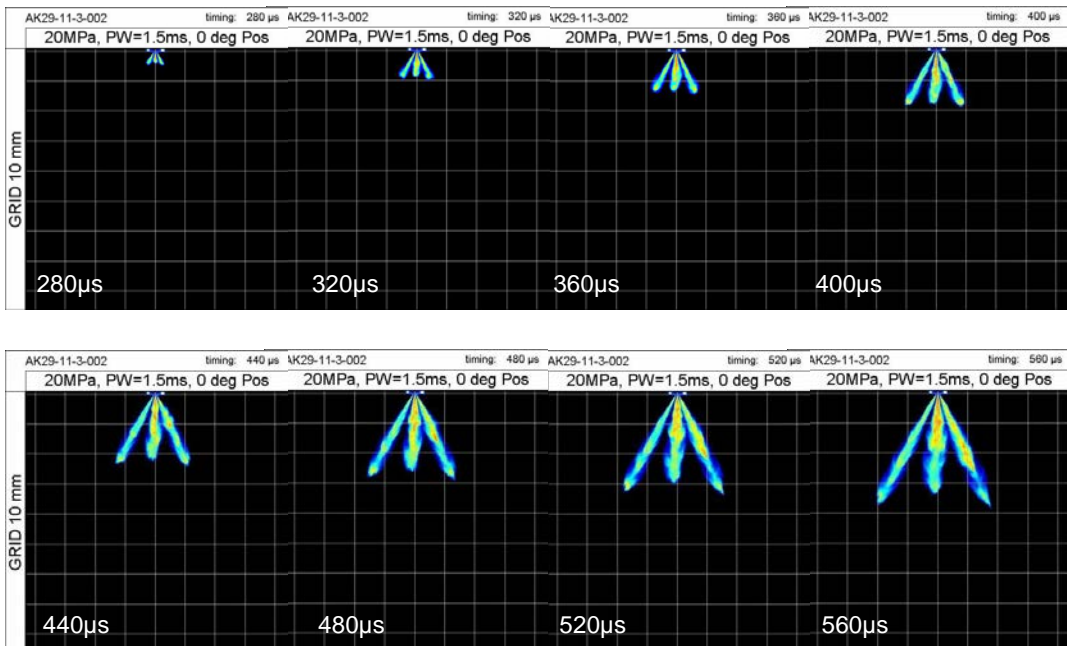
55

AK29-11-3-002 (Mie-Scatter): 10MPa, 90° orientation



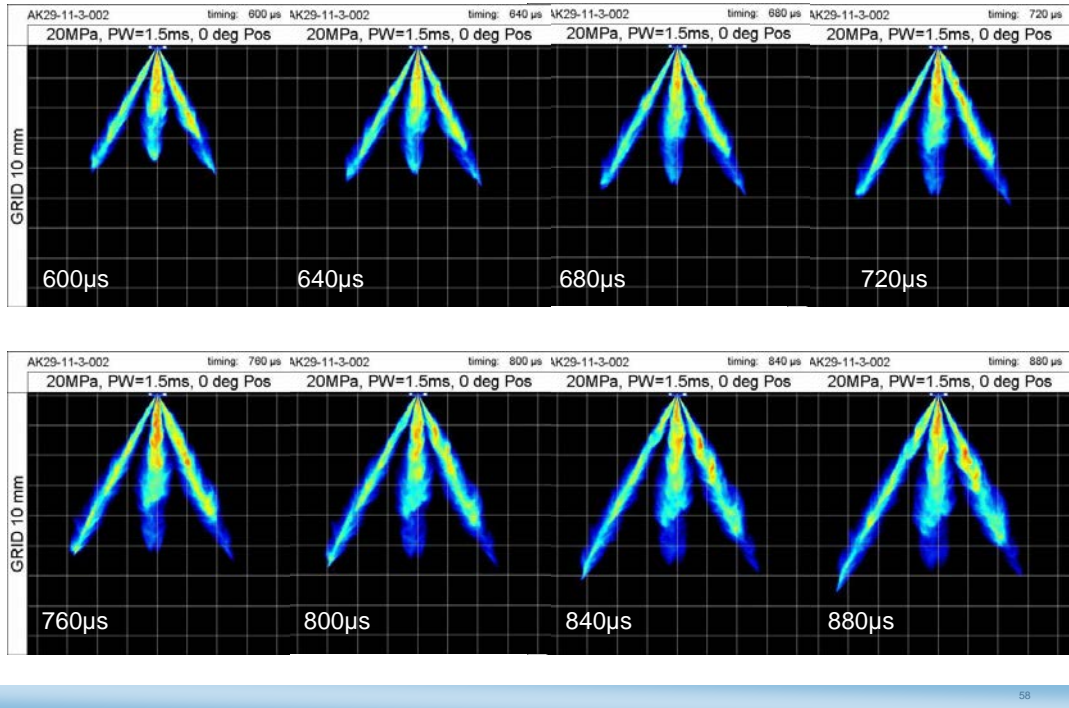
56

AK29-11-3-002 (Mie-Scatter): 20MPa, 0° orientation

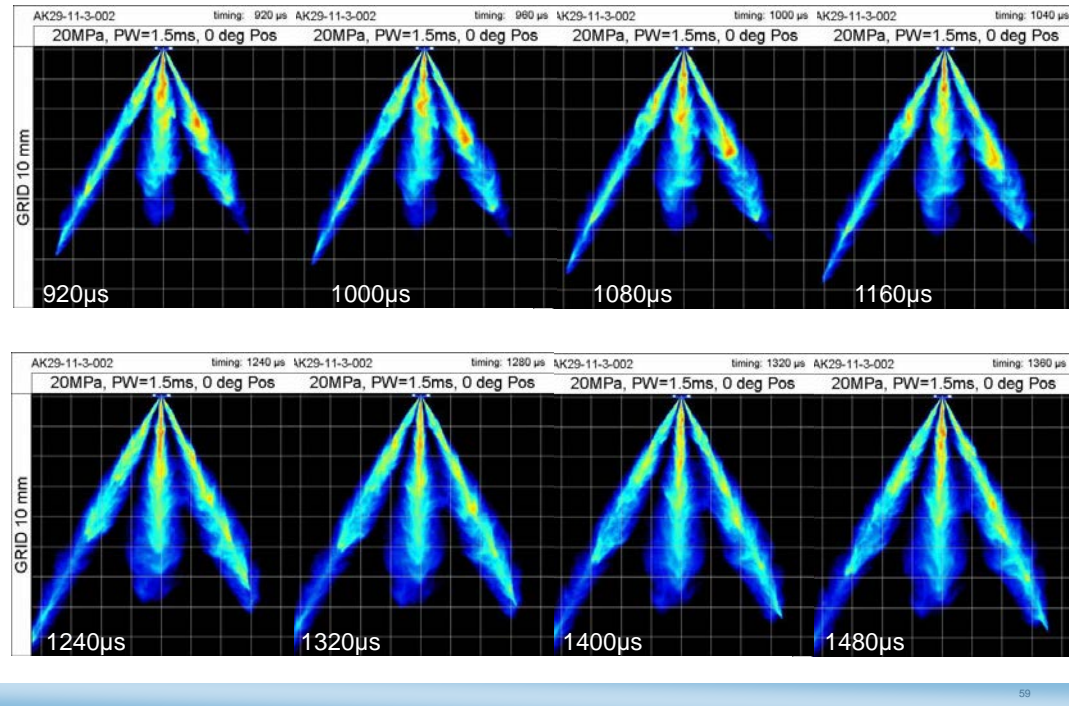


57

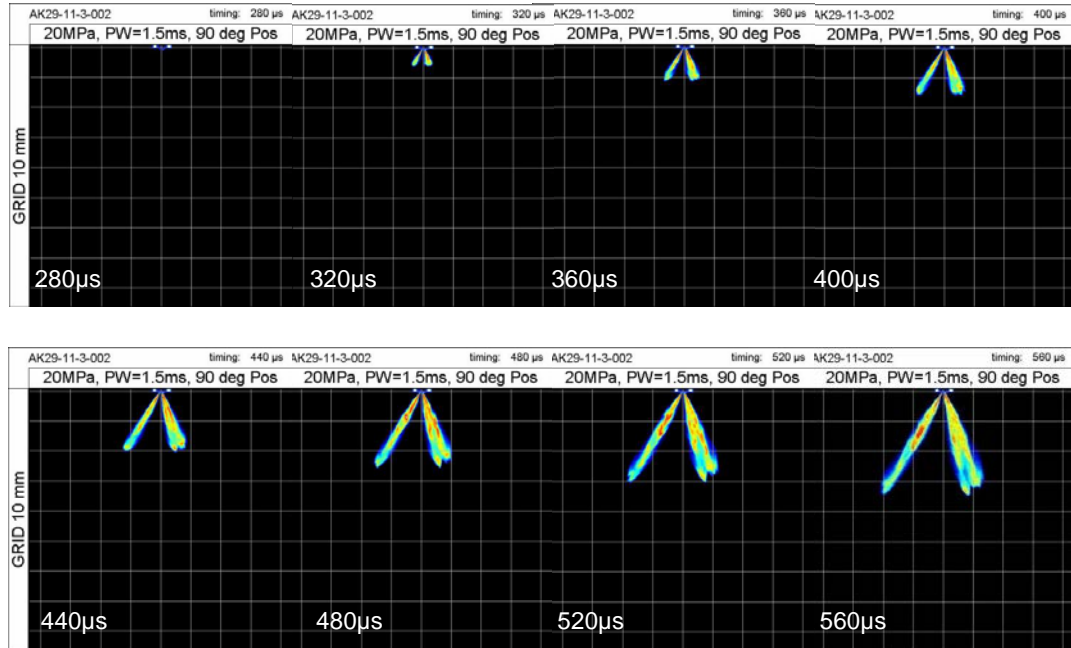
AK29-11-3-002 (Mie-Scatter): 20MPa, 0° orientation



AK29-11-3-002 (Mie-Scatter): 20MPa, 0°orientation

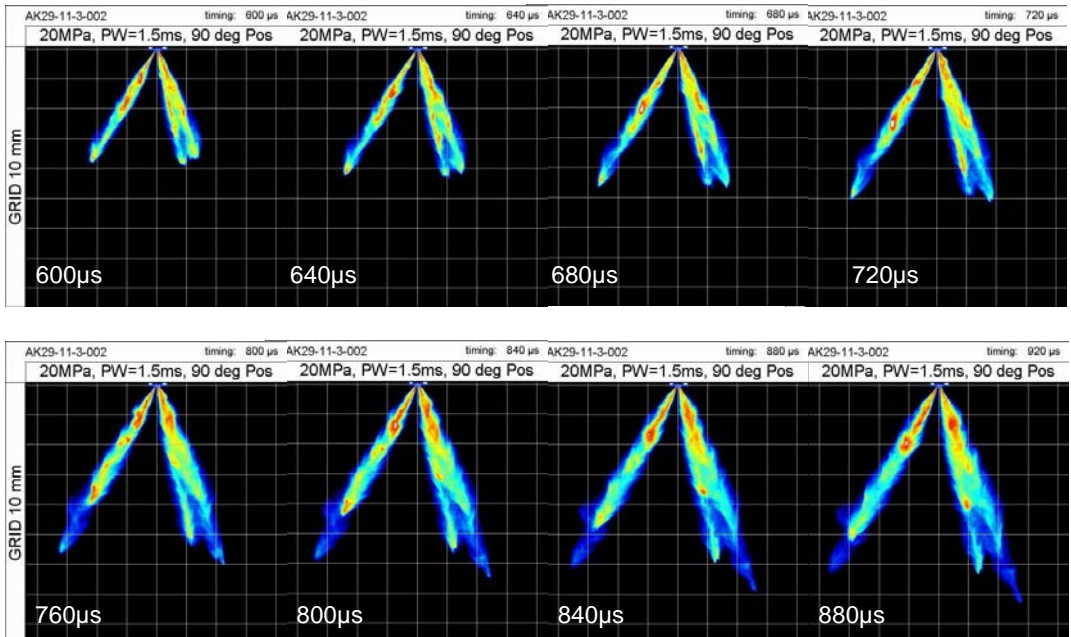


AK29-11-3-002 (Mie-Scatter): 20MPa, 90° orientation



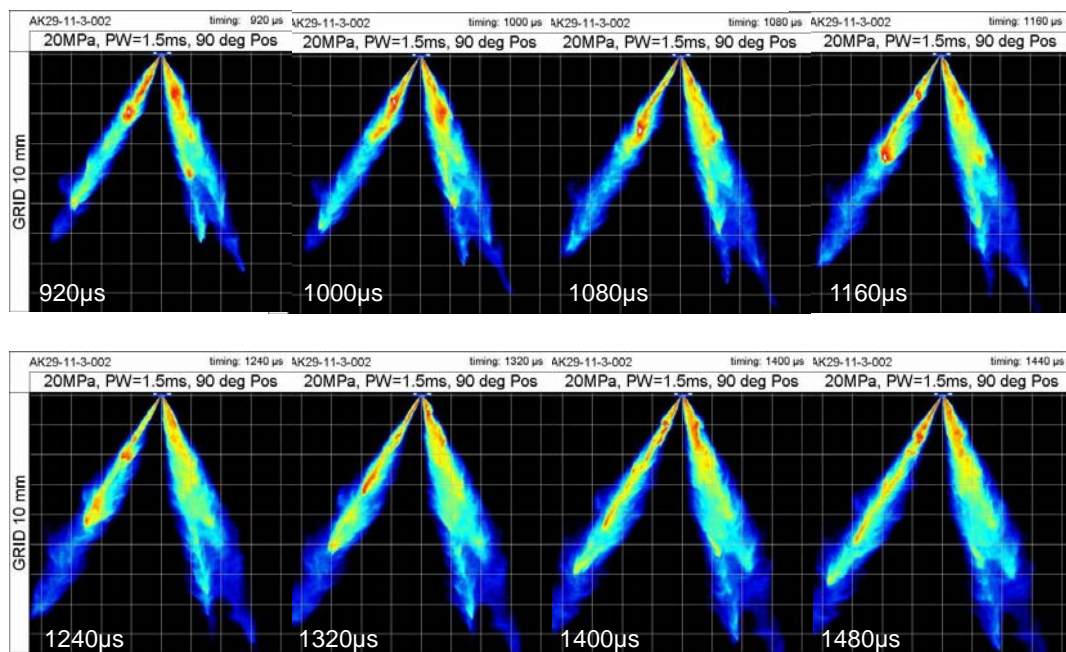
60

AK29-11-3-002 (Mie-Scatter): 20MPa, 90° orientation



61

AK29-11-3-002 (Mie-Scatter): 20MPa, 90°orientation

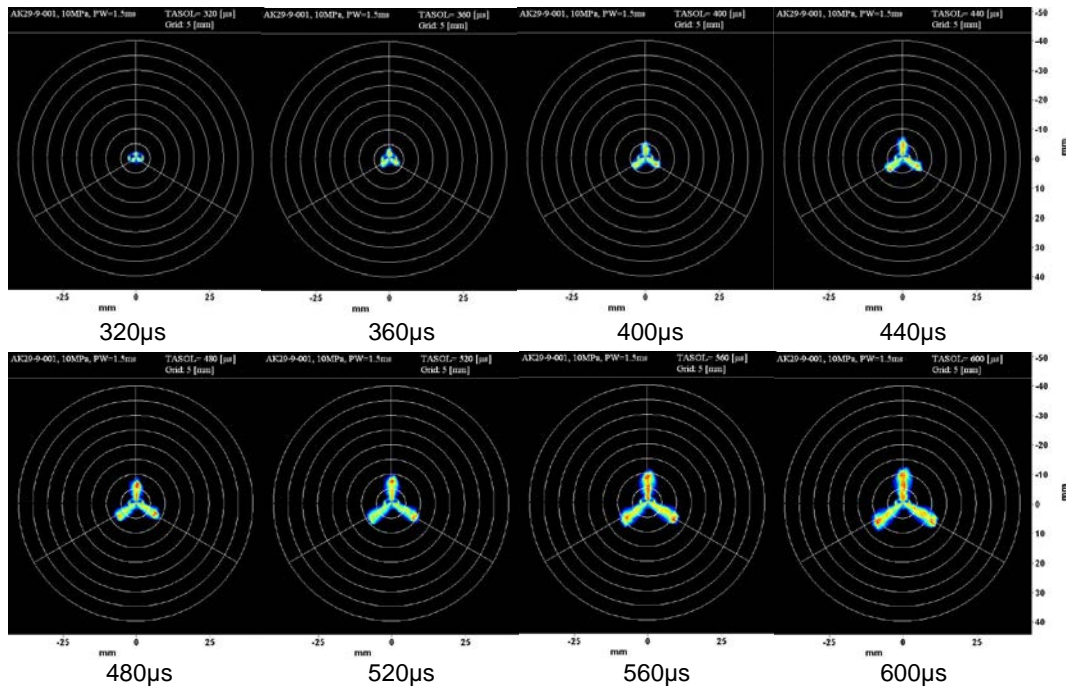


APPENDIX G MIE SCATTER IMAGES, SIDE VIEW

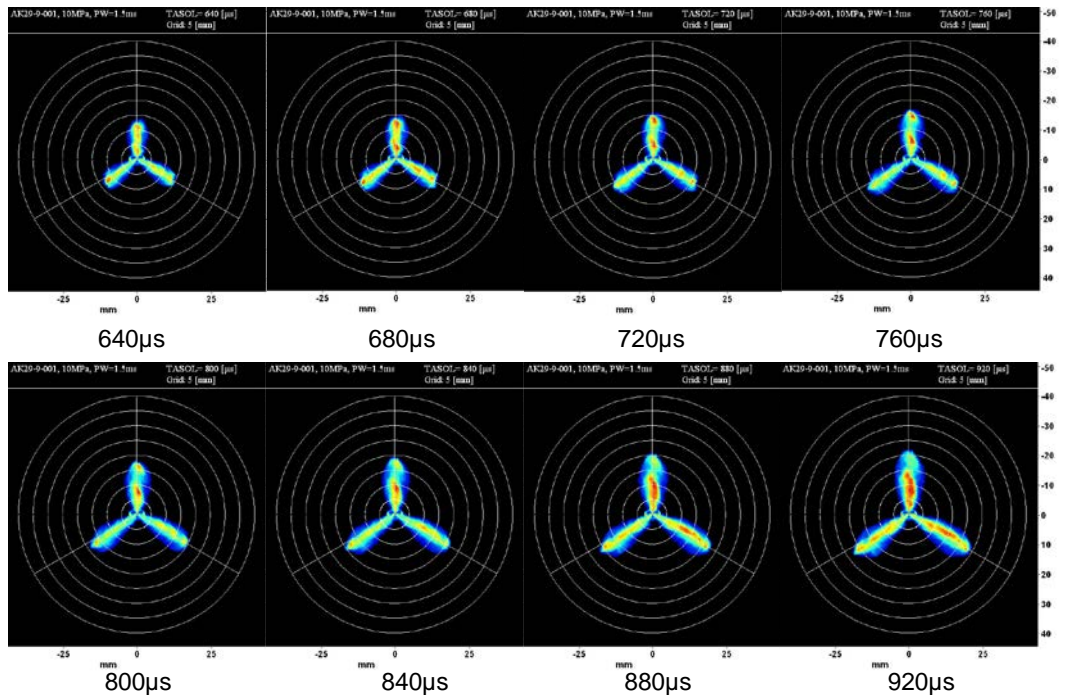
High speed Mie Imaging (144 images) of Spray plumes from bottom view, Luxembourg Spray lab

Image #	Seat #	d (mm)	β	l/d	(l+L)/d	D/d	Inj. Pres.	Mie Scatter Time Images (μ s)
1-8	AK29-9-001	$\approx .20$	30°	1.1	na	na	10MPa	320,360,400,440,470,520,560,600
9-16	AK29-9-001	$\approx .20$	30°	1.1	na	na	10MPa	640,680,720,760,800,840,880,920
17-24	AK29-9-001	$\approx .20$	30°	1.1	na	na	10MPa	1000,1080,1160,1240,1320,1400, 1480, 1560
1-8	AK29-9-001	$\approx .20$	30°	1.1	na	na	20MPa	320,360,400,440,470,520,560,600
9-16	AK29-9-001	$\approx .20$	30°	1.1	na	na	20MPa	640,680,720,760,800,840,880,920
17-24	AK29-9-001	$\approx .20$	30°	1.1	na	na	20MPa	1000,1080,1160,1240,1320,1400, 1480, 1560
1-8	AK29-10-3-003	$\approx .15$	30°	1.1	3.96	2.5	10MPa	320,340,400,440,480,520,560,600
9-16	AK29-10-3-003	$\approx .15$	30°	1.1	3.96	2.5	10MPa	640,680,720,760,800,840,880,920
17-24	AK29-10-3-003	$\approx .15$	30°	1.1	3.96	2.5	10MPa	1000,1080,1160,1240,1320,1400, 1480, 1560
1-8	AK29-10-3-003	$\approx .15$	30°	1.1	3.96	2.5	20MPa	320,340,400,440,480,520,560,600
9-16	AK29-10-3-003	$\approx .15$	30°	1.1	3.96	2.5	20MPa	640,680,720,760,800,840,880,920
17-24	AK29-10-3-003	$\approx .15$	30°	1.1	3.96	2.5	20MPa	1000,1080,1160,1240,1320,1400, 1480, 1560
1-8	AK29-11-3-002	$\approx .15$	30°	3.96	na	na	10MPa	320,340,400,440,480,520,560,600
9-16	AK29-11-3-002	$\approx .15$	30°	3.96	na	na	10MPa	640,680,720,760,800,840,880,920
17-24	AK29-11-3-002	$\approx .15$	30°	3.96	na	na	10MPa	1000,1080,1160,1240,1320,1400, 1480, 1560
1-8	AK29-11-3-002	$\approx .15$	30°	3.96	na	na	20MPa	320,340,400,440,480,520,560,600
9-16	AK29-11-3-002	$\approx .15$	30°	3.96	na	na	20MPa	640,680,720,760,800,840,880,920
17-24	AK29-11-3-002	$\approx .15$	30°	3.96	na	na	20MPa	1000,1080,1160,1240,1320,1400, 1480, 1560

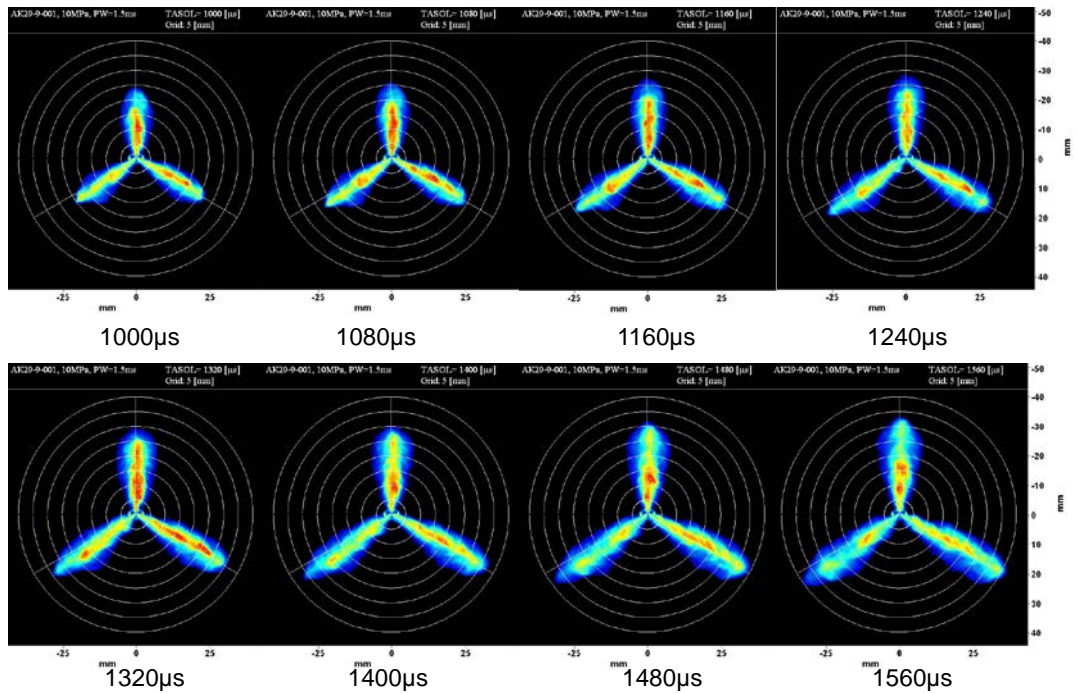
AK29-9-001 (Mie-Scatter Plume): 10MPa



AK29-9-001 (Mie-Scatter Plume): 10MPa

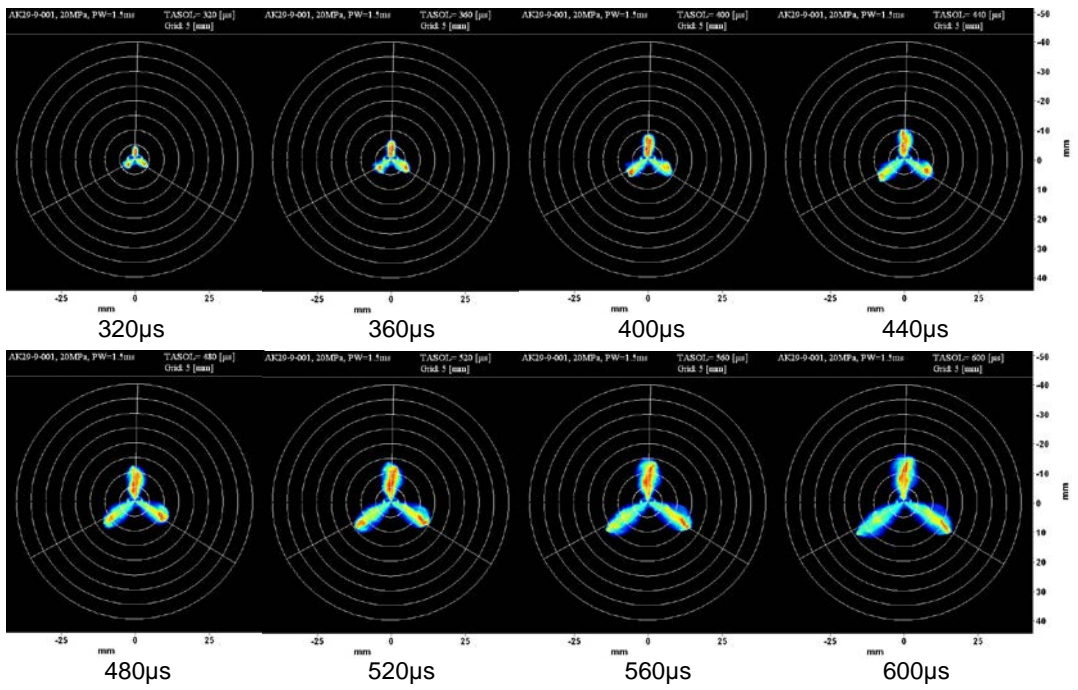


AK29-9-001 (Mie-Scatter Plume): 10MPa



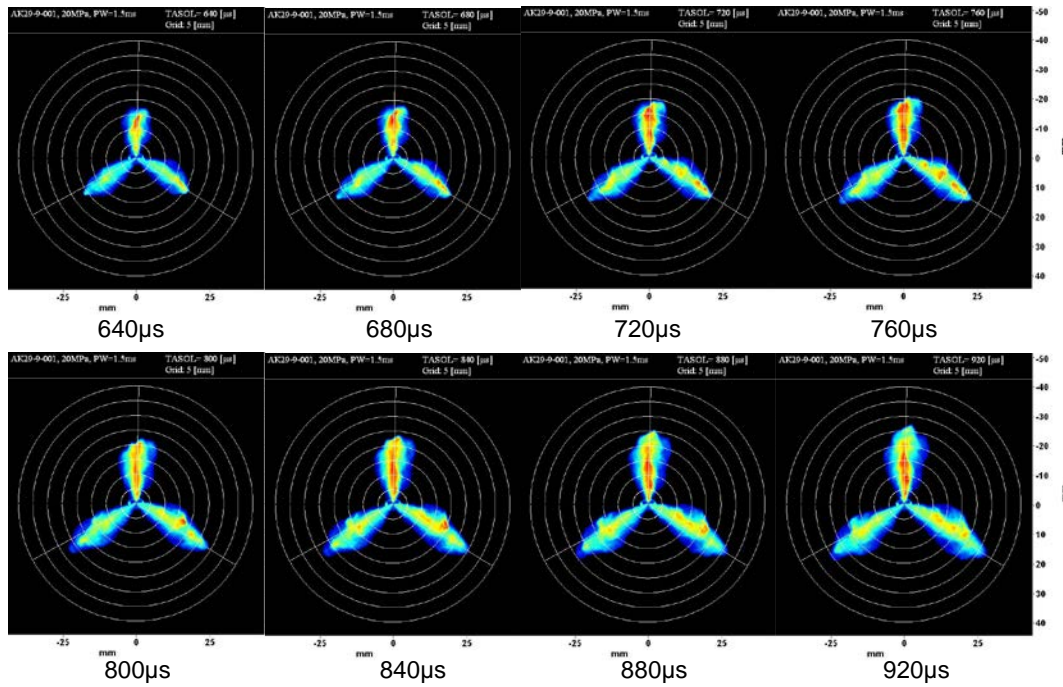
3

AK29-9-001 (Mie-Scatter Plume): 20MPa



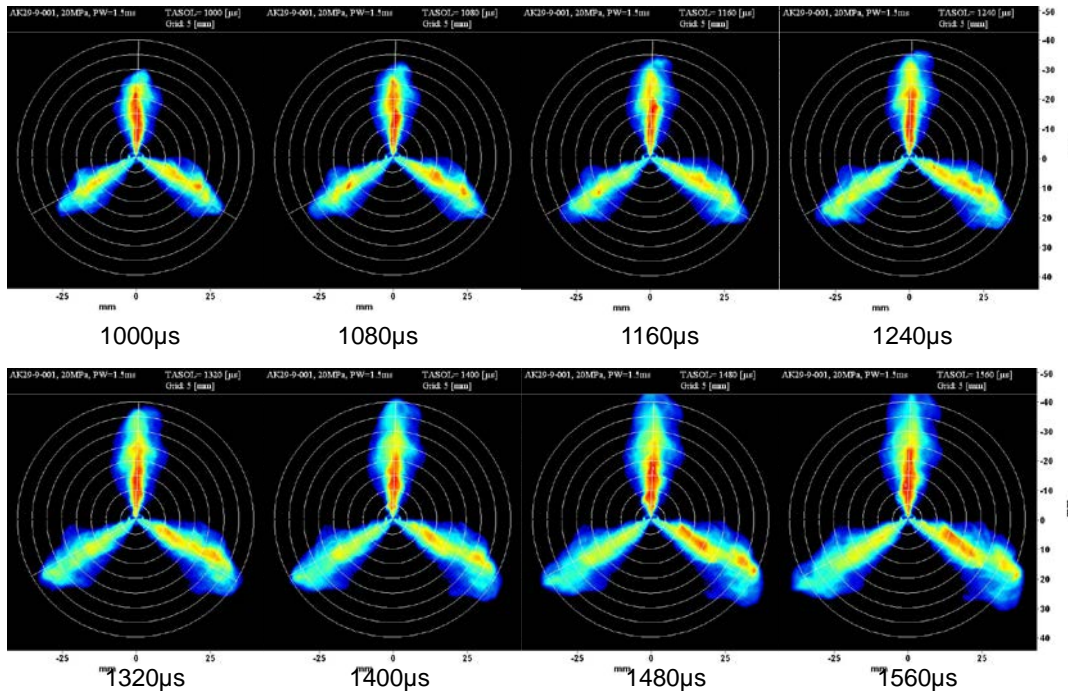
4

AK29-9-001 (Mie-Scatter Plume): 20MPa



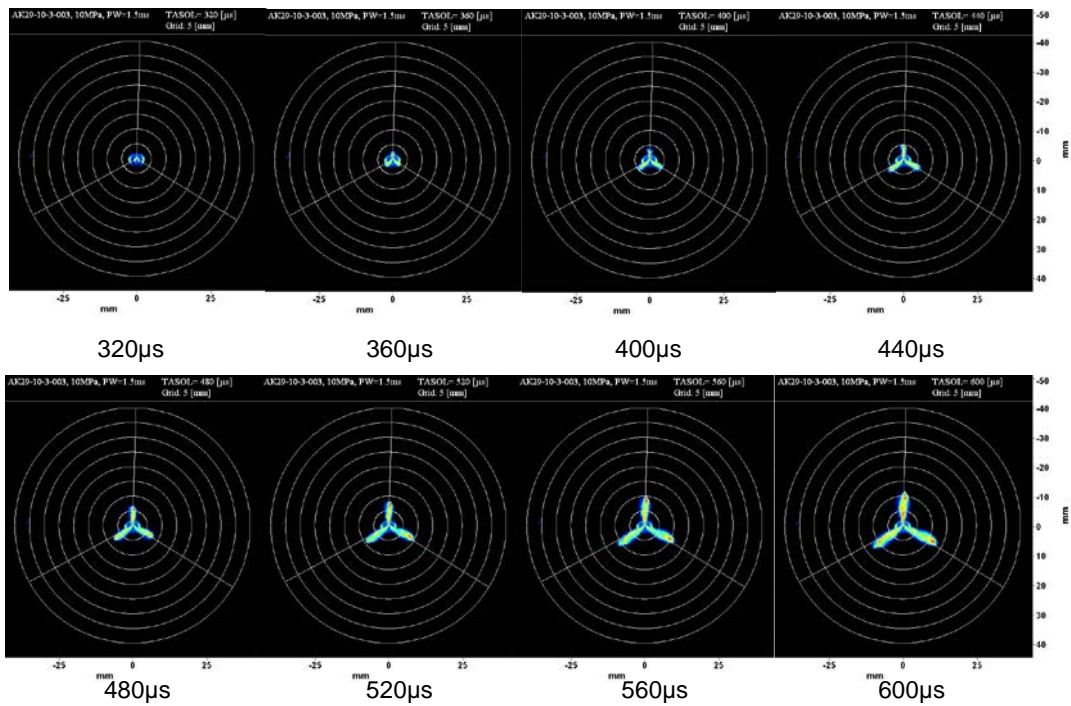
5

AK29-9-001 (Mie-Scatter Plume): 20MPa



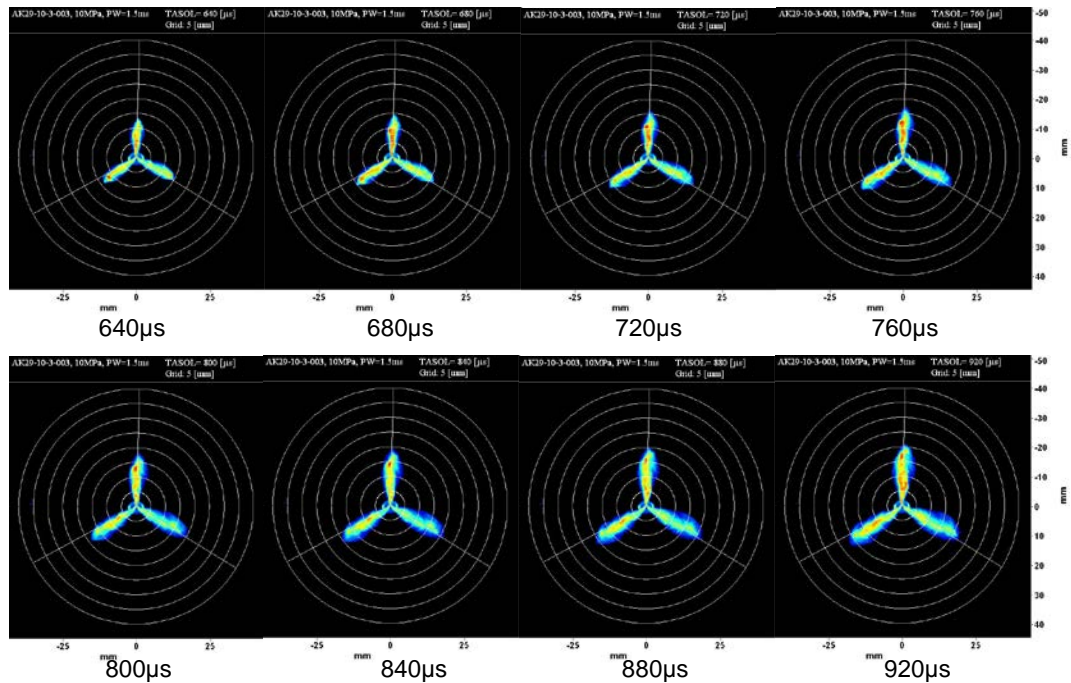
6

AK29-10-3-003 (Mie-Scatter Plume): 10MPa



7

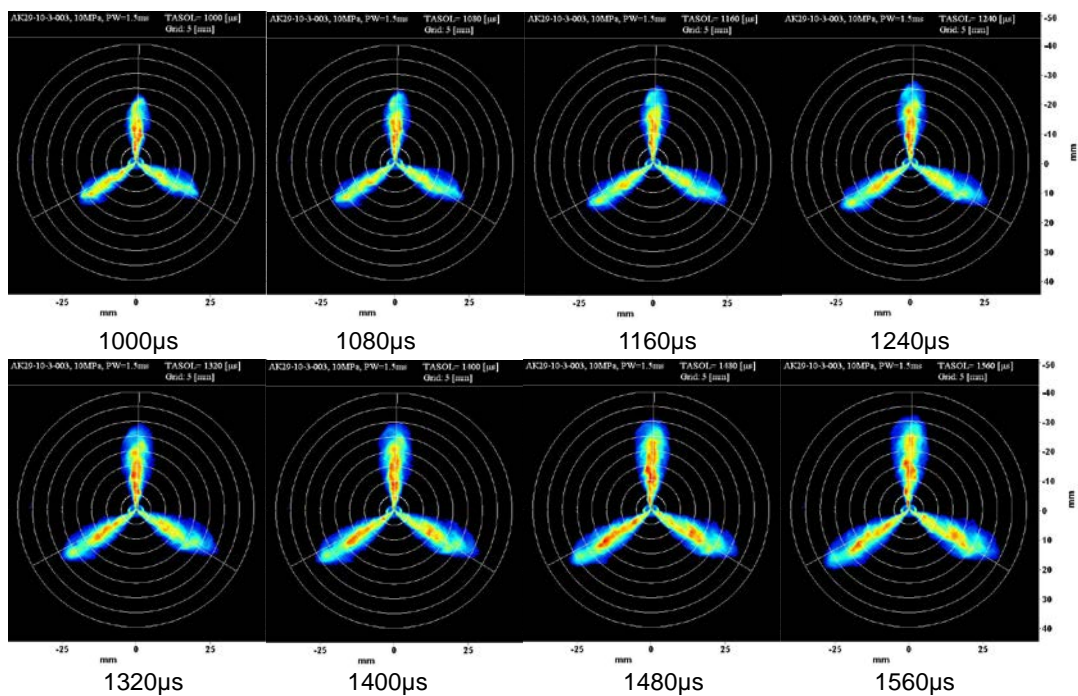
AK29-10-3-003 (Mie-Scatter Plume): 10MPa



8

AK29-10-3-003 (Mie-Scatter Plume):

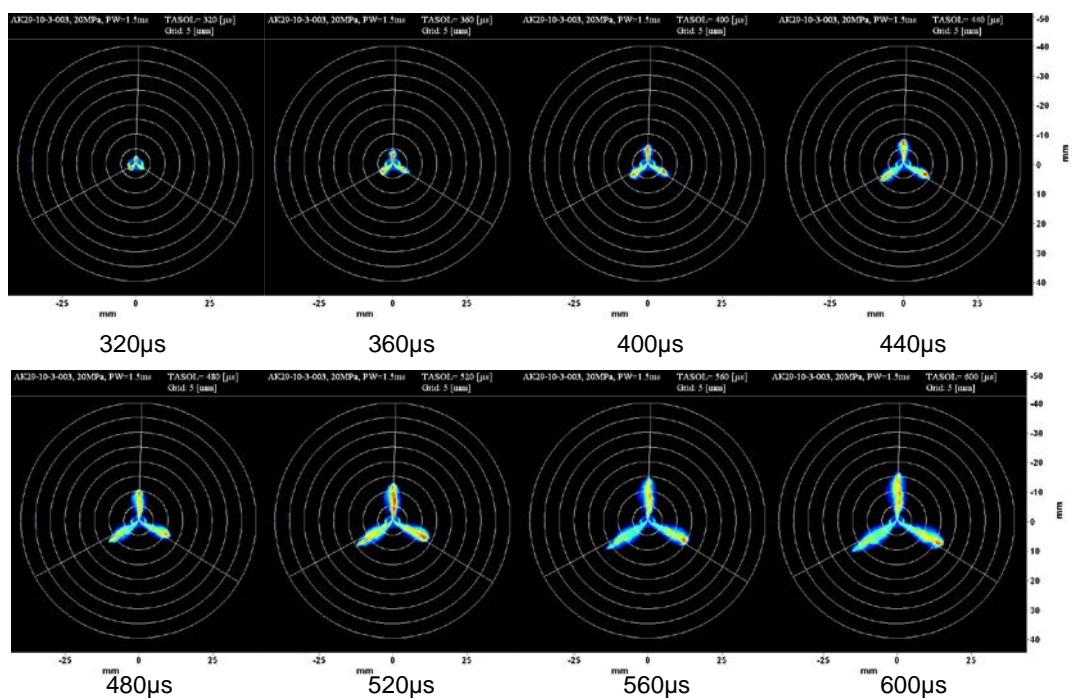
10MPa



9

AK29-10-3-003 (Mie-Scatter Plume):

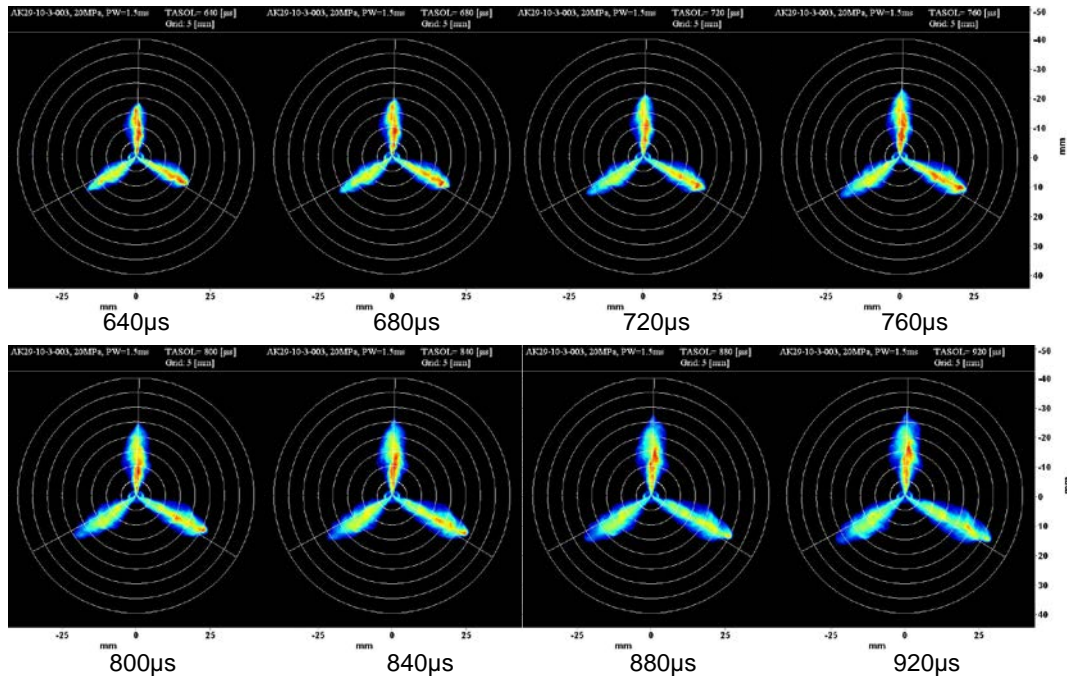
20MPa



10

AK29-10-3-003 (Mie-Scatter Plume):

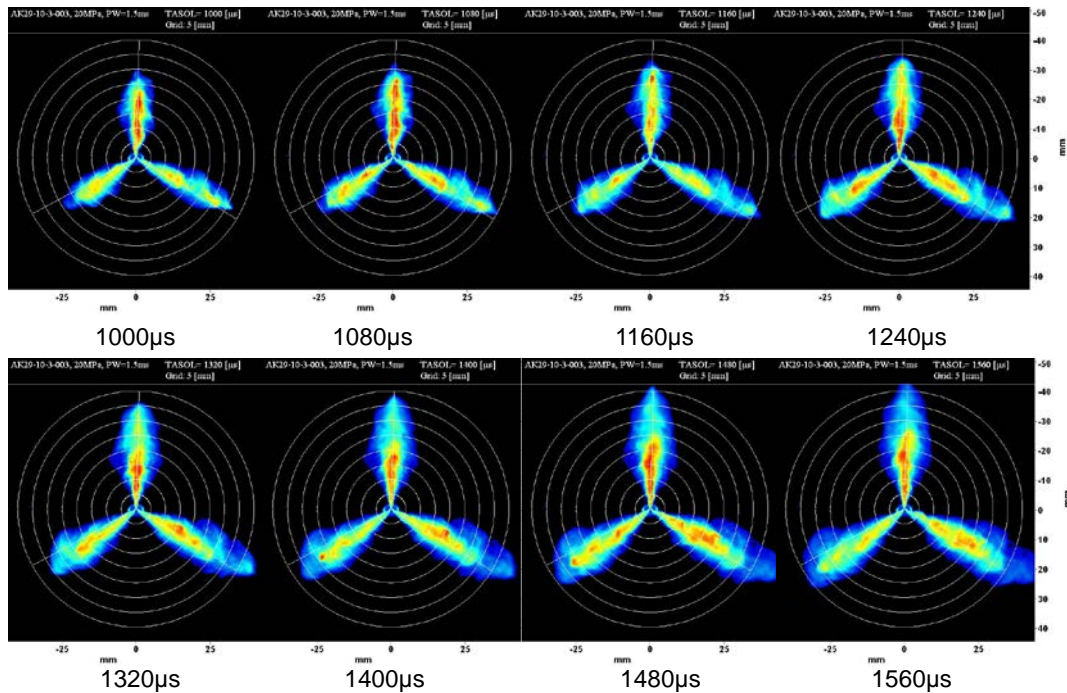
20MPa



11

AK29-10-3-003 (Mie-Scatter Plume):

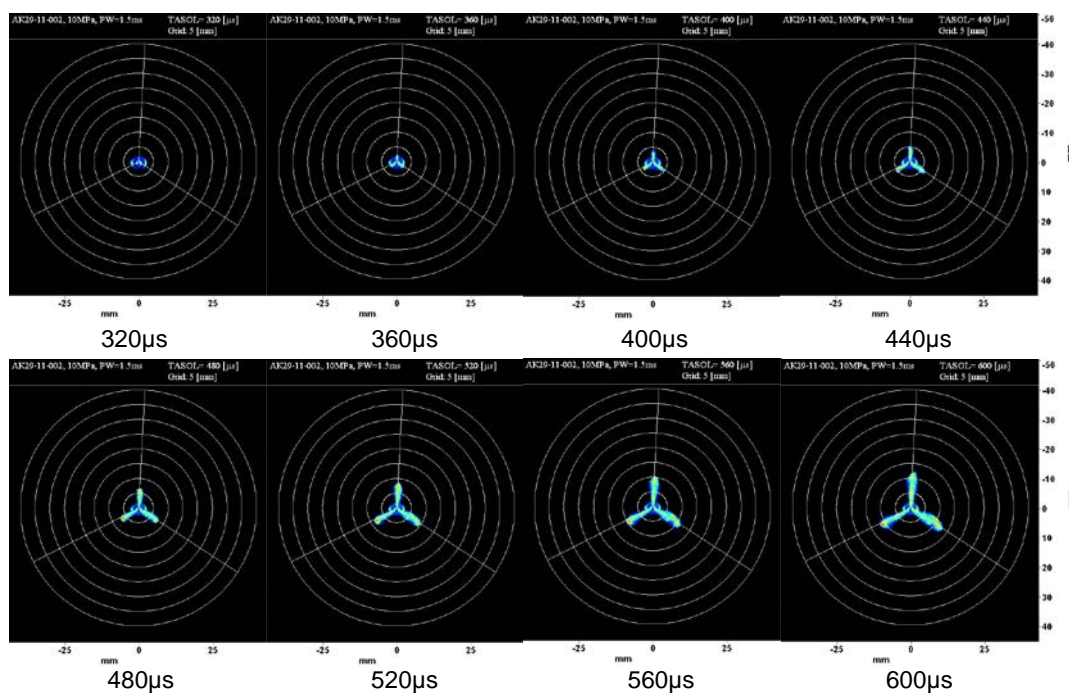
20MPa



12

AK29-11-3-002: (Mie-Scatter Plume)

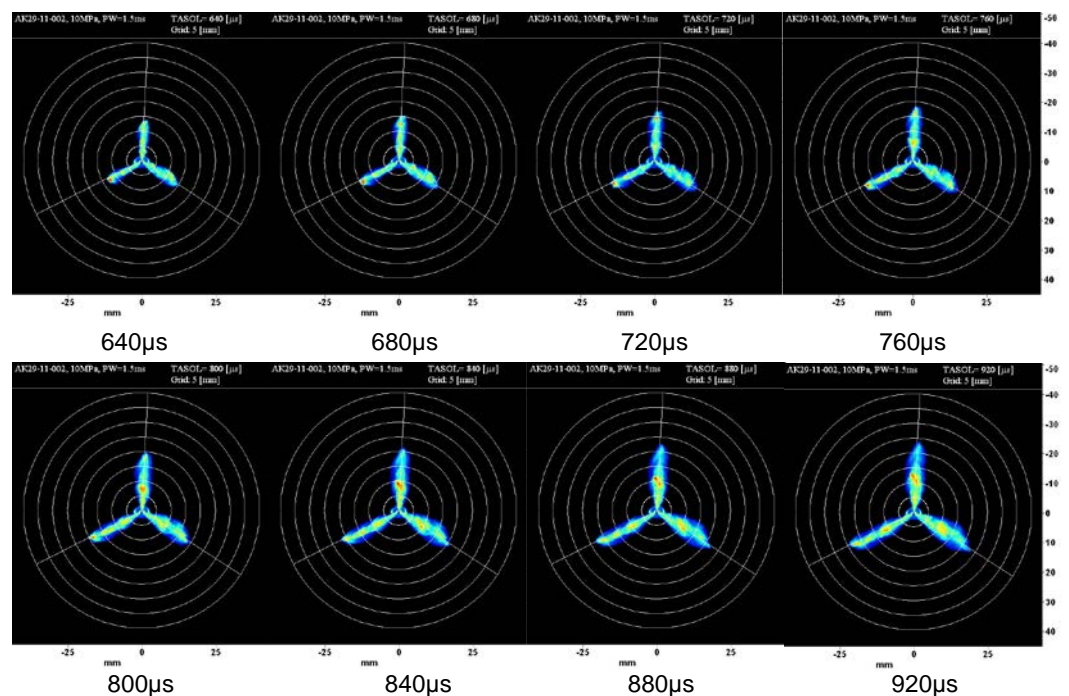
10MPa



13

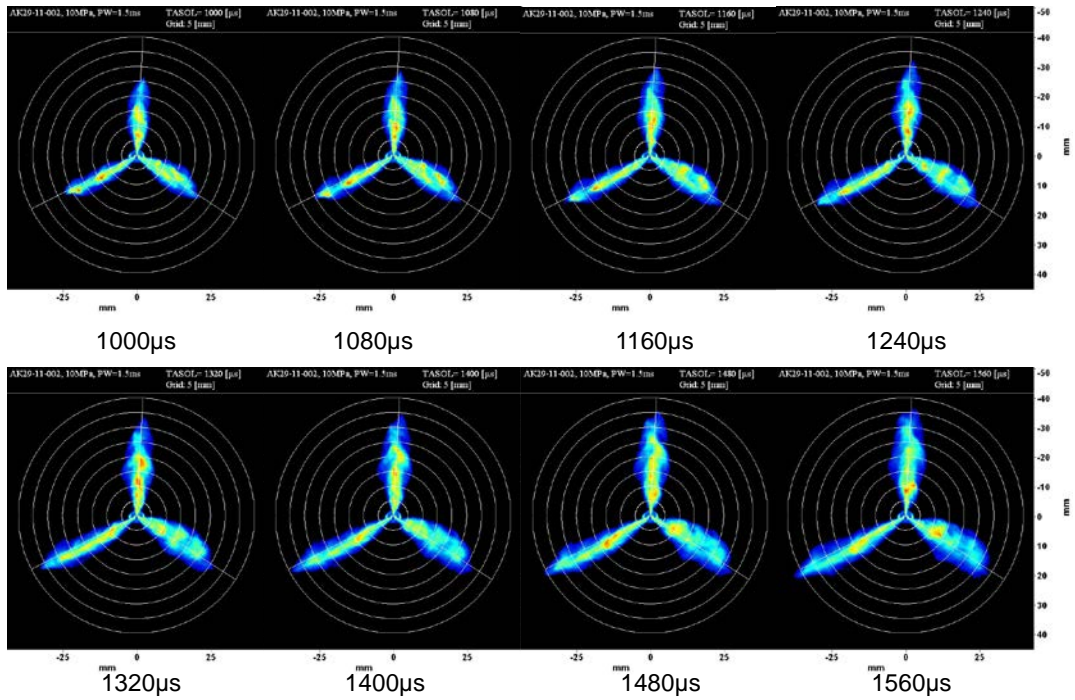
AK29-11-3-002: (Mie-Scatter Plume)

10MPa



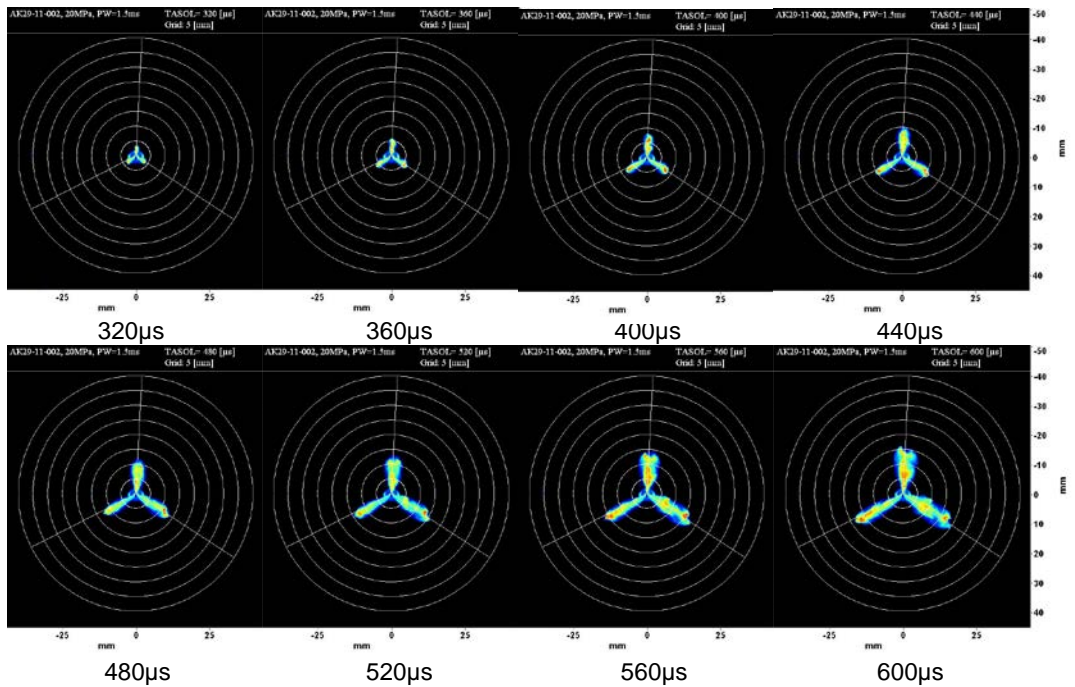
14

AK29-11-3-002: (Mie-Scatter Plume): 10MPa



15

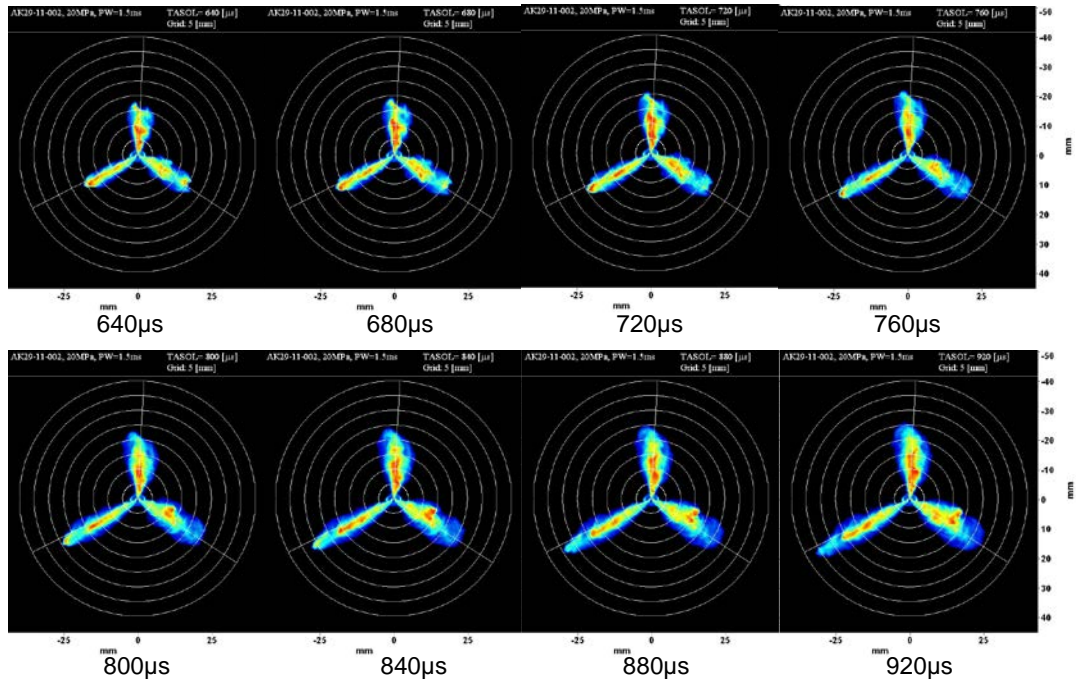
AK29-11-3-002: (Mie-Scatter Plume) 20MPa



16

AK29-11-3-002: (Mie-Scatter Plume)

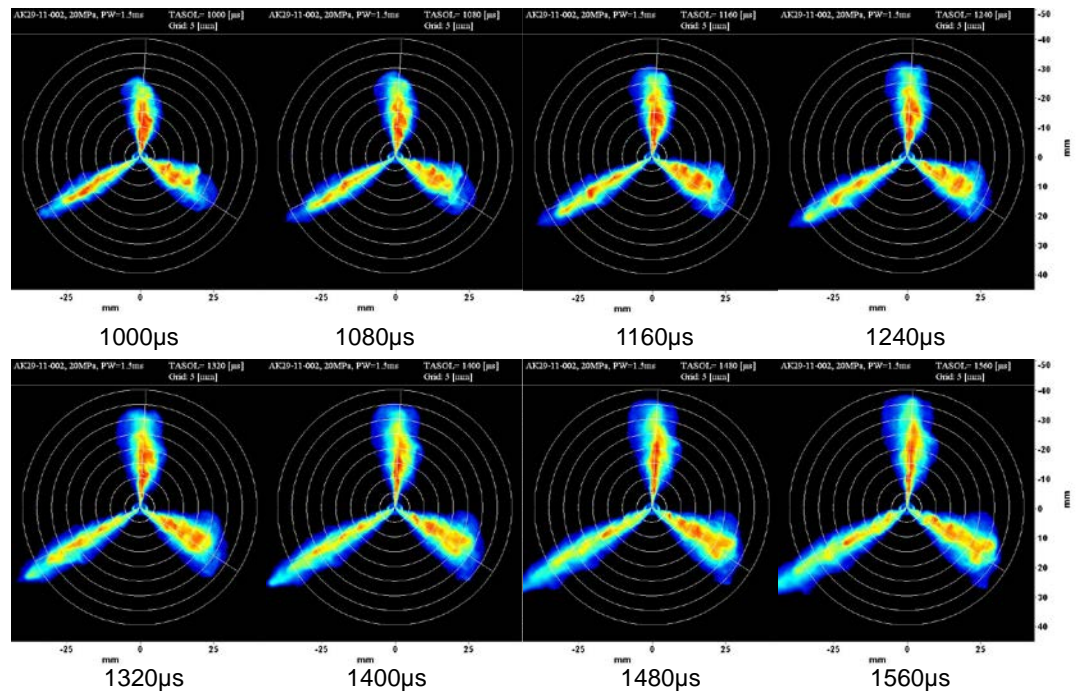
20MPa



17

AK29-11-3-002: (Mie-Scatter Plume):

20MPa

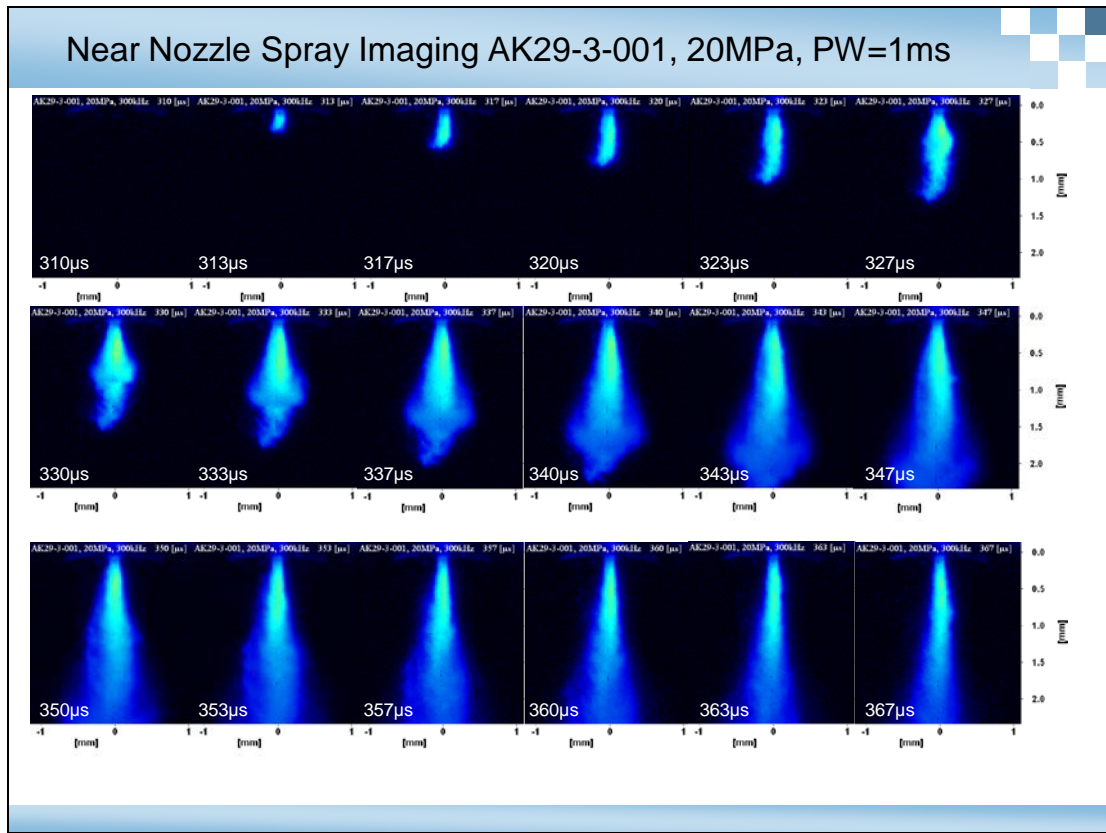


18

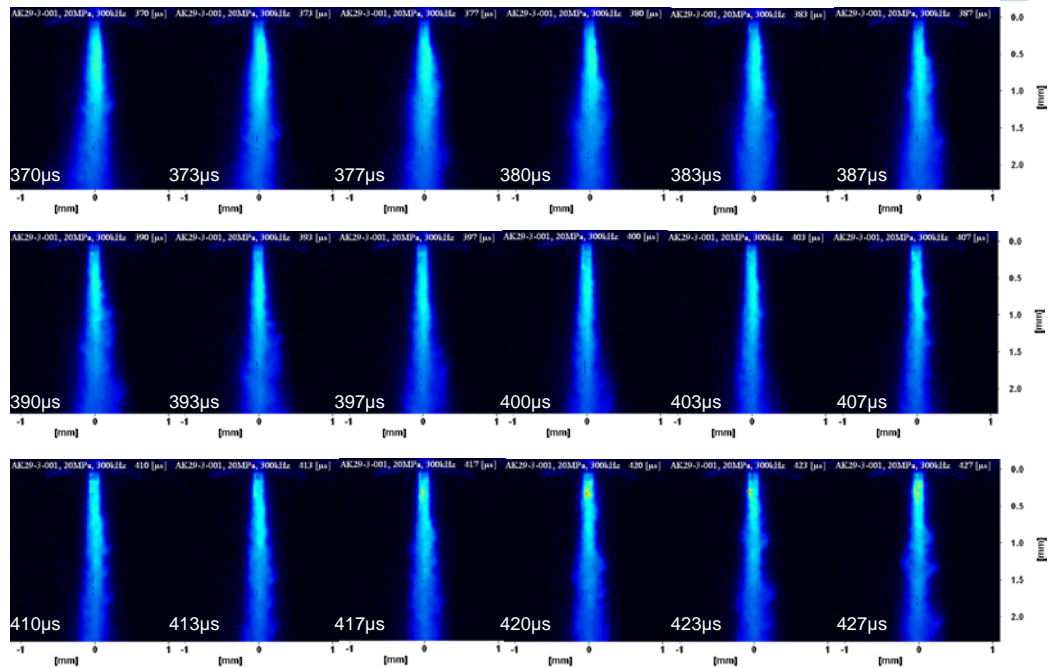
APPENDIX H MIE SCATTER IMAGES, BOTTOM VIEW

High speed Mie Imaging of near-field injector spray from side view, Luxembourg Spray lab

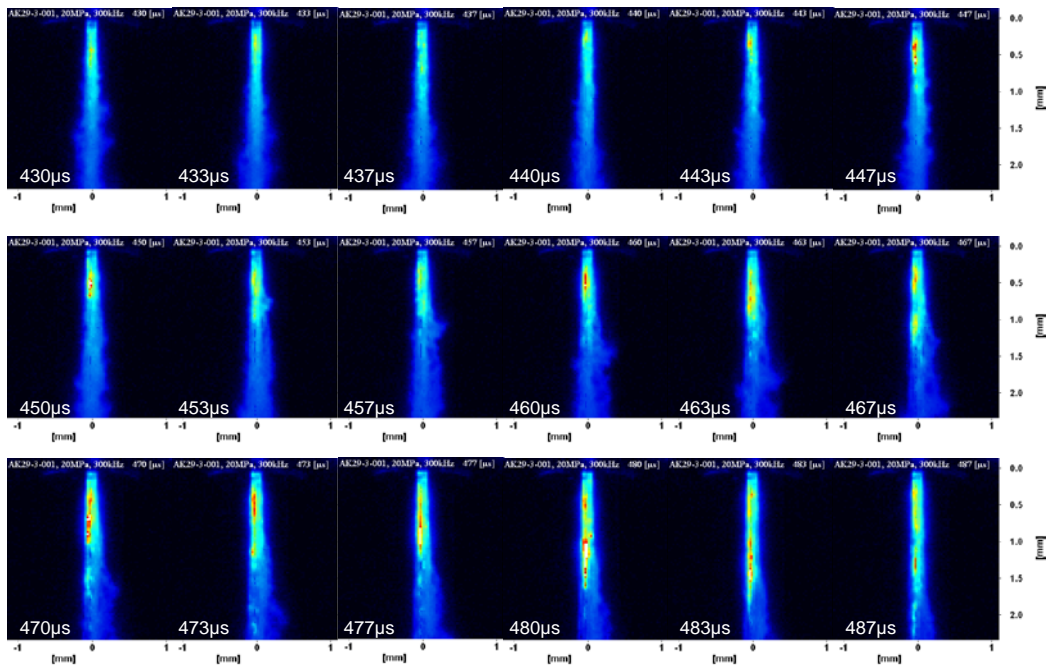
Image #	Seat #	d (mm)	β	l/d	(l+L)/d	D/d	Inj. Pres.	Pulse Width	Mie Scatter Time Images (μ s)
1-18	AK29-3-001	≈ 20	0°	1.1	na	na	20MPa	1 ms	310,313,317,320,323,327,330,333,337,340,343,347,350,353,357,360,363,367
19-26	AK29-3-001	≈ 20	0°	1.1	na	na	20MPa	1 ms	370,373,377,380,383,387,390,393,397,400,403,407,410,413,417,420,423,427
27-44	AK29-3-001	≈ 20	0°	1.1	na	na	20MPa	1 ms	430,433,437,440,443,447,450,453,457,460,463,467,470,473,477,480,483,487
45-62	AK29-3-001	≈ 20	0°	1.1	na	na	20MPa	1 ms	1300,1310,1320,1330,1340,1350,1360,1370,1380,1390,1400,1410,1420,1430,1440,1450,1460,1470
63-90	AK29-3-001	≈ 20	0°	1.1	na	na	20MPa	1 ms	1480,1490,1500,1510,1520,1530,1540,1550,1560,1570,1580,1590,1600,1610,1620,1630,1640,1650



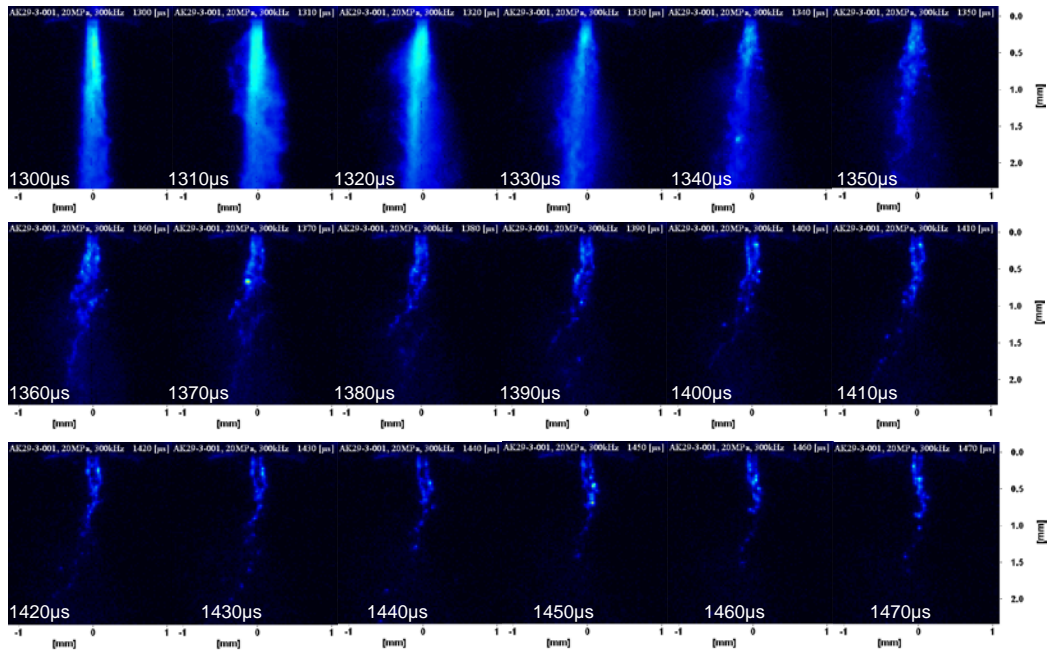
Near Nozzle Spray Imaging AK29-3-001, 20MPa, PW=1ms



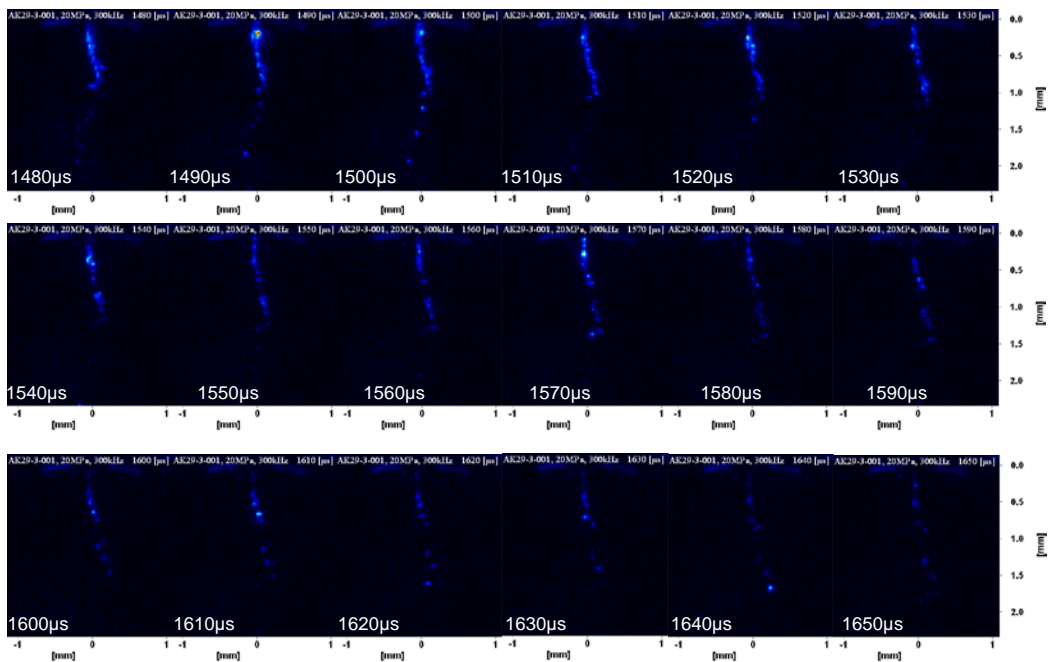
Near Nozzle Spray Imaging AK29-3-001, 20MPa, PW=1ms



Near Nozzle Spray Imaging AK29-3-001, 20MPa, PW=1ms Closing Behavior



Near Nozzle Spray Imaging AK29-3-001, 20MPa, PW=1ms Closing Behavior

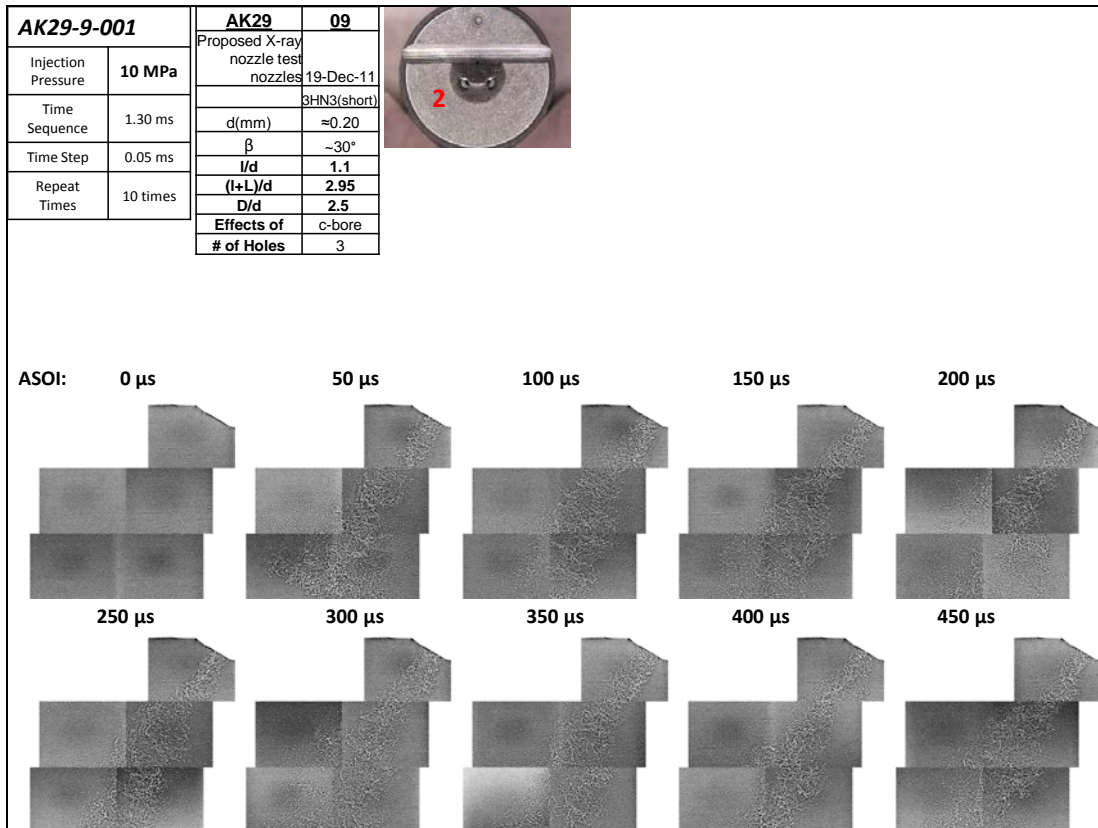
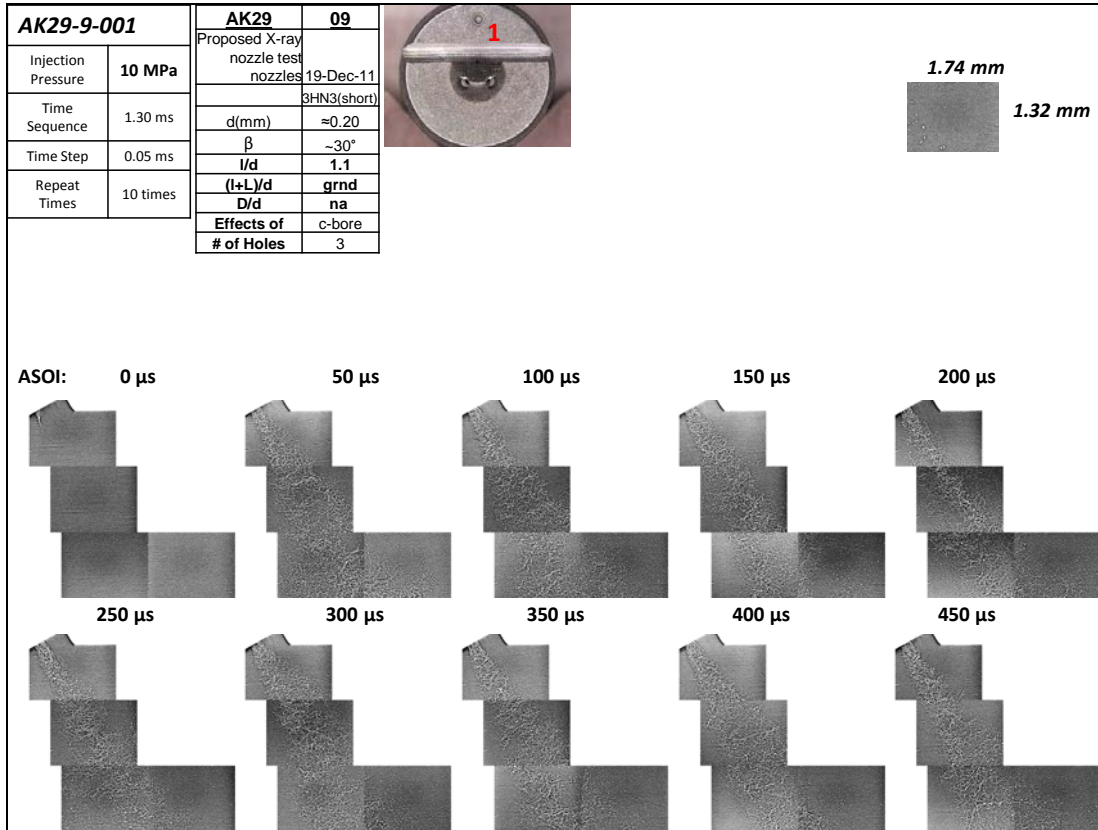


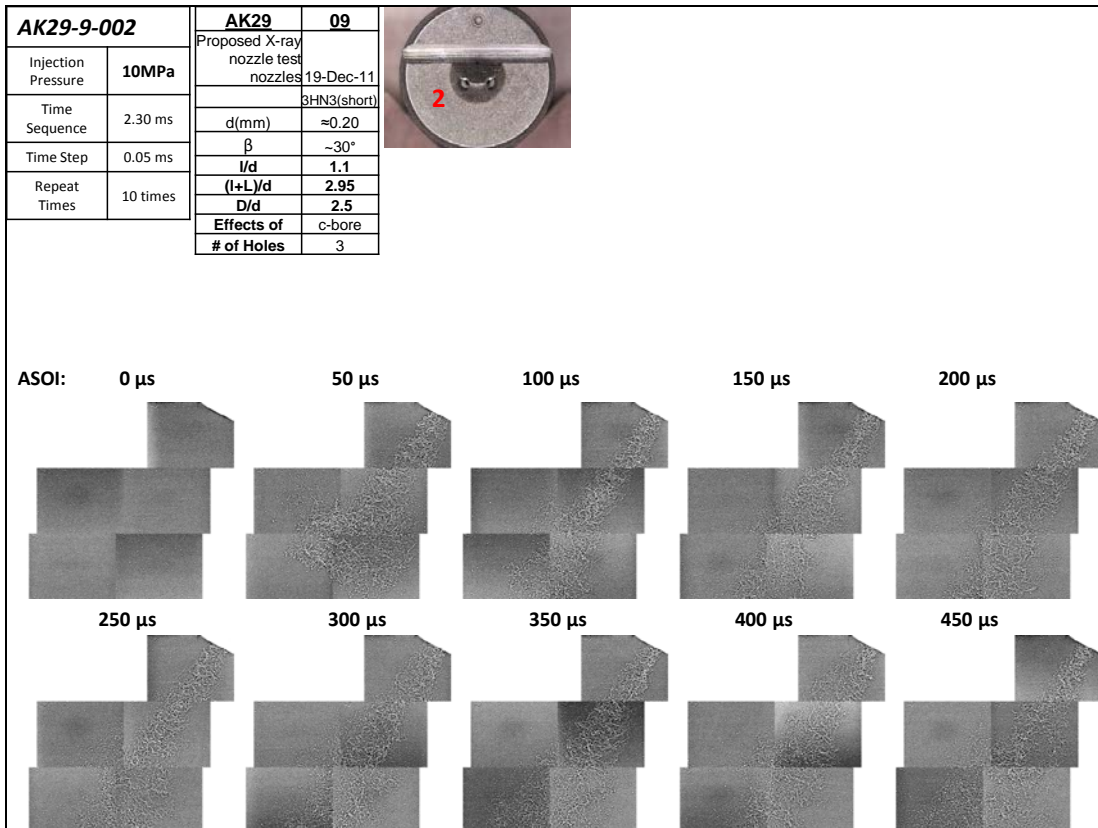
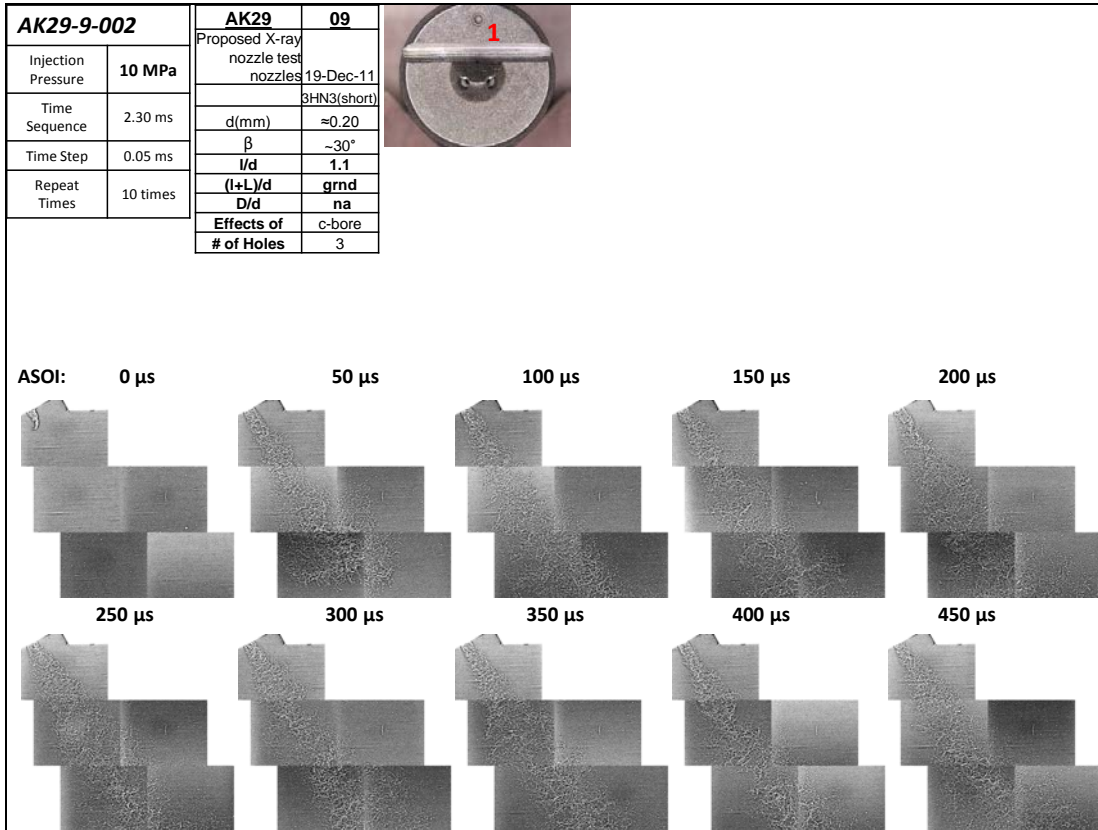
APPENDIX I PHASE-CONTRAST X-RAY IMAGES

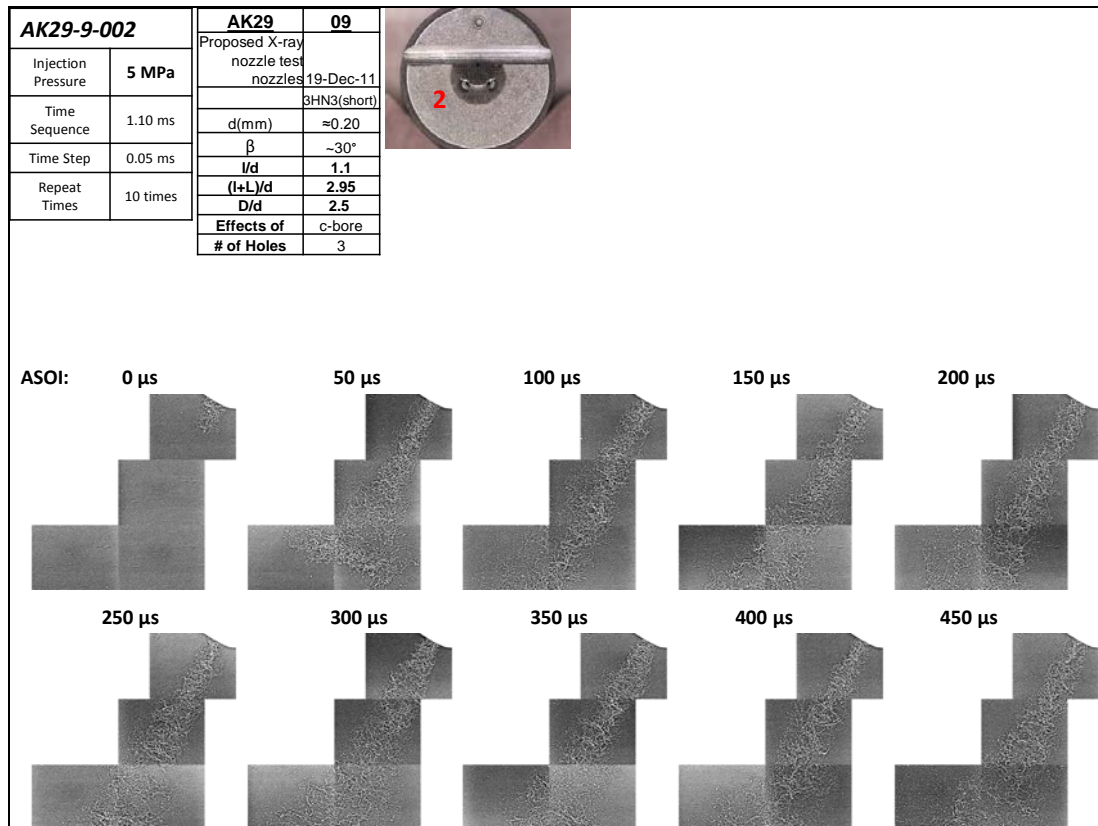
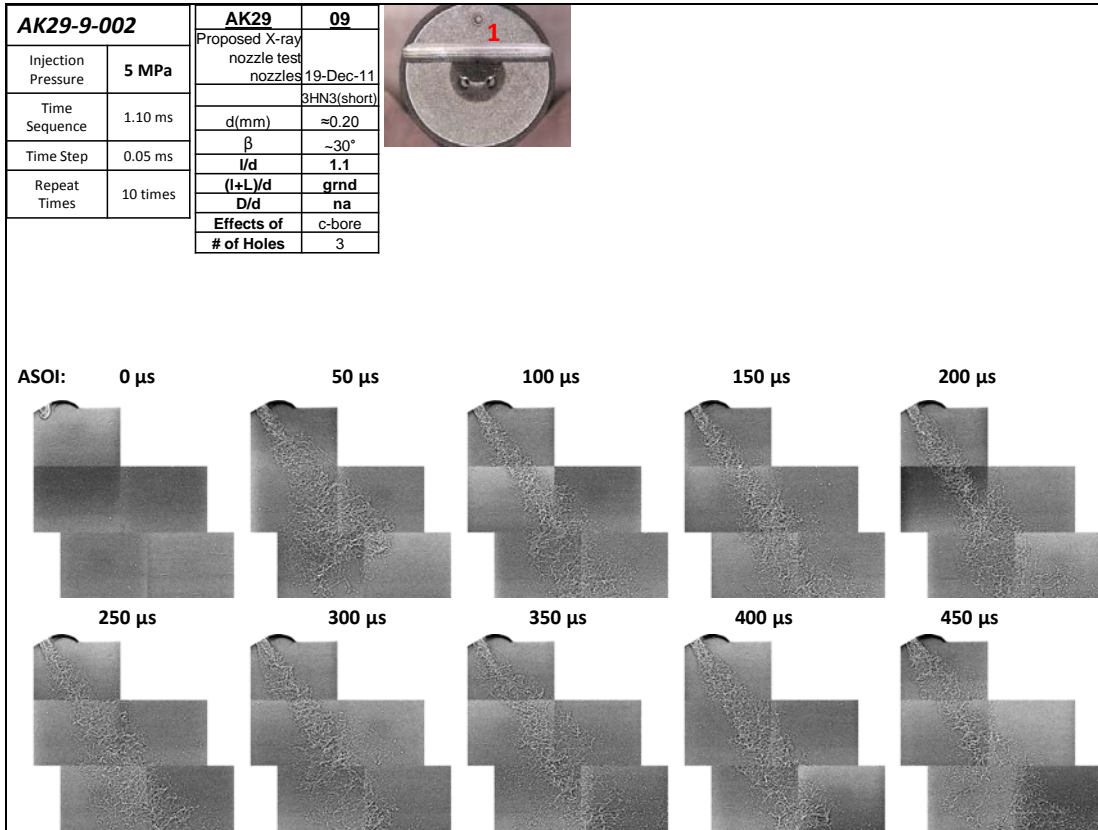
Phase Contrast X-ray image mosaics (100 mosaics) from Argonne testing 3-hole injectors

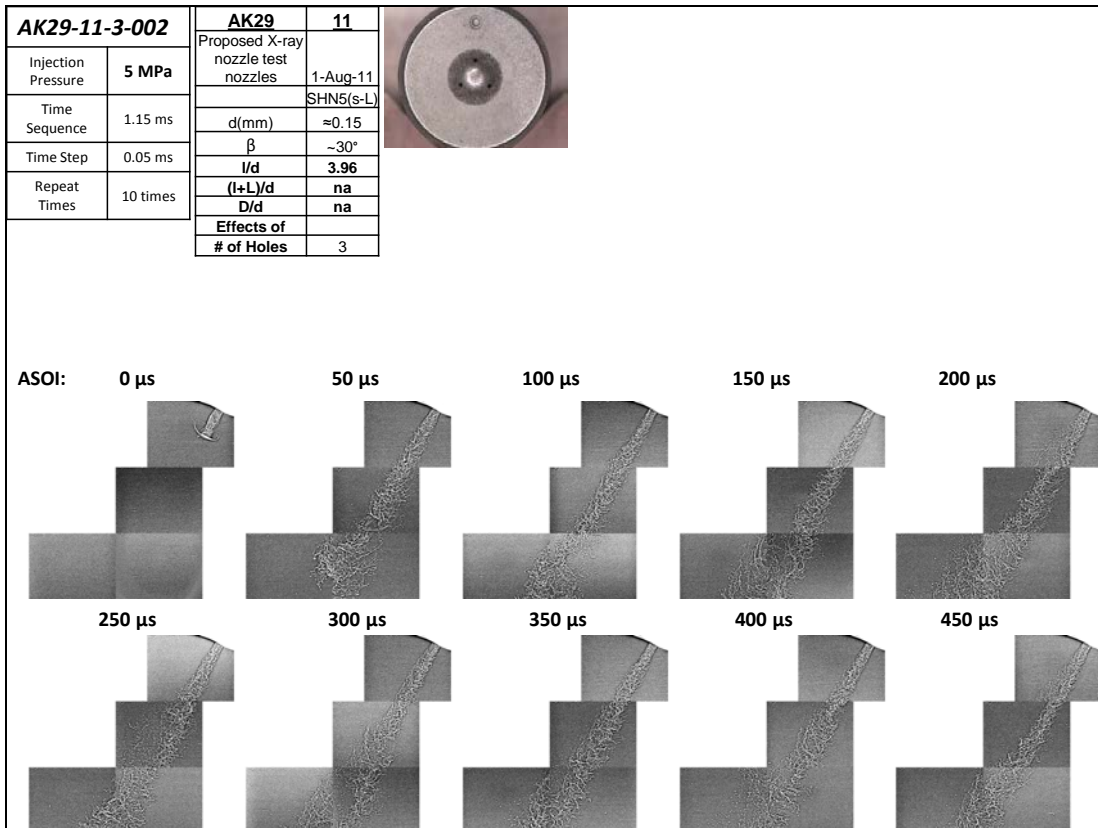
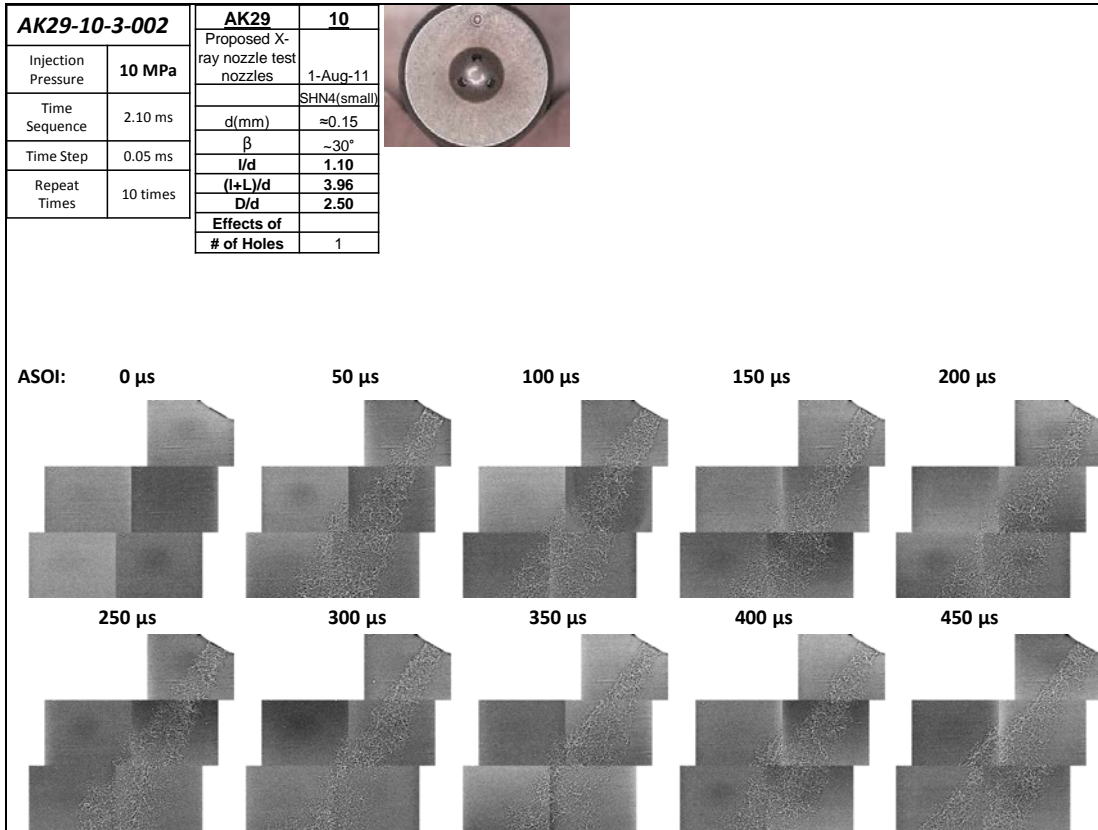
Each image is comprised of a mosaic of 4-5 image captures selected for spatial and temporal coherence to represent spray

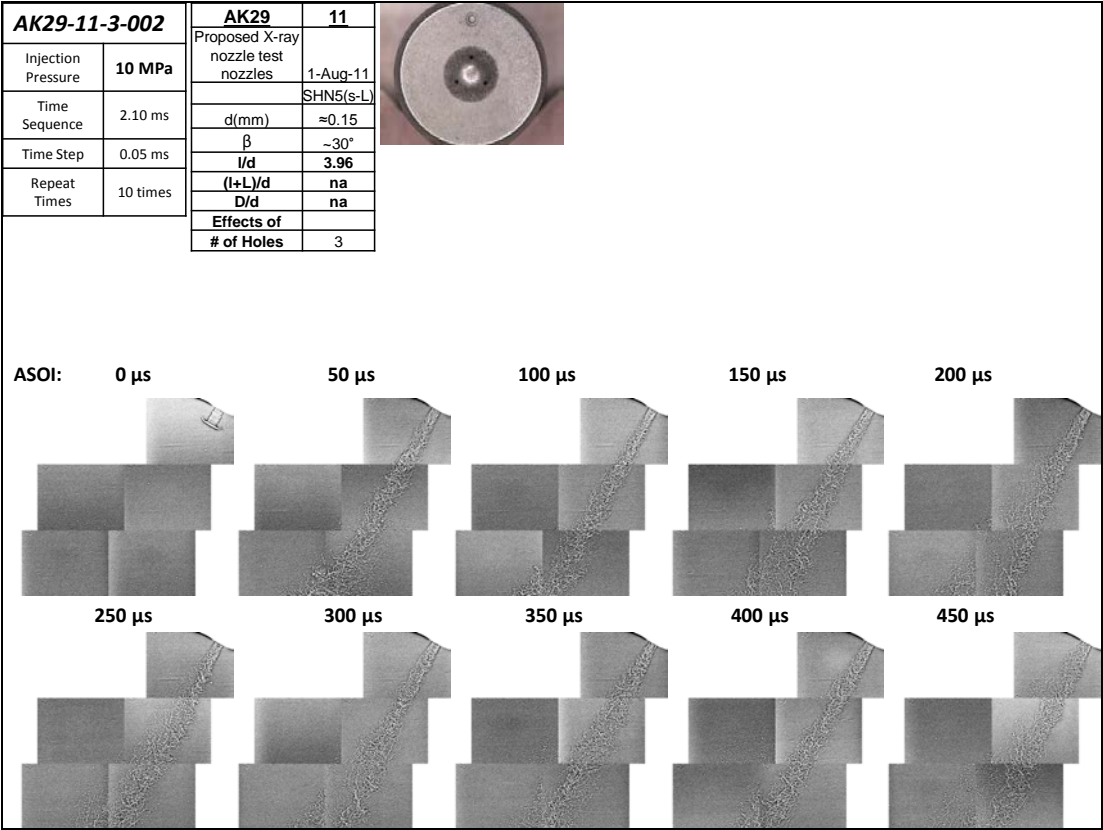
Mosaic #	Seat #	Hole #	d (mm)	β	l/d	(l+L)/d	D/d	Inj. Pres.	View Angle	X-ray Time Images (μ s)
1-10	AK29-9-001	1	$\approx .20$	30°	1.1	na	na	10MPa	0°	0,50,100,150,200, 250,300,350,400, 450
1-10	AK29-9-001	2	$\approx .20$	30°	1.1	2.95	2.5	10MPa	0°	0,50,100,150,200, 250,300,350,400, 450
1-10	AK29-9-002	1	$\approx .20$	30°	1.1	na	na	10MPa	0°	0,50,100,150,200, 250,300,350,400, 450
1-10	AK29-9-002	2	$\approx .20$	30°	1.1	2.95	2.5	10MPa	0°	0,50,100,150,200, 250,300,350,400, 450
1-10	AK29-9-002	1	$\approx .20$	30°	1.1	na	na	5MPa	0°	0,50,100,150,200, 250,300,350,400, 450
1-10	AK29-9-002	2	$\approx .20$	30°	1.1	2.95	2.5	5MPa	0°	0,50,100,150,200, 250,300,350,400, 450
1-10	AK29-10-3-002		$\approx .15$	30°	1.1	3.96	2.5	5MPa	0°	0,50,100,150,200, 250,300,350,400, 450
1-10	AK29-10-3-002		$\approx .15$	30°	1.1	3.96	2.5	10MPa	0°	0,50,100,150,200, 250,300,350,400, 450
1-10	AK29-11-3-002		$\approx .15$	30°	3.96	na	na	5MPa	0°	0,50,100,150,200, 250,300,350,400, 450
1-10	AK29-11-3-002		$\approx .15$	30°	3.96	na	na	10MPa	0°	0,50,100,150,200, 250,300,350,400, 450











REFERENCES

- [1] Yi, J., Wooldridge, S., Coulson, G., Hilditch, J. et al., "Development and Optimization of the Ford 3.5L V6 EcoBoost Combustion System," *SAE Int. J. Engines* 2, pp. 1388-1407, 2009.
- [2] Kirwan, J., Shost, M., Roth, G., and Zizelman, J., "3-Cylinder Turbocharged Gasoline Direct Injection: A High Value Solution for Low CO₂ and NO_x Emissions," *SAE Int. J. Engines* 3(1), pp. 355-371, 2010.
- [3] Bakker, A., "Applied Computational Fluid Dynamics, Lecture 8 – Turbulence," 2006.
- [4] Reynolds, O., "On the dynamical theory of turbulent incompressible viscous fluids and the determination of the criterion," *Phil. Trans. Royal Soc. London A* v. 186, pp. 123-164, 1894.
- [5] Richardson, L., F., "Weather Prediction by Numerical Process," 1922.
- [6] Kolmogorov, A., "The local structure of turbulence in incompressible viscous fluid," *Dokl. Akad. Nauk., Vol. 30*, pp. 301-305, 1941.
- [7] Reitz, R., D., and Bracco F., V., "Mechanism of Atomization of a Liquid Jet," *Phys. Fluids*, 25, p. 1730 – 1742, 1982.
- [8] Reitz, R., D., "Modeling Atomization Processes in High-Pressure Vaporizing Sprays," *Atom. & Spray Tech.*, 3, pp. 309-337, 1987.
- [9] Lin, S., P. and Reitz, R., D., "Drop and Spray Formation from a Liquid Jet," *Annu. Rev. Fluid Mech.*, 30, pp. 85-105, 1998.
- [10] O'Rourke, P.J., and Amsden, A.A., "The TAB Method for Numerical Calculation of Spray Droplet Breakup," *SAE Technical Paper 872089*, 1987.

- [11] Smagorinsky, J., "General Circulation Experiments with the Primitive Equations," *Monthly Weather Review*, 91, 1963.
- [12] Deardorff, J., W., "A Numerical study of three-dimensional turbulent channel flow at large Reynolds numbers," *J. Fluid Mech.* 41, p. 453, 1970.
- [13] Bakker, A., "Applied Fluid Dynamics, Lecture 12 - LES," [Online].
- [14] Boussinesq, J., "Essai sur la Théorie des Eaux Courantes," *Mém. prés. par div.*, vol. 23, pp. 1-680, 1877.
- [15] Schmitt, F., G., "About Boussinesq's turbulent viscosity hypothesis: historical remarks and a direct evaluation of its validity," *Comptes Rendus Mécanique*, vol. 335, no. 9-10, pp. 617-627, 2007.
- [16] Prandtl, L., "Bericht über Untersuchungen zur ausgebildeten Turbulenz," *Zs. angew. Math. Mech.* 5, pp. 136-139, 1925.
- [17] Wilcox, D., "Turbulence Modeling for CFD," DCW Industries, Inc, LA Canada, CA, 1993.
- [18] Sagaut, P., *Large Eddy Simulation for Incompressible Flows*, 3rd edition, Springer, 2005.
- [19] Leonard, A., "Energy cascade in large-eddy simulations of turbulent fluid flows," *Adv. in Geophys. A* 18, pp. 237-248, 1974.
- [20] Germano, M., "Turbulence : the filtering approach," *J. Fluid Mech.*, vol. 238, pp. 325-336, 1992.
- [21] Lilly, D., K., "A proposed modification of the Germano subgrid-scale closure method," *Physics of Fluids*, pp. 633-636, 1992.
- [22] Yoshizawa, A. and Horiuti, K., "A Statistically-Derived Subgrid-Scale Kinetic Energy Model for the Large Eddy Simulation of Turbulent Flows," *J. Phys. Soc. Japan*, 54 (8), pp.

2834-2839, 1985.

- [23] Weller, H.G., Tabor, G., Jasak, C., Fureby, C., "A tensorial approach to computational continuum mechanics using object-oriented techniques," *Journal of Computational Physics*, vol. 12, no. 6, pp. 56-74, 1998.
- [24] Arai, M., Shimizu, M. and Hiroyasu, H., "Break-up Length and Spray Angle of a High Speed Jet," *Proceedings of ICLASS '85, Paper IB/4*, July 1985.
- [25] Soteriou, C., E. and Andrews, R., J., "Cavitation Hydraulic Flip and Atomization in Direct Injection Diesel Sprays," *Proceedings of IMechE, Paper C465/051/93*, 1993.
- [26] Chaves, H., Knapp, M., Kubitzek, A., Obermeier, F., et. al., "Experimental Study of Cavitation in the Nozzle Hole of Diesel Injectors Using Transparent Nozzles," *SAE Technical Paper 950290*, 1995.
- [27] Lai, M., Wang, T., Xie, X., Han, J. et al., "Microscopic Characterization of Diesel Sprays at VCO Nozzle Exit," *SAE Technical Paper 982542*, 1998.
- [28] Wu, P., K., Miranda, R., F., and Faeth, G., M., "Effects of Initial Flow Conditions on Primary Breakup of Non Turbulent and Turbulent Round Liquid Jets," *Atomiz. Sprays*, 1995.
- [29] Andriotis A., Gavaises, M., and Arcoumanis, C., "Vortex Flow and Cavitation in Diesel Injector Nozzles," *J. Fluid Mechanics*, 610 (1), pp. 195-215, 2008.
- [30] Andriotis A. and Gavaises, M., "Influence of Vortex flow and Cavitation on Near-Nozzle Diesel Spray Dispersion Angle," *Atomiz. Sprays*, 19(3), 2009.
- [31] Lai, M.C., Zheng, Y., Xie, X., Moon, S. et. al., "Characterization of the Near-Field Spray and Internal Flow of Single-Hole and Multi-Hole Sac Nozzles Using Phase Contrast X-ray

- Imaging and CFD," *SAE Int. J. Engines* 4(1), pp. 703-719, 2011.
- [32] Das, S., Chang, S., and Kirwan, J., "Spray Pattern Recognition for Multi-Hole Gasoline Direct Injectors Using CFD Modeling," *SAE Technical Paper 2009-01-1488*, 2009.
- [33] Befrui, B., Corbinelli, G., D'Onofrio, M., and Varble, D., "GDI Multi-Hole Injector Internal Flow and Spray Analysis," *SAE Technical Paper 2011-01-1211*, 2011.
- [34] Lai, M., Zheng, Y., Shost, M., Xie, X. et al, "Characterization of Internal Flow and Spray of Multihole DI gasoline Spray using X-ray Imaging and CFD," *SAE Technical Paper 2011-01-1881*, 2011.
- [35] Albina, F.O., Muzaferija, S., Peric, M., "Numerical Simulation of Jet Instabilities," *Proceedings of ILASS-Europe 2000, Darmstadt (Germany), Sep. 2000*, 2000.
- [36] Klein, M. and Janika, J., "Large-eddy Simulation of the primary Breakup of a Spatially Developing Liquid Film," *Proceedings of International Conference on Atomization and Sprays (ICLASS), Sorrento (Italy), July 2003*, 2003.
- [37] Klein, M., "Direct Numerical Simulation of a Spatially Developing Water Sheet at Moderate Reynolds Number," *Int. J. Heat Fluid Flow*, 26, pp. 722-731, 2005.
- [38] Sander, W. and Weigand, B., *Direct Numerical Simulation of Primary Breakup Phenomena in liquid Sheets in Science and Engineering*, Springer, 2007, p. 223 – 236.
- [39] Sander, W. and Weigand, B., "Direct numerical simulation and analysis of instability enhancing parameters in liquid sheets at moderate Reynolds numbers," *Phys. Fluids* 20, 2008.
- [40] Befrui, B., Corbinelli, G., Robart, D., Reckers, W., et. al., "LES Simulation of the Internal Flow and Near-Field Spray Structure of an Outward-Opening GDi Injector and Comparison

- with Imaging Data," *SAE Technical Paper 2008-01-0137*, 2008.
- [41] Corbinelli, G., Befrui, B., and Reckers, W., "Large Eddy Simulation and Optical Studies of the Primary Break-up of a Thin Planar-Sheet Liquid Jet," *SAE Int. J. Fuels Lubr.* 3(1), pp. 266-276, 2010.
- [42] Hung, D., Harrington, D., Gandhi, A., Markle, L., et. al., "Gasoline Fuel Injector Spray Measurement and Characterization - A New SAE J2715 Recommended Practice," *SAE Int. J. Fuels Lubr.* 1(1), pp. 534-548, 2009.
- [43] Rivera, E., Mastro, N., Zizelman, J., Kirwan, J. et. al., "Development of Injector for the Direct Injection Homogeneous Market using Design for Six Sigma," *SAE Technical Paper 2010-01-0594*, 2010.
- [44] Malvern Instruments, "www.Malvern.com," 15 9 2014. [Online]. Available: www.malvern.com. [Accessed 15 9 2014].
- [45] de Villiers, E., Gosman, A., and Weller, H., "Large Eddy Simulation of Primary Diesel Atomization," *SAE Technical Paper 2004-01-0100*, 2004.
- [46] de Villiers, E., *The Potential of Large Eddy Simulation for the Modeling of Wall Bounded Flows PhD Thesis*, London: Imperial College of Science, Technology and Medicine, 2006.
- [47] Brackbill, J. U., Kothe, D. B., Zemach, C., "A Continuum Method for Modelling surface Tension," *J. Comp. Phys.*, 100, pp. 335-354, 1992.
- [48] Ubbink, O., *Numerical Prediction of Two Fluid Systems with Sharp Interfaces*, University of London, 1997.
- [49] Weller, H., *A New Approach to VOF-based Interface Capturing Methods for Incompressible and Compressible Flows*, 2008.

- [50] Gomma, H., Kumar, S., Huber, C., Weigand, B. and Peters, B., "Numerical Comparison of 3D Jet Breakup Using a Compression Scheme and an Interface Reconstruction Based VOF," in *Proceedings ILASS – Europe 2011, 24th European Conference on Liquid Atomization and Spray Systems*, Estoril, Portugal, 2011.
- [51] Jasak, H., Weller, H., G., Gosman, A., D., "High Resolution NVD Differencing Scheme for Arbitrary Unstructure Meshes," *Int. J. Numer. Math Fluids*, vol. 31, pp. 431-449, 1999.
- [52] Jeong, J. and Hussain, F., "On the identification of a vortex," *J. Fluid Mechanics*, vol. 285, pp. 69-94, 1995.
- [53] Hunt, J., C., R., Wray, A., A. and Moin, P., "Eddies, Stream and Convergence Zones in Turbulent Flows," *Center for Turbulence Research Report S88, 193*, p. 193, 1998.
- [54] "OpenCFD Ltd., OpenFOAM – User Guide,," 2010. [Online]. Available: <http://www.opencfd.com>.
- [55] Issa, R.I., "Solution of the Implicitly Discretized Fluid Flow Equations by Operator Splitting," *J. Comp. Phys.* 62, pp. 40-65, 1986.
- [56] Befrui, B., Corbinelli, G., Spiekermann, P., Shost, M., Lai, M-C., et. al., "Large Eddy Simulation of GDI Single-Hole Flow and Near-Field Spray," *SAE Int. J. Fuels Lubr.* 5(2), pp. 620-636, 2012.
- [57] Payri, R., Salvador, F. J., Gimeno, J., Zapata, L. D., "Diesel Nozzle Geometry Influence on Spray Liquid Phase Fuel Penetration in Evaporative Conditions," *J. Fuel*, 87 (7), pp. 1165 - 1176, 2008.
- [58] Kong, J. and Bae, C., "Effect of Tapered Nozzle Hole on Spray Characteristics of High Pressure Diesel Injection," in *11th International Annual Conference on Liquid Atomization*

and Spray Systems, Vail, Colorado, 2009.

- [59] Som, S., Ramirez, A.I., Longman, D. E., Aggarwal, S.K., "Effect of Nozzle Orifice Geometry on Spray, Combustion and Emission Characteristics under Diesel Engine Conditions," *J Fuel*, 90, pp. 1267-1276, 2011.
- [60] Befrui, B., Aye, A., Spiekermann, P., Varble, D. Shost, M., Lai, M-C., et. al., "GDI Skew-Angled Nozzle Flow and Near-Field Spray," *SAE Technical Paper 2013-01-0255*, 2013.
- [61] Shi, J., M., Wenzlawski, K., Helie, J., Nuglisch, H., Cousin, J., "URANS & SAS analysis of flow dynamics in a GDI nozzle," in *ILASS- Europe 23rd Annual Conference on Liquid Atomization and Spray Systems*, Brno (Czech Republic), 2010.
- [62] Pitcher, G., Wigley, G., "The Droplet Dynamics of Diesel Fuel Sprays under Ambient and Engine Conditions," *ASME*, vol. 2, pp. 571-586, 1991.
- [63] Xie, X., Lai, M.-C., Moon, S., Liu, Z., Gao, J., Dufresne, E., Fezza, K., Wang, J., "Ultrafast X-ray Phase-Contrast Imaging of High-Speed Fuel Sprays from a Two-Hole Diesel Nozzle," in *ILASS Americas 22nd Annual Conference on Liquid Atomization and Spray Systems*, Cincinnati, OH, 2010.
- [64] Gao, J., Reitz, R., D., Ghandhi, J., B., Wang, J., Liu, Z., P., "A Study of the Primary Breakup Process and Macroscale Characteristics of Impinging Diesel Spray Nozzles," in *ICLASS 11th Triennial International Annual Conference on Liquid Atomization and Spray Systems*, Vail CO, 2009.
- [65] Gao, J., Liu, Z., Moon, S., Xie, X., Dufresne, E., et. al., "Morphology of Diesel sprays from single-Orifice Micronozzles," in *ILASS Americas 22nd Annual Conference on Liquid Atomization and Spray Systems*, Cincinnati, OH, 2010.

- [66] Mitroglou, N., *Multi-Hole Injectors for Direct Injection gasoline Engines, PhD Thesis*, London, UK: The City University of London, 2006.
- [67] Papoulias, D., Giannadakis, E., Mitroglou, N., Gavaises, M., et. al., "Cavitation in Fuel Injection Systems for Spray-Guided Direct Injection Gasoline Engines," *SAE Technical Paper 2007-01-1418*, 2007.
- [68] Shost, M., Lai, M., Befrui, B., Spiekermann, P., et. al., "GDi Nozzle Parameter Studies Using LES and Spray Imaging Methods," *SAE Technical Paper 2014-01-1434*, 2014.
- [69] Befrui, B., Spiekermann, P., Shost, M., Lai, M., -C., "VoF-LES Studies of GDi Multi-Hole Nozzle Plume Primary Breakup and Comparison with Imaging Data," in *ILASS-Europe 25th European Conference on Liquid Atomization and Spray Systems*, chania, Greece, 2013.
- [70] Befrui, B. and D'Onofrio, M., "Primary Atomization of a GDi Multi-Hole Plume Using VOF-LES Method," *SAE Technical Paper 2014-01-1125*, 2014.

ABSTRACT**EVALUATION OF NOZZLE GEOMETRY ON HIGH PRESSURE
GASOLINE DIRECT INJECTION SPRAY ATOMIZATION**

by

MARK ANTHONY SHOST**December 2014****Advisor:** Professor Ming-Chai Lai**Major:** Mechanical Engineering**Degree:** Doctor of Philosophy

This research presents a critical study of injector nozzle geometry on high-pressure Gasoline Direct Injection, GDi, injector spray morphology. The study was conducted with the aid of multi-fluid Volume-of-Fluid, Large-Eddy-Simulation, VOF-LES, method. Alternative nozzle geometries, that are the subject of current interest including varying nozzle hole length to diameter ratio, counterbore presence and nozzle-hole skew-angle geometry, are studied in detail in order to provide insight into their specific influence on spray plume targeting and jet primary breakup characteristics. A comparison of the simulation results with near-field shadowgraph and Mie scatter imaging as well as phase-contrast X-ray imaging is provided. When near-field experimental imaging validated the simulation results further investigation of the fundamental flow mechanism internal to the injector was studied using VOF-LES to gain insight to the cause of spray morphology changes within the injector valve group. The complementary analysis of Computational Fluid Dynamics method and empirical data supported definitive conclusions on nozzle design parameter effects for l/d , skew angle, counterbore for varying injection pressure as well as provided an understanding of the underlying physical mechanisms involved to engender the resulting spray plume characteristics.

AUTOBIOGRAPHICAL STATEMENT

Mark A. Shost, currently Director of Powertrain Application Engineering at Chrysler, responsible for Powertrain Engine and Transmission calibration, On-Board-Diagnostic calibration, CARB certification, corporate criteria emissions planning and exhaust aftertreatment specification.

2012-2013, Vice President of Powertrain Engineering at Tula, Led engineering activities to create and integrate real-time cylinder-event-based powertrain controls with advanced signal processing, resulting in a unique, digital engine that achieves the best possible fuel efficiency over the engine's speed and load operating conditions.

2009-2012, Product Line Executive and European Regional Director residing in Luxembourg for Gasoline Engine Management Systems for Delphi Powertrain, this General Management position was P&L responsible for air & fuel systems, electronic controllers and full gasoline ems. The product portfolio generates \$800M in revenue supported by 1,200 salaried and 2,500 hourly employees worldwide. Global responsibilities included board member for Korean Joint Venture.

1985-2009, Joined GM and held engineering positions of increasing responsibility to Director for engine management systems portfolio generating \$3B in revenue. Established integrated technology plans including; operating budgets, and capital spending, balancing business growth and cost. Direct reports included 12 product-line chief engineers in seven global technical centers leading an organization of 3,100 employees. Led Mexico Technical Center growth to 2,500 engineers and held various chief engineer roles. R&D leadership for product development and innovation utilizing; robust engineering, Extensive background in manufacturing, program management, and product launch, as well as quality improvement and cost reduction initiatives using Six Sigma DFSS, Shainin Red X & Green Y, and Value Engineering tools.

Inventor on 16 United States Patents

5,033,327 5,090,364 5,129,373 5,588,404 6,392,406 6,463,951 6,467,495 6,595,485
6,766,819 6,788,054 6,830,232 6,851,306 6,889,546 7,279,133 7,800,379 8,464,690

The Pennsylvania State University

BSME, Engineering, 1981–1985

- Activities and Societies: Tau Beta Pi - The Engineering Honor Society, Pi Tau Sigma
- Treasurer - Mechanical Engineering Honor Society

University of Rochester - William E. Simon Graduate School of Business Administration

MBA, Business Administration, 1990–1992

- Attended under General Motors Fellowship
- Activities and Societies: Beta Gamma Sigma - The International Honor Society
- Recognizing Business Excellence

Wayne State University

MSME, Mechanical Engineering, 2006-2009

- 2009–2014 Achieved Doctoral Candidacy Status towards Ph.D. in Mechanical Engineering, dissertation study of GDi injector spray, completion planned in 2014